

Sheffield Hallam University

Vibrational spectroscopy to monitor controlled drug release from hydrophilic matrices

ZAHOOR, Farah Deeba

Available from the Sheffield Hallam University Research Archive (SHURA) at:

<http://shura.shu.ac.uk/30215/>

A Sheffield Hallam University thesis

This thesis is protected by copyright which belongs to the author.

The content must not be changed in any way or sold commercially in any format or medium without the formal permission of the author.

When referring to this work, full bibliographic details including the author, title, awarding institution and date of the thesis must be given.

Please visit <http://shura.shu.ac.uk/30215/> and <http://shura.shu.ac.uk/information.html> for further details about copyright and re-use permissions.

**Vibrational Spectroscopy to Monitor Controlled Drug Release from
Hydrophilic Matrices**

Farah Deeba Zahoor

A thesis submitted in partial fulfilment of the requirements of
Sheffield Hallam University
for the degree of Doctor of Philosophy

November 2021

Declaration

I hereby declare that:

1. I have not been enrolled for another award of the University, or other academic or professional organisation, whilst undertaking my research degree.
2. None of the material contained in the thesis has been used in any other submission for an academic award.
3. I am aware of and understand the University's policy on plagiarism and certify that this thesis is my own work. The use of all published or other sources of material consulted have been properly and fully acknowledged.
4. The work undertaken towards the thesis has been conducted in accordance with the SHU Principles of Integrity in Research and the SHU Research Ethics Policy.
5. The word count of the thesis is 46081

Name	<i>Farah Deeba Zahoor</i>
Date	<i>November 2021</i>
Award	<i>PhD</i>
Faculty	<i>College of Business, Technology and Engineering</i>
Director(s) of Studies	<i>Professor Chris Sammon</i>

Abstract

Approximately 40% of drugs currently marketed and 90% of all drugs under development show poor and varied aqueous solubility at the different pH values encountered along the gastrointestinal tract. The pH-dependent release profile exhibited by these drugs often leads to poor bioavailability and ultimately means that many do not make it to licence. To mitigate against this and to inform future drug development, it is important to understand the dissolution behaviour of these types of drugs at a molecular level.

This thesis explores the use of ATR-FTIR imaging to gain an insight into the within-tablet dynamics of a sparingly soluble, weakly basic drug that has been incorporated into a hydrophilic matrix. This approach provides a chemical insight into the nature of drug, polymer matrix, excipients and water in a formulation undergoing dynamic changes including ionisation, dissolution, hydration, swelling and particle dislocation. Specifically, this work uses tablets manufactured using an HPMC polymer matrix incorporating 20% w/w itraconazole as the model drug which has a pK_a of 3.7 and is practically insoluble at pH 7, both with and without the addition of the organic acid modifiers (citric acid, betaine HCl, cysteine HCl and glycine HCl) to control the local pH.

In placebo HPMC tablets, ATR-FTIR imaging, supplemented by optical imaging, showed that hydration and swelling was independent of the pH of the media. However, when the ionic strength of the hydrating medium was adjusted, rapid formation of the gel layer was observed at low ionic strength, while increased ionic strength was shown to interfere with HPMC hydration, resulting in the suppression of the expansion of the gel layer.

Hydration and dissolution studies conducted on HPMC tablets loaded with 20% w/w IT were limited to the use of low ionic strength media only. From the dissolution studies, the release of IT from these tablets was shown to be significantly greater at pH 1.5 when compared with that at pH 7. Optical measurements showed that the swelling of 20% w/w IT loaded HPMC tablets was greater at pH 1.5 over the period of the hydration in comparison to the pH 7 environment. ATR-FTIR imaging data revealed that at pH 1.5 the IT was ionised, becoming soluble and there was evidence of IT particle translocation into the diffusion front and eventually out into the surrounding medium. However, at pH 7, the IT remained in the free base form, largely within the tablet core and the swelling front, with less evidence of IT particle translocation. From both the optical measurements and ATR-FTIR imaging studies, it was shown that the swelling capacity of the gel layer in IT loaded tablets was reduced at pH 7 in comparison to pH 1.5 indicating that the poor solubility of IT retarded hydration.

Exploring the impact of organic pH modifiers on the release of IT from the HPMC matrix at a 10% w/w and 30% w/w loading, enhanced dissolution at pH 7 of the IT was observed in comparison to tablets without any modifier. From both the optical imaging and ATR-FTIR imaging data, the gel layer expansion was shown to be greater at higher pH modifier loading for all systems. However, the magnitude of swelling differed between the modifier systems over the hydration period and a greater amount of swelling was observed with the betaine HCl and citric acid in comparison to the cysteine HCl and glycine HCl. The results indicated that, of the organic acid modifiers selected, tablets containing cysteine HCl provided the greatest enhancement of release of IT. These findings were consistent with the ATR-FTIR imaging results, where the greatest reduction in the intensity of the spectral band assigned to the free base form of IT, was also observed in tablets containing the cysteine HCl modifier.

Acknowledgements

I gratefully acknowledge Sheffield Hallam University for funding my PhD and Bristol Myers-Squibb (BMS) for their invaluable expertise and for providing me with the materials to undertake my experimental work.

I would like to thank my supervisory team, Professor Chris Sammon and Dr Kerstin Mader at Sheffield Hallam, Dr Jon Brown at BMS and Professor Pete Timmins at the University of Huddersfield. Special thanks must go to Chris Sammon and Pete Timmins for their invaluable support and encouragement and enthusiasm throughout the project.

Other staff in MERI to whom I am indebted include: Paul Allender and Gary Robinson for their technical assistance and the amazing engineering expertise they provided throughout my studies; Matt Kitchen and Dr Francis Clegg for their support and help in ways too numerous to mention; Dr Nataalka Johnson for providing me with advice and technical assistance and Laura McLaughlin for helping me to optimise my photography set-up.

I am eternally grateful to my family for all their support: my sisters Sarah and Yasmin (I promise we'll make time for more shopping trips now!); my parents and my brother who are not here to share this moment with me but who steered me in the right direction and guided me and in particular my Pie for continually pushing, nagging, cajoling and encouraging me throughout my PhD. It's no exaggeration to say that without his support it would not have been possible for me to get to this stage and as such I would like to dedicate this thesis to him.

Finally, I could not write these acknowledgements without giving thanks to Allah who has blessed me with so much in life and who decreed for me the opportunity to complete this work, Alhamdulillah.

Table of Contents

Declaration	ii
Abstract	iii
Acknowledgement	iv
Table of Contents	v
List of Figures	xi
List of Equations	xxii
List of Tables	xxv
List of Abbreviations	xxvii
1.0 Introduction	1
1.1 Project Rationale	1
1.2 Aims and Objectives	1
1.3 References	3
2.0 Literature Review	4
2.1 Drug Release	4
2.1.1 The Biopharmaceutics Classification System (BCS)	4
2.1.2 The Importance of Acidity and pKa values in Drug Dissolution	5
2.1.3 Poorly-Soluble Drugs	7
2.1.3.1 Strategies for Improving Bioavailability of Poorly-Soluble Drugs	9
2.2 Solid Oral Dosage Forms	14
2.2.1 Types of Drug Release Mechanism from Solid Oral Dosage Forms	14
2.2.2 Methods to Monitor Drug Release	16
2.3 Hydrophilic Matrices and HPMC	21
2.3.1 Structure and Chemistry of HPMC	22
2.3.2 Drug Release from Hydrophilic Matrices	25
2.3.3 HPMC as a Model Hydrophilic Matrix	25
2.3.3.1 Effect of Polymer (HPMC) Concentration	29
2.3.3.2 Effect of Polymer (HPMC) Viscosity	30
2.3.3.3 Effect of Polymer (HPMC) Particle Size	30
2.3.4 Monitoring Swelling Behaviour of HPMC on Hydration	31
2.3.5 Quantification of Drug Release from Hydrophilic Matrices	34

2.4 Itraconazole-a Model Poorly-Soluble Drug	36
2.5 Conclusion	37
2.6 References	38
3.0 Experimental	48
3.1 Analytical Techniques	48
3.1.1 Infrared Spectroscopy	48
3.1.1.1 Electromagnetic Radiation	48
3.1.1.2 Absorbance and Transmittance Relationship and Beer Lambert Law	50
3.1.1.3 The IR Spectral Region and Molecular Spectroscopy	51
3.1.1.4 Practical Aspects of IR Spectroscopy	53
3.1.1.4.1 FTIR spectrometer	54
3.1.1.4.2 Detectors Used for FTIR	55
3.1.1.4.3 Optimisation of Spectral Acquisition	56
3.1.1.4.4 Transmission IR Spectroscopy	57
3.1.1.4.5 ATR-FTIR	58
3.1.1.4.6 Near-Infrared	61
3.1.1.4.7 ATR-FTIR Imaging	63
3.1.1.4.8 Micro-FTIR Imaging	65
3.2 Dissolution	68
3.3 Raman Spectroscopy	70
3.3.1 Principles of Raman Spectroscopy	70
3.3.2 Raman Microscopy	74
3.4 Data Processing Methods for Image Analysis	78
3.4.1 Univariate Data Analysis Approach	78
3.4.2 Multivariate Data Analysis Approach	80
3.4.3 Principal Components Analysis (PCA)	82
3.4.4 Partial least squares (PLS)	83
3.5 References	84
4.0 Preparation and Characterisation of Tablets and Their Constituents	91
4.1 Significance of Itraconazole Forms in Pharmaceutical Applications	93
4.2 Preparation of Different Forms of Itraconazole	96
4.2.1 Itraconazole Monohydrochloride	96
4.2.2 Itraconazole Dihydrochloride	96
4.2.3 Itraconazole Trihydrochloride	97

4.2.4 Amorphous Itraconazole	97
4.3 Characterisation of Constituent Materials	98
4.3.1 Determination of Itraconazole Structure Using X-Ray Powder Diffraction (XRPD)	98
4.3.2 Confirmation of Protonation of Itraconazole Structure by Nuclear Magnetic Resonance (NMR) Spectroscopy	98
4.3.3 ATR-FTIR Imaging of Reference Materials	98
4.3.4 SEM Morphological Analysis of Constituents	99
4.3.5 Particle Size Analysis of IT, HPMC and pH Modifier Powders	99
4.4 Preparation of 20% w/w Itraconazole Tablets and Formulations Containing pH Modifiers	100
4.4.1 Tablet Blending	100
4.4.2 Tablet Compaction	101
4.5 Characterisation of Tablets	102
4.5.1 Quantification of Loadings Using Near Infrared Spectroscopy (NIR)	102
4.5.2 Distribution of Constituents Within the Tablet Matrix Using Raman Microscopy	102
4.6 Results and Discussion	103
4.6.1 Analysis of Different Itraconazole Compounds	103
4.6.1.1 Formation of Amorphous Itraconazole Using Differential Scanning Calorimetry (DSC)	103
4.6.1.2 Confirmation of Amorphous and Crystalline Itraconazole Forms using XRPD	104
4.6.1.3 Confirmation of Protonated Itraconazole by Proton NMR	106
4.6.1.4 ATR-FTIR of the Different Forms of Itraconazole	107
4.6.2 ATR-FTIR Analysis of Reference Materials	110
4.6.3 Morphology and Particle Size Analysis of API, Polymer and pH Modifier	112
4.6.3.1 SEM Analysis to Determine Morphology	112
4.6.3.2 Particle Size Analysis	113
4.6.4 Content Uniformity of Itraconazole Loading and Heterogeneity of Tablets	114
4.6.4.1 Content Uniformity and Distribution of 20% w/w Itraconazole with 10% w/w and 30% w/w pH Modifier Tablets Using Near Infrared (NIR)	114

4.6.4.2 Content Uniformity and Distribution of Itraconazole and pH Modifier within the Tablets Using Raman Microscopy	130
4.6.4.3 Summary of Raman Distribution Data	153
4.7 Summary	156
4.8 References	157
5.0 Investigation of Within-Tablet Dynamics for Extended Release of Itraconazole from a HPMC Matrix Tablets Using ATR-FTIR Imaging	161
5.1 Introduction	161
5.2 Materials and Methods	162
5.2.1 Materials	162
5.2.2 Preparation and Characterisation of Tablets	162
5.2.3 Content Uniformity of Itraconazole Loading and Heterogeneity of Tablets	162
5.3 <i>In Vitro</i> Release Studies	163
5.4 Collection of ATR-FTIR Images	163
5.5 Hydration Experiments using ATR- FTIR Imaging	163
5.6 Optical Imaging to Determine to Radial and Axial Swelling	166
5.7 Results and Discussion	166
5.7.1 Content Uniformity and Distribution of 20% w/w Itraconazole Tablets Using Near Infrared (NIR) and Raman Microscopy	166
5.7.2 <i>In Vitro</i> Release Studies	166
5.7.3 ATR-FTIR Imaging of Reference Materials	167
5.7.4 ATR-FTIR Imaging of HPMC Tablets	167
5.7.5 FTIR Imaging Hydration Experiments on Pure 20% w/w IT Loaded Tablets	170
5.7.6 Investigating the Nature of IT Particles Within Different pH Environments	173
5.7.7 Characterisation of the Different Forms of IT	176
5.7.8 Physical Swelling Kinetics- Radial and Axial Swelling results on 20%w/w IT Loaded Tablets	179
5.8 Summary	183
5.9 Conclusions	184
5.10 References	186
6.0 Optimisation of IT Release from HPMC Tablets by Incorporating Organic Acid pH Modifiers	188
6.1 Introduction	188
6.2 Materials and Methods	192

6.2.1 Materials	192
6.2.2 Preparation and Characterisation of Tablets	193
6.2.3 Content Uniformity of Itraconazole Loading and Heterogeneity of Tablets	193
6.3 Morphology and Particle Size Analysis of IT, HPMC and Organic pH Modifiers	194
6.4 <i>In Vitro</i> Release Studies	194
6.5 Collection of ATR-FTIR Images	195
6.6 Hydration Experiments Using ATR- FTIR Imaging	195
6.7 Optical Imaging to Determine to Radial Swelling	195
6.8 Multivariate Curve Resolution Alternating Least Squares Analysis (MCR-ALS)	195
6.9 Results and Discussion	196
6.9.1 ATR-FTIR Imaging of Reference Materials	196
6.9.2 Content Uniformity and Distribution of 20% w/w Itraconazole with 10% w/w and 30% w/w pH Modifier Tablets using Near Infrared (NIR) and Raman Microscopy	196
6.9.3 Analysis of the Morphology and Particle Size Determination of IT, HPMC and Organic pH Modifiers	197
6.9.4 ATR-FTIR Imaging of HPMC Tablets Containing 10% w/w and 30% w/w Organic acid	197
6.9.5 FTIR Imaging Hydration Experiments on 20% w/w IT tablets With Organic Acid at 10% w/w and 30% w/w Loading.	203
6.9.6 ATR-FTIR Spectra of Anhydrous and Hydrated Organic Acids	212
6.9.7 MCR Analysis of 30% w/w Modifier Placebo Systems	214
6.9.8 MCR Analysis on 20% w/w IT with and without pH Modifier	220
6.9.9 Determination of pH in Solution Following Hydration Experiments using ATR-FTIR Imaging	230
6.9.10 <i>In Vitro</i> Release Studies	230
6.9.11 Characterisation of the Different Forms of IT	234
6.9.12 Physical Swelling Kinetics-Radial Swelling Results on 20% w/w IT Loaded Tablets with and without Organic Acid pH Modifier	237
6.10 Summary	241
6.11 References	243
7.0 Conclusions and Future Work	247

7.1 Conclusions	247
7.1.1 HPMC and Binary HPMC/IT System	247
7.1.2 20% w/w IT Tablets with the Incorporation of Organic Acid pH Modifiers	249
7.2 Recommendations for Future Work	250
7.2.1 Preparation and Characterisation of Tablets	250
7.2.2 Testing of Tablets and Optimising of Drug Release	250
7.2.3 Refinement of MCR-ALS Methodology	251
8.0 Appendix	253
Appendix 1 Histogram Data for Tablets with 10% w/w Organic Acid Modifier Formulation with 20% w/w IT	253
Appendix 2 ATR-FTIR images collected over the time course of hydration period for placebo and 20% w/w IT loaded tablets	257
Appendix 3 ATR-FTIR images collected over the time course of hydration period for tablets containing organic acid pH modifier at 10% w/w and 30% w/w loading with and without IT	261
Appendix 4 MCR-ALS distribution images and corresponding factors tablets containing 30% w/w organic acid pH modifier with and without IT	279
Appendix 5 Axial and Radial optical swelling images collected over the time course of hydration period for placebo and 20% w/w IT loaded tablets	281
Appendix 6 Radial optical swelling images collected over the time course of hydration period for tablets containing organic acid pH modifier at 10% w/w and 30% w/w loading with and without IT	301
Appendix 7 Publication	349

Figure Numbers

Figure Number	Figure Title	Page Number
2.1	Biopharmaceutics classification system (BCS) as defined by US FDA and Amidon <i>et al.</i> [1]	4
2.2	Schematic of variation of pH in the gastrointestinal tract (adapted from Wikimedia Commons-public domain)	9
2.3	Schematic comparing (a): immediate, burst and controlled drug release profiles; (b): immediate, biphasic burst and controlled drug release profiles. Adapted from [39] [40] [46]	16
2.4	Schematic presentation of compaction flow-through cell used in ATR-IR imaging linked to a UV detector shown on the right for quantitative measurement of dissolved drug. Reprinted from [65], with permission from Elsevier	20
2.5	The chemical structure of HPMC (taken from Wikimedia Commons-public domain)	23
2.6	Overview of HPMC synthesis (R = -H, -CH ₃ , or -CH ₂ CH(OH)CH ₃). Reprinted from [80], with permission from the American Chemical Society	23
2.7	Schematic explaining nomenclature used for METHOCEL K100M cellulose ether (adapted from The Dow Chemical Company 2000) [77] [81]	24
2.8	Diagram showing the evolving fronts within a hydrating hydrophilic matrix tablet. Reproduced with permission from Therapeutic Delivery as agreed by Newlands Press Ltd Timmins <i>et al.</i> [70]	26
2.9	Schematic showing the release mechanism of drugs from hydrophilic matrix tablets. Adapted from Alderman [14]	27
2.10	Schematic diagram of different stages of polymeric disentanglement. Adapted from Siepmann <i>et al.</i> [87]	28
2.11	Time series of fluorescence images in situ of hydrating HPMC matrices in aqueous medium containing NaCl (0.5, 0.6 and 0.75 M) and 0.008% w/v Congo Red. The dashed line represents the initial tablet boundary at t=0. The images are coded for fluorescence intensity from white (highest) to black (lowest) as indicated by the wedge. The bright regions indicate areas of high fluorescence, highlighting regions of polymer hydration where the fluorophore has penetrated. Hydration medium maintained at 37°C. Ex 488/Em > 510 nm. Scale bar = 750 μm. Reprinted from [98], with permission from Elsevier	33

2.12	Schematic showing variables that impact on drug release mechanism and kinetics from hydrophilic matrix tablet. Adapted from [74] by permission from Springer Nature	34
2.13	The chemical structure of Itraconazole	36
3.1	The electromagnetic spectrum highlighting the infrared region	48
3.2	Simplified vibrational energy level diagram showing the transition that occurs when infrared light is absorbed by a molecule	49
3.3	Schematic diagram of the vibrational modes of (a) water; (b) carbon dioxide; (c) degenerate modes carbon dioxide	53
3.4	Schematic of Michelson Interferometer	54
3.5	Schematic overview showing the process of generating of a mid- FTR spectrum using Attenuated Total Reflectance. Adapted from [6]	55
3.6	Schematic representation of transmission experimental setup	57
3.7	Schematic explaining ATR principle. Adapted from [14] [17]	59
3.8	A summary of the energy transition processes for Near-Infrared	62
3.9	Schematic of Golden Gate ATR-FTIR accessory used for FTIR imaging. Adapted from [3] [17]	63
3.10	Schematic of ATR-FTIR imaging set-up with a 64 x 64 FPA detector. Adapted from [32]	64
3.11	Schematic of micro FTIR imaging in (a) transmission set-up (b) reflectance and (c) ATR. Adapted from [3] [17]	66
3.12	Schematic (a) Basket USP I and (b) Paddle USP II dissolution set-up. Adapted from [46]	70
3.13	Jablonski energy level diagram illustrating Rayleigh and Raman scattering adapted from [48]	71
3.14	Schematic showing key constituents of a typical Raman microscope	75
3.15	(a) Schematic of three-dimensional data cube recorded during a chemical imaging experiment on a HPMC tablet and (b) extracted images to show distribution of water, drug and polymer within the tablet matrix. Reproduced from [72] with permission from Elsevier	79

3.16	Unfolding of the hyperspectral datacube in the bi-dimensional matrix D. bilinear decomposition of the matrix D into its constituents: C, concentration matrix; ST, spectra matrix; E, residual matrix. Reproduced from [72] with permission from Elsevier	82
3.17	Diagrammatic representation of PLS process. Adapted from [81]	83
4.1	Dissolution profiles for Sporanox (commercial form, green) and IT cocrystals with L-malic acid (red), L-tartaric acid (blue), succinic acid (orange) and crystalline IT in 0.1 M HCl at 25 °C. Reprinted from [7], with permission from the American Chemical Society	94
4.2	Itraconazole molecule highlighting carbon position	95
4.3	DSC trace showing the heat profiles obtained from the formation of amorphous itraconazole	104
4.4	XRPD trace obtained from the as received free base (as received) itraconazole confirming crystalline form	105
4.5	XRPD trace obtained from the amorphous itraconazole	105
4.6	Stacked plot of all three proton NMRs showing the deshielding shifts of the key signals at H18, H16 and H9	106
4.7	Structure of itraconazole highlighting the protonation sites	107
4.8	Average ATR-FTIR spectrum obtained from the as received free base itraconazole	108
4.9	Comparison of average ATR- FTIR spectrum obtained from the free base (black line) and amorphous (red line) itraconazole highlighting (a) $\nu(\text{C}=\text{O})$, (b) $\nu(\text{C}-\text{O})$ and $\nu(\text{C}-\text{Cl})$	109
4.10	Comparison of average ATR- FTIR spectra obtained from the free base (black line), IT dihydrochloride (red line) and IT monohydrochloride (blue line)	110
4.11	Average ATR-FTIR imaging spectra obtained from reference materials, highlighting $\delta(\text{OH})$, $\nu(\text{C}-\text{O})$ and $\nu(\text{C}=\text{C})$ in water, HPMC and IT respectively. Highlighted bands (indicating which functional group was used) used for peak area integration for images to show (representing) distribution of water, IT and HPMC	111
4.12	Average ATR-FTIR imaging spectra obtained from the organic acid modifiers, highlighting the position of $\nu(\text{C}=\text{O})$ in citric acid, cysteine HCl, betaine HCl and glycine HCl respectively	112

4.13	Representative SEM images for itraconazole, HPMC grade K100M, glycine HCl, betaine HCl and cysteine HCl	113
4.14	NIR spectra obtained from a low and high concentration IT (0% and 45%) standard highlighting the spectral region used for PLS model	116
4.15	NIR spectra obtained from a low and high concentration (8% w/w and 70% w/w) of modifier for (a) cysteine HCl; (b) citric acid; (c) betaine HCl and glycine HCl highlighting the spectral region used for PLS model	116
4.16	PLS plot of calculated versus actual concentration levels for the binary system (HPMC and itraconazole)	118
4.17	PLS plot of calculated versus actual concentration levels for the betaine formulation (betaine HCl and IT in HPMC matrix) for: (a) itraconazole; (b) betaine HCl	119
4.18	PLS plot of calculated versus actual concentration levels for the cysteine HCl formulation (cysteine HCl and IT in HPMC matrix) for: (a) itraconazole; (b) cysteine HCl	120
4.19	PLS plot of calculated versus actual concentration levels for the citric acid formulation (citric acid and IT in HPMC matrix) for (a) itraconazole; (b) citric acid	121
4.20	PLS plot of calculated versus actual concentration levels for the glycine HCl formulation (glycine HCl and IT in HPMC matrix) for: (a) itraconazole; (b) glycine HCl	122
4.21	Raman spectra obtained from (a) itraconazole and (b) HPMC highlighting the bands and the corresponding functional group used to generate the distribution images	131
4.22	Raman Distribution images and corresponding histograms obtained from the 20% IT w/w tablets for the three tablets analysed (a) showing IT (based on the band observed at 1614 cm^{-1} and b) shows the ratio of band intensities (selected markers) to represent IT:HPMC	132
4.23	Average spectra profiles (n=3) obtained from Raman maps on 20% w/w Itraconazole tablets (binary system)	135
4.24	Raman reference spectra obtained from (a) citric acid; (b) cysteine HCl; (c) glycine HCl and (d) betaine HCl	136
4.25	Raman distribution images and corresponding histogram for 10% w/w citric acid with 20% w/w itraconazole formulation showing a) citric acid; b) IT and c) ratio of pH modifier/itraconazole	138

4.26	Raman distribution images and corresponding histogram for 10% w/w betaine HCl with 20% w/w itraconazole formulation showing a) betaine HCl; b) IT and c) ratio of pH modifier/itraconazole	140
4.27	Raman distribution images and corresponding histogram for 10% w/w cysteine HCl with 20% w/w itraconazole formulation showing a) cysteine HCl; b) IT and c) ratio of pH modifier/itraconazole	142
4.28	Raman distribution images and corresponding histogram for 10% w/w cysteine HCl with 20% w/w itraconazole formulation showing a) cysteine HCl; b) IT and c) ratio of pH modifier/itraconazole	144
4.29	Raman distribution images and corresponding histogram for 30% w/w citric acid with 20% w/w itraconazole formulation showing a) citric acid; b) IT and c) ratio of pH modifier/itraconazole	146
4.30	Raman distribution images and corresponding histogram for 30% w/w cysteine HCl with 20% w/w itraconazole formulation showing a) cysteine HCl; b) IT and c) ratio of pH modifier/itraconazole	148
4.31	Raman distribution images and corresponding histogram for 30% w/w betaine HCl with 20% w/w itraconazole formulation showing a) betaine HCl; b) IT and c) ratio of pH modifier/itraconazole	150
4.32	Raman distribution images and corresponding histogram for 30% w/w glycine HCl with 20% w/w itraconazole formulation showing a) glycine HCl; b) IT and c) ratio of pH modifier/itraconazole	152
4.33	Average spectra profiles obtained from Raman maps on 10% w/w pH modifier with 20% w/w Itraconazole for (a) citric acid; (b) cysteine HCl; (c) glycine HCl and (d) betaine HCl tablets	154
4.34	Average spectra profiles obtained from Raman maps on 30% w/w pH modifier with 20% w/w Itraconazole for (a) citric acid; (b) cysteine HCl; (c) glycine HCl and (d) betaine HCl tablets	155

5.1	Schematic of different fronts of a hydrating hydrophilic tablet, looking down onto the upper tablet surface as if one could see through it, highlighting dry core, swelling, diffusion and erosion fronts. Adapted from [5] with permission from Therapeutic Delivery as agreed by Newlands Press Ltd. (b): Schematic of ATR-FTIR imaging set-up over the course of the hydration period using a Focal Plane Array (FPA) detector. Reprinted from [6] with permission from the American Chemical Society	165
5.2	Schematic of tablet placement on ATR crystal	165
5.3	Dissolution profiles for 20% w/w IT loaded tablets at pH 1.5 and 7 (n=6)	167
5.4	Selected ATR-FTIR images were collected over the time course of hydration experiments for placebo tablets in low and high ionic strength solutions at pH 1.5 and pH 7 showing (a) water and (b) HPMC distribution. Images were generated using methods described in section 4.5. The dotted lines in the first column of images denotes the boundary between the tablet and air/water	168
5.5	ATR-FTIR images of HPMC/water peak area ratio images over hydration period, showing HPMC gel layer evolution for (a) pH 1.5; (b) pH 7 low ionic strength solutions; (c) pH 1.5; (d) pH 7 high ionic strength solutions	170
5.6	ATR-FTIR peak area integration images over hydration period, showing: (a) distribution of water; (b) distribution of HPMC; (c) HPMC:water peak area ratio images, showing HPMC gel layer evolution for pH 1.5 and 7; (d) distribution of total IT. The dotted lines in the first column of images denotes the approximate boundary between the tablet and air/water	172
5.7	ATR-FTIR images tracking an IT particle at selected time points at (a) pH 1.5 and (b) pH 7 (interface indicated by dashed white line in last pane), (c) Plot showing movement of 5 discrete particles at each pH over time ($p < 0.05$), FTIR spectra from selected pixels across the IT particle, showing that the particles are IT rich at the 28-minute time-point for (d) pH 1.5 and (e) pH 7	175

5.8	(a) Average ATR-FTIR imaging spectra obtained from IT free base, IT monohydrochloride and IT dihydrochloride with dotted line indicating $\nu_s(\text{CH})$ at 2821 cm^{-1} (b) ATR-FTIR peak area integrated images generated using band at 2821 cm^{-1} . (c) average ATR-FTIR imaging spectra highlighting $\nu(\text{CH})$ at 0, 33 and 198 minute timepoints for 20% w/w IT loaded tablets at pH 1.5 and 7 (d) average ATR-FTIR imaging spectra obtained from IT free base, IT monohydrochloride and 198 minute timepoint for 20% /w IT loaded tablet at pH 1.5	178
5.9	Radial optical images obtained from 0 and 180 minute timepoints for swelling experiments conducted on HPMC placebo tablets at pH 1.5 and 7	180
5.10	Axial optical images obtained from 0 and 180 minute timepoints for swelling experiments conducted on HPMC placebo tablets at pH 1.5 and 7	180
5.11	Radial optical images obtained from 0 and 180-minute timepoints for swelling experiments conducted on 20% w/w IT tablets at pH 1.5 and 7	181
5.12	Axial optical images obtained from 0 and 180-minute timepoints for swelling experiments conducted on 20% w/w IT tablets at pH 1.5 and 7	181
5.13	Percentage swelling data (n=6) obtained from HPMC placebo tablets at pH 1.5 and 7 (a) axial (b) radial measurements	182
5.14	Percentage swelling data (n=6) obtained from 20% w/w IT loaded tablets from(a) axial (b) radial measurements	182
6.1	Selected ATR-FTIR images collected over the hydration period for 10% w/w organic acid placebo tablets at pH 7 showing: (a) distribution of water; (b) distribution of HPMC; (c) distribution of ionised organic acid (citric acid, cysteine HCl, betaine HCl and glycine HCl). The dotted lines in the first column of images denote the approximate boundary between the tablet and air/water	199
6.2	Selected ATR-FTIR images were collected over the time course of hydration experiments for 30% w/w organic acid placebo tablets at pH 7 showing: (a) distribution of water; (b) distribution of HPMC; (c) distribution of ionised organic acid (citric acid, cysteine HCl, betaine HCl and glycine HCl). The dotted lines in the first column of images denotes the approximate boundary between the tablet and air/water	200

6.3	ATR-FTIR images of HPMC/water peak area ratio images over hydration period, showing HPMC gel layer evolution at pH 7 for: (a) (i) 100% HPMC; (ii) 10% w/w citric acid; (iii) 10% w/w cysteine HCl; (iv) 10% betaine HCl w/w; (v) 10% w/w glycine HCl and (b) (i) 100% HPMC; (ii) 30% w/w citric acid; (iii) 30% w/w cysteine HCl; (iv) 30% w/w betaine HCl; (v) 30% w/w glycine HCl	202
6.4	ATR-FTIR peak area integration images for 20% w/w IT and 10% w/w pH modifier over the hydration period, showing: (a) distribution of water; (b) distribution of HPMC; (c) distribution of total IT; (d) distribution of ionised organic acid. The dotted lines in the first column of images denote the approximate boundary between the tablet and air/water	204
6.5	Overlaid ATR-FTIR spectra of IT free base, cysteine HCl, betaine HCl and glycine HCl highlighting overlap of band $\nu(\text{C}=\text{C})$ from IT and the discrete $\nu(\text{C}=\text{N})$ used for the total IT distribution	205
6.6	Extracted ATR-FTIR spectrum from pixel $x=381$, $y=23$ (denoted by the red dotted line) from 30% w/w glycine+20% w/w IT ATR-FTIR imaging experiment, compared with the average ATR-FTIR imaging reference spectrum of glycine HCl and free base itraconazole; b) The image distribution based on the carbonyl band at 1735cm^{-1} representing glycine HCl	206
6.7	ATR-FTIR peak area integration images for tablets containing 20% IT w/w and 30% w/w pH modifier over the hydration period, showing distribution of: (a) water; (b) HPMC; (c) total IT; (d) ionised organic acid. The dotted lines in the first column of images denote the approximate boundary between the tablet and air/water	209
6.8	Extracted ATR-FTIR spectrum from pixel $x=314$, $y=41$ (denoted by the red dotted line) from 30% w/w glycine+20% w/w IT ATR-FTIR imaging experiment, compared with the average ATR-FTIR imaging reference spectrum of glycine HCl and free base itraconazole; b) the image distribution based on the carbonyl band at 1735cm^{-1} representing glycine HCl	210
6.9	ATR-FTIR peak area integration ratio images (HPMC:water) showing gel layer evolution for 10% w/w and 30% w/w pH modifier tablets with 20% w/w IT for (i) 20% IT tablet; (ii) citric acid; (iii) cysteine HCl; (iv) betaine HCl and (v) glycine HCl	212
6.10	Equation showing deprotonation of carboxylic acids to form the carboxylate ion	213

6.11	ATR-FTIR spectra of (a) anhydrous citric acid and ionised citric acid (b) anhydrous betaine HCl and ionised betaine HCl (c) anhydrous cysteine HCl and ionised cysteine HCl and (d) anhydrous glycine HCl and ionised glycine HCl	214
6.12	(a) Distribution images for 30% w/w citric acid placebo formulation showing (i) citric acid (ATR-FTIR imaging); (ii) MCR-ALS citric acid; (iii) MCR-ALS ionised citric acid and (b): MCR-ALS factor with a comparison to the corresponding ATR-FTIR reference spectrum for (i) citric acid; (ii) ionised citric acid	217
6.13	(a): Distribution images for 30% w/w glycine HCl w/w placebo formulation showing (i) glycine HCl (ATR-FTIR imaging); (ii) MCR-ALS glycine HCl; (iii) MCR-ALS ionised glycine HCl and (b) MCR-ALS factor with a comparison to the corresponding ATR-FTIR reference spectrum for (i) glycine HCl; (ii) ionised glycine HCl	218
6.14	(a): Distribution images for 30% w/w cysteine HCl placebo formulation showing (i) cysteine HCl (ATR-FTIR imaging); (ii) MCR-ALS cysteine HCl distribution and (b): MCR-ALS ionised cysteine HCl factor shown with a comparison to the cysteine HCl ATR-FTIR reference spectrum	219
6.15	(a): Distribution images for 30% w/w betaine HCl placebo formulation showing (i) ionised betaine HCl (ATR-FTIR imaging); (ii) MCR-ALS ionised betaine HCl distribution and (b): MCR-ALS factor (predominantly showing $\delta(\text{OH})$) and corresponding ATR-FTIR reference spectrum of ionised betaine HCl	220
6.16	(a) Distribution images of 20% w/w IT formulation at pH 1.5 and 7 showing distribution of (i) IT free base at pH 1.5; (ii) IT free base at pH; (iii) MCR-ALS free base IT at pH 1.5; (iv) MCR-ALS free base IT at pH 7; (v) MCR-ALS possible different form of IT at pH 1.5; (vi) MCR-ALS possible different form of IT at pH 7 and (b): MCR-ALS factor and corresponding ATR-FTIR reference spectrum for (i) IT free base; (ii) MCR-ALS factor and corresponding ATR-FTIR reference spectrum for IT free base, amorphous IT and possible different form of IT	221
6.17	(a) ATR-FTIR peak area Integrated images for 30% w/w citric acid with 20% w/w IT formulation showing distribution of (i) IT free base; (ii) MCR-ALS possible different form of IT; (iii) MCR-ALS citric acid distribution; (vi) ionised citric acid distribution and (b): MCR-ALS corresponding factor and corresponding ATR-FTIR reference spectrum for (i) IT free base; (ii) possible different form of IT; (iii) citric acid; (iv) ionised citric acid	223

6.18	(a) Distribution images for 30% w/w betaine HCl with 20% w/w IT formulation showing distribution of (i) IT free base (ATR-FTIR imaging); (ii) MCR-ALS free base IT; (iii) MCR-ALS possible different form of IT (iv) betaine HCl (ATR-FTIR imaging); (vi) MCR-ALS betaine HCl and (b) MCR-ALS corresponding factor and corresponding ATR-FTIR reference spectrum for (i) IT free base; (ii) possible different form of IT; (iii) betaine HCl	225
6.19	(a) Distribution images for 30% w/w glycine HCl with 20% w/w IT formulation showing distribution of (i) IT free base (ATR-FTIR imaging); (ii) MCR-ALS free base IT; (iii) MCR-ALS possible different form of IT; (iv) MCR-ALS ionised glycine HCl and (b): MCR-ALS corresponding factor and corresponding ATR-FTIR reference spectrum for (i) IT free base; (ii) possible different form of IT; (iii) ionised glycine HCl	227
6.20	(a) Distribution images for 30% w/w cysteine HCl with 20% w/w IT formulation showing distribution of (i) IT free base (ATR -FTIR imaging); (ii) MCR-ALS free base IT; (iii) MCR-ALS possible different form of IT; (iv) MCR-ALS possible different form of IT; (v) cysteine HCl (ATR-FTIR imaging); (vi) MCR-ALS cysteine HCl and (b): MCR-ALS corresponding factor and corresponding ATR-FTIR reference spectrum for (i) IT free base; (ii) possible different form of IT; (iii) possible different form of IT; (iv) cysteine HCl	229
6.21	UV dissolution profiles showing the percentage itraconazole released from the HPMC matrix as a function of time for the 10% w/w pH modifier+20% w/w IT formulations (citric acid, cysteine HCl, betaine HCl and glycine HCl) at pH 7 and 20% w/w IT placebo at pH 1.5 and 7	232
6.22	UV dissolution profiles showing the percentage itraconazole released from the HPMC matrix as a function of time for the 30% w/w pH modifier+20% w/w IT formulations (citric acid, cysteine HCl, betaine HCl and glycine HCl) at pH 7 and 20% w/w IT placebo at pH 1.5 and 7	233
6.23	UV dissolution profiles showing the percentage itraconazole released from the HPMC matrix as a function of time for the 10% w/w and 30% w/w pH modifier +20% w/w IT formulations (citric acid, cysteine HCl, betaine HCl and glycine HCl) at pH 7 and 20% w/w IT placebo at pH 1.5 and 7	233

6.24	(a): ATR-FTIR peak area integrated images generated using band at 2821 cm ⁻¹ for the formulations containing 20% w/w IT with the 10% w/w organic acid modifier; (b) average ATR-FTIR imaging spectra highlighting $\nu(\text{CH})$ at 2821 cm ⁻¹ obtained from IT free base, IT monohydrochloride reference spectra and for the 1, 19, 128 and 198 minute timepoints for 20% w/w IT loaded tablets with 30% w/w organic acid modifier (b) citric acid (c) cysteine HCl (d) betaine HCl (e) glycine HCl	235
6.25	(a): ATR-FTIR peak area integrated images generated using band at 2821 cm ⁻¹ for the formulations containing 20% w/w IT with the 30% w/w organic acid modifier; (b) average ATR-FTIR imaging spectra highlighting $\nu(\text{CH})$ at 2821 cm ⁻¹ obtained from IT free base, IT monohydrochloride reference spectra and for the 1, 19, 128 and 198 minute timepoints for 20% w/w IT loaded tablets with 30% w/w organic acid modifier (b) citric acid (c) cysteine HCl (d) betaine HCl (e) glycine HCl	236
6.26	Percentage swelling data obtained from the radial measurements from (a) 10% w/w placebo organic acid pH modifier formulations (b) 10% w/w organic acid pH modifier formulations with 20% w/w IT. Examples of optical images obtained from 0 and 180 minute timepoints for citric acid, betaine HCl, glycine HCl and cysteine HCl (c) 10% w/w placebo organic acid pH modifier formulations and (d) 10% w/w organic acid pH modifier formulations with 20% w/w IT	238
6.27	Percentage swelling data obtained from the radial measurements from (a) 30% w/w placebo organic acid pH modifier formulations (b) 30% w/w organic acid pH modifier formulations with 20% w/w IT. Examples of optical images obtained from 0 and 180 minute timepoints for citric acid, betaine HCl, glycine HCl and cysteine HCl (c) 30% w/w placebo organic acid pH modifier formulations and (d) 30% w/w organic acid pH modifier formulations with 20% w/w IT	240

List of Equations

Equation Number	Equation	Page Number
2.1	$K_a = \frac{[H_3O^+][A^-]}{[HA]}$	6
2.2	$pK_a = -\log_{10} K_a$	6
2.3	$pH = pK_a + \log\left(\frac{[A^-]}{[HA]}\right)$	6
2.4	$HA + H_2O \leftrightarrow H_3O^+ + A^-$	6
2.5	$\frac{M_t}{M_0} = k\sqrt{t}$	34
2.6	$M_t/M_\alpha = kt^n$	35
2.7	$M_t/M_\alpha = k(t - l)^n$	35
3.1	$v = c/\lambda$	48
3.2	$\Delta E = E_1 - E_0 = hv$	49
3.3	$\bar{\nu} = \frac{1}{\lambda} = \frac{v}{c}$	49
3.4	$T = \frac{I}{I_0}$	50
3.5	$A = -\log T = -\log \frac{I}{I_0}$	50
3.6	$A = \epsilon cl$	50
3.7	$f = -kx$	51

- 3.8 $k = 4\pi^2 v^2 m$ 51
- 3.9 $E_v = hv \left(n + \frac{1}{2} \right)$ 51
- 3.10 $v = \frac{1}{2\pi c} \sqrt{\frac{k}{\mu}} \quad \mu = \frac{m_1 m_2}{m_1 + m_2}$ 52
- 3.11 $SNR \propto \sqrt{\text{number of scans}}$ 56
- 3.12 $\theta_c = \sin^{-1} \left(\frac{n_2}{n_1} \right)$ 58
- 3.13 $E = E_0 \exp \left[-\frac{2\pi}{\lambda_1} (\sin^2 \theta - n_{21}^2)^{\frac{1}{2}} Z \right]$ 58
- 3.14 $\frac{\lambda}{2\pi n_1 \sqrt{\sin^2 \theta - (n_1/n_2)^2}}$ 59
- 3.15 $r = \frac{0.61\lambda}{NA}$ 65
- 3.16 $NA = n \sin \theta$ 65
- 3.17 $I_R = (I_L \sigma_R X) PC$ 72
- 3.18 $\Delta/\bar{v} = \left(\frac{1}{\lambda_0} - \frac{1}{\lambda_1} \right)$ 73
- 3.19 $u = aE$ 73
- 3.20 $D = \frac{1.22\lambda}{NA}$ 76

3.21	$p = \frac{0.61\lambda}{NA}$	76
3.22	$A = \log\left(\frac{I}{I_0}\right) c\epsilon d$	81
3.23	$D = CS^T + E$	81
3.24	$D = TP^T + E$	82
4.1	$100 s/\bar{X}$	125
4.2	$AV = M - \bar{X} + ks$	125

Table Numbers

Table Number	Table Title	Page Number
2.1	Classification of acids and bases according to strength [4]	5
2.2	Approaches available to enhance dissolution in GI tract or to increase dissolution of a poorly soluble drug [24] [25]	10
2.3	Summary of different release mechanisms	14
2.4	Grades of HPMC used for pharmaceutical oral controlled release	24
3.1	Properties of commonly used ATR crystals [21]	61
4.1	Drug and Matrix materials used for all formulations	92
4.2	pH modifiers used for formulations	92
4.3	Chemicals used for preparation of itraconazole salts	93
4.4	Concentration of constituents used in the tablet formulations	101
4.5	FTIR spectral band assignments for itraconazole	108
4.6	Peak positions for the $\nu(\text{C}=\text{O})$ used to generate the ATR-FTIR distribution Images for the organic acids	112
4.7	Particle size distribution data obtained from the starting materials (mean \pm SD, n= 3)	114
4.8	Spectral regions selected for quantification of itraconazole and pH modifiers for the PLS model	117
4.9	PLS model results based on the optimised spectral ranges for the 20% w/w IT (binary system n=6)	123
4.10	PLS model results based on the optimised spectral ranges for the 10% w/w pH modifier placebo tablets (n=6)	127
4.11	PLS model results based on the optimised spectral ranges for the 30% w/w tablets pH modifier placebo tablets (n=6)	127
4.12	PLS model results based on the optimised spectral ranges for the 10% w/w pH modifier with 20% w/w itraconazole tablets (n=6)	128
4.13	PLS model results based on the optimised spectral ranges for the 30% w/w pH modifier with 20% w/w itraconazole tablets (n=6)	129

4.14	Statistical data obtained from histograms for 20% w/w IT binary system	135
4.15	Selected absorption bands used to generate the Raman distribution maps for the organic acids	137
6.1	Comparison of pK_a and aqueous solubility of various pH modifiers (values taken from the literature)	193
6.2	pH measurements obtained from remaining hydration solution after ATR-FTIR imaging experiments from the 30% w/w modifier + 20% w/w IT w/w formulations	230
6.3	pH measurements obtained from 0, 30, 60, 120 and 180 minute dissolution solutions remaining from the 30% w/w modifier + 20% w/w IT formulations	232

List of Abbreviations

AV	Acceptance value
API	Active pharmaceutical ingredient
ATR	Attenuated total reflection
ASTM	American Society for Testing and Materials
BCS	Biopharmaceutics Classification System
CCD	Charge coupled detectors
DSC	Differential scanning calorimetry
FDA	U.S.A Food and Drug Administration
FPA	Focal plane array
FTIR	Fourier transform infrared
GI	Gastrointestinal tract
HPMC	Hydroxypropyl methylcellulose
IR	Infrared
IT	Itraconazole
I	Ionic strength
MCR	Multivariate curve resolution
MCR-ALS	Multivariate curve resolution-alternating least squares
MCT	Mercury-cadmium-telluride
NCEs	New chemical entities
NIR	Near Infrared Imaging
NMR	Nuclear magnetic resonance
PCA	Principal component analysis
PLS	Partial least squares
RI	Refractive index
RSD	Relative standard deviation
SEM	Scanning electron microscopy
SD	Standard Deviation
SNR	Signal-to-noise ratio
T _g	Glass transition temperature
USP	United States Pharmacopeia
UV	Ultraviolet

μm	Micrometre
QC	Quality control
XRD	X-ray powder diffraction

1.0 Introduction

1.1 Project Rationale

One of the major challenges facing the pharmaceutical sector today is the number of drugs that fail to translate from development stage into marketable medicinal products due to the problems associated with their poor solubility at pH 7, which can result in reduced or variable bioavailability [1]. It has been reported that 40–60% of new chemical entities (NCEs) fall into the category of being poorly water soluble [2]. This presents ongoing challenges to the pharmaceutical industry as the most common approach for drug delivery is still by oral administration [3].

During the formulation of hydrophilic matrices, extensive screening of successive iterations is usually necessary to achieve a desired *in vitro* dissolution profile. In an industrial context, the United States Pharmacopeia ("USP") dissolution test and discernment of drug release remains the universal tool for the development, production, and quality control (QC) of oral solid dosage forms. However, the USP dissolution test does not provide microscopic temporal and spatial information and its use in elucidating the mechanism of drug release from the formulation matrix is limited.

To address this problem of poor availability there are a number of approaches that have been adopted, some of which are explored in Chapter 2. These include salt formation, amorphous solid dispersions, cyclodextrin complexes and the incorporation of pH modifiers into the tablet matrix [3].

1.2 Aims and Objectives

The aim of this work will be to incorporate itraconazole - a weakly basic drug - into a hydrophilic hydroxypropylmethylcellulose (HPMC) polymer and to explore the application of mid-FTIR imaging to monitor the hydration of the HPMC polymer and migration of the drug in the diffusion zone over time.

The work will aim to illustrate the procedure for mapping the drug release and water penetration as a function of time and position within the tablet matrix, offering previously unobtainable insights into the mechanistic phenomena underpinning the release.

To achieve the above, the following objectives will be met:

- Review of the literature to gain an understanding of the experimental approach researchers have adopted to investigate the release of poorly soluble drugs from tablet matrices and methodology currently adopted to address the problem of poorly soluble drugs.
- Preparation and characterisation of model formulation(s) using Raman, Attenuated Total Reflectance Fourier transform infrared (ATR-FTIR), Differential Scanning Calorimetry (DSC) and X-ray powder diffraction (XRD).
- To develop an *in situ* Mid-IR spectroscopic imaging technique for studying concomitantly the release of poorly soluble drug, HPMC and other excipients from HPMC hydrophilic matrices.
- To compare the spectroscopic data of drug release to HPMC matrix performance in standard USP II dissolution test procedures and identify possible correlations.
- To study and explore the impact of ionic strength on the gel layer behaviour and growth of HPMC matrices using ATR-FTIR imaging.
- To gain an insight into the conversion of the free base form of the drug to the ionised state during hydration in low pH, as weakly soluble drugs are considerably more soluble in low pH environments [4].
- To incorporate an organic acid pH modifier into the HPMC and itraconazole formulation to make use of the pH dependent solubility of the poorly soluble drug.

1.3 References

- [1] S. Kalepua and V. Nekkanti, "Insoluble drug delivery strategies: review of recent advances and business prospects," *Acta Pharmaceutica Sinica B*, vol. 5, no. 5, pp. 442-453, 2015.
- [2] A. Shoaib , B. Mangla, S. Javed, M. H. Sultan, S. S. Alqahtani and F. Shakeel, "Vicissitudes of liquid crystals for solubility enhancement of poorly soluble drugs," *Journal of Molecular Liquids*, vol. 321, p. 114924, 2021.
- [3] G. Tambosi, P. F. Coelho, S. Luciano, I. C. S. Lenschow, M. Zétola, H. K. Stulzer and B. R. Pezzini, "Challenges to improve the biopharmaceutical properties of poorly water-soluble drugs and the application of the solid dispersion technology," *Matéria (Rio de Janeiro)*, vol. 23, no. 4, p. e12224, 2018.
- [4] J. Van Der Weerd and S. G. Kazarian, "Release of Poorly Soluble Drugs from HPMC Tablets Studied by FTIR Imaging and Flow-Through Dissolution Tests," *Journal of Pharmaceutical Sciences*, vol. 94, no. 9, p. 2096–2109, 2005.

2.0 Literature Review

2.1 Drug Release

2.1.1 The Biopharmaceutics Classification System (BCS)

The BCS system and the corresponding guidance issued by the food and drug administration (FDA) in combination with work based on Amidon *et al.* [1] categorises drugs into four classes based on their aqueous solubility and permeability [2] as shown in Fig. 2.1. The development of the BCS system has significantly aided and equipped the pharmaceutical industry to gain greater insight into *in vivo* performance of BCS class II compounds which exhibit low solubility and high permeability. As this category of API exhibit low *in vivo* absorption and bioavailability [3]. As a result of this, poorly water-soluble drugs still present ongoing challenges in transforming these into feasible medicinal products. The bioavailability of BCS class II drugs is considered to be dissolution rate limited. Therefore, understanding the drug release mechanism is essential for improving the design and ensuring success of solid oral dosage forms.

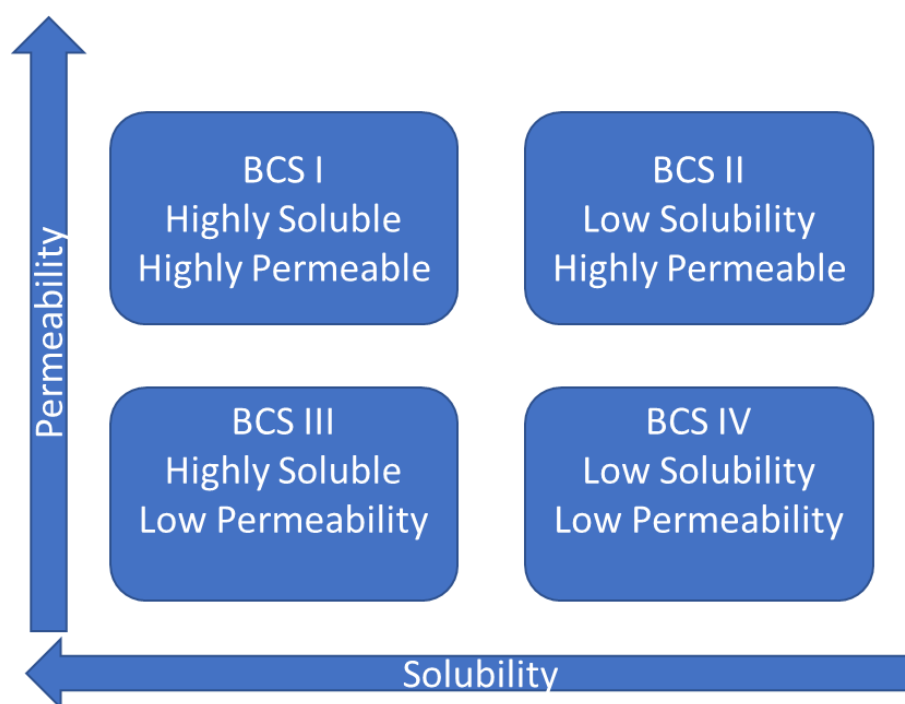


Fig. 2.1: Biopharmaceutics classification system (BCS) as defined by US FDA and Amidon *et al.* [1]

2.1.2 The Importance of Acidity and pK_a values in Drug Dissolution

Using the pK_a value as a measure of strength, pharmaceuticals are categorised as acids or bases (Table 2.1). The determination of the pK_a value of an API is a crucial parameter for all ionisable functional groups in order to determine the strength of acids and bases. Most pharmaceuticals can be classed as non-ionisable, ionised, weak acids, weak bases, or salts [4].

Table 2.1: Classification of acids and bases according to strength [4]

Strength	pK_a	
	Acids	Bases
Very Strong	<0	14
Strong	0-4.5	9.5-14
Weak	4.5-9.5	4.5-9.5
Very weak	9.5-14	0-4.5
Extremely weak	14	<0

The release characteristics of a drug can be improved in an aqueous environment depending on the ionisation characteristics (pK_a), which in turn has a direct influence on the drug formulation approach. Hence knowledge pertaining to the pK_a and molecular properties of the drug are essential to ensuring a successful release profile [5].

For solution-based drugs, the pK_a value(s) of the drug can critically affect factors associated with its formulation. pK_a values have a large effect on the aqueous solubility of the drug and generally the ionised form of a drug has a greater solubility in water compared to the un-ionised form [5]. Solubility is a key physicochemical parameter to ensuring successful drug delivery and is routinely investigated by the pharmaceutical industry [5].

The strength of the acid, i.e. the extent of dissociation, can be determined by the following equilibrium:

$$K_a = \frac{[H_3O^+][A^-]}{[HA]} \quad \text{Equation 2.1}$$

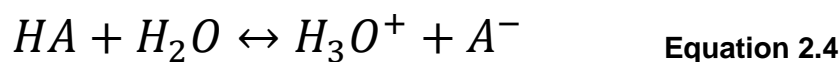
The equilibrium constant K_a provides a measure of the strength of the acid and can be referred to in several ways. These include the following: acid dissociation constant, ionisation constant or the acidity constant. This relates to the dissociation of the acid and is calculated based on the concentrations of the reacting species [6]:

$$pK_a = -\log_{10} K_a \quad \text{Equation 2.2}$$

Strong acids have a high K_a , which relates to a high degree of dissociation. The strength of an acid is more commonly reported as pK_a (negative logarithm of K_a) values due to the small numbers generated from K_a [7].

$$pH = pK_a + \log \left(\frac{[A^-]}{[HA]} \right) \quad \text{Equation 2.3}$$

The pK_a value is strongly related to the pH of the solution, and the Henderson-Hasselbalch equation describes how the pH relates the equilibrium concentration of the dissociated acid $[A^-]$ and non-dissociated acid $[HA]$ respectively:



For new drugs to be successful, properties such as absorption, distribution, metabolism and excretion (ADME) are critical factors that need to be taken into consideration. For an ionisable drug these properties are highly influenced by the pK_a values of the

functional groups [8]. Therefore, poor physicochemical properties of solid dosage forms can drastically hinder early stage (preclinical) development and ultimate release to market of new drugs [9].

At the early stage of drug discovery, the pK_a values are determined as part of the physicochemical profiling of the molecule and this is revisited for regulatory purposes at the later stage of development for verification [8].

pK_a determinations are generally carried out using potentiometric and spectrophotometric methodologies [10] [11]. Alternatively, ionisation behaviour can be predicted from the functional groups with acid-base character within a molecule using the pK_a of the conjugate acid which is sometimes referred to as pK_{aH} [12].

2.1.3 Poorly-Soluble Drugs

Drugs having an aqueous solubility below 0.1 mg/mL (100 μ g/mL) have been described as being 'poorly soluble' [13], although the terms 'poorly soluble' and 'weakly soluble' appear to be used interchangeably in the literature.

Poorly soluble ionisable drugs will exhibit different dissolution behaviour within the physiological pH range. Weakly basic compounds exhibit a marked increase in solubility at low pH while being practically insoluble at neutral pH [13] [14] [15]. A significant number of new drugs in development fall into this category [16], although the phenomenon may be ameliorated to a degree by incorporating pH-modifiers within the matrix to yield improved *in vivo* performance [17]. A further method to achieve an improved oral bioavailability is by the creation of a water-soluble salt form of the weakly basic drug [18].

Oral dosage forms are the preferred route for drug administration due to factors including lower cost associated with manufacturing and patient preferences in comparison to other options (transdermal, inhalation, etc) [19]. However, there are a number of considerations that can affect oral drug absorption which include the drugs

physicochemical properties such as pK_a , crystallinity, solubility, the form in which the drug is administered and the physiological environment, such as the range of pH values encountered [20].

One concern with oral drug delivery is the significant variation of the bioavailability of the drug due to a number of factors which include: limited dissolution, drug release, solubility and rapid precipitation [19].

With poorly soluble drugs such as albendazole, danazol and felodipine [21] the solubility is pH dependent and is affected by the range of pH encountered throughout the gastrointestinal tract (Fig. 2.2) and therefore fall into the BCS II category (Fig. 2.1). For ionisable basic drugs, the pH environment plays a critical role for the solubility and ultimately the absorption. Weakly basic drugs are protonated at low pH, leading to rapid solubilisation; conversely these types of drugs when present in the deprotonated state at higher pH - namely in intestinal fluid (pH7.35-7.45) - result in the presence of the poorly soluble un-ionised form which leads to incomplete drug release [19] [22]. Achieving a pH-independent drug release is a key factor in ensuring, reliable and consistent drug therapy [15].

It has been reported by Loftsson and Brewster that nearly 40% of oral drugs available on the market fall into the category of poorly soluble drugs ($<100 \mu\text{g/mL}$) [23].

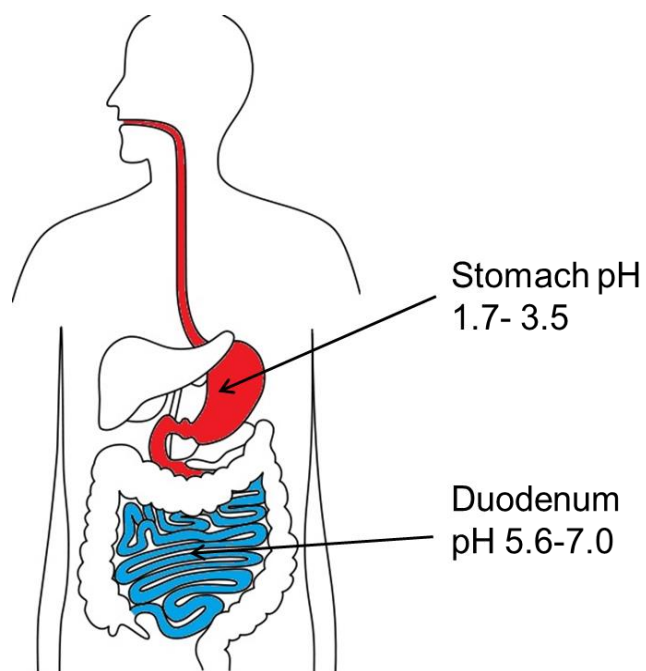


Fig. 2.2: Schematic of variation of pH in the gastrointestinal tract (adapted from Wikimedia Commons-public domain)

2.1.3.1 Strategies for Improving Bioavailability of Poorly-Soluble Drugs

For the successful development of oral formulations of poorly soluble drugs a range of methodologies have been developed and these can be categorised as physical or chemical modifications (Table 2.2) [24].

Table 2.2: Approaches available to enhance dissolution in GI tract or to increase dissolution of a poorly soluble drug [25] [26]

Physical Modifications	Particle size reduction	Micronisation Nanosuspensions
	Modifications of crystal structure	Polymorphs Pseudopolymorphs (e.g. hydrates)
	Complexation/solubilisation	Co-crystals Use of surfactants Use of cyclodextrins Use of polymeric micelles Use of further colloid-forming excipients
	Drug dispersions in carriers	Eutectic mixtures Amorphous solid dispersions and solid solutions
Chemical Modifications		Salts Soluble prodrugs Drug-excipient conjugates

Some examples of the chemical and physical modifications employed to enhance the bioavailability of poorly soluble drugs are discussed in the following paragraphs.

The bioavailability of poorly soluble drugs can be improved by the formation of a prodrug: The definition of a prodrug is a biologically inactive compound that undergoes conversion to an active drug during the body's metabolic process. Conversion to the active form can occur by different mechanisms such as by the action of specific enzymes [27].

Another method uses cyclodextrins, which can be classified as either natural or derived cyclodextrins. These are cyclic oligosaccharides of R-D-glucopyranose units linked by α -(1, 4) glycosidic and consists of hydrophobic central cavity with an outer hydrophilic surface. The natural cyclodextrins are usually substituted with the addition of polar groups which provide enhanced aqueous availability whilst maintaining the hydrophobic cavity [28]. Thus, allowing the formation of hydrophilic inclusion complex with water-insoluble lipophilic drugs resulting in solubilisation [29]. Cyclodextrin complexes are widely used in drug delivery systems in the pharmaceutical industry to increase aqueous bioavailability and stability of poorly soluble drugs.

Taupata *et al.* explored the use of binary and ternary cyclodextrin complexes formulated with three types of cyclodextrin derivatives in order to improve the dissolution of the model drug itraconazole. The authors concluded that all the formulation approaches investigated improved the *in vitro* bioavailability and the dissolution of the itraconazole, with the ternary complex (HP-b-CD or HBen-b-CD and Soluplus) exhibiting the greatest enhancement of itraconazole [28].

A drug, which is typically amorphous can be molecularly dispersed in a highly soluble carrier to form a solid dispersion. These formulations are proving to be a promising strategy to improve the bioavailability of poorly soluble drugs. The early work carried out on solid dispersions by Chiou and Riegelman defined them as the dispersion of one or more active ingredients in an inert carrier matrix at solid-state prepared by the melting (fusion), solvent or melting-solvent method [30].

Solid dispersions are generally obtained from melt and solvent evaporation methods and the approach involves reducing the particle size significantly and therefore improving drug wettability, hence providing a greatly enhanced bioavailability of the drug [16]. Drug particles incorporated into solid dispersions are found to have a higher degree of posterity [28].

Commonly employed methods such as milling or micronisation are used as strategies to improve solubility of poorly soluble drugs on the basis of the increased surface area. However, size reduction is limited to around 2-5 μm with these types of approaches and frequently this is insufficient to improve drug dissolution rates [31].

Solid dispersions have shown to provide a faster release rate and an increased bioavailability in comparison to the traditional formulations of the same drugs [16]. Authors have reported such improvements to be quite considerable, with increases of up to four hundred-fold being achieved [32]. One of the main principles associated with these formulations is to achieve an amorphous state which is more soluble than the crystalline form [33].

Reduction of particle size is a commonly used approach to improve the bioavailability of poorly soluble drugs [34]. A decrease in particle size provides an increase in the surface area resulting in enhancement of solubility of the drug.

Salt formation is frequently used and has proven to be successful at increasing solubility and dissolution rates of acidic and basic drugs. As the salts of these drugs generally have higher solubilities in comparison to their acid and base forms [18]. The main advantage of this approach is the considerable increase in drug solubility, potentially greater than three orders of magnitude being achieved [35].

In the period 1995 to 2006 40% of the new chemical entities approved by the FDA were in the salt form. From these approved salts of basic drugs, over half of these were prepared with hydrochloric acid, indicating the predominance of this salt form [18].

However, one of the problems associated with the use of salts in drug development is that salt forms are prepared from organic solvents (acetone, dichloromethane) and a salt which is isolated from an organic solvent. These salts will almost certainly behave differently when encountering an aqueous environment and could potentially lead to poor drug stability and conversion to the free acid or base form.

Organic pH-modifiers such as citric acid, succinic acid and tartaric acid are widely used in oral dosage forms and have successfully shown to enhance the dissolution rate and bioavailability of poorly water-soluble compounds [36]. In terms of formulation, this approach is one of the simplest and is usually a first-line strategy for improving the dissolution rate and bioavailability of poorly soluble drugs, generally used in combination with other solubilizing methods such as the use of surfactants, cyclodextrins or cosolvents [27]. The most frequent approach for weakly soluble basic drugs to achieve a pH independent drug release profile is based on the incorporation of organic acids within the formulation. They work by keeping the pH within the drug formulation low and hence in the intestinal pH-range, resulting in enhanced dissolution behaviour and bioavailability of the drug.

Previous researchers [37] have monitored the effects of citric acid, tartaric acid and succinic acid on drug release in various of 10-30% from a cellulose acetate and beeswax tablet matrix. The author concluded that the addition of an organic acids did not sufficiently enhance the dissolution rate of the drug in the pH 7.4 environment. However, when the pH of the dissolution medium was increased during the run, higher levels of drug dissolution were observed.

Depending on the organic acid selected and the pK_a , different dissolution rates can be observed from the tablet matrix [37].

2.2 Solid Oral Dosage Forms

2.2.1 Types of Drug Release Mechanism from Solid Oral Dosage Forms

Drug release mechanisms from solid oral dosages can be described in a number of ways and a brief overview is shown in Table 2.3 [38] [39]:

Table 2.3: Summary of different release mechanisms

Release Mechanism	Characterisation
Immediate	Released rapidly after administration.
Extended or controlled	Within the body, the API is released slowly at a predetermined or constant rate.
Pulsatile	Within the body, the API is released over a period of time in pulses.
Targeted or delayed	API release is delayed until it reaches a targeted area of the body.
Burst	An initial large dose of drug is released before the release rate reaches a stable profile.

A comparison of the immediate, burst and controlled drug release profiles is presented in Fig. 2.3 [39] [40]. Immediate release (Fig. 2.3a) allows the drug to dissolve in the gastrointestinal contents without delaying or prolonging the dissolution or absorption of the drug. Many drugs fall into this category and this is particularly important if a fast onset of action is required for therapeutic reasons such as relieving the symptoms of pain. An example of this is a tablet containing a painkiller such as paracetamol, where a rapid disintegration in the GI is essential in order to allow a fast uptake into the body [41].

With burst release the drug is released at a higher rate initially, which is followed by a more sustained release and often leads to a shorter total drug release time [42]. The main issue with burst release is that it is not easily controlled and can be quite variable. The underlying causes of burst release mechanisms are not fully understood and are

thought to be attributed to a variety of physical and chemical process parameters [39]. Burst release is frequently observed in micro and nano particles prepared from poly lactic-co-glycolic acid (PLGA). For sustained and controlled drug release formulations containing PLGA particles, this can be problematic as they often exhibit biphasic release profiles (with different drug release rates for each phase) [43]. Controlled drug release systems also exhibit burst release behaviour during the first hours of immersion. This is usually due to loss of the drug located in close proximity to the particle surface [42]. This can also arise when a poorly entrapped drug easily diffuses out of the carrier during the initial contact with the biological fluid. HPMC matrices often show burst release at the start of a dissolution run. It has been proposed that this phenomenon could be the result of release of drug from within the gel layer in the early stages of dissolution, before the internal concentration gradients within the gel have stabilised [44]. Ravivarapu *et al.* compared microparticles prepared from different molecular weight PLGA and found a greater initial burst release due to the low molecular weight, higher porosity and surface roughness. Differences in physicochemical properties of particles e.g. shape and size contribute significantly to the prevalence of burst release from PLGA polymeric matrices due to a higher surface to volume ratio.

With extended release systems the drug is released over a longer duration. This is advantageous as the frequency of dosing is reduced. Extended release of a drug can be achieved using sustained or controlled-release drug delivery systems [41].

In some instances, it is imperative that the drug selectively interacts with the relevant tissue; in these scenarios, it is important to optimise drug release to achieve targeting [41]. One example of this approach is the use of nanoparticle-based drug delivery systems. These are extensively use for the treatment of tumours [45].

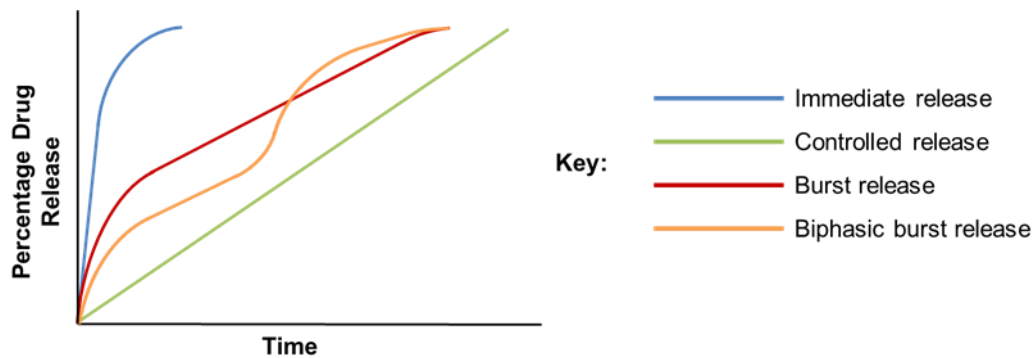


Fig. 2.3: Schematic comparing immediate, controlled, burst and biphasic burst drug release profiles. Adapted from [39] [40] [46]

2.2.2 Methods to Monitor Drug Release

To overcome the problems associated with BCS class II (poorly soluble, basic drugs) drugs, it is essential to gain an insight into the within-tablet dynamics and release behaviour (dissolution) of the drug, including the stability and transformations to the potential different forms (ionised, amorphous) at the molecular level. One way to investigate this is by using Attenuated Total Reflection-Fourier Transform Infrared (ATR-FTIR) spectroscopic imaging, which can provide detection of drug, polymer and other excipients within the tablet matrix and which enables the monitoring of the release behaviour simultaneously of these components when the tablet undergoes hydration [47].

Previous studies by Kazarian [8] have shown that Mid-IR spectroscopic imaging in Attenuated Total Reflectance (ATR) mode can successfully be applied to monitor real time hydration processes of solid dosage forms *in situ*.

Currently, a common approach for pharmaceutical companies is to use the dissolution method [48] for assessing controlled drug release from solid oral dosage forms [49]. Drug release data can be obtained by measuring the drug content in solution as a function of time using UV spectroscopy or High-Performance Liquid Chromatography (HPLC). This

method provides a basic knowledge of the drug concentration in solution; however, it does not provide an in-depth understanding on the mechanism of drug release [50].

Imaging techniques have also been used to investigate and characterise drug release mechanisms from solid oral dosage forms and these include:

- Magnetic resonance imaging (MRI) [51],
- Confocal imaging [44] [52]
- Near Infrared Imaging (NIR) [53]
- FTIR imaging [54] [55]
- Raman Spectroscopy [56]

Several groups have used ATR-FTIR imaging to study drug release mechanisms from solid oral dosage forms which use an HPMC polymer matrix [50] [57] [58] [59]. The advantages associated with using spectroscopic imaging techniques is that these setups rely on the bonds between atoms in the molecule absorbing infrared energy to provide a characteristic chemical fingerprint and are not reliant upon on the addition of chemical dyes/labelling methods in order to identify/monitor particular chemical moieties/bonds [50]. Other advantages include minimal sample preparation and sample size. This can be explained by the fact that the penetration depth of IR light in the sample for ATR measurements is independent of sample thickness and therefore tablets of any thickness can be analysed [50]. Another advantage is that strongly absorbing molecules such as water do not pose a problem with this type of measurement due to a smaller depth of penetration [60]. However, a limitation of this approach is that the area analysed may not capture the compositional changes of the tablet as a whole ($\sim 640 \times 640 \mu\text{m}^2$). Using the approach of mosaic imaging ("stitching" of images together) can be used to provide an overall view of the tablet, however this can be very time consuming [61].

Furthermore, the use of FTIR imaging techniques are proving to be popular with the

pharmaceutical industry as they provide a greater understanding of the mechanism of drug release. Currently this sector is very much dependent on the dissolution approach described above, in which drug mechanism can only be inferred [50]. FTIR imaging instrumentation uses a focal plane array detector (FPA), which contains multi - channel detectors consisting of an array of small detector elements, facilitating the collection of multiple spectra simultaneously. FTIR images can be obtained in transmission, reflection or ATR mode.

- Transmission mode- the infrared light passes through the sample.
- Reflection mode - the infrared light is reflected from the surface of the sample
- ATR mode- the infrared light is totally internally reflected through sample– crystal interface, the crystal is a material of high refractive index (such as diamond, germanium or silicon).

To perform FTIR imaging, various methodologies have been developed. Koenig and co-researchers [62] worked on an approach where FTIR imaging was used in transmission mode to understand dissolution and drug release [62]. However, the major disadvantage of using transmission is the limitation on sample thickness and a prerequisite is to have thin samples when used in conjunction with water. Pharmaceutical tablets would require microtoming and this has proven to be problematic. Collecting images in reflection mode requires the sample surface to be smooth [54]. Because of this restriction, ATR-FTIR imaging has become the preferred approach [57]. With this method, the tablet is pressed onto the ATR crystal with the dissolution cell on top. However, this can impact on the water penetration and the formation of the gel layer as the dissolution medium is only in contact with the sides of the tablet [57]. In order to overcome this, Puncochová *et al.* have used ATR-FTIR imaging in conjunction with magnetic resonance imaging (MRI) to obtain a more comprehensive and in-depth understanding of the chemical and physical processes that occur during dissolution.

Keles *et al.* studied the release of the growth hormone hGH from gamma-irradiated Poly(D,L-lactide-co-glycolide) and polylactic acid (PLGA/ PLA) micro particles using

ATR-FTIR imaging in order to gain a better understanding of how gamma radiation impacts on the hGH release kinetics. This research focused on using FTIR imaging to investigate the release of protein or peptides from a single micro-particle *in situ*, providing important information about the release mechanism [55].

ATR-FTIR imaging enables multiple spectra to be collected simultaneously, allowing a chemical image of the material to be generated relatively quickly [63] [64]. From this, information about the polymer, drug and water distribution can be gained simultaneously. The advantage of this approach is the ability to provide characterisation of the molecular species present and morphology of the polymer matrix [64]. ATR-FTIR images consist of spectral and spatial information and therefore requires additional steps for converting the data into chemically and physically significant information. There are several methodologies for doing this, the simplest being to plot the peak height or peak area of a band from a known component.

ATR-FTIR imaging has previously been used to study the mechanism of drug release from HPMC matrices [50] [57] [58]. Niacinamide incorporated into an HPMC matrix was used as a model system [65]. Work by van der Weerd and Kazarian described an approach to studying drug release from a tablet by using a combination of chemical imaging via ATR-FTIR imaging and dissolution. The tablet was compacted directly onto the ATR crystal and dissolution of the tablet was also investigated by flowing the dissolution medium through the ATR cell and thence to a UV detector, to quantify the amount of dissolved drug (Fig. 2.4) [65]. The compaction device was designed such that the flowing medium was only introduced when the tablet had been compacted, therefore combining imaging and the measurement of dissolved drug in the dissolution medium as a function of time. This work focused on using a partial least squares (PLS) calibration to obtain quantitative analysis for the concentration of water, polymer and drug as a function of time as opposed to images based on absorbance of a particular band of each component. Comparable data was then obtained from conventional dissolution tests for validation [65].

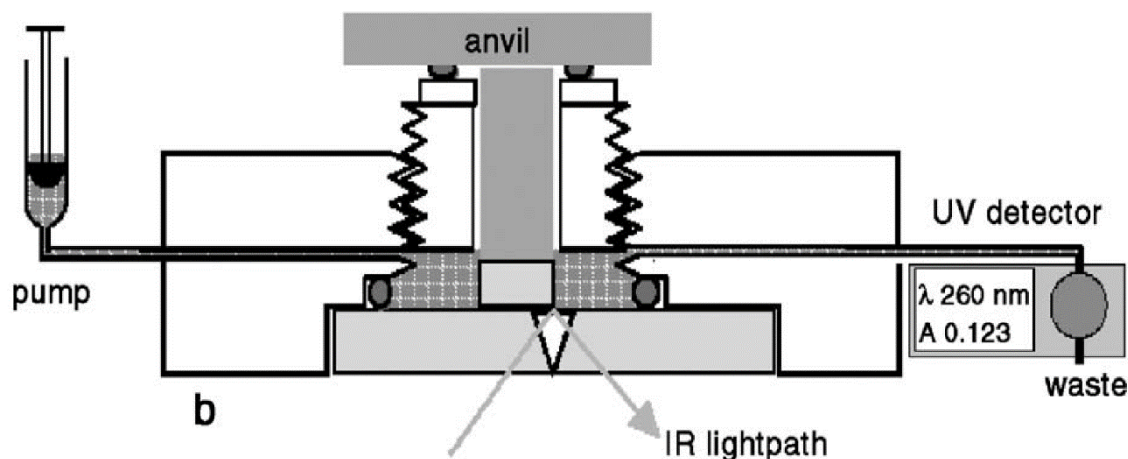


Fig. 2.4: Schematic presentation of compaction flow-through cell used in ATR-IR imaging linked to a UV detector shown on the right for quantitative measurement of dissolved drug. Reprinted from [65], with permission from Elsevier

Hifumi *et al.* have used ATR-FTIR imaging to investigate the influence of different polymer matrices on drug release. They studied ibuprofen loaded HPMC films as a rapid release model and ibuprofen loaded polyvinylpyrrolidone (PVP) films for extended release. The authors used a bespoke transparent flow cell placed over the polymer film and positioned such that at least half of the ATR crystal was covered. They were able to discern information on the distribution of the components in each system, the rate of water ingress, dissolution behaviour of the different components within the polymer films and interactions between the excipients and drug. They were also able to show that, by controlling the local pH and ionic strength around the HPMC films by incorporating a pH modifier and a hydrophobicity modifier to the PVP-based films, drug release behaviour could be controlled [66].

Ewing *et al.* used ATR-FTIR imaging combined with a polydimethylsiloxane microfluidic device to monitor the behaviour and release of ibuprofen *in situ* under flowing conditions at pH 1 and 7. It was reported that the low pH environment inhibited the release of the drug due to conversion from the molecularly dispersed ibuprofen to the crystalline form [67].

Near-IR (NIR) imaging can also be used in a similar way to ATR-FTIR imaging to monitor and determine drug release profiles from tablets under flowing conditions [56] and it has the advantage that analysis can be performed through the thickness of a tablet [68]. However, one of the disadvantages to this approach is the reliance upon multivariate analysis to elucidate information from the sample due to the broad absorption bands generated from an NIR spectrum [69]. In mid-IR spectroscopy the origin of fundamental vibrations of chemical moieties are better understood, reducing the ambiguity of band assignments and aiding interpretation.

Wray *et al.* were able to use NIR imaging with an FPA detector and Raman spectroscopy to investigate the dissolution of a whole tablet in combination with a custom designed flowing dissolution cell which was used for both techniques. The research focused on a model drug with a pKa of 3.98 which readily disproportionates. This is a common problem with pharmaceuticals and gaining a better understanding of this would be advantageous in order to overcome these effects [56].

2.3 Hydrophilic Matrices

Hydrophilic matrix tablets based on hydroxypropyl methylcellulose (HPMC) are a favourable choice for oral extended drug release dosage forms especially for weakly soluble drugs. The reasons for this include the knowledge base for the technology, regulatory status, low cost, ease of manufacture and relative inertness [70] [71] [72]. Due to their swelling properties, they have gained considerable popularity in the formulation of oral dosage formulations. Also, the good compression characteristics of cellulose ethers exhibit means they can be directly compressed to form sustained release swellable matrices. HPMC/cellulose derivatives are used in a wide range of applications, some of which include the pharmaceutical, food and textile industries [73].

2.3.1 Structure and Chemistry of HPMC

Cellulose is a plant-based carbohydrate, the structure having repeating anhydroglucose units. This is a hydrophilic material and a natural polymer, however due to its highly

crystalline nature and because of the strong intramolecular and intermolecular interactions, pure cellulose is insoluble in water. By changing the ordered crystalline regions of cellulose by the incorporation of chemical groups, solubility can be achieved [73].

HPMC, also known as hypromellose, is a cellulosic-based polymer with methoxylic and hydroxypropoxylic groups substituted onto the anhydroglucose backbone. The chemical structure of HPMC is shown in Fig. 2.5. HPMC is available in a variety of grades based on the extent of substitution and viscosity. The ratio of methoxyl and hydroxypropyl substitution have a significant impact on the polymer properties such as solubility and the viscosity of the polymer solution. In addition to this the physicochemical properties of HPMC are strongly affected by the molecular weight which ranges from 10,000 to 1,500,000 Da [74] [75]. For use in pharmaceutical applications, the United States Pharmacopeia distinguishes four different grades of HPMC, classified according to their relative hydroxypropyl and methoxy content as shown in Table 2.4 [76] [77].

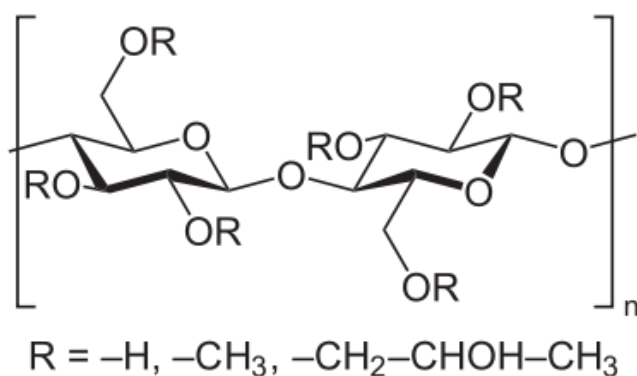


Fig. 2.5: The chemical structure of HPMC (taken from Wikimedia Commons-public domain)

HPMC is produced by treating pulped cellulose with a solution of caustic soda. Burdock reported the use of an 18% sodium hydroxide solution [78]. In order to introduce the propyl and hydroxyl methyl groups, the caustic cellulose pulp is reacted with methylene chloride and propylene oxide (Fig. 2.6) [79].

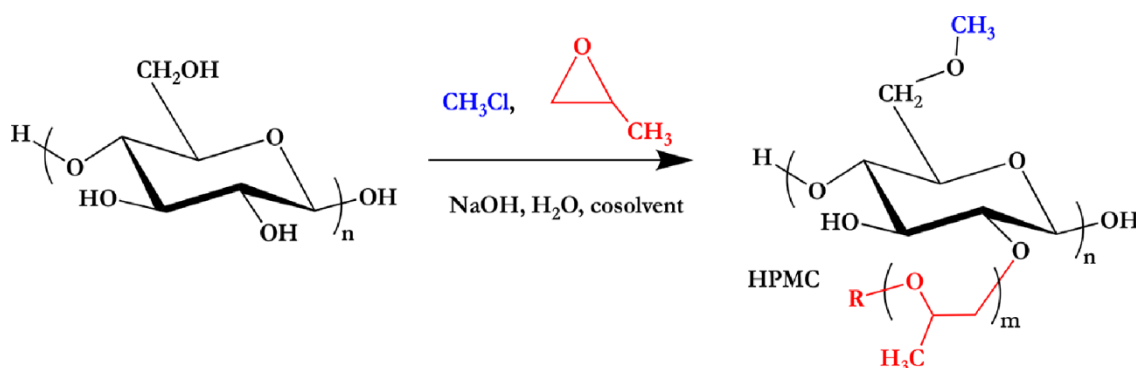


Fig. 2.6: Overview of HPMC synthesis (R = -H, -CH₃, or -CH₂CH(OH)CH₃). Reprinted from [80], with permission from the American Chemical Society

Table 2.4: Grades of HPMC used for pharmaceutical oral controlled release

HPMC TYPE	USP Type	Methoxy %	Hydroxypropoxy %
K	2208	19-24	4-12
E	2910	28-30	7-12
F	2906	27-30	4-7.5
J	1828	16.5-20	0.93-1.15

The HPMC used in this study was K100M CR Premium grade. The letter 'K' in the prefix denotes the HPMC chemistry (cellulose ether type) and the K type is a hydroxypropyl methylcellulose product as are E and F [77] [81]. The number after the letter refers to the viscosity grade in millipascal-seconds (m.Pa.s) for the product measured in 2% aqueous solution at 20°C. The letter M is used represent a multiplication factor of 1000. The 'CR' denotes controlled release grades [77] [81]. This is summarised in Fig. 2.7.

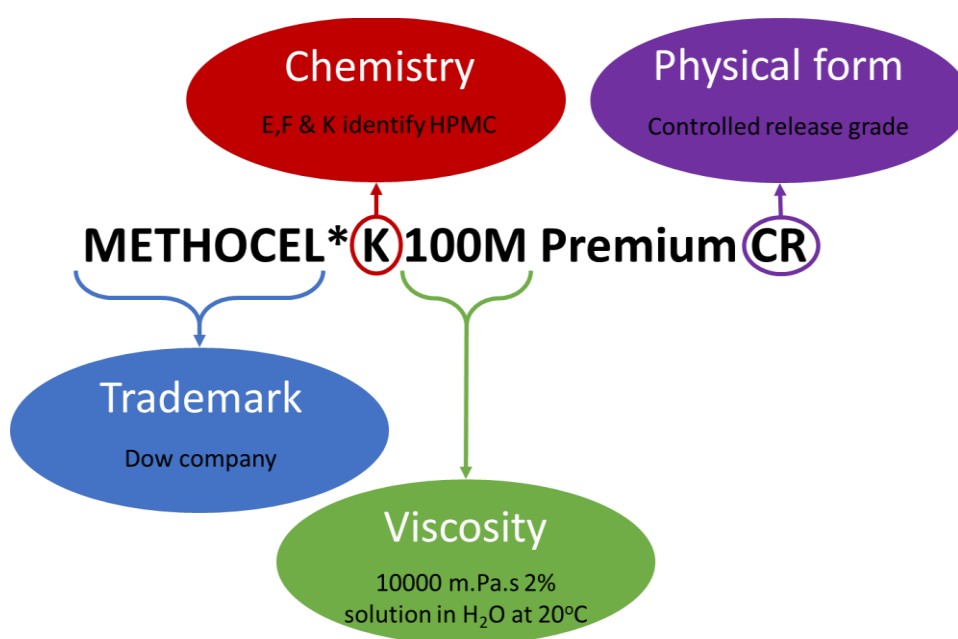


Fig. 2.7: Schematic explaining nomenclature used for METHOCEL K100M cellulose ether (adapted from The Dow Chemical Company 2000) [77] [81]

2.3.2 Drug Release from Hydrophilic Matrices

Oral drug delivery commonly uses a hydrophilic polymer matrix for dosing and the control of release.

Swellable matrices consist of a compressed mixture, with key constituents being a hydrophilic polymer and the drug. These types of matrices rapidly hydrate when in contact with water and form a gel layer of hydrated polymer (highly concentrated polymer, described as a highly entangled polymer chain network) around the tablet matrix controlling release of the drug by hindering water ingress [14]. The hydration of the polymer progresses by ingress of fluid into the tablet over time and contributes to controlling the release of the drug by modulating the rate of water ingress [14], however, drug dissolution in, and diffusion through the matrix, as well as erosion of the hydrated polymer under shear at the interface between the gel layer and the bulk medium also contribute to drug release.

2.3.3 HPMC as a Model Hydrophilic Matrix

Understanding the mechanisms controlling the rate of drug release from an HPMC hydrophilic matrix tablet can be pursued by considering the movement of three fronts inside the evolving matrix tablet over time (Fig. 2.8): the boundary between yet-to-be hydrated polymer and hydrated polymer (swelling front); between hydrated polymer and bulk aqueous medium (erosion front); within the hydrated gel where undissolved drug is in equilibrium with dissolved drug (diffusion front) [70] [82]. These are the key factors of understanding the mechanism of drug release from hydrophilic matrices and the key parameters for tailoring and controlling the release of drugs from these types of matrices [70]. Drug release kinetics can be determined from the movement of the erosion front.

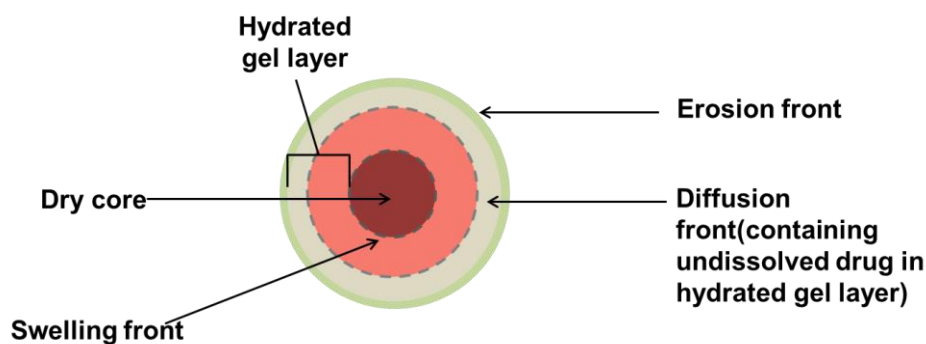


Fig. 2.8: Diagram showing the evolving fronts within a hydrating hydrophilic matrix tablet. Reproduced with permission from Therapeutic Delivery as agreed by Newlands Press Ltd Timmins *et al.* [70]

The mechanism of drug release outlined by Ford [79] is as follows: initial, rapid release of drug on hydration, followed by either controlled diffusion through the gel layer or continual exposure of fresh drug due to erosion. The author also concluded that the release of water-soluble drug controls diffusion, while for poorly-soluble drugs, erosion of the matrix is the dominating factor in release [79], thereby confirming there is a direct correlation between drug solubility and the drug release mechanism (Fig. 2.9).

It has previously been reported [83] that in hydrophilic matrices with sparingly or slightly soluble drugs, solid drug particles are transported within the gel layer by polymer swelling, so-called translocation. The presence of solid drug particles in the gel layer impaired the swelling of the polymer matrix due to restricting the disentanglement of the polymer chains. Furthermore, a correlation between decreased drug solubility and erosion of the matrix was observed. However, the methodology used by Bettini *et al.* [83] does not provide chemical information pertaining to solid drug particles. For poorly soluble drugs in hydrophilic matrices, the erosion mechanism of the hydrated polymer is important as it is this erosion that results in the liberation of undissolved drug [83].

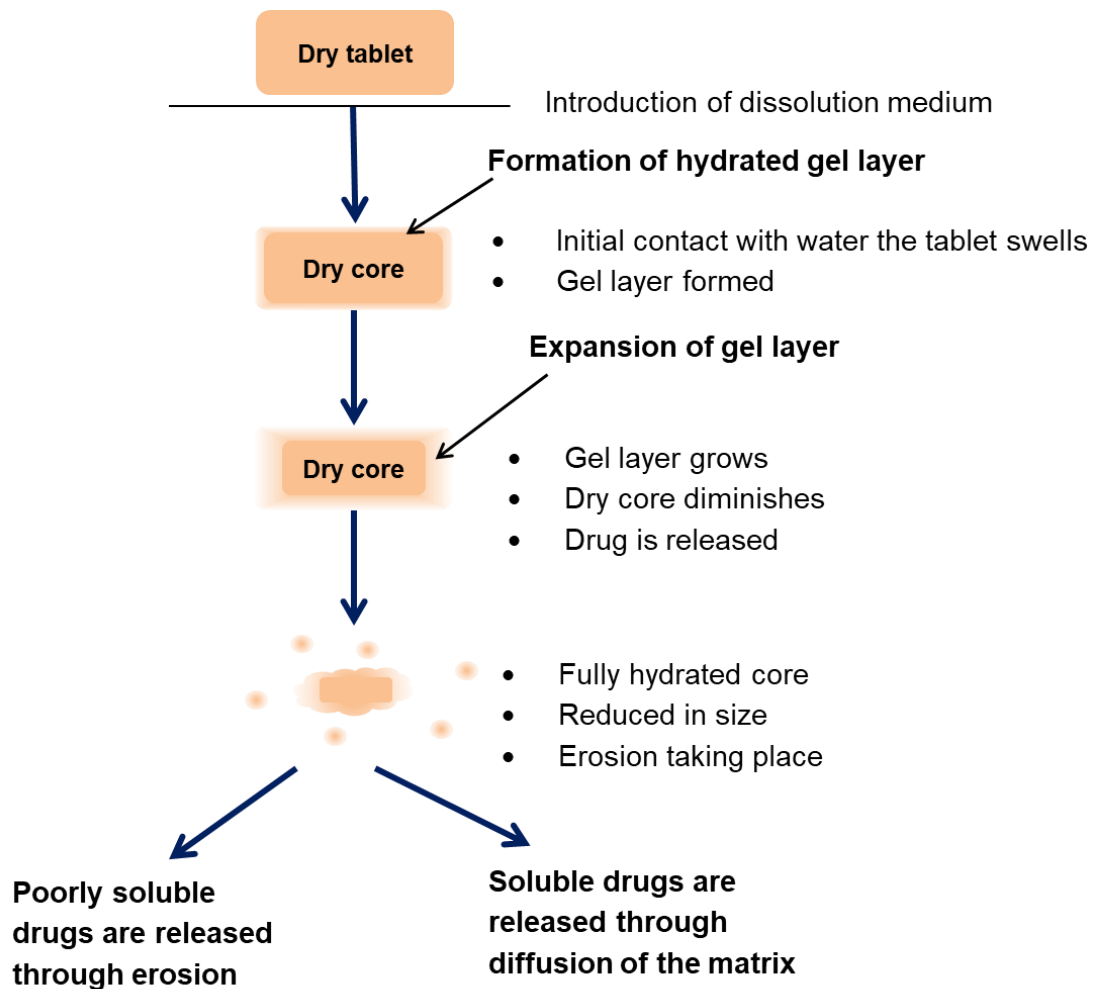


Fig. 2.9: Schematic showing the release mechanism of drugs from hydrophilic matrix tablets. Adapted from Alderman [14]

An important consideration for controlled drug release from hydrophilic matrices is the glass transition temperature (T_g) of the polymer [76]. The T_g of HPMC is 154-184 °C [84], meaning that at ambient conditions it exhibits glassy behaviour [79]. However, exposure to water/dissolution media results in a decrease in T_g such that the polymer is in a rubbery state at ambient temperature.

Maderuelo *et al.* [85] related the different stages of HPMC hydration and formation of the so-called gel layer to these changes in glass transition temperature. The authors state that the gel layer forms as a result of a decrease in the glass transition temperature, whereby the polymer undergoes a progressive change (structure and composition) in the matrix from a glassy to a rubbery state (the gel layer) resulting in swelling [85].

Furthermore, water ingress also leads to polymer chains uncoiling and extending, producing more sites for hydrogen bonding which in turn leads to swelling [79] [86].

The disentanglement mechanism during polymer dissolution as described by Siepmann *et al.* [87] (Fig. 2.10) highlights a polymer concentration gradient (also referred to as the gel layer [70]) when water comes into contact with HPMC tablet matrices. Siepmann describes the polymer network as a dense matrix, in which the macromolecules are restricted (non-swollen polymer). When the polymer comes into contact with water, relaxation of the polymer chains occurs and the mobility of the macromolecules increases significantly, which results in a decrease in polymer concentration and an increase in volume expansion of the system. The entangled polymer chains can undergo disentanglement or modification of their entanglement configuration. As its concentration decreases the ratio of disentangled polymer chains increases in comparison to the newly formed entangled macromolecules, meaning the HPMC matrix is eroded. The disentangled polymer diffuses through the gel layer into the surrounding solution and is observed by a distinct polymer concentration gradient [87].

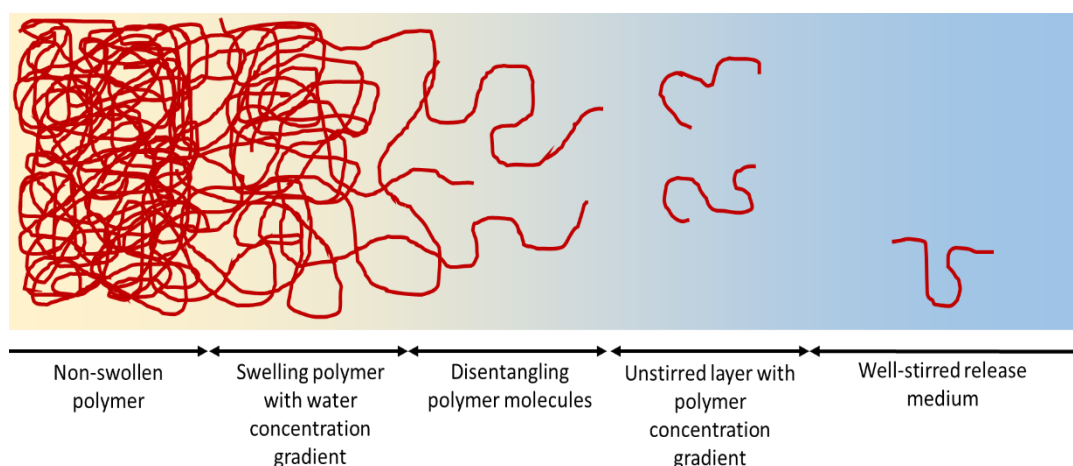


Fig. 2.10: Schematic diagram of different stages of polymeric disentanglement.

Adapted from Siepmann *et al.* [87]

The kinetics of the process described is affected by the polymer chain length and with longer chains it is slower due to the higher degree of entanglement within the tablet matrix

[88] and differences in water ingress and swelling are observed between a high and low molecular weight HPMC polymer.

Siepmann *et al.* suggested that the drug release mechanism from HPMC based formulations is highly dependent on the device design parameters such as the composition and geometry (size & shape) of the delivery system [76].

For example, the thickness of the gel layer plays a crucial role in the drug release process and essentially depends on the drug dose and the viscosity of the polymer.

Novaka *et al.* identified the following factors that influence drug release from a hydrophilic matrix [89]:

- Viscosity and particle-size distribution of the polymer;
- Ratio of the polymer to drug;
- Polymer grade;
- Compression pressure;
- Thickness of the tablet;
- Particle size of the drug;
- Entrapped air in the tablets;
- Molecular geometry of the drug;
- Solubility of the drug;
- The presence of excipients.

2.3.3.1 Effect of Polymer (HPMC) Concentration

There is a consensus that increased polymer concentration leads to a decrease in drug release rate. Ford *et al.* studied the effects of various formulation variables on the release rate of promethazine hydrochloride from HPMC tablet matrices and concluded the major controlling factor was the drug to polymer ratio. It was also concluded that increasing the particle size (45–63 to 500–700 μm) of the promethazine hydrochloride only yielded an additional 12% increase in the dissolution rate of the drug. Concluding, changes in drug

particle size only marginally yielded an increase in the promethazine hydrochloride [90] [91].

2.3.2.2 Effect of Polymer (HPMC) Viscosity

Investigations carried out on how differing viscosities of HPMC impact on drug release from hydrophilic matrices confirm that the drug release is reduced with increasing polymer viscosity. This is due to faster swelling of the polymer side chains, which form a stronger gel structure and which in turn hinders drug release.

Rahman *et al.* [92] looked at a range of different grades of viscosity for HPMC matrices (K100M, K15M, K4M and K100LV) used for oral controlled drug release in conjunction with the drug diclofenac sodium. The authors found significant differences in the drug release profiles depending on the viscosity grade of the HPMC matrix, with higher viscosity grade (K100M) producing a slower release of diclofenac sodium in comparison to the other grades [92].

Nokhodchi *et al.* explored the effect of different particles sizes (<45-350 μm) on the tensile strength of HPMC compacts of different viscosity grades. The researchers concluded that particle size had a marked effect on the tensile strength properties of the compacts. A clear relationship was observed, with a reduction in particle size leading to an observed increase in the tensile strength for all the different grades of HPMC investigated (K4M, K100M, K15M and K100). The authors concluded that the smallest particle size in combination with the lowest viscosity grade (K100) resulted in compacts exhibiting greater mechanical strength. It was also proposed that K4M and K100 are superior grades for sustained release formulations, due to their high tensile strength properties [81] [93].

2.3.3.3 Effect of Polymer (HPMC) Particle Size

Ford *et al.* have shown that HPMC particle size can have a significant effect on drug release from these types of matrices. Studies conducted on propranolol hydrochloride concluded that the drug release can be impacted on by the particle size of the polymer

matrix. The researchers found the drug release rate decreased as the particle size of HPMC reduced from $>355\ \mu\text{m}$ to $150\text{--}210\ \mu\text{m}$, however subsequent reduction on the particle size ($75\text{--}150\ \mu\text{m}$ and $<75\ \mu\text{m}$) did not impact on the release rate [79] [94]. However, coarser particles of HPMC ($>355\ \mu\text{m}$) can prevent sustained release as they are considered to hydrate too slowly, potentially leading to a burst release [79]. Studies carried out [95] have attributed this to the HPMC particles not being able to coalesce to adjacent particles, causing the matrix to disintegrate. It is also postulated that the coarser particles of the polymer allow water ingress and disintegration to occur prior to the gel layer forming which prevents the internal drug from dissolution [79].

2.3.4 Monitoring Swelling Behaviour of HPMC on Hydration

Previous studies have incorporated non-diffusing insoluble markers to gain insight and quantify swelling within the gel layer of hydrophilic HPMC matrix tablets. The movement of the fluorescent markers was tracked and observed using a confocal laser scanning microscope [96]. Interestingly, analysis of the tracks indicated a wave of expansion that started and was greatest at the exterior, moving inwards towards the core. The findings also suggested that as deeper layers started to expand, swelling continued in the outer layers.

HPMC is chemically stable over the physiological pH range [79], however, the swelling properties of HPMC are strongly influenced by the ionic strength of the medium [97] [98]. The ionic strength can vary considerably in the fluid within the gastrointestinal tract (GI) and depending on fasted and fed states, can range from $0\text{--}0.5\ \text{mol/L}$, impacting on drug release from a hydrophilic polymer matrix [97]. Many different approaches have been used to investigate the formation of the hydrated gel layer and the impact of ionic strength employing a range of techniques [99] [100].

Several techniques have been employed to investigate the swelling properties and characterize the formation of the gel layer. These include optical imaging which is a common approach to detecting the water enhancing front and works on the basis of

detecting changes in refractive index at the interface of the polymer gel and tablet core, also referred to as the glassy core [57]. Other techniques that are utilised to investigate the swelling of hydrophilic matrices are: ¹Hydrogen nuclear magnetic resonance (NMR), confocal laser scanning microscopy and ATR-FTIR.

Researchers have also investigated swelling of HPMC tablet matrices using a technique based on scattered light passing through the hydrating matrix. This enabled them to identify the swelling front and follow swelling evolution of the tablet matrix *in situ* without any physical constraints in both radial and axial directions [101] [102]. Other techniques which have been used to investigate the gel layer structure and gel thickness of these types of matrices include texture analysis [103].

Franz Hoffmeister in 1888 discovered salts had different effects on the stability of proteins from egg whites in water. Hoffmeister observed that some salts would cause the proteins to precipitate out of solution whilst some would enhance the stability of the solution. Following this, researchers have formulated an ordering of the salts which is commonly referred to as the Hofmeister series or lyotropic series [104]. The impact of ionic salts on the swelling of HPMC is dependent on their rank order in the Hofmeister series with higher valency ions being more potent.

More recently, Williams *et al.* reported high concentrations of sugars can accelerate drug release from hydroxypropyl methylcellulose (HPMC) matrices. This is due to the sugars suppressing polymer hydration due to particle swelling and coalescence being inhibited. This prevents a coherent diffusion barrier forming and therefore water penetrates the interior of the matrix. The authors studied the effect of sucrose in a range of different ionic strengths and found an increase in gel layer thickness with type of sugar and slower drug release concentrations achieved below 0.5M. At higher concentrations (0.6-0.8M), disruption of the gel formation is observed which caused a marked increase of drug release [105].

Bajwa *et al.* used real-time confocal fluorescence imaging to investigate movement and migration during the early stages of HPMC gel layer formation in the radial direction using the fluorophore Congo red, which selectively binds with the cellulosic unit and hence acts as a marker for the hydrated HPMC [98]. Fluorescent images obtained from HPMC tablet matrices hydrating in a range of different ionic strength solutions of sodium chloride (0.5M, 0.6M and 0.75M) for selected time points were examined (Fig. 2.11). The authors found with the 0.5M sodium chloride solution the images show a coherent gel layer formation in contrast to the 0.75 M which show little evidence of a gel layer. The authors concluded that gel layer growth was suppressed with increasing salt concentration of the hydration medium [98].

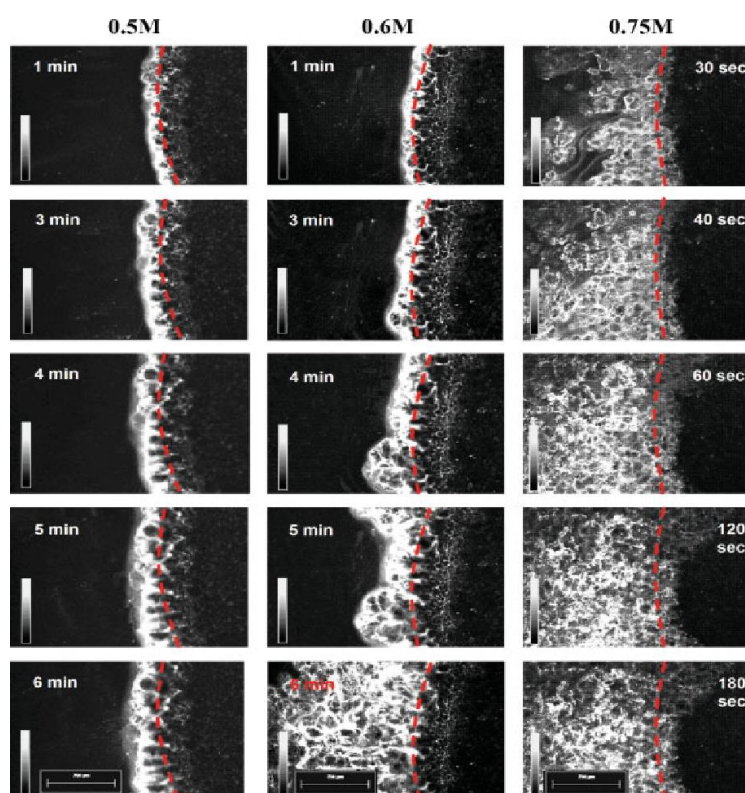


Fig. 2.11: Time series of fluorescence images in situ of hydrating HPMC matrices in aqueous medium containing NaCl (0.5, 0.6 and 0.75 M) and 0.008% w/v Congo Red. The dashed line represents the initial tablet boundary at $t=0$. The images are coded for fluorescence intensity from white (highest) to black (lowest) as indicated by the wedge. The bright regions indicate areas of high fluorescence, highlighting regions of polymer hydration where the fluorophore has penetrated. Hydration medium maintained at 37°C. Ex 488/Em > 510 nm. Scale bar = 750 μm .

Reprinted from [98], with permission from Elsevier

2.3.5 Quantification of Drug Release from Hydrophilic Matrices

Higuchi [106] derived a simple equation (2.5) that allowed for the quantification of a drug release from thin ointment films which can also be applied to other types of drug delivery methods such as controlled release transdermal patches or films for oral controlled drug delivery.

$$\frac{M_t}{M_0} = k\sqrt{t} \quad \text{Equation 2.5}$$

Where k is the Higuchi Constant, M_t is the amount of drug dissolved at time t , M_0 is the drug in the original dry tablet.

This pivotal equation allowed the possibility of facilitating device optimization and gaining an understanding of the underlying drug release mechanisms. Also, drug release from a matrix can be controlled by optimizing factors such as the concentration of the drug within the matrix, drug solubility and porosity and tortuosity of the polymer matrix system (shape and size) [74]. Therefore polymer, drug and formulation related variables that affect drug release kinetics can be carefully manipulated to achieve the desired release kinetics (Fig. 2.12) [74].

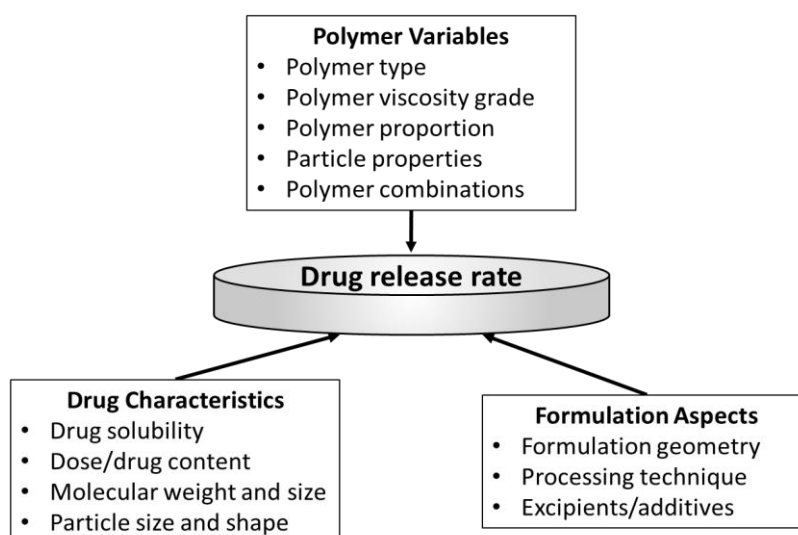


Fig. 2.12: Schematic showing variables that impact on drug release mechanism and kinetics from hydrophilic matrix tablet. Adapted from [74] by permission from Springer Nature

Some authors have stated that Higuchi's equation may not be valid for hydrophilic matrix systems [70]. For swellable matrices such as HPMC the important rate controlling mechanisms are diffusion, swelling and erosion [107], therefore exhibiting a mixed mechanism of release. Diffusion can be described using Fick's second law and the following mathematical models derived by Korsmeyer-Peppas (Equation 2.6). This provides a more comprehensive description of drug release from polymeric systems (referred to as the power law) and importantly takes into account the HPMC-based drug delivery system [107] [108]:

$$M_t/M_\alpha = kt^n \quad \text{Equation 2.6}$$

Where M_t/M_α represents the fraction of drug release, k is the diffusion constant, which considers the structural and geometric characteristics of the tablet, t is the release time and n is the release exponent indicative of the mechanism of drug release and which varies according to geometry of the dosage form (slab $n=0.5$, cylinder $=0.45$ and sphere $=0.43$).

This has been modified further (Equation 2.7) by Ford to take into account burst effects or lag times [79].

$$M_t/M_\alpha = k(t - l)^n \quad \text{Equation 2.7}$$

Where l is the lag time.

It should be noted that other mathematical models have been developed to determine the release kinetics from swellable matrices, but it is critical when applying them that the relevant factors associated with the system under investigation are taken into consideration [79].

2.4 Itraconazole-a Model Poorly-Soluble Drug

As discussed in section 1.1, the pharmaceutical sector has a requirement to improve the release of poorly soluble drugs and increase their bioavailability. Itraconazole was selected as a model drug for this work as it fits the profile of a poorly soluble drug: a weak base ($pK_a=3.7$), a highly lipophilic drug and practically insoluble at pH 7 [20]. According to the BCS classification, itraconazole falls into a class II category, which refers to drugs that exhibit low solubility and high permeability (Fig. 2.1) [19]. Itraconazole presents one of the most difficult challenges to the pharmaceutical industry due its extremely low aqueous solubility (1 ng/mL at pH 7). Even in favourable conditions (pH 1) the solubility is $\sim 4 \mu\text{g/mL}$, which is equivalent to 1mg of dissolved IT in 250 mL of solution [20] [109] [110].

Itraconazole is an azole antifungal agent, which contains imidazole and triazole groups (Fig. 2.13) and is a 1:1:1:1 racemic mixture of four diastereomers (two enantiomeric pairs), each possessing three chiral centres. It is used to treat a range of fungal infections, which include blastomycosis, histoplasmosis paracoccidioidomycosis and chronic disseminated aspergillosis [111].

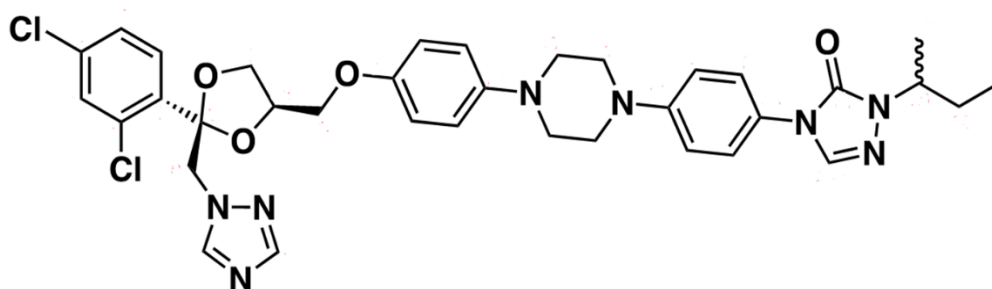


Fig. 2.13: The chemical structure of Itraconazole

2.5 Conclusion

This chapter has highlighted the challenges associated with the development of sustained release oral solid dosage formulations incorporating pH dependent sparingly soluble drugs. HPMC, the gel forming hydrophilic polymer used to make oral dosage forms in this study was introduced and a brief explanation as to how it functions as a controlled release matrix was provided. Using hydrophilic matrices to form semi-permeable gel layers thereby controlling release can be complicated by changes in the dissolution profile of drugs at different pH along the GI tract. Strategies to provide a favourable/consistent local pH, such as incorporating weak organic acids, can impact on hydration, gel layer formation and tablet swelling kinetics. A brief survey of suitable analytical tools to help understand the competing dynamics involved in hydration and drug release from hydrophilic matrices was provided, with a strong focus on the vibrational spectroscopic tools used in this study. Finally, the anti-fungal drug itraconazole, IT, which was used as a model drug in this work was introduced. The characteristics that make it suitable for this study were highlighted.

2.6 References

- [1] G. L. Amidon, H. Lennernäs, S. P. S. Vinod and J. R. Crison, "A Theoretical Basis for a Biopharmaceutical Drug Classification: The Correlation of in Vitro Drug Product Dissolution and in Vivo Bioavailability," *Pharm Res*, vol. 12, p. 413–420, 1995.
- [2] Food and Drug Administration, "Waiver of In Vivo Bioavailability and Bioequivalence Studies for Immediate-Release Solid Oral Dosage Forms Based on a Biopharmaceutics Classification System," Food and Drug Administration, 2017. [Online]. Available: <https://www.fda.gov/media/70963/download>. [Accessed 03 04 2020].
- [3] Y. Umemoto, S. Uchida, T. Yoshida, K. Shimada, H. Kojima, A. Takagi, S. Tanaka, Y. Kashiwagura and N. Namiki, "An effective polyvinyl alcohol for the solubilization of poorly water-soluble drugs in solid dispersion formulations," *Journal of Drug Delivery Science and Technology*, vol. 55, p. 101401, 2020.
- [4] G. A. Stephenson, A. Aburub and T. A. Woods, "Physical Stability of Salts of Weak Bases in the Solid-State," *J Pharm Sci.*, vol. 100, no. 5, pp. 1607-17, 2011.
- [5] D. T. Manallack, R. J. Prankerd, E. Yuriev, T. I. Oprea and D. K. Cha, "The Significance of Acid/Base Properties in Drug Discovery," *Chem Soc Rev.*, vol. 42, no. 2, p. 485–496, 2013.
- [6] L. Samuelsen, R. Holm, A. Lathuile and C. Schönbeck, "Buffer solutions in drug formulation and processing: How pKa values depend on temperature, pressure and ionic strength," *International Journal of Pharmaceutics*, vol. 560, pp. 357-364, 2019.
- [7] P. M. Dewick, *Essentials of Organic Chemistry: For Students of Pharmacy Medicinal Chemistry and Biological Chemistry*, John Wiley & Sons Ltd, 2006.
- [8] J. Comer and K. Box, "High-Throughput Measurement of Drug pKa Values for ADME Screening," *Journal of the Association for Laboratory Automation*, vol. 8, no. 1, pp. 55-59, 2003.
- [9] A. Shevchenko, I. Miroshnyk, L.-O. Pietilä, J. Haarala, J. Salmia, K. Sinervo, S. Mirza, B. v. Veen, E. Kolehmainen, Nonappa and J. Yliruusi, "Diversity in Itraconazole Cocrystals with Aliphatic Dicarboxylic Acids of Varying Chain Length," *Cryst. Growth Des.*, vol. 13, no. 11, p. 4877–4884, 2013.
- [10] J. Peeters, P. Neeskens, J. P. Tollenaere, P. V. Remoortere and M. E. Brewster, "Characterization of the Interaction of 2-Hydroxypropyl- β -cyclodextrin With Itraconazole at pH 2, 4, and 7," *J Pharm Sci.*, vol. 91, no. 6, p. 1414–1422, 2002.
- [11] S. Sanlı, F. Basaran, N. Sanlı, B. Akmeşe and I. Bulduk, "Determination of Dissociation Constants of Some Antifungal Drugs by Two Different Methods at 298 K," *Journal of Solution Chemistry*, vol. 42, p. 1976–1987, 2013.
- [12] D. Allwood, "pKa and pKaH in Organic Chemistry," You Tube, 17 02 2020. [Online]. Available: <https://www.youtube.com/watch?v=Px7RIY8Ad9I>. [Accessed 17 06 2020].

- [13] T. Takagi, . C. Ramachandran, M. Bermejo, S. Yamashita, L. X. Yu and G. L. Amidon, "A Provisional Biopharmaceutical Classification of the Top 200 Oral Drug Products in the United States, Great Britain, Spain, and Japan," *Mol. Pharm.*, vol. 3, no. 6, p. 631–643, 2006.
- [14] D. A. Alderman, "A review of cellulose ethers in hydrophilic matrices for oral controlled-release dosage forms.," *International Journal of Pharmaceutical Technology and Product Manufacture*, vol. 5, pp. 1-9, 1984.
- [15] P. Timmins, A. M. Delargy and J. R. Howard, "Optimization and Characterization of a pH Independent Extended-Release Hydrophilic," *Pharmaceutical Development and Technology*, vol. 2(1), pp. 25-31, 1997.
- [16] T. Vasconcelos, B. Sarmiento and P. Costa, "Solid dispersions as strategy to improve oral bioavailability of poor water soluble drugs," *Drug Discovery Today*, vol. 12, no. 23–24, p. 1068–1075, 2007.
- [17] D. J. Good, R. Hartley, N. Mathias, J. Crison, G. Tirucherai, P. Timmins, M. Hussain, R. Haddadin, O. Koo, F. Nikfar and N. K. Fung, "Mitigation of Adverse Clinical Events of a Narrow Target Therapeutic Index Compound through Modified Release Formulation Design: An in Vitro, in Vivo, in Silico, and Clinical Pharmacokinetic Analysis," *Mol. Pharmaceutics*, vol. 12, no. 12, p. 4434–4444, 2015.
- [18] A. T. Serajuddin, "Salt formation to improve drug solubility," *Advanced Drug Delivery Reviews*, vol. 59, no. 7, p. 603–616, 2007.
- [19] A. Y. Abuhelwa, D. B. Williams, R. N. Upton and D. J. R. Foster, "Food, gastrointestinal pH, and models of oral drug absorption," *European Journal of Pharmaceutics and Biopharmaceutics*, vol. 112, p. 234–248, 2017.
- [20] A. Domínguez-Gil Hurlé, A. Sánchez Navarro and M. J. García Sánchez, "Therapeutic drug monitoring of itraconazole and the relevance of pharmacokinetic interactions," *Clinical Microbiology and Infection*, vol. 2, no. 7, pp. 97-106, 2006.
- [21] M. Vogt, Kunath K and J. B. Dressman , "Dissolution improvement of four poorly water soluble drugs by cogrinding with commonly used excipients," *Eur J Pharm Biopharm.*, vol. 68, no. 2, pp. 330-7, 2007.
- [22] H. Kranz and T. Wagner , "Effects of formulation and process variables on the release of a weakly basic drug from single unit extended release formulations," *European Journal of Pharmaceutics and Biopharmaceutics*, vol. 36, no. 1, pp. 70-76, 2006.
- [23] T. Loftsson and M. E. Brewster, "Pharmaceutical applications of cyclodextrins: basic science and product development," *J. Pharm. Pharmacol.*, vol. 62, p. 1607–1621, 2010.
- [24] K. T. Savjani, A. K. Gajjar and J. K. Savjani, "Drug Solubility: Importance and Enhancement Techniques," *ISRN Pharmaceutics*, vol. 2012: 195727, 2012.

- [25] M. Kuentz , R. Holm and D. P. Elder , “Methodology of oral formulation selection in the pharmaceutical industry,” *European Journal of Pharmaceutical Sciences*, vol. 87, pp. 136-163, 2016.
- [26] C. Leuner and J. Dressman, “Improving drug solubility for oral delivery using solid dispersions,” *European Journal of Pharmaceutics and Biopharmaceutics*, vol. 50, no. 1, pp. 47-60, 2000.
- [27] M. Rodriguez-Aller, D. Guillaume, J.-L. Veuthey and R. Gurny, “Strategies for formulating and delivering poorly water-soluble drugs,” *Journal of Drug Delivery Science and Technology*, vol. 30, no. Part B, pp. 342-351, 2015.
- [28] T. Taupitz , J. B. Dressman , C. M. Buchanan and S. Klein, “Cyclodextrin-water soluble polymer ternary complexes enhance the solubility and dissolution behaviour of poorly soluble drugs. Case example: Itraconazole,” *European Journal of Pharmaceutics and Biopharmaceutics*, vol. 83, no. 3, pp. 378-387, 2013.
- [29] T. Loftsson , “Cyclodextrins and the Biopharmaceutics Classification System of Drugs,” *Journal of Inclusion Phenomena and Macrocyclic Chemistry*, vol. 44, no. 6, p. 63–67, 2002.
- [30] W. Chiou and S. Riegelman, “Pharmaceutical applications of solid dispersion systems,” *J. Pharm. Sci.*, vol. 60, pp. 1281-1302, 1971.
- [31] C. W. Pouton, “Formulation of poorly water-soluble drugs for oral administration: Physicochemical and physiological issues and the lipid formulation classification system,” *European Journal of Pharmaceutical Sciences*, vol. 29, no. 3-4, p. 278–287, 2006.
- [32] S. A. Said, H. M. Fatatry and A. S. Geneidi, “Coprecipitates of tolbutamide with polyvinylpyrrolidone and fusion mixtures with macrogol,” *Aust. J. Pharm. Sci.*, vol. 53, pp. 42-45, 1974.
- [33] S. Sinha, M. Ali, S. Baboota, A. Ahuja, A. Kumar and J. Ali, “Solid Dispersion as an Approach for Bioavailability Enhancement of Poorly Water-Soluble Drug Ritonavir,” *AAPS PharmSciTech*, vol. 11, no. 2, p. 518–527, 2010.
- [34] P. Khadka , . J. Ro , H. Kim, I. Kim, J. Tae Kim , H. Kim , J. M. Cho , G. Yun and J. Lee, “Pharmaceutical particle technologies: An approach to improve drug solubility, dissolution and bioavailability,” *Asian Journal of Pharmaceutical Sciences*, vol. 9, pp. 304-316, 2014.
- [35] B. J. Boyd, C. A. Bergström, Z. Vinarov, M. Kuentz, J. Brouwers, P. Augustijns, M. Brandl, A. Bern, A. Bernkop-Schnürch, N. Shrestha, V. Prétat, A. Müllertz, A. Bauer-Brandl and V. Jannin, “Successful oral delivery of poorly water-soluble drugs both depends on the intraluminal behavior of drugs and of appropriate advanced drug delivery systems,” *European Journal of Pharmaceutical Sciences*, vol. 137, p. 104967, 2019.
- [36] D. Fleishera, R. Bong and B. H. Stewart , “Improved dissolution and absorption of ketoconazole in the presence of organic acids as pH-modifiers,” *European Journal of Pharmaceutical Sciences*, vol. 76, pp. 225-230, 2015.

- [37] K. E. Gabr , “Effect of organic acids on the release patterns of weakly basic drugs from inert sustained release matrix tablets,” *European Journal of Pharmaceutics and Biopharmaceutics*, vol. 38, pp. 199-202, 1992.
- [38] “upperton.com,” Upperton Pharma Solutions, [Online]. Available: <https://www.upperton.com/28th-january-2020-tablets-a-general-overview/>. [Accessed 07 May 2020].
- [39] X. Huang and C. S. Brazel, “On the importance and mechanisms of burst release in matrix-controlled drug delivery systems,” *Journal of Controlled Release* , vol. 73, p. 121–136, 2001.
- [40] A. V. Ewing, “ATR-FTIR Spectroscopic Imaging to Study Drug Release and Tablet Dissolution,” London Imperial College, London, 2016.
- [41] T. Rades and . Y. Perrie, “Controlling drug delivery,” in *Fasttrack: Pharmaceutics - Drug Delivery and Targeting*, Pharmaceutical Press, 2009, pp. 1-53.
- [42] C. R. de Azevedo, M. v. Stosch, M. S. Costa, A. M. Ramos, M. M. Cardoso, F. Danhier, V. Préat and R. Oliveira, “Modeling of the burst release from PLGA micro- and nanoparticles as function of physicochemical parameters and formulation characteristics,” *International Journal of Pharmaceutics*, vol. 532, no. 1, pp. 229-240, 2017.
- [43] J. V. Andhariya, R. Jog, J. Shena, J. Shen, S. Choi, Y. Wang, Y. Zou and D. J. Burgess, “In vitro-in vivo correlation of parenteral PLGA microspheres: Effect of variable burst release,” *Journal of Controlled Release*, vol. 314, pp. 25-37, 2019.
- [44] S. R. Pygall , S. Kujawinski , P. Timmins and C. D. Melia , “Mechanisms of drug release in citrate buffered HPMC matrices,” *International Journal of Pharmaceutics*, vol. 370, no. 1-2, pp. 110-120, 2009.
- [45] Y. Hee Yun, L. Byung Kook and K. Park, “Controlled Drug Delivery: Historical perspective for the next the next generation,” *Journal of Control Release*, vol. 219, p. 2–7, 2015.
- [46] A. Singh, H. Dubey, I. Shukla and D. P. Singh, “Pulsatile Drug Delivery System: an Approach of Medication according to Circadian Rhythm,” *Journal of Applied Pharmaceutical Science*, vol. 02, no. 03, pp. 166-176, 2012.
- [47] J. Van Der Weerd and S. G. Kazarian, “Release of Poorly Soluble Drugs from HPMC Tablets Studied by FTIR Imaging and Flow-Through Dissolution Tests,” *Journal of Pharmaceutical Sciences*, vol. 94, p. 2096–2109, 2005.
- [48] V. Gray, G. Kelly, M. Xia, C. Butler, S. Thomas and S. Mayock, “The Science of USP 1 and 2 Dissolution: Present Challenges and Future Relevance,” *Pharm. Res.*, pp. 26, 1289–1302, 2009.
- [49] F. Tres, J. D. Patient, P. M. Williams, K. Treacher, J. Booth, L. P. Hughes, S. A. C. Wren, J. W. Aylott and J. C. Burley, “Monitoring the Dissolution Mechanisms of Amorphous Bicalutamide Solid Dispersions via Real-Time Raman Mapping,” *Mol. Pharmaceutics*, vol. 12, no. 5, p. 1512–1522, 2015.

- [50] S. Kazarian and K. L. Chan, "Applications of ATR-FTIR spectroscopic imaging to biomedical samples," *Biochimica et Biophysica Acta (BBA) - Biomembranes*, vol. 1758, no. 7, p. 858–867, 2006.
- [51] J. C. Richardson, R. W. Bowtell, K. Mäder and C. D. Melia, "Pharmaceutical applications of magnetic resonance imaging (MRI).," *Advanced Drug Delivery Reviews*, vol. 57, no. 8, pp. 1191-1209, 2005.
- [52] H. D. Williams , R. Ward , A. Culy, I. J. Hardy and C. D. Melia, "Designing HPMC matrices with improved resistance to dissolved sugar," *International Journal of Pharmaceutics*, vol. 401, no. 1-2, pp. 51-59, 2010.
- [53] L. Weiyong, A. Woldu, L. Araba and D. Winstead, "Determination of Water Penetration and Drug Concentration Profiles in HPMC-Based Matrix Tablets by Near Infrared Chemical Imaging," *Journal of Pharmaceutical Sciences*, vol. 99, no. 7, pp. 3081-3088, 2010.
- [54] K. L. A. Chan, S. V. Hammond and S. G. Kazarian, "Applications of Attenuated Total Reflection Infrared Spectroscopic Imaging to Pharmaceutical Formulations," *Anal. Chem.*, vol. 75, pp. 2140-2146, 2003.
- [55] H. Keles , A. Naylor , F. Clegg and C. Sammon, "Studying the release of hGH from gamma-irradiated PLGA microparticles using ATR-FTIR imaging," *Vibrational Spectroscopy*, vol. 71, p. 76–84, 2014.
- [56] P. S. Wray , W. E. Sinclair, J. W. Jones and G. S. Clarke, "The use of in situ near infrared imaging and Raman mapping to study the disproportionation of a drug HCl salt during dissolution," *International Journal of Pharmaceutics*, vol. 493, pp. 198-207, 2015.
- [57] K. Punčochová , A. V. Ewing , M. Gajdošová , N. Sarvašová, S. Kazarian, J. Beránek and F. Štěpánek, "Identifying the mechanisms of drug release from amorphous solid dispersions using MRI and ATR-FTIR spectroscopic imaging," *International Journal of Pharmaceutics*, vol. 483, no. 1–2, p. 256–267, 2015.
- [58] P. S. Wray, G. S. Clarke and S. G. Kazarian, "Application of FTIR Spectroscopic Imaging to Study the Effects of Modifying the pH Microenvironment on the Dissolution of Ibuprofen from HPMC Matrices," *Journal of Pharmaceutical Sciences*, vol. 100, no. 11, pp. 4745-4755, 2011.
- [59] F. D. Zahoor, K. T. Mader, P. Timmins, J. Brown and C. Sammon, "Investigation of Within-Tablet Dynamics for Extended Release of a Poorly Soluble Basic Drug from Hydrophilic Matrix Tablets Using ATR-FTIR Imaging," *Mol. Pharmaceutics* , vol. 17, no. 4, p. 1090–1099, 2020.
- [60] S. G. Kazarian and K. L. A. Chan, "ATR-FTIR spectroscopic imaging: recent advances and applications to biological systems," *Analyst*, vol. 138, pp. 1940-1951, 2013.
- [61] K. L. A. Chan, S. V. Hammond and S. G. Kazarian, "Applications of Attenuated Total Reflection Infrared Spectroscopic Imaging to Pharmaceutical Formulations," *Anal. Chem.*, vol. 75, no. 9, pp. 2140-2146, 2003.

- [62] C. Coutts-Lendon, N. Wright, E. V. Mieso and J. L. Koenig, "The use of FTIR imaging as an analytical tool for the characterization of drug delivery," *J. Controlled Release*, vol. 93, p. 223–248, 2003.
- [63] A. Ewing, G. Clarke and S. G. Kazarian, "Stability of indomethacin with relevance to the release from amorphous solid dispersions studied with ATR-FTIR spectroscopic imaging," *European Journal of Pharmaceutical Sciences*, vol. 60, p. 64–71, 2014.
- [64] K. Chan and S. Kazarian, "Visualisation of the heterogeneous water sorption in a pharmaceutical formulation under controlled humidity via FT-IR imaging," *Vibrational Spectroscopy*, vol. 35, no. 1-2, pp. 45-49, 2004.
- [65] J. Van der Weerd and S. G. Kazarian, "Combined approach of FTIR imaging and conventional dissolution tests applied to drug release," *Journal of Controlled Release*, vol. 98, no. 2, p. 295– 305, 2004.
- [66] H. Hifumia, A. V. Ewing and S. G. Kazarian, "ATR-FTIR spectroscopic imaging to study the drying and dissolution of pharmaceutical polymer-based films," *International Journal of Pharmaceutics*, vol. 515, no. 1-2, p. 57–68, 2016.
- [67] A. V. Ewing, G. S. Clarke and S. G. Kazarian, "Attenuated total reflection-Fourier transform infrared spectroscopic imaging of pharmaceuticals in microfluidic devices," *Biomicrofluidics*, vol. 10, no. 2, 2016.
- [68] A. Eustaquio, P. Graham, R. D. Jee, A. C. Moffatt and A. D. Trafford, "Quantification of paracetamol in intact tablets using near-infrared transmittance spectroscopy," *Analyst*, vol. 123, p. 2303–2306, 1998.
- [69] A. V. Ewing and S. G. Kazarian, "Recent advances in the applications of vibrational spectroscopic imaging and mapping to pharmaceutical formulations," *Spectrochimica Acta Part A: Molecular and Biomolecular Spectroscopy*, vol. 197, pp. 10-29, 2018.
- [70] P. Timmins, D. Desai, W. Chen, P. Wray, J. Brown and S. Hanley, "Advances in mechanistic understanding of release rate control mechanisms of extended-release hydrophilic matrix tablets," *Therapeutic delivery*, vol. 7, no. 8, p. 553–572, 2016.
- [71] L. K. N. Nihar R. Pani, "Development of controlled release tablet by optimizing HPMC: Consideration of theoretical release and RSM," *Carbohydrate Polymers*, vol. 104 , p. 238–245, 2014.
- [72] J. Pajander, S. Baldursdottir, J. Rantanen and J. Østergaard, "Behaviour of HPMC compacts investigated using UV-imaging," *International Journal of Pharmaceutics*, vol. 427, no. 2, p. 345–353, 2012.
- [73] C. Ding, M. Zhang and G. Li, "Preparation and characterization of collagen/hydroxypropyl methylcellulose (HPMC) blend film," *Carbohydrate Polymers*, vol. 119, p. 194–201, 2015.

- [74] M. V. Varma, A. M. Kaushal, A. Garg and S. Garg, "Factors Affecting Mechanism and Kinetics of Drug Release from Matrix-Based Oral Controlled Drug Delivery Systems," *American Journal of Drug Delivery*, vol. 2, no. 1, pp. 43-57, 2004.
- [75] S. Baghel, H. Cathcart and N. J. O'Reilly, "Polymeric Amorphous Solid Dispersions: A Review of Amorphization, Crystallization, Stabilization, Solid-State Characterization, and Aqueous Solubilization of Biopharmaceutical Classification System Class II Drugs," *Journal of Pharmaceutical Sciences*, vol. 105, no. 9, pp. 2527-2544, 2016.
- [76] J. Siepmann and N. A. Peppas, "Modeling of drug release from delivery systems based on hydroxypropyl methylcellulose (HPMC)," *Advanced Drug Delivery Reviews*, vol. 48, no. 2-3, p. 139-157, 2001.
- [77] DOW, "Using METHOCEL Cellulose Ethers for Controlled Release of Drugs in Hydrophilic Matrix Systems," July 2000. [Online]. Available: <https://www.colorcon.com/products-formulation/all-products/download/677/2063/34?method=view>. [Accessed 09 04 2020].
- [78] G. Burdock, "Safety assessment of hydroxypropyl methylcellulose as a food ingredient," *Food and Chemical Toxicology*, vol. 45, no. 12, p. 2341-2351, 2007.
- [79] J. L. Ford, "Design and Evaluation of Hydroxypropyl Methylcellulose Matrix Tablets for Oral Controlled Release: A Historical Perspective," in *Hydrophilic Matrix Tablets for Oral Controlled Release*, P. Timmins, S. R. Pygall and D. R. Melia, Eds., New York, AAPS Advances in the Pharmaceutical Sciences Series, vol 16. Springer, 2014, pp. 17-51.
- [80] H. C. Arca, L. I. Mosquera-Giraldo, V. Bi, L. S. Taylor and K. J. Edgar, "Pharmaceutical Applications of Cellulose Ethers and Cellulose Ethers," *Biomacromolecules*, vol. 19, no. 7, p. 2351-2376, 2018.
- [81] A. Nokhodchi, S. Raja, P. Patel and K. Asare-Addo, "The Role of Oral Controlled Release Matrix Tablets in Drug Delivery Systems," *BioImpacts*, vol. 2, no. 4, pp. 175-187, 2012.
- [82] P. Colombo, R. Bettini, G. Massimo, P. L. Catellani, P. Santi and N. Peppas, "Drug diffusion front movement is important in drug release control from swellable matrix tablets," *Journal of Pharmaceutical Sciences*, vol. 84, no. 8, p. 991-997, 1995.
- [83] R. Bettini, P. L. Catellani, P. Santi, G. Massimo, N. A. Peppas and P. Colombo, "Translocation of drug particles in HPMC matrix gel layer: effect of drug solubility and influence on release rate," *Journal of Controlled Release*, vol. 70, no. 3, p. 383-391, 2001.
- [84] P. Sakellariou, R. C. Rowe and E. F. White, "The thermomechanical properties and glass transition temperatures of some cellulose derivatives used in film coating," *International Journal of Pharmaceutics*, vol. 27, no. 2-3, pp. 267-277, 1985.
- [85] C. Maderuelo, A. Zarzuelo and J. M. Lanao, "Critical factors in the release of drugs from sustained release hydrophilic matrices," *Journal of Controlled Release*, vol. 154, no. 1, pp. 2-19, 2011.

- [86] M. U. Ghorri and B. R. Conway, "Hydrophilic Matrices for Oral Control Drug Delivery," *American Journal of Pharmacological Sciences*, vol. 3, no. 5, pp. 103-109, 2015.
- [87] J. Siepmann, H. Kranz, R. Bodmeier and N. A. Peppas, "HPMC-matrices for controlled drug delivery: a new model combining diffusion, swelling, and dissolution mechanisms and predicting the release kinetics. Pharmaceutical mechanisms and predicting the release kinetics.," *Pharmaceutical Research*, vol. 16, no. 11, pp. 1748-56, 1999.
- [88] P. Colombo, R. Bettini, P. Santi and N. A. Peppas, "Swellable matrices for controlled drug delivery: gel-layer behaviour, mechanisms and optimal performance," *Pharmaceutical Science & Technology Today*, vol. 3, no. 6, pp. 198-204, 2000.
- [89] S. D. Novaka, E. Šporara, S. Baumgartnerb and F. Vrečer, "Characterization of physicochemical properties of hydroxypropyl methylcellulose (HPMC) type 2208 and their influence on prolonged drug release from matrix tablets," *Journal of Pharmaceutical and Biomedical Analysis*, vol. 66, p. 136–143, 2012.
- [90] J. L. Ford, M. H. Rubinstein and J. E. Hogan, "Formulation of sustained release promethazine hydrochloride tablets using hydroxypropyl-methylcellulose matrices," *International Journal of Pharmaceutics*, vol. 24, no. 2-3, pp. 327-338, 1985.
- [91] J. L. Ford, M. H. Rubinstein and J. E. Hogan, "Propranolol hydrochloride and aminophylline release from matrix tablets containing hydroxypropylmethylcellulose," *International Journal of Pharmaceutics*, vol. 24, no. 2-3, pp. 339-350, 1985.
- [92] R. M. S. Roy, S. Das, M. K. Jha, T. Begum, M. Q. Ahsan, M. S. Islam and M. S. Reza, "Evaluation of various grades of hydroxypropyl methylcellulose matrix systems as oral sustained release drug delivery systems," *Journal of Pharmaceutical Sciences and Research*, vol. 3, pp. 930-938, 2011.
- [93] A. Nokhodchi, M. H. Rubinstein and J. L. Ford, "The effect of particle size and viscosity grade on the compaction properties of hydroxypropylmethylcellulose 2208," *International Journal of Pharmaceutics*, vol. 126, pp. 189-197, 1995.
- [94] K. Mitchell, J. L. Ford, D. J. Armstrong, P. N. Elliott, J. E. Hogan and C. Rostron, "The influence of the particle size of hydroxypropylmethylcellulose K15M on its hydration and performance in matrix tablets," *International Journal of Pharmaceutics*, vol. 100, no. 1-3, pp. 175-179, 1993.
- [95] M. E. Campos-Aldrete and L. Villafuerte-Robles, "Influence of the viscosity grade and the particle size of HPMC on metronidazole release from matrix tablets," *European Journal of Pharmaceutics and Biopharmaceutics*, vol. 43, no. 2, pp. 173-178, 1997.
- [96] J. Alder, A. Jayan and C. Melia, "A Method for Quantifying Differential Expansion within Hydrating Hydrophilic Matrixes by Tracking Embedded Fluorescent Microspheres," *Journal of Pharmaceutical Sciences*, vol. 88, no. 3, pp. 371-377, 1999.

- [97] K. Asare-Addo, M. Levina, A. R. Rajabi-Siahboomi and A. Nokhodchi, "Effect of ionic strength and pH of dissolution media on theophylline release from hypromellose matrix tablets—Apparatus USP III, simulated fasted and fed conditions," *Carbohydrate Polymers*, vol. 86, no. 1, pp. 85-93, 2011.
- [98] G. S. Bajwa, K. Hoebler, C. Sammon, P. Timmins and C. D. Melia, "Microstructural imaging of early gel layer formation in HPMC matrices," *Journal of Pharmaceutical Sciences*, vol. 95, no. 10, pp. 2145-2157, 2006.
- [99] U. Mikac, A. Sepe, J. Kristl and S. Baumgartner, "A new approach combining different MRI methods to provide detailed view on swelling dynamics of xanthan tablets influencing drug release at different pH and ionic strength," *Journal of Controlled Release*, vol. 145, no. 3, pp. 247-256, 2010.
- [100] X. Ming Xu, Y. M. Song, Q. N. Ping, Y. Wang and X. Y. Liu, "Effect of Ionic Strength on the Temperature-Dependent Behavior of Hydroxypropyl Methylcellulose Solution and Matrix Tablet," *Journal of Applied Polymer Science*, vol. 102, no. 4, pp. 4066-4074, 2006.
- [101] P. Gao and R. H. Meury, "Swelling of hydroxypropyl methylcellulose matrix tablets. 1. Characterization of swelling using a novel optical imaging method," *Journal of Pharmaceutical Sciences*, vol. 85, no. 7, pp. 725-731, 1996.
- [102] P. Gao and R. H. Meury, "Swelling of hydroxypropyl methylcellulose matrix tablets. 2. Mechanistic study of the influence of formulation variables on matrix performance and drug release," *Journal of Pharmaceutical Sciences*, vol. 85, no. 7, pp. 732-740, 1996.
- [103] S. Zuleger, R. Fassihi and B. C. Lippold, "Polymer particle erosion controlling drug release. II. Swelling investigations to clarify the release mechanism," *International Journal of Pharmaceutics*, vol. 274, pp. 23-37, 2002.
- [104] V. Mazzini and V. S. J. Craig, "What is the fundamental ion-specific series for anions and cations? Ion specificity in standard partial molar volumes of electrolytes and electrostriction in water and non-aqueous solvents," *Chem. Sci.*, vol. 8, p. 7052–7065, 2017.
- [105] H. D. Williams, R. Ward and I. J. Hardy, "The extended release properties of HPMC matrices in the presence of dietary sugars," *Journal of Controlled Release*, vol. 138, no. 3, pp. 251-259, 2009.
- [106] J. Siepmann and N. A. Peppas, "Higuchi equation: Derivation, applications, use and misuse," *International Journal of Pharmaceutics*, vol. 418, no. 1, pp. 6-12, 2011.
- [107] J. Siepmann and N. A. Peppas, "Modeling of drug release from delivery systems based on hydroxypropyl methylcellulose (HPMC)," *Advanced Drug Delivery Reviews*, vol. 64, pp. 163-174, 2012.
- [108] K. K. Jain, *Drug Delivery Systems*, Springer Science & Business Media, 2008.
- [109] T. Parikh, H. K. Sandhu, T. T. Talele and A. T. M. Serajuddin, "Characterization of Solid Dispersion of Itraconazole Prepared by Solubilization in Concentrated

Aqueous Solutions of Weak Organic Acids and Drying," *Pharmaceutical Research*, vol. 33, no. 6, pp. 1456-1471, 2016.

[110] T. Tao, Y. Zhao, J. Wu and B. Zhou, "Preparation and evaluation of itraconazole dihydrochloride," *International Journal of Pharmaceutics*, vol. 367, p. 109–114, 2009.

[111] F. C. Odds, "Itraconazole — a new oral antifungal agent with a very broad spectrum of activity in superficial and systemic mycoses," *Journal of Dermatological Science*, vol. 5, no. 2, pp. 65-72, 1993.

3.0 Experimental

3.1 Analytical Techniques

3.1.1 Infrared Spectroscopy

3.1.1.1 Electromagnetic Radiation

The electromagnetic spectrum encompasses a range of radiation types including visible, IR and UV light, microwaves and radio waves (Fig. 3.1). These all travel at the same speed however, they differ in their wavelength and frequency.

Frequency ν is defined as the number of wave cycles that pass through a point in one second and is measured in Hertz (Hz).

Wavelength λ is the length of one complete wave cycle and is measured in metres (m).

The wavelength is inversely proportional to the frequency as shown by the following equation:

$$\nu = c/\lambda \quad \text{Equation 3.1}$$

Where c is the speed of light

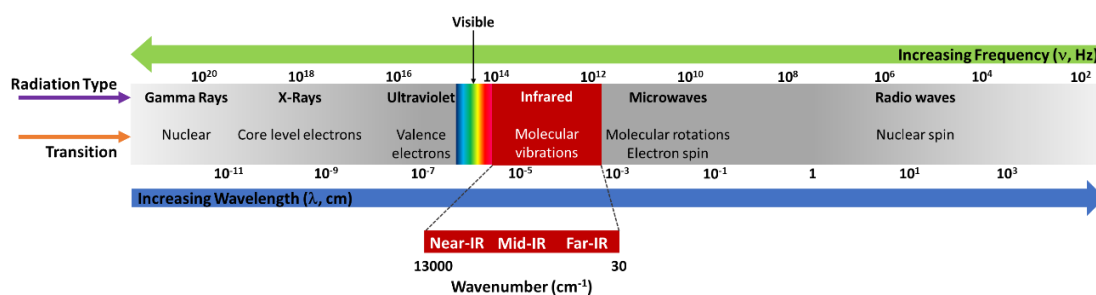


Fig. 3.1: The electromagnetic spectrum highlighting the infrared region

Light consists of discrete packets of energy referred to as photons. The energy of a photon is the product of its frequency and Planck's constant. Infrared spectroscopy is the study of transitions of molecules between different quantised energy levels. In this process a photon from the incident infrared radiation source excites a molecule which

undergoes a transition from ground state to a higher energy state as shown in Fig. 3.2 below.

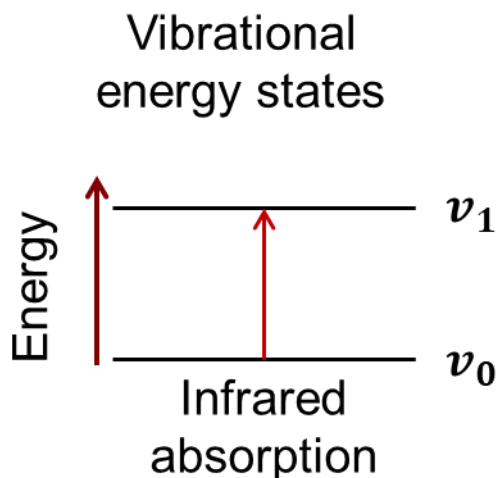


Fig. 3.2: Simplified vibrational energy level diagram showing the transition that occurs when infrared light is absorbed by a molecule

The difference in energy between any two energy levels determines the frequency of light absorbed during a transition between the two levels. The energy of the light emitted from a particular transition can be calculated according to the *Bohr-Einstein* condition:

$$\Delta E = |E_1 - E_0| = h\nu \quad \text{Equation 3.2}$$

where ν the frequency of the light absorbed/emitted and h is Planck's constant. $h\nu$ is a quantum of energy referred to as a photon.

Vibrational spectroscopists and chemists use the reciprocal wavelength ($1/\lambda$) which is the number of wavelengths per unit distance (typically quoted in cm^{-1}) as a measure of the frequency of radiation. This is represented by the following:

$$\bar{\nu} = \frac{1}{\lambda} = \frac{\nu}{c} \quad \text{Equation 3.3}$$

3.1.1.2 Absorbance and Transmittance Relationship and Beer Lambert Law

As light passes through a sample, a degree of absorption takes place and this attenuation of radiation can be described quantitatively by transmittance and absorbance (Equation. 3.4 and 3.5 respectively).

$$T = \frac{I}{I_0}$$

Equation 3.4

$$A = -\log T = -\log \frac{I}{I_0}$$

Equation 3.5

Where I is the light intensity after it passes through the sample and I_0 is the initial light intensity.

It is possible to quantitatively measure the degree of absorption based on the Beer-Lambert Law and the concentration of the compound of interest can be determined from the IR absorbance using the following equation:

$$A = \epsilon cl$$

Equation 3.6

where A is the absorption, ϵ is the molar absorptivity, l is the pathlength, and c is the concentration of the specific analyte.

Absorbance is the more accepted unit for expressing the attenuation of radiation because it has a linear relationship with the concentration of the analyte.

3.1.1.3 The IR Spectral Region and Molecular Spectroscopy

The IR region can be subdivided into three portions (Fig. 3.1):

- 1) Near IR 13,000 to 4,000 cm^{-1}
- 2) Mid IR 4000 to 400 cm^{-1}
- 3) Far IR 400 to 10 cm^{-1}

Infrared radiation can be considered as primarily thermal energy, which induces strong molecular vibrations in covalent bonds. However, not all the vibrations within a given molecule will give rise to an absorption band in the infrared region. For a material to absorb radiation in the infrared region there must be resonance among the frequencies of the infrared radiation and molecular vibration and a change in the dipole moment must take place.

The simplest theoretical model of vibrational spectroscopy is that of vibrations of a harmonic oscillator [1]. The atomic stretching can be approximated by a mechanical model corresponding to a mass m connected to a spring with no mass displacement of the molecule along the axis of the spring [2].

If the spring obeys Hooke's law, the strength, f , applied is proportional to the molecule movement according to:

$$f = -kx \quad \text{Equation 3.7}$$

where k is the spring constant and x is displacement of the molecule.

From this equation the potential energy and vibrational energy can be determined:

$$k = 4\pi^2\nu^2m \quad \text{Equation 3.8}$$

With this approach the frequency is only dependent on k and m and can be improved using quantum mechanics. Vibrational energy like all the energies of the molecule are quantised and can be calculated from the Schrödinger equation [3] [4]:

$$E_v = h\nu \left(n + \frac{1}{2} \right) \quad \text{Equation 3.9}$$

h is Planck's constant

ν is the fundamental vibrational energy

n is the vibrational quantum number (0,1,2,3,..)

For a diatomic model the harmonic model can be used to calculate fundamental frequencies observed in a spectrum.

Hooke's law can be transformed to reflect this:

$$\nu = \frac{1}{2\pi c} \sqrt{\frac{k}{\mu}} \qquad \mu = \frac{m_1 m_2}{m_1 + m_2} \qquad \text{Equation 3.10}$$

ν = frequency

c = speed of light

k = force constant (bond strength)

μ = reduced mass

The vibrational frequencies of a chemical bond are affected by the mass of the atoms in the bond and the strength of the bond. This relationship can be explained by Hooke's law (Equation 3.10).

In accordance with Hooke's law:

- 1) Frequency is directly related to bond strength. The stronger the bond, the faster the bonds vibrate and therefore absorbance will occur at higher frequencies. Therefore, a C=C stretching vibration is observed at a higher frequency than that of C-C.
- 2) The lighter the atoms linked by the bond, the faster the bond vibrates, resulting in radiation absorbance of higher frequencies.

Molecules vibrate in many different ways (vibrational modes) and these range from the simple motions of two atoms in a diatomic molecule to the complex motions of atoms in a polyatomic molecule. Consider a molecule with N atoms; each of these atoms can undergo translational, vibrational and rotational motion in the x , y and z direction, i.e. $3N$

degrees of freedom. Three degrees of freedom are needed to describe the position in Cartesian space of the molecule and, in the case of a non-linear polyatomic, three more degrees of freedom are needed to describe the rotational motion of the molecule. The remaining $3N - 6$ degrees of freedom describe the fundamental vibrations of that molecule, e.g. water (Fig. 3.3(a)). In the case of linear molecules, only two degrees of freedom are required to describe the rotational motion, leaving $3N - 5$ fundamental vibrational modes. Carbon dioxide is an example of a linear molecule (Fig. 3.3(b)) [2] [5].

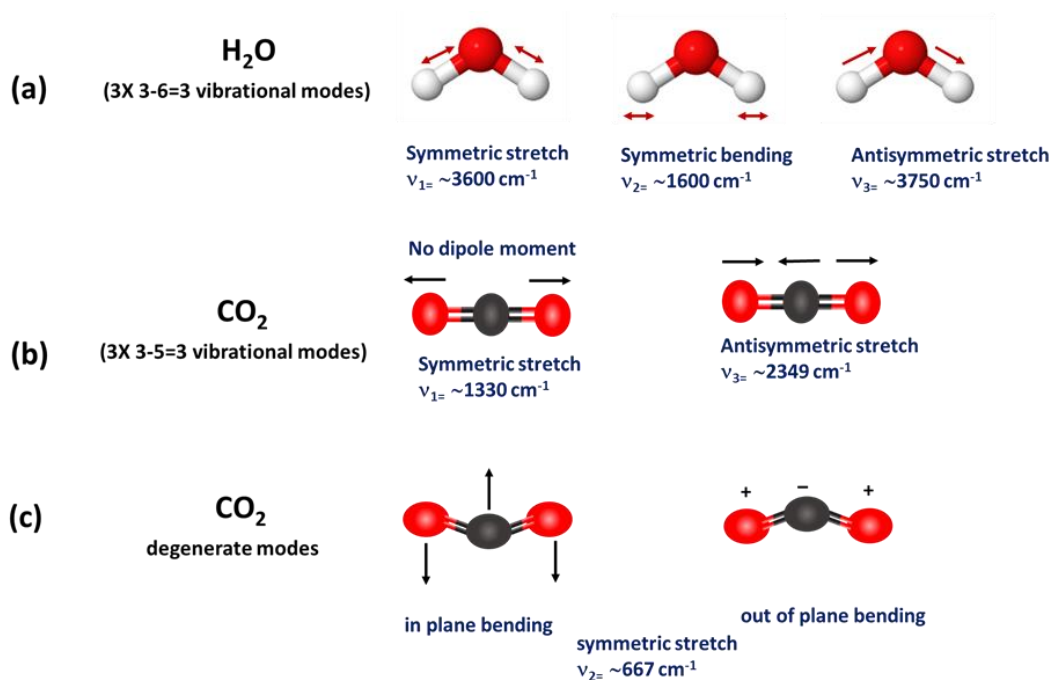


Fig. 3.3: Schematic diagram of the vibrational modes of (a) water; (b) carbon dioxide; (c) degenerate modes carbon dioxide

There are two types of molecular vibrations referred to as stretching and bending. Stretching changes the bond length and bending vibrations change the bond angle and there are four types of bending vibrations (rocking, scissoring, wagging and twisting).

3.1.1.4 Practical Aspects of IR Spectroscopy

3.1.1.4.1 FTIR spectrometer

An FTIR spectrometer is typically based on a Michelson Interferometer as shown in Fig. 3.4. This consists of a beam splitter, a fixed mirror and a moving mirror. The interferometer divides the beam of radiation using a beam splitter, generating a path

difference between the beams resulting in constructive and destructive interference. The beams are recombined to produce an interference signal measured as a function of optical path difference by a detector and known as an interferogram. The interferogram is a function of time and is converted to the frequency domain by a mathematical approach known as Fourier transform to provide a spectrum (Fig. 3.5).

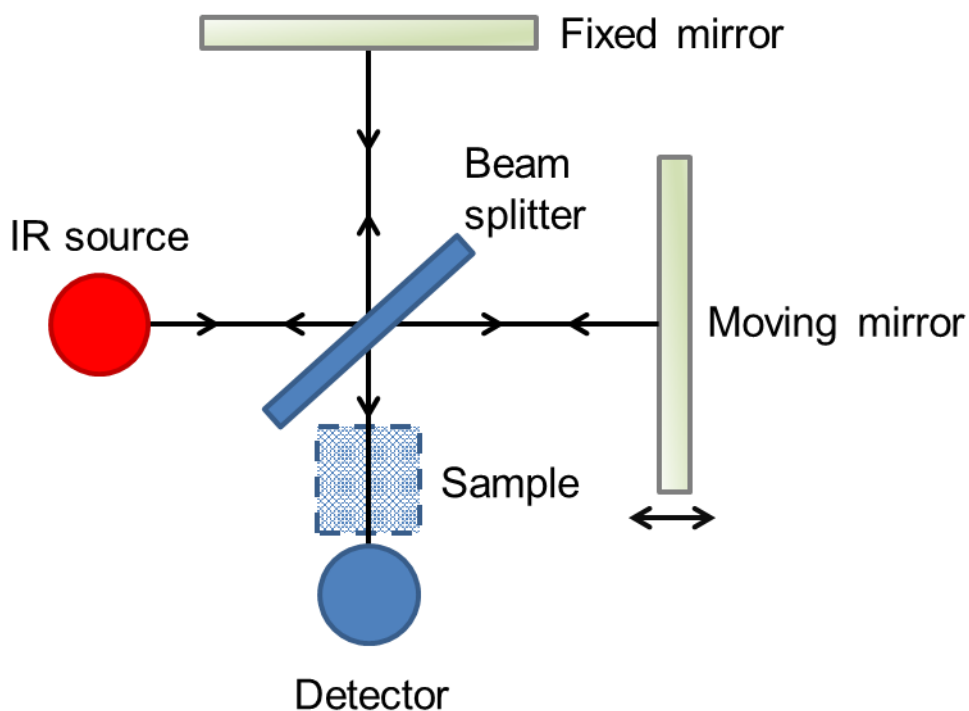


Fig. 3.4: Schematic of Michelson Interferometer

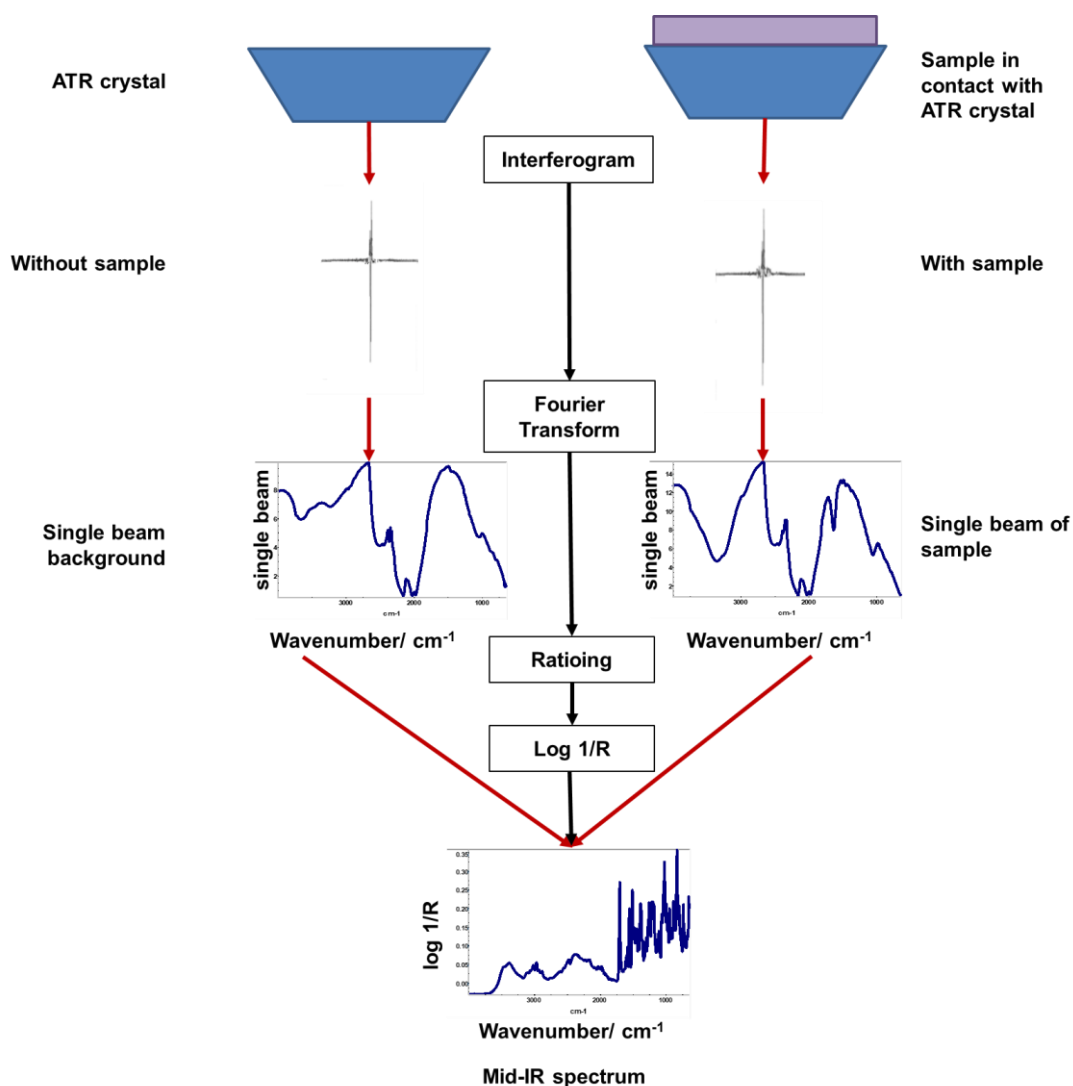


Fig. 3.5: Schematic overview showing the process of generating of a mid- FTR spectrum using Attenuated Total Reflectance. Adapted from [6]

3.1.1.4.2 Detectors Used for FTIR

There are two basic categories of detectors used for infrared spectroscopy, either thermal detectors or photoconducting (also known as 'photon') detectors.

Thermal detectors are made from materials such as deuterated triglycine sulfate (DTGS). These operate at room temperature and can be used over a wide spectral range. This type of detector measures the total energy absorbed from the infrared beam by detecting changes in temperature of an absorbing material. This category of detectors can be further subdivided into different types i.e. thermocouples, pyroelectric detectors and bolometers. The main disadvantages with these types of detectors are a slow response time and lower sensitivity relative to other types of detectors [7].

Photon detectors consist of semiconductor-based materials, such as mercury cadmium telluride (MCT) or lead sulfide. The photons of radiation are absorbed by the semiconductor material producing electrons which can be measured. Commercially, these detectors are sold as narrow band gap (type A). Altering the mercury:cadmium ratio influences the bandwidth, thereby impacting on the operating spectral range [7]. The MCT-A detectors operate at the temperature of liquid nitrogen (-196 °C). The major advantage of this type of detector is their sensitivity and speed compared to the DTGS resulting in an improved signal-to-noise ratio (S/N) [7] [8].

3.1.1.4.3 Optimisation of Spectral Acquisition

FTIR spectrometers are based on rapid scans and signal to noise can be reduced by adding multiple scans together in a process known as co-adding. The SNR is directly proportional to the square root of the number of scans used to collect the data [9].

$$SNR \propto \sqrt{\text{number of scans}} \quad \text{Equation 3.11}$$

In FTIR the resolution relates to the ability of the spectrometer to distinguish between two closely spaced spectral features. An increase in spectral resolution is achieved by increasing the optical retardation (optical path difference between stationary and moving mirrors).

However, there is trade-off between increasing the resolution and the S/N, as high-resolution spectra will have more noise. Also, increasing the resolution and the number of scans will generate a longer collection time [6].

Most FTIR spectrometers have a laser, usually HeNe and the main purpose of this is to determine the precise position of the moving mirror and hence the optical path difference [6] [10].

3.1.1.4.4 Transmission IR Spectroscopy

This is a commonly used approach for FTIR measurements and this technique can be used for analysing solid, liquid and gas samples. In transmission mode, the sample is placed directly into the infrared beam. As the IR beam passes through the sample, the transmitted energy is measured (Fig. 3.6). In a transmission measurement a spectrum is collected that is an average of the bulk properties of the sample. In order to analyse a solid material in transmission mode, sample preparation is usually required before the analysis and a prerequisite is that the sample must be optically transparent in order to ensure the light is being transmitted to the detector. Sample preparation can be time consuming and ensuring a transparent sample is produced can be problematic. Powdered samples are diluted with a non-absorbing material such as potassium bromide and pressed, producing a transparent disc for analysis. Other approaches include dispersing solid materials in a nujol mull (mineral oil). Nujol mull is an ideal choice as it has a limited number of absorbance bands in the IR region [11]. Analysis of liquids is carried out by sandwiching the material between two IR transparent windows usually of an alkali halide such as sodium chloride.

The transmission approach is used extensively to analyse thin samples because of the requirement for short pathlengths (<10 μm) therefore suited for thin films or tissues, however it cannot be used to analyse thick samples such as tablets [12].

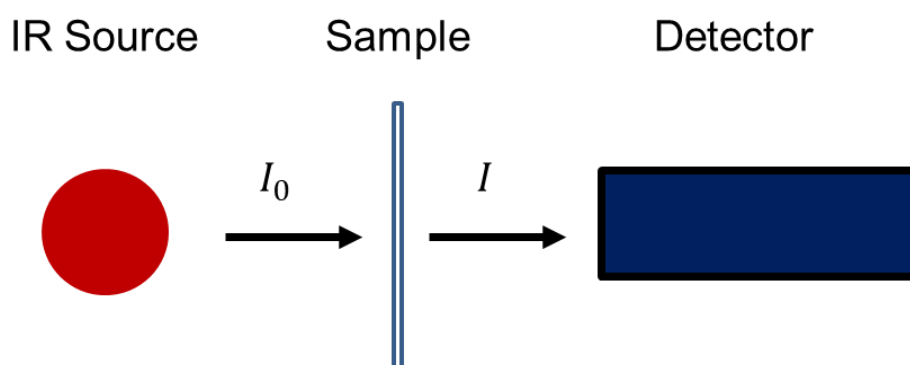


Fig. 3.6: Schematic representation of transmission experimental setup

3.1.1.4.5 ATR-FTIR

Attenuated total reflectance (ATR) is based on a beam of radiation propagating through a crystal of high refractive index at an angle greater than the critical angle which undergoes total internal reflection when it reaches an interface with a material with a lower refractive index (e.g. air or a sample surface). A schematic of the ATR principle is shown in Fig. 3.7. The critical angle can be defined in accordance with Snell's law (Equation 3.12).

$$\theta_c = \sin^{-1} \left(\frac{n_2}{n_1} \right) \quad \text{Equation 3.12}$$

Where n_1 and n_2 are the refractive indices of the ATR crystal and the sample in contact respectively [13].

An evanescent wave forms which decays a few micrometres beyond the crystal surface into the sample, consequently ATR only probes the near-surface of a sample. An exponential decay of the evanescent field is observed in the less dense medium in accordance with the following equation [14] [15]:

$$E = E_0 \exp \left[- \frac{2\pi}{\lambda_1} (\sin^2 \theta - n_{21}^2)^{\frac{1}{2}} Z \right] \quad \text{Equation 3.13}$$

E is the value of the electric field at distance Z into the sample

E_0 is the electric field amplitude at the surface of the sample

θ is angle of incidence

λ_1 is wavelength of the radiation in the ATR crystal in air

n_{21} is the ratio of the refractive indices ($n_{21} = n_2 / n_1$)

Harrick and du Pre provide a description for the distance through which the evanescent wave travels using penetration depth (d_p) which is defined as the depth E_0 at which the electric field amplitude falls to a value $E = E_0 \exp^{-1}$ (evanescent wave intensity exponentially decays to e^{-1} of its value at the interface (Fig. 3.7) and is defined by the following equation [12] [14] [16]:

$$d_p = \frac{\lambda}{2\pi n_1 \sqrt{\sin^2 \theta - (n_1/n_2)^2}} \quad \text{Equation 3.14}$$

λ is the wavelength of light

θ is the angle of incidence

Researchers have shown in practice the actual sampling depth is approximately $3 \times d_p$ [15].

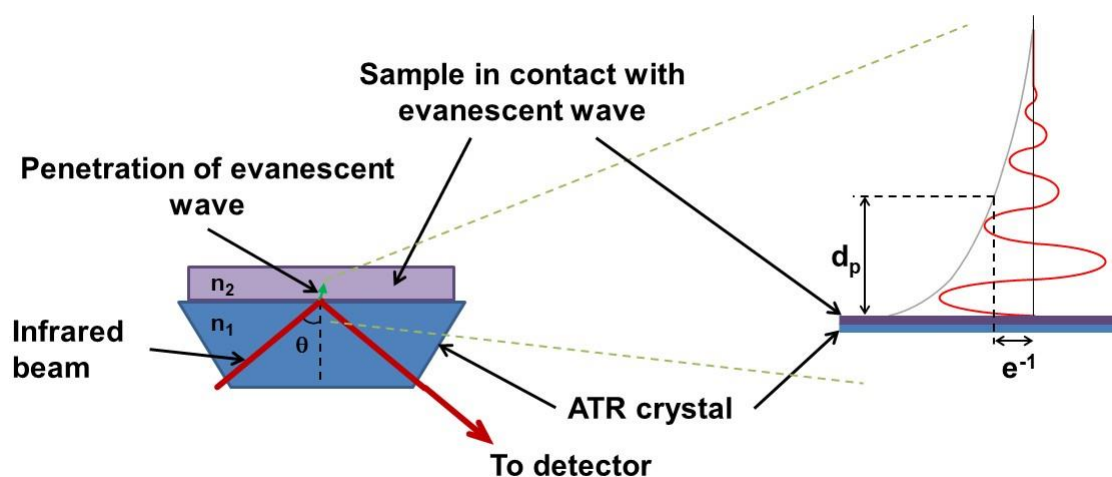


Fig. 3.7: Schematic explaining ATR principle. Adapted from [14] [17]

From equation 3.14 the depth of penetration of the IR beam is determined by the refractive index (RI) of the IR transparent ATR crystal. Because it is preferable to have a small depth of penetration, materials with a high refractive index are predominantly used, as attenuated total reflectance is not achievable with materials of a low refractive index. A range of different materials are available for ATR crystals and these are outlined in Table 3.1. The refractive index of the crystal must be significantly greater than that of the sample or else internal reflectance will not occur. Diamond (RI = 2.4) crystals are generally commonly used as they are chemically inert to corrosive materials and more robust in terms of hardness and durability. However, materials containing a high proportion of carbon black (filler) content such as tyres are inherently difficult to analyse with a diamond ATR crystal and the spectra generated from these materials can be distorted and dominated by a sloping baseline. This is due to a mismatch of the refractive

index of the ATR crystal and that of the sample, therefore germanium (RI = 4) or silicon (RI = 3.4) are usually more suitable crystals (Table 3.1) for these types of materials [18].

The ATR-FTIR approach is becoming increasingly popular in the medical field for detection of brain tumours from analysis of blood serum [19]. This provides rapid confirmation and avoids lengthy delays in diagnosis [19]. Researchers have shown this approach to be capable of discriminating between cancerous and non-cancerous blood serum and determine the cancer severity relatively quickly (10 min) using 1 μ l of serum from a patient with an FTIR with ATR configuration and diamond crystal [20].

One of the advantages of the ATR-FTIR methodology is that solids, liquids and powders can be analysed without the requirement for any sample preparation or sample dilution. However, good optical contact must be established between the ATR crystal and sample, otherwise this can result a poor quality spectrum. Also, for comparative purposes applying a set/constant pressure is crucial, this is generally overcome with the use of a torque wrench set to an appropriate value.

Table 3.1: Properties of commonly used ATR crystals [21]

Material	Refractive Index	Spectral Range (cm⁻¹)	Depth of penetration at 45°, 1000 cm⁻¹ (μm)	Hardness (Knoop)
Diamond	2.40	45,000-10	1.66	9000
ZnSe	2.43	20,000-500	1.66	130
Germanium	4.01	5000-600	0.65	550
Silicon	3.42	10,000-100	0.81	11150

3.1.1.4.6 Near-Infrared

Near-Infrared (NIR) provides information about combination bands and molecular overtones (Fig. 3.8) and is useful in probing bulk material because NIR can typically penetrate much further into the sample than mid-IR. NIR spectra show overtones and combination of fundamental vibrations e.g. for the following functional groups: C-H, N-H and O-H [22]. These types of bands are complex, which renders them difficult to interpret because they are typically very broad bands which arise from absorptions in overlapping wavelengths and which are ambiguous. It is therefore very problematic when trying to interpret specific features and assign them to specific chemical components [23]. To address this, results generated from NIR are processed in a variety of ways, including principal component analysis and partial least squares in order to provide quantitative information [24] [25].

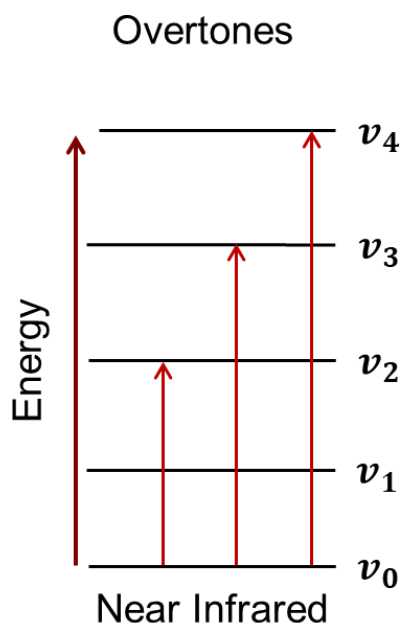


Fig. 3.8: A summary of the energy transition processes for Near-Infrared

Because NIR spectroscopy allows for samples to be analysed quickly, directly, and non-destructively without the requirement for sample preparation, it is ideally suited for production control purposes, for industries such as the polymer and pharmaceutical sectors. This methodology is commonly adopted for the analysis of tablets to determine the assay of the API within the formulation. Eustaquio *et al.* [24] investigated NIR for quantification and assaying of tablets containing paracetamol. They found the technique to be a viable alternative to the traditional UV spectrometry approach. The pharmaceutical sector has been actively encouraged by the food and drug administration (FDA) to implement technologies such NIR in the production of drug products as part of the Process Analytical Technology (PAT) program [26] [27]. This is because the technique can be used in a variety of ways in the manufacture of pharmaceuticals and to assist in the improved quality of the final drug product, e.g. to monitor the blending process in order determine the homogeneity of an API in a solid dosage form, moisture content, polymorph screening method etc. [27].

3.1.1.4.7 ATR-FTIR Imaging

Mid Infrared chemical imaging set-ups in macro mode (without the use of a microscope) are achieved using ATR accessories with a diamond or germanium crystal and a mercury cadmium telluride (MCT-A) detector. The ATR accessory used in this study was the Golden Gate produced by Specac and was designed specifically for FTIR imaging (Varian) [28]. A schematic highlighting the internal optics and the IR beam path are shown below in Fig. 3.9.

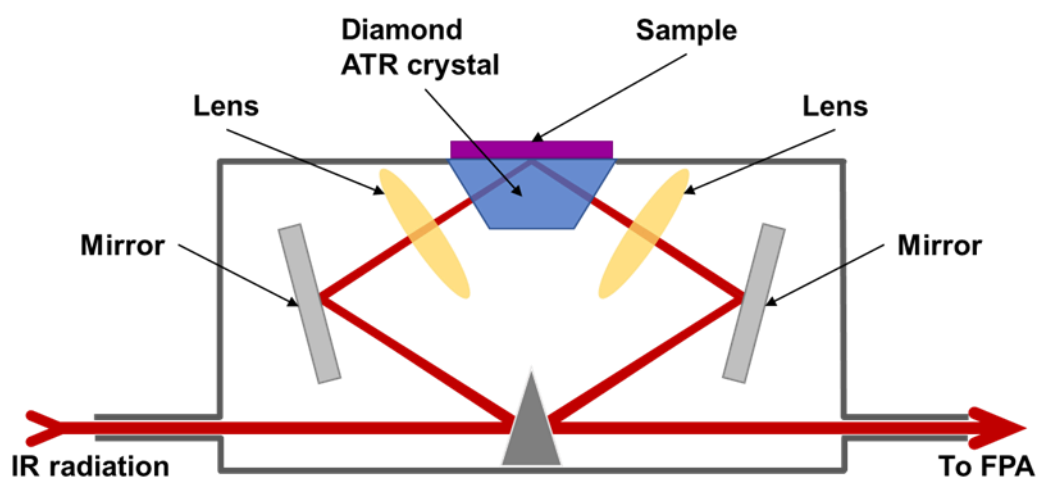


Fig. 3.9: Schematic of Golden Gate ATR-FTIR accessory used for FTIR imaging. Adapted from [3] [17]

The FTIR imaging approach permits the collection of images from an area $\sim 640 \times 640 \mu\text{m}$ with a spatial resolution of $\sim 10 \mu\text{m}$ and a temporal resolution of ~ 30 seconds [29]. Traditional ATR-FTIR spectroscopy is not location-specific, spectra being an average of the sample area in contact with the ATR crystal. More recently, FTIR Imaging spectrometers have been developed in which spectra can be acquired from specific locations on the ATR crystal. This is achieved by using a focal plane array (FPA) detector which was originally designed for military and surveillance purposes [30]. The FPA is a 2D device used for the infrared region of the electromagnetic spectrum and consists of a grid array of detectors in which each pixel acts as an individual detector and therefore an entirely separate infrared spectrum can be obtained from each pixel [31]. The FPA

detector allows the spatially resolved spectral information from all areas of a sample simultaneously. The principle is illustrated in Fig. 3.10.

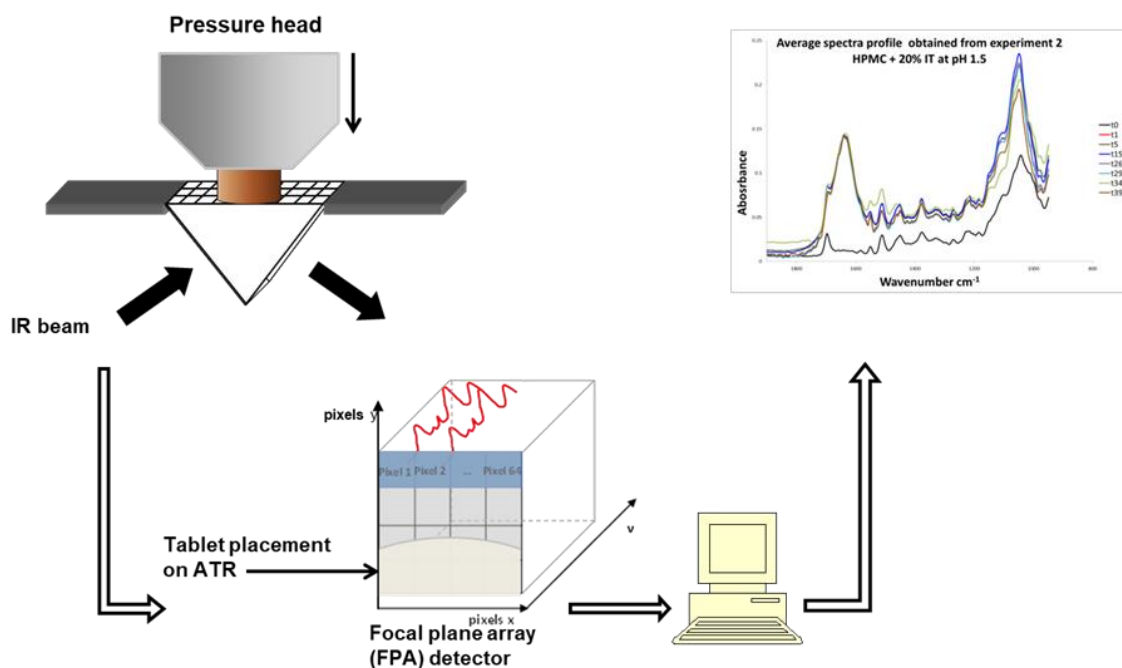


Fig. 3.10: Schematic of ATR-FTIR imaging set-up with a 64 x 64 FPA detector.
Adapted from [32]

One of the most challenging aspects of this approach in this project was maintaining a good contact between the collection optics of the FTIR imaging system (ATR crystal) and the oral solid dosage sample during hydration experiments. This is because poor contact between the sample and ATR crystal will result in lower absorbance, leading to weaker intensities and hence variability between images acquired [33]. However, with swellable matrices, the contact upon hydration improves due to the differences in refractive index of the dry versus the hydrated tablet. Over the timeframe of the experiment successful imaging of tablet swelling can therefore be observed due to the formation of the gel layer establishing enhanced contact with the ATR crystal [17] [33]. Researchers have shown that Mid-IR spectroscopic imaging in ATR mode can successfully be applied to monitor real time hydration processes of pharmaceutical solid dosage forms *in situ* [34].

The resolution of the FPA detector determines the number of pixels and therefore the number of spectra generated. Currently the best commercial FPA detectors have a pixel resolution of 128 * 128 providing the capability to produce 16,384 individual spectra from one image [31]. However, a 64*64 pixel detector is also commonly used and this provides 4096 spectra from a single chemical image.

For FTIR imaging using an FPA detector the achievable spectral range to collect a mid-Infrared spectrum is typically 4000–950 cm⁻¹. Lenses are incorporated within the ATR accessory to focus the infrared beam on to the diamond crystal which has a surface area of 4 mm², allowing 4 times the magnification of the imaged sample [35].

3.1.1.4.8 Micro-FTIR Imaging

Micro-FTIR imaging can also be performed in ATR, transmission or transflection mode where an infrared microscope is used in conjunction with the FTIR spectrometer and an FPA detector. A schematic describing the three different approaches is shown in Fig. 3.11.

For the micro-ATR approach, the spatial resolution is described by the Rayleigh criterion as shown in Equation 3.15 [17]:

$$r = \frac{0.61\lambda}{NA}$$

Equation 3.15

$$NA = n \sin \theta$$

Equation 3.16

where *NA* is the numerical aperture of system and is defined as the product of the refractive index of the medium in which the sample is immersed (*n*₁) and sin *θ*, where *θ* is the half angle the angular aperture [36].

λ is the wavelength of light

r is the distance required to completely resolve two nearby objects (*2r*)

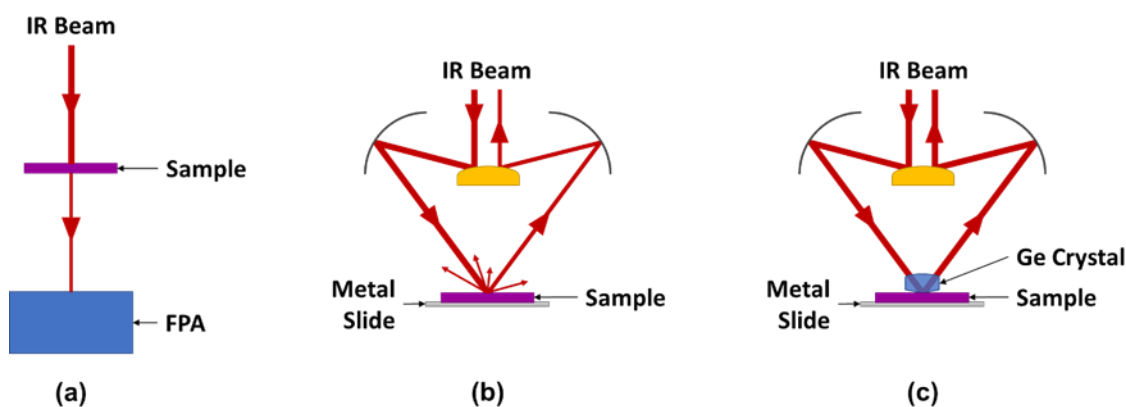


Fig. 3.11: Schematic of micro FTIR imaging in (a) transmission set-up (b) reflectance and (c) ATR. Adapted from [3] [17]

Unlike immersion microscopy, which has a requirement for a high index liquid, micro-ATR imaging uses a hemispherical crystal. The infrared light enters the hemispherical crystal without refraction and therefore an increase in the value of n is observed. Germanium (Ge) (refractive index ~ 4) is commonly used as the crystal as this provides a greater spatial resolution. This is due to the greatly increased numerical aperture of the micro-ATR objective through the high refractive index of the crystal [17]. Authors have demonstrated a four-fold increase in spatial resolution compared to the same microscope used in transmission mode using a Ge crystal, with an achievable spatial resolution of $4 \mu\text{m}$ [33]. This is particularly advantageous for imaging of biomedical samples. However, the downside to a higher spatial resolution is a smaller field of view $64 \times 64 \mu\text{m}$.

Researchers have carried out imaging of colon biopsies using Micro ATR-FTIR spectroscopy with a new hemispherical large radius Ge crystal ($\theta=28 \text{ mm}$) compared to a small Ge crystal ($\theta=3.5 \text{ mm}$). This permits a greater amount of infrared light to probe the sample and collection by the detector which advantageously decreases the acquisition time whilst improving the overall signal-to-noise ratio of the spectra [37].

In FTIR microscopy Cassegrain objectives are frequently used as glass is problematic in that it absorbs all the IR light. The infrared beam is focused on the sample through a

reflective Cassegrain condenser and the transmitted or reflected light is collected by a Cassegrain objective and then focused onto the FPA detector [10].

Using micro FTIR imaging in transflection mode, the sample must be deposited on a reflective substrate. The IR beam passes through the sample to the substrate, where it is reflected back through the sample to the detector. The principle of transflection is shown in Fig. 3.11(b).

Emanuel *et al.* have successfully used FTIR imaging in transflection mode to investigate visualization and quantification of extracellular matrix (ECM) composition of intervertebral discs without the requirement for the lengthy process of histopathologic preparation and immunohistochemical staining. Using more traditional methods such as histology and magnetic resonance it is difficult to detect or quantify subtle changes in the ECM. The authors were able to use FTIR imaging to study subtle changes in ECM composition and structure using chemical bonds as markers from collagens and proteoglycans to provide insight into early-stage intervertebral disc degeneration [38].

Micro-FTIR imaging in transmission mode has been used extensively in cancer studies with the aid of spectral biomarkers to determine the presence of cancer in biological materials [39] [40] as molecular differences can be detected between normal and diseased tissues. The advantage of this approach is that it allows for continuous monitoring of treatment response and tracking of disease progression in comparison to conventional screening and diagnostic methods [40].

Verdonck *et al.* carried out a feasibility study into using FTIR imaging as a potential diagnostic tool to identify characteristics of epithelial cells in breast tissue and the stroma (chemical changes occur in the stroma near a tumor). Using the technique, the authors were successfully able to distinguish between the main breast tissue (normal) cell types from epithelial cells associated with the tumor [41].

3.2 Dissolution

Dissolution testing was widely adopted in the 1970s with the introduction of a standardised approach using the United States Pharmacopeia apparatus, referred to as USP I and II and with the guidance published by the United States Food and Drug Administration (FDA). However, the United States Pharmacopeia now have four dissolution apparatus used for developing drug dissolution methodologies for solid oral dosage forms [42]. These are as follows:

- Apparatus one: Baskets (USP I)
- Apparatus two: Paddles (USP II)
- Apparatus three: Reciprocating cylinder (USP III)
- Apparatus four: Flow through cell (USP IV)

Dissolution is routinely used in the pharmaceutical sector to aid drug formulation development and more commonly in a quality control capacity for batch release and stability testing as required and mandated by regulatory agencies. Initially this technique was developed for solid oral dosage forms but now has a much wider scope, including controlled release formulations, suspensions and transdermal patches [43]. However, the main reason for using *in vitro* dissolution testing is to predict *in vivo* performance of the drug [44]. During this time the dissolution approach was much simpler as most of the drugs under development had sufficient solubility and were categorised as BCS 1 and 3 and were incorporated in conventional tablet or capsule formulations [45].

Monitoring the release of the API from the dosage form during dissolution test is commonly carried out using UV spectroscopy. Before commencement of the dissolution testing, it is important to acquire a spectrum of the drug to determine whether the UV absorbance wavelength of the fully released drug from the tablet matrix is within the range of the spectrophotometer. In accordance with the FDA methodology, analysis is carried out on six of the same dosage forms in order to determine statistical significance. The dissolution vessel is cylindrical in design with a hemispherical bottom and a paddle

is used to stir the dissolution medium at rate specified by the USP method. USP I and USP II are the commonly used methods for dissolution (schematic shown in Fig. 3.12). The temperature inside the vessel is maintained at $37^{\circ} \text{C} \pm 0.3^{\circ} \text{C}$. Conventional dissolution uses 900 mL of dissolution and sometimes with a solubiliser in order to achieve sink conditions.

Depending on the methodology, either 500 mL or 900 mL of dissolution medium is used (usually phosphate buffer for pH 7 or 0.1N for pH 1.2). The USP monograph for a drug product defines the specifications, such as assay and dissolution requirements. For known formulations the recommended methods for dissolution can be located from the FDA dissolution methods database [46].

Known aliquots are withdrawn from each of the dissolution vessels at specified time intervals, either manually or using an automated system and the concentration of API is measured using UV as a function of time. Drug release profiles (percentage drug dissolved vs. time) can be generated following completion of the dissolution test. It is important to note that this type of analysis is not intended to provide mechanistic insight into the drug release as the methodology does not reflect or mimic the highly complex and dynamic *in vivo* conditions encountered in the GI tract.

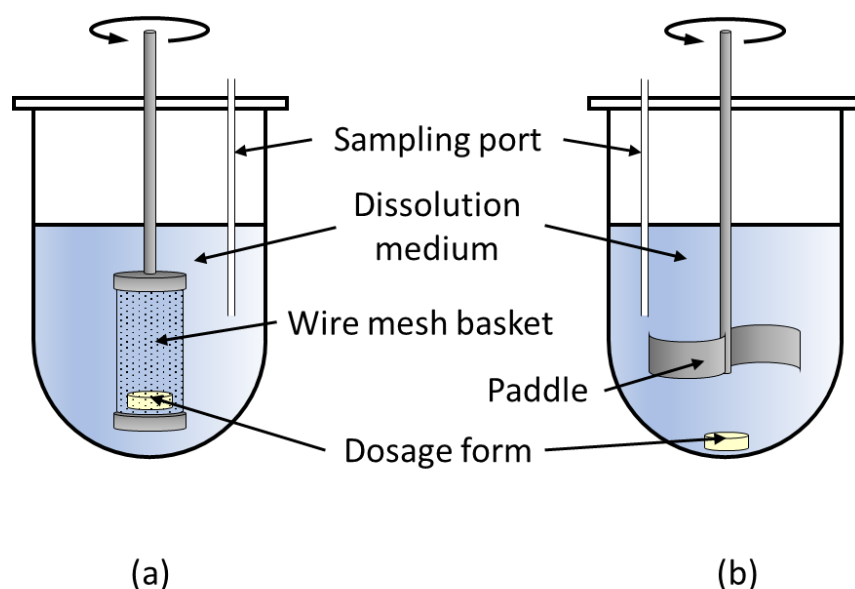


Fig. 3.12: Schematic (a) Basket USP I and (b) Paddle USP II dissolution set-up.
Adapted from [46]

3.3 Raman Spectroscopy

3.3.1 Principles of Raman Spectroscopy

The Raman effect was first reported in 1928 by Raman and Krishnan [47] and from this understanding, the technique of Raman spectroscopy was developed. Raman spectroscopy is a complementary technique to infrared spectroscopy and is similar in that it also provides information about the chemical bonds within a compound. Raman spectroscopy is a scattering technique and is based on the inelastic scattering (Raman scattering) of incident radiation through its interaction with vibrating molecules and hence it probes the molecular vibration (vibrational, rotational and low-frequency modes). The process of scattering can take place with or without an exchange in energy between the incident radiation and the molecule, as discussed in the following paragraphs.

There are three potential outcomes associated with scattering and these are represented diagrammatically in Fig. 3.13.

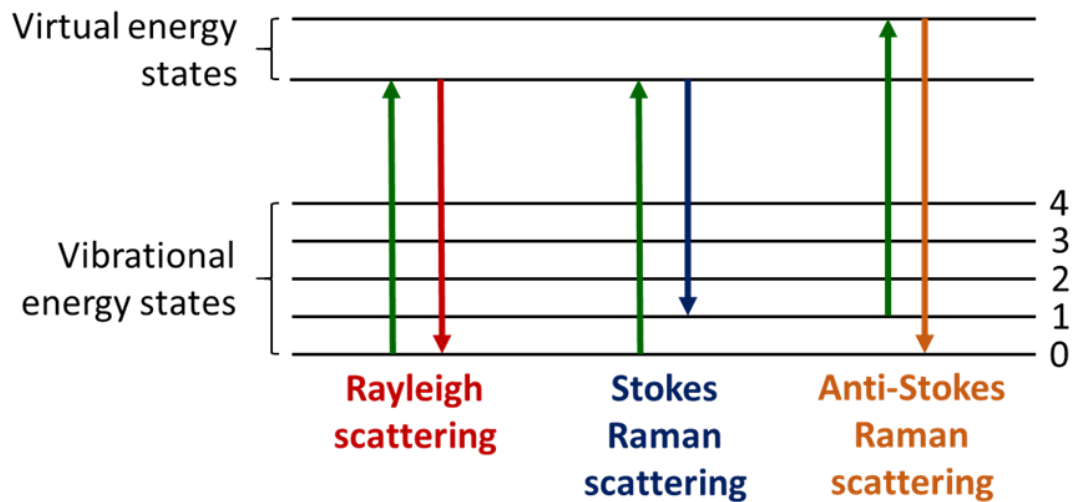


Fig. 3.13: Jablonski energy level diagram illustrating Rayleigh and Raman scattering adapted from [48]

- Stokes scattering-** (Raman) results from a scattered photon, whose energy differs from the incident radiation. If, during the scattering process, nuclear motion is induced, it will result in energy transfer either from the incident photon to the molecule (referred to as Stokes Scattering) or from the molecule to the scattered photon (referred to as Anti-Stokes Scattering). This process is referred to as inelastic and results in the scattered photon having a lower energy and a higher wavelength than the incident photon [49].
- Anti-stokes scattering-** This type of scattering is rarely used because it is a weaker process than the stokes scattering and is temperature dependent, governed by Boltzmann's law. If a molecule is in an excited vibrational state when an incident photon is scattered, the process is known as anti-Stokes scattering and results in the scattered photon having higher energy and a lower wavelength than the incident photon.

- **Rayleigh scattering**- With this scattering process, the light interacts with the molecule which causes distortion (also referred to as polarizability) of the electrons around the nuclei to form a temporary state known as a virtual state. If, in this scattering process, only the electron cloud is distorted and the photon returns to the starting position, the photons are scattered with the same frequency as the incident radiation. This scattering process is regarded as elastic scattering and is the dominant process. i.e., no net change in the energy between the incident radiation and the molecules within a sample [49].

Raman scattering is a very weak phenomenon in that one in every 10^6 - 10^8 photons that are scattered are Raman scattered [49].

In order to explain the origin of Raman spectra, it is necessary to consider the classical theory of scattering when photons from a laser interact with the electron cloud of a covalent bond in a molecule [50].

A relationship can be established to show that the Raman scattering intensity is proportional to the number of molecules being illuminated. This permits the use of Raman spectroscopy for quantitative analysis.

$$I_R = (I_L \sigma_R X) P C \quad \text{Equation 3.17}$$

Where I_R is the measured Raman intensity, I_L is the laser intensity in photons per second and σ_R is the absolute Raman cross section in $\text{cm}^2/\text{molecule}$ and X is the experiment constant, P is the sample path length in cm and C is the concentration in $\text{molecules}/\text{cm}^3$ [51].

In Raman Spectroscopy an intense source of monochromatic ultraviolet, visible or infrared radiation, typically from a laser, irradiates a sample surface where there is then an exchange of quantised vibrational energy.

The Raman spectrum is obtained from the frequency difference between incident radiation and the scattered photons. This is referred to as Raman shift and is calculated using the equation 3.18.

$$\Delta/\bar{\nu} = \left(\frac{1}{\lambda_0} - \frac{1}{\lambda_1} \right) \quad \text{Equation 3.18}$$

Selection rules for Raman differ to those for IR. For a vibration to be IR active there must be a change in the dipole moment during vibration and for Raman active modes there has to be a dipole induced during the scattering of light by the molecule [52].

The Raman process arises due to the polarizability of a molecule and as such is a measure of molecular polarisability (the degree of distortion of the electronic cloud) [47]. Distortion is easier for the electron clouds of molecules and atoms that are further away from the nucleus in comparison to those closer to the nuclei and hence a stronger polarisability.

Raman scattering can be described by understanding the process of an oscillating electric field interacting with a polarisable molecule. The presence of an electric field, E , induces polarisation (α) of an atom/molecule. The induced dipole μ (sometimes shown as P) is determined by the following equation:

$$u = \alpha E \quad \text{Equation 3.19}$$

Therefore, the magnitude of this induced dipole moment is proportional to the electric field.

Understanding the results generated from Raman spectroscopy requires the interpretation of vibrational modes in spectra where the frequencies of vibrational peaks can be attributed to the chemical functional group of the material being analysed. The position and intensity of a Raman band is used to characterise chemical functional groups [53]. Also, frequency shifts of specific vibrational modes can provide insight into potential changes in the chemical composition of the molecules within a material [54].

Not all vibrations are active in Raman scattering. As a Raman selection rule, nonpolar groups and ring structures are known to be Raman active chemical groups that generate strong peaks and are often well-resolved in the Raman spectra. Conversely polar groups containing vibrational modes assigned to stretching and bending vibrations (e.g. water) do not dominate the spectra, unlike in NIR and IR spectroscopy [55].

3.3.2 Raman Microscopy

Raman microscopy is a combination of a Raman spectrometer with an optical confocal microscope. Raman microscopy is a commonly used configuration of Raman spectroscopy employed for research purposes and was the set-up used for this project. It is described in further detail in this section.

A typical Raman microscopy set up is illustrated schematically in Fig. 3.14. The main components of a Raman microscope are the laser source, microscope, Rayleigh filter, grating and the detector. The excitation laser beam is directed onto the sample through the objective lens, and the scattered light is collected along the same beam path. The Raman light is then separated using a grating and dispersed on to a CCD detector. Raman detectors are commonly 2D charge coupled detectors (CCDs). The configuration also contains an aperture which allows the setup to be used in confocal mode which narrows the focal plane. This allows the depth of field to be controlled by eliminating the undesired signal from outside the focal plane. This approach can be adopted for depth profiling. The laser spot size can be determined by the magnification of the objective used and the laser optics aperture (slit size). The Raman wavenumber region can be calibrated in a number of ways, including using a reference sample with a known Raman spectrum such as a silicon wafer (520 cm^{-1}) or using gas emission lines such as argon or neon to calibrate the over the entire range of the grating.

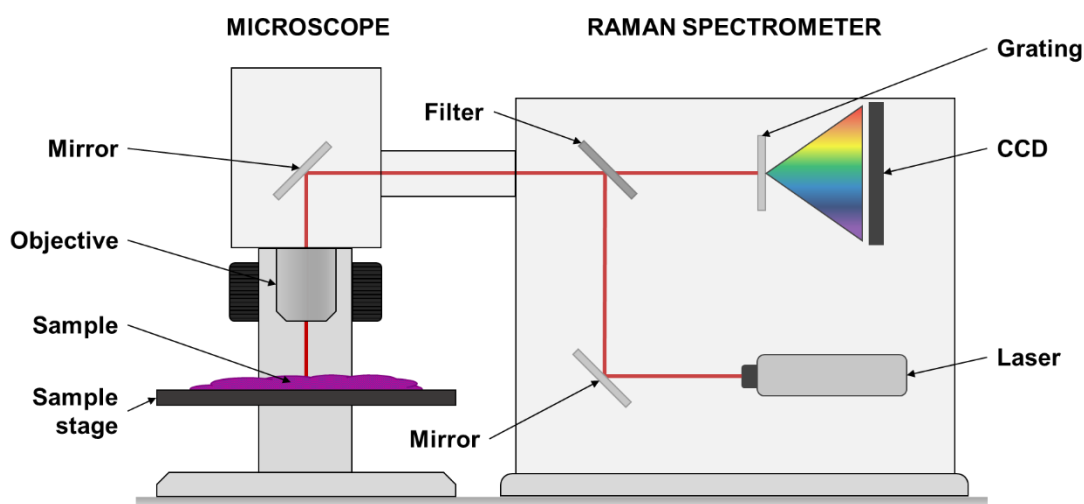


Fig. 3.14: Schematic showing key constituents of a typical Raman microscope

The technique can be used to analyse organic and inorganic materials. Advantageously minimal quantities of sample can be analysed and does not usually require any sample preparation. Similarly, to FTIR the breadth of materials that can be analyzed include solids, liquids and gases. However, Raman analysis on gases can be more difficult due to the inherently low scattering. This is because of the low density of molecules present in a given volume [49]. With Raman, the observed peak positions pertaining to the chemical structure of a material are independent of the excitation wavelength. However, variations in the intensity and resolution may be observed when using different laser wavelengths [56].

Raman spectroscopy is generally a non-destructive technique; however, some materials are prone to laser damage. This is indicated by the presence of localized darkening, which is manifested visually and can be observed from the optical image of the sample. Also, depending on the degree of damage, bands associated with carbon may be present in the Raman spectrum. This is usually overcome by reducing the laser power. The resolution in a Raman spectrometer is determined by the grating. Types of grating that are commonly used vary from 300 to 1800 groove/mm, the latter giving higher resolution [57]. Better grating dispersion and enhanced resolution is obtained with more grooves per millimetre [58]. With Raman, the spatial resolution is dependent on the size of the

laser beam and the laser spot size (D) is determined by the equation below (Equation. 3.20) [59].

$$D = \frac{1.22\lambda}{NA} \quad \text{Equation 3.20}$$

where λ is the wavelength of the laser, and NA is the numerical aperture of the microscope objective being used.

The achievable spatial resolution (p) using an optical microscope is obtained by modifying the above equation to give equation:

$$p = \frac{0.61\lambda}{NA} \quad \text{Equation 3.21}$$

However, it should be noted that modern Raman spectrometers are computer controlled and the software will typically display the spatial resolution to the user. With such systems, a resolution of 2 μm or less is achievable.

Raman microscopy has been used extensively over the years in the surface analysis of works of art to determine the chemical composition of pigments in order to produce a timeline of origin. This facilitates establishing authenticity and selecting the correct pigments for restoration work [60].

The technique is used routinely for the analysis of different forms of the same drug molecule (polymorphism) in preference to other techniques. This is because the risks associated with conversion to other forms is minimized as Raman affords the advantage of no sample contact and preparation [49]. Also, using Raman is particularly advantageous for polymorph analysis as the technique permits the investigation of low frequency bands ($<100 \text{ cm}^{-1}$) which provide valuable information on crystal lattice vibrations [61]. Researchers [62] [63] have shown that Raman analysis using near-infrared excitation can successfully be used for the evaluation of pharmaceutical products contained within packaging material. Niemczyk *et al.* were able to obtain

quantitative information on the levels of Bucindolol using Raman spectroscopy on intact gel capsules and from gel capsules contained within blister packs [62]. One advantage of this approach is the ability to rapidly determine the existence of counterfeit painkillers and to confirm if the API dosage differs significantly from that stated on the packaging or the expected API [63].

Traditionally, the pharmaceutical industry relied on validation studies on the end product to assess the quality of the finalised product. However, the US Food and Drug Administration (FDA) in 2004 introduced Process Analytical Technology (PAT) which provided a way forward for the pharmaceutical sector to assess the quality of the API during the manufacturing process [64]. This essentially involves the use of *in situ* analytical equipment such as thermocouple, pH probe and vibrational spectroscopy techniques such as NIR and Raman and chromatography-based techniques to facilitate a safe approach to analysis in real-time [65].

Raman spectroscopy has been widely used to determine the presence of cancer in blood samples and tissue [66] [67] as it can detect changes associated with molecular composition in cells and tissues, such as proteins and nucleic acids originating from a tumor. Nargis *et al.* have shown that Raman spectroscopy can be used as a diagnostic tool in the early detection of breast cancer in blood plasma samples [66].

One of the advantages of Raman spectroscopy over other techniques such as X-ray diffraction and X-Ray fluorescence when analyzing inorganic oxides is that it can be used to identify elements and their associated oxidation states. One example of this is iron oxide which can exist as magnetite (Fe_3O_4), hematite ($\alpha\text{-Fe}_2\text{O}_3$), goethite ($\alpha\text{-FeOOH}$), etc. [68]. However, high laser power can be detrimental as it can cause conversion from one oxide form to another.

One of the main problems associated with Raman spectroscopy is the issue of fluorescence interference which arises when the laser excitation line is partially absorbed and re-emitted. Fluorescence could be associated with the sample, or impurities within the

sample that may exist. The fluorescence signal generally dominates the Raman spectrum in the form of a large background across the spectral region as it is a much more photon-efficient process than Raman scattering.

There are several ways to overcome fluorescent problems such as “burning out” the fluorescence, also referred to as photo bleaching, which involves leaving the sample exposed to the laser for a longer a period. Alternatively, a higher laser wavelength can be used, however, this approach may give rise to reduced intensity as there is a relationship between Raman signal and the power of laser wavelength. Raman scattering intensity is proportional to $1/\lambda^4$ [69].

Other methods include using software for fluorescence subtraction, however, this approach should be used with caution as spectral information may be lost or distorted. Fluorescence is particularly prevalent in biological based materials.

On occasion, the cosmic spikes may appear in the spectrum. This is caused by high energy photons, commonly referred to as cosmic rays, striking the CCD detector. Another limitation of the technique is that some materials are weak Raman scatterers and hence difficulties arise when analysing these types of materials by Raman spectroscopy.

3.4 Data Processing Methods for Image Analysis

3.4.1 Univariate Data Analysis Approach

One of the primary advantages of using FTIR imaging over single point FTIR is that it combines both spatial and spectral information, with the ability to generate thousands of spectra from a single image. However, this often presents challenges when it comes to interpreting the data and the spectral information required is not easily extractable, particularly when dealing with large datasets. One of the simplest approaches is to generate chemical distribution maps by plotting the intensities of a characteristic absorption band of interest (peak area/peak height, ratios, etc.) as a function of spatial position on a selected sample area [70] (Fig. 3.15). A colour coded scheme (“false colour

image”) is usually applied to the intensity values in order to provide and aid interpretation. However, applying this univariate approach can present inherent challenges when it comes to interpretation of a complex matrix of spectral data. As these can be affected by matrix effects, overlapping of characteristic bands [71], variations in water and carbon dioxide levels over the duration of an experiment and the presence of dead pixels (arising from detector anomalies which can manifest as missing or zero values).

FTIR imaging data can be considered as a “hyper cube” and can be presented as a “hyperspectral” image which is comprised of four dimensions [71]:

- x and y spatial dimensions
- x and y spectral dimensions
- intensity dimensions

Within the image, each pixel represents an entirely separate, complete infrared spectrum.

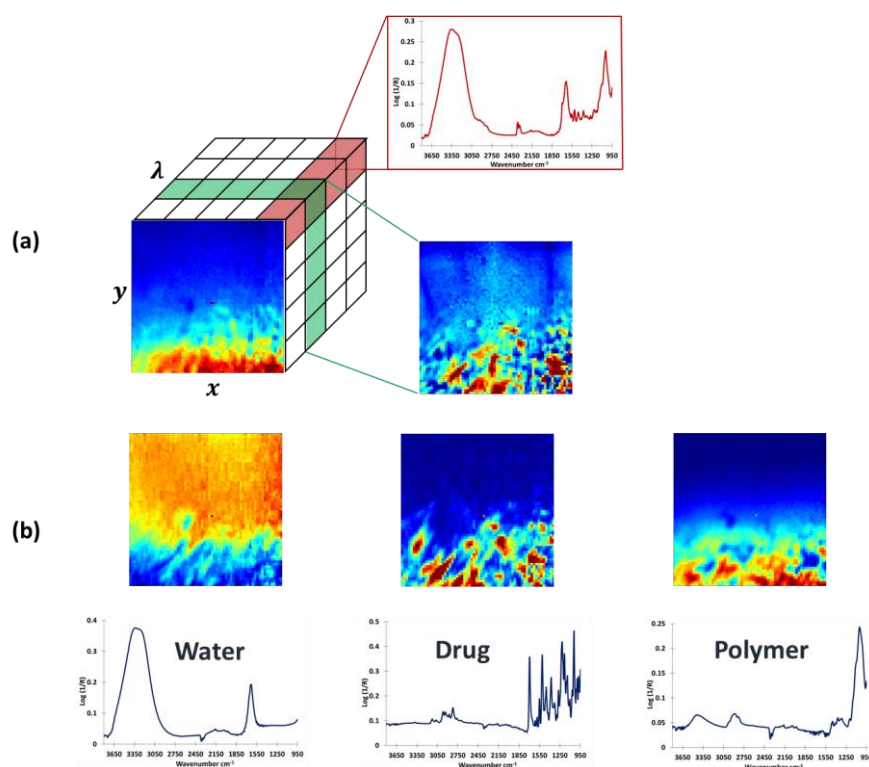


Fig. 3.15: (a) Schematic of three-dimensional data cube recorded during a chemical imaging experiment on a HPMC tablet and (b) extracted images to show distribution of water, drug and polymer within the tablet matrix. Reproduced from [72] with permission from Elsevier

The univariate approach is predominately used in Raman and mid-infrared spectroscopy, since the spectra exhibit sharp unambiguous peaks. However, difficulty arises when specific and well-resolved peaks are not available, such as when the imaged samples consist of multiple compounds. In this case, it is sometimes difficult to find specific and well-resolved peaks. It is therefore necessary to apply a statistical or multivariate data analysis approach (MCR) [73].

The most commonly applied multivariate methods include principal components analysis (PCA) and multivariate curve resolution - alternating least squares (MCR-ALS). Both these statistical approaches attempt to deconvolute the data into 'factors' that can be attributed to the individual components within the dataset and 'loadings' which are related to the concentration of the factors.

3.4.2 Multivariate Data Analysis Approach

MCR is used for a range of analytical and the most popular MCR algorithm, due to its flexibility, is Multivariate Curve Resolution by Alternating Least Squares (MCR-ALS), proposed by Tauler [74].

Using an MCR-ALS algorithm with ATR-FTIR imaging, spatially resolved chemical images and corresponding resolved FTIR spectra of the individual, pure chemical species within a complex, unknown sample can be generated. This approach is particularly suited to unknown compositions or quantification without a calibration set.

The first step of the chemometric data analysis procedure (MCR-ALS) is to create a data matrix, **D**. Usually, the spectral region will be cropped to focus on a region of interest. As a starting point, an estimate of the potential number of pure components is required and this is generally obtained from methods such as principal component analysis (PCA). MCR methods are based on a bilinear model and the assumption that Beer's law is valid for the spectroscopic system investigated, hence the observed spectra are linear

combinations of the spectra of the pure components within the system as shown below (Equation 3.22).

$$A = \log \left(\frac{I}{I_0} \right) c \epsilon d \quad \text{Equation 3.22}$$

The logarithm of incident radiant intensity (I) divided by transmitted radiant intensity (I_0) is equal to the product of substance concentration (c), the molar attenuation coefficient (ϵ) and the pathlength which is the depth of penetration of the evanescent wave for ATR (d).

The experimental data matrix can be decomposed and expressed mathematically as:

$$D = CS^T + E \quad \text{Equation 3.23}$$

Where C is the concentration profile matrix, S^T is the resolved spectral matrix, and E is the residual error matrix [75]. A diagrammatic representation of the decomposition of the experimental set is shown in Fig. 3.16 [73].

MCR is an iterative method and optimisation of C and S^T are achieved using ALS until convergence is achieved. In order to generate chemically meaningful results, constraints can be applied in each iteration to reduce the number of possible outputs for C and S^T . The constraints for vibrational spectroscopy are usually non-negativity thereby ensuring the concentration and the spectral profile are equal to or greater than zero [76].

The challenges with MCR arise due to co-linearity and over estimation of the initial number of factors.

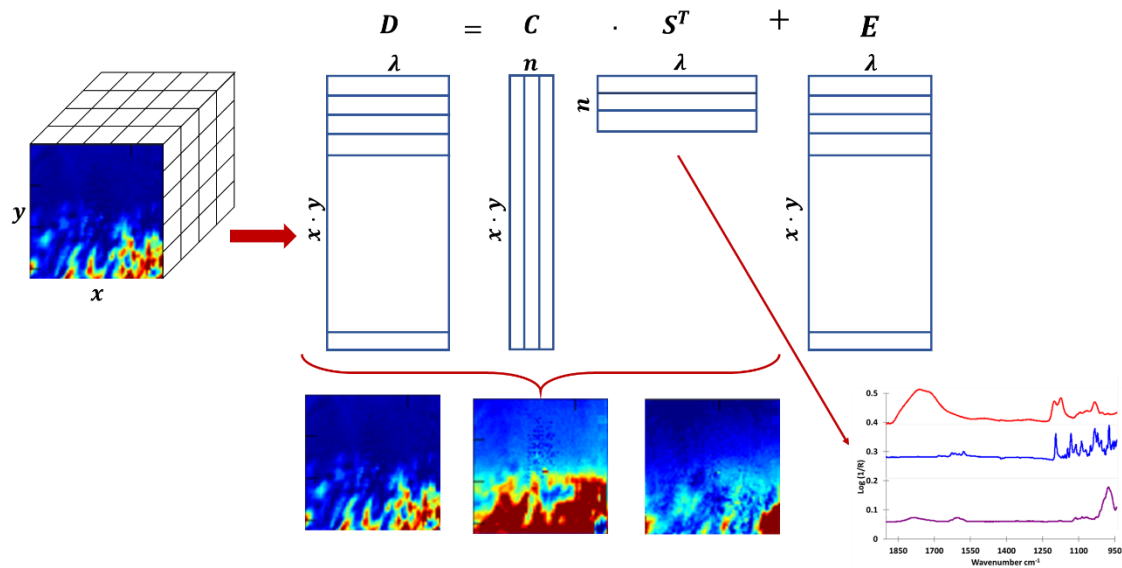


Fig. 3.16: Unfolding of the hyperspectral datacube in the bi-dimensional matrix D . bilinear decomposition of the matrix D into its constituents: C , concentration matrix; S^T , spectra matrix; E , residual matrix. Reproduced from [72] with permission from Elsevier

3.4.3 Principal Components Analysis (PCA)

PCA is a multivariate statistical technique used for simplifying complex data sets and the aim is to reduce the dimensionality of the data matrix. This is achieved by the creation of principal components which are new, uncorrelated variables from the original data set [77]. PCA is widely used in pharmaceutical research as an exploratory approach.

PCA decomposes the hyperspectral data cube into two matrices, a set of scores containing the new calculated principal component and the loading profile (relates to the weights for each variable in the dataset), as shown in the equation below [78]:

$$D = TP^T + E \quad \text{Equation 3.24}$$

where T is the $M \times Q$ score matrix, P is the $N \times Q$ loading matrix, E is the $M \times N$ model residual matrix and Q is the number of principal components (PCs).

3.4.4 Partial Least Squares (PLS)

PLS is another example of a multivariate data analysis method which is widely used as the chemometric tool of choice to extract quantitative information from spectroscopic data and is used in a variety of fields including medicine, food research, oil analysis and pharmacology [79] [80]. This approach is based on a linear relationship and uses a simple and convenient calibration method for resolving spectral data sets. It requires a calibration, prepared with pure materials distributed over a suitable concentration range. PLS is used for creating predictive models and establishes relationships between input and output variables.

PLS uses blocks of information referred to as X and Y blocks. X blocks denote spectra and Y blocks relate to information that needs to be predicted, e.g. concentrations or physical properties. Illustrated diagrammatically, PLS as can be visualised as shown in Fig. 3.17 [81].

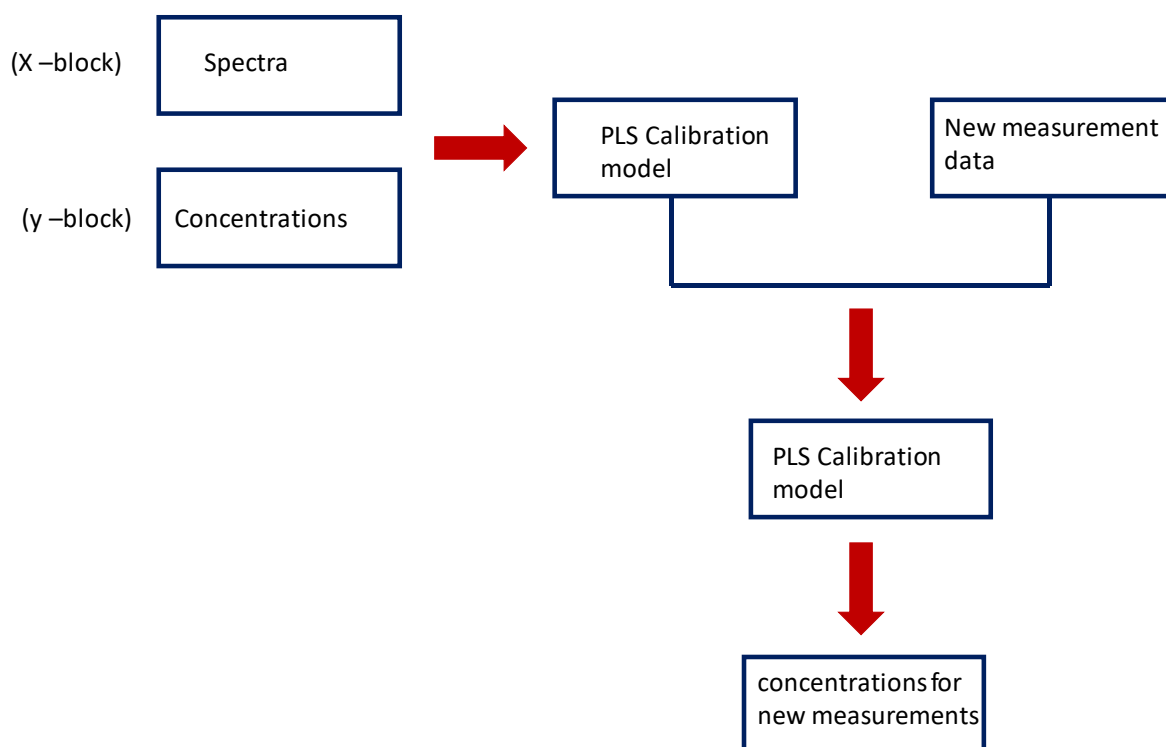


Fig. 3.17: Diagrammatic representation of PLS process. Adapted from [81]

3.5 References

- [1] S. C. Gad, *Pharmaceutical Manufacturing Handbook: Regulations and Quality*, New Jersey: John Wiley & Sons, 2008.
- [2] É. Dufour, "Chapter 1 - Principles of Infrared Spectroscopy," in *Infrared Spectroscopy for Food Quality Analysis and Control*, Academic Press, 2009, pp. 3-27.
- [3] H. Keles, *Mid-IR Imaging and Multivariate Analysis of Dynamic Processes in Pharmaceutically Relevant Microparticles*, 2014: Sheffield Hallam University, 2014.
- [4] D. Faivre, *Iron Oxides: From Nature to Applications*, John Wiley & Sons, 2016.
- [5] M. Derrick, D. Stulik and J. M. Landry, *Infrared Spectroscopy in Conservation Science*, Getty Conservation Institute, 2000.
- [6] A. Subramanian and L. Rodriguez-Saona, "Fourier Transform Infrared (FTIR) Spectroscopy," in *Infrared Spectroscopy for Food Quality Analysis and Control*, Dublin, Academic Press, 2009, pp. 146-173.
- [7] J. Coates, "Vibrational Spectroscopy: Instrumentation for Infrared and Raman Spectroscopy," *Applied Spectroscopy Reviews*, vol. 33, no. 4, pp. 267-425, 1998.
- [8] B. C. Smith, *Fundamentals of Fourier Transform Infrared Spectroscopy*, CRC Press, 1996.
- [9] D.-W. Sun, *Infrared Spectroscopy for Food Quality Analysis and Control*, Academic Press, 2009.
- [10] B. H. Stuart, *Infrared Spectroscopy: Fundamentals and Applications*, John Wiley & Sons, 2004.
- [11] J. L. Koenig, *Spectroscopy of Polymers*, New York: Elsevier science Inc., 1999.
- [12] C. Gendrin, Y. Roggo and C. Collet, "Pharmaceutical applications of vibrational chemical imaging and chemometrics: A review," *Journal of Pharmaceutical and Biomedical Analysis*, vol. 48, no. 3, pp. 533-553, 2008.
- [13] M. M. Mossoba, *Spectral Methods in Food Analysis: Instrumentation and Applications*, New York: CRC Press, 1998.
- [14] G. Lefèvre, T. Preočanin and J. Lützen, "Attenuated total reflection - Infrared spectroscopy applied to the study of mineral - aqueous electrolyte solution interfaces: a general overview and a case study," in *Infrared Spectroscopy - Materials Science, Engineering and Technology*, IntechOpen. <https://doi.org/10.5772/36459>, 2012, pp. 97-122.

- [15] F. M. Mirabella, "Strength of interaction and penetration of infrared radiation for polymer films in internal reflection spectroscopy," *Journal of Polymer Science Polymer Physics Edition*, vol. 21, no. 11, pp. 2403-2417, 1983.
- [16] F. M. Mirabella, "Handbook of Vibrational Spectroscopy," vol. 2, John Wiley & Sons, 2002, p. 1091–1102.
- [17] S. G. Kazarian and A. K. Chan, "Micro- and Macro-Attenuated Total Reflection Fourier Transform Infrared Spectroscopic Imaging," *Advanced Vibrational Spectroscopy*, vol. 64, no. 5, pp. 135A-152A, 2010.
- [18] T.-T. Do, . M. Celina and P. M. Fredericks, "Attenuated total reflectance infrared microspectroscopy of aged carbon-filled rubbers," *Polymer Degradation and Stability*, vol. 77, p. 417–422, 2002.
- [19] H. J. Butler , J. M. Cameron , C. A. Jenkins, G. Hithell, S. Hume , N. T. Hunt and M. J. Bake, "Shining a light on clinical spectroscopy: Translation of diagnostic IR, 2D-IR and Raman spectroscopy towards the clinic," *Clinical Spectroscopy*, vol. 1, no. 100003, 2019.
- [20] J. R. Hands , G. Clemens, R. Stables, K. Ashton, A. Brodbelt, C. Davis, T. P. Daw, M. D. Jenkinson, R. W. Lea, C. Walker and . M. J. Baker, "Brain tumour differentiation: rapid stratified serum diagnostics via attenuated total reflection Fourier-transform infrared spectroscopy," *Journal of Neuro-Oncology*, vol. 127, p. 463–472, 2016.
- [21] A. Materials, "Attenuated Total Reflection (ATR) Mode – Advantages for FT-IR Spectroscopy," August 2015. [Online]. Available: <https://sites.chem.colostate.edu/diverdi/c431/experiments/infrared%20spectroscopy%20-%20transmission%20and%20attenuated%20total%20reflectance/references/AZO%20Materials%20ATR.pdf>. [Accessed 25 April 2020].
- [22] S. Türker-Kaya and C. W. Huck, "A Review of Mid-Infrared and Near-Infrared Imaging: Principles, Concepts and Applications in Plant Tissue Analysis," *Molecules*, vol. 22, no. 168, pp. 1-20, 2017.
- [23] G. Reich, "Near-infrared spectroscopy and imaging: Basic principles and pharmaceutical applications," *Advanced Drug Delivery Reviews*, vol. 57, no. 8, p. 1109–1143, 2005.
- [24] A. Eustaquio , P. Graham, R. Jee , A. Moffatt and A. D. Trafford, "Quantification of paracetamol in intact tablets using near-infrared transmittance spectroscopy," *Analyst*, vol. 123, p. 2303–2306, 1998.
- [25] K. Varmuza, *Chemometrics in Practical Applications*, Viena: InTech, 2012.
- [26] Food and Drug Administration, "FDA (2004a) PAT: A framework for innovative pharmaceutical development, manufacturing, and quality assurance, Guidance

- for industry,” 2004 September. [Online]. Available: (www.fda.gov/cder/guidance/6419fnl.pdf. [Accessed 27 05 2020].
- [27] E. Räsänen and N. Sandler , “Near infrared spectroscopy in the development of solid dosage forms,” *Journal of Pharmacy and Pharmacology*, vol. 59, no. 2, p. 147–159, 2007.
- [28] Specac LTD, “https://www.specac.com/en,” [Online]. Available: https://www.specac.com/en/documents/instructional/2i-10600-5-golden-gate-imaging-atr. [Accessed 27 05 2020].
- [29] H. Keles , A. Naylor , F. Clegg and C. Sammon, “Studying the release of hGH from gamma-irradiated PLGA microparticles using ATR-FTIR imaging,” *Vibrational Spectroscopy*, vol. 71, p. 76–84, 2014.
- [30] E. N. Lewis, P. J. Treado, R. C. Reeder, G. M. Story, A. E. Dowrey, C. Marcott and I. W. Levin, “Fourier transform spectroscopic imaging using an infrared focal-plane array detector,” *Analytical Chemistry*, vol. 67, pp. 3377-3381, 1995.
- [31] K. M. Dorling and M. J. Baker, “Rapid FTIR chemical imaging: highlighting FPA detectors,” *Trends in Biotechnology*, vol. 31, no. 8, pp. 437-438, 2013.
- [32] F. D. Zahoor, K. T. Mader, P. Timmins, J. Brown and C. Sammon, “Investigation of Within-Tablet Dynamics for Extended Release of a Poorly Soluble Basic Drug from Hydrophilic Matrix Tablets Using ATR–FTIR Imaging,” *Molecular Pharmaceutics*, vol. 17, no. 4, p. 1090–1099, 2020.
- [33] S. G. Kazarian and K. L. Chan, “New Opportunities in Micro- and Macro-Attenuated Total Reflection Infrared Spectroscopic Imaging: Spatial Resolution and Sampling Versatility,” *Applied Spectroscopy*, vol. 57, no. 4, pp. 381-389, 2003.
- [34] S. G. Kazarian and A. . K. L. Chan , ““Chemical Photography” of Drug Release,” *Macromolecules*, vol. 36, no. 26, pp. 9866-9872, 2003.
- [35] S. Kazarian and K. L. Chan, “Applications of ATR-FTIR spectroscopic imaging to biomedical samples,” *Biochimica et Biophysica Acta (BBA) - Biomembranes*, vol. 1758, no. 7, p. 858–867, 2006.
- [36] H. J. Gulley-Stahl, S. B. Bledsoe, A. P. Evan and A. J. Sommer, “The Advantages of an Attenuated Total Internal Reflection Infrared Microspectroscopic Imaging Approach for Kidney Biopsy Analysis,” *Applied Spectroscopy*, vol. 64, no. 1, pp. 15-22, 2010.
- [37] C. L. Song and S. G. Kazarian, “Micro ATR-FTIR spectroscopic imaging of colon biopsies with a large area Ge crystal,” *Spectrochimica Acta Part A: Molecular and Biomolecular Spectroscopy*, vol. 228, no. 117695 , pp. 1386-1425, 2020.
- [38] K. S. Emanuel, K. T. Mader, M. Peeters, I. Kingma, C. M. V. P.-P. Rustenburg, C. Sammon and T. H. Smit, “Early changes in the extracellular matrix of the

- degenerating intervertebral disc, assessed by Fourier transform infrared imaging,” *Osteoarthritis and Cartilage*, vol. 26, no. 10, pp. 1400-1408, 2018.
- [39] D. C. Fernandez, R. Bhargava, S. M. Hewitt and I. W. Levin, “Infrared spectroscopic imaging for histopathologic recognition,” *Nature biotechnology*, vol. 23, no. 4, pp. 469-474, 2005.
- [40] K.-Y. Su and W.-L. Lee, “Fourier Transform Infrared Spectroscopy as a Cancer Screening and Diagnostic Tool: A Review and Prospects,” *Cancers (Basel)*, vol. 12, no. 15, p. 115, 2020.
- [41] M. Verdonck, A. Denayer, B. Delvaux, S. Garaud, R. D. Wind, C. Desmedt, C. Sotiriou, K. Willard-Gallo and E. Goormaghtigh, “Characterization of human breast cancer tissues by infrared imaging,” *Analyst*, vol. 141, no. 2, p. 606–619, 2016.
- [42] A. Siew, “Dissolution Testing,” *Pharmaceutical Technology*, vol. 40, no. 11, pp. 56-64, 2016.
- [43] M. Siewert, J. Dressman, C. K. Brown and V. P. Shah, “FIP/AAPS Guidelines to Dissolution/in Vitro Release Testing of Novel/Special Dosage Form,” *AAPS PharmSciTech*, vol. 4, no. 1, p. 43–52, 2003.
- [44] Food and Drug Administration FDA, “Guidance for Industry Dissolution Testing of Immediate Release Solid Oral Dosage Forms,” 1997. [Online]. Available: <https://www.fda.gov/media/70936/download>. [Accessed 16 april 2020].
- [45] H. Grady , D. Elder , G. K. Webst, Y. Mao , Y. Lin, T. Flanagan , J. Mann , A. Blanchard, M. J. Cohen , J. Lin, F. Kesisoglou, A. Hermans , A. Abend, . L. Zhang and D. Curran , “Industry’s View on Using Quality Control, Biorelevant, and Clinically Relevant Dissolution Tests for Pharmaceutical Development Registration and Commercialization,” *Journal of Pharmaceutical Sciences*, vol. 107, no. 1, pp. 34-41, 2018.
- [46] M. Long and Y. Chen , “Developing Solid Oral Dosage Forms,” in *Chapter 14 - Dissolution Testing of Solid Products*, San Diego, Academic Press, 2009, pp. 319-340.
- [47] H. M. Mansour and A. J. Hickey, “Raman Characterization and Chemical Imaging of Biocolloidal Self-Assemblies, Drug Delivery Systems, and Pulmonary Inhalation Aerosols: A Review,” *AAPS PharmSciTech* , vol. 8 , no. 4, 2007.
- [48] K. J. I. Ember, M. A. Hoeve, S. L. McAughtrie, M. S. Bergholt, B. J. Dwyer, M. M. Stevens, K. Faulds, S. J. Forbes and C. J. Campbell, “Raman spectroscopy and regenerative medicine: a review,” *Regenerative Medicine*, vol. 2, no. 12, 2017.
- [49] E. Smith and G. Dent, *Modern Raman Spectroscopy – A Practical Approach*, NJ: Hoboken, Wiley, 2019.
- [50] M. J. Pelletier, *Analytical Applications of Raman Spectroscopy*, Wiley, Bodmin, 1999.

- [51] S. Sasic and Y. Ozaki, *Raman, Infrared, and Near-Infrared Chemical Imaging*, New Jersey: John Wiley & Sons, 2011.
- [52] J. Coates, "Interpretation of Infrared Spectra, A Practical Approach," in *Encyclopedia of Analytical Chemistry*, John Wiley & Sons, 2006, p. 10815–10837.
- [53] D.-W. Sun, *Modern Techniques for Food Authentication*, Academic Press, 2018.
- [54] T. Yang, B. Zhao and L. He, "Raman instruments for food quality evaluation," in *Evaluation Technologies for Food Quality*, Woodhead Publishing Series in Food Science, Technology and Nutrition, 2019, pp. 119-143.
- [55] R. Kizil and J. Irudayaraj, "Chapter 6 - Spectroscopic Technique: Fourier Transform Raman (FT-Raman) Spectroscopy," in *Modern Techniques for Food Authentication (Second Edition)*, Academic Press, 2018, pp. 193-217.
- [56] K. B. Ferreira, A. G. Oliveira and J. A. Gomes, "Raman spectroscopy of automotive paints: Forensic analysis of variability and spectral quality," *Spectroscopy Letters*, vol. 50, no. 2, pp. 102-110, 2017.
- [57] "Horiba.co," Horiba, [Online]. Available: <https://www.horiba.com/uk/scientific/products/raman-spectroscopy/raman-academy/raman-tutorial/>. [Accessed 14 05 2020].
- [58] J. R. Ferraro, K. Nakamoto and C. W. Brown, *Introductory Raman Spectroscopy*, Elsevier Science & Technology, 2003.
- [59] I.-M. Chou and A. Wang, "Application of laser Raman micro-analyses to Earth and planetary materials," *Journal of Asian Earth Sciences*, vol. 145, no. B, pp. 309-333, 2017.
- [60] A. Kudelski, "Analytical applications of Raman spectroscopy," *Talanta*, vol. 76, no. 1, pp. 1-8, 2008.
- [61] R. Deidda, P.-Y. Sacre, M. Clavaud, L. Coïc, H. Avohou, P. Hubert and E. Ziemons, "Vibrational spectroscopy in analysis of pharmaceuticals: Critical review of innovative portable and handheld NIR and Raman spectrophotometers," *TrAC Trends in Analytical Chemistry*, vol. 114, pp. 251-259, 2019.
- [62] T. M. Niemczyk, M. M. Delgado-Lopez and F. S. Allen, "Quantitative Determination of Bucindolol Concentration in Intact Gel Capsules Using Raman Spectroscopy," *Analytical Chemistry*, vol. 70, pp. 2762-2765, 1998.
- [63] J. Omar, A. Boix and F. Ulberth, "Raman spectroscopy for quality control and detection of substandard painkillers," *Vibrational Spectroscopy*, vol. 111, p. 103147, 2020.
- [64] B. Nagy, A. Farkas, E. Borbás, P. Vass, Z. Kristóf Nagy and G. Marosi, "Raman Spectroscopy for Process Analytical Technologies of Pharmaceutical Secondary Manufacturing," *AAPS PharmSciTech*, vol. 20, no. 1, pp. 1-16, 2019.

- [65] A. Chanda, A. M. Daly, D. A. Foley, M. A. LaPack, S. Mukherjee, J. D. Orr, G. L. Reid, D. R. Thompson and H. W. Ward, "Industry Perspectives on Process Analytical Technology: Tools and Applications in API Development," *Organic Process Research & Development*, vol. 19, no. 1, pp. 63-83, 2015.
- [66] H. F. Nargis, H. Nawaz, A. Ditta, T. Mahmood, M. I. Majeed, N. Rashid, M. Muddassar, H. N. Bhatti, M. Saleem, K. Jilani, F. Bonnier and H. J. Byrne, "Raman spectroscopy of blood plasma samples from breast cancer patients at different stages," *Spectrochimica Acta Part A: Molecular and Biomolecular Spectroscopy*, vol. 222, no. 117210, pp. 1-8, November 2019.
- [67] J. Depciuch, B. Tołpa, P. Witek, K. Szmu, E. Kaznowska, M. Osuchowski, P. Król and J. Cebulski, "Raman and FTIR spectroscopy in determining the chemical changes in healthy brain tissues and glioblastoma tumor tissues," *Spectrochimica Acta Part A: Molecular and Biomolecular Spectroscopy*, vol. 225, no. 117526, pp. 1-8, 2020.
- [68] S. Das and J. M. Hendry, "Application of Raman spectroscopy to identify iron minerals commonly found in mine wastes," *Chemical Geology*, vol. 290, no. 3-4, pp. 101-108, 2011.
- [69] S. Yang, B. Li, M. N. Slipchenko, A. Akkus, N. G. Singer, Y. N. Yeni and O. Akkus, "Laser Wavelength Dependence of Background Fluorescence in Raman Spectroscopic Analysis of Synovial Fluid from Symptomatic Joints," *Journal of Raman Spectroscopy*, vol. 44, no. 8, p. 1089–1095, 2013.
- [70] G. Sciutto, P. Oliveri, S. Prati, E. Catelli, I. Bonacini and R. Mazzeo, "A Multivariate Methodological Workflow for the Analysis of FTIR Chemical Mapping Applied on Historic Paint Stratigraphies," *International Journal of Analytical Chemistry*, vol. 4938145, 2017.
- [71] Y. Wang, X. Yao and R. Parthasarathy, "Characterization of interfacial chemistry of adhesive/dentin bond using FTIR chemical imaging with univariate and multivariate data processing," *Journal of Biomedical Materials Research Part A*, vol. 91, no. 1, pp. 251-62, 2009.
- [72] P.-Y. Sacré, P. Lebrun, P.-F. Chavez, C. De Bleye, L. Netchacovitch, E. Rozet, R. Klinkenberg, B. Streeel, P. Hubert and E. Ziemons, "A new criterion to assess distributional homogeneity in hyperspectral images of solid pharmaceutical dosage forms," *Analytica Chimica Acta*, vol. 818, pp. 7-14, 2014.
- [73] P. Y. Sacré, C. D. Bleye, P.-F. Chavez, L. Netchacovitch, P. Hubert and E. iemons, "Data processing of vibrational chemical imaging for pharmaceutical applications," *Journal of Pharmaceutical and Biomedical Analysis*, vol. 101, pp. 123-140, 2014.
- [74] R. Tauler, "Multivariate curve resolution applied to second order data," *Chemometrics and Intelligent Laboratory Systems*, vol. 30, pp. 133-146, 1995.

- [75] J. P. Smith, F. C. Smith and K. S. Booksh, "Multivariate Curve Resolution–Alternating Least Squares (MCR-ALS) with Raman Imaging Applied to Lunar Meteorites," *Applied Spectroscopy*, vol. 72, no. 3, p. 404-419, 2018.
- [76] A. B. Câmara, L. S. d. Carvalho, C. L. de Morais, L. A. de Lima, H. O. de Araújo, F. M. de Oliveira, and K. M. de Lima, "MCR-ALS and PLS coupled to NIR/MIR spectroscopies for quantification and identification of adulterant in biodiesel-diesel blends," *Fuel*, vol. 210, pp. 497-506, 2017.
- [77] B. Balan , . A. S. Dhaulaniya , . R. Jamwal, K. K. Sodhi, S. Kelly, A. Cannavan and D. K. Singh, "Application of Attenuated Total Reflectance-Fourier Transform Infrared (ATR-FTIR) spectroscopy coupled with chemometrics for detection and quantification of formalin in cow milk," *Vibrational Spectroscopy*, vol. 107, no. 103033, pp. 1-7, 2020.
- [78] J. M. Amigo, "Practical issues of hyperspectral imaging analysis of solid dosage forms," *Analytical and Bioanalytical Chemistry*, vol. 398, p. 93–109, 2010.
- [79] I. Singh , P. Juneja and B. Kaur, "Pharmaceutical Applications of Chemometric Techniques," *International Scholarly Research Notices*, vol. Article ID 795178, pp. 1-14, 2013.
- [80] A. Biancolillo and F. Marini, "Chemometric Methods for Spectroscopy-Based Pharmaceutical Analysis," *Frontiers in Chemistry*, vol. 6, p. 576, 2018.
- [81] T. Dearing, "Fundamentals of Chemometrics and Modeling," [Online]. Available: <https://depts.washington.edu/cpac/Activities/Meetings/documents/DearingFundamentalsofChemometrics.pdf>.

4.0 Preparation and Characterisation of Tablets and Their Constituents

In the following chapter, a description of the characterisation of the API, polymer and excipients (highlighted in Table 4.1 and 4.2) is presented. The work was undertaken using a range of analytical techniques to gain an insight into the components of the system. The purpose of this was to better understand the effect of variables such as particle size and processing parameters used on the overall tablet formulation. Having gained an understanding of the constituents, further analysis was then performed on the blended formulations after pressing into tablets.

Because itraconazole exists in different forms such as the salt form, amorphous and crystalline, it is important to be able ascertain which is present when conducting dissolution studies. In order to identify potential spectroscopic markers for these reference materials, powders of the different forms were prepared (salt, amorphous and crystalline) [1] [2] [3].

NIR spectroscopy was applied to assess its potential for quantitative determination of the loadings of itraconazole and the different pH modifiers explored in this study. An additional requirement from these tests was to ensure the loadings of the API and pH modifiers within the tablets are consistent and reproducible as this is a prerequisite for ultimately being able to draw reliable conclusions from the various dissolution tests. Calibration models were developed from NIR spectral data using PLS regression.

This project focused on 4 pH modifiers: cysteine HCl, betaine HCl, glycine HCl and citric acid and tablet formulations were trialled both with and without their incorporation. The pH modifiers were incorporated into the tablets at 10% w/w and 30% w/w, initially with just HPMC (referred to as placebo) to provide a benchmark. Further tests were then undertaken using tablets which also included itraconazole at 20% w/w.

The API, polymer and pH modifiers used in this project are shown in Table 4.1 and 4.2.

The materials used to synthesise the different itraconazole salts are shown in Table 4.3.

Table 4.1: Drug and matrix materials used for all formulations

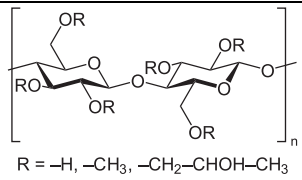
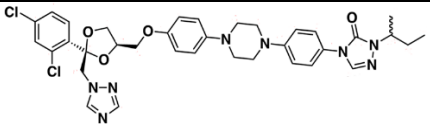
Material	Structure	Supplier
HPMC	 <p>R = -H, -CH₃, -CH₂-CHOH-CH₃</p>	K100M CR Premium grade
Itraconazole		Acros Organics 99%

Table 4.2: pH modifiers used for formulations

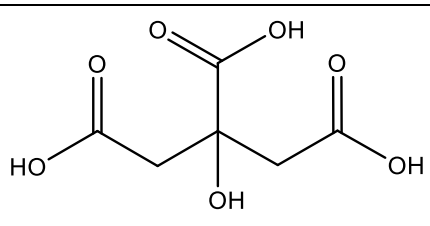
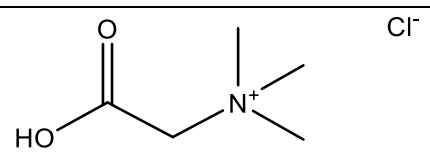
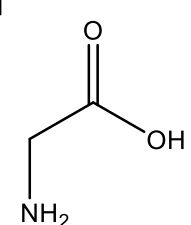
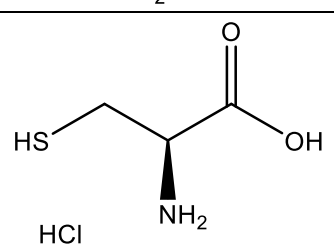
Material	Structure	Supplier
Citric Acid		Sigma Aldrich ACS reagent ≥99.0%
Betaine HCl	 <p>Cl⁻</p>	Sigma Aldrich ≥99.0%
Glycine HCl	<p>HCl</p> 	Sigma Aldrich ≥99% (HPLC)
L-Cysteine HCl	 <p>HCl</p>	Acros Organics 98%

Table 4.3: Chemicals used for preparation of itraconazole salts

Material	Supplier & grade
Dichloromethane	Sigma Aldrich, HPLC grade
Itraconazole	Acros Organics, 99%
Acetone	Sigma Aldrich, HPLC grade
Hydrogen chloride	Sigma Aldrich reagent Plus(R), >=99%
Hydrochloric acid	Sigma Aldrich 11.42 mmol, laboratory reagent grade

4.1 Significance of Itraconazole Forms in Pharmaceutical Applications

Most active pharmaceutical ingredients (APIs) such as itraconazole can exist in many forms and this can change their properties, leading to different physical, chemical, mechanical, and biopharmaceutical performance (bioavailability, permeability, etc). Solid forms of APIs can exist as crystalline forms including polymorphs, hydrates, solvates, co-crystals and salts, as well as amorphous forms, all of which can impact drug release mechanism.

Itraconazole is marketed in the amorphous solid dispersion form incorporated in HPMC that is coated onto inert sugar beads (Sporanox). Research carried out on the formulation showed a significant reduction (40%) in the bioavailability of the drug when administered in humans in a fasted state [4]. To achieve maximum absorption, the Sponarox formulation should be taken with food and in the presence of an acidic gastric

environment, as low pH is the most favourable environment for the itraconazole release [5].

In the literature, several strategies to enhance the bioavailability and dissolution rate of IT have been reported [6]. These include modifying the chemical and physical properties of the drug. Tao *et al.* and Bagavatula *et al.* have prepared IT salts by reacting IT with concentrated HCl [2] [3]. However, difficulties with the manufacturing process for the salts means this approach is not easily scalable and chemical instability associated with the salts in the dosage form can cause reversion back to the free base form [6].

Remenar *et al.* explored the possibility of cocrystals of IT with various water-soluble organic acids and reported improved dissolution of itraconazole using L-malic acid, L-tartaric acid and succinic acid [7]. The researchers reported that the cocrystal forms achieved from 4 to 20 times higher concentrations in 0.1 N HCl than the crystalline IT and comparable concentrations to the amorphous form. A comparison of the dissolution profiles for the cocrystal forms to the commercially available Sporanox (amorphous form) and crystalline IT are shown in Fig.4.1.

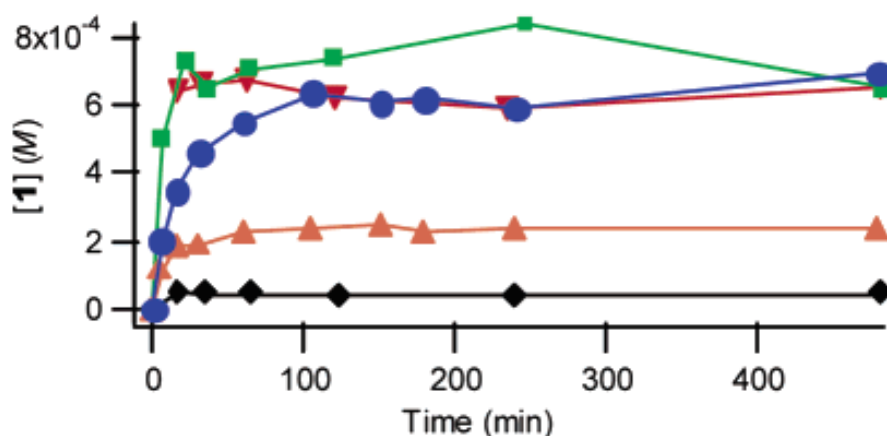


Fig. 4.1: Dissolution profiles for Sporanox (commercial form, green) and IT cocrystals with L-malic acid (red), L-tartaric acid (blue), succinic acid (orange) and crystalline IT in 0.1 M HCl at 25 °C. Reprinted from [7], with permission from the American Chemical Society

Badawi *et al.* prepared itraconazole crystalline nanoparticles as a methodology for improving the bioavailability of the drug and reported an improvement of 3.77 to 8.59 times in the percentage drug dissolved compared to the pure itraconazole [8].

Itraconazole is a weak base and although generally only the nitrogen on the piperazine ring ($pK_a \sim 3.7$) is considered for pK_a determinations, itraconazole has several potential ionisation sites [9] [10]. The Itraconazole molecule consists of a piperazine and two triazole groups, all of which have potential sites for protonation (Fig. 4.2). There are three easily ionizable nitrogens which are located between C9 and C10 on the triazole group and the two on the piperazine ring (C18-19) [11]. Peeters *et al.* state that there are four possible ionisable nitrogens in the itraconazole molecule, however, the authors do not highlight or refer to these in the structure or provide all the pK_a values [12]. The authors determined one of the pK_a s to ~ 4 using potentiometric and spectrophotometric methods and state the pK_{a3} is $\sim 1.5-2$ based on predicting/calculating the expected pK_a . The authors reported the remaining ionisable nitrogens are not protonated [12]. The logical option for the fourth protonation site would be the nitrogen located in proximity to C25 as this is part of a ring system which is not already protonated. However, this is unlikely as it would be energetically unfavorable to force another positive charge into the triazole.

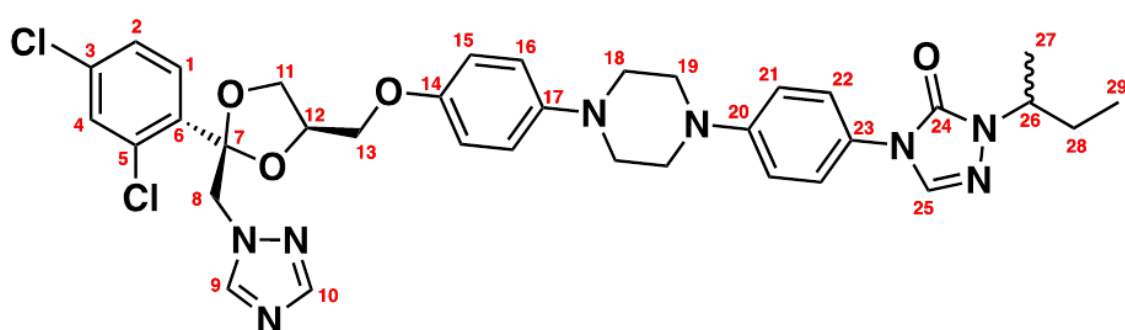


Fig. 4.2: Itraconazole molecule highlighting carbon position

Inkman and Holzgrabe performed proton (1H) and carbon (^{13}C) nuclear magnetic resonance spectroscopy on itraconazole and the analysis confirmed the piperazine nitrogen between C17 and C18 (N26 notation used by the authors) exhibited the highest

proton affinity. With the addition of excess acid, the authors also postulate, using semiempirical calculations, that the triazole ring is protonated between C9 and C10 (N11 notation used by the authors) [13].

4.2 Preparation of Different Forms of Itraconazole

4.2.1 Itraconazole Monohydrochloride

Itraconazole monohydrochloride salt was prepared in accordance with the procedure defined by Bagavatula *et al.* [2] in which 1 g of itraconazole was dissolved in approximately 10 mL of dichloromethane in a rotary evaporator flask. To this solution, approximately 400 mg of concentrated hydrochloric acid (HCl) was added and dissolved. The suspension was heated at 50° C for 1 hour under reflux. After one hour this was removed and placed on a rotary evaporator and a vacuum was applied. The reaction was continued for one hour to form a precipitate of the salt.

4.2.2 Itraconazole Dihydrochloride

Itraconazole salt was prepared using the procedure defined by previous researchers [3]. Itraconazole (1 g) was transferred to a round bottom flask containing 20 mL of acetone. This suspension was heated under reflux under a low flow of hydrogen chloride (HCl) gas until a clear solution was formed (approximately 20 minutes). After a further few minutes the precipitate was formed. The reaction mixture was left under reflux with the HCl bubbling through the mixture for a period of 2 hours. This was allowed to cool and the salt was collected by washing the filtrate with acetone and drying in an oven at 100°C.

4.2.3 Itraconazole Trihydrochloride

Itraconazole trihydrochloride preparation was conducted following the methodology stated by Shevchenko *et al.* [11]. Itraconazole (5 g) was transferred to a round bottom flask containing 100 mL of acetone. HCl gas was produced by reacting sodium chloride with sulphuric acid and drying through magnesium sulphate.

The anhydrous HCl was bubbled through the itraconazole/acetone mixture and the temperature was increased to 40° C and then reduced to 25° C. Approximately 15 minutes later a clear solution should have formed, followed by the formation of a precipitate. However, despite following the procedure, precipitation of the salt did not take place. This was possibly due to the HCl gas retaining some moisture, thus inhibiting the precipitate formation.

4.2.4 Amorphous Itraconazole

Amorphous itraconazole was prepared by melt quenching using Differential Scanning Calorimetry (DSC). This technique also permitted the formation of the compound to be confirmed simultaneously, as DSC traces were recorded over the temperature range adopted.

Approximately 60 mg of as-received (nominally crystalline) free base itraconazole was transferred into a DSC aluminium pan and sealed by crimping. DSC was performed using a Perkin Elmer DSC 8000 system. Under a nitrogen atmosphere, the itraconazole was heated above its melting temperature, and then crash cooled and reheated to form amorphous itraconazole. The parameters used were as follows: heat 25-200° C at 30° C/min; cool 200-0° C at 100° C/min; heat 0-200° C at 30° C/min; cool to ambient temperature.

4.3 Characterisation of Constituent Materials

4.3.1 Determination of Itraconazole Structure Using X-Ray Powder Diffraction (XRPD)

X-ray powder diffraction (XRPD) was performed on the itraconazole powders in order to verify the formation of the amorphous form and to confirm the as-received free base itraconazole was indeed crystalline. Data was collected using a Panalytical X-ray diffractometer (Panalytical X'Pert PRO) equipped with a Cu K-alpha radiation source operating at 40 kV and 40 mA, using an Xcelerator detector. 1 mg of powder was mounted on a low-background silicon wafer for each sample, with a drop of acetone. XRD data was collected over the range 10-80°.

4.3.2 Confirmation of Protonation of Itraconazole Structure by Nuclear Magnetic Resonance (NMR) Spectroscopy

NMR spectroscopy was conducted to confirm the formation of the monohydrochloride and dihydrochloride salts of itraconazole.

The samples of itraconazole and the hydrochloride salts were dissolved in deuterated dimethyl sulfoxide (d6-DMSO) and the spectra were recorded on a Bruker Avance DPX-400 NMR spectrometer operating at a resonance frequency of 400 MHz (1H) or 100 MHz (13C). The chemical environments in both molecules were fully assigned using 1H NMR and 13C NMR experiments. The 1H and 13C chemical shifts of equivalent positions in both compounds were then compared in order to observe any significant changes in chemical shift. Chemical shift values were interpreted for confirmation on the sites of protonation.

4.3.3 ATR-FTIR Imaging of Reference Materials

Reference spectra were collected of the different forms of itraconazole, HPMC, 0.1N HCl acid, tris buffer and the organic pH modifiers using the following mid-IR spectroscopic method. Images were collected using a Varian 680-IR spectrometer coupled to a

temperature controlled Specac Golden Gate single reflection attenuated total reflectance sampling accessory using a 64 x 64 focal plane array detector, at a spectral resolution of 8 cm⁻¹ using 8 co-additions. The average spectrum from all pixels was obtained from each image to generate reference spectra in the same configuration as the hydration experimental data.

4.3.4 SEM Morphological Analysis of Constituents

Scanning Electron Microscopy (SEM) was used to provide images of the IT and HPMC for the purposes of determining an insight into the morphology of the particles.

The analysis was carried out on a FEI Quanta 3D SEM equipped with a tungsten filament as the electron source and a secondary electron (SE) detector for imaging. The powders were dispersed on a self-adhesive conductive carbon tab mounted onto an aluminium stub and sputter-coated with a 15 nm layer of gold to render them electrically conductive before obtaining the SEM micrographs. All samples were examined using an electron beam with a spot size of 4 and an accelerating voltage of 20 kV.

4.3.5 Particle Size Analysis of IT, HPMC and pH Modifier Powders

Particle size distribution of the materials was measured using Malvern Mastersizer 3000 with Aero S dry unit (Malvern Instruments Ltd., Worcestershire, United Kingdom). 1 g of dry sample was placed into the cell and particle size parameters corresponding to the 10th, 50th, 90th (μm percentile of particles (D_{10} , D_{50} , D_{90})) were detected and recorded. All samples were measured in triplicate and the distribution was presented as an average value. The data was processed using Malvern Mastersizer software v3.81.1908.020.

4.4 Preparation of 20% w/w Itraconazole Tablets and Formulations Containing pH Modifiers

4.4.1 Tablet Blending

Blending of powders is a key step in the pharmaceutical manufacturing process, as it ensures a homogenous distribution of a drug and the excipients, such as sugar, starch and cellulose lactose within the bulk matrix. The pharmaceutical sector assesses the quality of blended powder formulations with an invisible thief sampling procedure, which is followed by off-line chemical analysis. Another common approach is to carry out in-line measurement when using NIR spectroscopy [14].

Blending mechanisms can be classified as convection, diffusion or shear. Convective blending encompasses gross movement of particles within the blend, whereas diffusion is a slow blending process where individual particles are distributed upon blending into the newly formed interface. Lastly, the shear mechanism of blending comprises blending of material while passing along forced slip planes which can aid in breaking agglomerates and facilitate blending [15] [16].

Tumbler, convective, hopper and fluidization are the four main types of blending equipment available on the market [17]. Tumble blending is the most commonly used approach for blending powders in the pharmaceutical and food industries. This is due to the low energy consumption ($< 1 \text{ kW/m}^3$) [18], suitability for mixing of friable particles and ease of cleaning after blending [18]. Mixing time and speed of mixing are the key process parameters for this type of process.

With tumble blending, the container is mounted such that it can be rotated about an axis. The tumbling action facilitates shear mixing and diffusive mixing [19].

In this study, prior to producing the tablets, the different formulations were mixed using tumble blending (Stuart STR4 rotator drive) for 5 hours at approximately 30 rpm for the binary formulation (HPMC and Itraconazole). All subsequent formulations were blended

for 20 minutes. The powders were transferred to a container which was positioned horizontally using Velcro straps attached to the rotating shaft.

The different formulations blended and pressed into tablets for this study are shown in Table 4.4.

Table 4.4 Concentration of constituents used in the tablet formulations

Constituent	HPMC	Itraconazole	pH modifier (citric acid, cysteine HCl, glycine HCl, betaine HCl)
Loading (% w/w)	80	20	0
	90	0	10
	70	0	30
	70	20	10
	50	20	30

4.4.2 Tablet Compaction

Flat-faced matrix tablets (10 mm diameter) containing 90 mg total powder were manufactured by direct compression on a Specac Atlas manual press (Specac, Orpington, UK) using a compaction pressure of 625 MPa and a 5-minute compaction time.

4.5 Characterisation of Tablets

4.5.1 Quantification of Loadings Using Near Infrared Spectroscopy (NIR)

Tablet composition was quantified using Near Infrared Spectroscopy. The tablets were placed in a custom designed sample holder and NIR transmittance spectra were collected using a Thermo Scientific Nicolet iS50 FTIR spectrometer equipped with a deuterated triglycine sulfate (DTGS) detector (ThermoScientific, Maddison, USA). Spectra were collected by averaging 256 scans over a spectral range of 11500-2800 cm^{-1} , at a resolution of 4 cm^{-1} .

The spectral information below 7157 cm^{-1} was discarded due to complete absorbance of the NIR radiation. The spectral region chosen for the PLS analysis for the selected regions ranged from 9515-7157 cm^{-1} (TQ analyst software, version 9.7.027).

4.5.2 Distribution of Constituents Within the Tablet Matrix Using Raman Microscopy

The distribution of IT and the pH modifiers within the HPMC matrix was determined using Raman microscopy. Raman maps were generated using a Thermo DXR2 Raman Spectrometer with a 633 nm laser, equipped with a CCD detector and a 600 l/mm grating. Data was collected using an Olympus X10 microscope objective, 3.5 mW laser power, with an estimated spot size of 2.5 μm , a collection time of 2 seconds with 2 exposures and collected over the spectral range 3500 to 100 cm^{-1} . The aperture slit size was set to 50 μm . Spectra were recorded using Omnic for Dispersive Raman software (version 9.6.238). Area maps (2 mm x 2 mm) were collected across the surface of six tablets, with a 100 μm step size (441 spectra collected in total). Raman reference spectra were also collected from the HPMC, itraconazole (as-received free base) and each of the organic acid pH modifiers to identify distinct bands which could be used to directly discriminate (used as markers) each of the components in the tablet maps and facilitate the

generation of the distribution maps and the corresponding histograms. The distribution maps and histograms were generated using ISys 5.0 chemical imaging software (Malvern Instruments, Malvern, UK). Vector normalisation was applied to the raw data prior to generating the chemical distribution maps. This is a commonly adopted approach on spectroscopic data because it helps minimize the effects of potential variations in the sample [20] [21].

4.6 Results and Discussion

4.6.1 Analysis of Different Itraconazole Compounds

4.6.1.1 Formation of Amorphous Itraconazole Using Differential Scanning Calorimetry (DSC)

The DSC results for the formation of the amorphous itraconazole are presented in Fig. 4.3. The results show that on the initial heating of the itraconazole, an intense melting peak was observed at approximately 171° C. However, after crash cooling followed by reheating, the DSC trace showed no endothermic peak at 171° C, indicating a morphological change from the crystalline to the amorphous form. It should be noted that a small feature at approximately 95° C is observed on the reheat cycle (red traces). Based on the literature this could potentially relate the presence of a glass transition [22].

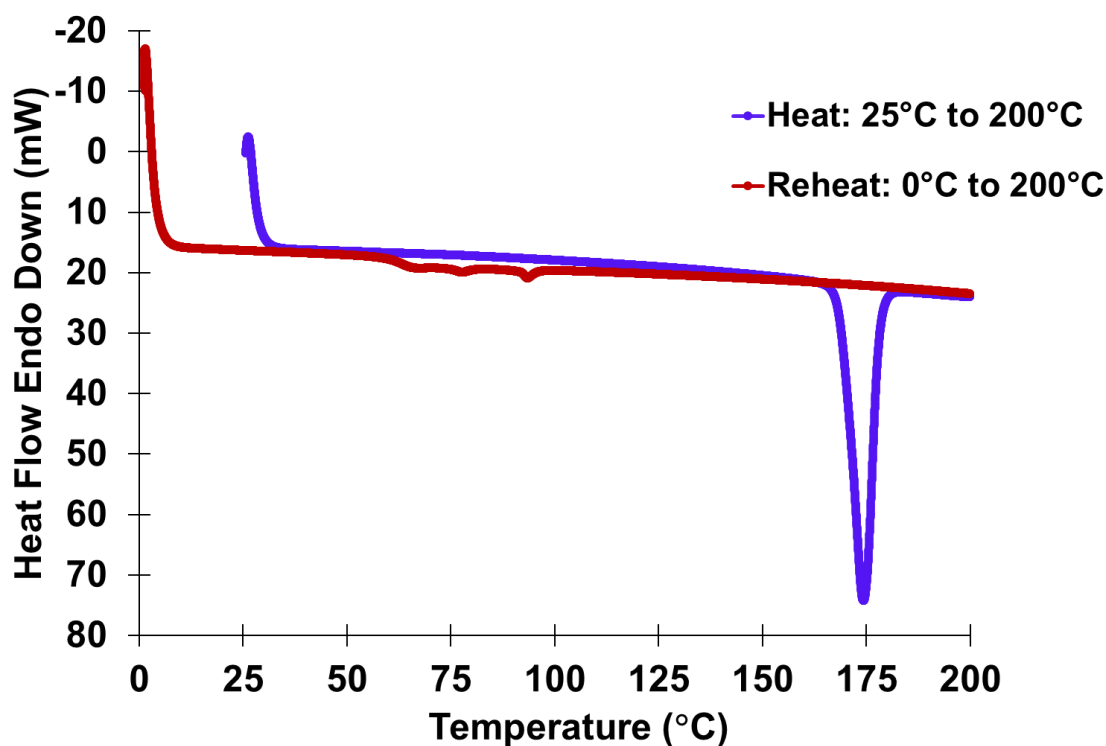


Fig. 4.3: DSC trace showing the heat profiles obtained from the formation of amorphous itraconazole

4.6.1.2 Confirmation of Amorphous and Crystalline Itraconazole Forms Using XRPD

Fig. 4.4 and 4.5 show the XRPD results obtained from the as-received free base and amorphous itraconazole created from the melt quenching procedure carried out using the DSC and described in Section 4.2.4. The peaks present in Fig. 4.4 are indicative of a crystalline structure, while the absence of peaks in Fig. 4.5 confirms the amorphous form.

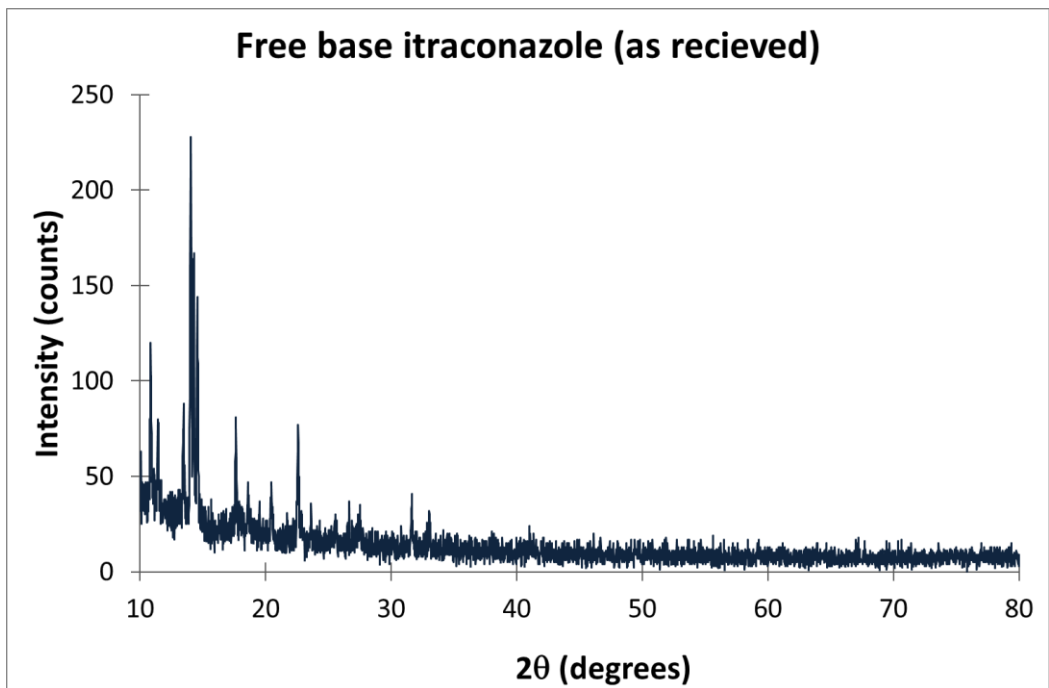


Fig. 4.4: XRPD trace obtained from the as-received free base itraconazole confirming crystalline form

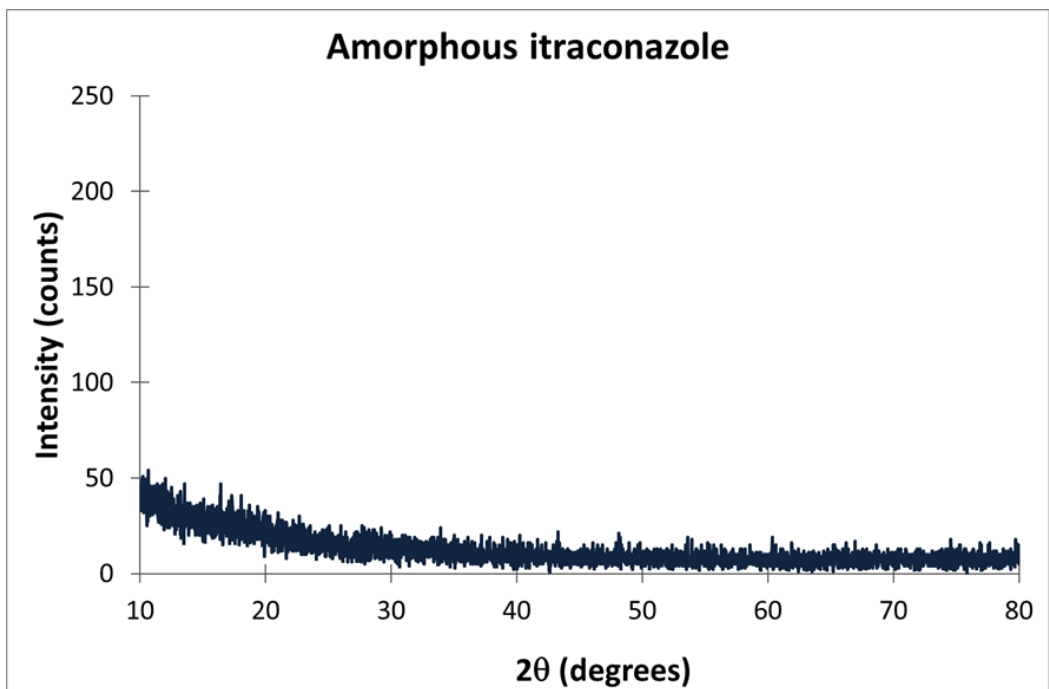


Fig. 4.5: XRPD trace obtained from the amorphous itraconazole

4.6.1.3 Confirmation of Protonated Itraconazole by Proton NMR

From the NMR results (Fig. 4.6), the main site of protonation was proposed to be the nitrogen between C17 and C18 as the environments around this position experienced a strongly deshielding effect in transitioning from the freebase to the hydrochloride salt, consistent with their close proximity to a cationic hypervalent nitrogen atom. The change in chemical shifts of the adjacent aromatic ring, in particular C16 and C14, are also consistent with disruption of the lone pair conjugation from this nitrogen into the π system. There are a number of basic nitrogen atoms in itraconazole and each is likely to contribute a protonated form to an overall equilibrium mixture but based on the NMR analysis, the major contributor to the structure is protonation at the nitrogen between C17 and C18. This confirms that the site of protonation for the monohydrochloride is the piperazine nitrogen (Fig. 4.7), as this has the highest proton affinity. The confirmation of the preferential protonation site is in agreement with the literature [13].

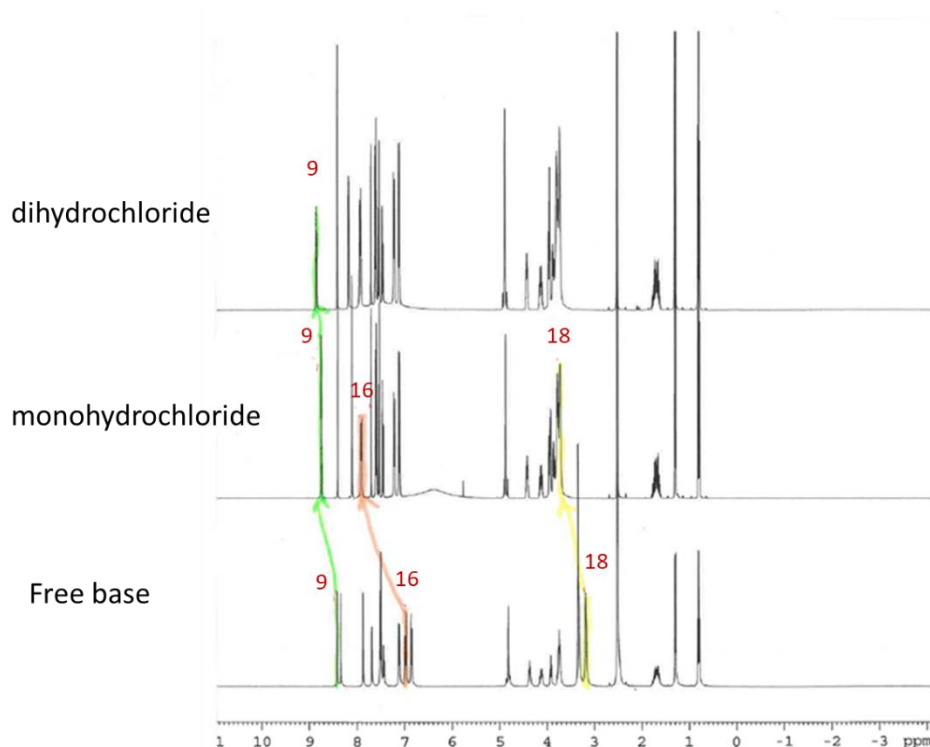


Fig. 4.6: Stacked plot of three proton NMRs showing the deshielding shifts of the key signals at H18, H16 and H9.

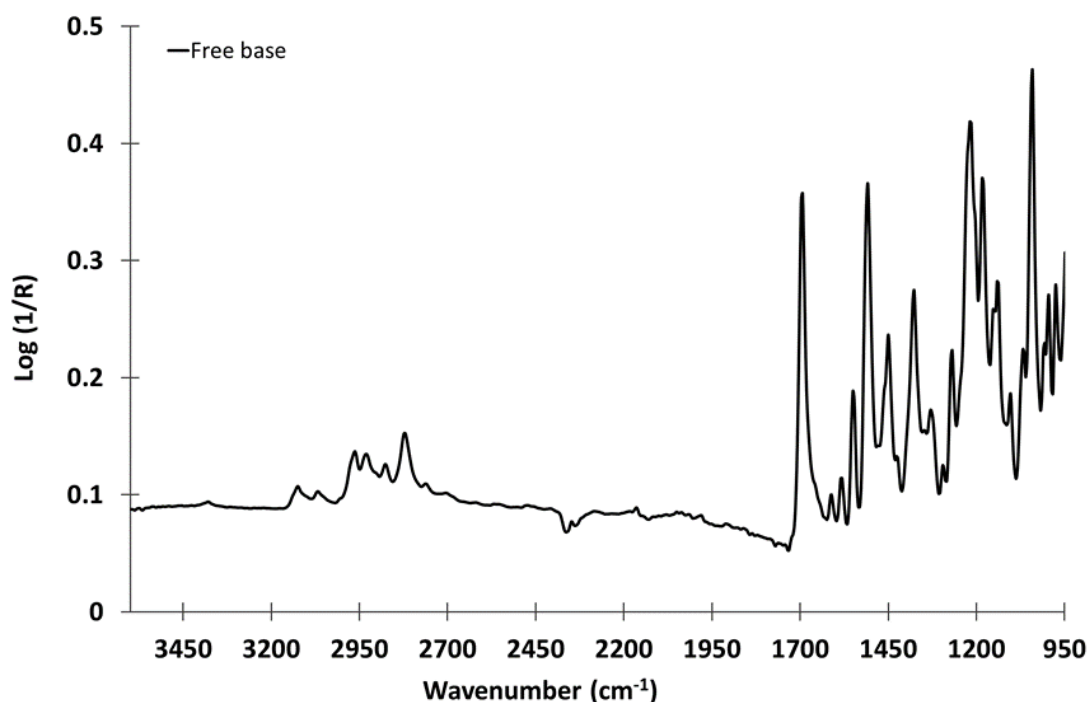


Fig. 4.8: Average ATR-FTIR spectrum obtained from the as-received free base itraconazole

Table 4.5: FTIR spectral band assignments for itraconazole

Peak position cm^{-1}	Assignment
3124, 3068	Aromatic C-H stretching
2821, 2876, 2930, 2962	Aliphatic C-H stretching
1694	C=O stretching
1583, 1549	C=N stretching
1508, 1450, 1377	Aromatic C=C stretching
1217, 1182, 1140	C-O and C-N stretching
1042	Aromatic C-Cl stretching

The average ATR-FTIR spectrum of the amorphous form was compared to the as-received free base itraconazole (overlaid spectra in Fig. 4.9). The main spectral differences observed were associated with the following bands: the $\nu(\text{C}=\text{O})$, $\nu(\text{C}-\text{O})$ and $\nu(\text{C}-\text{Cl})$. The carbonyl of the triazol-3-one group in the amorphous itraconazole (Fig. 4.9) was observed at 1697 cm^{-1} . In the free base form, the band is narrower and a shift of 4 cm^{-1} to lower wavenumber was observed. A shift was also observed for the $\nu(\text{C}-\text{O})$ band observed at 1224 and 1217 cm^{-1} for the amorphous and free base forms. Marked differences were also observed with the shape of the $\nu(\text{C}-\text{Cl})$ band, broader and at a

lower wavenumber position in comparison to the spectrum obtained from the free base form.

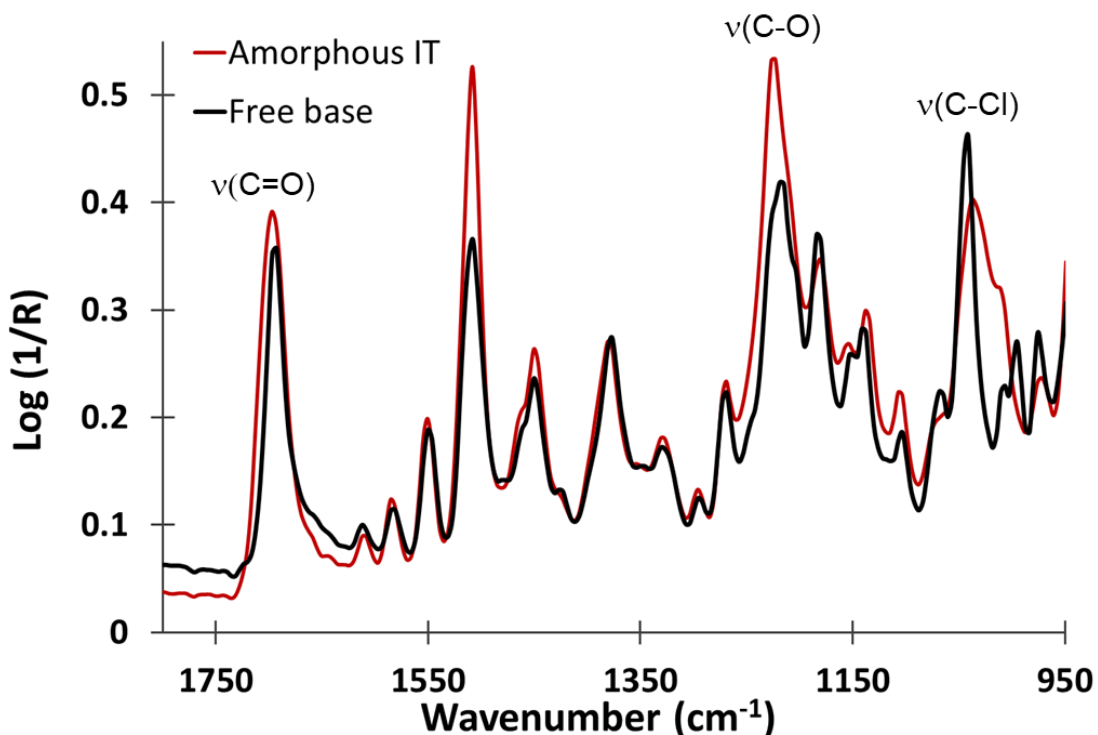


Fig. 4.9: Comparison of average ATR- FTIR spectrum obtained from the free base (black line) and amorphous (red line) itraconazole highlighting (a) $\nu(\text{C}=\text{O})$, (b) $\nu(\text{C}-\text{O})$ and (c) $\nu(\text{C}-\text{Cl})$

The average FTIR spectra obtained from the itraconazole hydrochloride and dihydrochloride are presented in Fig. 4.10. Evidence of salt formation was confirmed from the broad feature observed at approximately 2365-1946 cm⁻¹ which is typically attributed to acid salts [3]. Also, to further corroborate the formation of the salt forms is the loss of the band at 2821 cm⁻¹ which is present in the free base form and is assigned to the CH symmetric stretching vibrations of the methyl group (dotted line in Fig. 4.10).

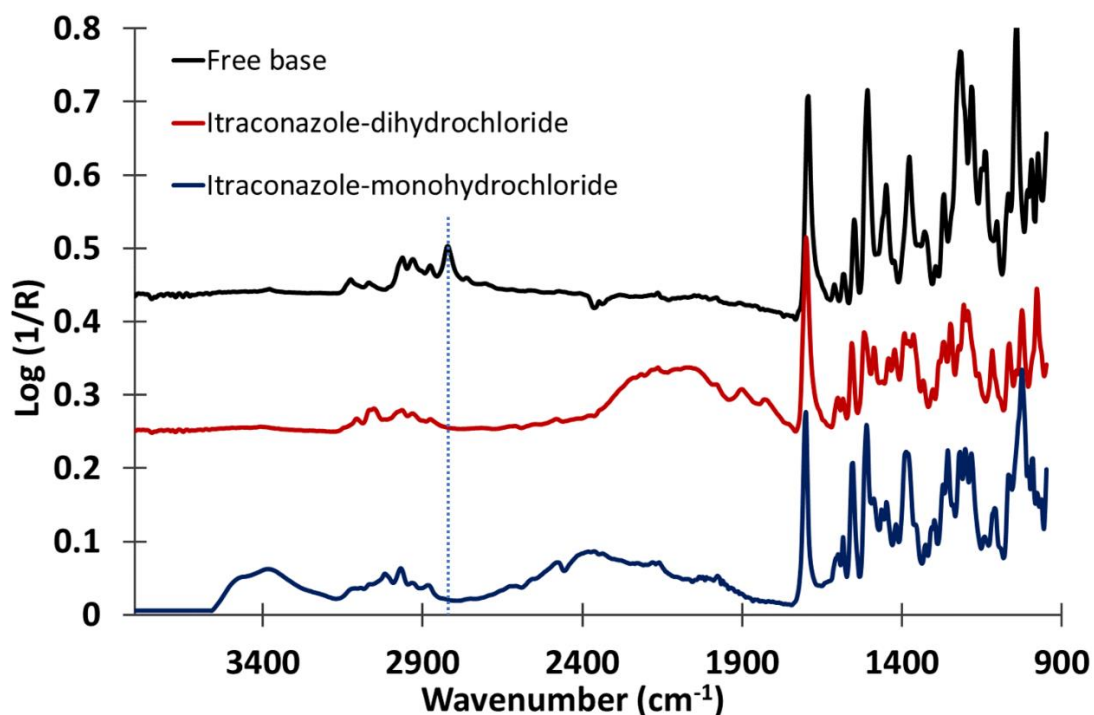


Fig. 4.10: Comparison of average ATR- FTIR spectra obtained from the free base (black line), IT dihydrochloride (red line) and IT monohydrochloride (blue line)

4.6.2 ATR-FTIR Analysis of Reference Materials

Averaged spectra profiles (generated as described in section 4.3.3) of the reference materials were used to identify a suitable peak which could be attributed to a functional group relating to the compound of interest (water, drug or polymer). From this it was possible to generate chemical images of each component during a dissolution experiment (Fig. 4.11). The bands of interest were shown to be the $\delta(\text{OH}) \sim 1620 \text{ cm}^{-1}$ for water (used as a marker for tris buffer and 0.1 N HCl, due to water being the main component), $\nu(\text{C-O}) \sim 1041 \text{ cm}^{-1}$ for HPMC and aromatic $\nu(\text{C=C}) \sim 1510 \text{ cm}^{-1}$ for the total IT distribution.

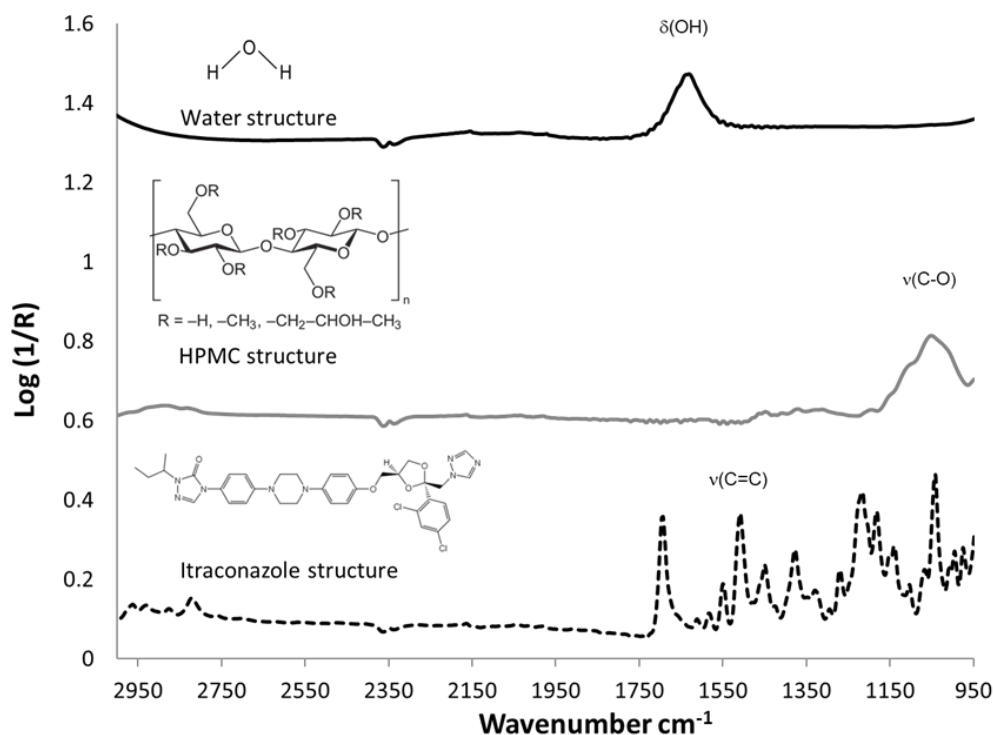


Fig. 4.11: Average ATR-FTIR imaging spectra obtained from reference materials, highlighting $\delta(\text{OH})$, $\nu(\text{C-O})$ and $\nu(\text{C=C})$ in water, HPMC and IT respectively. Highlighted bands (indicating which functional group was used) used for peak area integration for images to show (representing) distribution of water, IT and HPMC

Spectra profiles generated from the average of the ATR-FTIR images obtained from the organic acid pH modifiers are presented in Fig 4.12. These were used to identify species-specific bands from which it was possible to generate chemical images. For each of the organic acids, the $\nu(\text{C=O})$ band was identified as the most suitable as this did not overlap with the $\delta(\text{OH})$ upon ionisation. Table 4.6 shows the peak positions of the $\nu(\text{C=O})$ used to generate the ATR-FTIR distribution images for each of the organic acids investigated in this study.

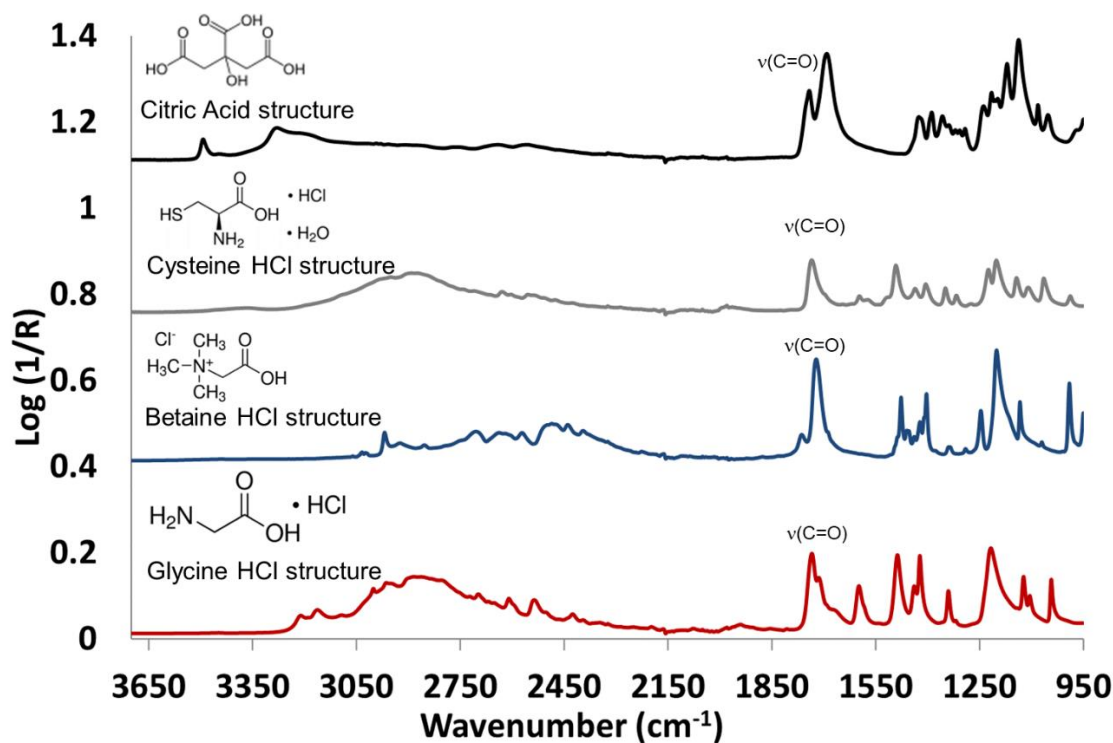


Fig. 4.12: Average ATR-FTIR imaging spectra obtained from the organic acid modifiers, highlighting the position of $\nu(\text{C}=\text{O})$ in citric acid, cysteine HCl, betaine HCl and glycine HCl respectively

Table 4.6: Peak positions for the $\nu(\text{C}=\text{O})$ used to generate the ATR-FTIR distribution Images for the organic acids

Organic Acid pH Modifier	Peak position of $\nu(\text{C}=\text{O})/\text{cm}^{-1}$
Citric Acid	1742
Betaine HCl	1764
Glycine HCl	1734
Cysteine HCl	1735

4.6.3 Morphology and Particle Size Analysis of API, Polymer and pH Modifier

4.6.3.1 SEM Analysis to Determine Morphology

The SEM images obtained from the as-received itraconazole, HPMC and the pH modifiers used in this study are presented in Fig. 4.13. Due to the large variation in particle size, the micrographs reproduced here were selected to best show particle morphology and so magnifications differ in each.

The image obtained from the itraconazole shows the needle-like crystal structure of the API while the image of HPMC shows agglomerated fibres and particles which have combined to form larger elongated structures.

SEM images obtained from the glycine HCl and betaine HCl show clusters of agglomerated particles with a range of different sizes and dimensions. SEM images of cysteine HCl featured rod-like structures with a more regular shape and size and images of citric acid showed individual particles with a range of different sizes.

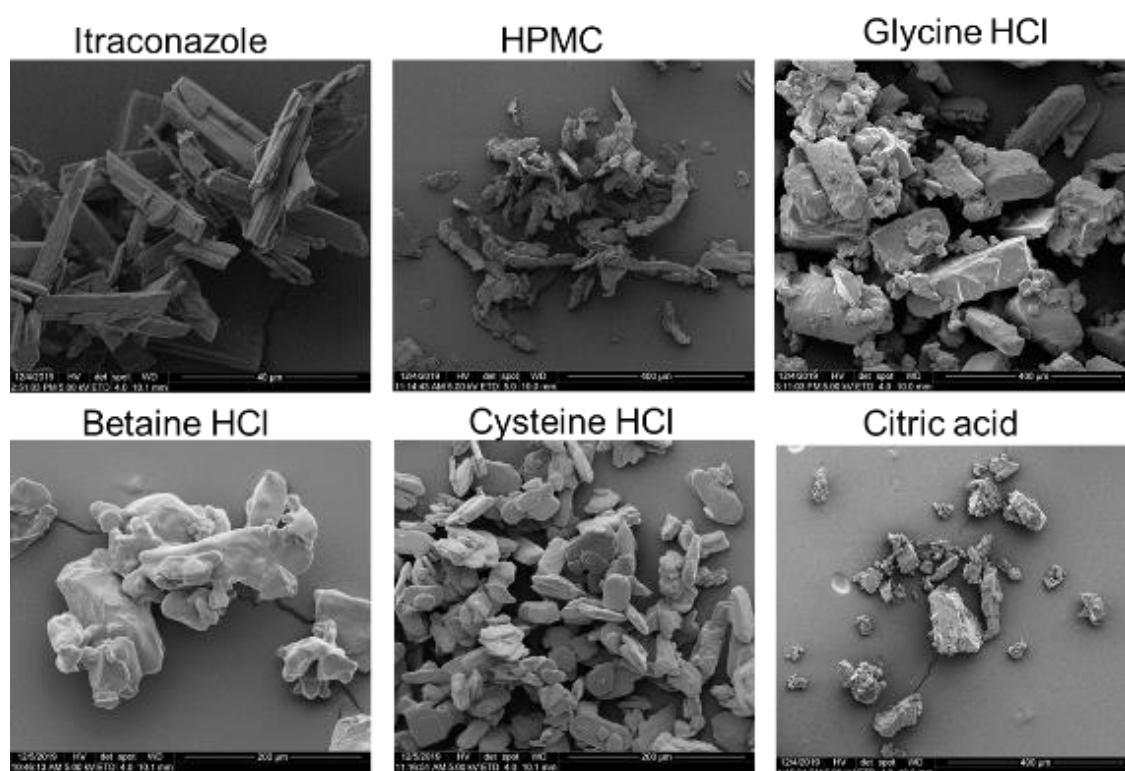


Fig. 4.13: Representative Secondary Electron SEM images for itraconazole, HPMC grade K100M, glycine HCl, betaine HCl and cysteine HCl

4.6.3.2 Particle Size Analysis

The particle size results obtained from the itraconazole, HPMC and the organic acid pH modifiers are presented below in Table 4.7.

Based on the based median 50% volume percentile (d_{50}), the particle size analysis confirms the itraconazole and cysteine HCl have the smallest particle sizes (8 μm and 41 μm respectively) followed by the glycine HCl. A similar particle size range was observed

for the HPMC, glycine HCl betaine HCl and citric acid (128 μm -171 μm), with the betaine HCl exhibiting the largest particle size (171 μm). It is well documented in the literature that particle size of the API and excipient can impact on the flowability as well as the compression behaviour of solid dosage forms [25]. The particle size range obtained from the starting materials was 10–300 μm , apart from the itraconazole (3-8 μm observed for the D_{10} and D_{50} , respectively). These values fall within the range typically used for manufacturing solid dosage forms, being optimal for good flow characteristics [26].

Table 4.7: Particle size distribution data obtained from the starting materials (mean \pm SD, n= 3)

Material	Size Distribution		
	$D_{10}/\mu\text{m}$	$D_{50} /\mu\text{m}$	$D_{90}/\mu\text{m}$
Itraconazole	2.6 \pm 0.3	7.7 \pm 0.6	21.3 \pm 1.2
HPMC	65.0 \pm 1.0	128.3 \pm 0.6	211.7 \pm 3.8
Glycine HCl	46.3 \pm 0.6	150.0 \pm 0.0	222.0 \pm 0.0
Betaine HCl	51.3 \pm 3.5	171.3 \pm 6.7	253.0 \pm 1.7
Cysteine HCl	16.7 \pm 4.6	41.1 \pm 6.0	90.0 \pm 7.9
Citric Acid	45.7 \pm 3.8	160.3 \pm 0.6	254.3 \pm 0.6

4.6.4 Content Uniformity of Itraconazole Loading and Heterogeneity of Tablets

4.6.4.1 Content Uniformity and Distribution of 20% w/w Itraconazole with 10% w/w and 30% w/w pH Modifier Tablets Using Near Infrared (NIR)

The primary purpose of using PLS was to be able to rapidly quantify the levels of drug and pH modifier in the tablets for each of the systems prepared in this project and to have confidence that these quantities were consistent for each tablet within a batch.

For each of the PLS models, standard mixtures were blended to generate the predictive model. The calibration standards were prepared from the concentration ranges predicted by the algorithm within the TQ analyst software v7.2.0.161 (Thermo Electron Corp, Waltham, MA, USA). This avoids co-linear constituent concentrations, which would mean that no linear relationship would be observed between the two components within the prepared standards (drug and pH modifier). In total thirteen standards were prepared and used for the calibration plots.

Separate PLS calibration models were built for each modifier system, optimising the spectral range, the number of spectral regions and the number of principal components. The accuracy, predictive ability and robustness of the different models was assessed using a high correlation coefficient (R). The calibration models were built using algorithm PLS one, which uses a unique set of principal components for everything within the system. PLS one is advantageous for systems that have a wider range of concentrations and composition within the formulation.

No pre-processing methods were employed. Models were constructed initially using the entire spectral region and then reduced by identifying the prominent bands representing the IT and organic acid pH modifier (Fig. 4.14 and Fig. 4.15). These were determined by comparing the intensity of the peaks associated with a low and a high concentration of the constituent (see Fig. 4.14 and 4.15). For the IT, 0% w/w IT (pure HPMC) and 45% w/w IT were used as low and high concentration standards, respectively. For each modifier, standards were prepared containing approximately 10% w/w and 68% w/w.

The PLS parameters used (spectral regions and factors) are summarised in Table 4.8. For all the constituents except betaine HCl, one spectral region was used for the PLS quantification. The selected NIR spectral regions for the itraconazole and each of the pH modifiers are shown below in the grey highlighted regions in Fig. 4.14 and 4.15. Also, spectral areas were eliminated where no energy was reaching the detector.

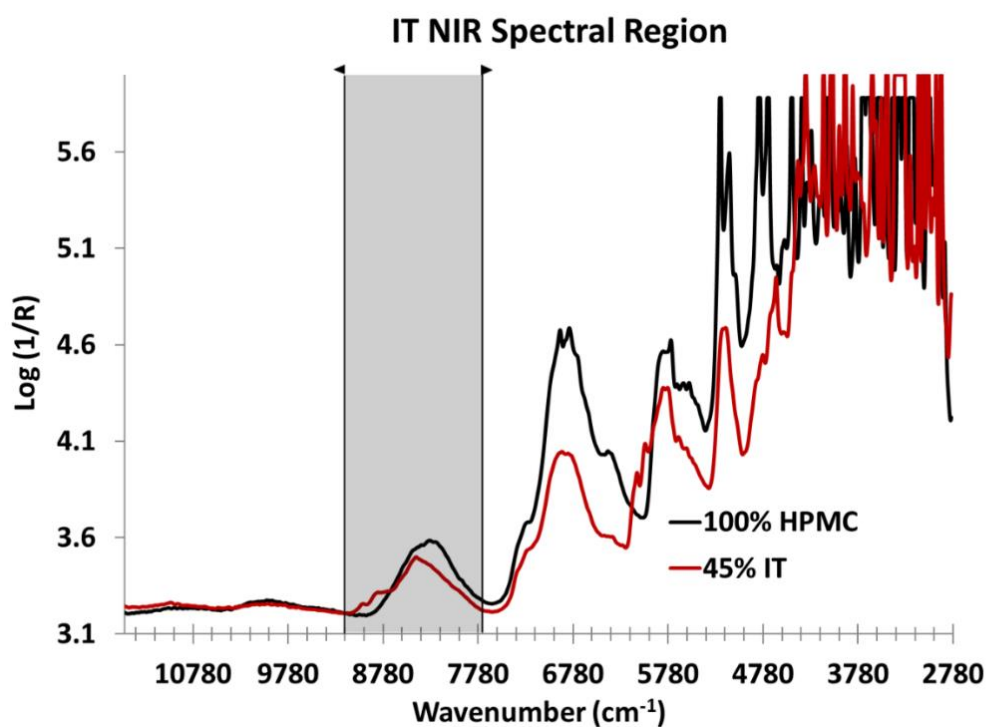


Fig. 4.14: NIR spectra obtained from a low and high concentration IT (0% and 45%) standard highlighting the spectral region used for PLS model

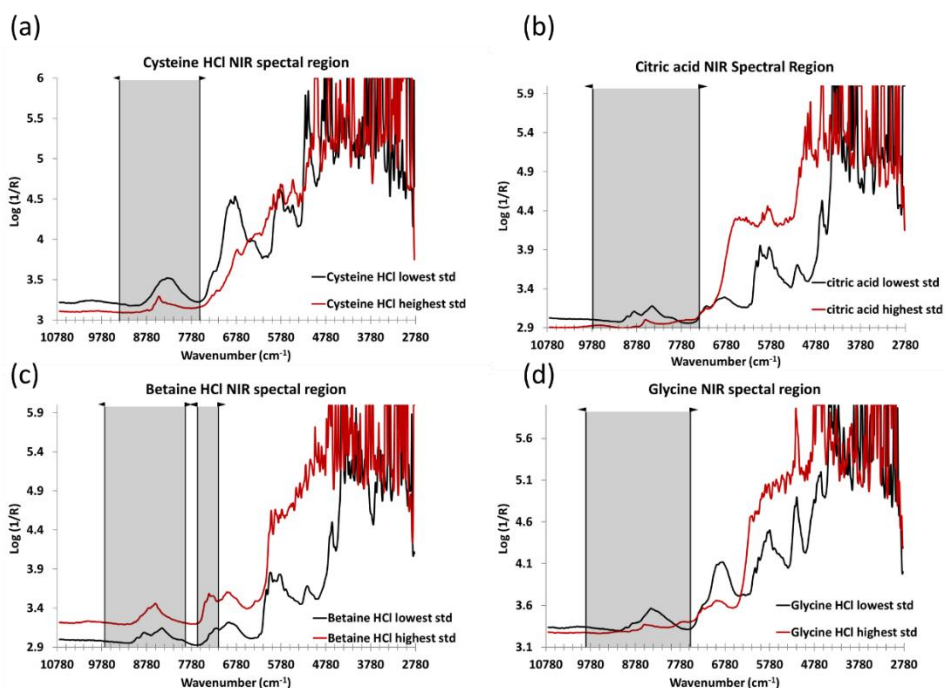


Fig. 4.15: NIR spectra obtained from a low and high concentration (8% w/w and 70% w/w) of modifier for (a) cysteine HCl; (b) citric acid; (c) betaine HCl and glycine HCl highlighting the spectral region used for PLS model

The number of factors used for the PLS model was determined using the predicted residual sum of squares (PRESS) plot diagnostic function in the TQ analyst software. This determines the optimal number of factors for the model, i.e. the factors at the point where the PRESS is minimum. No changes were made to the suggested number of factors and a minimum number of factors were used as this ensures the avoidance of over-fitting, which can lead to a poorly performing model which ultimately impacts on the prediction accuracy for unknown samples.

The robustness of the model and its ability to predict the drug and pH modifier content was tested using a validation set and a prediction set consisting of 6 tablets for each formulation. The validation of a calibration model is an important step in the process of verifying the suitability of a model and should take place prior to implementation of the method. This aids verification of the accuracy of the model.

Table 4.8: Spectral regions selected for quantification of itraconazole and pH modifiers for the PLS model

Formulation	Spectral Region 1 (cm ⁻¹)	Spectral Region 2 (cm ⁻¹)	Optimal Number of Factors	
			Modifier	IT
Itraconazole binary system	9157-7774	-	-	4
Betaine HCl+IT	9515-7671	7601-7157	4	4
Citric acid+IT	9260-7695	-	4	2
Cysteine HCl+IT	9175-7580	-	3	4
Glycine HCl+IT	9264-7552	-	3	4

Plots of the calculated concentration versus the actual concentration, so-called concentration correlation plots, for each of the tablet components are presented in Fig. 4.16 to Fig. 4.20 for the NIR calibration models. These plots show a good correlation between calculated and predicted values (R value of 0.99) and prediction performance

for these PLS models with validation values closely distributed along the ideal correlation line.

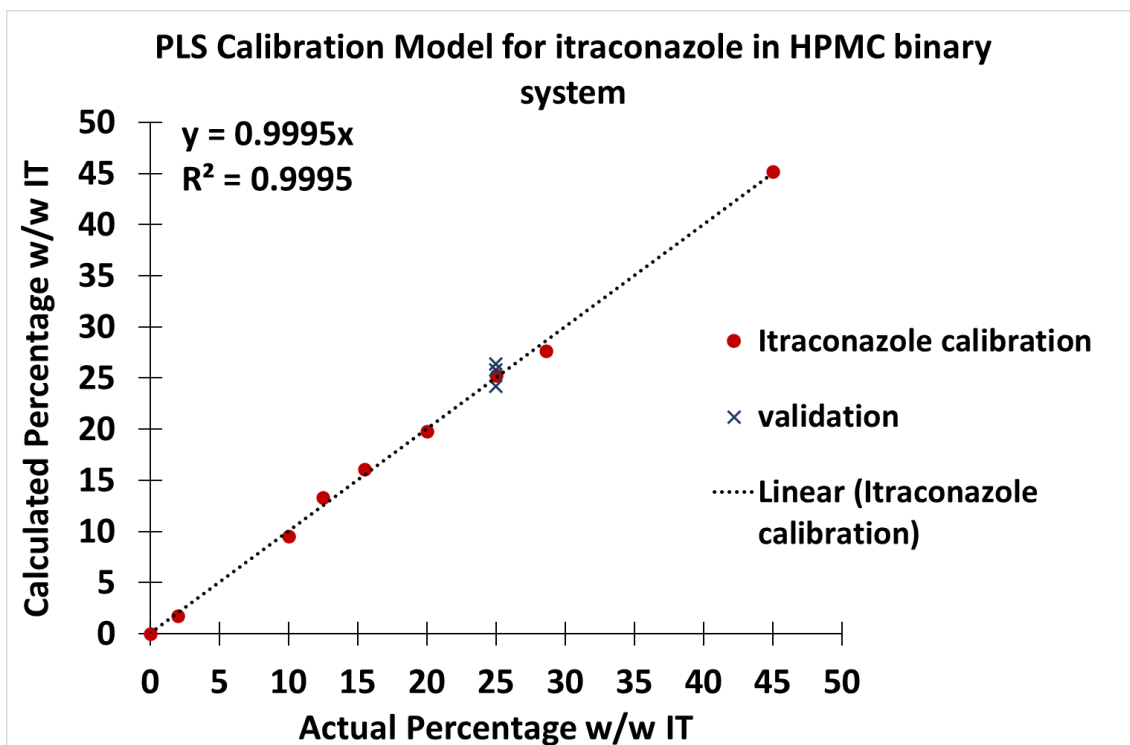


Fig. 4.16: PLS plot of calculated versus actual concentration levels for the binary system (HPMC and itraconazole)

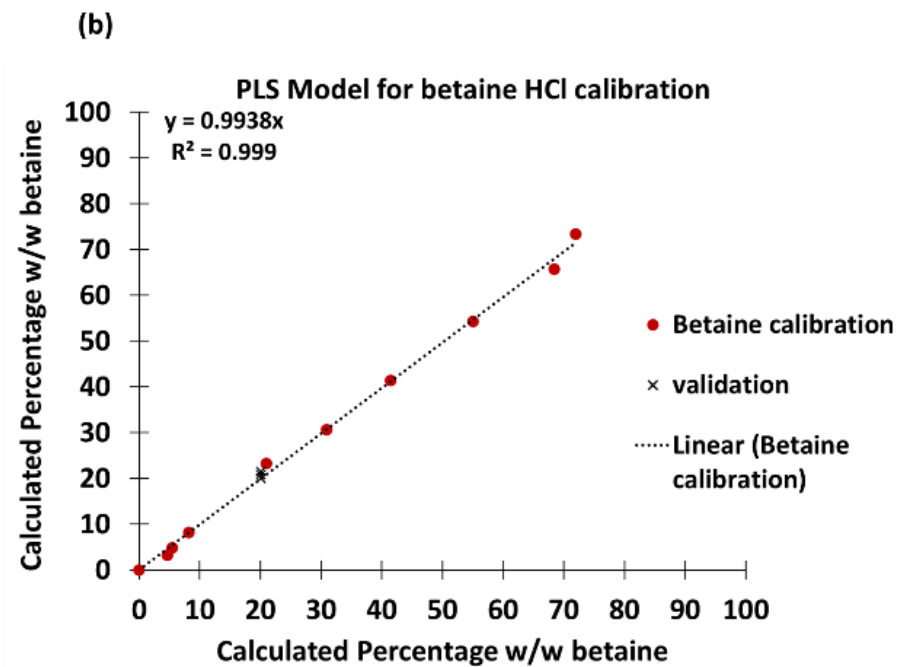
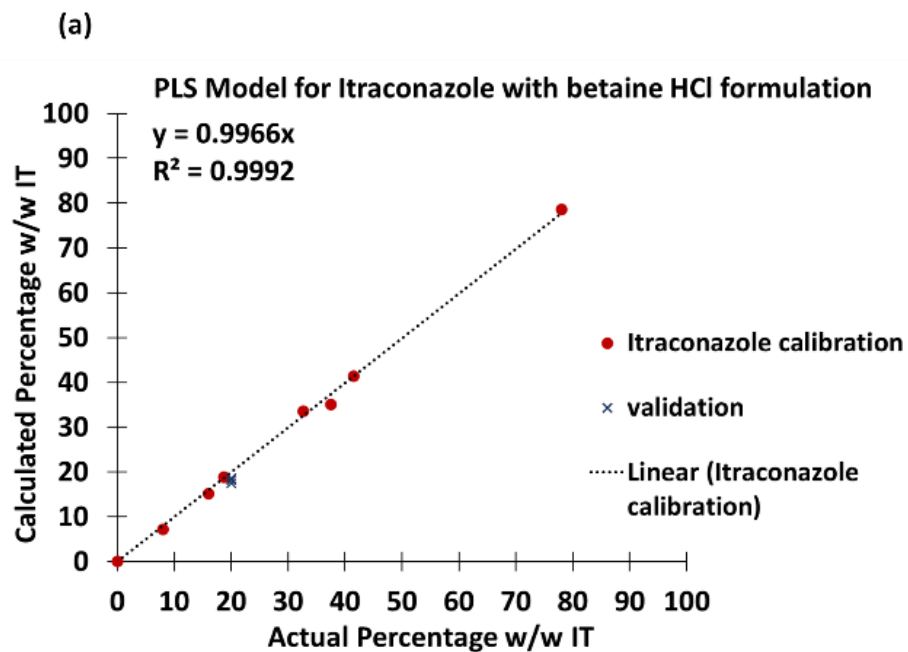


Fig. 4.17: PLS plot of calculated versus actual concentration levels for the betaine formulation (betaine HCl and IT in HPMC matrix) for: (a) itraconazole; (b) betaine HCl

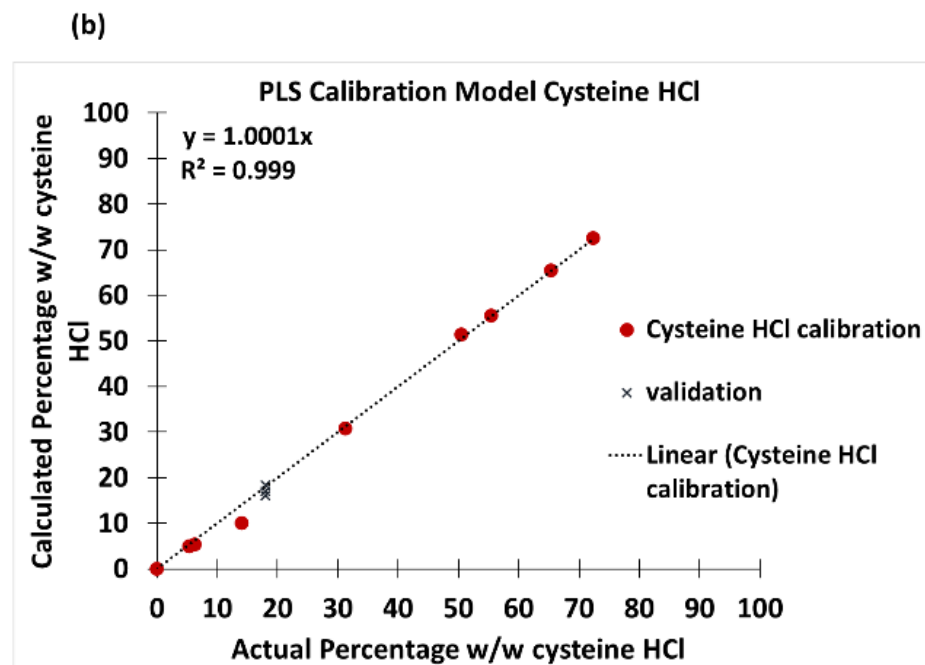
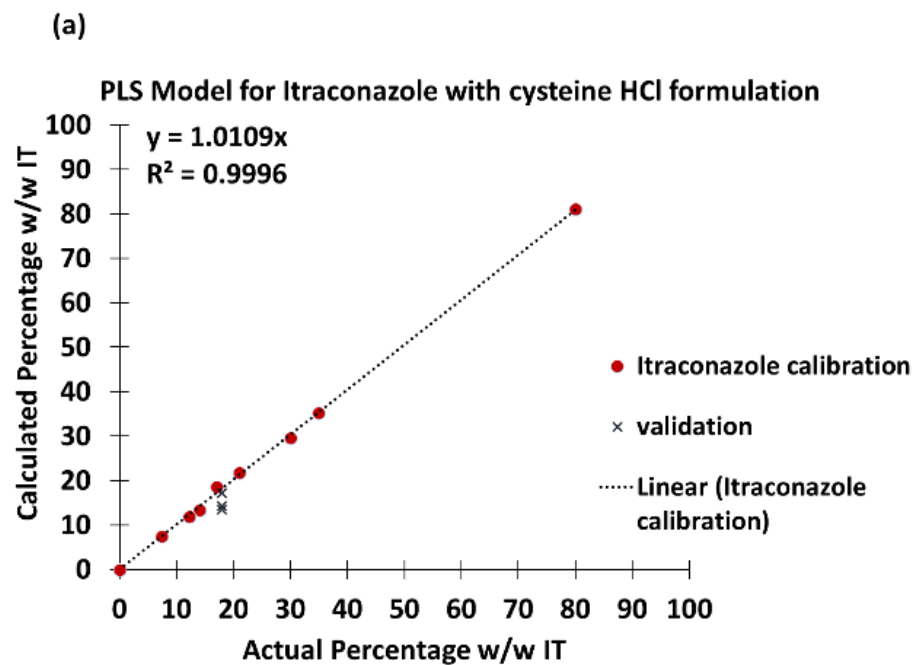


Fig. 4.18: PLS plot of calculated versus actual concentration levels for the cysteine HCl formulation (cysteine HCl and IT in HPMC matrix) for: (a) itraconazole; (b) cysteine HCl

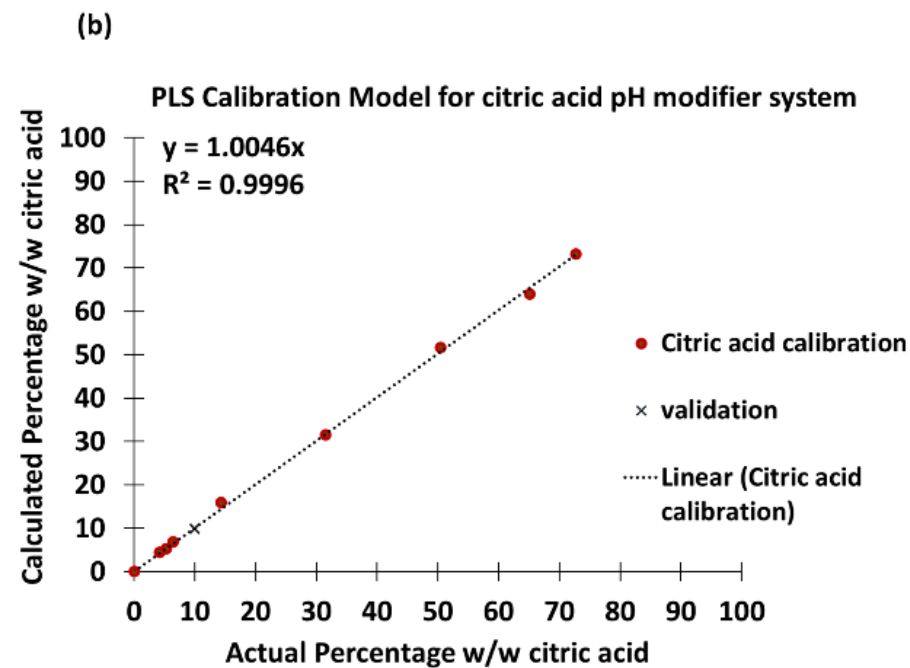
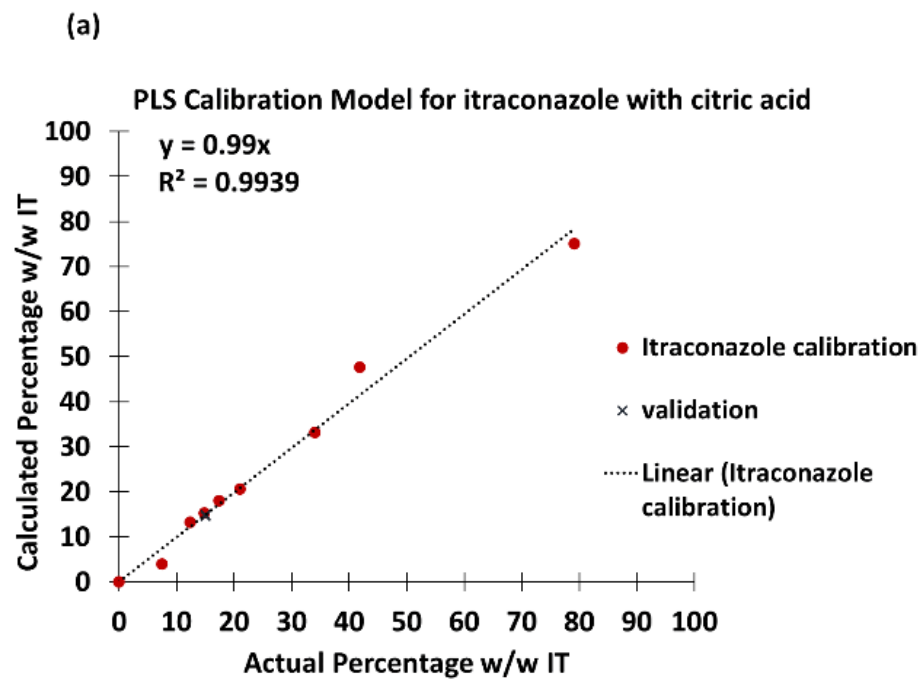


Fig. 4.19: PLS plot of calculated versus actual concentration levels for the citric acid formulation (citric acid and IT in HPMC matrix for (a) itraconazole; (b) citric acid

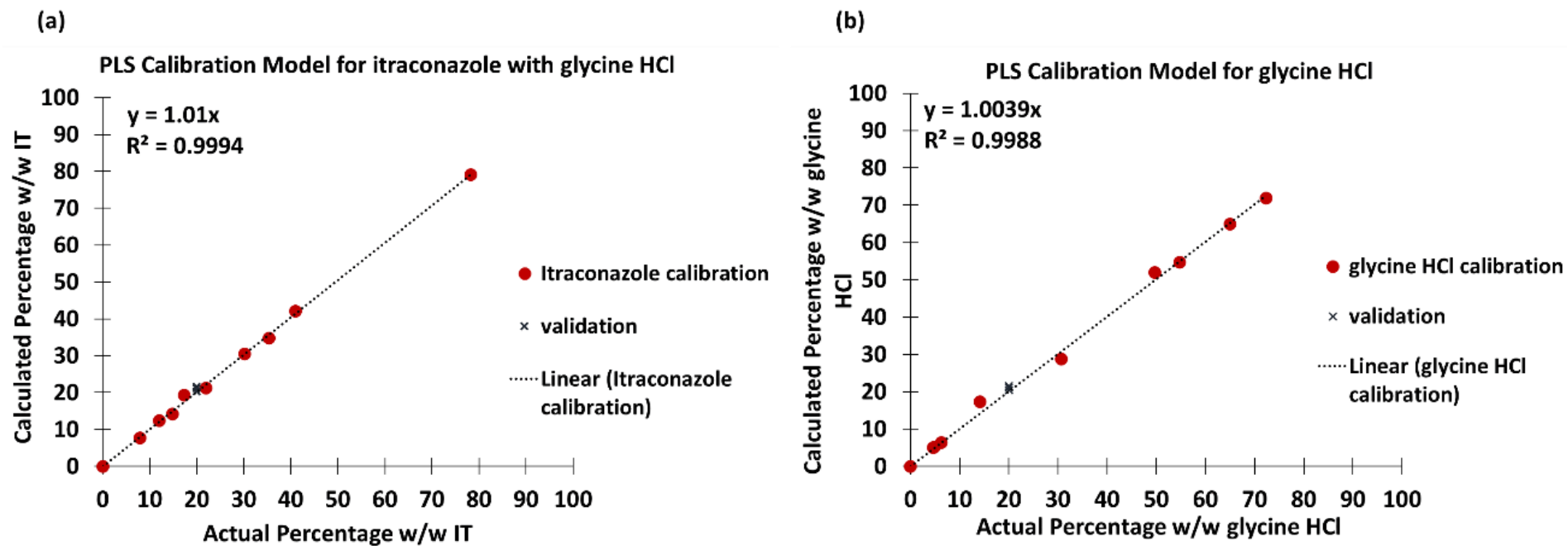


Fig. 4.20: PLS plot of calculated versus actual concentration levels for the glycine HCl formulation (glycine HCl and IT in HPMC matrix) for: (a) itraconazole; (b) glycine HCl

Initially, quantification was carried out on the 20% w/w IT tablets (n=6) and the data generated from this analysis is presented in Table 4.9.

Table 4.9: PLS model results based on the optimised spectral ranges for the 20% w/w IT (binary system n=6)

Tablet	20% w/w IT tablets (binary system)
Tablet 1	18.44
Tablet 2	19.47
Tablet 3	19.21
Tablet 4	19.17
Tablet 5	20.05
Tablet 6	20.44
Average	19.46
SD	0.7
RSD (%)	3.6
Acceptance level	12.7

The six tablets analysed by the NIR-PLS method show good agreement with regards the expected percentage of itraconazole in each tablet (20% w/w) and a mean of 19.46% and a relative standard deviation of 3.6% was obtained. The results confirm that the strategy adopted successfully produced tablets with a consistent concentration of API.

Tables 4.10 and 4.11 show the calculated quantities for the components within the tablets for the 10% w/w and 30% w/w pH modifier placebo formulations, respectively. Values were obtained from the NIR PLS models computed over the selected spectral ranges and six tablets were prepared and analysed for each formulation.

The data shows that the prediction performance of the PLS model is in line with the expected levels of the pH modifier, with the relative standard deviation below 6% (ranging from 1.6 to 5.1%) for all the 10% w/w and 30% w/w pH modifier placebo formulations. This suggests that the values are comparable to those reported in the literature by other researchers [27] and are within the stipulated USP criteria for acceptance testing for content uniformity on compacting tablets, which states: “The Relative Standard Deviation (RSD) is no greater than 6.0%” [28]. The approach adopted

confirms that reproducible tablets are created which contain the expected concentrations of pH modifier.

The NIR PLS data generated for the tablets containing 10% w/w modifier and 30% w/w modifier with 20% w/w itraconazole is presented in Tables 4.12 and 4.13. Again, a good agreement was obtained between the calculated concentration values in comparison to the expected concentration of organic acid modifier and itraconazole in the tablets. With a relative standard deviation of <5.5% for the calculated itraconazole in the 10% w/w modifier +20% w/w IT systems and for the 30% w/w modifier +20% w/w IT systems. This indicates that all tablets are inside the United States Pharmacopeia (USP) range of up to 6.0%, although in some cases, they were close to the acceptable limit. The USP is used as an industry standard by the pharmaceutical sector, however, is not a regulatory body.

A relative standard deviation of up to 6.3 %, ranging from 2.2% (30% w/w glycine HCl) to 6.3% (10% w/w betaine HCl), was observed for the calculated levels of the modifiers in both the 10% w/w modifier +20% w/w IT systems and for the 30% w/w modifier +20% w/w IT systems. Again, this confirms that the overall strategy adopted produced consistent and as-expected concentrations of organic acid modifier within the tablets.

The data processing methodology adopted for the NIR analysis could potentially be optimised by improving the signal-to-noise and utilising data pre-processing steps (baseline correction, etc.) prior to applying the PLS model [29]. This could help eliminate artefacts caused during measurement, which in turn would improve the prediction performance or interpretation and improve the relative standard deviation [29].

The approach to quantification of API and pH modifier in oral dosage forms is commonly carried out using chromatographic techniques such as HPLC. These methods are time-consuming and labour-intensive and furthermore require the destruction of the tablet. Also, several methods may have to be employed to quantify the different constituents within the tablet. By comparison, the NIR technique adopted in this project provides a

rapid approach to quantifying the levels of API and pH modifier simultaneously, while the tablet remains intact following analysis [30].

Content uniformity results are reported in the literature in several ways, either in terms of relative standard deviation (RSD) and/or acceptance value, with the former being more prevalent in research papers. The RSD is the standard deviation (s) of the drug content in the samples analysed, expressed as the percentage of the mean [18] and is determined by the following equation:

$$100 s/\bar{X} \quad \text{Equation 4.1}$$

The use of an acceptance value is defined by several bodies, including the United States Pharmacopeia (USP), the European Pharmacopeia and the Japanese Pharmacopeia. It also forms the basis for assessment in the ASTM Standard E2810. The acceptance value is determined from an analysis of either 10 or 30 tablets, based on the recommendation as outlined in the United States Pharmacopeia (USP), European Pharmacopoeia and ASTM standard (American Society for Testing and Materials) [28] [31].

The acceptance value (AV) is calculated from the following equation [[28]:

$$AV = |M - \bar{X}| + ks \quad \text{Equation 4.2}$$

Where:

- M is the reference value;
- \bar{X} is the mean of the individual contents, expressed as a percentage of the label claim (LC);
- k is the acceptability constant, 2.4 where n = 10 and 2.0 where n = 30;
- s is the sample standard deviation.

As noted, the USP criteria refers to the tablet label claim (% label claim) rather than the mean analytical value.

The value for M is dependent on T, the target content per dosage unit. In this study, T is 100% LC for each constituent. The following criteria then apply:

1. If \bar{X} is less than 98.5% LC, then $M = 98.5\% \text{ LC}$;
2. If \bar{X} is between 98.5 and 101.5% LC, then $M = \bar{X}$;
3. If \bar{X} is greater than 101.5% LC, then $M = 101.5 \text{ LC}$.

The content uniformity requirement is assumed to be met if AV is equal to or less than 15 [31] [32]. It should be noted that the value of the acceptability constant is based on a sample of either 10 or 30 tablets. However, for the purpose of this study, it was decided that preparation and analysis of 6 tablets per formulation was sufficient to provide indicative results.

Applying the above criteria to the NIR data generated for all the tablets prepared in this study, most tablets conform to the requirement (Tables 4.9-4.13). However, some of the tablets fall just outside the range and these are as follows:

- 10% w/w cysteine HCl +20% w/w IT (both modifier and IT, acceptance value of 15.5 and 15.6 respectively, data in table 4.12)
- 10% w/w betaine HCl +20% w/w IT (modifier only, acceptance value of 15.7, data in table 4.12)
- 30% w/w citric HCl +20% w/w IT (itraconazole only, acceptance value of 15.5, data in table 4.13)

However, it should be noted that this criterion is designed for the pharmaceutical sector where large batch of tablets are manufactured under controlled and optimised conditions (particle size matching, blending parameters, etc).

Table 4.10: PLS model results based on the optimised spectral ranges for the 10% w/w pH modifier placebo tablets (n=6)

Tablet	% w/w betaine HCl	% w/w cysteine HCl	% w/w citric acid	% w/w glycine HCl
Tablet 1	9.52	10.29	9.66	11.29
Tablet 2	10.32	10.68	9.89	10.89
Tablet 3	10.5	10.58	10.03	10.93
Tablet 4	9.73	10.33	10.24	10.61
Tablet 5	10.89	10.99	10.43	10.31
Tablet 6	10.21	10.74	9.01	10.46
Average	10.20	10.60	9.88	10.75
SD	0.5	0.3	0.5	0.4
RSD (%)	4.9	2.5	5.1	3.3
Acceptance level	12.5	10.8	12.0	14.6

Table 4.11: PLS model results based on the optimised spectral ranges for the 30% w/w tablets pH modifier placebo tablets (n=6)

Tablet	% w/w betaine HCl	% w/w cysteine HCl	% w/w citric acid	% w/w glycine HCl
Tablet 1	28.46	32.24	28.30	30.77
Tablet 2	31.68	32.22	28.61	33.54
Tablet 3	31.84	32.76	32.88	29.99
Tablet 4	31.34	31.79	28.85	30.87
Tablet 5	32.62	32.32	27.65	29.53
Tablet 6	30.02	31.28	29.21	31.2
Average	30.99	32.10	29.08	30.98
SD	1.5	0.5	1.5	1.4
RSD (%)	4.9	1.6	5.0	4.5
Acceptance Value	13.8	9.6	13.3	12.9

Table 4.12: PLS model results based on the optimised spectral ranges for the 10% w/w pH modifier with 20% w/w itraconazole tablets (n=6)

Tablet	% w/w Citric acid	% w/w Itraconazole	% w/w Glycine HCl	% w/w Itraconazole	% w/w Cysteine HCl	% w/w Itraconazole	% w/w Betaine HCl	% w/w Itraconazole
Tablet 1	10.1	21.31	9.48	20.65	9.51	21.36	9.94	19.02
Tablet 2	9.81	21.23	9.86	20.12	10.63	20.67	9.09	19.84
Tablet 3	9.32	21.81	10.04	20.21	10.09	20.86	10.73	20.55
Tablet 4	9.34	20.28	9.93	19.49	11.15	21.03	10.29	19.65
Tablet 5	10.89	21.33	10.44	19.72	10.41	21.66	10.89	20.27
Tablet 6	9.74	21.16	10.18	20.29	10.48	21.31	10.11	19.45
Average	9.87	21.19	9.99	20.08	10.38	21.15	10.18	19.80
SD	0.6	0.5	0.3	0.4	0.5	0.4	0.6	0.6
RSD (%)	5.9	2.4	3.2	2.1	5.3	1.7	6.3	2.8
Acceptance Value	14.0	17	7.8	6.1	15.5	15.6	15.7	12.4

Table 4.13: PLS model results based on the optimised spectral ranges for the 30% w/w pH modifier with 20% w/w itraconazole tablets (n=6)

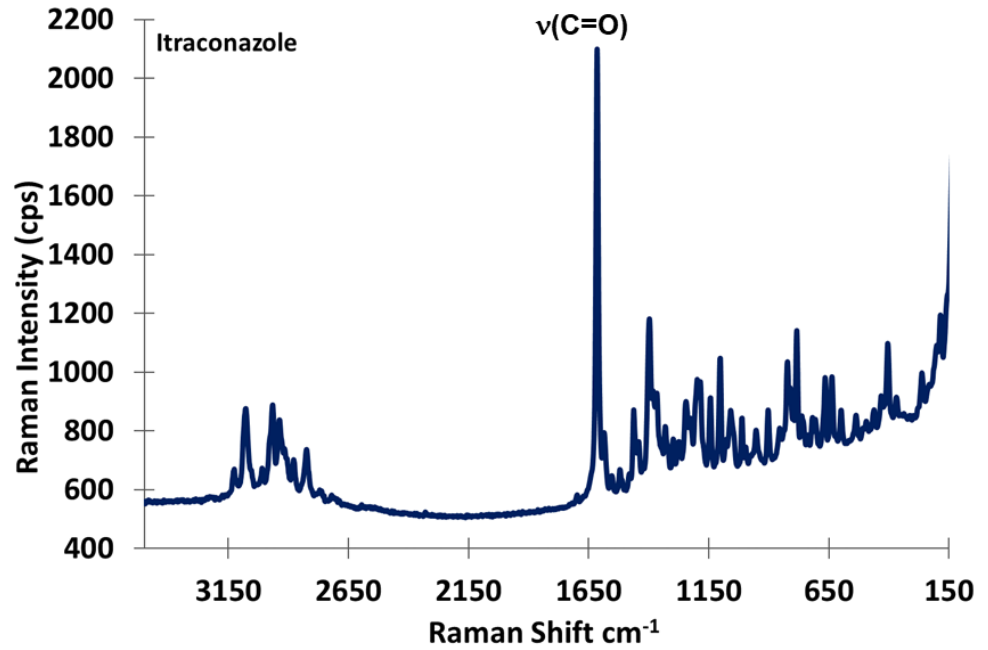
Tablet	% w/w Citric acid	% w/w Itraconazole	% w/w Glycine HCl	% w/w Itraconazole	% w/w Cysteine HCl	% w/w Itraconazole	% w/w Betaine HCl	% w/w Itraconazole
Tablet 1	31.25	21.25	32.19	21.85	28.18	19.88	30.00	19.25
Tablet 2	30.68	21.21	33.79	19.54	27.05	19.25	31.78	21.16
Tablet 3	29.29	20.39	33.07	20.37	27	18.99	30.13	21.9
Tablet 4	29.12	21.43	32.87	20.78	26.77	19.66	30.07	19.21
Tablet 5	32.41	20.88	32.88	20.87	26.5	18.65	29.87	19.58
Tablet 6	30.04	20.57	34.26	19.89	26.58	19.92	29.10	19.85
Average	30.47	20.96	33.18	20.55	27.01	19.39	30.16	20.16
SD	1.3	0.4	0.7	0.8	0.6	0.5	0.9	1.1
RSD (%)	4.1	2.0	2.2	4.0	2.3	2.7	2.9	5.5
Acceptance Value	10.1	15.5	15.0	12.7	13.4	12.8	7.1	14.2

4.6.4.2 Content Uniformity and Distribution of Itraconazole and pH Modifier within the Tablets Using Raman Microscopy

The Raman spectra obtained from the HPMC and itraconazole are presented below in Fig. 4.21. The spectra were used to identify the most suitable bands which represented the HPMC and IT. The most appropriate bands were found to be the $\sim 2839\text{ cm}^{-1}$ in HPMC (attributable to the $\nu(\text{CH})$) and 1614 cm^{-1} for itraconazole (attributable to the $\nu(\text{C}=\text{O})$).

The band at 1614 cm^{-1} and 2829 cm^{-1} were then used to determine the IT:HPMC ratio for each of the six tablets. This is a common approach adopted for analysing data generated from vibrational spectroscopy-based techniques [33]. It eliminates issues relating to background fluctuations etc, thereby providing a method for normalising the data and enabling a more robust and useful method of comparing distributions relating to a particular component within a sample [33]. The ratio for this work was produced using peak heights.

(a)



(b)

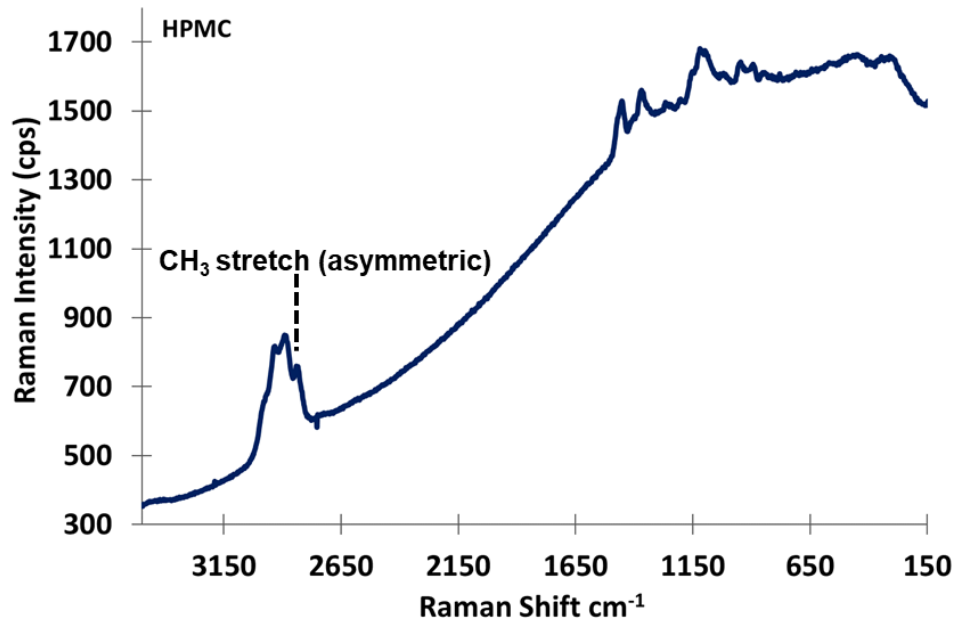


Fig. 4.21 Raman spectra obtained from (a) itraconazole and (b) HPMC highlighting the bands and the corresponding functional group used to generate the distribution images

Fig. 4.22 (a) shows the distribution of IT, based on the $\nu(\text{C}=\text{O})$ band $\sim 1614 \text{ cm}^{-1}$, in the three tablets analysed and Fig. 4.22 (b) shows the ratio of IT:HPMC, as described.

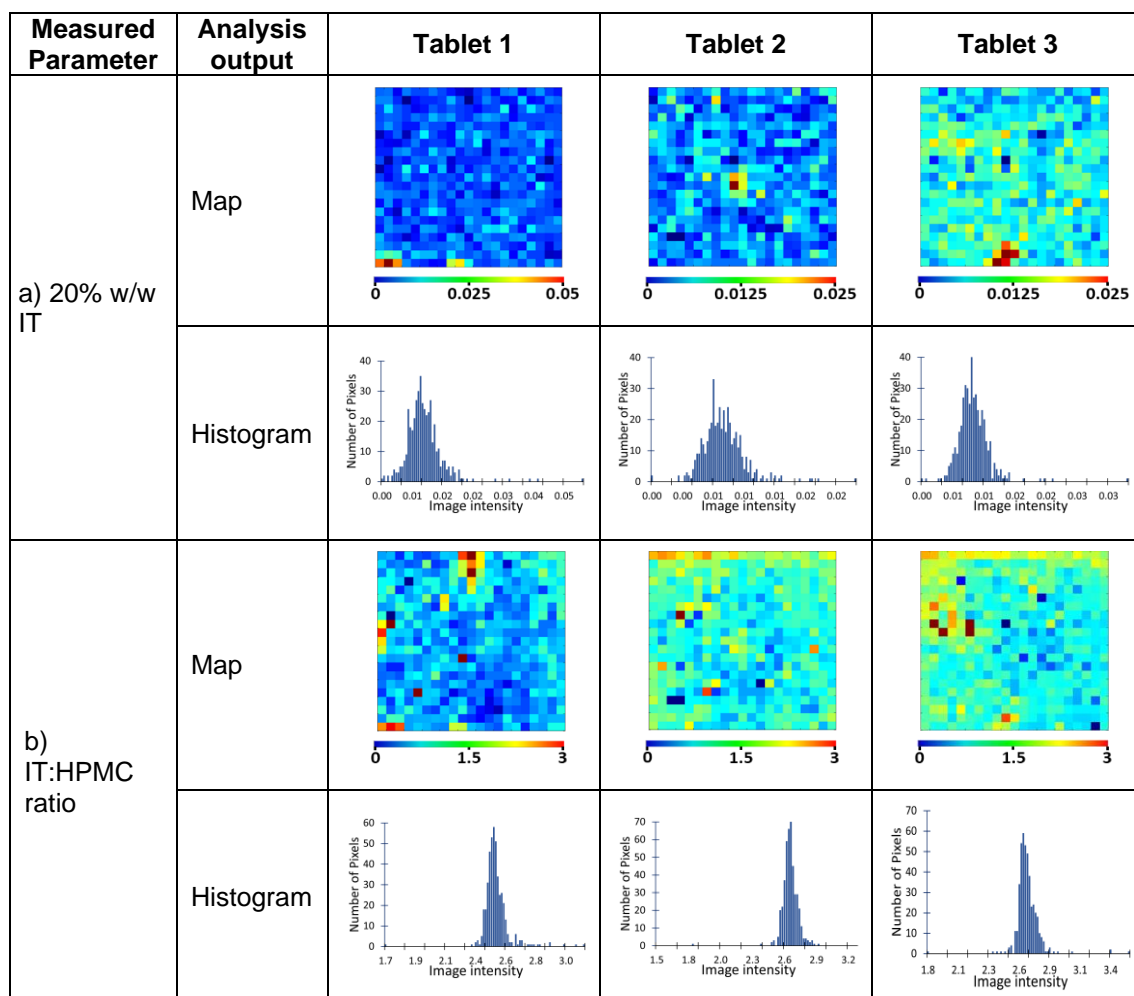


Fig. 4.22 Raman Distribution images and corresponding histograms obtained from the 20% IT w/w tablets for the three tablets analysed (a) showing IT (based on the band observed at 1614 cm^{-1} and b) shows the ratio of band intensities (selected markers) to represent IT:HPMC

With these maps, it is possible to make a visual, qualitative assessment of the spatial distribution of IT and pH modifier. However, without a means of quantification, the magnitude of any concentration variability cannot be determined and as such it is difficult to ascertain where highly localised regions of either IT or pH modifier exist and how this translates into differences in the concentration of the constituents within the tablet matrix. In order to provide an additional means of assessing the uniformity of distribution for the IT and organic acid pH modifier within the tablet matrix, the associated histogram for the distribution maps were generated. This approach is often adopted when assessing the homogeneity of components within oral dosage forms and for comparing sample-to-sample variability from the same batch, or from different processing methods [34] [35].

The histogram represents the distribution of the pixel values in the image, which can be related to the concentration of the constituent. The parameters that can be obtained from the histogram are the mean (relative abundance), standard deviation, skewness and kurtosis of pixel intensity distribution in the mapped/imaged area [34] [36].

The skewness indicates the level of symmetry of the distribution and for a normal distribution this would be zero [34]. Negative values indicate the data are skewed to the left and conversely positive values are indicative of a skew to the right [34] [37].

In the literature there seems to be a variety of ways that kurtosis has been defined some of which refer to the “degree of peakedness of distribution” (positive kurtosis shown as a peaked distribution and a negative kurtosis indicated by a flat distribution) [38] and a value of three is also used as a measure for a standard normal distribution (Gaussian distribution) [34] [39]. Both the skew and kurtosis describe a deviation from a normal distribution. The mean values relate to the abundance (concentration) of the constituent/parameter analysed.

The Raman distribution images obtained from the peak area integrated maps obtained from the 20% w/w IT tablets (n=3) are presented in Fig. 4.22. The scale bar displayed with the distribution images indicates the changes in Raman intensity, with the blue

colour indicating the lower IT or organic acid pH modifier distribution in the mapped area. Conversely, higher levels are shown in the red colour. The corresponding histograms are also presented in Fig. 4.22. It should be noted that the histogram plots show the pixel values at a particular intensity.

The results indicate that the distribution of itraconazole (Fig. 4.22a) is essentially uniform and little difference was observed across the multiple tablets analysed. However, it should be noted a few high intensity pixels are observed images, which can be related to higher levels of IT in these areas (denoted by the red colour).

The corresponding histogram plots show the number of pixels with a particular intensity, which also look very similar across the tablets analysed. The statistical data (Table 4.14) for the corresponding histograms also confirms a degree of reproducibility is observed for the three tablets analysed, as indicated by the mean and standard deviation values. A similar range of values observed for the kurtosis (0.99-1.5) and skew (0.10-0.34). Although the distributions are not considered to be normal (kurtosis 3 and skew 0), reasonable compositional homogeneity was discernible for the IT distribution.

The corresponding IT:HPMC ratio images are presented in Fig. 4.22b and again, a similar distribution is observed. However, the corresponding images show a tall peak with a narrow base which is more akin to a Gaussian distribution, in comparison to a broader profile observed for the IT distribution, indicating the IT is indeed homogeneously distributed. This engenders confidence that the method employed for the preparation of tablets provides a uniform distribution of the IT in the HPMC matrix.

Table 4.14: Statistical data obtained from histograms for: 20% w/w IT binary system

Parameter	Tablet	Mean	Standard Deviation	Kurtosis	Skew
IT intensity	1	0.01	0.00	1.30	0.34
	2	0.01	0.00	1.50	0.31
	3	0.01	0.00	0.99	0.10
IT:HPMC ratio	1	2.50	0.06	3.70	1.30
	2	2.66	0.07	2.20	0.40
	3	2.67	0.06	1.80	0.25

The average spectra profiles (Fig. 4.23) generated from the Raman maps are also very similar for the three tablets analysed. This again confirms that the strategy adopted for synthesising the tablets was successful at producing uniformly distributed IT within the tablet matrix.

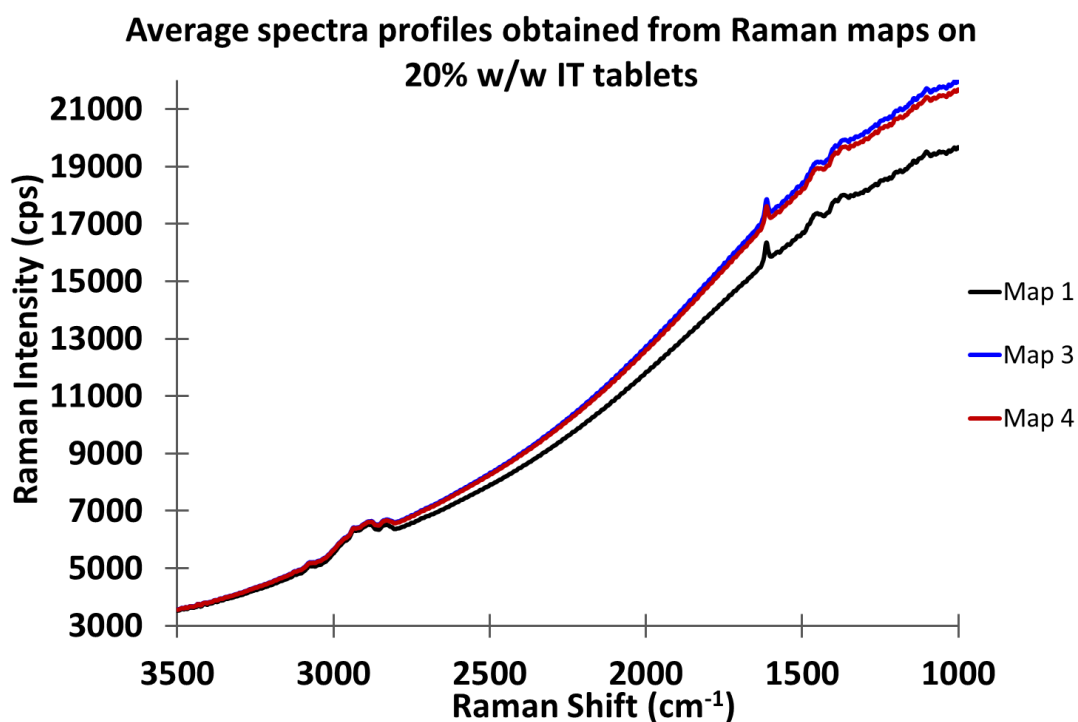


Fig. 4.23: Average spectra profiles (n=3) obtained from Raman maps on 20% w/w Itraconazole tablets (binary system)

Raman reference spectra were also generated from the organic acid modifiers and these are presented in Fig. 4.24.

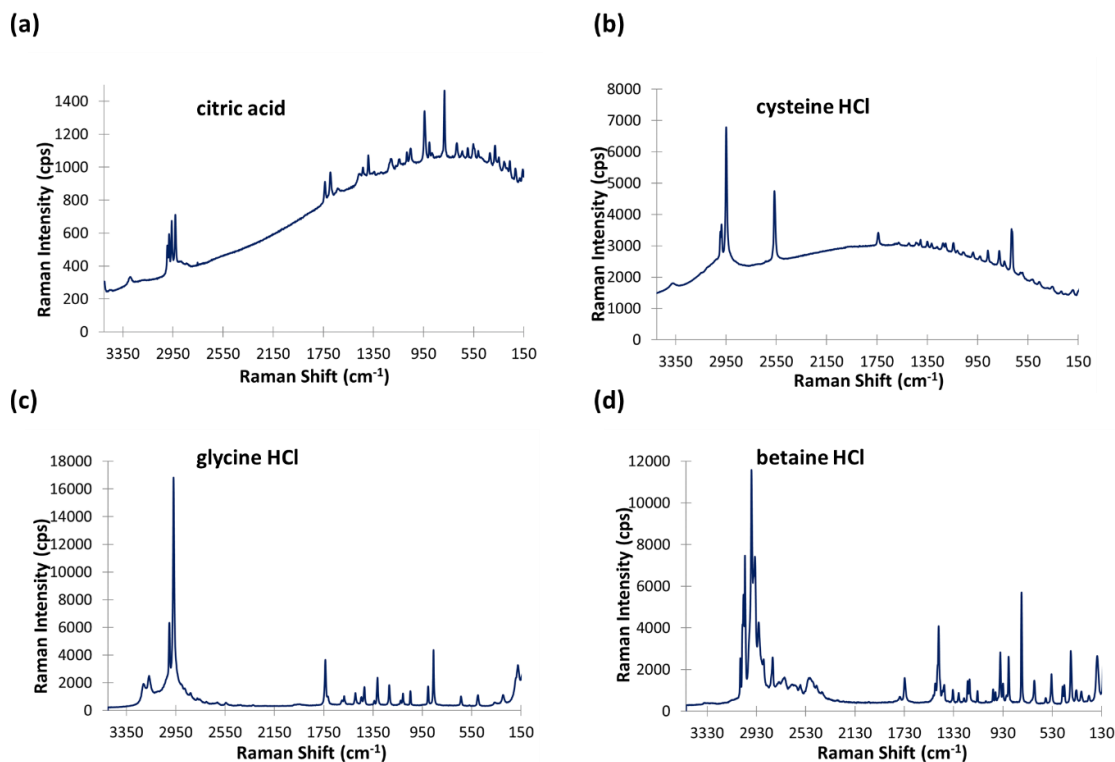


Fig. 4.24: Raman reference spectra obtained from (a) citric acid; (b) cysteine HCl; (c) glycine HCl and (d) betaine HCl

To investigate how well the itraconazole and the pH modifiers were distributed within the HPMC matrix, appropriate bands were identified (discrete spectral marker) which could be assigned to the IT and each organic acid pH modifier. For IT, the carbonyl band observed at 1614 cm⁻¹ was selected, while for the pH modifiers, bands were identified from the spectra in Fig. 4.24. The chosen bands are identified in Table 4.15.

Table 4.15 Selected absorption bands used to generate the Raman distribution maps for the organic acids

Organic Acid	Raman band and position
Betaine HCl	$\nu(\text{C=O})\sim 1728\text{ cm}^{-1}$
Cysteine HCl	$\nu(\text{S-H})\sim 2564\text{ cm}^{-1}$
Citric acid	$\nu(\text{C=O})\sim 1736\text{ cm}^{-1}$
Glycine HCl	$\nu(\text{C=O})\sim 1736\text{ cm}^{-1}$

Having identified appropriate bands, peak area integrated distribution maps were generated along with peak height ratio images (itraconazole:modifier). Similar to the 20% w/w IT system, histograms and the corresponding statistical information was obtained from each Raman map. The statistical data produced from the histograms (mean, standard deviation, skew and kurtosis) is shown in Tables 1-4 in Appendix 1.

The Raman distribution maps and corresponding histograms generated for the 10% w/w citric tablets (n=3) are presented in Fig. 4.25. Comparing the image distribution maps across the triplicate set for the citric acid, IT and ratio, it can be seen that a similar distribution is observed in the three tablets and the distribution appears to be relatively homogeneous, with few areas where hotspots (high concentration shown by the red regions) are observed for the IT and citric acid. Examination of the histograms shows some variation in the distribution of the pixels, however the corresponding statistical data shown in Table 1 of Appendix 1 indicates a similar mean, kurtosis and skewness for each of the constituents within the triplicate set. The skew data and kurtosis data both confirm the distribution is not normal, i.e. the kurtosis is above 3 and the skew is above zero. However, a high degree of asymmetry is not apparent in the histogram plots, indicating that the distribution of the IT and citric acid is not considered to be heterogeneous [37].

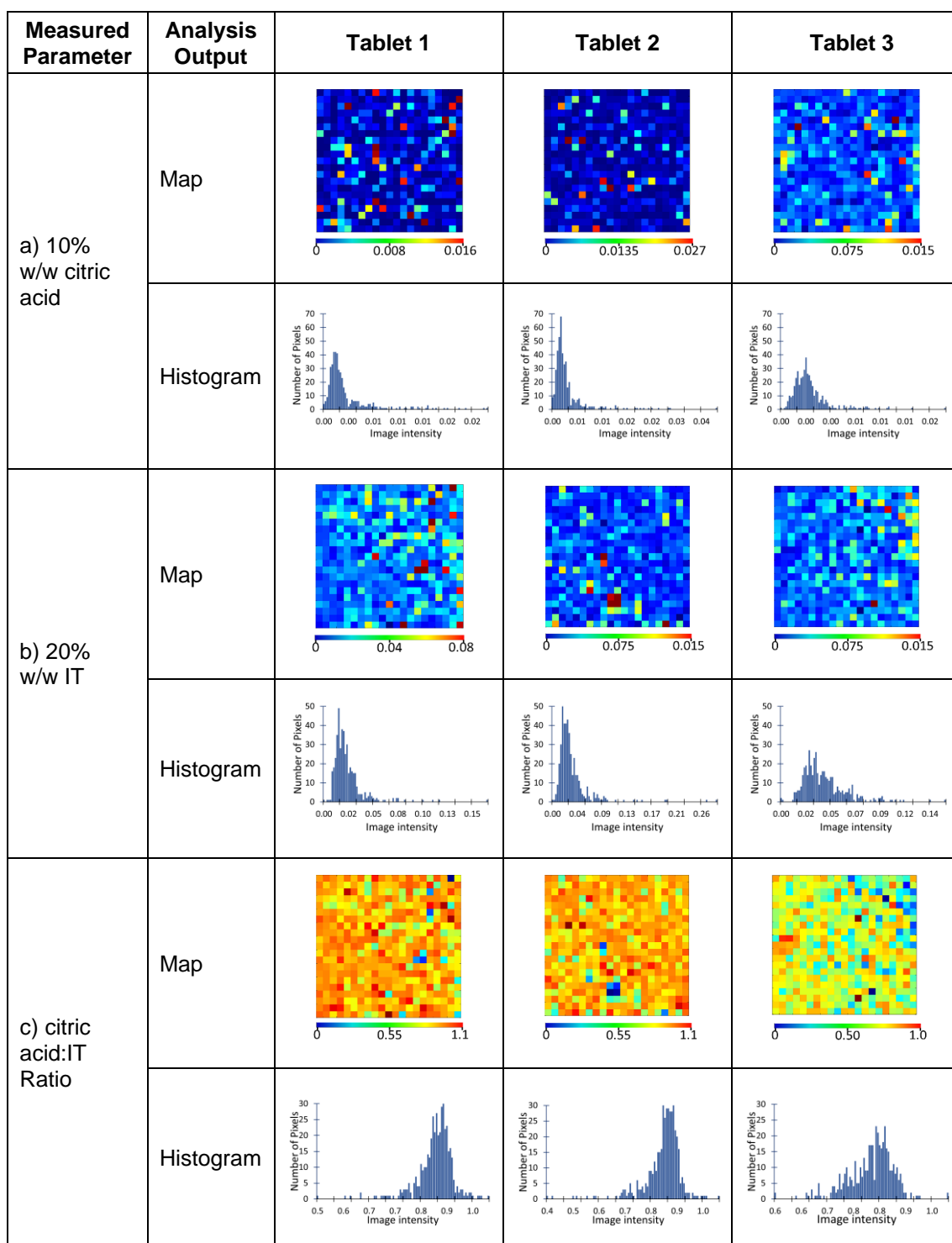


Fig. 4.25: Raman distribution images and corresponding histogram for 10% w/w citric acid with 20% w/w itraconazole formulation showing a) citric acid; b) IT and c) ratio of pH modifier/itraconazole

The Raman distribution maps and corresponding histograms generated for the 10% w/w betaine HCl +20% w/w IT tablets (n=3) are presented in Fig. 4.26. The distribution of the betaine HCl (Fig. 4.26a) for the 3 tablets analysed looks to be very similar, with very few areas of localised modifier, suggesting a uniform distribution. The corresponding histogram distributions are also very similar across the three tablets analysed, exhibiting a symmetric distribution with a narrow base and a sharp peak, supporting the assertion that the betaine HCl is homogeneously distributed. The maps relating to the IT distribution highlight some regions of localised IT hot spots (shown by the red colour), implying the possibility of clumping of the IT particles. Similarities were observed in the shape and distribution for the corresponding histograms. The images representing the betaine HCl:IT ratio show a uniform distribution, with a minimum of contrast, apart from the areas where localised IT is observed.

Comparing the statistical data presented in Table 2 of Appendix 1 (mean, standard deviation, kurtosis, and skew), similar values are obtained from the histograms for the tablets analysed. This confirms that there is reproducibility of the homogeneity within the three tablets analysed.

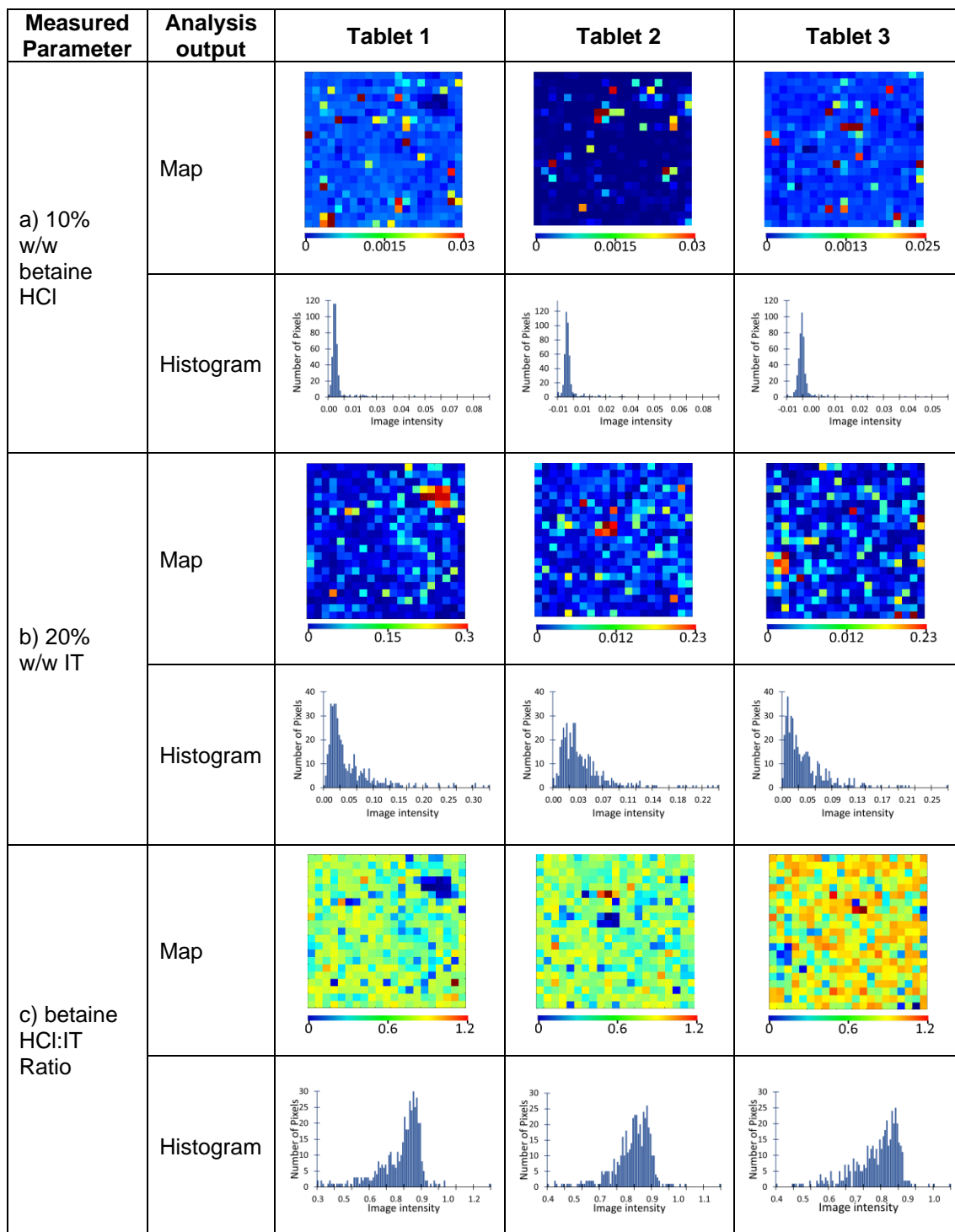


Fig. 4.26: Raman distribution images and corresponding histogram for 10% w/w betaine HCl with 20% w/w itraconazole formulation showing a) betaine HCl; b) IT and c) ratio of pH modifier/itraconazole

The Raman maps and histograms associated with the 10% w/w cysteine HCl +20% w/w IT are shown in Fig. 4.27. The images for the cysteine HCl (Fig. 4.27a) are similar for the three tablets analysed and the corresponding histogram distributions are also very similar with a narrow base and a sharp peak, suggesting that the modifier is uniformly distributed within the tablet matrix. The distribution images generated for the IT (Fig. 4.27b) are again very similar for the three tablets with some areas showing IT hotspots. The corresponding histograms have a wider base in comparison to the cysteine HCl modifier distributions, suggesting the distribution is not as homogeneous [37]. The images representing the cysteine HCl:IT ratio (Fig. 4.27c) show a relatively uniform distribution, apart from the areas where localised IT is observed within the tablet matrix. Similar statistical data (Table 3, Appendix 1) was obtained from the histogram plots associated with the constituents (cysteine HCl, IT and ratio). For the ratio, the kurtosis and skew the values are low and are near to what would be expected for normal distribution (3.9 and 0.83 respectively, based on the average across the triplicate set).

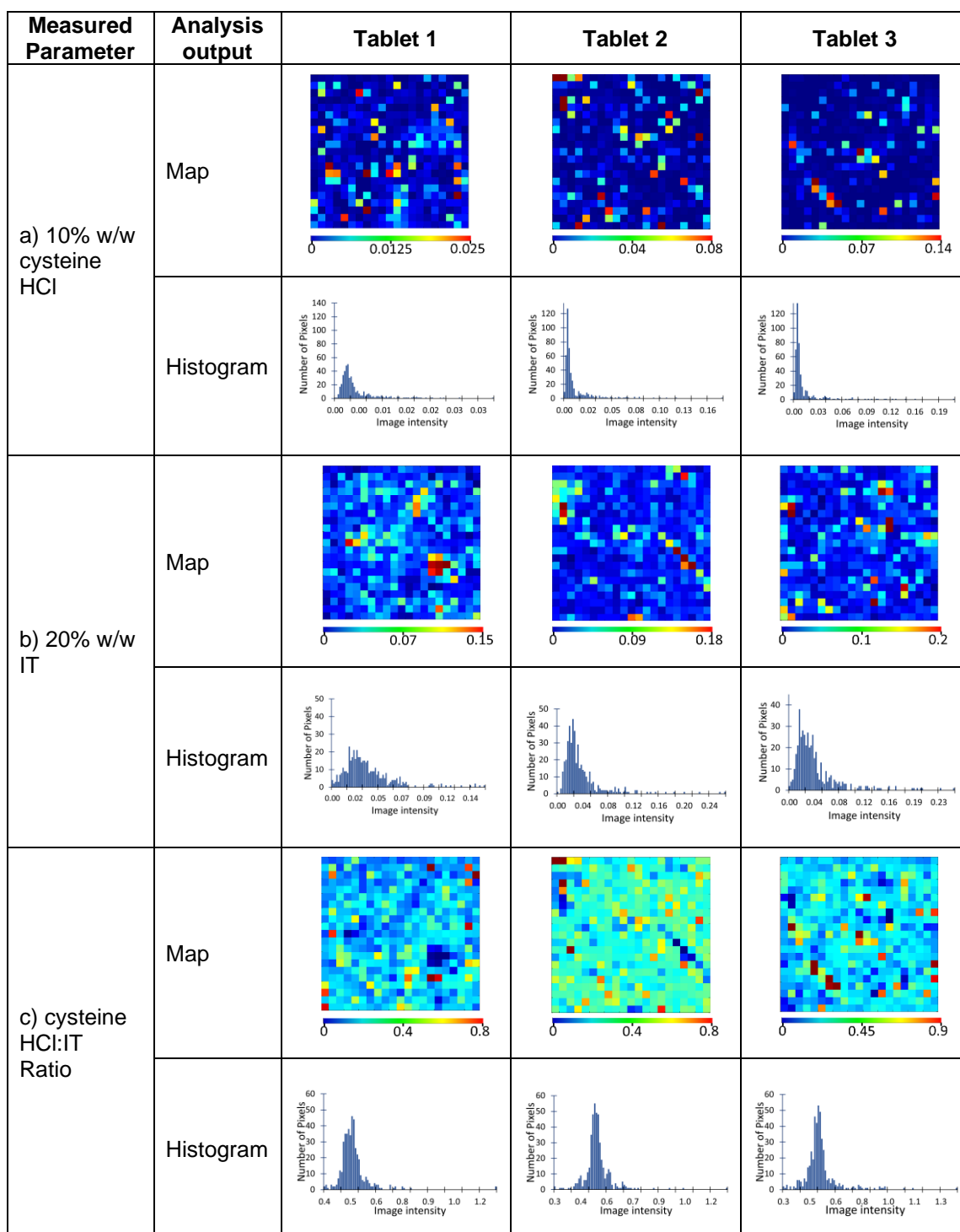


Fig. 4.27: Raman distribution images and corresponding histogram for 10% w/w cysteine HCl with 20% w/w itraconazole formulation showing a) cysteine HCl; b) IT and c) ratio of pH modifier/itraconazole

The Raman maps and histograms associated with the 10% w/w glycine HCl +20% w/w IT formulation are shown in Fig. 4.28. The distribution images for the glycine HCl (Fig. 4.28a) are similar for the three tablets analysed and show very little variation. However, the corresponding histogram distributions show some differences for the tablets

analysed, with those for tablets 1 and 3 having a narrow base, while that for tablet 2 exhibits a broader distribution. This suggests variable levels of homogeneity across the three tablets for the glycine distribution.

The distribution images generated for the IT (Fig. 4.28b) show localised regions of high intensity pixels (denoted by the red colour), which relate to a higher concentration of IT particles in these areas, suggesting the IT is not evenly distributed in some parts of the tablet. The corresponding histograms also exhibit have a broader distribution in comparison to the glycine HCl modifier distributions, also confirming the distribution is not as homogeneous.

The images representing the glycine HCl:IT ratio (Fig. 4.28c) show a relatively uniform distribution, apart from the areas where localised IT is observed within the tablet matrix. Similar histogram distributions were obtained for all three ratios. For the ratio, a satisfactory uniformity is confirmed by the mean, standard deviation, kurtosis and skew values of 0.8-0.83, 0.04-0.11, 0.28-0.77 and -0.36-1.11 respectively (Table 4, Appendix 1).

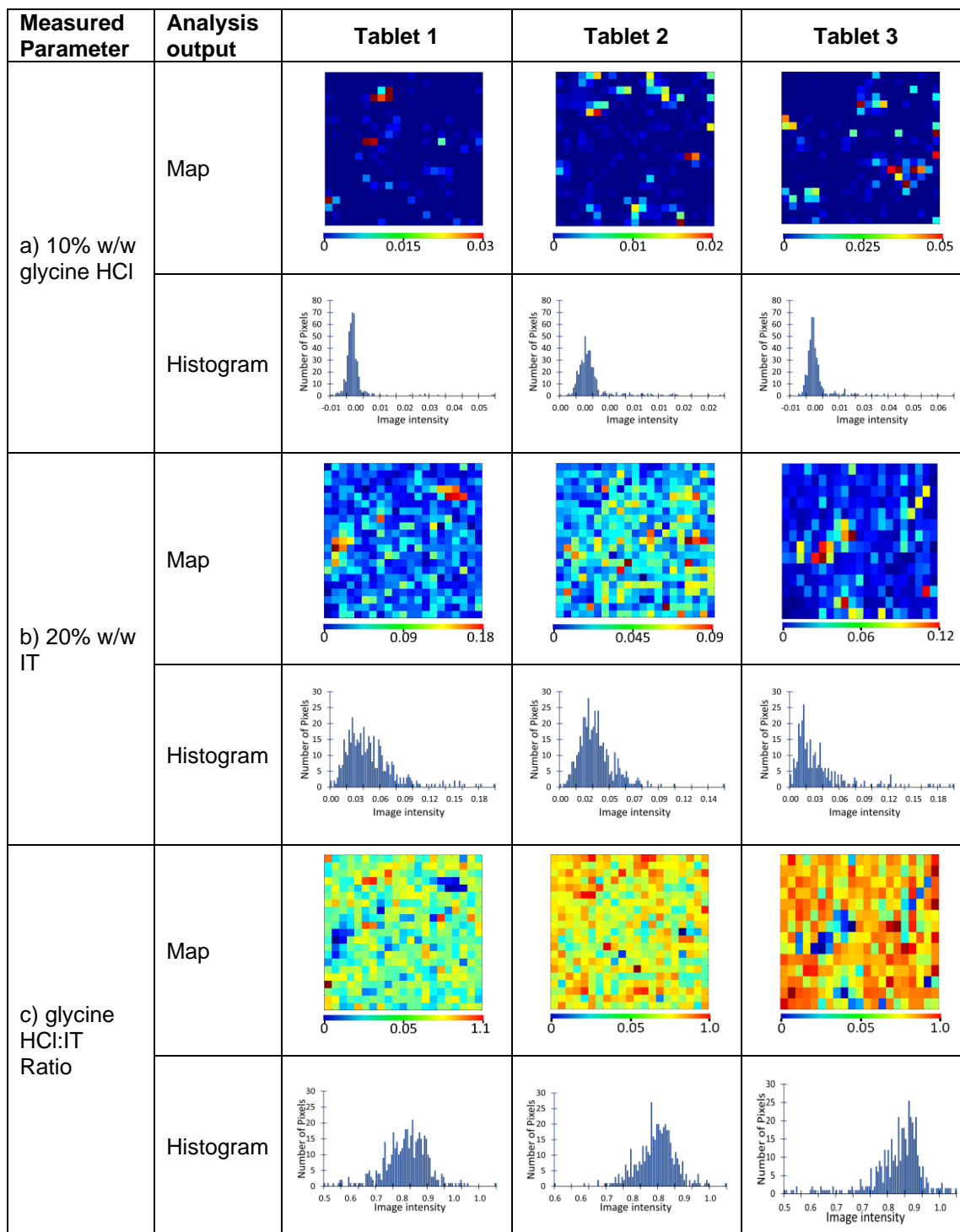


Fig. 4.28: Raman distribution images and corresponding histogram for 10% w/w cysteine HCl with 20% w/w itraconazole formulation showing a) cysteine HCl; b) IT and c) ratio of pH modifier/itraconazole

The Raman distribution maps and corresponding histograms obtained for the 30% w/w citric acid are presented in Fig. 4.29. The statistical values obtained from the histograms are shown in Table 5, Appendix 1.

Comparing the citric acid distribution for the three tablets (Fig. 4.29a) a similar distribution is observed, with a few localised areas of high citric acid concentration, denoted by the red colour. The corresponding histogram profiles are also very similar, exhibiting a tall peak with a long tail to the right, indicating a skewness greater than zero, potentially inferring a degree of inhomogeneity.

The data obtained from the IT (Fig. 4.29b) distribution also looks to be similar across the three tablets. It should be noted that several higher intensity pixels in the mapped region, relating to the IT, are evident in the images. However, these represent only a small proportion of the pixels in the overall map.

The distribution maps generated for the IT: citric acid ratio are presented in Fig. 4.29c and these are not dissimilar for the three tablets analysed. The corresponding histograms all exhibit a breadth of distribution which is indicative of a level of heterogeneity in the tablets.

The interpretation of the histograms is borne out by analysis of the statistical data (shown in Table 5, Appendix 1), in which comparable values for the standard deviation, kurtosis, and skew were calculated. This confirms that the method adopted for tablet preparation is capable of producing tablets with an acceptable degree of homogeneity to be used for further study.

The statistical data (Table 5, Appendix 1) obtained from the 30% w/w citric acid+20% w/w IT tablets shows similar ranges of values for the standard deviation, kurtosis, and skew, confirming the method adopted for tablet preparation produces reproducible tablets.

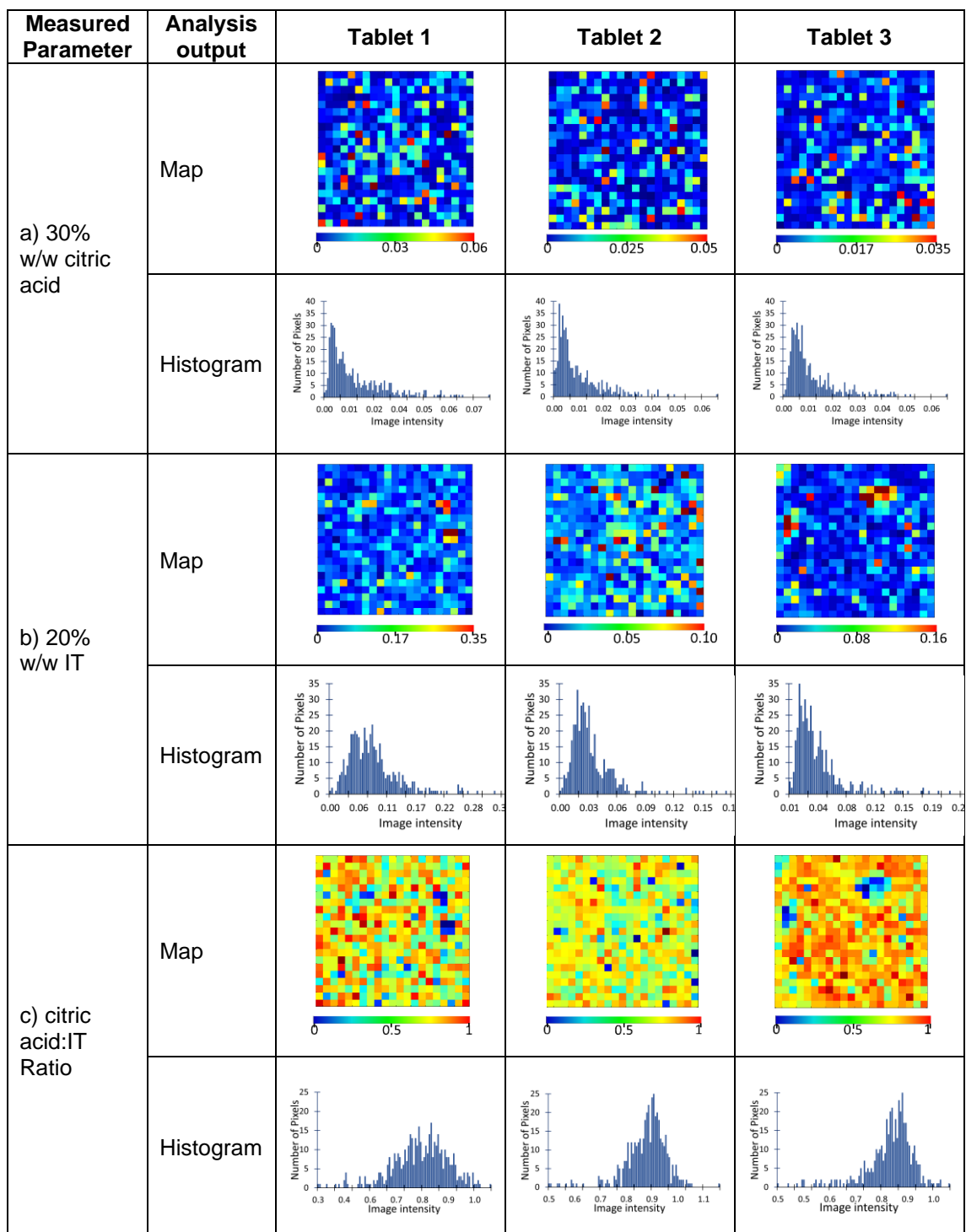


Fig. 4.29: Raman distribution images and corresponding histogram for 30% w/w citric acid with 20% w/w itraconazole formulation showing a) citric acid; b) IT and c) ratio of pH modifier/itraconazole

The Raman distribution maps, along with the histograms generated from the 30% w/w cysteine HCl+20% w/w IT tablets are presented Fig. 4.30. The distribution maps relating to the cysteine HCl (Fig. 4.30a) for tablet 1 show a small, localised region of higher intensity pixels in the mapped region, indicating a greater concentration of cysteine HCl in this area. Tablets 2 and 3 show a very similar distribution, with some areas exhibiting higher intensity pixels in the mapped area. The corresponding histograms all show some degree of asymmetry (narrow distribution with a long tail). The statistical data (Table 6, Appendix 1) shows very little difference in the skew values (2.29-2.65) and kurtosis (5.74-8.12).

The Raman images generated from the band used to represent the IT distribution (Fig. 4.30b) again show some areas of high intensity IT (denoted by the red colour) which appear to more abundant in tablet 1. The ratio images (Fig. 4.30c) look to be very similar for the three tablets analysed. The statistical data (Table 6, Appendix 1) from the histograms confirms the distribution is not considered to be normal, as confirmed by the kurtosis which is above 3 and the skew which is greater than 0 for all three tablets. While this indicates that the tablets have some heterogeneity, only a slight degree of asymmetry is apparent compared to a normal distribution.

Comparing the 10% w/w cysteine HCl Raman data with the 30% w/w cysteine HCl, similar distribution images (maps and histograms) for each of the parameters measured suggests that increasing the concentration of the cysteine has had little adverse impact on the blend uniformity of the tablets.

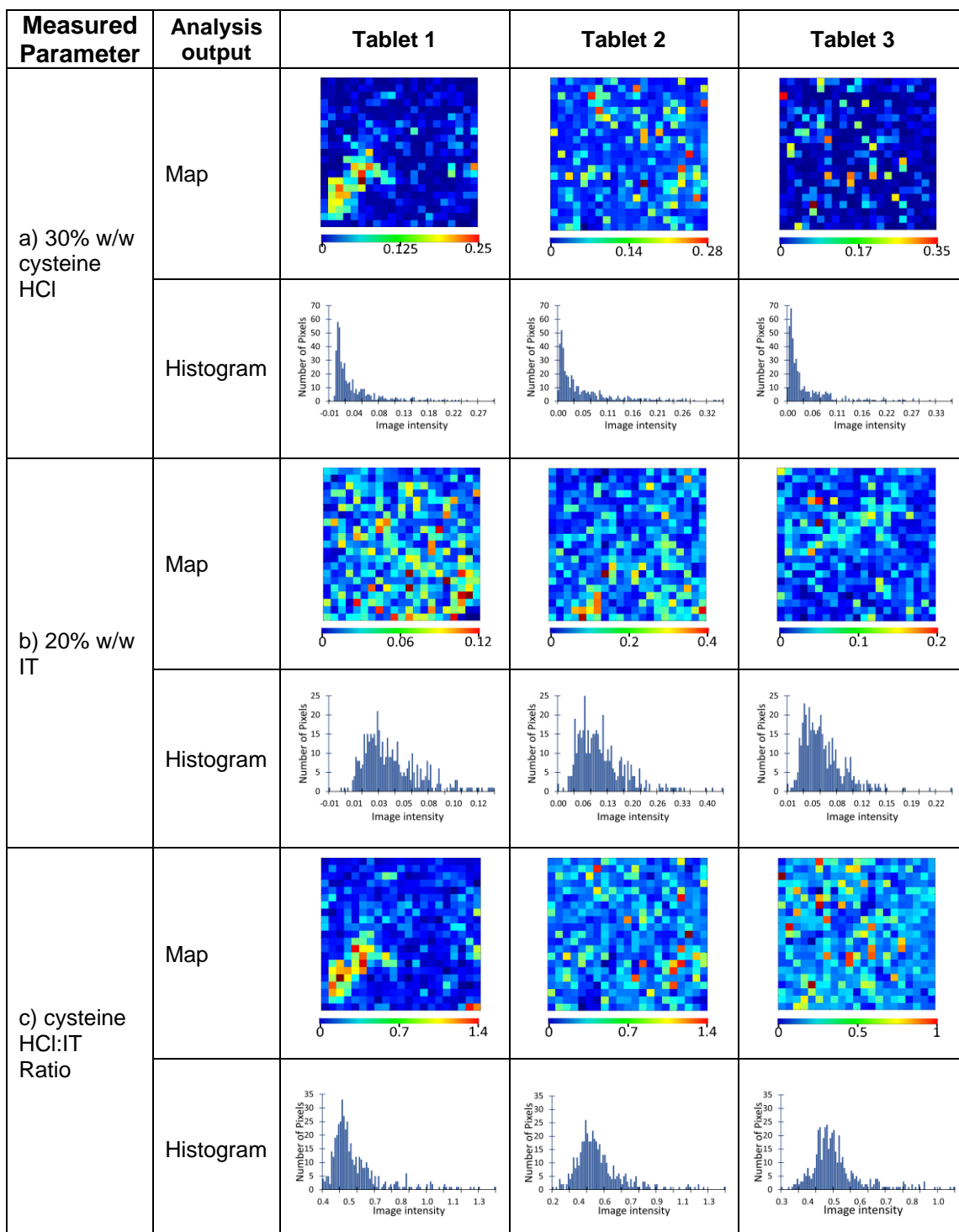


Fig. 4.30: Raman distribution images and corresponding histogram for 30% w/w cysteine HCl with 20% w/w itraconazole formulation showing a) cysteine HCl; b) IT and c) ratio of pH modifier/itraconazole

The content uniformity data for the 30% w/w betaine HCl+20% w/w formulation is presented in Fig. 4.31. The distribution (Raman images) attributable to the betaine HCl (Fig. 4.31a) appears to be very similar for the 3 tablets analysed and comparable to the 10% w/w betaine formulation, with very few areas of localised modifier, suggesting a uniform distribution. Comparing the statistical data (mean, standard deviation, kurtosis, and skew) shown in Table 7 Appendix 1, similar values are obtained from the histograms for the tablets analysed, thus confirming a degree of reproducibility with the tablet production method.

The corresponding histogram distributions are again very similar to the 10% w/w betaine+20% w/w IT formulation, exhibiting a symmetrical distribution with a narrow base and a sharp peak, the only apparent difference being that the 30% data shows some tailing to the right, indicating that the skewness is greater than zero. The same is observed for the 10% w/w betaine+20% w/w IT formulation, apart from the distribution for the betaine: IT ratio which exhibits a negatively skewed distribution (to the left) and has a value less than zero. For both formulations, the skewness (Table 2 and 7, Appendix 1) is not greater than ± 1.0 , essentially confirming the skewness is not substantial and the distribution is not far from being symmetrical [40]. This indicates that the betaine HCl is relatively homogeneously distributed at both the 10% w/w and 30% w/w levels.

Comparison of the results were obtained (maps and histograms) for each of the parameters measured for the 10% w/w and 30% w/w citric acid +20% w/w tablets show similar results, confirming that increasing the pH concentration does not appear to significantly affect the blend homogeneity.

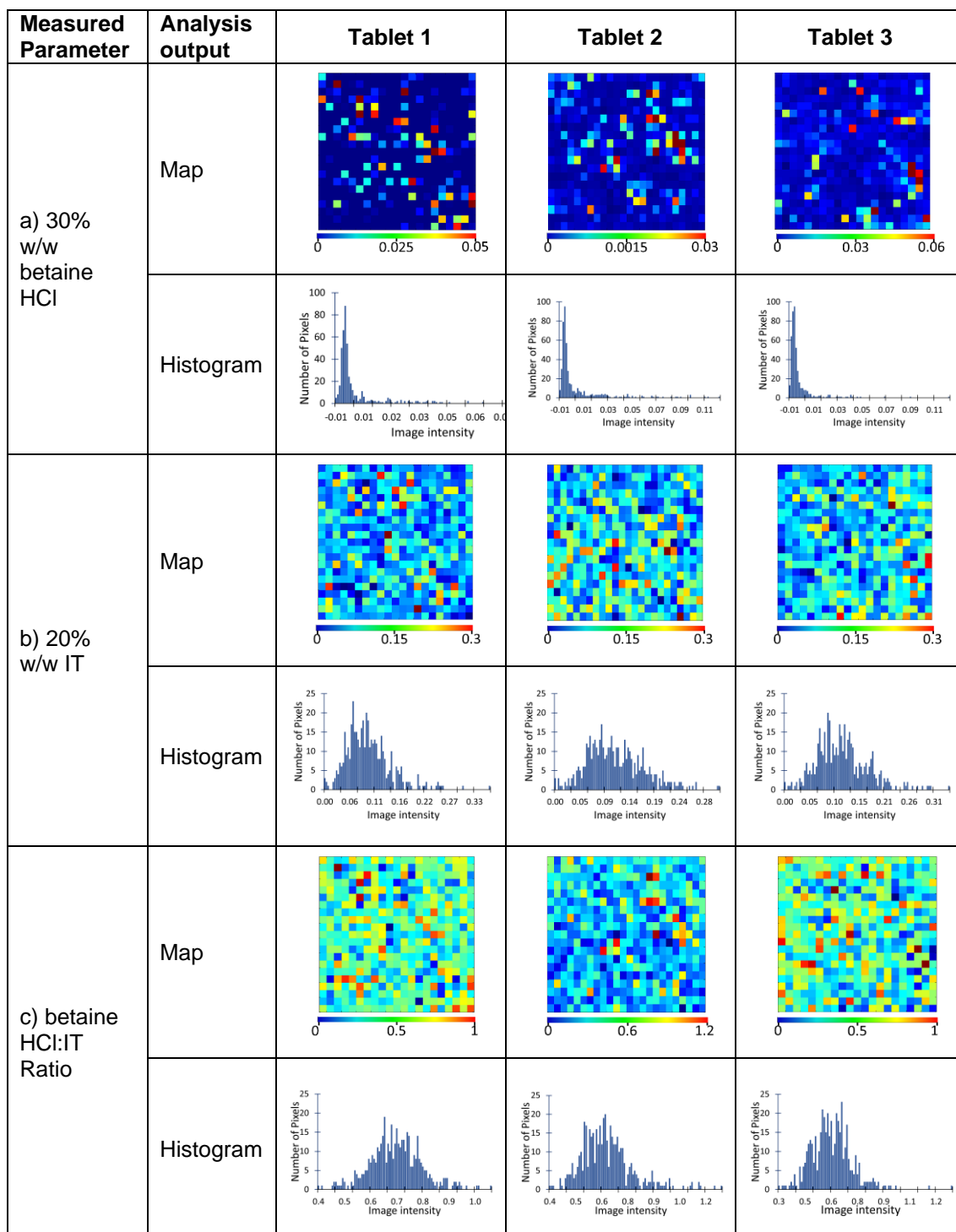


Fig. 4.31: Raman distribution images and corresponding histogram for 30% w/w betaine HCl with 20% w/w itraconazole formulation showing a) betaine HCl; b) IT and c) ratio of pH modifier/itraconazole

The Raman distribution images for the 30% w/w glycine +20% w/w IT, along with the corresponding histograms, are presented in Fig. 4.32.

The images representing the glycine HCl distribution are shown in Fig. 4.32a. They confirm that the distribution is very similar for the three tablets, with very few high intensity pixels, suggesting the glycine HCl is uniformly distributed. The corresponding histograms are again very similar and exhibit a long narrow peak, with evidence of minimum tailing to the right. The statistical data from the histograms (Table 8 in Appendix 1) also shows similar values for the mean (0.01 for all of three tablets), standard deviation (0.01-0.02), kurtosis (8.95-12.15) and skew (2.80-3.15) for the three tablets analysed. This provides reassurance that there is a high degree of reproducibility with the blending of the pH modifier.

The images representing the IT distribution are shown in Fig. 4.32b. Comparing these images it can be seen that tablet 2 exhibits intermediate intensity pixels (denoted by the yellow) in the mapped area in comparison to tablet 1 and 3. However, the corresponding histogram profiles all exhibit a broad distribution profile, with tablet 2 and 3 demonstrating a slight skewness to the left (-0.14 and -0.10 respectively). However, the values are not too dissimilar from the criteria used to describe a normal distribution (skewness =0) [40].

Comparable results were obtained (maps and histograms) for each of the parameters measured for the 10% w/w and 30% w/w glycine HCl +20% w/w tablets indicating the increase of the pH modifier concentration does not impact adversely on the blend homogeneity.

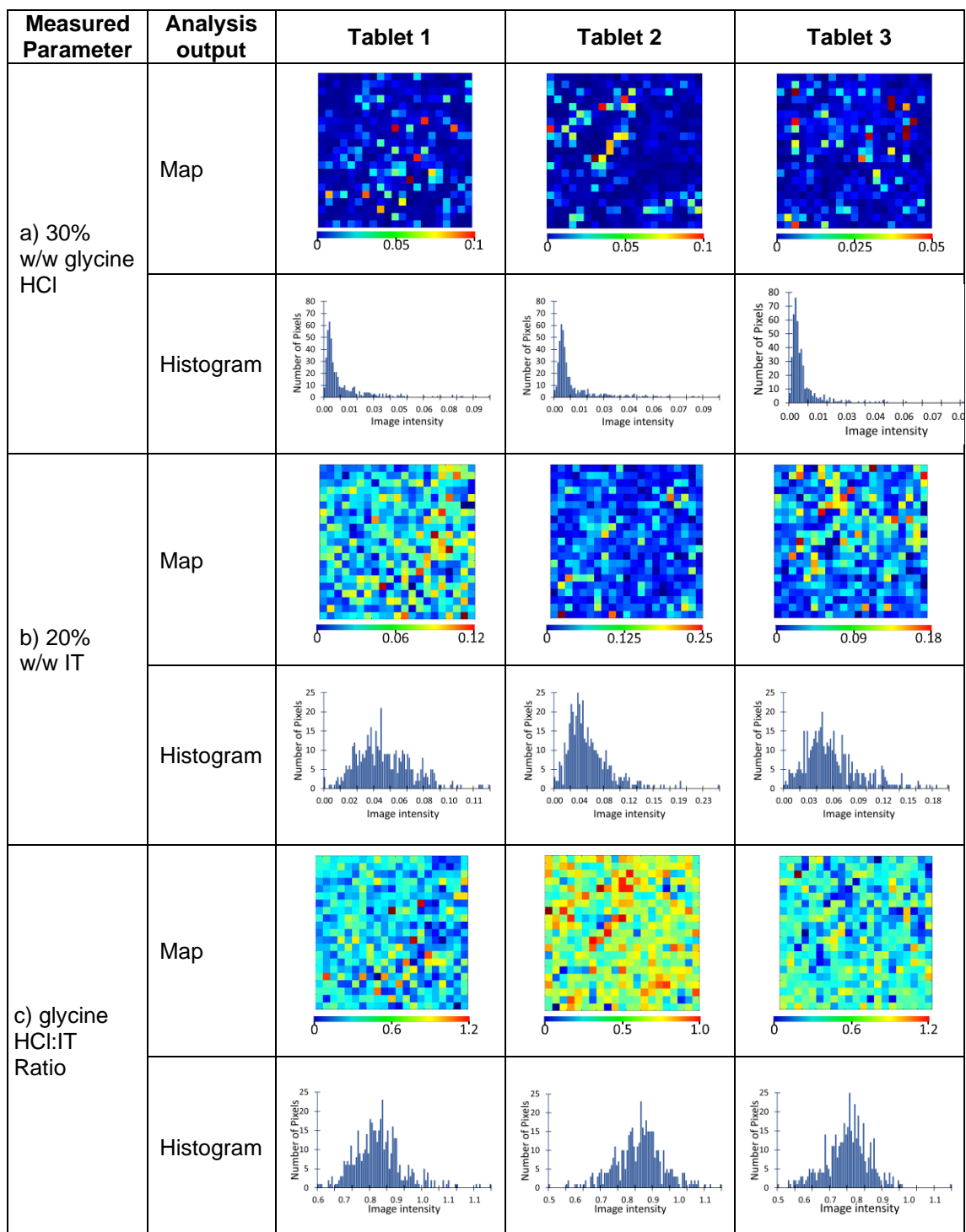


Fig. 4.32: Raman distribution images and corresponding histogram for 30% w/w glycine HCl with 20% w/w itraconazole formulation showing a) glycine HCl; b) IT and c) ratio of pH modifier/itraconazole

4.6.4.3 Summary of Raman Distribution Data

In general, it can be seen that a high intensity of IT in the distribution images corresponds to a low intensity in the modifier/IT ratio images (anti-correlation). It can therefore be concluded that the wavelengths/functional groups chosen as being indicative of the two components of interest were able to permit discrimination.

Some of the features observed could be associated with differences in particle size between the individual constituents and also the particle size distribution for each constituent. The project was reliant on the use of commercially sourced chemicals; in commercial pharmaceutical applications, particle size matching and control may minimise the variability observed.

Although the distributions do not fall into the category of a normal distribution (Kurtosis=3 and skew =0) and some degree of asymmetry is observed, none of the distributions exhibit severe non-uniformity, which would be manifested as a binomial distribution. Furthermore, within the triplicate sets set of tablets analysed, consistent images and histograms were acquired. Generally, a broader distribution is observed when IT is mapped, compared to some of the pH modifiers (cysteine HCl, glycine HCl and betaine HCl), suggesting it is less homogeneously distributed. This could be related to the small particle size of the IT ($7.7 \mu\text{m} \pm 0.6$ for d50) in comparison to the modifiers.

The Raman mapping results indicate that a reasonable degree of uniformity was achieved for the 20% w/w itraconazole and each of the pH modifiers at both 10% w/w and 30% w/w loadings. This is also verified by the average spectra profiles generated for each of the Raman maps (Fig. 4.33 and 4.34), confirming that the strategy adopted for preparing the tablets successfully created reproducible tablets with homogeneously distributed constituents.

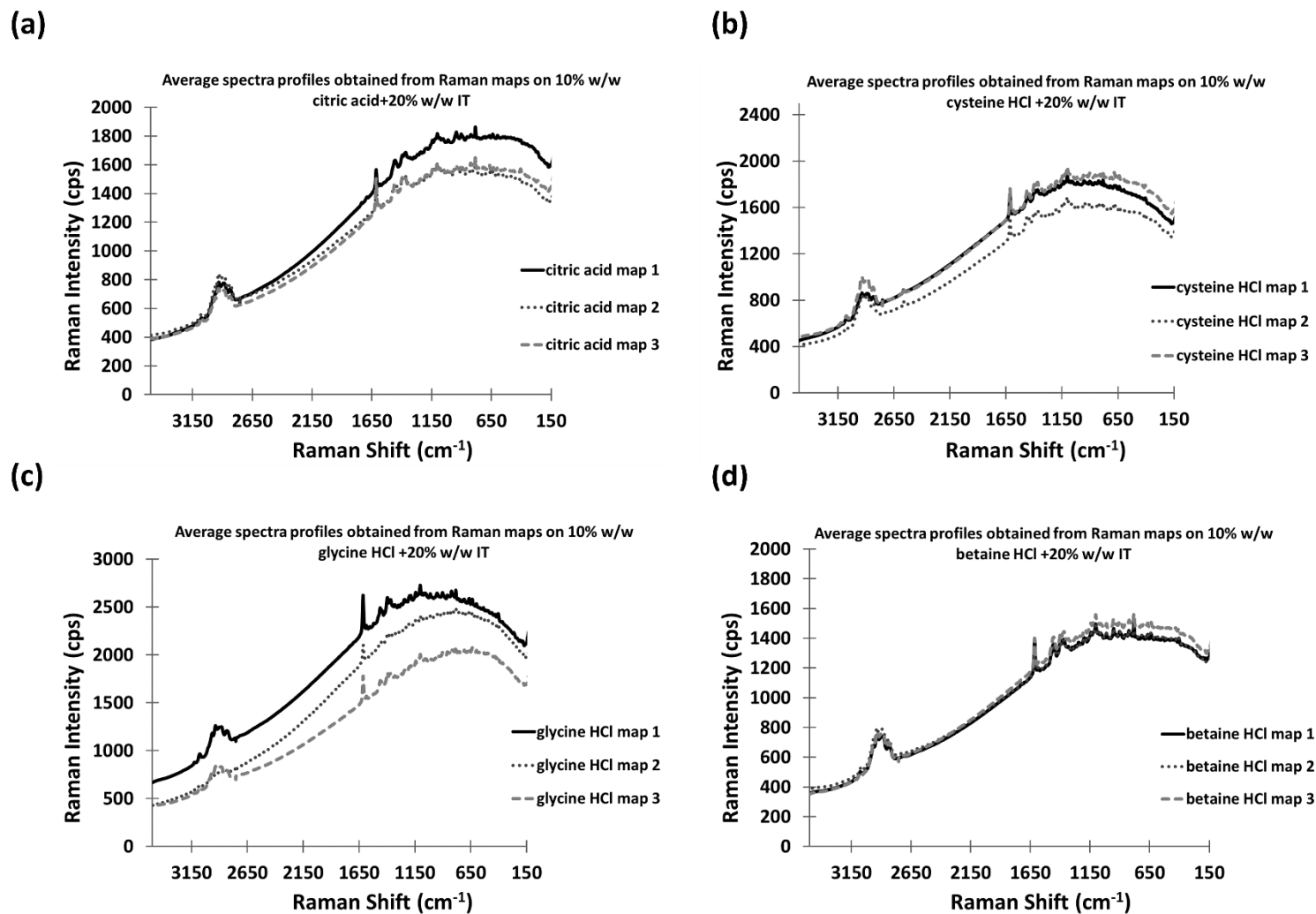


Fig. 4.33: Average spectra profiles obtained from Raman maps on 10% w/w pH modifier with 20% w/w Itraconazole for (a) citric acid; (b) cysteine HCl; (c) glycine HCl and (d) betaine HCl tablets

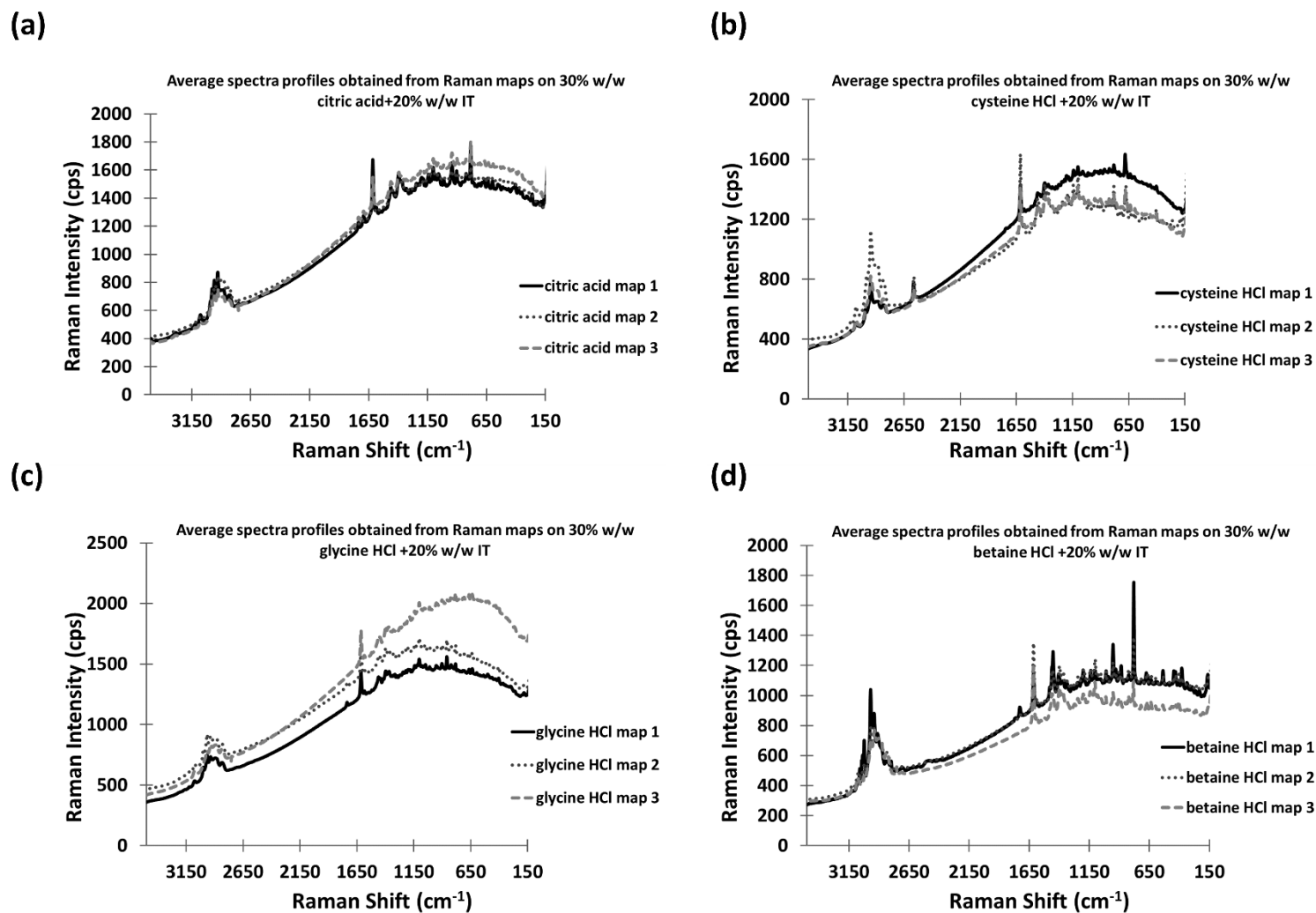


Fig. 4.34: Average spectra profiles obtained from Raman maps on 30% w/w pH modifier with 20% w/w Itraconazole for (a) citric acid; (b) cysteine HCl; (c) glycine HCl and (d) betaine HCl tablets

4.7 Summary

The IT salts and the amorphous form were successfully prepared and their structures confirmed using ATR-FTIR imaging and XRD. Suitable spectroscopic markers were identified to provide differentiation between the ionised and crystalline forms. Morphological analysis revealed that the 'as-received' IT powder was composed of needle/rod-like structures with an average particle length of 25 μm .

Discrete and unique spectroscopic markers were also identified for HPMC and the pH modifiers. These were used to generate peak area distribution images for both Raman maps and ATR-FTIR images.

NIR spectroscopy was successfully used to rapidly and non-destructively characterise the API and pH modifiers used for this project. The use of the PLS approach successfully permitted quantification of the concentrations of each the components of interest within a tablet. A calculated mean value of 19.5% w/w and a relative standard deviation of 3.6% were obtained for the 20% w/w IT tablet binary system (n=6).

Results obtained from the NIR analysis showed that calculated loading of the pH modifier and IT for both the 10% w/w and 30% w/w modifier formulations were in good agreement with expected concentrations, with maximum RSD values of 5.1% and 5.0%, respectively. This also means that all tablets are within the USP range of up to 6% RSD and acceptance values of up to 15. This indicates that the tablet preparation technique adopted was capable of producing tablets whose consistency is acceptable for further dissolution experiments.

From the Raman mapping data, it can be concluded that the pH modifier and IT appear to be uniformly distributed across the area of the mapped tablet. However, a small number of localised areas of high intensity were also observed, which could be due to a variation in the particle size of the different constituents (ranging from 7.7 μm for IT and 171 μm for betaine HCl).

4.8 References

- [1] S. Zhang, T. W. Y. Lee and A. H. L. Chow, "Crystallization of Itraconazole Polymorphs from Melt," *Cryst. Growth Des.*, vol. 16, no. 7, p. 3791–3801, 2016.
- [2] H. Bagavatula, S. Lankalapalli, V. V. K. Tenneti, N. M. R. Beeraka and . B. . T. Bulusu, "Comparative Studies on Solubility and Dissolution Enhancement of Different Itraconazole Salts and Their Complexes," *Advances in Pharmacology and Pharmacy*, vol. 2, no. 6, pp. 85-95, 2014.
- [3] T. Tao, Y. Zhao, J. Wu and B. Zhou, "Preparation and evaluation of itraconazole dihydrochloride," *International Journal of Pharmaceutics*, vol. 367, no. 1-2, p. 109–114, 2009.
- [4] K. D. Beule, "Itraconazole: pharmacology, clinical experience and future development," *International Journal of Antimicrobial Agents*, vol. 6, no. 3, pp. 175-181, 1996.
- [5] J. A. Barone, B. L. Moskovitz, J. Guarnieri, A. E. Hassell, J. L. Colaizz, R. H. Bierman and L. Jessen, "Enhanced Bioavailability of Itraconazole in Hydroxypropylb-Cyclodextrin Solution versus Capsules in Healthy Volunteers," *Antimicrobial Agents and Chemotherapy*, vol. 42, no. 7, p. 1862–1865, 1998.
- [6] T. Parikh, H. K. Sandhu, T. T. Talele and A. . T. M. Serajuddin, "Characterization of Solid Dispersion of Itraconazole Prepared by Solubilization in Concentrated Aqueous Solutions of Weak Organic Acids and Drying," *Pharmaceutical Research*, vol. 33, no. 6, pp. 1456-1471, 2016.
- [7] J. F. Remenar, S. L. Morissette, M. L. Peterson, B. Moulton, J. M. MacPhee, H. R. Guzman and O. Almarsson, "Crystal Engineering of Novel Cocrystals of a Triazole Drug with 1,4-Dicarboxylic Acids," *J. Am. Chem. Soc.*, vol. 125, no. 28, pp. 8456-8457, 2003.
- [8] A. A. Badawi, M. A. El-Nabarawi, D. A. El-Setouhy and S. A. Alsammit, "Formulation and Stability Testing of Itraconazole Crystalline Nanoparticles," *AAPS PharmSciTech* , vol. 12, no. 3, pp. 811-820, 2001.
- [9] H. S. Ghazal, A. M. Dyas, J. L. Ford and G. A. Hutcheon, "In vitro evaluation of the dissolution behaviour of itraconazole in bio-relevant media," *International Journal of Pharmaceutics*, vol. 366, no. 1-2, p. 117–123, 2009.
- [10] K. Zhang, H. Yu, Q. Luo, S. Yang, X. Lin, Y. Zhang, B. Tian and X. Tang, "Increased dissolution and oral absorption of itraconazole/Soluplus extrudate compared with itraconazole nanosuspension," *European Journal of Pharmaceutics and Biopharmaceutics*, vol. 85, no. 3 Part B, p. 1285–1292, 2013.
- [11] A. Shevchenko, L. M. Bimba, I. Miroshnyk, J. Haarala, K. Jelínková, K. Syrjänen, B. v. Veen, J. Kiesvaara, H. A. Santos and Y. Jouko , "A new cocrystal and salts of itraconazole: Comparison of solid-state properties, stability and dissolution

- behavior," *International Journal of Pharmaceutics*, vol. 436, no. 1-2, pp. 403-409, 2012.
- [12] J. Peeters, P. Neeskens, J. P. Tollenaere, P. V. Remoortere and M. E. Brewster, "Characterization of the Interaction of 2-Hydroxypropyl- β cyclodextrin With Itraconazole at pH 2, 4, and 7," *Journal of Pharmaceutical Sciences*, vol. 91, no. 6, p. 1414–1422, 2002.
- [13] E. Inkmann and U. Holzgrabe, " ^1H and ^{13}C nuclear magnetic resonance studies of the sites of protonation in itraconazole and fluconazole," *Journal of Pharmaceutical and Biomedical Analysis*, vol. 20, no. 1-2, pp. 297-307, 1999.
- [14] O. Scheibelhofer, N. Balak, P. R. Wahl, D. M. Koller, B. J. Glasser and J. G. Khinastcorre, "Monitoring Blending of Pharmaceutical Powders with Multipoint NIR Spectroscopy," *AAPS PharmSciTech*, vol. 14, no. 1, p. 1234–244, 2013.
- [15] R. Deveswaran, S. Bharath, B. V. Basavaraj, S. Abraham, S. Furtado and V. Madhavan, "Concepts and techniques of pharmaceutical powder mixing process: A current update," *Research J. Pharm. and Tech*, vol. 2, no. 2, p. 245–9, 2009.
- [16] H. Alyami, E. Dahmash and J. Bowen, "An investigation into the effects of excipient particle size, blending techniques and processing parameters on the homogeneity and content uniformity of a blend containing low-dose model drug," *PLOS ONE*, vol. 12, no. 16 e0178772, 2017.
- [17] E. P. Maynard, "Mixing & Blending," *Powder & Bulk Solids*, 9 July 2007. [Online]. Available: <https://www.powderbulksolids.com/article/mixing-blending-1>. [Accessed 05 May 2020].
- [18] C. A. Anderson and N. L. Velez, "Chapter 6 Blending and Characterization of Pharmaceutical Powders Carl A. Anderson and Natasha L. Velez," in *Particles and Nanoparticles in Pharmaceutical Products Design, Manufacturing, Behavior and Performance*, AAPS Advances in the Pharmaceutical Sciences Series, 2018, pp. 233-275.
- [19] B. Mittal, "How to Develop Robust Solid Oral Dosage Forms from Conception to Post-Approval," in *Chapter 4 - Pharmaceutical Unit Operations*, Academic Press, 2017, pp. 69-95.
- [20] O. Ryabchykov, J. Popp and T. Bocklitz, "Fusion of MALDI Spectrometric Imaging and Raman Spectroscopic Data for the Analysis of Biological Samples," *Frontiers in Chemistry*, vol. 6, no. 257, pp. 1-10, 2018.
- [21] K. H. Liland, A. Kohler and N. K. Afseth, "Model-based pre-processing in Raman spectroscopy of biological samples," *Journal of Raman Spectroscopy*, vol. 47, no. 6, p. 643–650, 2016.
- [22] S. P. Bhardwaj, K. K. Arora, E. Kwong, A. Templeton, S.-D. Clas and R. Suryanarayanan, "Mechanism of Amorphous Itraconazole Stabilization in

Polymer Solid Dispersions: Role of Molecular Mobility," *Mol. Pharmaceutics*, vol. 11, no. 11, p. 4228–423, 2014.

- [23] D. Allwood, *NMR interpretation of itraconazole*. [Email]. 16 June 2020.
- [24] A. A. Al-Badr and H. El-Subbagh, "Itraconazole: Comprehensive profile," in *Profiles of Drug Substances, Excipients and Related Methodology*, Academic Press, 2009, pp. 193-261.
- [25] M. Kumar, R. Bhatia and R. K. Rawal, "Applications of various analytical techniques in quality control of pharmaceutical excipients," *Journal of Pharmaceutical and Biomedical Analysis*, vol. 157, pp. 122-136, 2018.
- [26] H. G. Merkus, G. M. H. Meesters and W. Oostra, *Particles and Nanoparticles in Pharmaceutical Products Design, Manufacturing, Behavior*, AAPS Advances in the Pharmaceutical Sciences Series, 2018.
- [27] A. Pestieau, F. Krier, G. Thoorens, A. Dupont, P.-F. Chavez, E. Ziemons, P. Hubert and B. Evrard, "Towards a real time release approach for manufacturing tablets using NIR spectroscopy," *Journal of Pharmaceutical and Biomedical Analysis*, vol. 98, pp. 60-67, 2014.
- [28] T. U. S. Pharmacopeia, *The United States pharmacopeia 30–National Formulary 25*, Rockville, MD: United States Pharmacopeial Convention, 2007.
- [29] M. Schoot, C. Kapper, G. H. Kollenburg, G. J. Postma, G. v. Kessel, L. M. Buydens and J. J. Jansen, "Investigating the need for preprocessing of near-infrared spectroscopic data as a function of sample size," *Chemometrics and Intelligent Laboratory Systems*, vol. 204, no. 104105, 2020.
- [30] S. Lohumi, M. S. Kim, J. Qin and B.-K. Cho, "Raman imaging from microscopy to macroscopy: Quality and safety control of biological materials," *TrAC Trends in Analytical Chemistry*, vol. 93, pp. 183-198, 2017.
- [31] 19, ASTM Designation: E2810, "Standard Practice for Demonstrating Capability to Comply with the Test for Uniformity of Dosage Units," 2021. [Online]. Available: <https://www.astm.org/e2810-19.html>. [Accessed 31 May 2021].
- [32] J. Cruz and M. Blanco, "Content uniformity studies in tablets by NIR-C," *Journal of Pharmaceutical and Biomedical Analysis*, vol. 56, no. 2, pp. 408-412, 2011.
- [33] S. Kumar, T. Verma, R. Mukherjee, A. Freek, K. Somasundaram and S. Umamathy, "Raman and infra-red microspectroscopy: towards quantitative evaluation for clinical research by ratiometric analysis," *Chem. Soc. Rev.*, vol. 45, pp. 1879-1900, 2016.
- [34] T. Pucherta, D. Lochmann, J. C. Menezes and G. Reicha, "A multivariate approach for the statistical evaluation of near-infrared chemical images using Symmetry Parameter Image Analysis (SPIA)," *European Journal of Pharmaceutics and Biopharmaceutics*, vol. 78, no. 1, pp. 117-124, 2011.

- [35] P.-Y. Sacréa, P. Lebrun, P.-F. Chavez, C. De Bleye, L. Netchacovitch, E. Rozet, R. Klinkenberg, B. Streef, P. Hubert and E. Ziemons, "A new criterion to assess distributional homogeneity in hyperspectral images of solid pharmaceutical dosage forms," *Analytica Chimica Acta*, vol. 818, pp. 7-14, 2014.
- [36] C. L. Robbe , D. S. Lester, E. N. Lewis, X. L. Yu, E. H. Jefferson and A. S. Hussain, "Near-infrared spectral imaging for quality assurance of pharmaceutical products: Analysis of tablets to assess powder blend homogeneity," *AAPS PharmSciTech*, vol. 3, no. 3, p. 1–15, 2002.
- [37] C. Gendrin , Y. Roggo , C. Spiegel and C. Collet, "Monitoring galenical process development by near infrared chemical imaging: One case study," *European Journal of Pharmaceutics and Biopharmaceutics*, vol. 68, no. 3, p. 828–837, 2008.
- [38] Z. Liang , J. Wei, . J. Zhao, H. Liu, B. Li, J. Shen and C. Zheng, "The Statistical Meaning of Kurtosis and Its New Application to Identification of Persons Based on Seismic Signals," *Sensors*, vol. 8, no. 8, pp. 5106-5119, 2008.
- [39] NIST/SEMATECH, "NIST/SEMATECH e-Handbook of Statistical Methods," NIST/SEMATECH, 30 10 2013. [Online]. Available: <https://www.itl.nist.gov/div898/handbook/eda/section3/eda35b.htm>. [Accessed 03 06 2021].
- [40] N. K. D. Devi, N. N. Rao, M. Anurad, P. Naveena, P. Sravani and Y. S. Sree, "Validation of particle size distribution in pharmaceutical excipients," *Annals of Biological Research*, vol. 6, no. 6, pp. 1-7, 2015.

5.0 Investigation of Within-Tablet Dynamics for Extended Release of Itraconazole from a HPMC Matrix Tablets Using ATR-FTIR Imaging

5.1 Introduction

The aim of the work for this chapter was to use a poorly water-soluble, weakly basic and lipophilic model drug system to develop an insight how these types of drugs behave within the tablet matrix. Itraconazole (IT) was selected as the chosen model drug as although it is not a candidate for oral extended delivery from a hydrophilic matrix system it met the stated criteria for a suitable model compound for this work in that it exhibits pH-dependent and poor solubility, close to 1 ng/mL at pH 7 and 4 µg/mL at pH 1 [1], with a pK_a of 3.7. This is well inside the physiological pH range and characteristic of the most challenging compounds which might be considered for delivery from hydrophilic matrix systems. It is also very amenable to the spectroscopic imaging approaches applied in this work. In this chapter ATR-FTIR imaging was used to monitor the hydration of HPMC and migration of the itraconazole in the diffusion front over time. The influence of ionic strength on the formation of the HPMC gel layer was also investigated.

ATR-FTIR imaging allowed dissolution to be studied in real-time, mapping both the location of the drug and its chemical characteristics (e.g. ionisation state) as it dissolved. The behaviour of salt forms of a drug within polymeric systems has been characterised previously. However, the combined assessment of poor solubility, very weakly basic drug and excipients and water in a formulation undergoing dynamic changes including ionisation, dissolution, hydration, swelling, particle dislocation with a view to informing future product design has not been reported [2]. The application of this approach will permit a greater understanding of the factors controlling drug release and enable a more effective quality-by-design approach to formulating HPMC matrix tablets.

5.2 Materials and Methods

5.2.1 Materials

Tablet constituents used in this chapter are listed in Chapter 4 (Table 4.1). For the hydration studies two different hydrating media were used to investigate pH effects; these were 0.1 M HCl solution (pH 1.5) and tris(hydroxymethyl)aminomethane hydrochloride buffer solution (tris buffer, purchased from Sigma Aldrich, molecular biology grade pH 7.2). The pHs were selected on the basis these are commonly used to simulate the gastric and intestinal fluids and cover the physiological pH range of the GI tract. In order to explore the influence of ionic strength on the hydration of the HPMC two different ionic strength solutions were investigated (0.1M and 1M). In order to minimise Hofmeister series-like effects, ionic strength was managed by using monovalent buffering agents [3]. The 0.1 M HCl was prepared by diluting concentrated HCl 37% with deionised water having a resistivity of 18.2 MΩ. For the low ionic strength tris buffer, a 0.1 M solution was prepared by carrying a 10-fold dilution of the as-received solution. To obtain the high ionic strength solutions a 1 M concentration was used. For the 1 M tris solution, the as-received buffer was used. For the high ionic strength solution at low pH, sodium chloride (general purpose grade, Fischer Scientific) was added to the 0.1 N HCl solution to increase the ionic strength to 1 M.

5.2.2 Preparation and Characterisation of Tablets

Formulations were prepared and compacted in accordance with the methodology outlined in Chapter 4, section 4.4.

5.2.3 Content Uniformity of Itraconazole Loading and Heterogeneity of Tablets

The PLS method used to calculate/predict the values of the API loadings within the prepared tablet matrix is described in section 4.5.1 of Chapter 4.

The Raman methodology for assessing the distribution of the API within the HPMC matrix is described in section 4.5.2 of Chapter 4.

5.3 *In Vitro* Release Studies

Dissolution studies were carried out using Agilent 708 (708-DS; Agilent Technologies, Santa Clara, CA, USA) on the 20% w/w IT formulation (n=6) in 900 mL of 0.1N HCl and 0.1M tris buffer using the USP Type-II method. A paddle speed of 75 rpm and a temperature of 37 ± 0.5 °C was used in all experiments [4]. A 5 mL aliquot was withdrawn at different time intervals and assayed for IT using ultraviolet–visible spectroscopy (Agilent Cary 60, Agilent Technologies, Santa Clara, CA, USA) by measuring the absorbance at 257 nm.

5.4 Collection of ATR-FTIR Images

Mid-IR spectroscopic images were collected using a Varian 680-IR spectrometer (Agilent Technologies LDA UK Limited, Stockport, UK) coupled to a variable temperature Golden Gate single reflection ATR sampling accessory (Specac, Orpington, UK) held at 37°C. Images were collected at a spectral resolution of 8 cm^{-1} with 8 co-additions. It was observed that an S/N advantage can be obtained by using a large number of background scans whilst maintaining the speed advantage of having fewer sample scans. Therefore, blank ATR crystal images at a resolution of 8 cm^{-1} and 256 co-additions were used as a background reference for image processing.

5.5 Hydration Experiments using ATR- FTIR Imaging

Hydration studies on the tablets were performed as follows and shown schematically in Fig 5.1.

Each tablet was placed on the ATR crystal such that approximately one-third of the ATR crystal surface was covered, thereby ensuring the dissolution medium could only be introduced from one side of the crystal (Fig. 5.2). Pressure was then applied to the tablet using a sapphire anvil and a good optical contact between the sample and the ATR

crystal was confirmed by checking the quality of the image of the dry tablet, this limited swelling in the axial direction. A polyester ring, of larger diameter than the tablet itself to permit unimpeded radial expansion, was sealed around the tablet and 5 mL of sonicated pH 7 tris buffer or 0.1 N (pH 1.5) HCl (37°C) was carefully added from one side of the crystal as hydrating medium.

Hydration was studied over a 3 hour period at a temperature of 37° C, images were collected every 2 min for the first 10 min, every 10 min over the following 70 min and every 20 min for the remainder of the experiment. Chemical images for each component in the system were generated by plotting the peak area of the bands at 1630, 1510 and 1041 cm^{-1} to show the distribution of water, IT and HPMC respectively using ISys 5.0 chemical imaging software (Malvern Instruments, Malvern, UK).

It should be noted that this experimental arrangement permits only observation of swelling and water ingress, particle translocation if it occurs and dissolution/diffusion of the drug in the hydrated matrix. It is not capable of monitoring erosion due to the low shear environment that exists within the cell. However, this is not considered to be a limitation in this context as it still allows assessment of within-tablet dynamics due to hydration and swelling at pH values within the tablet where drug will be insoluble (high pH medium) or have some solubility (low pH medium).

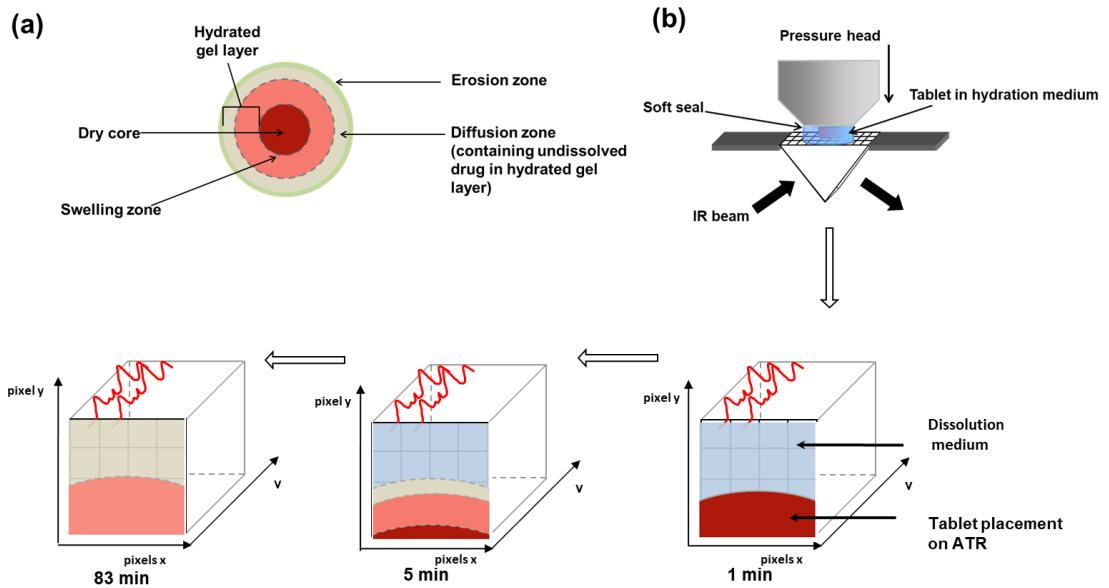


Fig. 5.1 (a): Schematic of different fronts of a hydrating hydrophilic tablet, looking down onto the upper tablet surface as if one could see through it, highlighting dry core, swelling, diffusion and erosion fronts. Adapted from [5] with permission from Therapeutic Delivery as agreed by Newlands Press Ltd. (b): Schematic of ATR-FTIR imaging set-up over the course of the hydration period using a Focal Plane Array (FPA) detector. Reprinted from [6] with permission from the American Chemical Society

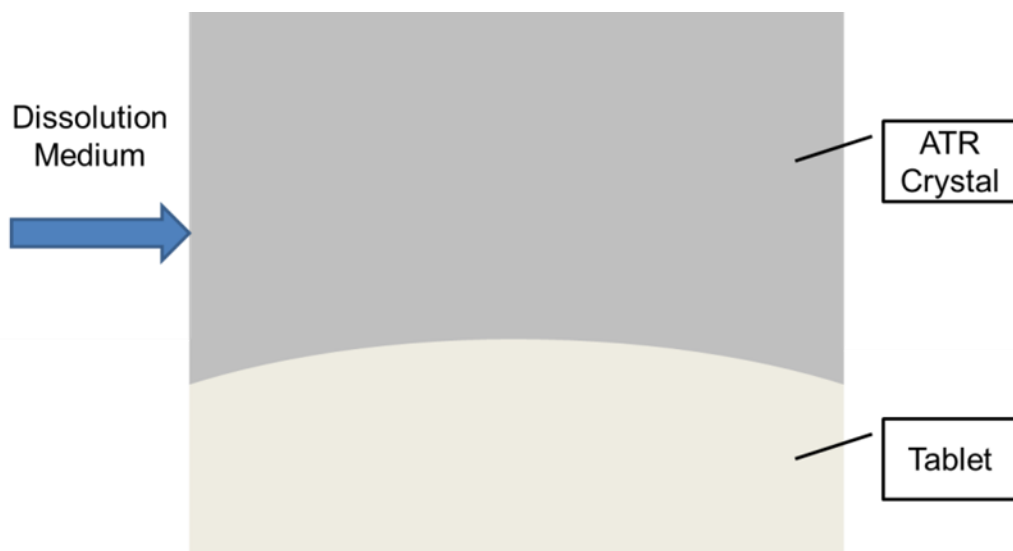


Fig. 5.2: Schematic of tablet placement on ATR crystal

5.6 Optical Imaging to Determine to Radial and Axial Swelling

Optical images of the axial and radial swelling were collected using two Canon 5D MK3 digital cameras equipped with 100 mm macro lenses, arranged to capture axial and radial images of the tablets simultaneously. Images were obtained from the HPMC placebo and the 20% w/w IT loaded HPMC formulation in dissolution media at pH 1.5 and 7 (n=6). The tablets were placed onto a 3 prong polymeric sample holder located in a glass cell and 40 mL of either 0.1N HCl or 0.1M tris buffer was added. Images were collected at 5 minute intervals for a period of 180 minutes. Data analysis was conducted using image analysis software (ImageJ 1.52a) to determine to the area change in both the axial and radial dimensions. Dimensional changes of the drug loaded tablets immersed in media at the two different pHs were statistically compared using a two-way analysis of variance (ANOVA) to determine the statistical significance of any differences (Prism V 7.03).

5.7 Results and Discussion

5.7.1 Content Uniformity and Distribution of 20% w/w Itraconazole Tablets Using Near Infrared (NIR) and Raman Microscopy

The 6 tablets analysed by NIR show a reasonable agreement with the expected levels of itraconazole (20% w/w). The results are presented Chapter 4 section 4.6.4.1 (Table 4.8).

5.7.2 *In Vitro* Release Studies

Dissolution profiles obtained for the 20% w/w IT loaded tablets (Fig. 5.3) showed a marked difference in release rate between the two pHs. At pH 1.5 sustained release of IT was observed over the 24h experiment, although when the experiment was stopped at this point, only 24% of the contained IT had been released. In contrast, the same IT tablets in the pH 7 medium showed release to be less than 1% at 24 hours. There was no evidence of burst release during these measurements at either pH for this

API/polymer matrix. However, the results showed clear evidence of an increase in both dissolution rate and percentage IT release (associated with pH-dependent solubility profile of IT) in the pH 1.5 medium, as anticipated and in full agreement with previous studies [7].

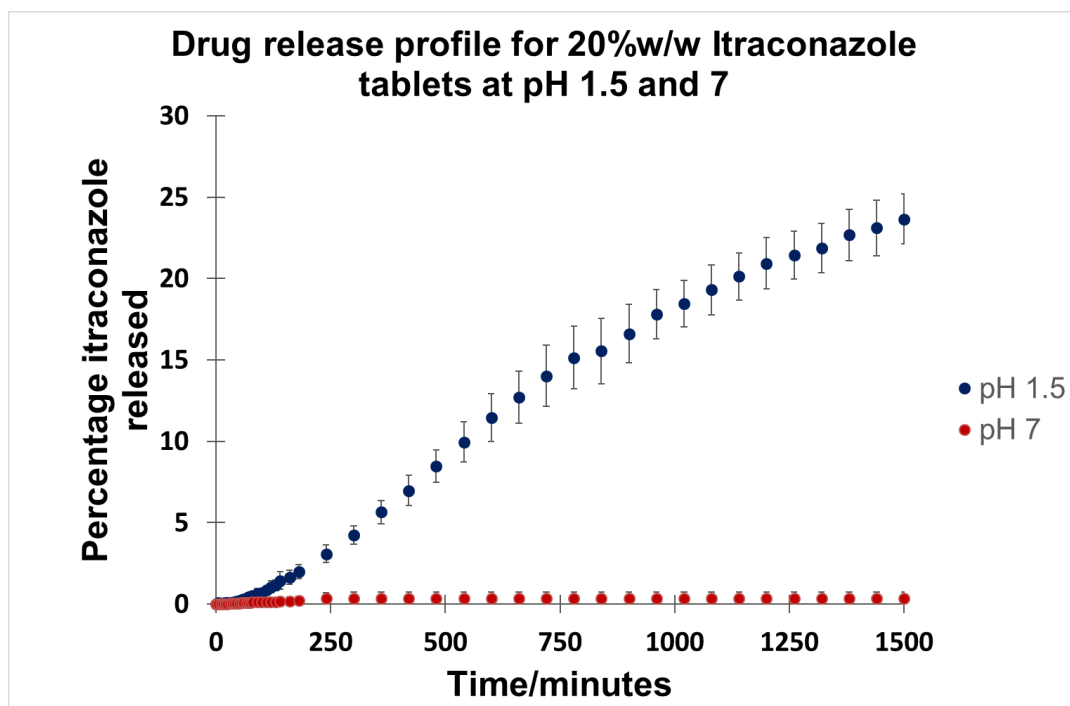


Fig. 5.3: Dissolution profiles for 20% w/w IT loaded tablets at pH 1.5 and 7 (n=6)

5.7.3 ATR-FTIR Imaging of Reference Materials

The spectroscopic markers identified for each of the reference materials in order to generate the chemical images are described section 4.6.2.

5.7.4 ATR-FTIR Imaging of HPMC Tablets

Mid-IR images of matrix tablet composed simply of HPMC hydrating at pH 1.5 and 7 using low and high ionic strength media over the 3-hour hydration period were generated using the bands identified in section 4.6.2 and show the evolution of the ingress of water into the tablet matrix and the growth of the gel layer. High intensity regions are coloured red, while low intensity regions are blue. Increasing intensity is denoted by the numerical values on the accompanying colour scale bars.

From the water distribution images (Fig. 5.4a) it is evident that water ingress occurs rapidly and full penetration throughout the tablet, visible within the field of view, occurs by around 19 minutes irrespective of the pH or ionic strength environment. HPMC distribution images show the (non-hydrated) tablet core is located towards the lower half of the images (Fig. 5.4b). The intensity of this dark red/yellow HPMC distribution in the high ionic strength medium at pH 1.5 and 7 (Fig. 5.4b (iii) and (iv)) is far greater throughout the duration of the experiment in comparison to the low ionic strength images (Fig. 5.4b(i) and (ii)).

Typical representative images from each data set are shown in this chapter, the remaining data is presented in Appendix 2.

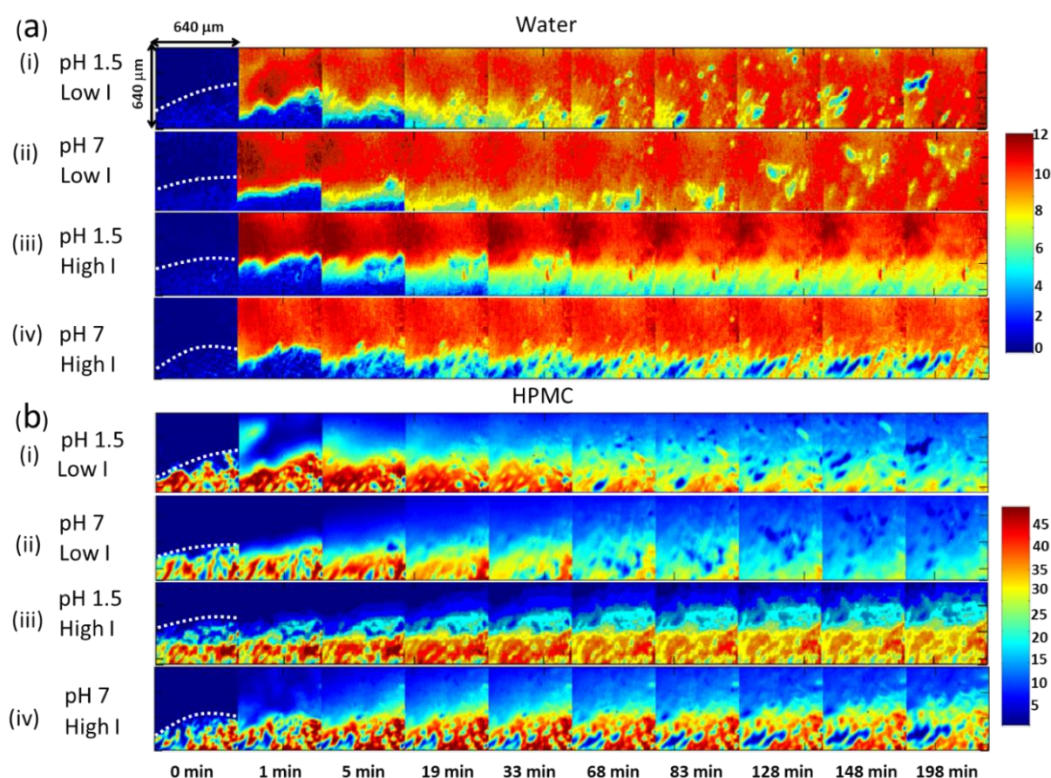


Fig. 5.4: Selected ATR-FTIR images were collected over the time course of hydration experiments for placebo tablets in low and high ionic strength solutions at pH 1.5 and pH 7 showing (a) water and (b) HPMC distribution. Images were generated using methods described in section 4.5. The dotted lines in the first column of images denotes the boundary between the tablet and air/water

To gain an insight into the gel layer behaviour, the peak area ratio of the $\nu(\text{C-O})$ in the HPMC and the $\delta(\text{OH})$ for water was plotted. The gel layer was defined as the cyan zone corresponding to values between 2.2 and 3.8, on the colour scale shown in Fig. 5.5 and consisted of a combination of water and polymer at varying concentrations. Fig. 5.5a and b clearly highlight the rapid formation of the gel layer at pH 1.5 and pH 7 in a low ionic strength environment. The dark red colour corresponded to regions with high polymer content. Conversely, regions of hydrated HPMC with increasing water content are denoted by the yellow, green and cyan zones respectively.

The gel layer behaviour is the same between the different pH environments for the pure HPMC with the same ionic strength (Fig 5.5). For the low ionic strength media (Fig. 5.5a and 5.5b), at both pH, initial swelling is observed from the 1 minute time point. The dry core diminishes rapidly and the gel layer recedes towards the edge of the field of view within the time frame of the experiment.

The images obtained from the tablets subjected to high ionic strength media at pH 1.5 and 7, show that swelling is observed from the outset the gel layer is much more stable over the duration of the experiment (Fig. 5.5c and 5.5d). This confirms that the ionic strength of the media had a significant impact on the gel layer behaviour. This is consistent with previous studies looking at the impact of ionic strength and HPMC gel formation [8] [9] [10], where the gel layer behaviour is shown to be independent of pH but highly dependent on the ionic strength of the medium. At higher ionic strength, less effective penetration of the water into the core and development of hydrated, swollen polymer gel layer is observed.

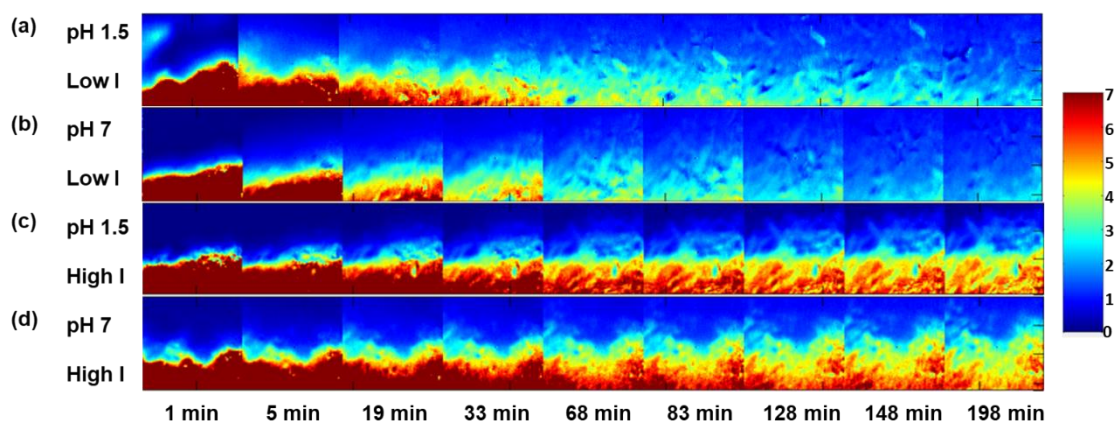


Fig. 5.5: ATR-FTIR images of HPMC/water peak area ratio images over hydration period, showing HPMC gel layer evolution for (a) pH 1.5; (b) pH 7 low ionic strength solutions; (c) pH 1.5; (d) pH 7 high ionic strength solutions

5.7.5 FTIR Imaging Hydration Experiments on Pure 20% w/w IT Loaded Tablets

To determine the influence of pH on IT-containing tablet matrices, the ionic strength of the hydration medium was matched whilst the pH was modified. The strategy adopted was to use the low ionic strength medium, thereby ensuring that any changes observed to the drug could be attributed to the pH environment alone.

Fig. 5.6 shows the results of the ATR-FTIR imaging hydration experiments performed on 20% w/w IT-loaded tablets hydrated with a low ionic strength medium (0.1 mol/L) at pH 1.5 and 7.

Fig. 5.6a, 5.6b and 5.6c show the water, HPMC distribution and gel layer evolution over the timeframe of the experiment. These results are similar to those observed with the IT-free HPMC tablets in a low ionic strength medium, shown in Figs. 5.4 and 5.5. However, interrogation of the gel layer images shown Fig. 5.6c over the hydration period appears to show visible differences between the swelling behaviour in the two pH environments.

The distribution and dispersion of the total IT over the hydration period (Fig. 5.6d) differs dramatically between the two pH environments. At pH 7, an environment where the drug

is very insoluble, the matrix expands and swells, taking some drug particles with it but the drug predominantly remains in the core and is not readily able to dissolve or disperse into the hydrating matrix, reflecting the *in vitro* dissolution data. However, at pH 1.5, as the HPMC matrix expands and swells the IT shows enhanced mobility and moves with the apparent diffusion front, which has improved definition and has more inherent structure at this pH. At pH 7 the diffusion front and the swelling front are likely to coincide. As indicated previously, the solubility of IT is very different in the two pH environments. It can be hypothesised that the additional structure within the diffusion front, evident at pH 1.5, is related to the pH-dependent solubility of IT [1] [11]. This has the potential to impact on the mechanism drug release kinetics [12] [13].

The FTIR imaging data confirms that the HPMC swelling is similar at each pH for the placebo but is measurably different when IT is incorporated into the tablet. This suggests the possibility of an additional mechanism affecting drug release kinetics beyond pH enabled drug solubility in the hydrated matrix. To explore this further and to inform the findings observed from the ATR-FTIR imaging, a program of work to determine the swelling kinetics of IT loaded tablets was conducted using optical imaging (see section 5.7.7).

Evidence of undissolved IT particle movement was observed in both pH environments. This phenomenon of drug particle translocation has previously been studied using optical methods [14]. Using ATR-FTIR imaging, as the HPMC matrix swells and expands, undissolved drug particles moving outward in the expanding hydrated gel layer can be followed without the need for other markers, such as dyes or glass beads [9], advantageously it is possible to also confirm the chemical form of the drug as the particle is moving.

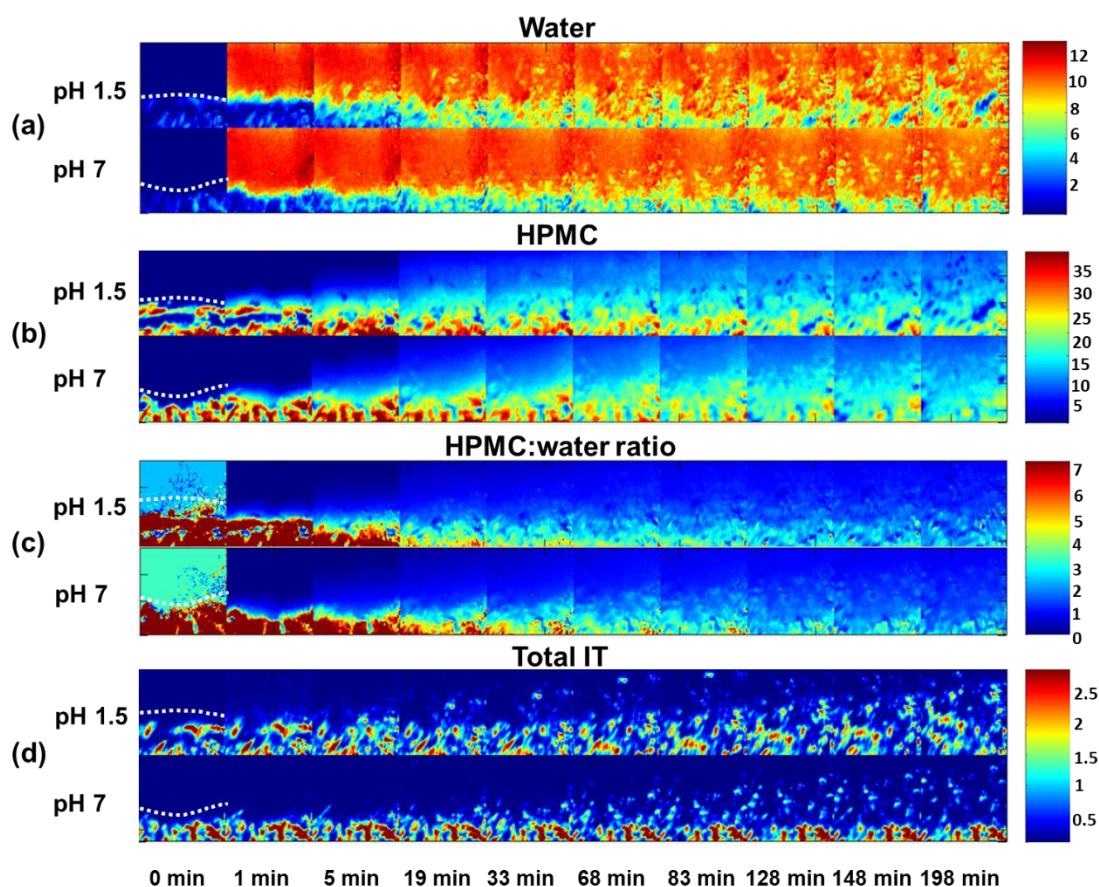


Fig. 5.6: ATR-FTIR peak area integration images over hydration period, showing: (a) distribution of water; (b) distribution of HPMC; (c) HPMC:water peak area ratio images, showing HPMC gel layer evolution for pH 1.5 and 7; (d) distribution of total IT. The dotted lines in the first column of images denotes the approximate boundary between the tablet and air/water

5.7.6 Investigating the Nature of IT Particles Within Different pH Environments

Expanding the diffusion front area of images at selected time point permits the exploration of the translocation of the IT particles in more detail (Fig. 5.7). In these enlarged images, it is possible to identify and track individual particles, an example of a tracked particle is highlighted at both pH 1.5 (Fig. 5.7a) and pH 7 (Fig. 5.7b) images. At each time point, the change in the position of the interface between the IT rich area and the surrounding medium was calculated. This was then subtracted from the measured distance of particles relative to their original position giving a measure of the relative movement of the particle and interface at each time point.

Five particles were tracked from the pH 1.5 and 7 datasets and their movement is plotted in Fig. 5.7c. It should be noted that due to the limited field of view of the ATR-imaging experimental set up, distances $>400\ \mu\text{m}$ away from the interface could not be measured. Differences were observed in the distribution and the number of particles between the pH 1.5 and 7 datasets suggesting that particles at pH 1.5 are moving a greater distance relative to the interface in comparison to those particles present in the pH 7 environment within the same timeframe. A two-way ANOVA determined that there was a statistically significant difference in the distance travelled by the particles in the pH 1.5 and 7 environments after 58 minutes ($p < 0.05$, $n = 5$). This is most likely attributable to the low solubility of IT at higher pH impacting on the water uptake and swelling capacity of the tablet in comparison to that at pH 1.5. For reference, the solubility of IT at pH 7 is reported to be 1 ng/mL and the solubility at pH 1.5 is 4 $\mu\text{g/mL}$ [1].

It is postulated that as IT has much greater solubility at pH 1.5 it therefore will dissolve out of the matrix, effectively leaving a more “porous” structure than that observed at pH 7. This more porous matrix clearly has different expansion properties upon hydration as evidenced by the different outward IT particle translocation. Differences in the expansion properties were not observed in the placebo. Ultimately, monitoring actual drug particle

movement by ATR-FTIR imaging, for a compound that shows pH dependent solubility, reveals more information pertaining to the nuances of the mechanism of drug release when compared to methods lacking chemical specificity, such as optical microscopy, to track glass beads.

Infrared spectra were extracted across the central line of the highlighted particles in the images obtained after 28 minutes at pH 1.5 and pH 7, to determine if changes in particle mobility were linked to changes in the IT chemistry (Fig. 5.7d and 5.7e). The infrared spectra from the translocated particles were shown to be IT rich, although evidence of water and HPMC was also observed at both pH values. Interestingly, the particle at pH 7 shows a greater intensity of HPMC across the particle in comparison to that at pH 1.5 as the edge of the diffusion front will be in different places due to the pH effect on IT solubility. Consequently, particles monitored will be located within different evolving fronts (swelling and diffusion) [5] [14] [15] depending on the pH environment. As the tablet hydrates, the polymer chains start to relax creating the swelling front [16], this and the diffusion fronts move out further as the tablet continues to hydrate, translocating any undissolved particles inside the diffusion front with them.

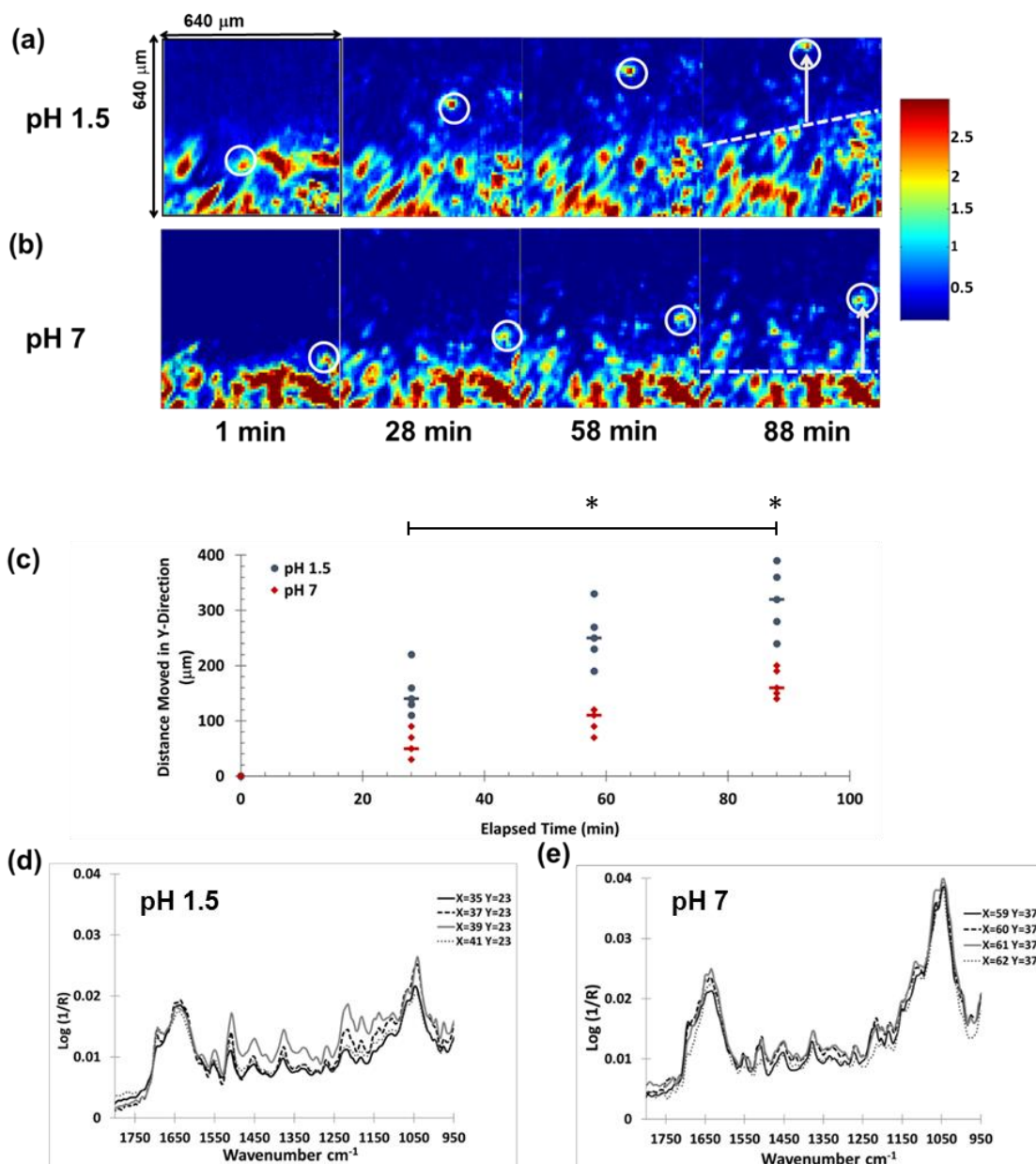


Fig. 5.7: ATR-FTIR images tracking an IT particle at selected time points at (a) pH 1.5 and (b) pH 7 (interface indicated by dashed white line in last pane), (c) Plot showing movement of 5 discrete particles at each pH over time ($p < 0.05$), FTIR spectra from selected pixels across the IT particle, showing that the particles are IT rich at the 28-minute time-point for (d) pH 1.5 and (e) pH 7

5.7.7 Characterisation of the Different Forms of IT

FTIR is sensitive to molecular structure, therefore it is reasonable to assume that spectroscopic differences will be associated with the different forms of IT (ionised/ non-ionised form). For the images generated here, showing the distribution of IT in Fig. 5.6d and Fig. 5.7a and b, the $\nu(\text{C}=\text{C}) \sim 1510 \text{ cm}^{-1}$ was used as the spectroscopic marker for IT. However, this band is present in both the ionised and un-ionised forms therefore it only shows the distribution of total IT. In order to ascertain that IR was sensitive to the different forms of IT, ATR-FTIR spectra were collected from IT salts (mono and dihydrochloride) prepared following procedures outlined previously [1] [17]. Clear differences were observed between spectra obtained from the free base and IT salts, predominantly in the C-H stretching region. The free base form exhibits a strong band at 2821 cm^{-1} associated with CH symmetric stretching vibrations of the methyl group (Fig. 5.8a) which disappears when the drug is ionised. Therefore the 2821 cm^{-1} band was used to generate peak area distribution images to show changes in IT chemistry over the course of the hydration period (Fig. 5.8b). A greater intensity of undissolved free base is observed in the tablet core (towards the bottom of the image) for the high pH medium over the duration of the experiment. In contrast for the low pH environment, the intensity of the free base reduces rapidly as it starts to partially ionise, as expected with IT being more soluble at low pH. From this it can be surmised that the IT is predominantly in the free base form in the images at the early time points at both pH 1.5 and pH 7. However, IT remains in the free base form for the duration of the experiment behind the swelling front, with a small number of undissolved particles extending towards the diffusion front at pH 7.

Conversely, at pH 1.5 IT is predominantly in the ionised form at later time points, as illustrated by the loss of the free base (Fig. 5.8b), extending through to the outer edge of the diffusion front most probably due to its improved solubility in comparison to the free base form.

A more detailed interrogation of the changes in chemistry of IT during the dissolution process can be performed by comparison of the infrared data extracted from the lowest 6 rows of pixels in these images. Binning the spectra within the pixels of the lowest six rows from images at 0, 33 and 198 minutes at both pH, it was possible to generate average spectra with sufficient S/N to elucidate differences in the IT chemistry between systems (Fig. 5.8c). It was observed that over the course of the dissolution experiment performed at pH 1.5 there was a subtle reduction in the intensity of the 2821 cm^{-1} band and a shift to higher wavenumber of the 2925 cm^{-1} band over time, which was indicative of a partial transformation of IT from the free base to the monohydrochloride form, shown more clearly in Fig. 5.8d. Whereas at pH 7, there is no reduction in the intensity of the 2821 cm^{-1} band indicating that at pH 7, the IT remains in the free base form, with an associated lower solubility.

ATR-FTIR imaging studies provide a direct understanding how the low solubility pH-dependent drug, with a pK_a in the physiological range, changes during the dissolution process. Following matrix swelling and expansion whilst tracking undissolved drug particles, in the way previous workers have tracked glass beads [14], it was possible to directly observe the relationship between particle translocation, drug solubility, ionisation state and distribution across the hydrated matrix at different media pHs. These factors will be important to drug release kinetics at different pH values.

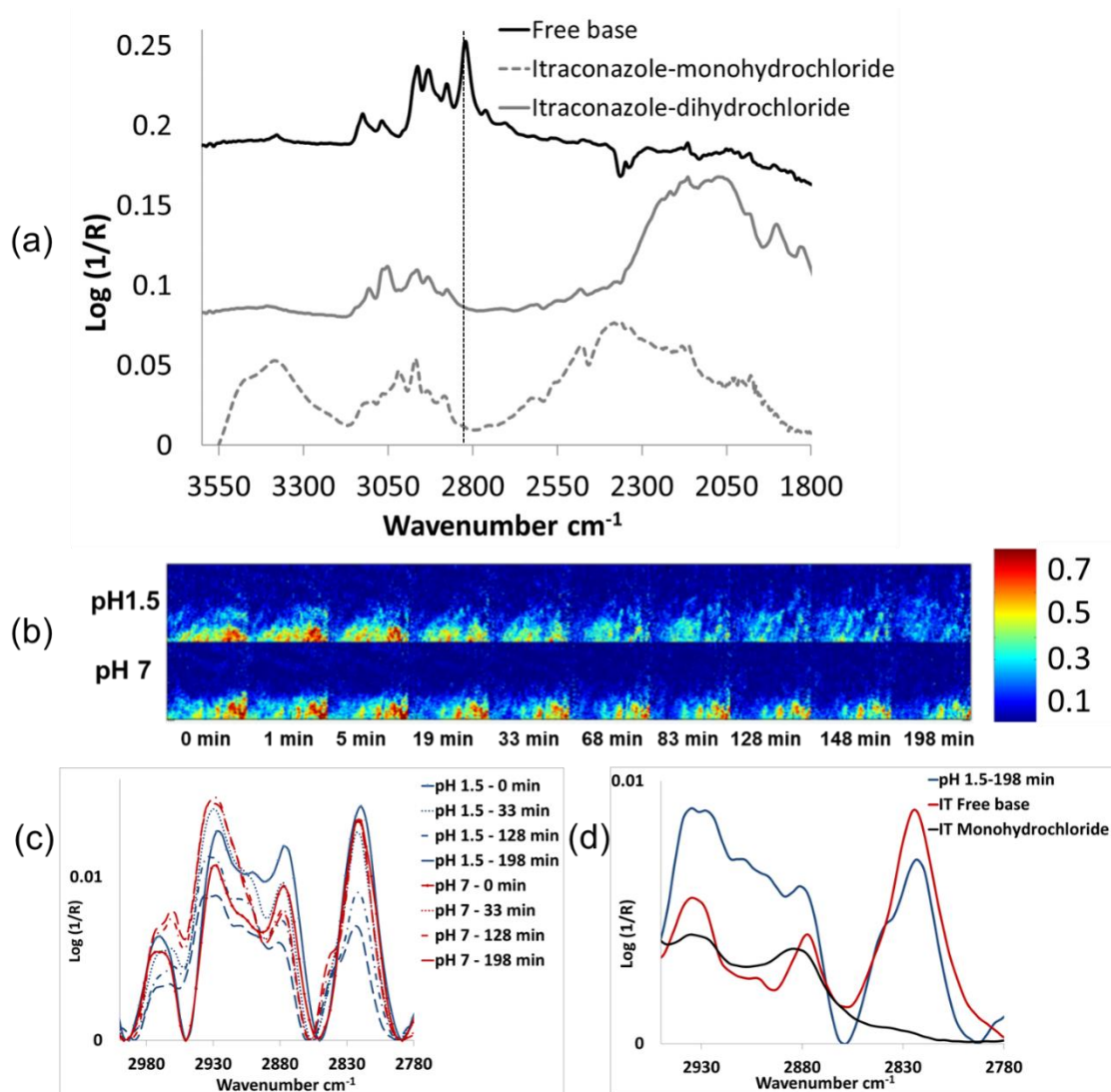


Fig. 5.8: (a) Average ATR-FTIR imaging spectra obtained from IT free base, IT monohydrochloride and IT dihydrochloride with dotted line indicating $\nu_s(\text{CH})$ at 2821 cm^{-1} (b) ATR-FTIR peak area integrated images generated using band at 2821 cm^{-1} . (c) average ATR-FTIR imaging spectra highlighting $\nu(\text{CH})$ at 0, 33 and 198 minute timepoints for 20% w/w IT loaded tablets at pH 1.5 and 7 (d) average ATR-FTIR imaging spectra obtained from IT free base, IT monohydrochloride and 198 minute timepoint for 20% /w IT loaded tablet at pH 1.5

5.7.8 Physical Swelling Kinetics- Radial and Axial Swelling Results on Placebo and 20% w/w IT Loaded Tablets

To supplement the ATR-FTIR data a series of swelling experiments were performed on both IT loaded and placebo tablets at pH 1.5 and pH 7. Examples of the optical images obtained from the placebo and 20% w/w IT loaded tablets for the 0 and 180-minute timepoint at pH 1.5 and 7 for the radial and axial measurements are shown in Fig. 5.9, Fig. 5.10, Fig. 5.11 and Fig. 5.12. The full set of optical images are shown in Appendix 5.

The results obtained from the swelling measurements confirmed that the swelling of placebo HPMC tablets was independent of pH (Fig. 5.13), however there were a distinct difference in swelling behaviour of the 20% w/w IT loaded tablets in the different pH environments (Fig. 5.14). A greater degree of swelling was observed at pH 1.5 over the period of the hydration. Statistical analysis was carried out on the 30, 60, 90, 150 and 180 minute time point data using a two-way ANOVA to determine if there is a significant difference in both axial and/or radial swelling between tablets in the pH 1.5 and 7 environments. The results indicate that no statistically significant difference was observed at the 30-minute time-point, however a significant difference ($p < 0.05$) was observed for the subsequent time points analysed. Statistical analysis was also carried out on the placebo data at the same time points, however no significant difference was found for either the axial or radial dimensions between the pH environments (Fig. 5.13). These findings are in agreement with the FTIR-ATR imaging data presented earlier and support the hypothesis that the reduced swelling capacity of the IT loaded tablets at pH 7, leads to a reduction in the translocation of IT particles in the diffusion layer and consequently, along with the poor solubility of IT under these conditions results in a retardation of IT release from these tablets.

		pH 1.5
		pH7
Dry Tablet	180 min Immersion	

Fig. 5.9: Radial optical images obtained from 0 and 180 minute timepoints for swelling experiments conducted on HPMC placebo tablets at pH 1.5 and 7

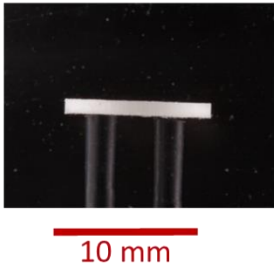
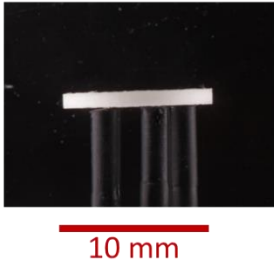
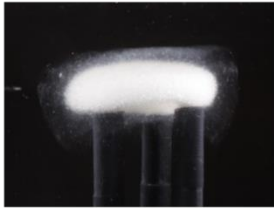
		pH 1.5
		pH7
Dry Tablet	180 min Immersion	

Fig. 5.10: Axial optical images obtained from 0 and 180 minute timepoints for swelling experiments conducted on HPMC placebo tablets at pH 1.5 and 7

		pH 1.5
		pH 7
Dry Tablet	180 min Immersion	

Fig. 5.11: Radial optical images obtained from 0 and 180 minute timepoints for swelling experiments conducted on 20% w/w IT tablets at pH 1.5 and 7

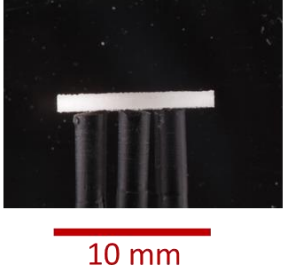
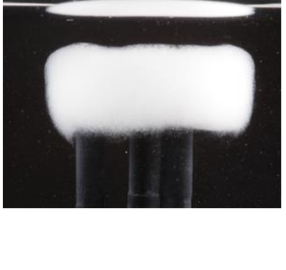
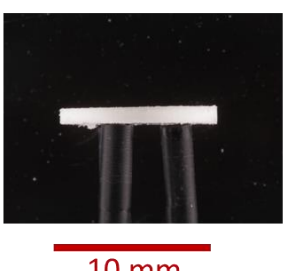
		pH 1.5
		pH 7
Dry Tablet	180 min Immersion	

Fig. 5.12: Axial optical images obtained from 0 and 180 minute timepoints for swelling experiments conducted on 20% w/w IT tablets at pH 1.5 and 7

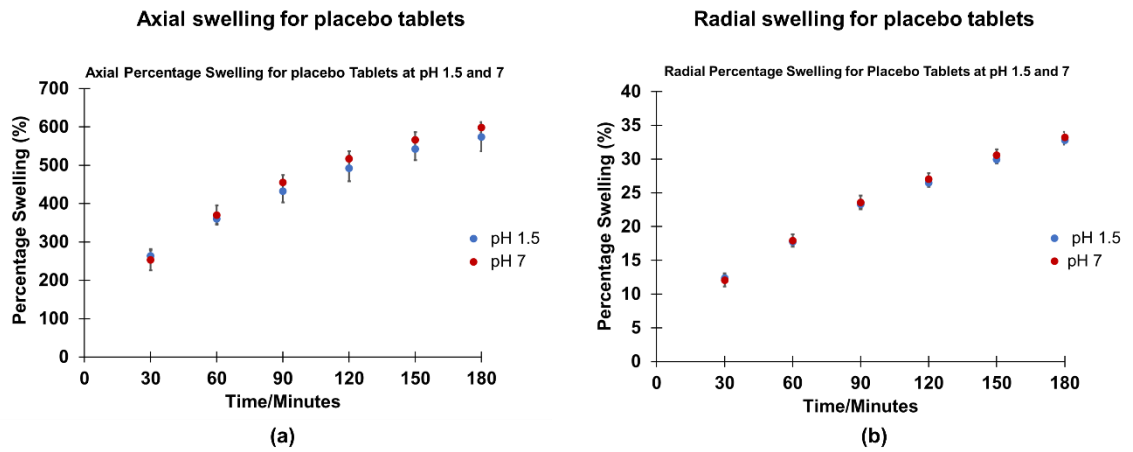


Fig. 5.13: Percentage swelling data (n=6) obtained from HPMC placebo tablets at pH 1.5 and 7 (a) axial (b) radial measurements

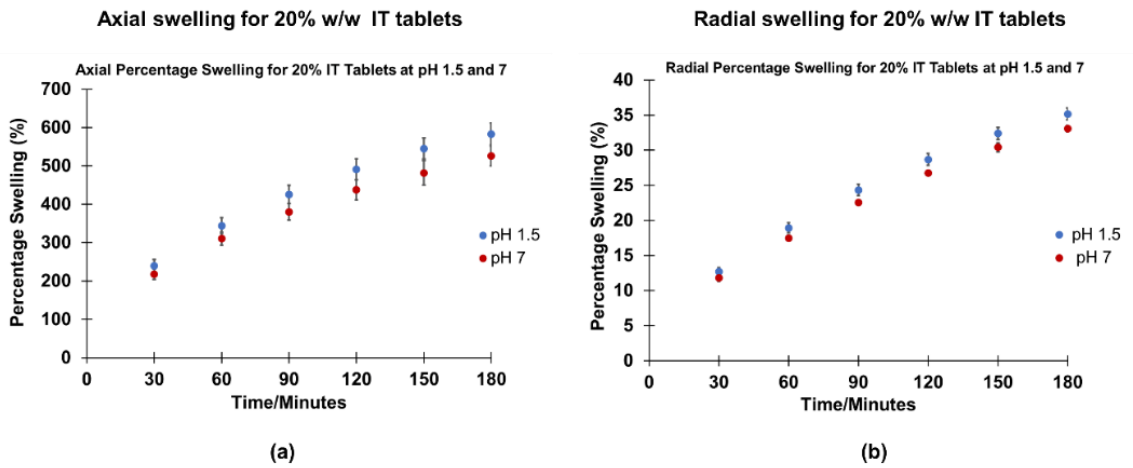


Fig. 5.14: Percentage swelling data (n=6) obtained from 20% w/w IT loaded tablets from (a) axial (b) radial measurements

5.8 Summary

Using ATR-FTIR imaging it has been shown that increasing the ionic strength of the hydration medium inhibits/restricts the formation of the HPMC swelling and gel layer formation. Rapid formation of the gel layer was observed with low ionic strength media, whilst high ionic strength was shown to interfere with the polymer hydration, resulting in the suppression of the expansion of the gel layer.

Evidence of particle translocation was observed in both pH 1.5 and 7 environments. The hydration experiments performed using ATR-FTIR imaging have also shown that the undissolved drug particles migrate with the gel layer as the outer shell of the polymer matrix hydrates and expands. The particles at pH 1.5 were shown to move a greater distance relative to the interface in comparison to the particles present in the pH 7 environment due, possibly as a result of the enhanced solubility of the ionised form of the itraconazole.

This was verified using optical swelling measurements conducted on the 20% w/w loaded tablets and confirmed a difference in swelling rate at pH 1.5 and 7. The tablets exposed to the low pH medium show a greater swelling rate and higher overall percentage swelling in comparison to those exposed to the pH 7 environment. No significant differences in the swelling behaviour were observed for placebo tablets.

As the matrix swells and hydrates at different pH, it was possible to gain an insight into the chemical characteristics of the drug, distinguish and detect the un-ionised form in both low and high pH environments. Un-ionised IT was observed predominately in the tablet core and remained localised in the pH 7 medium, in contrast, in pH 1.5 medium, as the drug dissolved and diffused through the matrix, it transformed from the un-ionised to the ionised form. Due to a combination of a low signal to noise ratio and the detection limits of ATR-FTIR imaging, it was not possible to verify the presence of the ionised itraconazole form in the surrounding medium at pH 1.5, despite observing an overall reduction of free base IT within the tablet images over time. Complementary dissolution

data clearly suggests that the concentration of IT in the surrounding medium does increase with time at pH 1.5. As stated previously, the aqueous solubility of IT is ~1 ng/mL at pH 7 and 4 µg/mL at pH 1 [1] these values are likely to be below the detection limits of the ATR-FTIR imaging method.

The methodology used in this work permits an understanding of the within-matrix dynamics of the drug and shows that drug mobility is very different in the two pH environments. It was possible to follow matrix swelling and expansion and track undissolved drug particles in the way previous workers have tracked glass beads [14]. However, it was possible to observe the changing chemical nature of the drug as a particle moved within the diffusion front. At pH 7 the drug remained in the free base form, which is poorly soluble and therefore largely stayed within the core and the swelling front. At pH 1.5 however, the IT was ionised, becoming more soluble and was able to migrate into the diffusion front and eventually out into the surrounding medium.

5.9 Conclusions

This work highlights the value of utilising ATR-FTIR imaging to elucidate factors affecting the release of a pH-dependent, poorly-soluble drug from a hydrophilic matrix. This approach permits an understanding of the within-matrix dynamics of the drug and shows that although evidence of particle translocation was observed in both pH 1.5 and 7 environments, drug mobility was very different between the two.

Using ATR-FTIR imaging to follow matrix swelling and expansion and track undissolved drug particles in the way previous workers have tracked glass beads [14], it was possible to observe the changing chemical nature of the drug as a particle moved within the diffusion front. At pH 7 the drug remained in the free base form, which is poorly-soluble and therefore largely stayed within the core and the swelling front. At pH 1.5 however, the IT was partially ionised, becoming more soluble and was able to migrate into the diffusion front and eventually out into the surrounding medium. The IT containing tablets exposed to the low pH medium show a higher swelling rate and greater overall

percentage swelling in comparison to those exposed to the pH 7 environment. No significant differences in the swelling behaviour were observed for placebo tablets.

Therefore, it can be concluded that differential drug solubility observed across the pH range is not the sole reason for different release rates within different pH environments. Additionally, the presence of non-dissolved drug negatively impacts upon matrix swelling resulting in translocated free base drug particles being in the swelling front at pH 7 and partially ionised drug particles in the diffusion front at pH 1.5. In combination, differences between the solubility of the two drug forms and swelling of the matrix affect the rate and percentage drug release at the two different pHs.

5.10 References

- [1] T. Tao, Y. Zhao, J. Wu and B. Zhou, "Preparation and evaluation of itraconazole dihydrochloride for the solubility and dissolution rate enhancement," *International Journal of Pharmaceutics*, vol. 367, no. 1-2, p. 109–114, 2009.
- [2] A. V. Ewing, G. S. Clarke and S. G. Kazarian, "Attenuated total reflection-Fourier transform infrared spectroscopic imaging of pharmaceuticals in microfluidic devices," *Biomicrofluidics*, vol. 10, no. 2, 2016.
- [3] S. R. Pygall, S. Kujawinski, P. Timmins and C. D. Melia, "The suitability of tris(hydroxymethyl) aminomethane (THAM) as a buffering system for hydroxypropyl methylcellulose (HPMC) hydrophilic matrices containing a weak acid drug," *International Journal of Pharmaceutics*, vol. 387, p. 93–102, 2010.
- [4] FDA U.S. Food and Drug Administration, "Dissolution Methods-itraconazole," [Online]. Available: https://www.accessdata.fda.gov/scripts/cder/dissolution/dsp_SearchResults.cfm. [Accessed 19 July 2019].
- [5] P. Timmins, D. Desai, W. Chen, P. Wray, J. Brown and S. Hanley, "Advances in mechanistic understanding of release rate control mechanisms of extended-release hydrophilic matrix tablets," *Therapeutic delivery*, vol. 7, no. 8, p. 553–572, 2016.
- [6] F. D. Zahoor, K. T. Mader, P. Timmins, J. Brown and C. Sammon, "Investigation of Within-Tablet Dynamics for Extended Release of a Poorly Soluble Basic Drug from Hydrophilic Matrix Tablets Using ATR-FTIR Imaging," *Mol. Pharmaceutics*, vol. 17, no. 5, p. 1090–1099, 2020.
- [7] X. Yin, L. S. Daintree, S. Ding, D. M. Ledger, B. Wang, W. Zhao, Q. Jianping and W. Wu, "Itraconazole solid dispersion prepared by a supercritical fluid technique: preparation, in vitro characterization, and bioavailability in beagle dogs," *Drug Design, Development and Therapy*, vol. 9, p. 2801–2810, 2015.
- [8] J. L. Ford, "Design and Evaluation of Hydroxypropyl Methylcellulose Matrix Tablets for Oral Controlled Release: A Historical Perspective," in *Hydrophilic Matrix Tablets for Oral Controlled Release*, P. Timmins, S. R. Pygall and D. R. Melia, Eds., New York, AAPS Advances in the Pharmaceutical Sciences Series, vol 16. Springer, 2014, pp. 17–51.
- [9] G. S. Bajwa, K. Hoebler, C. Sammon, P. Timmins and C. D. Melia, "Microstructural imaging of early gel layer formation in HPMC matrices," *Journal of Pharmaceutical Sciences*, vol. 95, no. 10, pp. 2145-2157, 2006.
- [10] X. Ming Xu, Y. M. Song, Q. N. Ping, Y. Wang and X. Y. Liu, "Effect of Ionic Strength on the Temperature-Dependent Behavior of Hydroxypropyl Methylcellulose Solution and Matrix Tablet," *Journal of Applied Polymer Science*, vol. 102, no. 4, pp. 4066-4074, 2006.

- [11] J. Peeters, P. Neeskens, J. P. Tollenaere, P. V. Remoortere and M. E. Brewster, "Characterization of the Interaction of 2-Hydroxypropyl- β cyclodextrin With Itraconazole at pH 2, 4, and 7," *Journal of Pharmaceutical Sciences*, vol. 91, no. 6, p. 1414–1422, 2002.
- [12] J. L. Ford, K. Mitchell, P. Rowe, D. J. Armstrong, P. N. Elliott, C. Rostron and J. E. Hogan, "Mathematical modelling of drug release from hydroxypropylmethylcellulose matrices: effect of temperature.," *International Journal of Pharmaceutics*, vol. 71, no. 1-2, p. 95–104, 1991.
- [13] P. Colombo, R. Bettini, P. Santi, A. De Ascentiis and N. A. Peppas, "Analysis of the swelling and release mechanisms from drug delivery systems with emphasis on drug solubility and water transport," *Journal of Controlled Release*, vol. 39, no. 2-3, pp. 231-237, 1996.
- [14] R. Bettini, P. L. Catellani, P. Santi, G. Massimo, N. A. Peppas and P. Colombo, "Translocation of drug particles in HPMC matrix gel layer: effect of drug solubility and influence on release rate," *Journal of Controlled Release*, vol. 70, no. 3, p. 383–391, 2001.
- [15] P. Colombo, R. Bettini, G. Massimo, P. L. Catellani, P. Santi and N. Peppas, "Drug diffusion front movement is important in drug release control from swellable matrix tablets," *Journal of Pharmaceutical Sciences*, vol. 84, no. 8, p. 991–997, 1995.
- [16] M. U. Ghori and B. R. Conway, "Hydrophilic Matrices for Oral Control Drug Delivery," *American Journal of Pharmacological Sciences*, vol. 3, no. 5, pp. 103–109, 2015.
- [17] H. Bagavatula, S. Lankalapalli, V. Tenneti, N. Beeraka and B. Bulusu, "Comparative Studies on Solubility and Dissolution Enhancement of Different Itraconazole Salts and Their Complexes," *Advances in Pharmacology and Pharmacy*, vol. 2, no. 6, pp. 85-89, 2014.

6.0 Optimisation of IT Release from HPMC Tablets by Incorporating Organic Acid pH Modifiers

6.1 Introduction

The aim of this programme of work was to investigate how the addition of pH modifiers (citric acid, betaine HCl, cysteine HCl and glycine HCl), differing in their pK_a and solubility, impacts on drug release from a hydrophilic matrix of a poorly-soluble drug with a pK_a in the physiological range. In an extension of the work carried out in Chapter 5, the same ATR-FTIR imaging methodology was also adopted to characterise the within-tablet dynamics for an HPMC polymer matrix incorporating 20% w/w itraconazole, with the addition of an organic acid pH modifier. As previously stated, itraconazole (IT) was selected as a model drug in this work as it exhibits the characteristics of having a pK_a of 3.7 and being practically insoluble at pH 7. This puts it into the biopharmaceutics classification system (BCS) of class II drugs, which are those having low solubility and high permeability. IT also has good infrared spectroscopic properties to facilitate imaging approaches [1].

Many strategies have been adopted to overcome the bioavailability problems associated poorly-soluble drugs to achieve a pH-independent dissolution profile from drugs of this classification. Approaches have included formation of salts [2], solid–lipid nanoparticles [3] and solid dispersions [4]. Another strategy is to incorporate a pH modifier into the tablet formulation [5] and it was this approach that was adopted for this study.

Tablets were prepared using 10% w/w and 30% w/w of the selected pH modifier, with a view to regulating the pH microenvironment within the tablet and hence enhancing drug release from the HPMC polymer matrix.

Incorporation of acidic pH modifiers within an oral dosage form is an advantageous approach for weakly basic drugs, because these are selected to manipulate the microenvironmental pH to provide a low pH environment within the tablet matrix and in

the gastrointestinal tract, therefore providing increased drug availability due the ionisation of the drug in the favorable pH conditions created [6]. The term 'microenvironment' has been coined by researchers in this field to identify a microscopic layer of saturated solution which forms around a solid particle during hydration [7].

The key to ensuring success with this approach is to ensure a pH modifier is selected that has adequate solubility and an appropriate pK_a to maintain the low pH environment. Ensuring the most appropriate pH modifier is selected for optimal release of a specific drug can be rather challenging and is quite involved. For example, if the pH modifier diffuses out of the tablet matrix more rapidly in comparison to the drug this will result in a decrease in the pH modifying effect over time. Therefore obtaining the desired microenvironment pH as a result of incorporating a pH modifier is a major challenge for regulating drug ionisation within a tablet matrix over the entire drug release period [6] and understanding the release behaviour of the pH modifier from an oral dose form is crucial to appreciate the impact on drug release [8].

Typically, organic acids such as citric, fumaric, tartaric and sorbic acid are used as pH modifiers in solid oral dosage forms. There are many characteristics associated with organic acids such as pK_a , solubility, chemical structure, particle size and molecular weight that can influence the drug dissolution profile of weakly soluble drugs. Also, the drug that the organic acid will be used with will also have an impact on the dissolution profile and properties such as solubility, pK_a and the composition of the dosage form would need to be taken into consideration [5] [9] [10]. It is well understood that the dissolution medium pH impacts on the dissolution rate of API's with a pH dependent solubility [11].

Due consideration to the concentration of the selected pH modifier within the formulation is required as it will impact on drug dissolution, manufacturability and tablet stability. High levels of pH modifier within a formulation could advantageously increase drug dissolution, while conversely leading to poor stability within the formulation [8]. In order to achieve complete dissolution of the drug, it has been suggested that the pH modifier

and drug particles need to coexist in the solid dosage form for the drug to fully dissolve or be released [12].

Siepe *et al.* have reported that the incorporation of poorly water-soluble organic acids such as fumaric acid were more effective than water-soluble organic acids in enhancing the dissolution rate of the drug dipyridamole from an HPMC tablet matrix due to their low aqueous solubility. The release of the organic acid coincided with that of the drug and provided a suitable acidic environment for the optimal release of the drug. The authors investigated the release rate of the drug using a range of different organic acids and found that fumaric acid provided 86.8% release followed by the citric acid at 65.6%, succinic acid at 51.7% and ascorbic acid at 4.18%, after a 6 hour dissolution time [13].

Adachi *et al.* investigated a range of organic acid pH modifiers (tartaric, citric, malic, succinic and aspartic acid) to improve the dissolution and bioavailability of a ketoconazole which is a weakly soluble drug with a pK_a of 6.5. The authors found that the water-soluble organics (citric acid and tartaric acid) provided an eight-fold increase in the dissolution of the drug at pH 6 compared to the ketoconazole only system [14]. The authors concluded that the poorly water-soluble acids were not as effective as the water-soluble organic acids. With the least effective water-soluble organic acid (succinic acid) exhibiting a lower drug release rate of ketoconazole in comparison to the citric, tartaric and malic acid modifiers, all of which have a higher aqueous solubility and a lower pK_a value in comparison to the succinic acid [14]. It should be noted, however, that these findings seem to contradict those of Siepe *et al.*

Cysteine HCl has been used as a pH modifier in the HPMC-based Wellbutrin 100 mg tablets to provide the API bupropion hydrochloride (pK_a 7.9) an acidic environment and stability due to the protonation of the of the N-H of the t- butyl amino group in the drug molecule. However, in the original formulation, a significant increase in dissolution rate was observed under storage conditions at 25° C/60% relative humidity. This was thought to be attributable to slow acid hydrolysis of HPMC under the storage conditions. This highlights the importance of HPMC to cysteine HCl ratio in stabilising the formulation.

The product was reformulated by increasing the ratio of HPMC to cysteine HCl (Hypromellose 2910: cysteine HCl 20% and 6% in the original formulation and Hypromellose 2910: cysteine HCl 33% and 6% in the revised formulation) [15] [16].

Authors conducted a pilot study to investigate the use of betaine HCl as a hydrochloric-based gastric supplement to produce a decrease in the gastric pH, therefore assisting the absorption of weakly basic drugs that exhibit a pH-dependent solubility. The betaine HCl was incorporated into solid dosage forms such as capsules and tablets, the advantage being that commencement of the acidification would only take place when the dosage form reaches the stomach, allowing the salt to dissociate and form the free HCl. The advantage of using betaine is that it is a naturally occurring substance which is present in foods such as beetroot, spinach and whole wheat foods. The authors concluded that the strategy of using betaine HCl was an effective methodology to rapidly reduce the gastric pH. Also, because the effect was temporary, it provided sufficient window for the dissolution of weakly soluble basic drugs [17].

Citric acid is a tricarboxylic acid and is a naturally occurring substance found in citrus fruits. It is widely used as an acidifying agent in pharmaceutical solid dosage forms. Citric acid is commonly used in pharmaceutical formulations, cosmetics dietary supplements and as a preservative in the food and beverage industry. The advantages of using citric acid are that it is relatively inexpensive and inherently safe [18] [19].

Others have reported incorporating high concentrations of extremely soluble organic acid modifiers such as citric acid or tartaric acid to generate a high osmotic pressure and /or ionic strength which undoubtedly impacts on the formation of the gel layer and release mechanism of the drug [10] [16] [20]. Also, other factors could potentially impact on the processing and stability of the solid dosage form when high levels of pH modifier are incorporated. Factors such as blending and compression of the solid dosage form could be influenced by the compaction properties of the pH modifier when present in high levels within the formulation [16].

The effect of amino acid pH modifiers incorporated into HPMC matrices with a poorly-soluble weakly basic drug and how these types of modifiers influence dynamics of the gel layer behaviour has not extensively been investigated. The strategy adopted for the current study was to use an organic pH modifier that is commonly used in oral dosage forms (citric acid) and to investigate amino acid-based modifiers such that the *pKa* is around 2 units lower than itraconazole, thus providing favourable acidic conditions to enhance the dissolution of the drug. To elucidate the potential release enhancement of IT in an HPMC tablet matrix using organic acid pH modifiers, the following were investigated: citric acid, cysteine HCl, glycine HCl and betaine HCl at a loading of 10% w/w and 30% w/w.

6.2 Materials and Methods

6.2.1 Materials

Tablet constituents used in this chapter are listed in Chapter 4 (Table 4.1 and 4.2). The tris(hydroxymethyl)aminomethane hydrochloride buffer solution (tris buffer, Sigma Aldrich, molecular biology grade pH 7.2) was used for the hydration, dissolution and optical imaging studies, the 0.1 M solution being prepared by carrying a 10-fold dilution of the as-received standard solution using 18 M Ω water. A 10% w/w and 30% w/w loading of the organic acid was incorporated into the HPMC-IT formulation. Table 6.1 shows the physiochemical properties of the organic acids used in this study.

Table 6.1: Comparison of pK_a and aqueous solubility of various pH modifiers (values taken from the literature)

Organic acid pH Modifier	Structure	pK_{a1}	Solubility Data g/100 mL
Citric Acid		3.1	59.2 [21]
Betaine HCl		2.4	64.7 [22]
Glycine HCl		2.3	82.5 [23]
Cysteine HCl		1.7	74 [24]

6.2.2 Preparation and Characterisation of Tablets

Formulations were prepared and compacted in accordance with the methodology outlined in Chapter 4.4.

6.2.3 Content Uniformity of Itraconazole Loading and Heterogeneity of Tablets

Whole tablets were analysed (n=6) using Near Infrared (NIR) spectroscopy and a PLS method was used to calculate/predict the values of the API and pH modifier loadings.

The methodology adopted is described in section 4.5.1 of Chapter 4.

Uniform distribution of the IT and organic acid modifier across the tablets was determined by Raman microscopy. The Raman methodology for assessing the distribution of the API and pH modifier within the HPMC matrix is described in section 4.5.2 of Chapter 4.

Raman microscopy has been demonstrated to be a suitable technique for determining content uniformity of an API and other excipients (organic acids) in tablet matrices due to enhanced spatial resolution (spot sizes less than 2 μm) and the capability to map larger areas, compared to other chemical mapping techniques [25].

6.3 Morphology and Particle Size Analysis of IT, HPMC and Organic pH Modifiers

Scanning Electron Microscopy (SEM) was used to generate images of the organic acids, IT and HPMC powders, for the purposes of determining the morphology of the starting materials. Particle size analysis was conducted using a Malvern Mastersizer particle size analyser. The methodology adopted is outlined in Chapters 4.3.4 and 4.3.5 respectively.

6.4 *In Vitro* Release Studies

Dissolution studies were carried out on the 20% w/w IT incorporated with the organic acid pH modifier at loadings of 10% w/w and 30% w/w (n=6). Analysis was carried out using an Agilent 708 dissolution tester in 900 mL of 0.1M tris buffer using the USP Type-II method. A paddle speed of 75 rpm and a temperature of $37\pm 0.5^\circ\text{C}$ was used in all experiments [26]. A 5 mL aliquot of dissolution medium was withdrawn at different time intervals and assayed for IT using ultraviolet–visible spectroscopy (Agilent Cary 60) by measuring the absorbance at 257 nm.

6.5 Collection of ATR-FTIR Images

Mid-IR spectroscopic images were collected using the approach described in Chapter 5, section 5.4 [27].

6.6 Hydration Experiments Using ATR- FTIR Imaging

Hydration studies on the tablets (n=3) were performed using the experimental arrangement described in Chapter, section 5.5.

6.7 Optical Imaging to Determine to Radial Swelling

Swelling experiments were performed in which optical images were collected using a Canon 5D MK3 digital camera equipped with a 100 mm macro lens, arranged to capture radial images of the tablet, as described previously in section 5.6 of Chapter 5. Images were obtained for all tablet formulations used in this study (n=6).

The tablets were placed onto a 3-prong polymeric sample holder located in a glass cell and 40 mL of 0.1M tris buffer was added. Images were collected at 5 minute intervals for a period of 180 minutes. Data analysis was conducted using image analysis software (ImageJ version 1.52a) to determine the area change in the radial dimension. Previous work (Chapter 5, section 5.6) focused on both radial and axial swelling measurements, however due to both of these providing similar results (Chapter 5, section 5.7.8), this chapter will only consider the radial dimension.

6.8 Multivariate Curve Resolution Alternating Least Squares Analysis (MCR-ALS)

MCR-ALS was performed using MCRv3.19.04 (V 1.6; Copyright © 2003-2001 Unilever) on the ATR-FTIR images for the combined pH 1.5 and 7 datasets with IT and the 30% w/w system without and without pH modifier. The spectral region selected was 1900-950 cm^{-1} and the MCR-ALS was carried out using 4 and 5 factors for the combined pH 1.5 and 7 dataset and factors 8 and 9 for the 30% w/w modifier formulation. User defined software parameters selected for the MCR-ALS analysis were non-linear iterative partial

least squares (NIPALS) decomposition method, alternating least squares was used to determine the optimal loadings (ALS constraints) and for decomposition of the images, non-negativity modified alternating least squares method was used within the software (MALS).

6.9 Results and Discussion

6.9.1 ATR-FTIR Imaging of Reference Materials

The spectroscopic markers identified for each of the reference materials, including the organic acid pH modifiers used for the generation of the chemical images, are described Chapter 4.6.2.

The $\nu(\text{C}=\text{O})$ band was used as a discrete marker to be representative of the concentration, nature and position of the organic acid modifier. These bands/markers were used to generate maps to show the distribution of each of the organic acid modifiers within the tablet.

6.9.2 Content Uniformity and Distribution of 20% w/w Itraconazole with 10% w/w and 30% w/w pH Modifier Tablets using Near Infrared (NIR) and Raman Microscopy

The NIR and PLS data generated from the tablets containing 10% w/w and 30% w/w pH modifier with and without itraconazole is presented in Chapter 4, section 4.6.4.1. In summary, a good agreement between the actual and predicted concentration levels was obtained for all components in all systems investigated.

Raman spectra were obtained from the organic acid modifiers to identify the most suitable (discrete marker) band to represent the modifier and generate the distribution maps from the prepared tablets. The methodology adopted is outlined in Chapter 4, section 4.6.4.2.

To summarise, the $\nu(\text{C}=\text{O})$ band was used as a marker to represent the betaine HCl ($\sim 1728 \text{ cm}^{-1}$), citric acid ($\sim 1736 \text{ cm}^{-1}$) and glycine HCl ($\sim 1736 \text{ cm}^{-1}$). The S-H stretching

mode observed at $\sim 2564\text{ cm}^{-1}$ was found to be the most suitable for generating the Raman distribution maps for the cysteine HCl.

6.9.3 Analysis of the Morphology and Particle Size Determination of IT, HPMC and Organic pH Modifiers

The secondary electron images obtained from the itraconazole, HPMC, glycine HCl, betaine HCl and citric acid powders are presented and discussed in section 4.6.3.1 of Chapter 4.

6.9.4 ATR-FTIR Imaging of HPMC Tablets Containing 10% w/w and 30% w/w Organic acid

Mid-IR images of matrix tablets composed solely of HPMC and the different loadings (10% w/w and 30% w/w) of each of the organic acids hydrating in the pH 7 medium over the 3 hour hydration period were generated using the bands identified in Chapter 4, section 4.6.2 and show the evolution of the hydration medium ingress into the tablet matrix and the growth of the gel layer (Fig. 6.1 and Fig. 6.2). Images were generated using methods described in Chapter 5, section 5.5. Typical representative images from each data set are shown in this chapter, the remaining data is presented in Appendix 3.

High intensity regions, which correspond to high concentrations, are coloured red, while low intensity regions, representing low concentrations, are blue. Differences in intensity for each component are denoted by the numerical values on the accompanying colour scale bars.

From the water distribution images for both the 10% w/w and 30% w/w loadings (Fig. 6.1a and Fig. 6.2a) it was evident that water ingress, determined by observing the colour change (blue to red) in the water distribution maps over time, was rapid and full penetration throughout the area of tablet visible within the field of view, occurred by ~ 19 minutes irrespective of the nature of the organic acid.

HPMC distribution images showed the (non-hydrated) tablet core located towards the lower half of the images (Fig. 6.1b and Fig. 6.2b) and this intensity is comparable for all

the weak acids, independent of loading. Upon hydration, the intensity of this dark red/yellow HPMC distribution in the 100% HPMC tablet image (Fig. 6.1b (i)) is similar to that obtained from tablets containing the citric acid, cysteine HCl and glycine 10% w/w pH modifiers. Conversely, high intensity, HPMC rich regions remain prevalent for longer for the 100% HPMC tablet throughout the duration of the experiment compared with tablet formulations containing each of the 30% w/w pH modifiers. This suggests a greater concentration of pH modifier within the formulation impacts on the hydration properties of HPMC. This could potentially be due to the highly soluble nature of the weak acid 'wicking' water through the HPMC. The betaine HCl exhibited a marked difference at both the 10% and 30% w/w loading in comparison with the other pH modifiers and the 100% HPMC. The tablet containing the 30% w/w betaine HCl (Fig. 6.2b (iv)) shows a rapid disappearance of the high intensity HPMC (dark red) in comparison to the citric acid, cysteine HCl and glycine HCl organic acids. This suggests that the presence of betaine HCl at 10% and 30% loadings disrupts the HPMC gel layer formation.

The ATR-FTIR distribution images shown in Fig. 6.1c and 6.2c represent the distribution of the 10% w/w and 30% w/w organic acid pH modifier. The images show a rapid dissolution of all the organic acids investigated in this study, with no non-hydrated citric acid, cysteine HCl, betaine HCl or glycine HCl detectable in the tablet matrix after 33 minutes in the ATR-FTIR images.

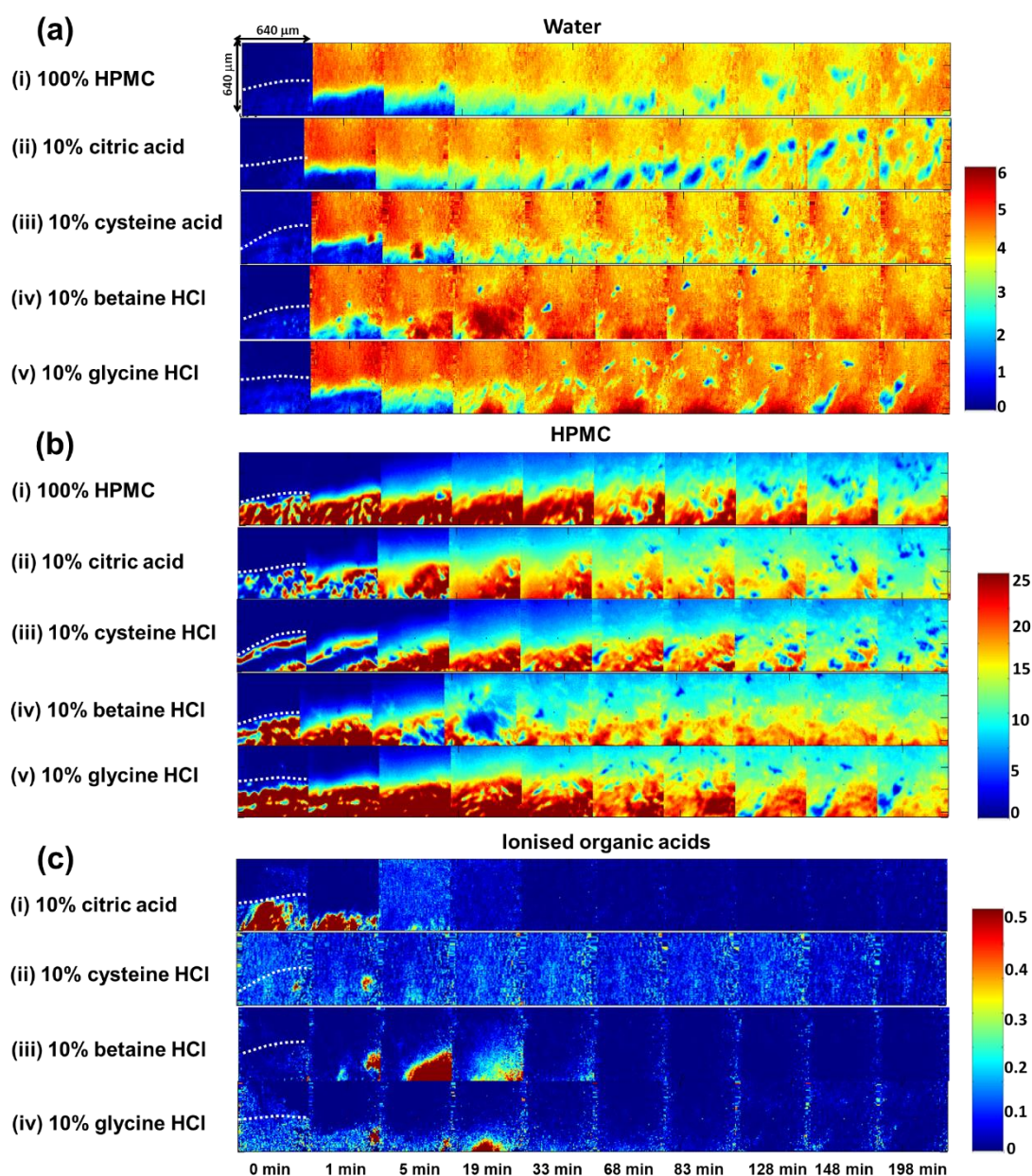


Fig. 6.1: Selected ATR-FTIR images collected over the hydration period for 10% w/w organic acid placebo tablets at pH 7 showing: (a) distribution of water; (b) distribution of HPMC; (c) distribution of ionised organic acid (citric acid, cysteine HCl, betaine HCl and glycine HCl). The dotted lines in the first column of images denote the approximate boundary between the tablet and air/water

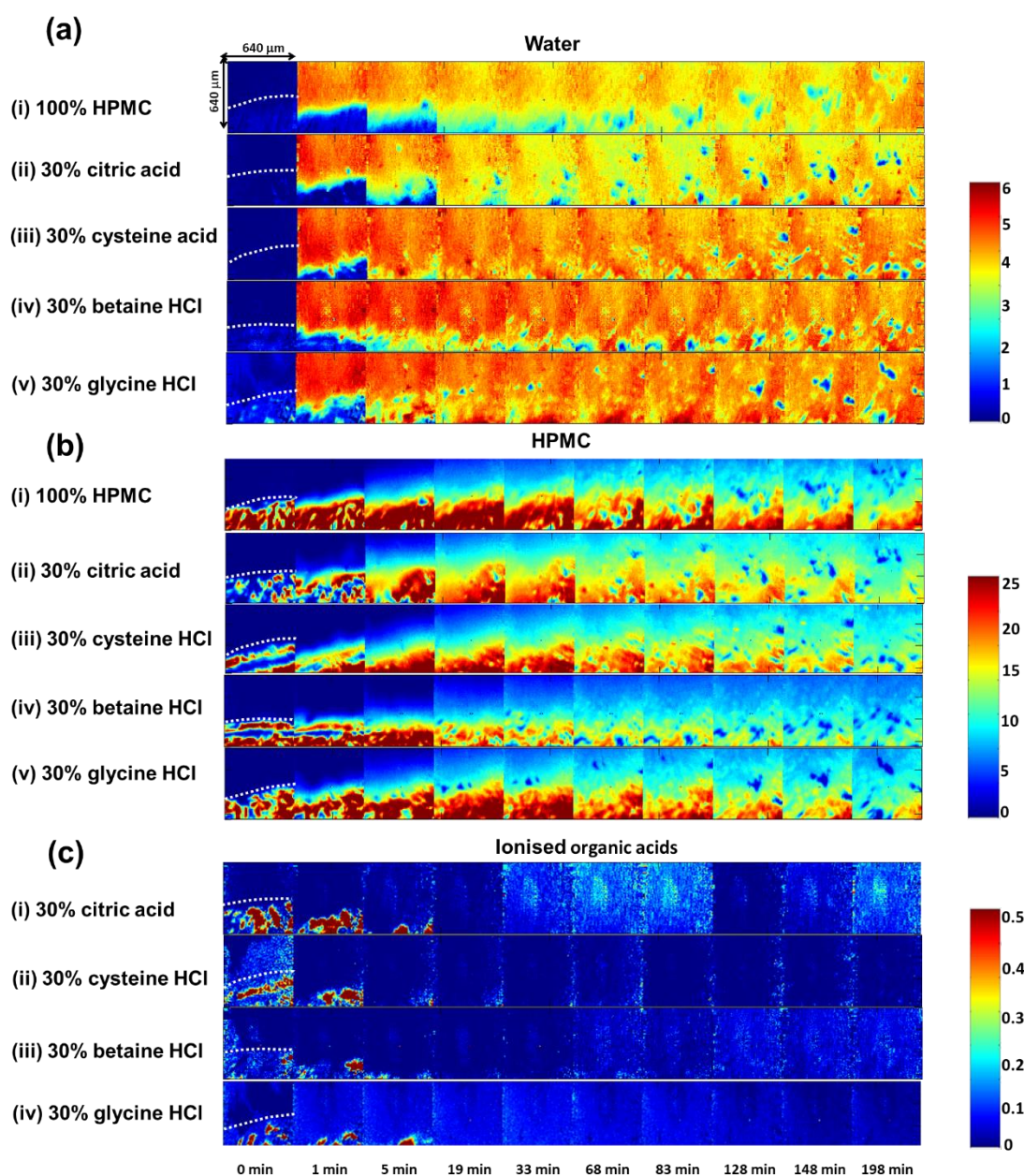


Fig. 6.2: Selected ATR-FTIR images were collected over the time course of hydration experiments for 30% w/w organic acid placebo tablets at pH 7 showing: (a) distribution of water; (b) distribution of HPMC; (c) distribution of ionised organic acid (citric acid, cysteine HCl, betaine HCl and glycine HCl). The dotted lines in the first column of images denotes the approximate boundary between the tablet and air/water

To gain an insight into the gel layer behaviour, the peak area ratio of the $\nu(\text{C-O})$ of the HPMC and the shoulder ($1566\text{-}1678\text{ cm}^{-1}$) of the $\delta(\text{OH})$ for water was plotted. The shoulder was used as opposed to all the $\delta(\text{OH})$, as in chapter 5, to ensure no contribution from the ionised pH modifier was included. As described in Chapter 5, section 5.7.4, the

gel layer was defined as the cyan zone corresponding to values between 2.2 and 3.8, on the colour scale shown in Fig. 6.2 and consisted of a combination of water and polymer at varying concentrations.

The dark red colour corresponded to regions of high intensity which correlate with high HPMC content. Conversely, regions of hydrated HPMC with increasing water content are denoted by the yellow, green and cyan zones, respectively.

Comparing the formulations containing the 10% w/w loading of the pH modifiers (Fig. 6.3a (ii)-(v)) to the 100% HPMC (Fig. 6.3a (i)), the citric acid and cysteine HCl exhibit the greatest similarity to the placebo for the gel layer development over the time frame of the experiment. It can be seen that the high intensity polymer region shown by the dark red colouration is more apparent and less diffuse across the hydration period. The images for the 10% w/w betaine HCl (Fig. 6.3a (iv)) pH modifier show a rapid reduction of the dark red colours assigned to the high polymer content regions. The 10% w/w glycine HCl (Fig. 6.3a (v)) images exhibit a more controlled reduction of the high intensity HPMC in comparison to the betaine HCl over the course of the experiment.

The gel layer behaviour for hydration of formulations containing 30% w/w organic acid modifier (Fig. 6.3b) was markedly different in comparison to that of the 100% HPMC (Fig. 6.3b (i)). A similar behaviour to the 10% w/w formulations was observed with the 30% w/w betaine HCl (Fig. 6.3b (iv)), in that the dry core diminishes more rapidly and the gel layer recedes towards the edge of the field of view within the time frame of the experiment in comparison to the other organic acid modifiers. The increased loading of the citric acid, betaine HCl and cysteine HCl modifier appears to accelerate the disappearance of the high intensity HPMC-rich regions. This suggests that not only are the citric acid, cysteine and betaine facilitating the rapid formation of the gel layer, but that the increased loading also affects the gel layer formation, which is potentially related to the ionic strength of the pH modifier and hence exerting a Hoffmeister like effect.

Comparing the ionic strength distribution images obtained from hydrating the 10% w/w and 30% w/w loadings of the glycine HCl modifier (Fig. 6.3a (v) and Fig. 6.3b (v)), increasing the loading does not appear to significantly impact on the gel layer formation. Comparable distributions are obtained for both 10% w/w and 30% w/w.

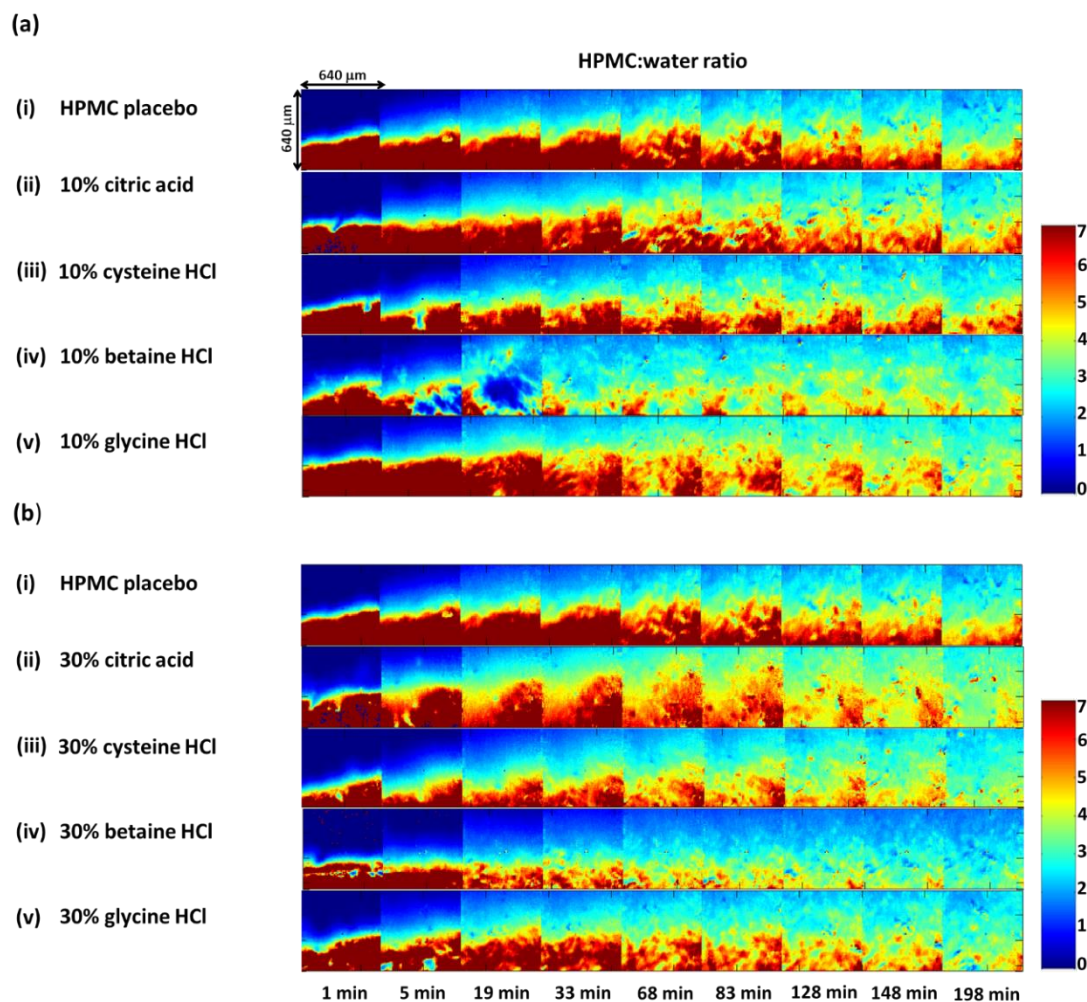


Fig. 6.3: ATR-FTIR images of HPMC/water peak area ratio images over hydration period, showing HPMC gel layer evolution at pH 7 for: (a) (i) 100% HPMC; (ii) 10% w/w citric acid; (iii) 10% w/w cysteine HCl; (iv) 10% betaine HCl w/w; (v) 10% w/w glycine HCl and (b) (i) 100% HPMC; (ii) 30% w/w citric acid; (iii) 30% w/w cysteine HCl; (iv) 30% w/w betaine HCl; (v) 30% w/w glycine HCl

6.9.5 FTIR Imaging Hydration Experiments on 20% w/w IT tablets With Organic Acid at 10% w/w and 30% w/w Loading

The ATR-FTIR peak area distribution images generated for water, HPMC, total IT and pH modifiers for the formulations containing the 20% w/w IT with a 10% w/w loading of the organic acid modifiers used in this study are presented in Fig. 6.4.

The peak area integrated images showing the water distribution (Fig. 6.4a) over the timeframe of the experiment are similar to those obtained for the 10% w/w modifier images without IT, in that water ingress is rapid and is present across the entirety of the field of view by 19 minutes.

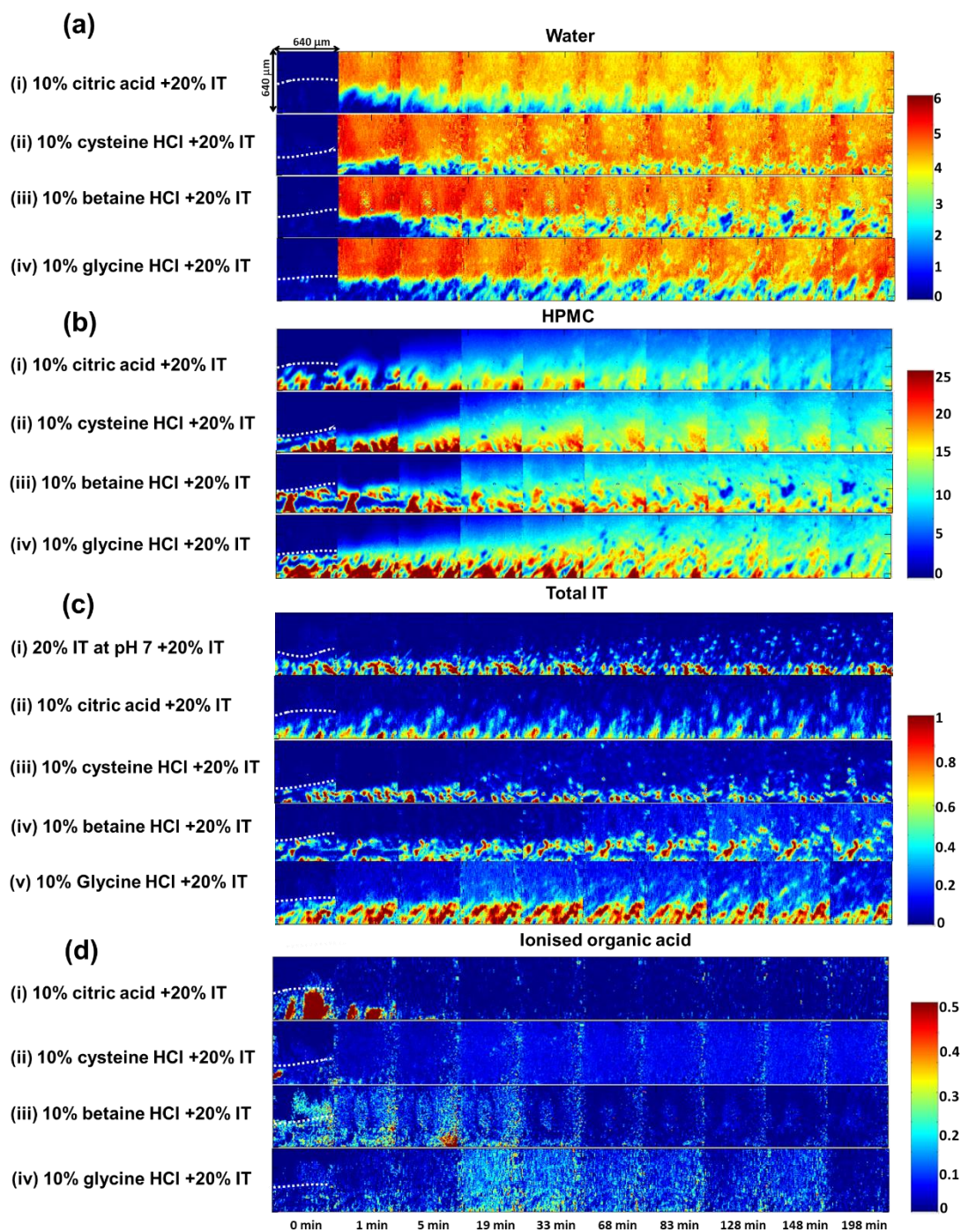


Fig. 6.4: ATR-FTIR peak area integration images for 20% w/w IT and 10% w/w pH modifier over the hydration period, showing: (a) distribution of water; (b) distribution of HPMC; (c) distribution of total IT; (d) distribution of ionised organic acid. The dotted lines in the first column of images denote the approximate boundary between the tablet and air/water

The ATR-FTIR images showing the total IT distribution for each system are presented in the Fig. 6.4c. The peak area integrated images were generated using the IT band at 1550 cm^{-1} corresponding to the $\nu(\text{C}=\text{N})$ (Fig. 6.5) instead of the band used previously (Chapter 5, section 5.5) at 1508 cm^{-1} ($\nu(\text{C}=\text{N})$) due to overlap observed with bands in the pH modifiers (cysteine HCl, betaine HCl and glycine HCl).

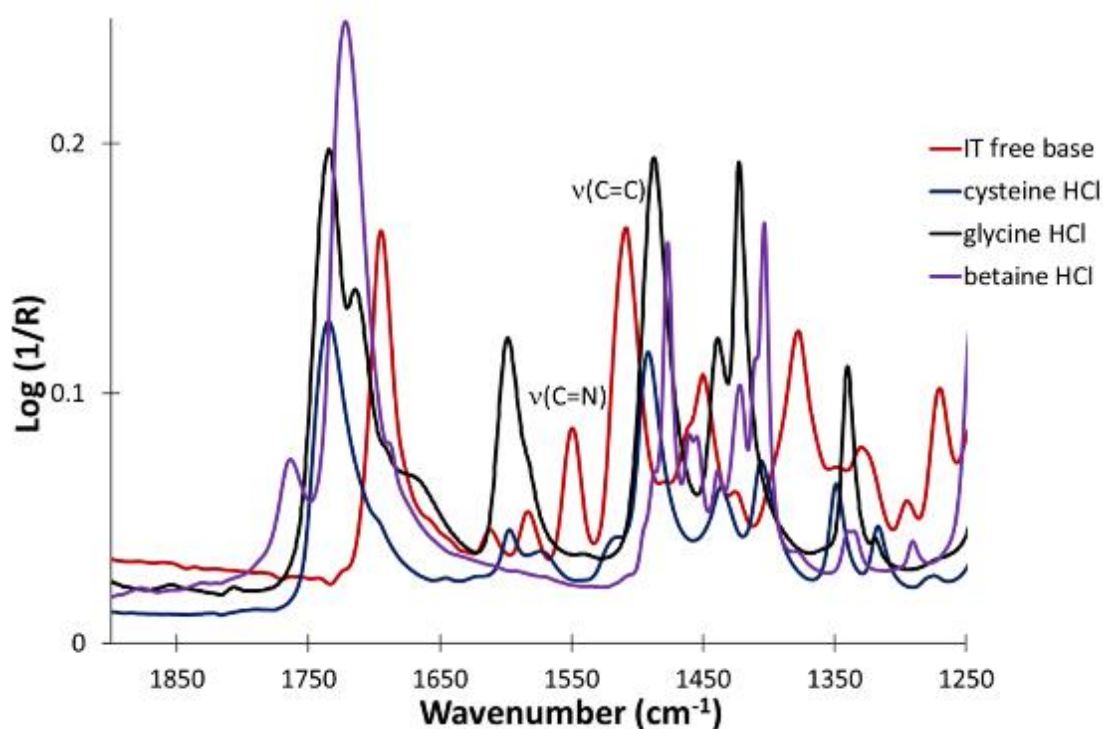


Fig. 6.5: Overlaid ATR-FTIR spectra of IT free base, cysteine HCl, betaine HCl and glycine HCl highlighting overlap of band $\nu(\text{C}=\text{C})$ from IT and the discrete $\nu(\text{C}=\text{N})$ used for the total IT distribution

IT distribution observed for the 10% w/w cysteine HCl and glycine HCl (Fig. 6.4c (iii) and Fig. 6.4c (iv)) formulations show a distinct reduction in the high intensity free base IT over the course of the hydration period which is denoted by the red colour on the scale bar. A subtle decrease for the citric acid intensity is observed, however this is not as pronounced as the cysteine HCl and glycine HCl systems. The IT images for the betaine formulation show enhanced mobility of the IT, however, from the images it is difficult to ascertain if there is a reduction of the free base over the timeframe of the experiment.

The peak area distribution images generated to track the pH modifier in each system are shown in Fig. 6.4d. As expected, due to the high solubility, the pH modifier rapidly

disappeared into the surrounding medium and out of the field of view. However, low levels of glycine HCl ((Fig. 6.4d iv)) are still evident in spectra obtained at the later timepoints (33 minutes Fig. 6.6a). This is confirmed by the presence of the carbonyl band observed at 1734 cm^{-1} which is associated with the glycine HCl and is not present in the ATR-FTR spectrum of itraconazole free base.

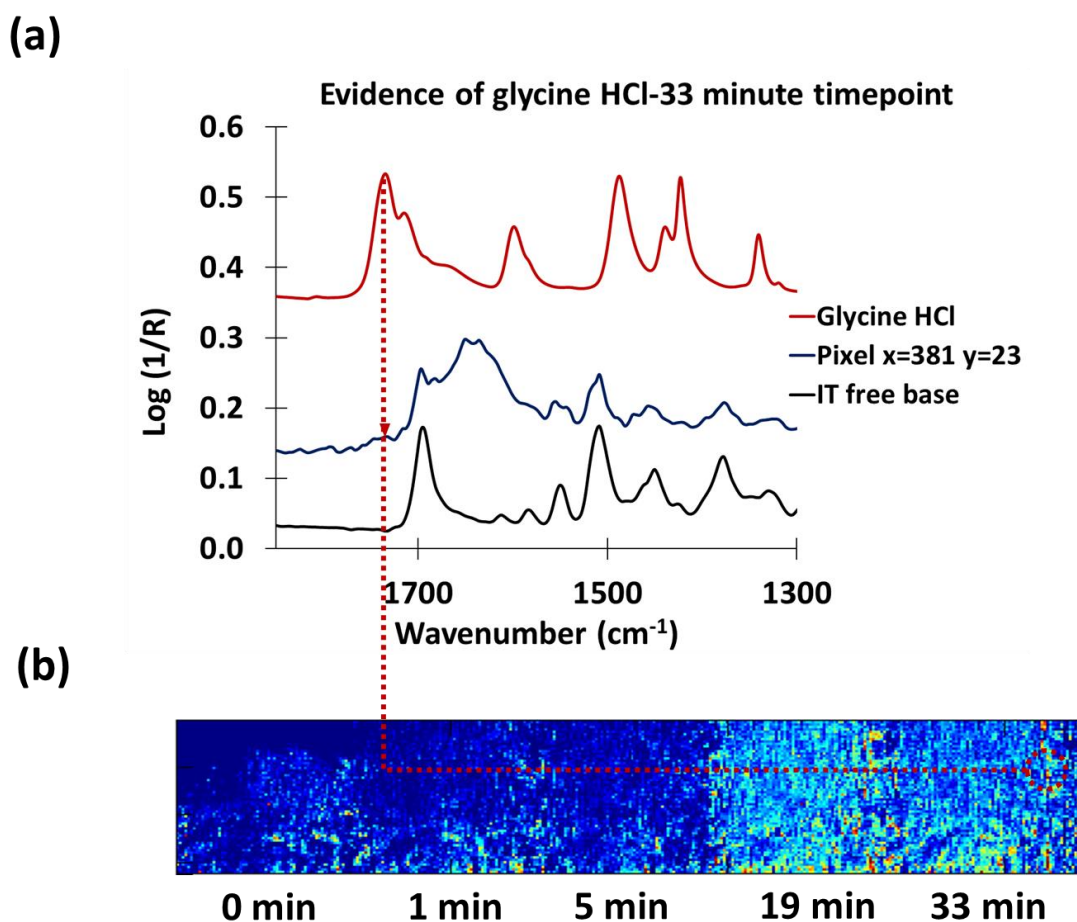


Fig. 6.6: Extracted ATR-FTIR spectrum from pixel $x=381$, $y=23$ (denoted by the red dotted line) from 30% w/w glycine+20% w/w IT ATR-FTIR imaging experiment, compared with the average ATR-FTIR imaging reference spectrum of glycine HCl and free base itraconazole; b) The image distribution based on the carbonyl band at 1735cm^{-1} representing glycine HCl

Fig. 6.7 shows the results of the ATR-FTIR imaging hydration experiments performed on 20% w/w IT-loaded tablets containing 30% w/w organic acid used in this study (citric acid, cysteine HCl, betaine HCl and glycine HCl) hydrated at pH 7 using 0.1 M/L tris buffer.

Fig. 6.7a and 6.7b show the water and HPMC distribution evolution over the duration of the experiment. The results appear to show a different behaviour of the HPMC during the process of hydration in comparison to the corresponding IT-free HPMC tablets with just the 30% w/w pH modifier (Fig. 6.2b) when hydrated at pH 7. This is shown in Fig. 6.7b (ii) to 6.7b (v). After the incorporation of IT, the HPMC-rich areas in the tablets dissipate more quickly over the time frame of the experiment (denoted by the red colour changing to yellow). However, overall, the ingress of water into the tablet matrix was found to be very similar to the 30% w/w placebo formulations (Fig. 6.2a), the inference being that the HPMC is being dissolved into the surrounding medium.

The distribution and dispersion of the total IT over the hydration period for the different modifiers are presented in Fig. 6.7c (ii) to 6.7c (v). The mobility and release of the IT for the citric acid tablets appears to be very similar to the 20% w/w IT formulation without modifier (Fig. 6.7c (i)), which is somewhat expected as the pK_a of the citric (3.1) is similar to that of the itraconazole (3.7). In comparison to the 10% w/w, the higher loading of citric seems creates an environment in which the drug remains more localised and less mobile.

However, in contrast, the formulation containing the glycine HCl, Fig. 6.7c (v), shows markedly enhanced itraconazole mobility, the IT moving with the apparent diffusion front. The betaine HCl Fig. 6.7c (iv) also shows greater enhanced mobility/dissolution of the itraconazole, although not to the same extent as the glycine HCl pH modifier. The cysteine HCl, betaine HCl and glycine HCl all show a reduction in the total IT over the timeframe of the experiment.

The movement of the organic acid pH modifiers is shown in Fig. 6.7d (i) to 6.7(iv). The behaviour of the organic acid modifiers in the IT-containing tablet appears to be very similar to that for the placebo formulations in that the rapid disappearance of the pH modifier is observed.

Researchers have concluded that for adopting the approach of using an organic acid within a solid dosage form, the organic acid modifier must be present over the entire drug release period to sustain the pH modifying effect. Thoma and Zimmer concluded that the amount of organic acid pH modifier present with the tablet core is directly related to the total release rates achieved [28]. A high percentage of acid is therefore required to maintain the acidic micro-pH. They also concluded that highly soluble organic acid pH modifiers such as citric acid and tartaric acid were less effective than modifiers such as succinic acid which are not as soluble [29].

One strategy adopted is to use a coating barrier to prevent the rapid diffusion of the organic acid out of the tablet matrix. This ensures an acidic micro-pH inside the tablet matrix, creating a favourable environment for a weakly basic drug to be released [28] [30].

The addition of weak acid to the formulation results in a faster overall reduction of IT in the tablet, although most of the IT still remains within the matrix. However, the nature of the IT loss is different. In the case of tablets containing pH modifier, exemplified most clearly in Fig. 6.7c (iii), the IT ionises, solubilises and moves from the field of view but once all the acid has dissolved this phenomenon stops. This therefore suggests that a decrease in the microenvironmental pH of the dosage form provides favourable conditions for the IT release. In the case of the 20% w/w IT tablet, clear evidence of IT translocation was observed for the duration of the experiment, indicating that the IT moving away from the tablet core remained unionised.

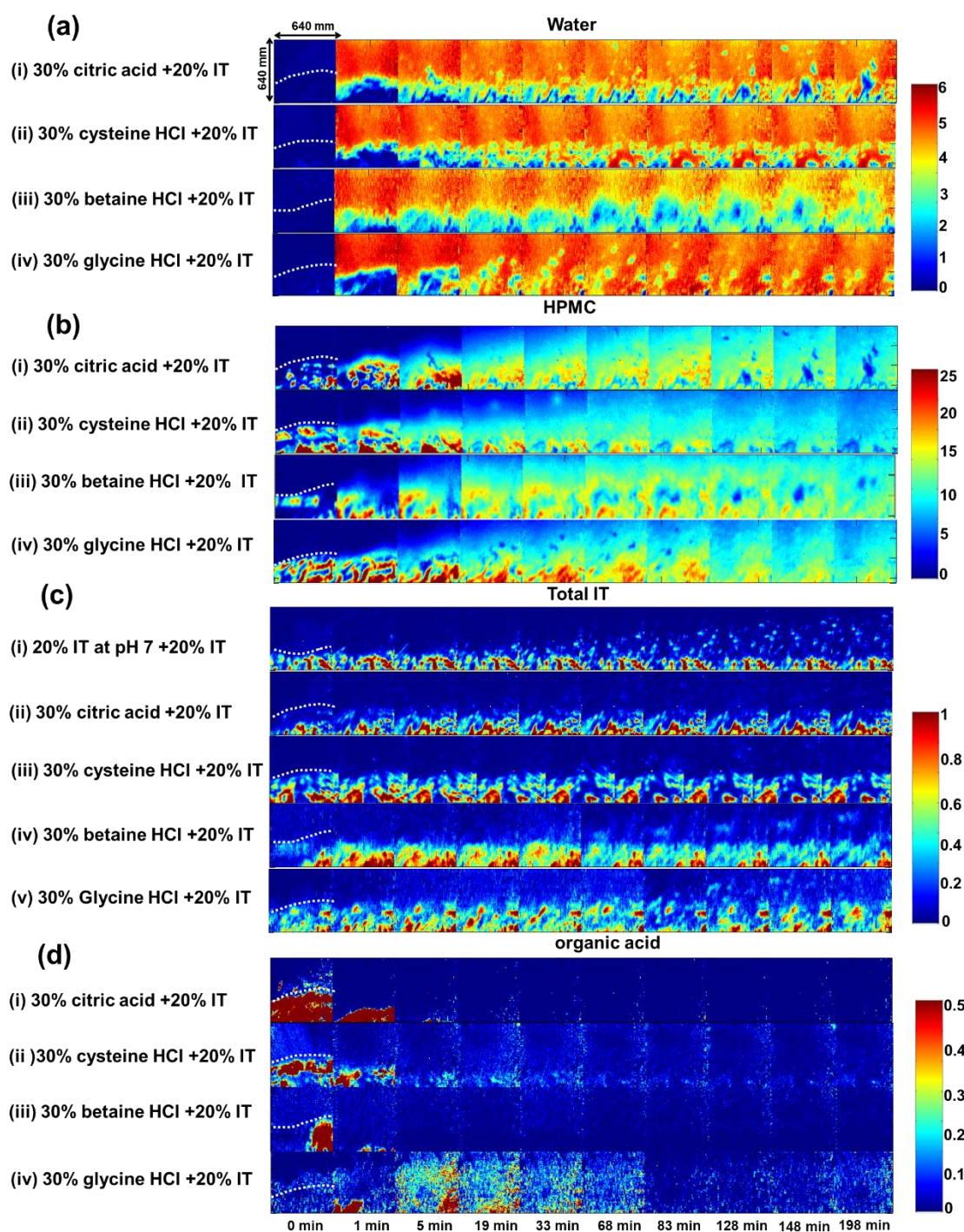


Fig. 6.7: ATR-FTIR peak area integration images for tablets containing 20% IT w/w and 30% w/w pH modifier over the hydration period, showing distribution of: (a) water; (b) HPMC; (c) total IT; (d) ionised organic acid. The dotted lines in the first column of images denote the approximate boundary between the tablet and air/water

Similarly, to the 10% w/w glycine HCl +20% w/w IT formulation, the distribution images for the 30% w/w glycine HCl loading also exhibit evidence of the modifier at the later time points (Fig. 6.8)

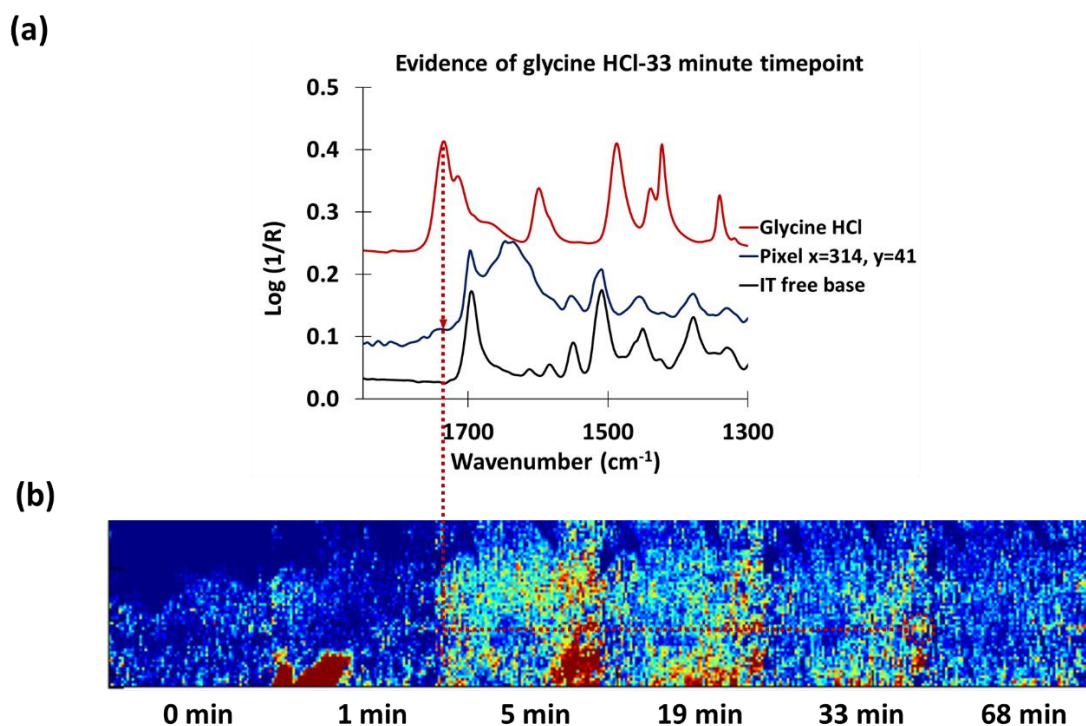


Fig. 6.8: Extracted ATR-FTIR spectrum from pixel $x=314$, $y=41$ (denoted by the red dotted line) from 30% w/w glycine+20% w/w IT ATR-FTIR imaging experiment, compared with the average ATR-FTIR imaging reference spectrum of glycine HCl and free base itraconazole; b) the image distribution based on the carbonyl band at 1735cm^{-1} representing glycine HCl

The gel layer (ratio of HPMC/water band) images are presented in Fig. 6.9 for both the 10% w/w and 30% w/w modifier formulations containing the 20% w/w IT. These were compared to the images obtained from 20% w/w IT tablets without modifier. With the 10% w/w modifier, differences are observed with the formation of the gel layer, but the behaviour is more comparable to the unmodified system than when 30% w/w modifier is used.

Comparing the ratio images obtained from the 10% w/w and 30% w/w modifier tablets, differences in the gel layer behaviour are apparent. For the tablets containing 10% w/w modifier, the gel layer (cyan regions) formation is less rapid. With 30% w/w modifier in

the tablet, the HPMC-rich regions (denoted by the red colour) disappear more quickly over the hydration period in comparison to the 10% w/w loadings. Furthermore, the gel layer formed in systems containing 10% w/w modifier is less voluminous than those with 30% w/w modifier.

Interrogation of the 30% w/w organic acid modifier images (Fig. 6.9b) over the hydration period show differences in swelling behaviour exhibited for the organic acid pH modifiers. In each case, a rapid disappearance of the high intensity band associated with HPMC (essentially representing the dry core) is observed. However, this is more pronounced for the cysteine and glycine HCl formulations with the gel layer receding towards the edge of the field of view, suggesting the combination of these pH modifiers and IT enhance the hydration kinetics of the HPMC polymer or better allow water penetration into the tablet. It is possible that the pH modifiers dissolve out quickly (due to their high solubility) and leave a porous matrix into which water can easily flow.

In summary the results suggest that increasing the pH modifier loading from 10% w/w to 30% w/w has a considerable impact on the gel layer, with the presence of greater concentrations of highly soluble pH modifier leaving a porous structure. This is further explored with macro swelling and is described later.

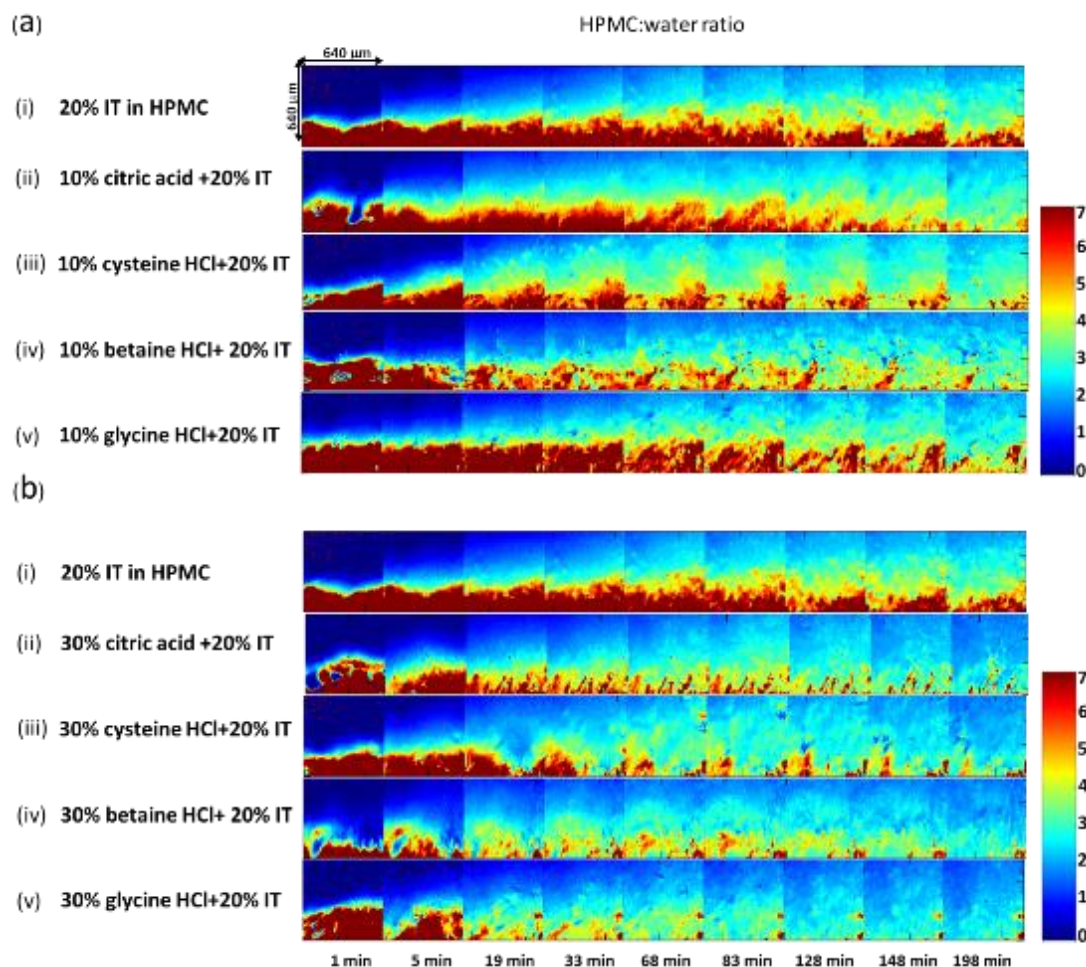


Fig. 6.9: ATR-FTIR peak area integration ratio images (HPMC:water) showing gel layer evolution for 10% w/w and 30% w/w pH modifier tablets with 20% w/w IT for (i) 20% IT tablet; (ii) citric acid; (iii) cysteine HCl; (iv) betaine HCl and (v) glycine HCl

6.9.6 ATR-FTIR Spectra of Anhydrous and Hydrated Organic Acids

The ATR-FTIR spectra of carboxylic acid-based organic acids exhibit strong absorption bands between 1690 cm^{-1} and 1750 cm^{-1} corresponding to the $\nu(\text{C}=\text{O})$ and $\nu(\text{C}-\text{OH})$ vibrations observed in the region of 1200 cm^{-1} to 1300 cm^{-1} . Deprotonation of the carboxylic acid results in the formation of the carboxylate ion, as shown in Fig. 6.10. The Mid-IR exhibits strong vibrational changes for the deprotonation of carboxylic acids (Fig. 6.11).

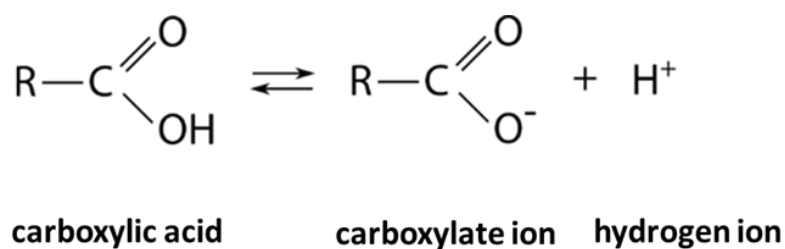


Fig. 6.10: Equation showing deprotonation of carboxylic acids to form the carboxylate ion

The ATR-FTIR spectrum obtained from anhydrous citric acid is shown in Fig. 6.11(a) (red spectrum) and the carbonyl groups are shown by two absorption bands observed at 1742 cm^{-1} and 1691 cm^{-1} . Hydration of the citric acid (blue spectrum) results in the shift of the $\nu(\text{C}=\text{O})$ to lower frequency and the formation of the carboxylate ion. The deprotonation of the organic acid results in a peak observed at $\sim 1396 \text{ cm}^{-1}$ which can be assigned to the symmetric stretching of the COO^- group and a strong band at 1218 cm^{-1} associated with the $\nu(\text{C}-\text{OH})$ stretching vibrational mode [31].

Strong spectral changes are also observed with the protonated amino acid organic modifiers ((Fig. 6.11(b)-Fig. 6.11(d)) with the shift of the $\nu(\text{C}=\text{O})$ 1734 cm^{-1} to 1741 cm^{-1} along with the peak observed at $\sim 1257 \text{ cm}^{-1}$ which is assigned to $\nu(\text{C}-\text{O})$ stretching [32] [33].

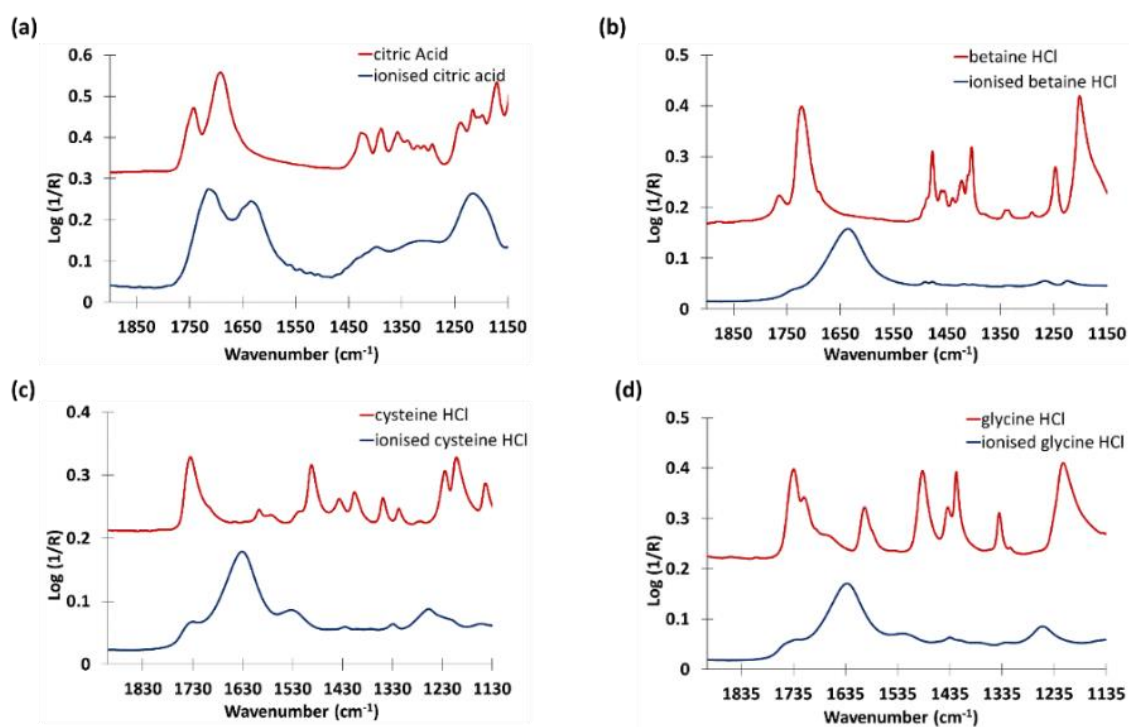


Fig. 6.11: ATR-FTIR spectra of (a) anhydrous citric acid and ionised citric acid (b) anhydrous betaine HCl and ionised betaine HCl (c) anhydrous cysteine HCl and ionised cysteine HCl and (d) anhydrous glycine HCl and ionised glycine HCl

6.9.7 MCR Analysis of 30% w/w Modifier Placebo Systems

Using the peak area integration approach to generate infrared images can be very problematic if the system under investigation contains several components with overlapping peaks of interest. The limiting factor with this approach is that either an isolated band is required or partial area of a peak to generate truly representative distinct images corresponding to the component of interest. Peak area integration (heat map intensities) and PCA are routine methodologies used for disseminating vibrational spectroscopy-based data. An alternative approach which can be used for imaging datasets generated from FTIR and Raman imaging is MCR-ALS.

The advantages of using an algorithm such as MCR-ALS is that the process takes into consideration the entire spectral region in order to identify the chemical compound/s present and provides a corresponding visual distribution of that compound within the sample [34]. The MCR approach can be used for chemical and biological based systems and data analysis can be performed comparatively quickly. The interpretation can be

relatively straightforward compared to approaches such as PCA and peak area integration [34]. The outputs that are obtained from an MCR-ALS analysis are a spectral signature for the pure component within a mixture, which is referred to as a factor and a corresponding distribution map of that component.

One of the disadvantages of using the MCR approach is that generation of distribution maps that do not reflect what is expected of the sample can be produced. These are generally artefacts that may be associated with the lack of data pre-processing or the poor quality of data or the volume of data submitted for analysis. Also, another issue with the MCR approach is that resolved contributions are more ambiguous. However, the pre-processing stage, i.e. using the appropriate constraints, can help to reduce or eliminate this and provide a unique output [35]. Additionally, the inherent problem with the presence of negative peaks can be problematic, however, this could also be resolved with a pre-processing step.

The types of pre-processing steps that are commonly employed prior to MCR analysis are baseline corrections, smoothing and area normalisation. The pre-processing steps are particularly important to remove any variation/interference that is not related to the chemical information in the spectra. With Raman spectra, a common example of interference is the issue of background fluorescence which could potentially be problematic for MCR analysis unless a pre-processing step was applied to correct for it.

The MCR approach was investigated in a feasibility study using the 30% w/w placebo and 30% w/w+20% w/w IT systems. The systems with 30% w/w pH modifier loading were selected in the expectation that the higher concentration would render the different forms of IT detectable and more readily distinguishable during MCR analysis, specifically the ionised form which is more likely to be prevalent at lower pH. Also, the technique could be useful to gain an insight into the dissolution behaviour of the non-hydrated and ionised forms of the pH modifiers over the course of the hydration period.

The factors and distribution images associated with the IT and pH modifiers are shown and discussed in this section. The remaining factors and images associated with the components (HPMC and water) are shown in Appendix 4.

Advantageously, organic acids that have carboxylic acids when hydrated and become ionised exhibit strong spectral changes. FTIR spectral bands observed in the anhydrous ATR-FTIR spectrum of citric acid exhibit carbonyl bands at 1742cm^{-1} and 1696cm^{-1} which disappear in aqueous solution to give one carbonyl band at 1714cm^{-1} and a strong band at 1218cm^{-1} .

The MCR results obtained for the 30% w/w citric acid placebo (Fig. 6.12) generated factors (spectrum) and distribution images that corresponded to the anhydrous and ionised forms of citric acid. The MCR distribution images for the citric acid (Fig. 6.12 a (i) and 6.12 a (ii)) are very similar to the peak area distribution images and the factors obtained from the analysis show a good spectral match with the corresponding ATR-FTIR reference spectra generated from the anhydrous and ionised citric acid are shown in Fig. 6.12b (i) and 6.12b (ii). The distribution images generated by the MCR-ALS analysis for the ionised citric acid which are presented in Fig. 6.12a (iii) show the presence of this form over the duration of the hydration period, however, it rapidly diminishes in intensity.

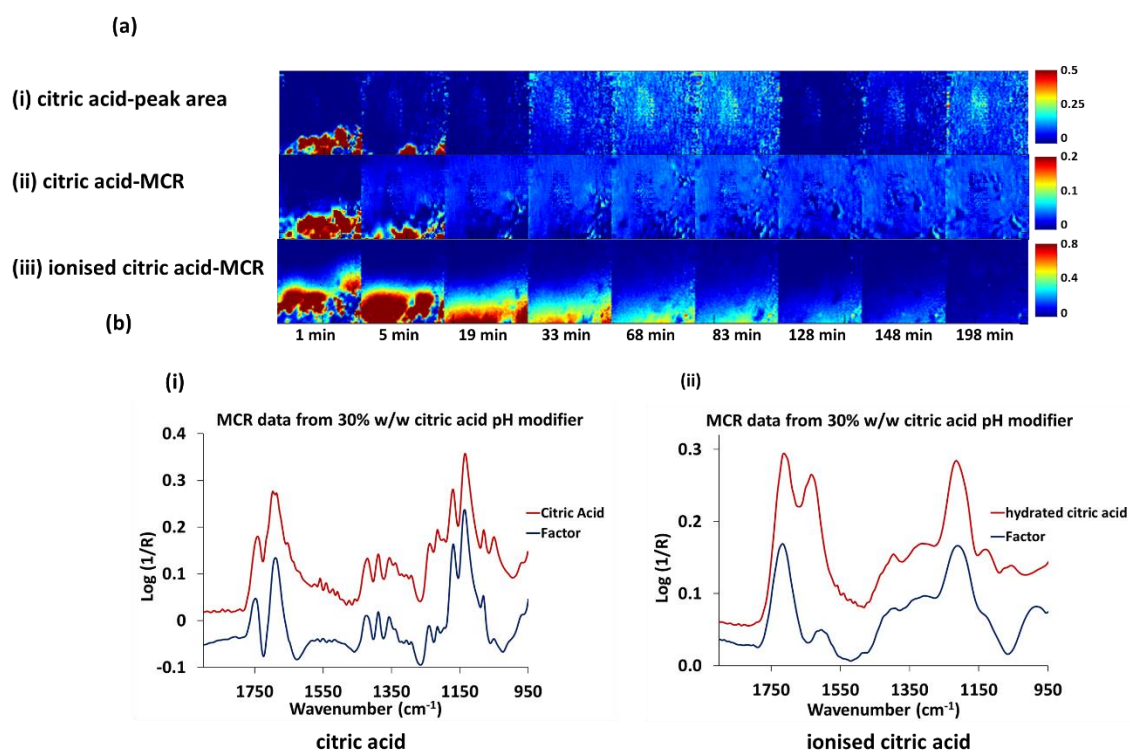


Fig. 6.12(a): Distribution images for 30% w/w citric acid placebo formulation showing (i) citric acid (ATR-FTIR imaging); (ii) MCR-ALS citric acid; (iii) MCR-ALS ionised citric acid and (b): MCR-ALS factor with a comparison to the corresponding ATR-FTIR reference spectrum for (i) citric acid; (ii) ionised citric acid

The MCR results obtained for the 30% w/w glycine HCl placebo are presented in Fig. 6.13. The MCR distribution images for the glycine HCl (Fig. 6.13a (ii)) show strong similarities with the peak area distribution FTIR images (Fig. 6.13a (i)) and the factors obtained from the analysis show a good spectral match with the corresponding ATR-FTIR reference spectra generated from the anhydrous and ionised glycine HCl (Fig 6.13b (i) and 6.13b (ii)). It should be noted that the ATR-FTIR reference spectrum of ionised glycine HCl included for the purpose of comparison exhibits a greater water content, indicated by the intense $\delta(\text{OH})$ at $\sim 1635 \text{ cm}^{-1}$. The distribution images generated by the MCR-ALS analysis for the anhydrous and ionised glycine HCl are presented in Fig. 6.13a (ii) and Fig. 6.13a (iii). The images show low intensity presence of both forms over the duration of the hydration period.

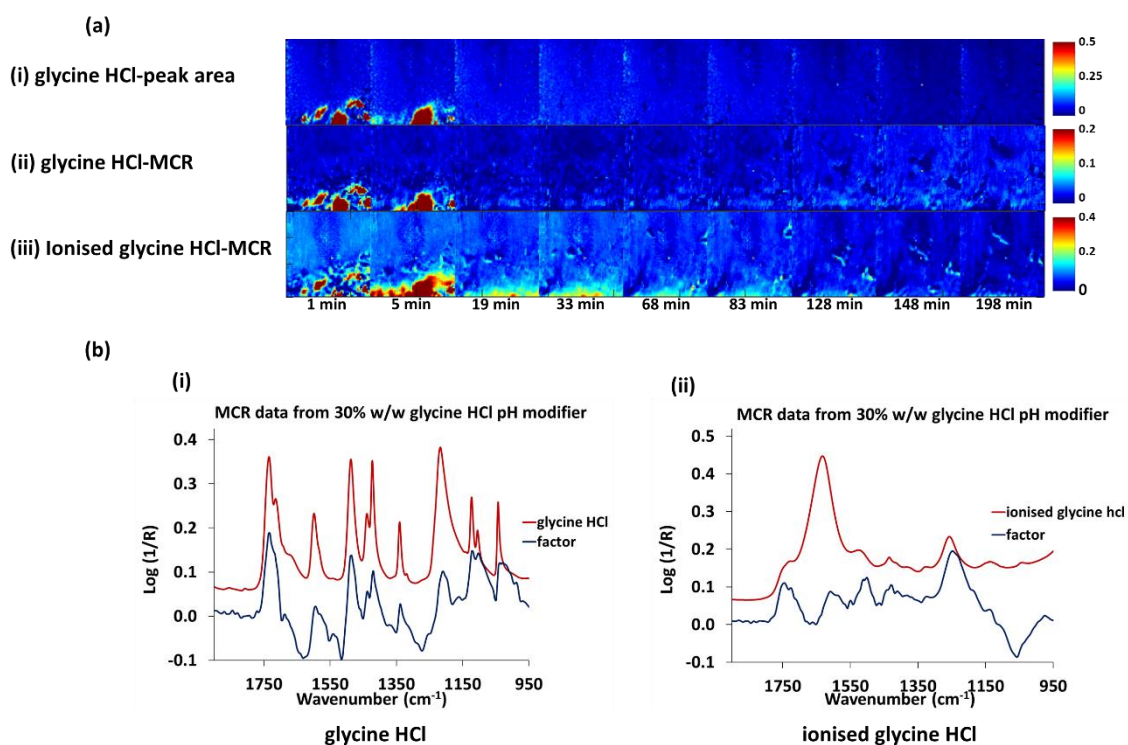


Fig. 6.13 (a): Distribution images for 30% w/w glycine HCl w/w placebo formulation showing (i) glycine HCl (ATR-FTIR imaging); (ii) MCR-ALS glycine HCl; (iii) MCR-ALS ionised glycine HCl and (b) MCR-ALS factor with a comparison to the corresponding ATR-FTIR reference spectrum for (i) glycine HCl; (ii) ionised glycine HCl

The MCR results generated for the 30% w/w cysteine HCl placebo are shown in Fig. 6.14. Only one factor associated with the cysteine HCl was observed from the analysis. The MCR distribution images for the cysteine HCl (Fig. 6.14a (ii)) do not show a good agreement with the peak area distribution FTIR images and evidence of low intensity cysteine HCl (light blue region) predominates in all of the images (Fig. 6.14a (i)). Similarly, the factors produced for the cysteine HCl show broad and less defined peaks in comparison to the sharp, well-resolved peaks observed in the reference spectrum of cysteine HCl (Fig. 6.14b). The system was investigated using 5, 6 and 7 factors and a reasonable output was not obtained for the modifier.

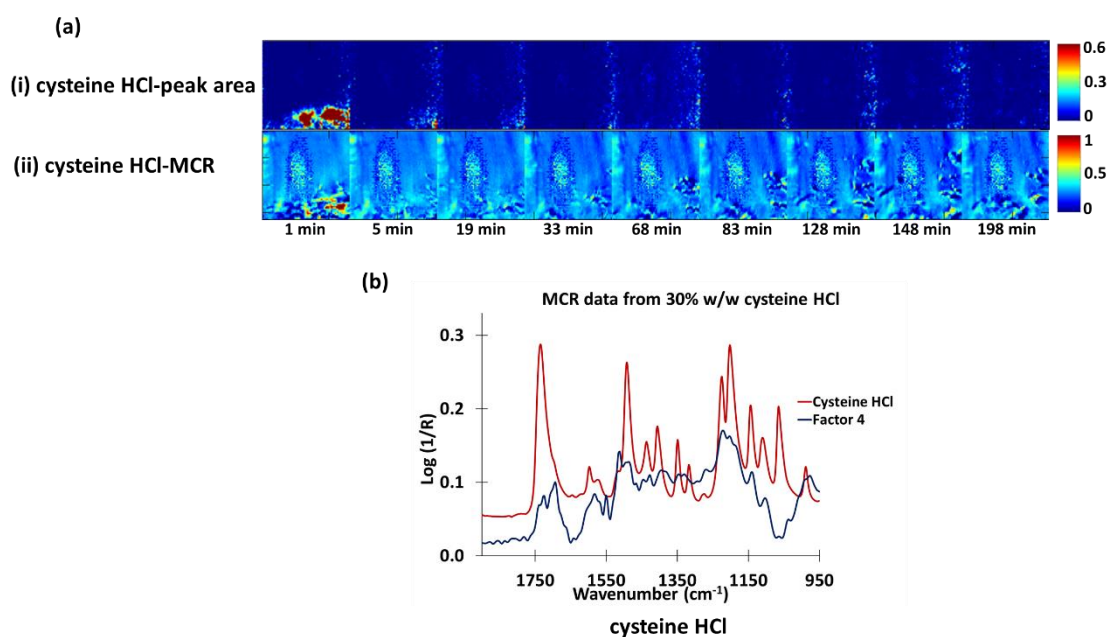


Fig. 6.14 (a): Distribution images for 30% w/w cysteine HCl placebo formulation showing (i) cysteine HCl (ATR-FTIR imaging); (ii) MCR-ALS cysteine HCl distribution and (b): MCR-ALS ionised cysteine HCl factor shown with a comparison to the cysteine HCl ATR-FTIR reference spectrum

The results from the MCR-ALS data analysis conducted on the 30% w/w betaine HCl placebo system are shown in Fig. 6.15. Only one factor was generated that could potentially be assigned to the ionised betaine HCl and this exhibited predominately a high degree of water, shown by the intense $\delta(\text{OH})$ observed at $\sim 1635 \text{ cm}^{-1}$.

The MCR-ALS distribution images show a small region of high intensity betaine HCl in the 1 minute timepoint, which is similar to what was obtained from the peak area integrated images. However, subsequent timepoints appear to be dominated by a background aberration.

Using the MCR-ALS approach for this system generated factors and distribution images that were not comparable to the reference data and from this it can be concluded that the approach adopted did not work as well for this system, compared to the other modifier systems studied.

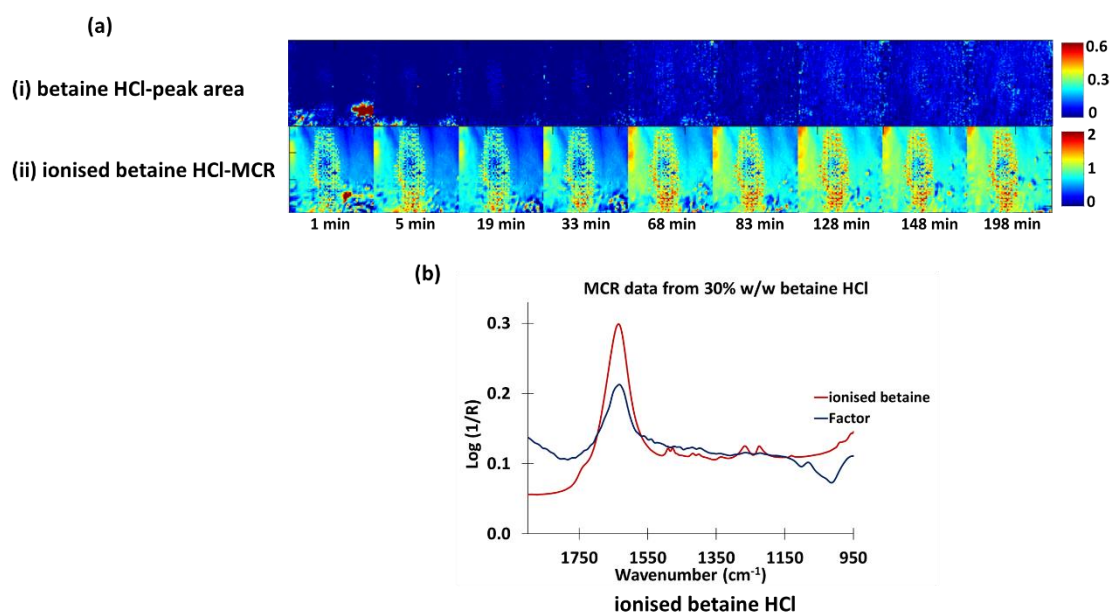


Fig. 6.15 (a): Distribution images for 30% w/w betaine HCl placebo formulation showing (i) ionised betaine HCl (ATR-FTIR imaging); (ii) MCR-ALS ionised betaine HCl distribution and (b): MCR-ALS factor (predominantly showing $\delta(\text{OH})$) and corresponding ATR-FTIR reference spectrum of ionised betaine HCl

6.9.8 MCR Analysis on 20% w/w IT with and without pH Modifier

To investigate the presence of other IT forms (amorphous and ionised) forming during the hydration of the tablets with incorporation of the pH modifiers, MCR analysis was carried out on the 20% w/w IT tablets hydrated at pH 1.5 and 7. The results from the MCR-ALS analysis (distribution images and corresponding factors) are presented below in Fig. 6.16.

Two potential IT forms were extracted from the analysis. The predominant form was shown to be the free base IT which agrees with the findings from Chapter 5. However, the additional IT factor reported from the MCR results does not correspond well to the spectra profile of the reference spectrum of the free base or amorphous form, however, there are some bands that are indicative of itraconazole, e.g. $\nu(\text{C}=\text{O})$, $\nu(\text{C}=\text{C})$ and $\nu(\text{C}-\text{Cl})$ observed at 1691 cm^{-1} , 1505 cm^{-1} and 1035 cm^{-1} respectively.

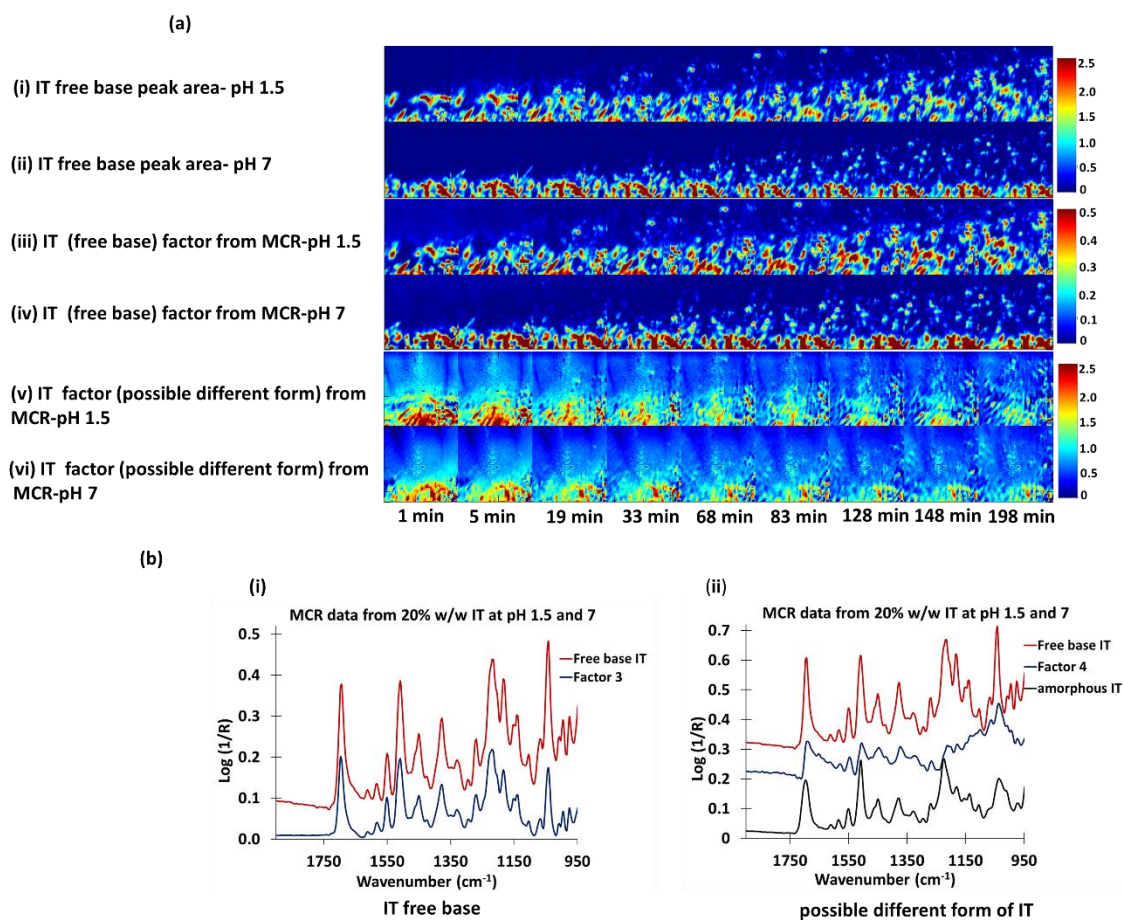


Fig. 6.16 (a): Distribution images of 20% w/w IT formulation at pH 1.5 and 7 showing distribution of (i) IT free base at pH 1.5; (ii) IT free base at pH; (iii) MCR-ALS free base IT at pH 1.5; (iv) MCR-ALS free base IT at pH 7; (v) MCR-ALS possible different form of IT at pH 1.5; (vi) MCR-ALS possible different form of IT at pH 7 and (b): MCR-ALS factor and corresponding ATR-FTIR reference spectrum for (i) IT free base; (ii) MCR-ALS factor and corresponding ATR-FTIR reference spectrum for IT free base, amorphous IT and possible different form of IT

The distribution images along with the factors from the MCR-ALS data analysis performed on the 30% w/w citric acid with the 20% w/w IT are presented below in Fig. 6.17a and Fig. 6.17b. Interestingly, two potential IT forms are generated from the MCR-ALS analysis. The distribution images for both IT forms bear strong similarities to the peak area integrated ATR-FTIR images of the IT free base, Fig. 6.17a (i). The factor presented in Fig. 6.17b (i) exhibited the strongest spectral match to the ATR-FTIR reference spectrum of IT free base. The second IT factor (Fig. 6.17b (ii)) generated from the MCR-ALS analysis also shows similarities to the free base and amorphous IT.

However, for this factor to be definitively assigned to the amorphous IT, the corresponding image would exhibit a diffuse distribution of IT as the amorphous IT would be expected to be more soluble [36].

For the anhydrous citric acid (Fig. 6.17a (v)) the MCR-ALS distribution images showed a rapid reduction of intensity from the 1 minute to the 5 minute time point, however, from 19 minutes onwards a residual amount of citric acid is present throughout the remaining hydration period, with little change in the intensity. This is somewhat unexpected due to the high solubility of citric acid, indeed it would be expected to disappear rapidly as indicated by the peak area integrated images (Fig. 6.17a (iv)). The corresponding factor ((Fig. 6.17b (iii)) is not a good spectral match in comparison to the ATR-FTIR reference spectra of the anhydrous form. The factor also exhibits characteristic peaks from the itraconazole (see highlighted region in Fig. 6.17b (iii)). The spectra profile appears to be a mixture anhydrous citric acid and free base itraconazole. This potentially implies a citric acid-itraconazole complex but is more likely due to the hydrophobic nature of the itraconazole preventing hydration of the citric acid.

The MCR-ALS data for the ionised citric is presented in Fig. 6.17a (vi). This form remains throughout the hydration period, with a rapid reduction observed over the timeframe of the experiment. The corresponding factor is a good spectral match in comparison to the ATR-FTIR reference spectrum of the ionised form. However, the reference spectrum exhibits evidence of water, which is apparent from the $\delta(\text{OH})$ observed at 1634 cm^{-1} .

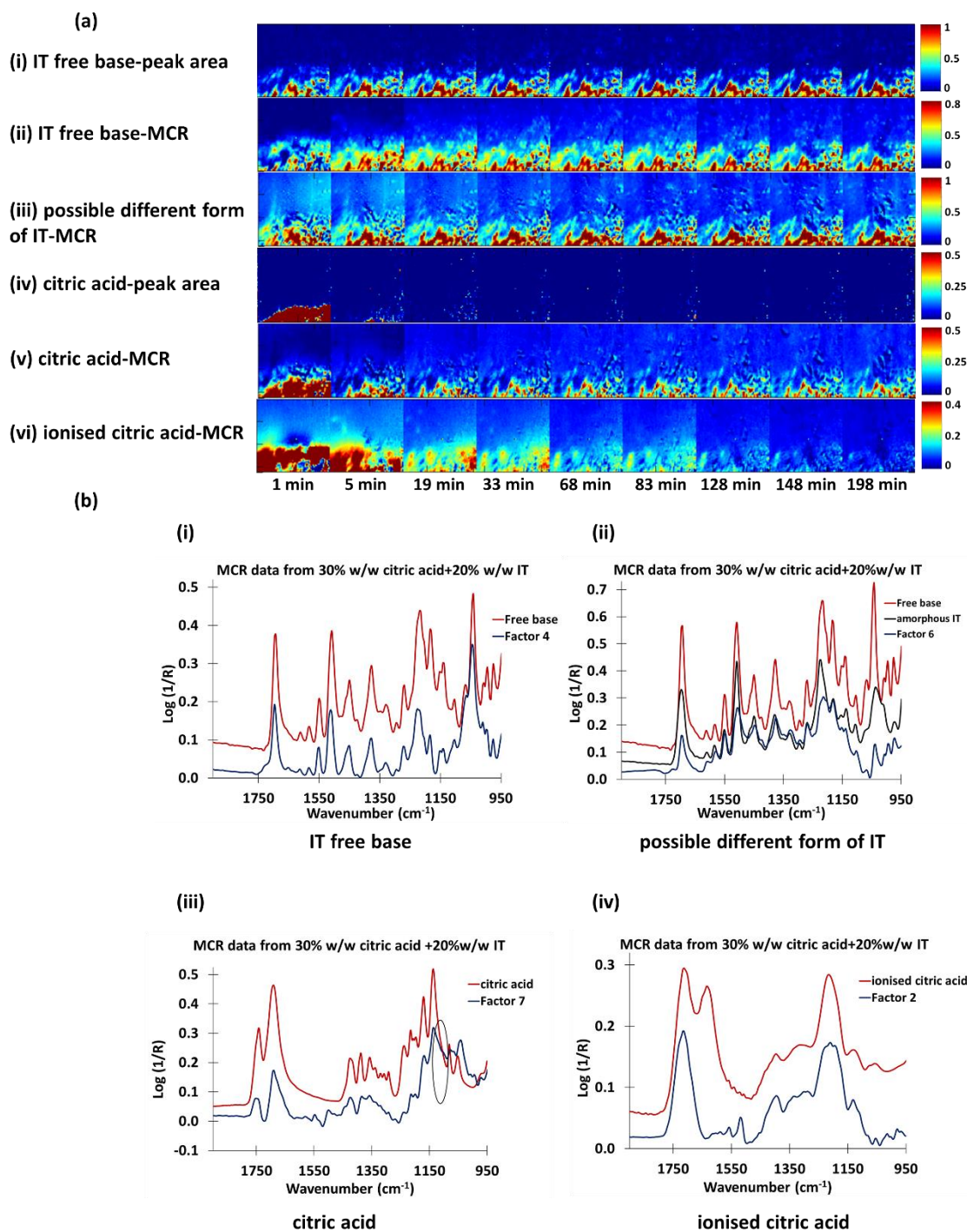


Fig. 6.17 (a): ATR-FTIR peak area Integrated images for 30% w/w citric acid with 20% w/w IT formulation showing distribution of (i) IT free base; (ii) MCR-ALS possible different form of IT; (iii) MCR-ALS citric acid distribution; (vi) ionised citric acid distribution and (b): MCR-ALS corresponding factor and corresponding ATR-FTIR reference spectrum for (i) IT free base; (ii) possible different form of IT; (iii) citric acid; (iv) ionised citric acid

The distribution images obtained from the MCR-ALS data analysis performed on the 30% w/w betaine HCl with the 20% w/w IT are shown below in Fig. 6.18(a). Similarly to the citric acid system, two possible IT forms (Fig. 6.18a (ii) and 6.18a (iii)) were observed from the MCR-ALS analysis. The MCR IT distribution image shown in Fig. 6.18a (ii) exhibits the closest match to the peak area integrated ATR-FTIR images of the IT free base ((Fig. 6.18a (i)). The corresponding factor shown in Fig. 6.18b (i) was also the strongest spectral match to the ATR-FTIR reference spectrum of IT free base.

The second distribution image assigned to IT shown in Fig. 6.18a (iii) shows a less intense and more diffuse distribution of the IT in comparison to the image assigned to the IT free base. The corresponding factor (Fig. 6.18b (ii)) also displays strong similarities to the average ATR-FTIR reference spectrum of amorphous IT.

The MCR-ALS distribution image obtained for the betaine HCl modifier is shown in Fig. 6.18a (v). The betaine HCl disappears rapidly after the 1 minute timepoint, which is also observed in the peak area integrated images for betaine HCl (Fig. 6.18a (iv)). However, the MCR images show evidence of low intensity betaine HCl (yellow region) throughout the hydration period. The corresponding factor from the MCR analysis is shown in Fig. 6.18b (iii) and exhibits broad bands in comparison to the ATR-FTIR reference spectrum of betaine HCl and appears not to be a good spectral match although there are some spectral similarities.

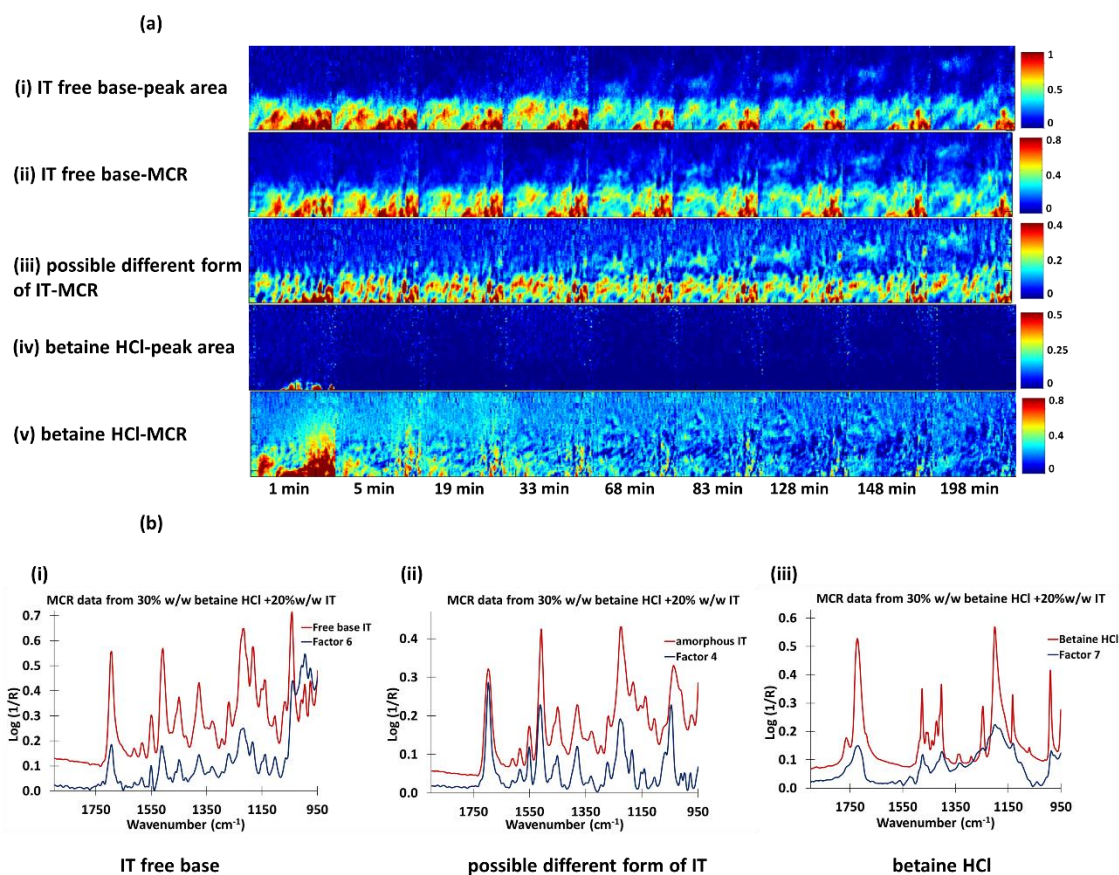


Fig. 6.18(a): Distribution images for 30% w/w betaine HCl with 20% w/w IT formulation showing distribution of (i) IT free base (ATR-FTIR imaging); (ii) MCR-ALS free base IT; (iii) MCR-ALS possible different form of IT (iv) betaine HCl (ATR-FTIR imaging); (v) MCR-ALS betaine HCl and (b) MCR-ALS corresponding factor and corresponding ATR-FTIR reference spectrum for (i) IT free base; (ii) possible different form of IT; (iii) betaine HCl

The distribution images (MCR and ATR-FTIR imaging) for the 30% w/w glycine HCl and 20% w/w IT system are shown below in Fig. 6.19(a). Similar to the citric acid and betaine HCl formulations, a good match was obtained with the peak area integrated images of the IT free base, shown in Fig. 6.19a (i) and 6.19a (ii). The corresponding factor is also a good spectroscopic match with the ATR-FTIR reference of IT free base, 6.19b (i). In addition to the IT free base, a distribution image and factor assigned to another form of IT was also observed (Fig. 6.19a (iii) and Fig. 6.19b (ii)). The IT distribution is more

diffuse and less intense than that observed for the IT free base form. The corresponding factor appears to be a better spectral match to the amorphous form (Fig. 6.19b (ii)).

Interestingly, a factor for the glycine HCl was not obtained from the MCR-ALS data analysis, which is most likely due to the rapid hydration and hence the rapid disappearance of this form. However, a factor and corresponding distribution image for the ionised form was produced. A good spectral match was obtained with the ATR-FTIR reference spectrum of the ionised glycine HCl, Fig. 6.19b (iii).

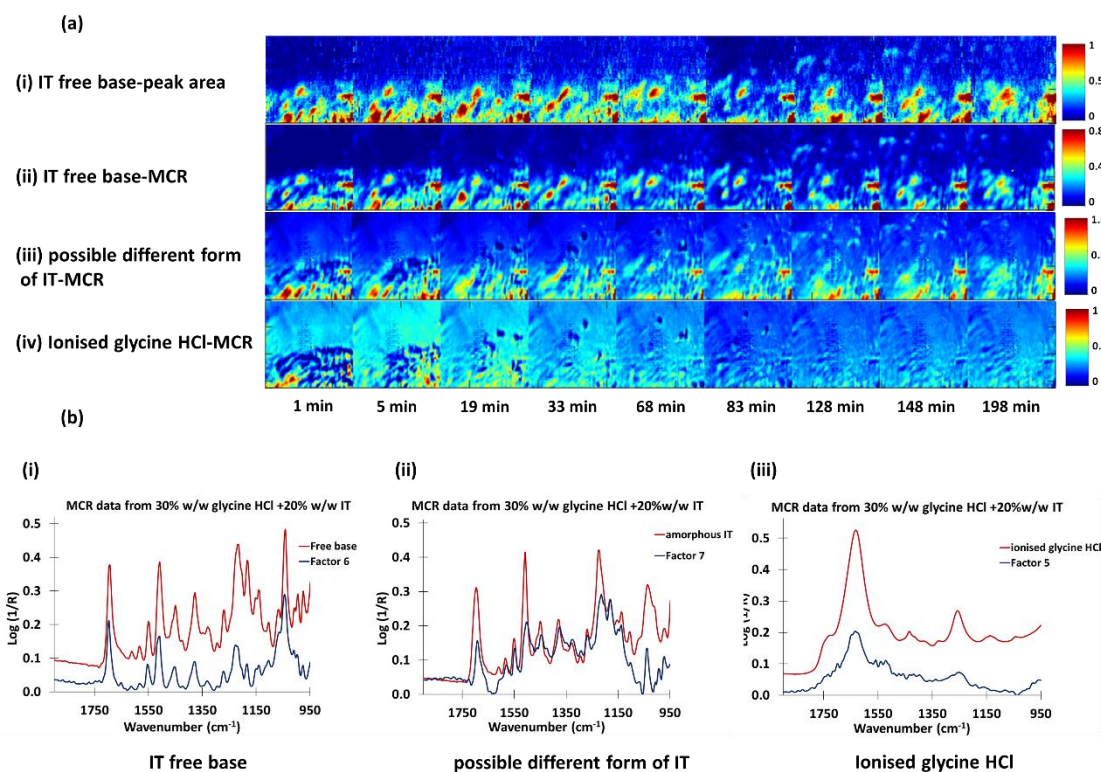


Fig. 6.19(a): Distribution images for 30% w/w glycine HCl with 20% w/w IT formulation showing distribution of (i) IT free base (ATR-FTIR imaging); (ii) MCR-ALS free base IT; (iii) MCR-ALS possible different form of IT; (iv) MCR-ALS ionised glycine HCl and (b): MCR-ALS corresponding factor and corresponding ATR-FTIR reference spectrum for (i) IT free base; (ii) possible different form of IT; (iii) ionised glycine HCl

The results from MCR-ALS data analysis performed on the 30% w/w cysteine HCl+20% w/w IT are shown in Fig. 6.20.

The output from the MCR analysis produced strong similarities (factors and distribution images) for the IT free base when compared to the ATR-FTIR reference spectrum and peak area integrated images for the IT free base. Two additional IT factors were also obtained from the MCR-ALS analysis (distribution images shown in Fig. 6.20a (iii) and Fig. 6.20a (iv)). From the additional IT factors, the one which produced the closest spectral match to the amorphous form is the one shown in Fig. 6.20b (ii) and the corresponding distribution image is shown in Fig. 6.20a (iii). However, the distribution profile is somewhat different to that which would be expected for an amorphous form, as

the IT is very much localised but it has lower intensity compared to images obtained for the free base form (red regions).

A distribution image for the cysteine HCl (Fig. 6.20a (vi)) obtained from the MCR-ALS analysis is initially (1 minute timepoint) in a good agreement with the ATR-FTIR peak area integrated images (Fig. 6.20a (v)). However, similarly to the citric acid system, low intensity residual cysteine HCl is observed throughout the hydration period. The corresponding factor shown in Fig. 6.20b (iv) is a reasonable spectroscopic match to the corresponding cysteine reference spectrum (shown in red).

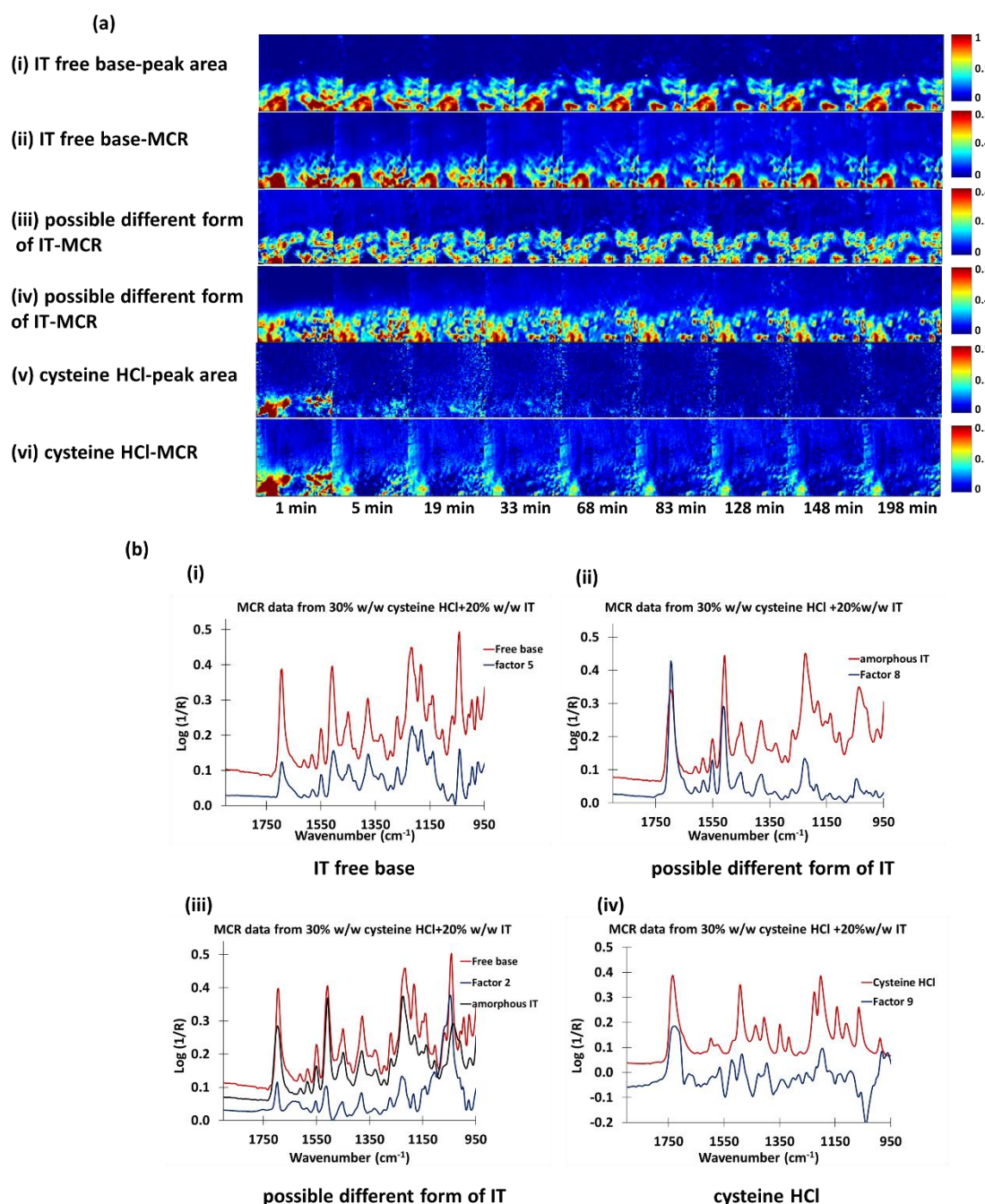


Fig. 6.20(a): Distribution images for 30% w/w cysteine HCl with 20% w/w IT formulation showing distribution of (i) IT free base (ATR -FTIR imaging); (ii) MCR-ALS free base IT; (iii) MCR-ALS possible different form of IT; (iv) MCR-ALS possible different form of IT; (v) cysteine HCl (ATR-FTIR imaging); (vi) MCR-ALS cysteine HCl and (b): MCR-ALS corresponding factor and corresponding ATR-FTIR reference spectrum for (i) IT free base; (ii) possible different form of IT; (iii) possible different form of IT; (iv) cysteine HCl

6.9.9 Determination of pH in Solution Following Hydration

Experiments using ATR-FTIR Imaging

Following the hydration experiments of the 20% w/w IT with 30% w/w organic acid modifier, the pH of the hydration solution was determined. All the solutions showed a considerable decrease from the initial pH of the tris buffer (pH 7) to a lower pH (Table 6.2). However, the cysteine HCl, betaine HCl and glycine showed a greater reduction in the pH (to values less than 2) which is associated with the release of the amino acids into the hydration medium. By comparison, the tablets containing the citric acid engendered a reduction of pH in the dissolution medium to pH 2.7. This may be somewhat expected due to the pK_a of the citric acid. It should be noted that the initial pH of the citric acid was tested in deionised water, in addition to 0.1M tris buffer and similar pH values were obtained. The results confirm that the release of cysteine HCl, betaine HCl or glycine HCl from the tablet formulation drives the pH of the tris hydration medium to a lower pH compared to the citric acid.

Table 6.2: pH measurements obtained from remaining hydration solution after ATR-FTIR imaging experiments from the 30% w/w modifier + 20% w/w IT formulations

Formulation (30% w/w Modifier+20% w/w IT)	Start pH	End pH
Glycine HCl	1.8	1.8
Betaine HCl	1.8	1.5
Cysteine HCl	1.8	1.9
Citric Acid	2.5	2.7

6.9.10 *In Vitro* Release Studies

Dissolution profiles obtained from the 20% w/w IT with the 10% w/w organic acid loaded tablets are shown in Fig. 6.21. The release profiles are very similar between the different modifiers investigated. Approximately 3% release is observed by the end of the dissolution period. The 10% w/w loading of the different organic acid modifiers did not achieve the 24% release obtained from the 20% w/w IT at pH 1.5 medium (Fig. 6.21).

However, all the organic acid pH modifiers provided a slightly higher release in comparison to the 20% w/w IT in pH 7 medium (Fig. 6.21).

Dissolution profiles obtained for the 20% w/w IT with the 30% w/w organic acid loaded tablets are presented in Fig. 6.22. The addition of the organic acid pH modifiers showed a similar IT release rate ranging from 2.3% to 2.8% for the citric acid and glycine HCl, respectively, after 24 hours. A slightly higher release rate was achieved by the end of the dissolution period by the incorporation of the betaine HCl and cysteine HCl (3.6% and 4.8% respectively). All the formulations achieved a greater release in comparison to the 20% w/w IT placebo under the same pH conditions. This also correlates with the findings from the ATR-FTIR imaging. However, none of the organic acid modifiers achieved the 24% release obtained from the 20% w/w IT in the pH 1.5 medium (Fig. 6.23). This can be rationalised due to the inability of the pH modifier to achieve the necessary pH change (from pH 7 to ~1) in the volume of tris buffer used in the dissolution set-up following release from the tablet matrix. To investigate this hypothesis further, pH measurements were obtained from the dissolution solutions from the 30% w/w organic acid modifier formulations (Table 6.3) at different timepoints (30, 60, 120 and 180 minutes). The pH values obtained from the solutions at the selected timepoints from the organic acid pH modifiers formulations all show an inability to reach the desired low pH for the itraconazole release (~1.5). All the solutions measured at the different timepoints showed a reading of approximately pH 4. The results from the dissolution work (Fig. 6.22) cannot therefore be directly correlated with the ATR-FTIR imaging results.

Also, the ATR-FTIR imaging data confirms the rapid release of the organic acid modifiers as the hydration medium penetrates the tablet matrix. It is well-documented that micro-environmental pH is influenced by release rates of pH modifiers, which in turn impacts on drug dissolution. Therefore, the rapid release of the organic acid modifier could potentially result in insufficient quantities remaining to modulate the required micro-environmental pH [37].

Comparing the 10% w/w and 30% w/w modifier systems, the 30% w/w cysteine HCl provides the greatest release of IT (Fig. 6.23).

Table 6.3: pH measurements obtained from 0, 30, 60, 120 and 180 minute dissolution solutions remaining from the 30% w/w modifier + 20% w/w IT formulations

Formulation (30% w/w Modifier+20% w/w IT)	pH at 0 mins	pH at 30 mins	pH at 60 mins	pH at 120 mins	pH at 180 mins
Glycine HCl	7	4.1	3.5	3.6	3.6
Betaine HCl	7	3.8	3.9	3.9	3.8
Cysteine HCl	7	3.5	3.7	3.8	3.8
Citric Acid	7	4.1	4.3	3.9	3.9

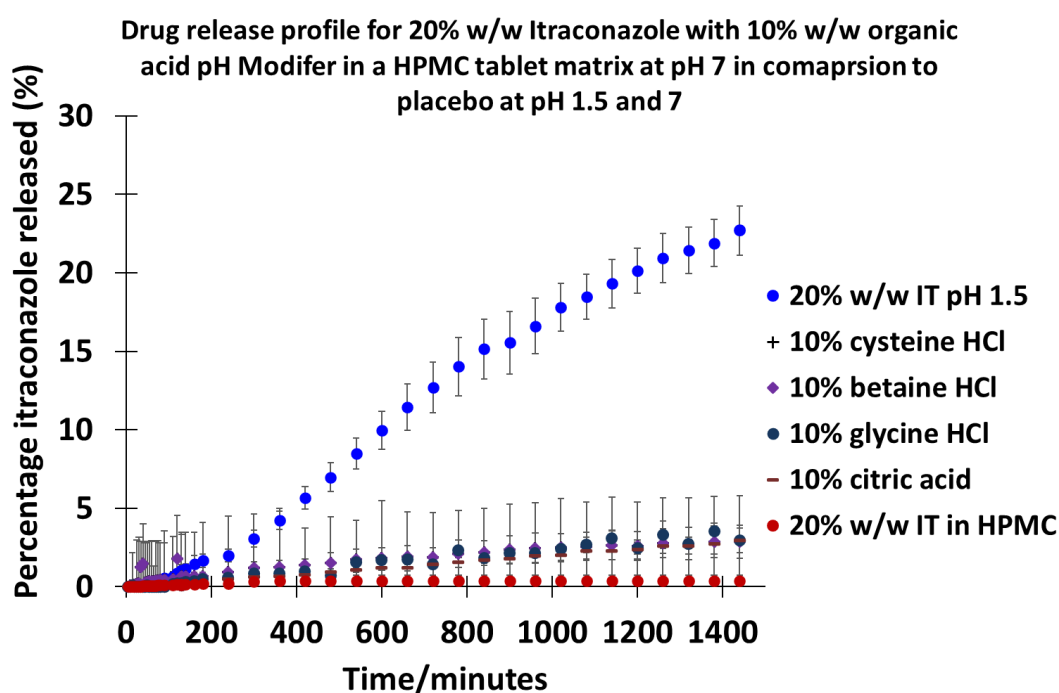


Fig. 6.21: UV dissolution profiles showing the percentage itraconazole released from the HPMC matrix as a function of time for the 10% w/w pH modifier+20% w/w IT formulations (citric acid, cysteine HCl, betaine HCl and glycine HCl) at pH 7 and 20% w/w IT placebo at pH 1.5 and 7

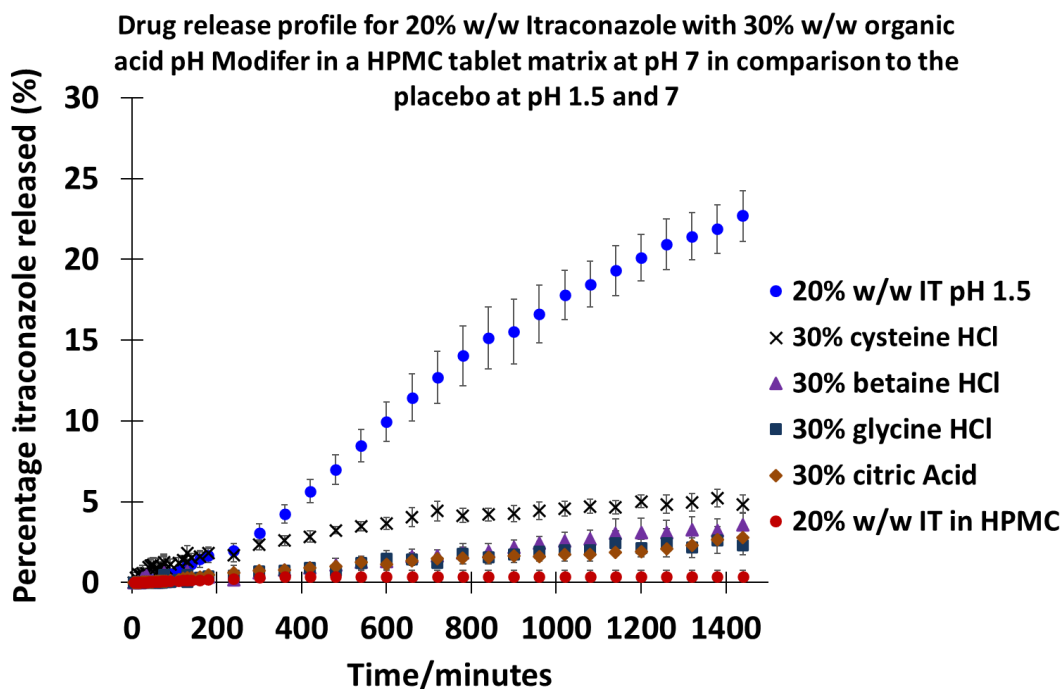


Fig. 6.22: UV dissolution profiles showing the percentage itraconazole released from the HPMC matrix as a function of time for the 30% w/w pH modifier+20% w/w IT formulations (citric acid, cysteine HCl, betaine HCl and glycine HCl) at pH 7 and 20% w/w IT placebo at pH 1.5 and 7

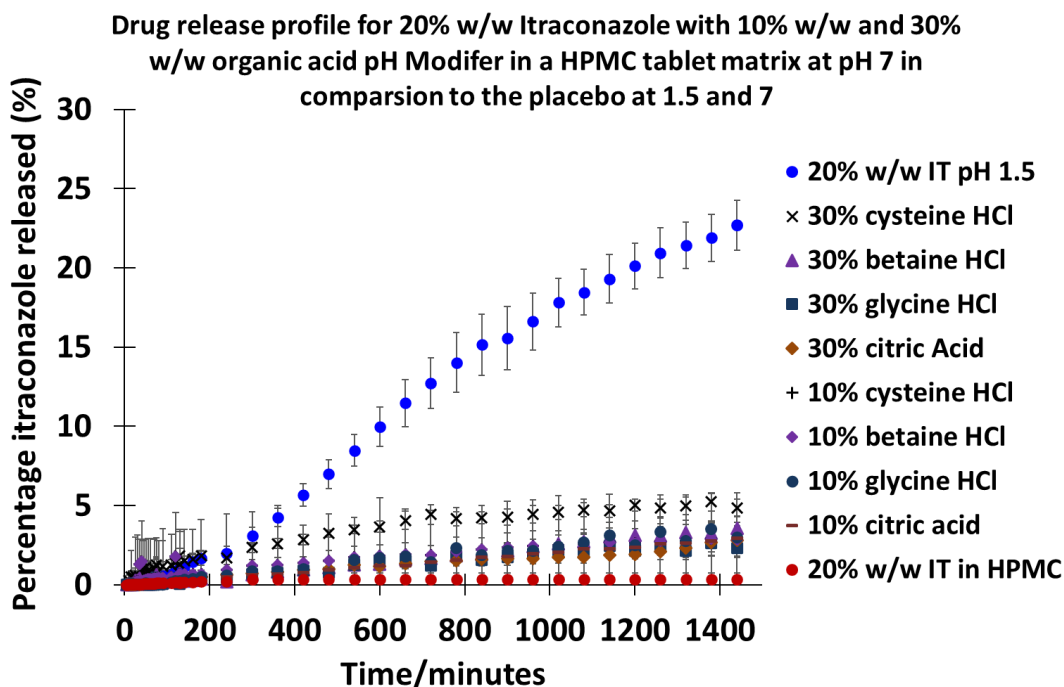


Fig. 6.23: UV dissolution profiles showing the percentage itraconazole released from the HPMC matrix as a function of time for the 10% w/w and 30% w/w pH modifier+20% w/w IT formulations (citric acid, cysteine HCl, betaine HCl and glycine HCl) at pH 7 and 20% w/w IT placebo at pH 1.5 and 7

6.9.11 Characterisation of the Different Forms of IT

To ascertain if the organic acid pH modifiers investigated in this study have the potential to influence the ionisation of the itraconazole, spectroscopic differences associated with the different forms of IT (ionised/non-ionised) were investigated. The band at 2821 cm^{-1} associated with CH symmetric stretching vibrations of the methyl group was used, as per previous studies [1], to generate peak area distribution to elucidate changes in IT chemistry over the course of the hydration period (Fig. 6.24a and 6.25a (i)-(iv)).

A similar strategy was adopted to the previous research (documented in Chapter 5, section 5.7.7) in order to carry out a more detailed analysis of the chemical changes occurring to the IT over the hydration period. Binning the spectra within the pixels of the lowest six rows from images at 1, 33, 128 and 198 minutes for all four formulations consisting of the IT and organic acid modifier generated average spectra with sufficient S/N to elucidate differences in the IT chemistry between systems (Fig. 6.24 and 6.25 (b)-(e)).

From the distribution images and the average ATR-FTIR spectra generated for the 10% w/w modifier +20% w/w IT formulations, a reduction in the free base intensity over the time frame of the experiment is observed with all formulations. The cysteine HCl showed a greater reduction in the free base intensity (Fig. 6.24a (ii) and Fig. 6.25c).

For the 30% w/w citric acid +20% w/w IT system, a greater intensity of undissolved free base is observed in the tablet core (towards the bottom of the image) and is seen to be increasing over the timeframe of the experiment. This is also highlighted in the corresponding average ATR-FTIR spectra shown in Fig. 6.25b. This can be rationalized by taking into account how the measurement is performed. With this technique, everything present within the evanescent field is measured and with the rapid disappearance of the citric acid, this leads to an increase in concentration of the other components within the system, i.e. the itraconazole.

The distribution images for the 20% w/w IT with the 30% w/w betaine HCl, 30% w/w cysteine HCl and 30% w/w glycine HCl (Fig. 6.25 (ii)-(iv)) modifier systems all show a small reduction in the free base intensity over the time frame of the experiment. This is shown more clearly in the corresponding average ATR-FTIR spectra shown in Fig. 6.25 (c) to 6.25 (e), suggesting that these pH modifiers are somewhat partially ionising the itraconazole, although the free base form is still predominating. From Fig. 6.25 (c) and (e), the cysteine HCl and glycine HCl show a greater reduction in the free base form in comparison to the betaine HCl.

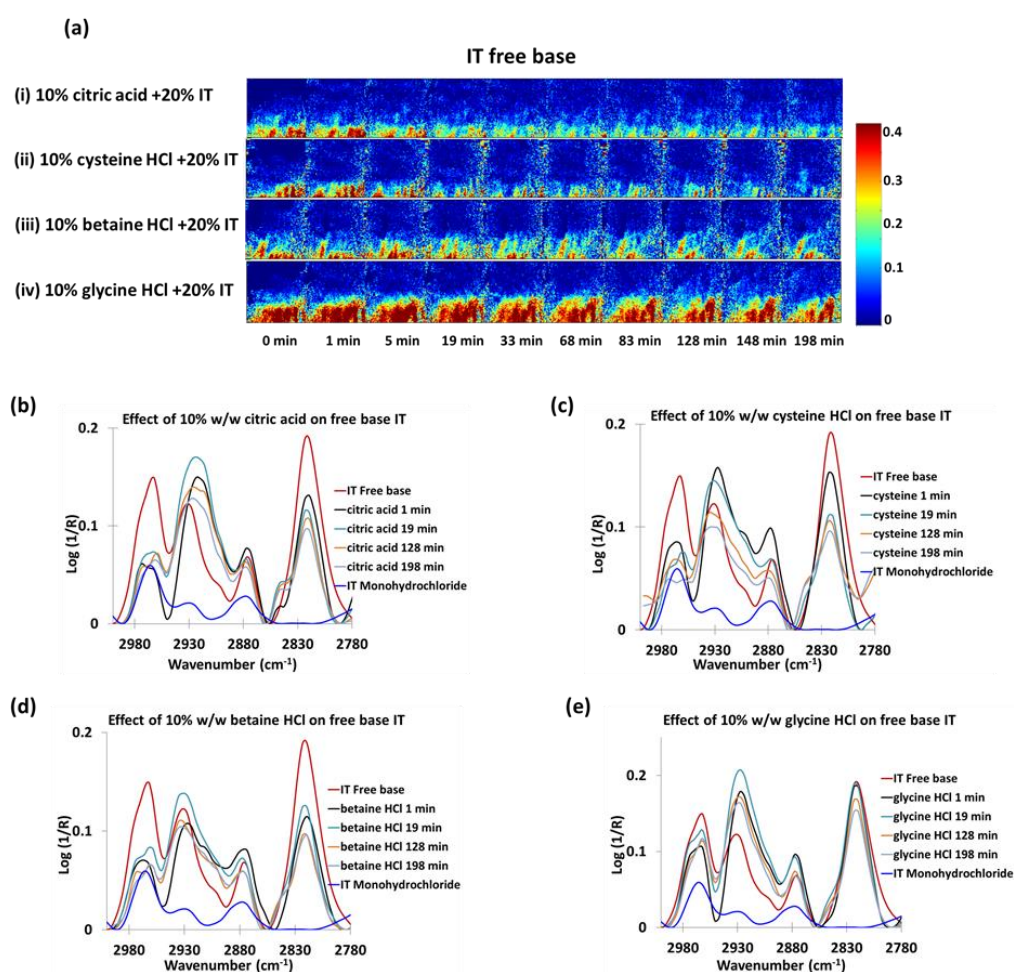


Fig. 6.24 (a): ATR-FTIR peak area integrated images generated using band at 2821 cm^{-1} for the formulations containing 20% w/w IT with the 10% w/w organic acid modifier; (b) average ATR-FTIR imaging spectra highlighting $\nu(\text{CH})$ at 2821 cm^{-1} obtained from IT free base, IT monohydrochloride reference spectra and for the 1, 19, 128 and 198 minute timepoints for 20% w/w IT loaded tablets with 30% w/w organic acid modifier (b) citric acid (c) cysteine HCl (d) betaine HCl (e) glycine HCl

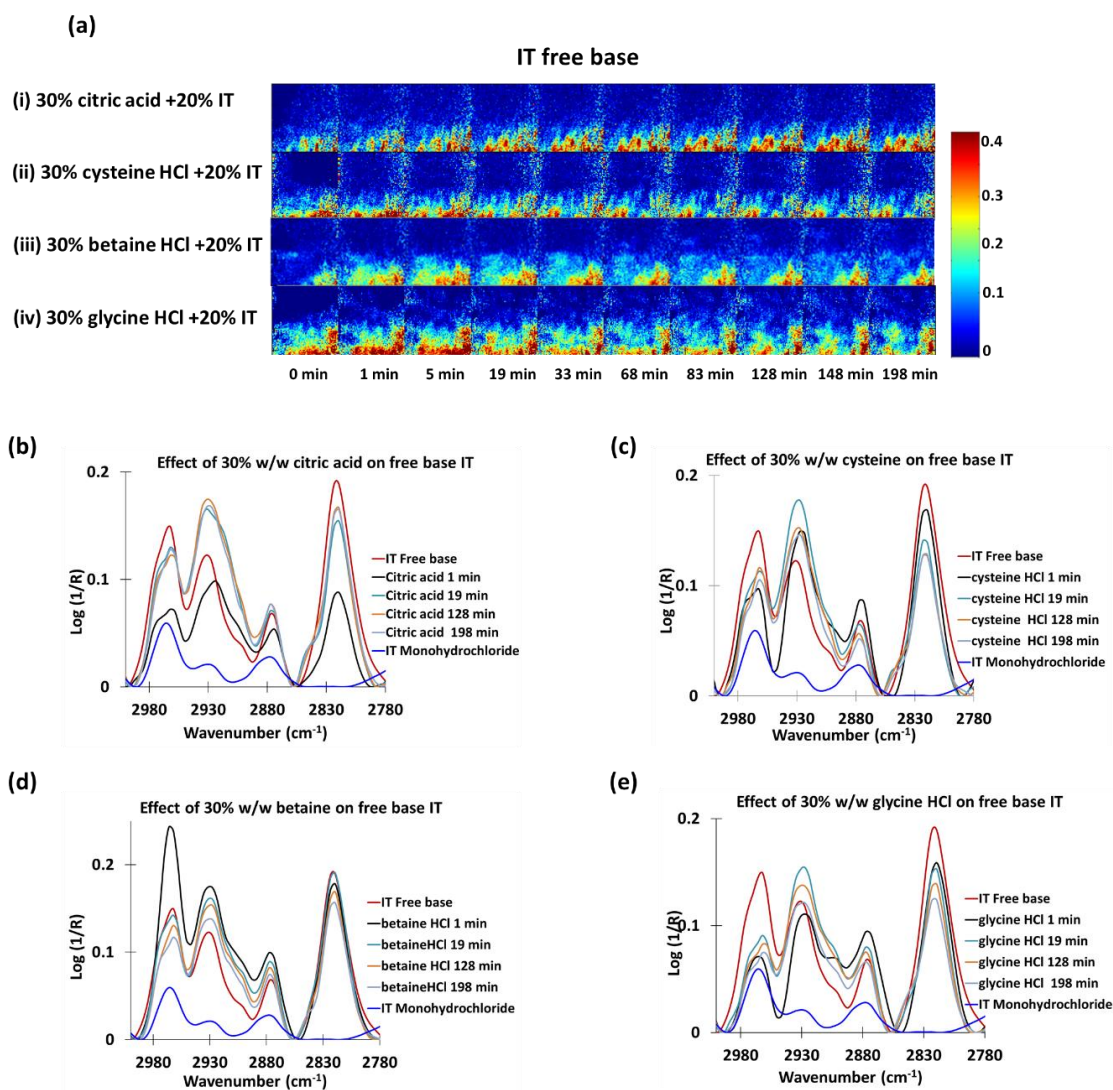


Fig. 6.25 (a): ATR-FTIR peak area integrated images generated using band at 2821 cm⁻¹ for the formulations containing 20% w/w IT with the 30% w/w organic acid modifier; (b) average ATR-FTIR imaging spectra highlighting $\nu(\text{CH})$ at 2821 cm⁻¹ obtained from IT free base, IT monohydrochloride reference spectra and for the 1, 19, 128 and 198 minute timepoints for 20% w/w IT loaded tablets with 30% w/w organic acid modifier (b) citric acid (c) cysteine HCl (d) betaine HCl (e) glycine HCl

6.9.12 Physical Swelling Kinetics-Radial Swelling Results on 20% w/w IT Loaded Tablets with and without Organic Acid pH Modifier

To gain further insight into the swelling behaviour of the pH modifier formulations and to complement the ATR-FTIR data, a series of swelling experiments were performed on both IT loaded (20% w/w) tablets containing organic acid pH modifiers (citric acid, cysteine HCl, betaine HCl and glycine HCl) and placebo tablets containing just the organic acid modifier (10% w/w and 30% w/w). Examples of the optical images obtained from the placebo (10% w/w organic acid modifier in HPMC) and 20% w/w IT with 10% w/w organic acid modifier loaded tablets for the 0 and 180 minute timepoints for the radial measurements are shown in Fig. 6.26b and Fig. 6.26d, respectively. The full set of optical images are shown in Appendix 6.

Macro swelling measurements conducted on the 10% w/w modifier containing formulations with and without IT are presented in Fig. 6.26a and Fig. 6.26c. The results show that the betaine HCl with and without the presence of the 20% w/w IT exhibits the greater volume of swelling. This also correlates with the ATR-FTIR imaging data generated by interrogating the gel layer behaviour of the organic acid modifiers (Fig. 6.3a). Similarities in the rate of swelling were observed with the other modifiers (glycine HCl, cysteine HCl and citric acid) when incorporated with the 20% w/w IT and without. For the systems containing 10% w/w pH modifier, the swelling behaviour over the hydration period was similar regardless of whether or not IT was incorporated into the tablet. Furthermore, in each case, the magnitude of swelling which occurred was comparable to the tablets without modifier, with the exception of the betaine HCl tablets. Both with and without IT, the swelling of betaine HCl-containing tablets was marginally higher than the others and this difference in percentage swelling increases over the hydration period.

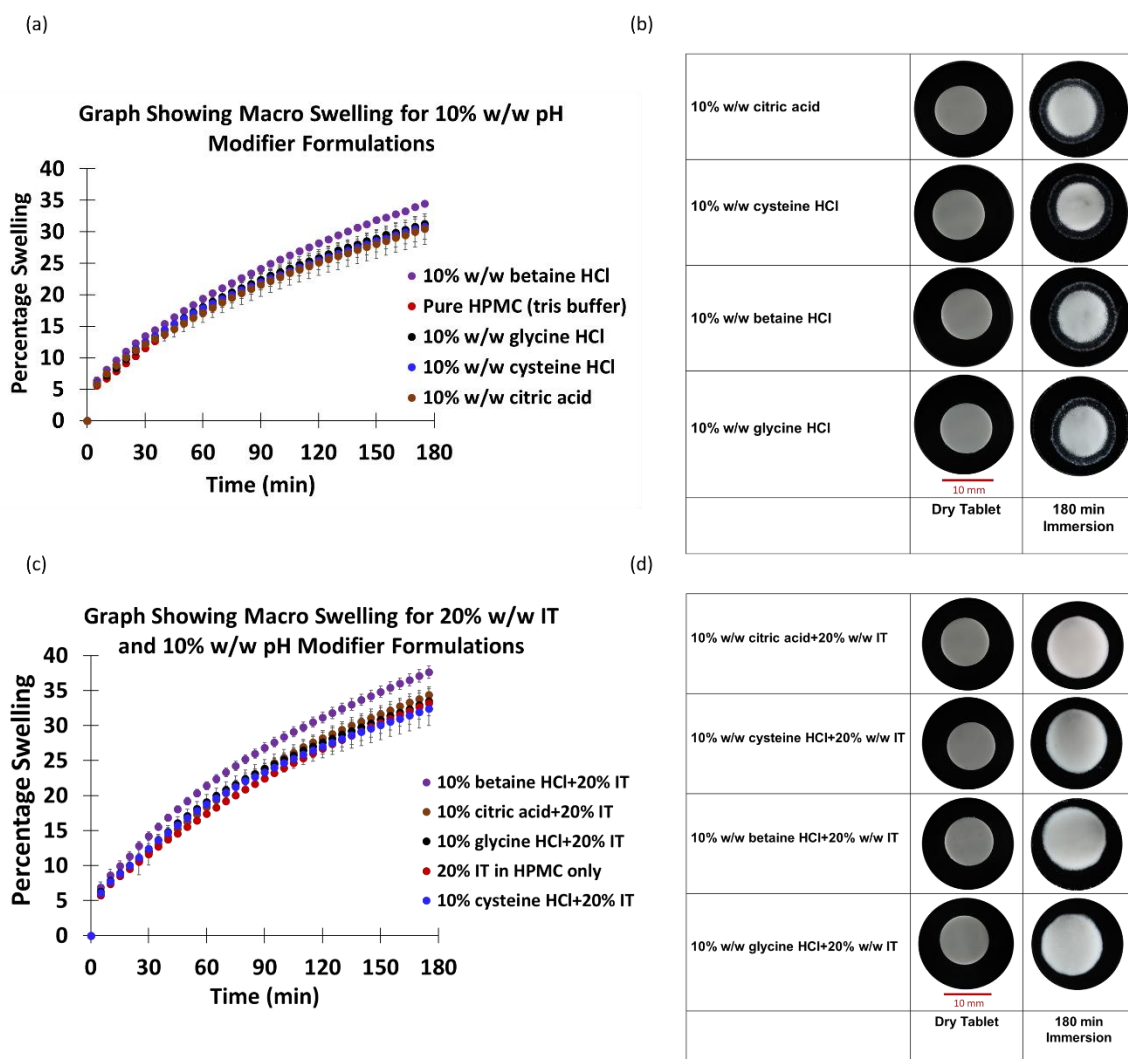


Fig. 6.26: Percentage swelling data obtained from the radial measurements from (a) 10% w/w placebo organic acid pH modifier formulations (b) 10% w/w organic acid pH modifier formulations with 20% w/w IT. Examples of optical images obtained from 0 and 180 minute timepoints for citric acid, betaine HCl, glycine HCl and cysteine HCl (c) 10% w/w placebo organic acid pH modifier formulations and (d) 10% w/w organic acid pH modifier formulations with 20% w/w IT

The results obtained from the swelling measurements from the 30% w/w organic acid pH modifier formulations with and without the 20% w/w IT are presented in Fig. 6.27. The data supports the ATR-FTIR findings in showing differences are observed with swelling rate for the different placebo formulations (Fig. 6.27 (a)). HPMC with the betaine HCl showed the greatest swelling rate, followed by the citric acid. With the cysteine HCl and glycine HCl, collapsing of the tablet structure was observed as the hydration progressed. This was more noticeable with the glycine HCl modifier, which starts to show loss of

tablet structure from approximately 25 minutes, in comparison to the cysteine HCl which was observable after 55 minutes. This is potentially due to glycine HCl and cysteine HCl having higher aqueous solubilities in comparison to citric acid and betaine HCl and thereby impacting on the structural integrity of the tablet. A similar swelling behaviour was observed with the IT and organic acid formulations (Fig. 6.27c and Fig. 6.27d) in that a greater amount of swelling was observed with the betaine HCl and citric acid in comparison to the cysteine HCl and glycine HCl (Fig. 6.27c and Fig. 6.27d). This therefore suggests that the swelling properties of the IT loaded tablets is somewhat related to the solubility of the pH modifier (Table 6.1).

Comparison of the 30% w/w modifier formulations with the pure HPMC swelling data (Fig. 6.27a) shows a trend which is comparable for the betaine HCl and citric acid modifiers over the course of the hydration period.

Comparing the 30% w/w modifier +20% w/w IT formulations (Fig. 6.27c), a greater degree (approximately 10-15%) of swelling is observed in comparison to the 20% w/w IT tablets without modifier. The 20% w/w IT data is more comparable to the results obtained from the cysteine HCl and glycine modifiers.

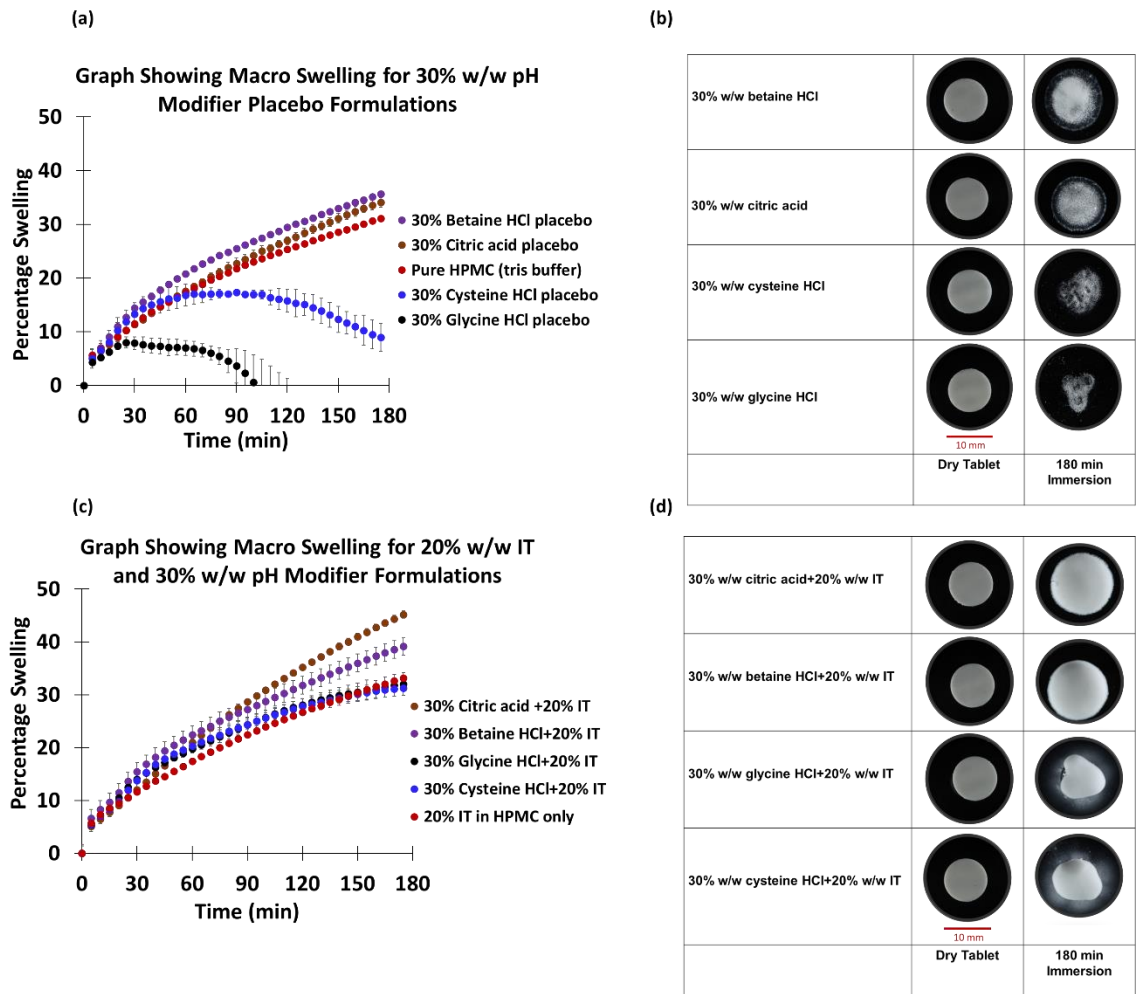


Fig. 6.27: Percentage swelling data obtained from the radial measurements from (a) 30% w/w placebo organic acid pH modifier formulations (b) 30% w/w organic acid pH modifier formulations with 20% w/w IT. Examples of optical images obtained from 0 and 180 minute timepoints for citric acid, betaine HCl, glycine HCl and cysteine HCl (c) 30% w/w placebo organic acid pH modifier formulations and (d) 30% w/w organic acid pH modifier formulations with 20% w/w IT

6.10 Summary

The macroscopic swelling data obtained from the 10% w/w betaine tablets exhibit a greater volume of swelling regardless of the presence of IT. The glycine HCl and cysteine HCl at the 30% w/w also appear to impact the swelling regardless of whether or not IT is present. However, in this case, visual observation suggests that the pH modifier affects the stability of the tablet. This is especially apparent when IT is not present and the swelling measurements suggest that, after initial swelling, the size of the tablets again decreases. This could be related to the solubility properties of these modifiers: as the glycine HCl and cysteine HCl are more soluble than the betaine HCl, it could be postulated that the modifier dissolves out of the tablet matrix, leaving a more porous and unstable structure.

At 10% w/w loading of organic acid modifier, the impact on gel layer formation rate appears to be greatest for tablets containing betaine HCl, followed by glycine HCl, while citric acid and cysteine HCl appear to have a lesser effect. In the case of the betaine-containing tablets, the HPMC-rich areas are almost entirely converted to gel layer, as indicated by the colours in the ATR images. At 30%, this trend remains the same, but the magnitude of the change brought about by the presence of the modifier is greater in every case.

Considering the tablets containing 20% w/w IT, differences in gel layer behaviour are observed between those tablets containing 10% pH modifier and those with 30%. All the organic acid modifiers at the 30% w/w loading show a rapid reduction in the high intensity HPMC-rich regions and a corresponding rapid formation of the gel layer, indicating the higher loading affects the kinetics of the hydration process. While this same trend was apparent in the tablets without IT, the effect is more pronounced in those containing IT.

Investigation into changes associated with the free base IT form to the ionised form show that 30% w/w cysteine HCl and glycine HCl provides the greatest reduction in the

observed IR signal from the free base form in comparison to the same loading for the citric acid and betaine HCl containing formulations.

The dissolution studies, of the same formulations, indicate the tablets with the cysteine HCl at 30% w/w loading provide a slightly enhanced release of the IT (4.8%) from the tablet matrix compared to the other modifiers at the same loading (glycine HCl, betaine HCl and citric acid). However, it should be noted that none of the modifiers were able to achieve dissolution profiles analogous to the tablets consisting only of 20% w/w IT (~24%) at pH 1.5.

The incorporation of the four organic pH modifiers explored in this study (citric, betaine HCl, cysteine HCl and glycine HCl) at the different loadings (10% w/w and 30% w/w) provided some degree of enhanced release (between 2.3% and 4.8%) of the itraconazole from the tablet matrix when compared to tablets containing no modifier.

The MCR analysis has provided further insight into the different forms of IT (for example amorphous) that may be formed when the tablet matrix undergoes dissolution. However, further refinement of this technique is required in order to ensure the approach is optimised for the formulations investigated in this study.

6.11 References

- [1] F. D. Zahoor, K. T. Mader, P. Timmins, J. Brown and C. Sammon, "Investigation of Within-Tablet Dynamics for Extended Release of a Poorly Soluble Basic Drug from Hydrophilic Matrix Tablets Using ATR-FTIR Imaging," *Mol. Pharmaceutics*, vol. 17, no. 4, p. 1090–1099, 2020.
- [2] S. Berge, L. Bighley and D. Monkhouse, "Pharmaceutical salts," *J. Pharm. Sci.*, vol. 66, no. 1, pp. 1-19, 1977.
- [3] G. Potta, S. Minemi, R. K. Nukala, C. Peinado, D. A. Lamprou, A. Urquhart and D. Douroumis, "Development of solid lipid nanoparticles for enhanced solubility of poorly soluble drugs," *J. Biomed. Nanotechnol.*, vol. 6, no. 6, pp. 634-640, 2010.
- [4] C. Le-Ngoc Vo, C. Park and B.-J. Lee, "Current trends and future perspectives of solid dispersions containing poorly water-soluble drugs," *European Journal of Pharmaceutics and Biopharmaceutics*, vol. 85, no. 3 Part B, pp. 799-813, 2013.
- [5] P. Timmins and S. R. Pygall, "Microenvironmental pH Control and Mixed Polymer Approaches to Optimise Drug Delivery with Hydrophilic Matrix Tablets," in *Hydrophilic Matrix Tablets for Oral Controlled Release*, New York, AAPS Advances in the Pharmaceutical Sciences, 2014, pp. 257-280.
- [6] Z. Xi, N. Sharma, A. Paprikar and S. Lin, "Development and evaluation of dipyridamole sustained release tablets containing micro-environmental pH modifiers," *Journal of Drug Delivery Science and Technology*, vol. 54, no. 101231, pp. 1-9, 2019.
- [7] Y. Kawabata, K. Wada, M. Nakatani, S. Yamada and S. Onoue, "Formulation design for poorly water-soluble drugs based on biopharmaceutics classification system: Basic approaches and practical applications," *International Journal of Pharmaceutics*, vol. 420, no. 1, pp. 1-10, 2011.
- [8] C. Taniguchi, Y. Kawabata, K. Wada, S. Yamada and S. Onoue, "Microenvironmental pH-modification to improve dissolution behavior and oral absorption for drugs with pH-dependent solubility," *Expert Opinion on Drug Delivery*, vol. 11, no. 4, pp. 505-516, 2014.
- [9] K. Dvořáčková, P. Doležel, E. Mašek, J. Muselík, M. Kejdušová and D. Vetchý, "The Effect of Acid pH Modifiers on the Release Characteristics of Weakly Basic Drug from Hydrophilic–Lipophilic Matrices," *AAPS PharmSciTech*, vol. 14, no. 4, p. 1341–1348, 2013.
- [10] S. R. Pygall, S. Kujawinski, P. Timmins and C. D. Melia, "Mechanisms of drug release in citrate buffered HPMC matrices," *International Journal of Pharmaceutics*, vol. 370, no. 1-2, pp. 110-120, 2009.

- [11] S. I. Farag Badawy and M. A. Hussain, "Microenvironmental pH Modulation in Solid Dosage Forms," *Journal of Pharmaceutical Sciences*, vol. 96, no. 5, pp. 948-959, 2007.
- [12] Y. Kawabata, K. Wada, M. Nakatani, S. Yamada and S. Onoue, "Formulation design for poorly water-soluble drugs based on biopharmaceutics classification system: Basic approaches and practical applications," *International Journal of Pharmaceutics*, vol. 420, no. 1, pp. 1-10, 2011.
- [13] S. Siepe , B. Lueckel , A. Kramer, . A. Ries and R. Gurny , "pH-independent release of a weakly basic drug from water-insoluble and -soluble matrix tablets," *International Journal of Pharmaceutics*, vol. 316, no. 1-2, pp. 14-20, 2006.
- [14] M. Adachi , Y. Hinatsu , K. Kusamo, H. Katsumi, T. Sakane, M. Nakatani, K. Wada and A. Yamamoto, "Improved dissolution and absorption of ketoconazole in the presence of organic acids as pH-modifiers," *European Journal of Pharmaceutical Sciences*, vol. 76, pp. 225-230, 2015.
- [15] M. L. Wells, S. O. Williams, R. A. Sanftleben, S. B. Balik and B. A. Evans, "Investigation into the Dissolution Rate Increase on Storage of Wellbutrin SR®100 mg Tablets," *Journal of the American Association of Pharmaceutical Scientists*, vol. 11, no. 1, pp. 113-119, 2010.
- [16] Y. Qiu and P. I. Lee, "Rational Design of Oral Modified-Release Drug Delivery Systems," in *Developing Solid Oral Dosage Forms (Second Edition): Pharmaceutical Theory and Practice*, Academic Press, 2017, pp. 519-554.
- [17] M. A. R. Yago, A. R. Frymoyer, G. S. Smelick, L. A. Frassetto, N. R. Budha, M. J. Dresser, J. A. Ware and L. Z. Benet, "Gastric Re-acidification with Betaine HCl in Healthy Volunteers with Rabeprazole-Induced Hypochlorhydria," *Mol Pharm.*, vol. 10, no. 11, p. 4032–4037, 2013.
- [18] A. Oryan, A. Kamali, A. Moshiri, H. Baharvand and H. Daemi, "Chemical crosslinking of biopolymeric scaffolds: Current knowledge and future directions of crosslinked engineered bone scaffolds," *International Journal of Biological Macromolecules*, vol. 107, no. Part A, pp. 678-688, 2018.
- [19] M. Sabzi, M. Javad, A. Masoud, M. Babaahmadi and N. Shafagh, "pH-dependent swelling and antibiotic release from citric acid crosslinked poly(vinyl alcohol) (PVA)/nano silver hydrogels," *Colloids and Surfaces B: Biointerfaces*, vol. 188, no. 110757, pp. 1-10, 2020.
- [20] H. D. Williams , R. Ward , I. J. Hardy and C. D. Melia, "The effect of sucrose and salts in combination on the drug release behaviour of an HPMC matrix," *European Journal of Pharmaceutics and Biopharmaceutics*, vol. 76, no. 3, pp. 433-436, 2010.
- [21] Merck, "Sigma Aldrich," [Online]. Available: <https://www.sigmaaldrich.com/content/dam/sigma->

aldrich/docs/Sigma/Product_Information_Sheet/c1909pis.pdf. [Accessed 02 06 2020].

- [22] G. W. Milne, *Drugs: Synonyms and Properties*, New York: Routledge, 2018.
- [23] Merck, "www.sigmaaldrich.com," [Online]. Available: <https://www.sigmaaldrich.com/MSDS/MSDS/DisplayMSDSPage.do?country=GB&language=en&productNumber=G2879&brand=SIGMA&PageToGoToURL=http%3A%2F%2Fwww.sigmaaldrich.com%2Fcatalog%2Fsearch%3Fterm%3DGlycine%2BHCl%26interface%3DAI%26N%3D0%26mode%3Dmatch%2520partia>. [Accessed 02 06 2020].
- [24] Merck, "www.sigmaaldrich.com," Sigma Aldrich, [Online]. Available: <https://www.sigmaaldrich.com/MSDS/MSDS/DisplayMSDSPage.do?country=US&language=en&productNumber=C1276&brand=SIGMA&PageToGoToURL=http%3A%2F%2Fwww.sigmaaldrich.com%2Fcatalog%2Fproduct%2Fsigma%2Fc1276%3Flang%3Den>. [Accessed 02 06 2020].
- [25] K. C. Gordona and C. M. McGoverin, "Raman mapping of pharmaceuticals," *International Journal of Pharmaceutics*, vol. 417, no. 1-2, p. 151–162, 2011.
- [26] FDA U.S. Food and Drug Administration, "Dissolution Methods-itraconazole," [Online]. Available: https://www.accessdata.fda.gov/scripts/cder/dissolution/dsp_SearchResults.cfm. [Accessed 19 July 2019].
- [27] H. Keles , A. Naylor , F. Clegg and C. Sammon, "Studying the release of hGH from gamma-irradiated PLGA microparticles using ATR-FTIR imaging," *Vibrational Spectroscopy*, vol. 71, p. 76–84, 2014.
- [28] K. Thoma and T. Zimmer, "Retardation of weakly basic drugs with diffusion tablets," *International Journal of Pharmaceutics*, vol. 58, no. 3, pp. 197-202, 1990.
- [29] K. Thoma and I. Ziegler, "The pH-independent release of fenoldopam from pellets with insoluble film coats," *European Journal of Pharmaceutics and Biopharmaceutics*, vol. 46, no. 1, pp. 105-113, 1998.
- [30] J. Ploen, J. Andersch, M. Heschel and C. S. Leopold, "Citric acid as a pH-modifying additive in an extended release pellet formulation containing a weakly basic drug," *Drug Development and Industrial Pharmacy*, vol. 35, no. 10, p. 1210–1218, 2009.
- [31] W. Chen , H. Shen , X. Zhu , Z. Xing and S. Zhang, "Effect of citric acid on structure and photochromic properties of WO₃-TiO₂-ZnO composite films prepared by a sol-gel method," *Ceramics International*, vol. 41, no. 10, pp. 12638-12643, 2015.
- [32] M. Wolpert and P. Hellwig, "Infrared spectra and molar absorption coefficients of the 20 alpha amino acids in aqueous solutions in the spectral range from 1800 to 500 cm⁻¹," *Spectrochimica Acta Part A Molecular and Biomolecular Spectroscopy*, vol. 64, no. 4, p. 987–1001, 2006.

- [33] D. Sebben and P. Pendleton, "Infrared spectrum analysis of the dissociated states of simple amino acids," *Spectrochimica Acta Part A: Molecular and Biomolecular Spectroscopy*, vol. 132, pp. 706-712, 2014.
- [34] J. Felten, H. Hall, J. Jaumot, T. Romà, A. de Juan and G. Andrés, "Vibrational spectroscopic image analysis of biological material using multivariate curve resolution-alternating least squares (MCR-ALS)," *Nature Protocols*, vol. 10, no. 2, pp. 217-240, 2015.
- [35] R. Tauler, "Application of non-linear optimization methods to the estimation of multivariate curve resolution solutions and of their feasible band boundaries in the investigation of two chemical and environmental simulated data sets," *Analytica Chimica Acta*, vol. 595, no. 1-2, p. 289-298, 2007.
- [36] J. Maincent, L. K. Najvar, W. R. Kirkpatrick, S. Huang, T. F. Patterson, N. P. Wiederhold, J. I. Peters and R. O. Williams, "Modified Release Itraconazole Amorphous Solid Dispersion to Treat *Aspergillus fumigatus*: Importance of the Animal Model Selection," *Drug Dev Ind Pharm.*, vol. 43, no. 2, p. 264-274., 2017.
- [37] D. T. Thao Truong, L. T. Phuong Ha, H.-G. Choi, H. Hyo-Kyung and L. Beom-Jin, "The roles of acidifiers in solid dispersions and physical mixtures," *International Journal of Pharmaceutics*, vol. 384, no. 1-2, p. 60-66, 2010.

7.0 Conclusions and Future Work

The overall conclusions are presented in this chapter along with proposed future work for the application of ATR-FTIR spectroscopic imaging to investigate the within-tablet dynamics of a poorly water-soluble drug in a HPMC matrix.

The aim of the work in this thesis was to explore the use of Mid-IR imaging as the primary technique to study the release mechanism of a weakly basic drug (IT) from an HPMC tablet matrix. The current knowledge gap with this category of drugs is the lack of understanding of the within-tablet dynamics due to the complexity of the mechanisms by which these drugs are released. This is further exacerbated by the limited information provided by conventional dissolution testing.

7.1 Conclusions

7.1.1 HPMC and Binary HPMC/IT System

The initial part of the study focused on the analysis of HPMC and HPMC tablets containing 20% w/w IT. From this work, the following conclusions were made:

- HPMC tablets containing 20% w/w IT were successfully prepared by tumble blending and direct compression and compacted using a press. IT loading was confirmed using NIR-PLS spectroscopy; analysis of six tablets gave a mean IT loading of 19.46% w/w with standard deviation of 0.7.
- Determination of blend uniformity was carried out by Raman microscopy on the 20% w/w IT tablets (n=3) and confirms the strategy adopted was successful at producing homogeneously distributed IT within the HPMC tablet matrix.
- The IT salts (monohydrochloride and dihydrochloride) and polymorphs (amorphous form) were successfully prepared, and their structures confirmed using ATR-FTIR imaging and XRD.
- The work undertaken in this project has successfully developed an ATR-FTIR spectroscopic imaging methodology to study the gel layer formation and release

behaviour of poorly-soluble weakly basic drug (IT) from a HPMC matrix in different pH environments (pH 1.5 and 7).

- Discrete spectroscopic markers for ATR-FTIR imaging were identified from all the starting materials and these were found to be the following: $\delta(\text{OH})$, $\nu(\text{C-O})$, $\nu(\text{C=C})$ and $\nu(\text{C-H})$ in water, HPMC, IT (total IT) and free base IT, respectively. These bands were successfully used to generate the peak area distribution maps from the data generated from ATR-FTIR imaging hydration experiments.
- Initial work carried out on the HPMC placebo tablets confirmed that high ionic strength hydration medium has a considerable impact on the HPMC gel layer formation and was shown to interfere with the polymer hydration, resulting in the suppression and expansion of the gel layer growth.
- Macro swelling conducted on the pure HPMC placebo tablets showed no significant difference between the different pH environments. However, the 20% w/w IT loaded tablets exhibited a greater swelling rate and higher overall percentage swelling in the pH 1.5 hydration medium in comparison to those exposed to the pH 7 for both axial and radial dimension, confirming that pH does indeed impact on the swelling properties.
- The ATR imaging was able to show that pH has an impact on the dissolution behaviour of the IT. At pH 7 the drug remained predominantly in the free base form and largely stayed within the tablet core and the swelling front. At pH 1.5 however, the IT was partially ionised as evidenced by the reduction of the $\nu(\text{C-H})$ observed at 2821 cm^{-1} (CH symmetric stretching vibration of the methyl group). This implies that at pH 1.5 the IT becomes more soluble and able to migrate into the diffusion front and eventually out into the surrounding medium, as proposed by other researchers.

7.1.2 20% w/w IT Tablets with the Incorporation of Organic Acid pH Modifiers

- NIR spectroscopy in conjunction with PLS was shown to be a successful technique for quantifying the IT and the organic acid pH modifier loadings simultaneously within the same tablets, for the different formulations prepared for this study. Furthermore, the calculated values were comparable to the predicted values, with all mean IT loadings lying within 1.2% of the intended value and 0.4% of the intended value for all pH modifiers mean loadings for the 10% w/w organic acid pH modifier formulations with 20% w/w IT. For the 30% w/w organic acid pH modifier formulations with IT, the mean IT and pH modifier loadings were within 1.0% and 3.2% of the predicted values respectively.
- Increasing the modifier loading from 10% w/w to 30% w/w with the incorporation of IT has a considerable impact on the rate the gel layer is formed, with a rapid formation when the organic acid modifier levels are increased. This was observed for all the organic acid modifiers used in this study.
- *In-vitro* dissolution studies showed that IT release from the tablet matrix is enhanced by the incorporation of the four organic pH modifiers explored in this study (citric, betaine HCl, cysteine HCl and glycine HCl). This was the case with both the 10% w/w and 30% w/w loadings and irrespective of the *pKa* or water solubility of the modifier.

Cysteine HCl provided the greatest enhancement (approximately 5%) in comparison to the citric acid, betaine HCl and glycine for both the 10% w/w and 30% w/w loading. The low release of the IT from the tablet matrix with the incorporation of the pH modifiers can be explained by the fact that none of the pH modifiers were effective at reducing the pH of the dissolution medium to a sufficiently low value to provide favourable conditions for the optimal release of the IT.

- Investigation into changes associated with the free base IT form to the ionised form show that cysteine HCl at both 10% w/w and 30% w/w loadings provides the greatest reduction in the free base form in comparison to the organic acid pH modifiers.
- MCR analysis has provided valuable insights into the different forms of IT that exist, however further optimisation with the use of data pre-treatment would be required.

7.2 Recommendations for Future Work

7.2.1 Preparation and Characterisation of Tablets

Confidence in the tablets used for dissolution experiments requires optimal tablet preparation and appropriate characterisation. For further work on this project, the following are proposed:

- Optimization of the tablet preparation procedure would be advantageous to ensure that all the raw materials used within the formulation are particle size matched and are similar in morphology to ensure differences attributable to these parameters can be eliminated when assessing their dissolution. Ideally, the particle size of the API should be similar to the excipients to reduce the potential for segregation and to avoid problems with powder flow when blending the mixtures. The blend uniformity and segregation of the API and excipient is markedly controlled by the particle size distribution.
- Raman imaging of the whole tablet would be advantageous to determine homogeneity of the API and pH modifier at a macro scale, rather than a small section of the tablet.

7.2.2 Testing of Tablets and Optimising of Drug Release

This study has shown that the incorporation of a pH modifier provides enhanced release of the IT, however due to time constraints of the project this could not be explored further. In order to optimise the IT release, the following should be considered:

- Shelf life (stability testing) and studies of gel strength by rheology/ texture analysis of the different tablet formulations with the incorporated organic acid modifier may be able to shed some light on the differences observed with the integrity of the tablet structure during the macro swelling experiments.
- Quantification of the pH modifier release from the tablet matrix, in addition to that of the IT levels obtained from the in-vitro dissolution studies, to facilitate further understanding of the release behaviour of the modifier and provide additional insight into the mechanism of drug release from the tablet matrix.
- Measurement of the microenvironmental pH (pH_M) of the tablet matrix using a pH meter or indicator dye media or nuclear magnetic resonance to determine the pH of the hydrated matrix; this is an important factor which influences the drug dissolution characteristics and is the key to achieving a pH independent release profile. Understanding of this will permit the comparison and effectiveness of the pH modifiers selected in this study to be determined. In addition to the pH_M , pH measurements of the tablet surface using a contact pH electrode to monitor pH changes of HPMC gel layer as the tablet matrix swells will permit further insight into the impact of the pH modifier on the gel layer.

7.2.3 Refinement of MCR-ALS Methodology

The feasibility study conducted on the tablets containing the 30% w/w organic acid pH modifier with and without the incorporation of IT provided a valuable insight into the chemical changes to the IT during the hydration of the tablet matrix. To explore this further the following would be beneficial:

- Further refinement of the MCR-ALS methodology including comparison of data pre-treatment methods (spectral pre-processing) such as de-noising, spectral correction and normalization.

- Using a more focused spectral region to aid with the detection and changes associated with the IT during the hydration process (free base and amorphous form) and the use of data binning to develop a more robust MCR-ALS model.

8.0 Appendix

Appendix 1: Histogram data for tablets with 10% w/w organic acid modifier formulation with 20% w/w IT

Table 1 Histogram data for: 10% w/w citric acid+20% w/w IT

Parameter	Tablet	Mean	Standard Deviation	Kurtosis	Skew
Citric acid intensity	1	0.002	0.002	6.78	2.49
	2	0.003	0.004	9.89	3.43
	3	0.002	0.002	5.69	2.07
IT intensity	1	0.02	0.01	1.25	1.91
	2	0.03	0.02	7.51	2.43
	3	0.04	0.02	1.90	1.22
Citric Acid: IT ratio	1	0.86	0.040	7.46	-1.76
	2	0.84	0.069	9.79	-2.23
	3	0.80	0.056	1.87	-0.81

Table 2: Histogram data for: 10% w/w betaine HCl+20% w/w IT

Parameter	Tablet	Mean	Standard Deviation	Kurtosis	Skew
Betaine HCl intensity	1	0.001	0.004	15.06	3.70
	2	0.001	0.003	12.86	3.15
	3	-0.001	0.002	12.70	2.54
IT intensity	1	0.05	0.04	2.95	1.72
	2	0.04	0.03	2.42	1.47
	3	0.04	0.03	1.87	1.45
Betaine HCl: IT ratio	1	0.80	0.10	1.09	-1.04
	2	0.82	0.10	1.02	-0.77
	3	0.81	0.10	0.51	-0.91

Table 3: Histogram data for 10% w/w cysteine HCl+20% w/w IT

Parameter	Tablet	Mean	Standard Deviation	Kurtosis	Skew
Cysteine HCl intensity	1	0.003	0.003	4.44	2.05
	2	0.007	0.012	6.97	2.57
	3	0.007	0.013	10.09	3.05
IT intensity	1	0.03	0.02	1.34	1.01
	2	0.03	0.02	3.68	1.83
	3	0.04	0.03	3.37	1.72
Cysteine HCl: IT ratio	1	0.50	0.06	4.81	1.44
	2	0.51	0.06	3.21	0.18
	3	0.51	0.07	3.78	0.88

Table 4: Histogram data 10% w/w glycine HCl+20% w/w IT

Parameter	Tablet	Mean	Standard Deviation	Kurtosis	Skew
Glycine HCl intensity	1	0.0015	0.003	5.38	0.92
	2	0.0015	0.002	7.74	2.44
	3	0.0014	0.005	7.56	2.44
IT intensity	1	0.05	0.02	4.6	1.7
	2	0.03	0.02	0.93	0.85
	3	0.03	0.05	3.6	1.87
Glycine HCl: IT ratio	1	0.80	0.07	0.77	-0.36
	2	0.83	0.04	0.28	-0.14
	3	0.80	0.11	0.33	-1.11

Histogram Data for Tablets with 30% w/w Organic Acid Modifier Formulation with 20% w/w IT

Table 5: 30% w/w citric acid+20% w/w IT formulation

Parameter	Tablet	Mean	Standard Deviation	Kurtosis	Skew
Citric acid intensity	1	0.02	0.01	0.98	1.26
	2	0.01	0.01	1.11	1.32
	3	0.01	0.01	2.02	1.54
IT intensity	1	0.08	0.04	0.83	0.92
	2	0.03	0.02	2.11	1.26
	3	0.04	0.02	2.83	1.57
Citric Acid: IT ratio	1	0.78	0.11	0.28	-0.43
	2	0.88	0.10	0.35	-0.39
	3	0.77	0.10	0.83	-0.10

Table 6: 30% w/w cysteine HCl+20% w/w IT formulation

Parameter	Tablet	Mean	Standard Deviation	Kurtosis	Skew
Cysteine HCl intensity	1	0.04	0.05	5.74	2.29
	2	0.03	0.03	4.57	2.03
	3	0.04	0.05	8.12	2.65
IT intensity	1	0.04	0.03	1.28	1.13
	2	0.11	0.06	3.45	1.52
	3	0.06	0.03	4.56	1.62
Cysteine HCl: IT ratio	1	0.57	0.15	5.72	2.23
	2	0.52	0.18	4.72	1.80
	3	0.54	0.11	3.85	1.68

Table 7: 30% w/w betaine HCl+20% w/w IT formulation

Parameter	Table t	Mean	Standard Deviation	Kurtosis	Skew
Betaine HCl intensity	1	0.002	0.008	6.56	2.60
	2	0.008	0.020	9.94	3.01
	3	0.004	0.007	10.32	2.96
IT intensity	1	0.10	0.05	3.12	1.26
	2	0.11	0.05	-0.03	0.45
	3	0.12	0.05	0.06	0.37
Betaine HCl: IT ratio	1	0.68	0.11	0.76	0.22
	2	0.66	0.12	0.41	0.52
	3	0.63	0.11	0.29	0.25

Table 8: 30% w/w glycine HCl+20% w/w IT formulation

Parameter	Table t	Mean	Standard Deviation	Kurtosis	Skew
Glycine HCl intensity	1	0.01	0.02	10.67	2.96
	2	0.01	0.01	8.95	2.80
	3	0.01	0.01	12.15	3.15
IT intensity	1	0.04	0.02	-0.23	0.33
	2	0.05	0.02	-0.27	0.38
	3	0.05	0.03	0.34	0.82
Glycine HCl: IT ratio	1	0.82	0.10	2.24	0.87
	2	0.82	0.10	0.86	-0.14
	3	0.78	0.10	0.83	-0.10

Appendix 2

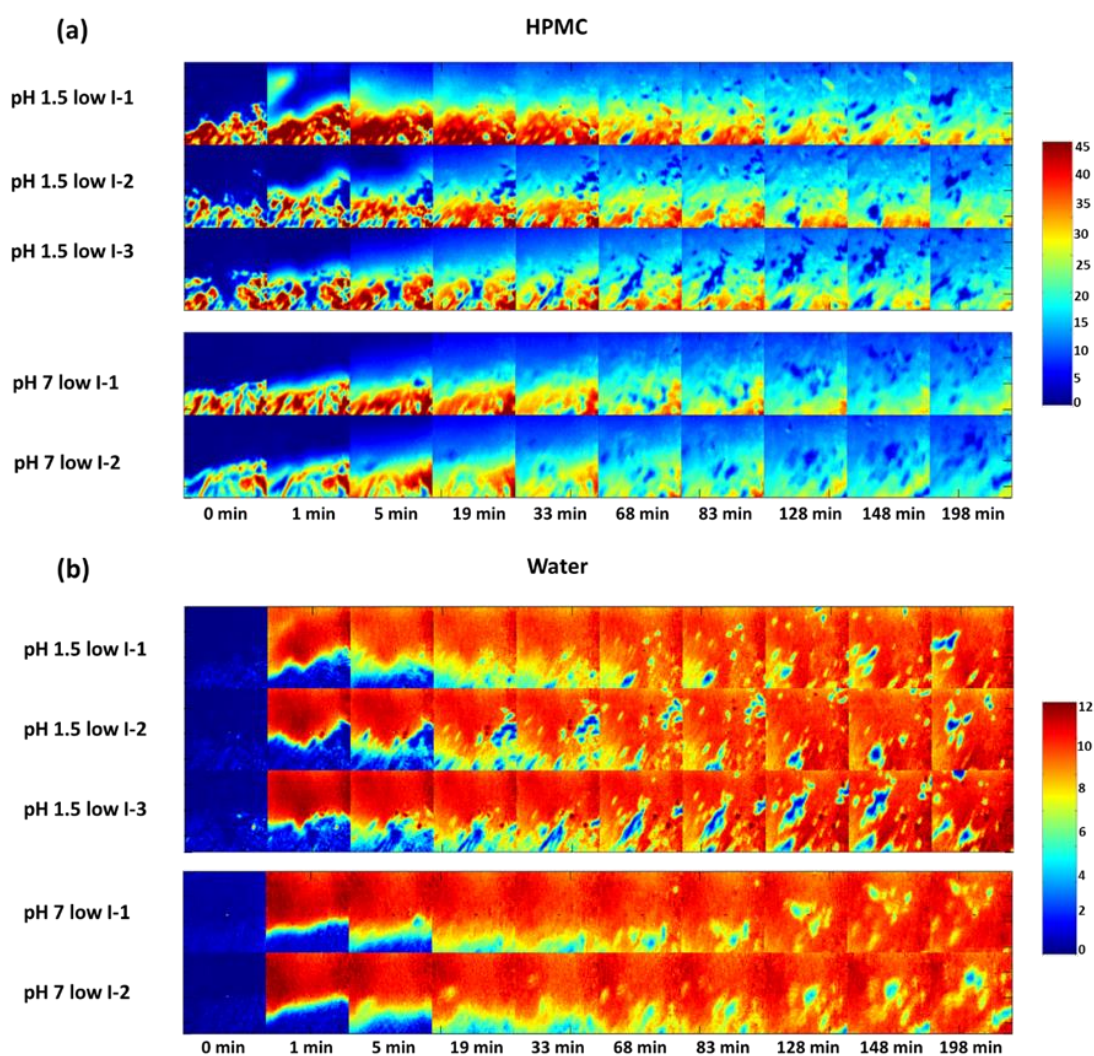


Fig. 1: ATR-FTIR images collected over the time course of hydration period for placebo tablets in low ionic strength solutions at pH 1.5 (n=3) and pH 7 (n=2) showing (a) water and (b) HPMC distribution. Images were generated using methods described in section 4.5

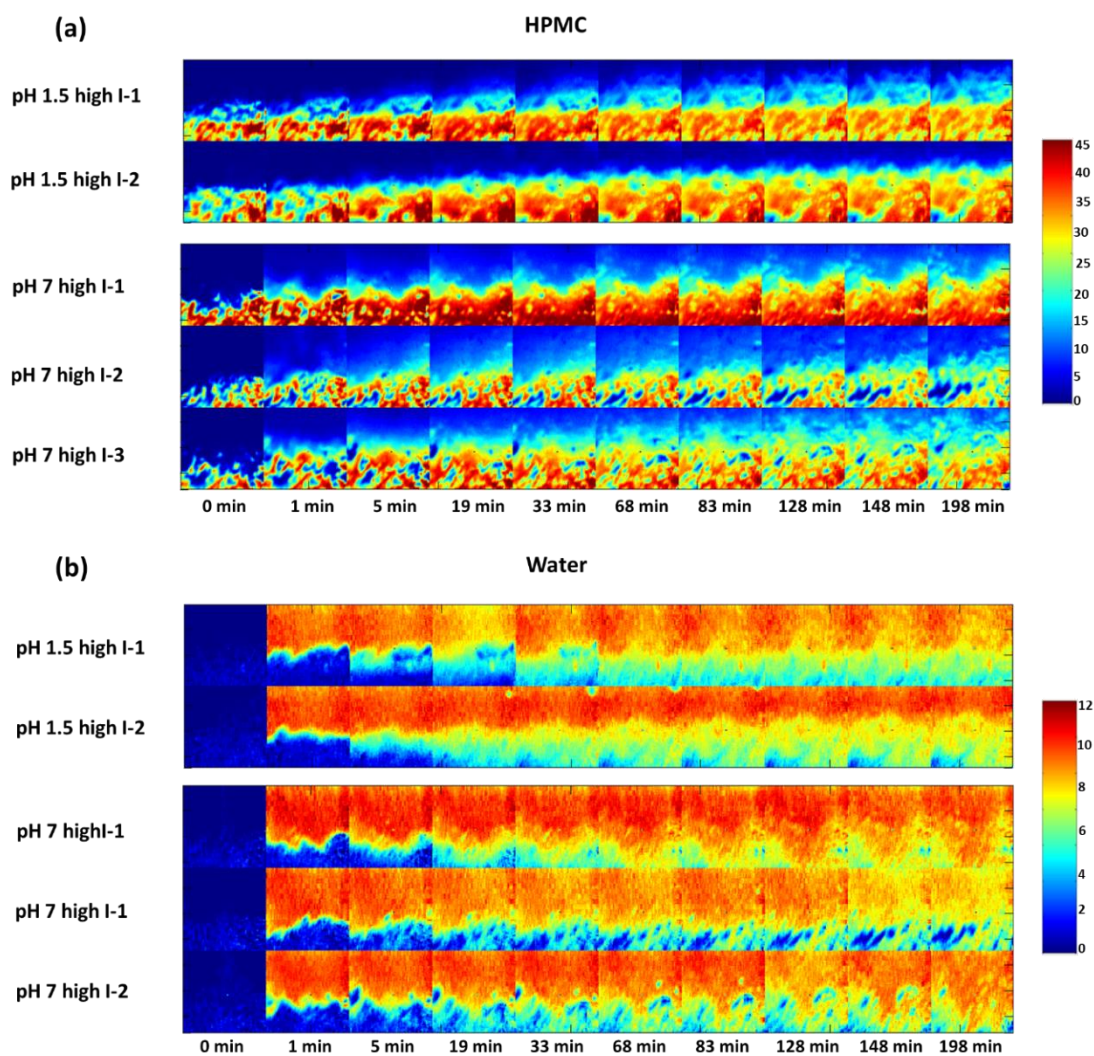


Fig. 2: ATR-FTIR images collected over the time course of hydration period for placebo tablets in high ionic strength solutions at pH 1.5 (n=2) and pH 7 (n=3) showing (a) water and (b) HPMC distribution. Images were generated using methods described in section 4.5

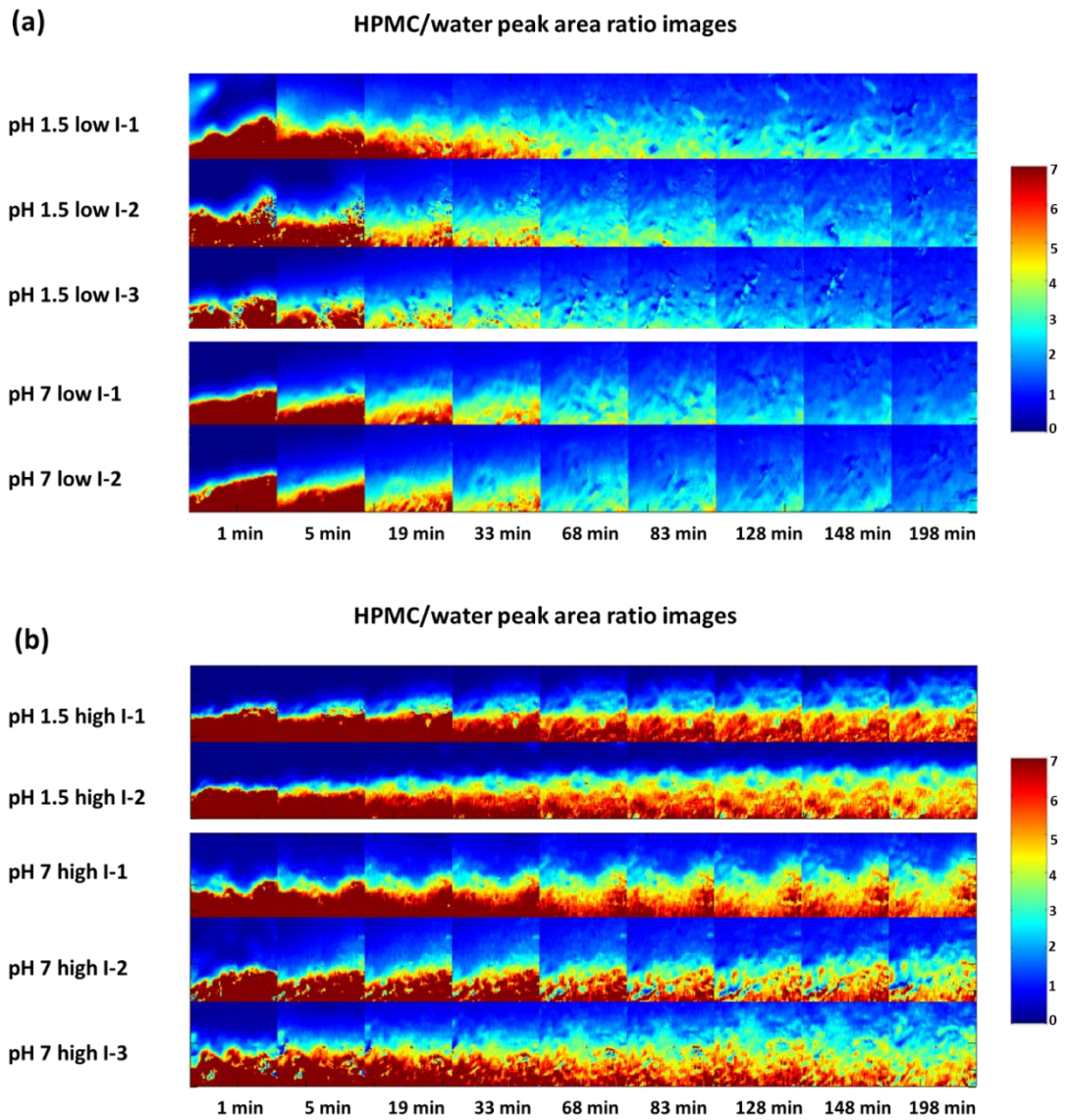


Fig. 3: ATR-FTIR images of HPMC/water peak area ratio images over hydration period for placebo tablets, showing HPMC gel layer evolution for (a) pH 1.5 and pH 7 low ionic strength solutions; (b) pH 1.5 and pH 7 high ionic strength solutions

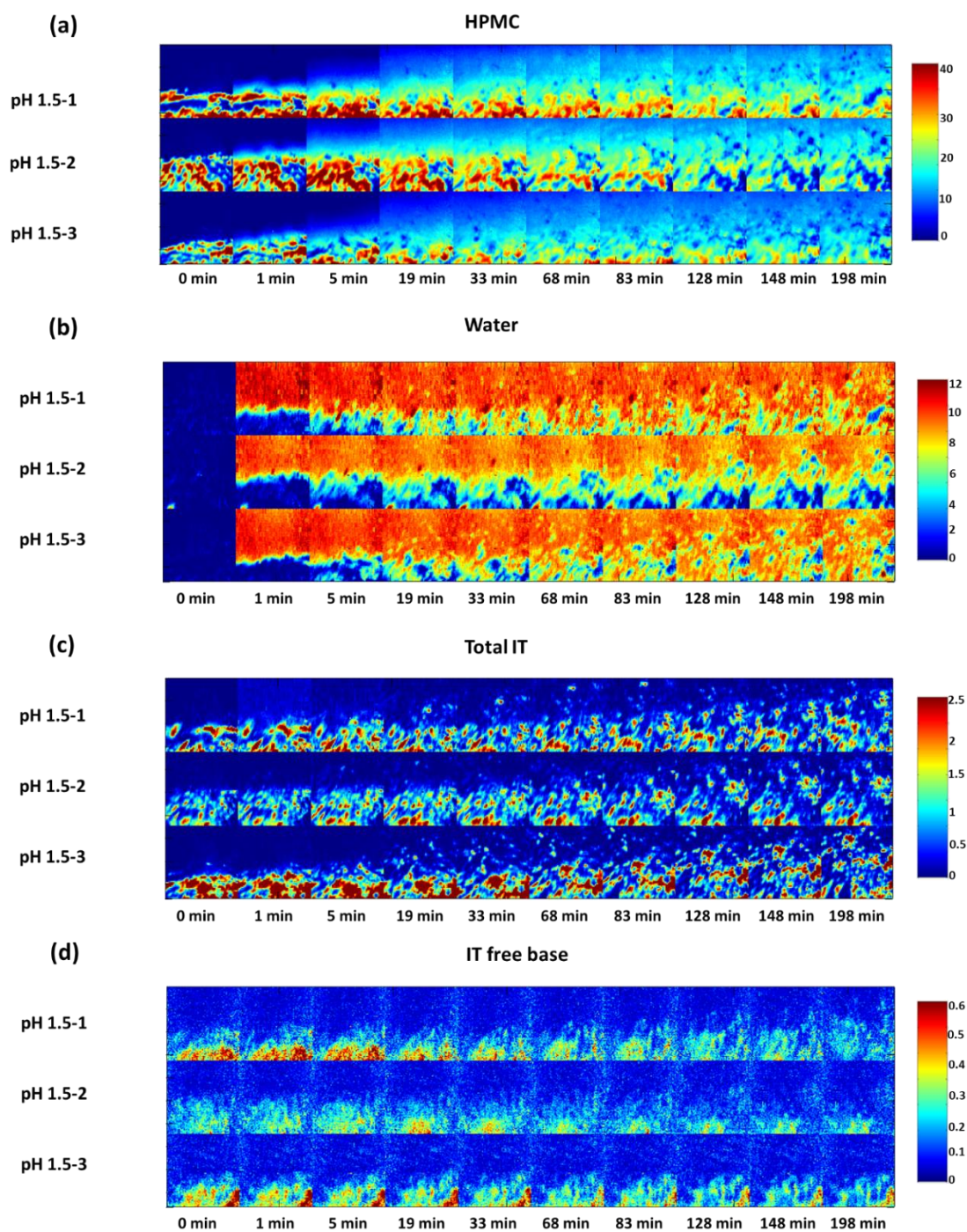


Fig. 4: ATR-FTIR peak area integration images over hydration period for 20% w/w IT tablets (n=3), showing: (a) distribution of water; (b) distribution of HPMC; (c) distribution of total IT; (d) distribution of free base IT

Appendix 3

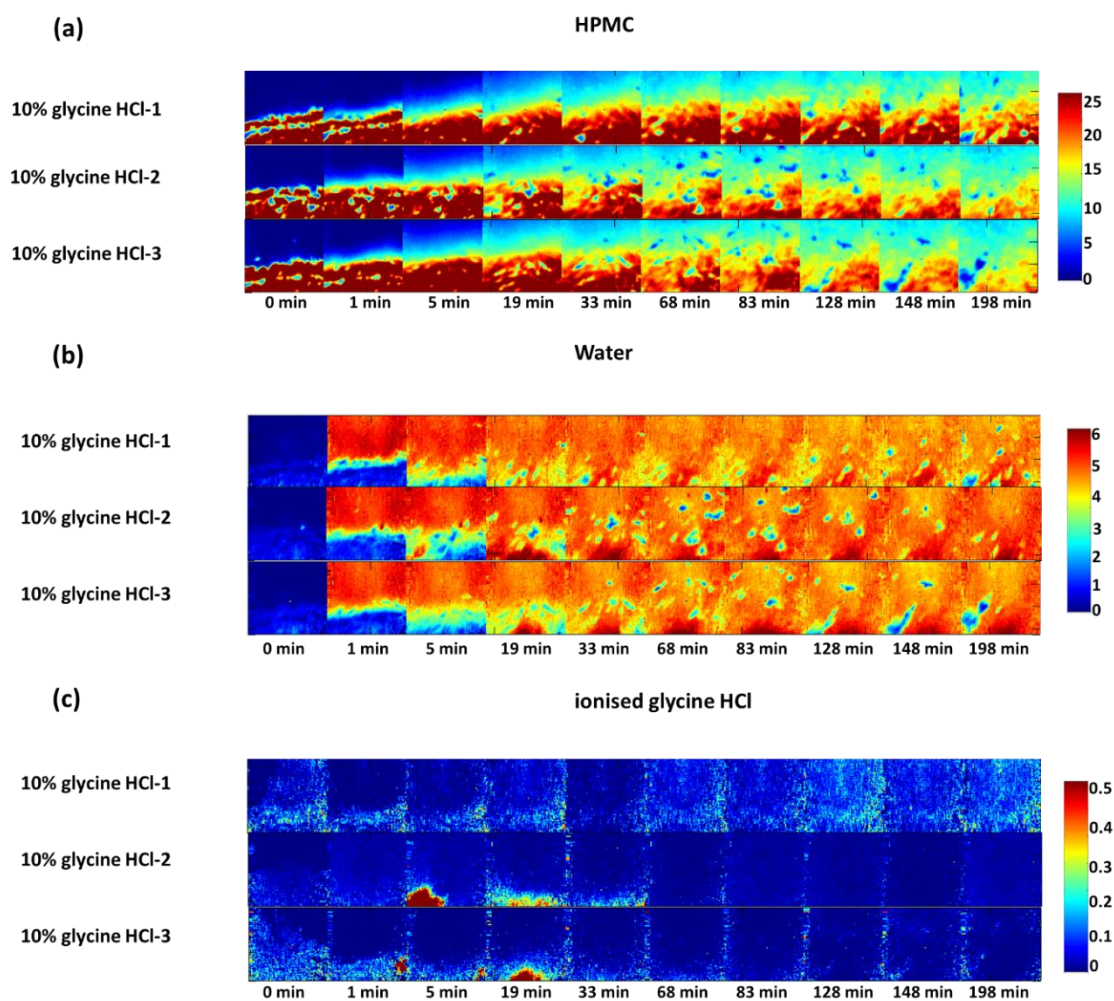


Fig. 5: ATR-FTIR images collected over the hydration period for 10% w/w glycine HCl tablets (n=3) at pH 7 showing: (a) distribution of HPMC; (b) distribution of water; (c) distribution of ionised glycine HCl

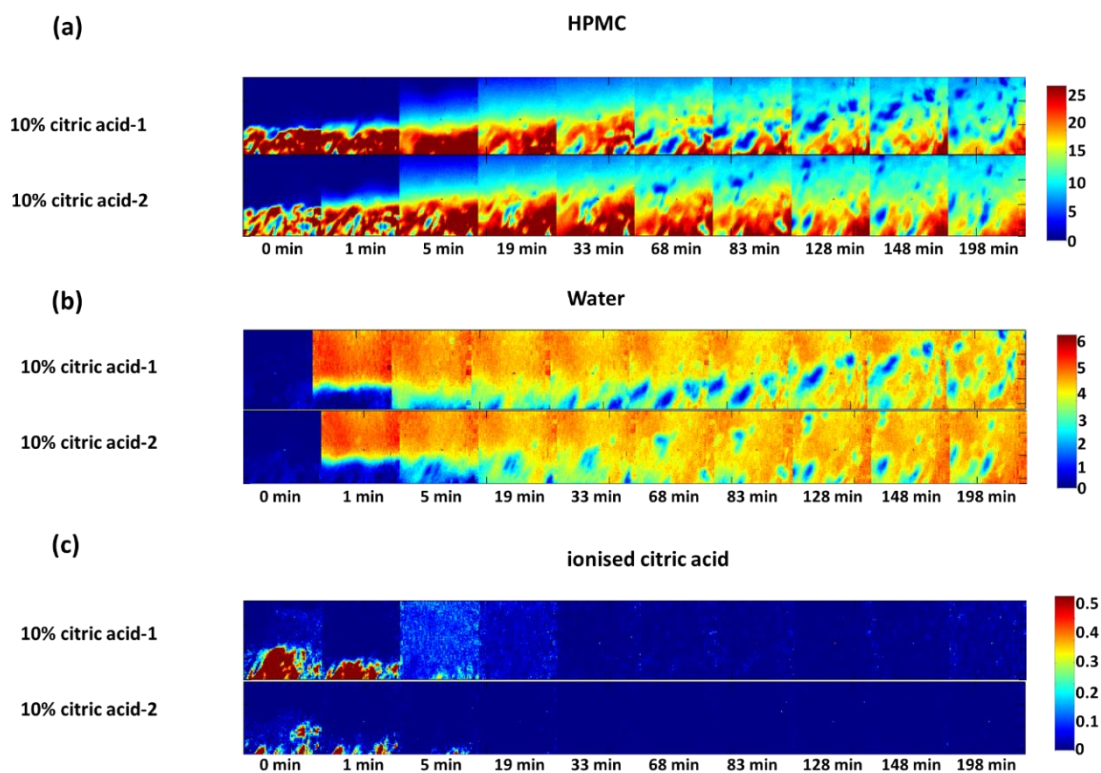


Fig. 6: ATR-FTIR images collected over the hydration period for 10% w/w citric acid tablets (n=2) at pH 7 showing: (a) distribution of HPMC; (b) distribution of water; (c) distribution of ionised citric acid

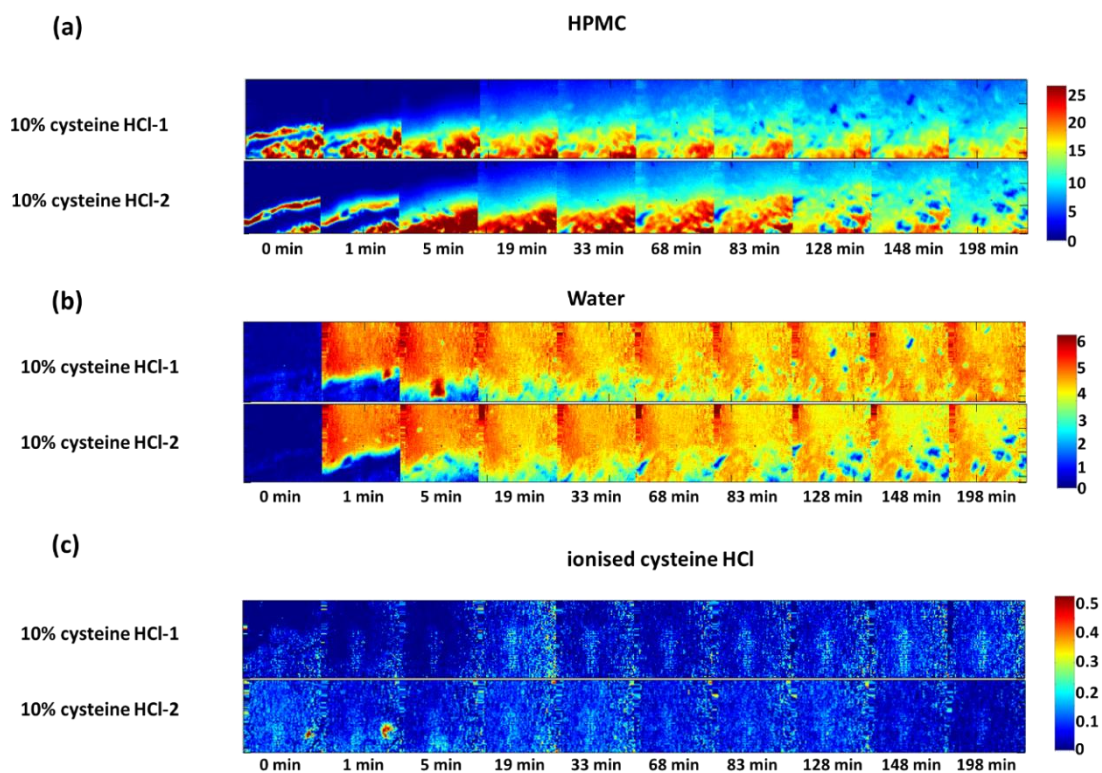


Fig. 7: Selected ATR-FTIR images collected over the hydration period for 10% w/w cysteine HCl tablets (n=2) at pH 7 showing: (a) distribution of HPMC; (b) distribution of water; (c) distribution of ionised cysteine HCl

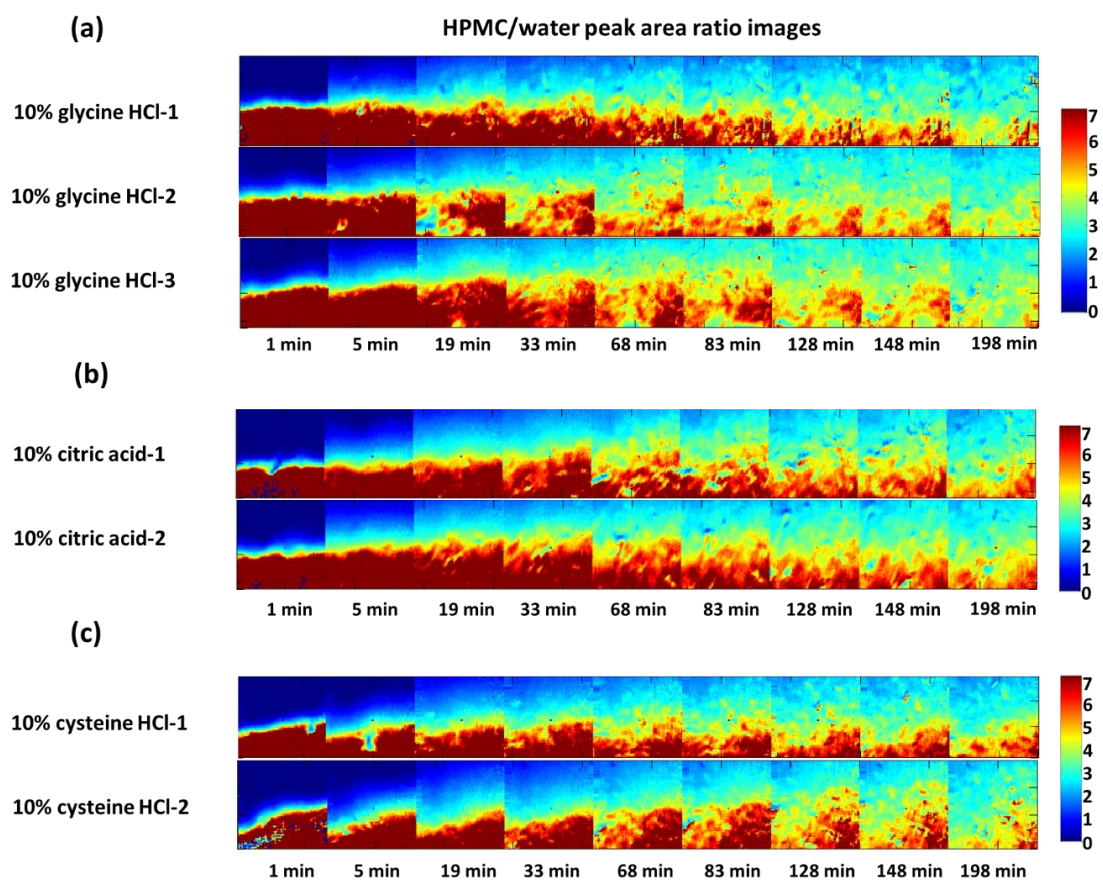


Fig. 8: ATR-FTIR images of HPMC/water peak area ratio images over hydration period for 10% w/w cysteine HCl tablets, showing HPMC gel layer evolution at pH 7 for (a) 10% w/w glycine HCl; (b) 10 % w/w citric acid; (c) 10% w/w cysteine HCl

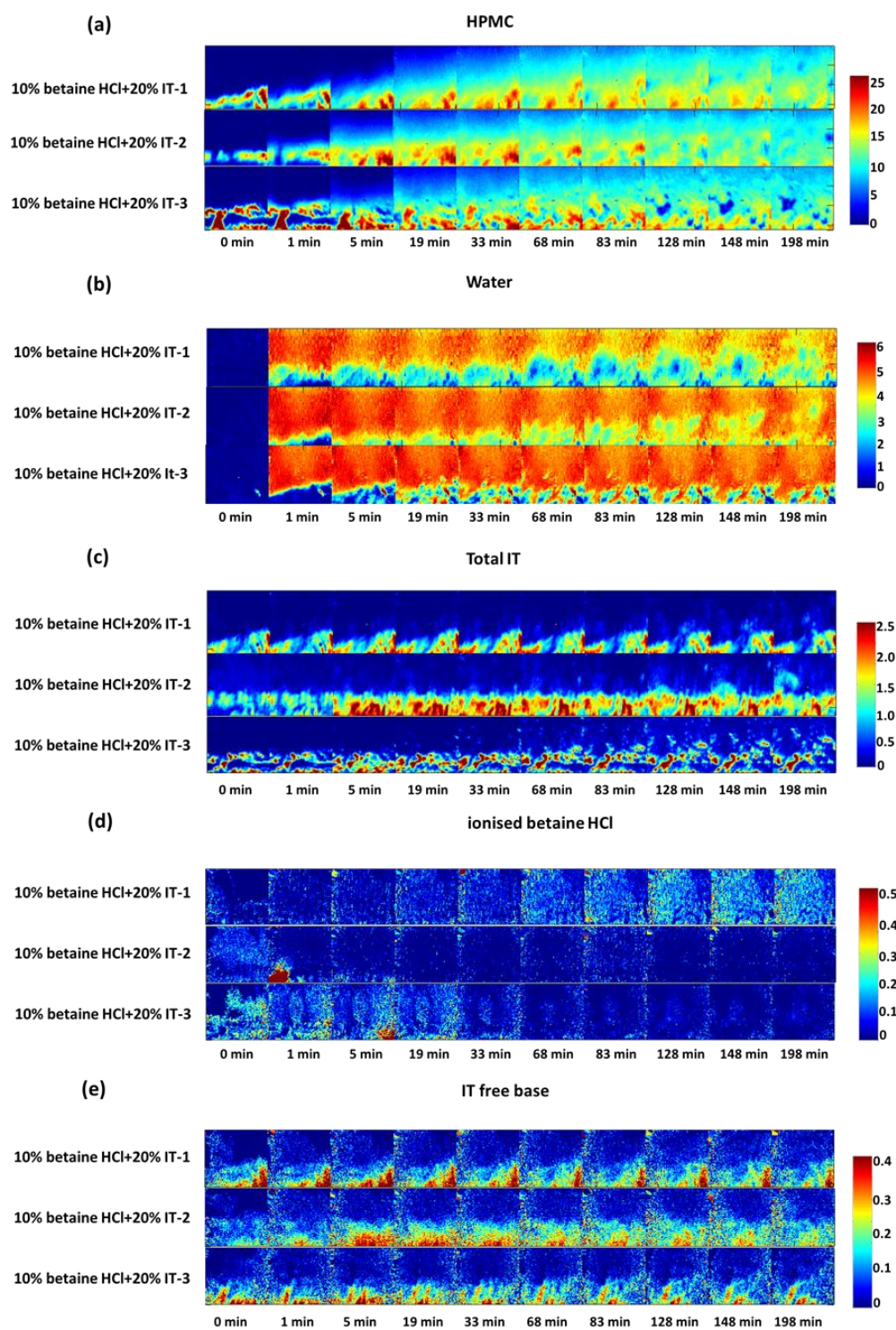


Fig. 9: Selected ATR-FTIR peak area integration images for 20% w/w IT and 10% w/w betaine HCl pH modifier tablets (n=3) over the hydration period, showing distribution of: (a) HPMC; (b) distribution of water; (c) distribution of total IT; (d) distribution of ionised betaine HCl

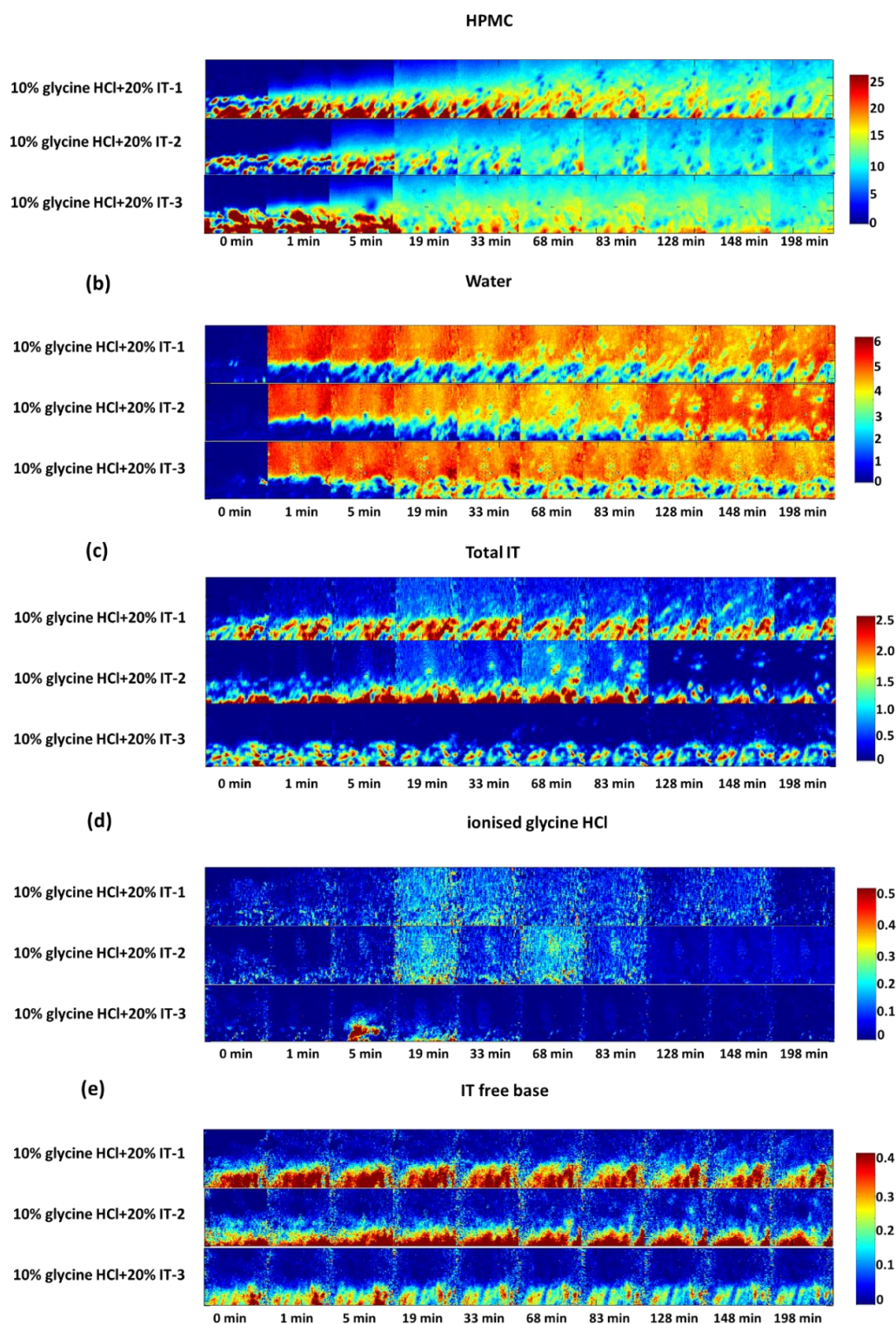


Fig. 10: Selected ATR-FTIR peak area integration images for 20% w/w IT and 10% w/w glycine HCl pH modifier tablets (n=3) over the hydration period, showing distribution of: (a) HPMC; (b) distribution of water; (c) distribution of total IT; (d) distribution of ionised glycine HCl

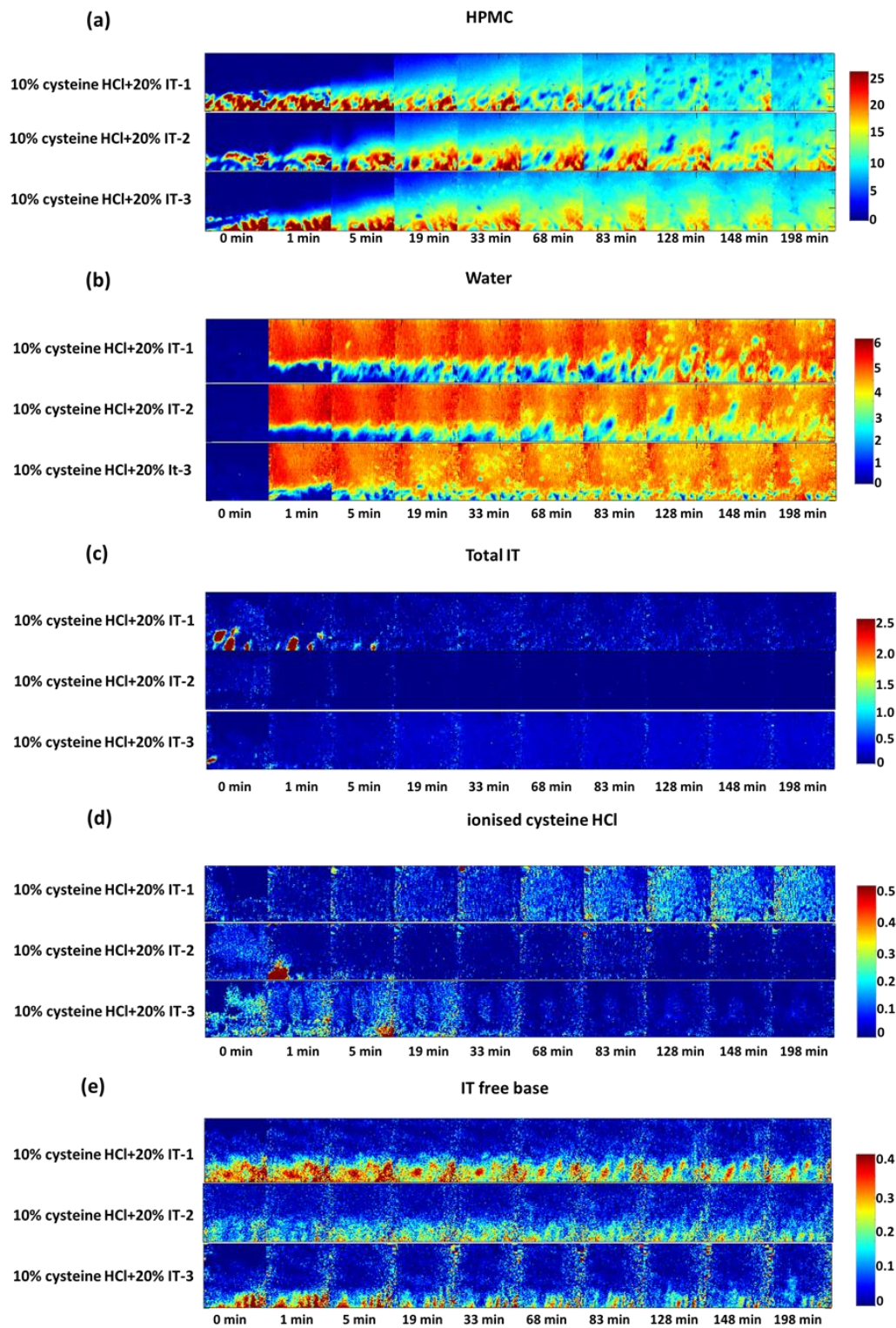


Fig. 11: Selected ATR-FTIR peak area integration images for 20% w/w IT and 10% w/w cysteine HCl pH modifier tablets (n=3) over the hydration period, showing distribution of: (a) HPMC; (b) distribution of water; (c) distribution of total IT; (d) distribution of ionised cysteine HCl

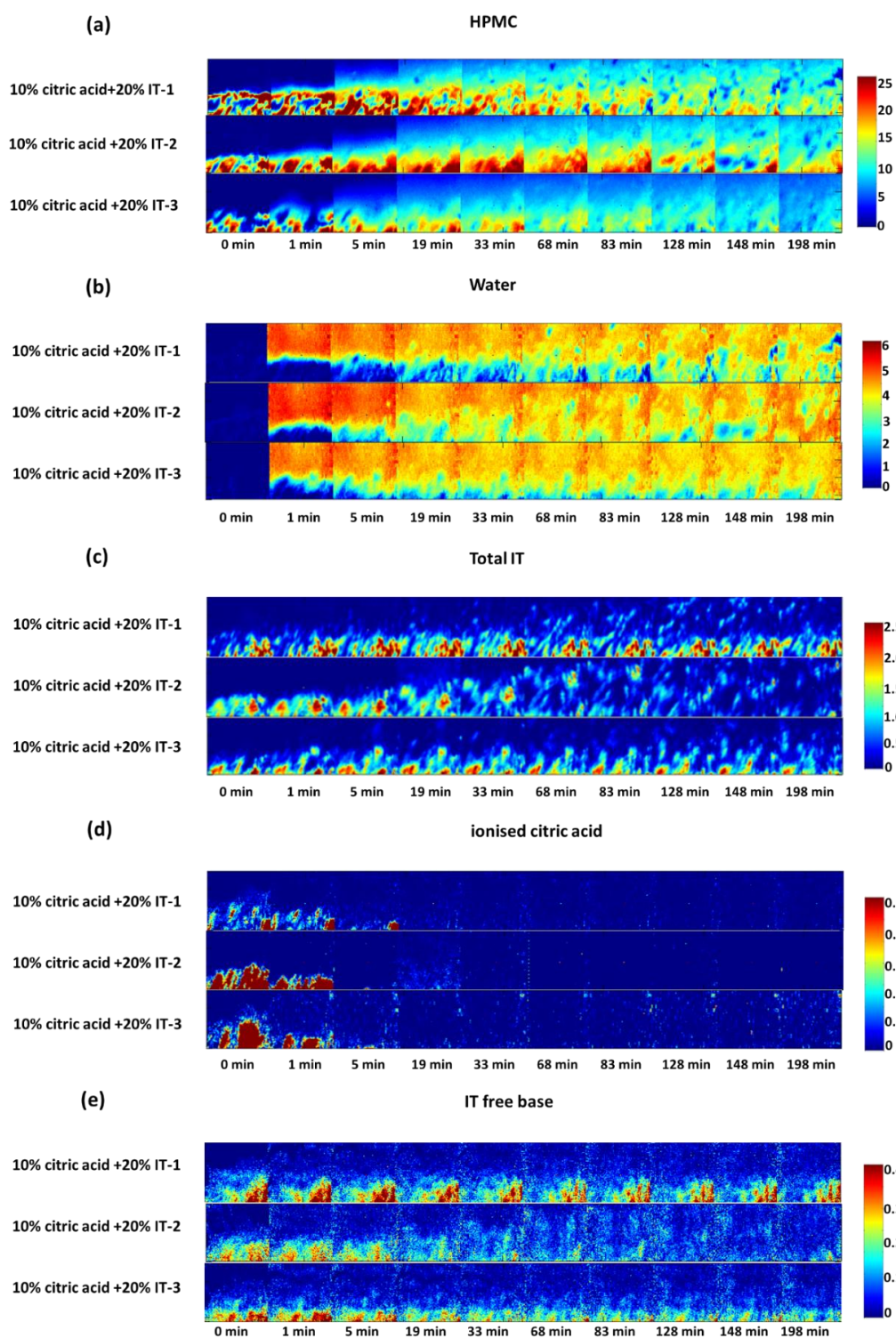


Fig. 12: Selected ATR-FTIR peak area integration images for 20% w/w IT and 10% w/w citric acid pH modifier tablets (n=3) over the hydration period, showing distribution of: (a) HPMC; (b) distribution of water; (c) distribution of total IT; (d) distribution of ionised citric acid

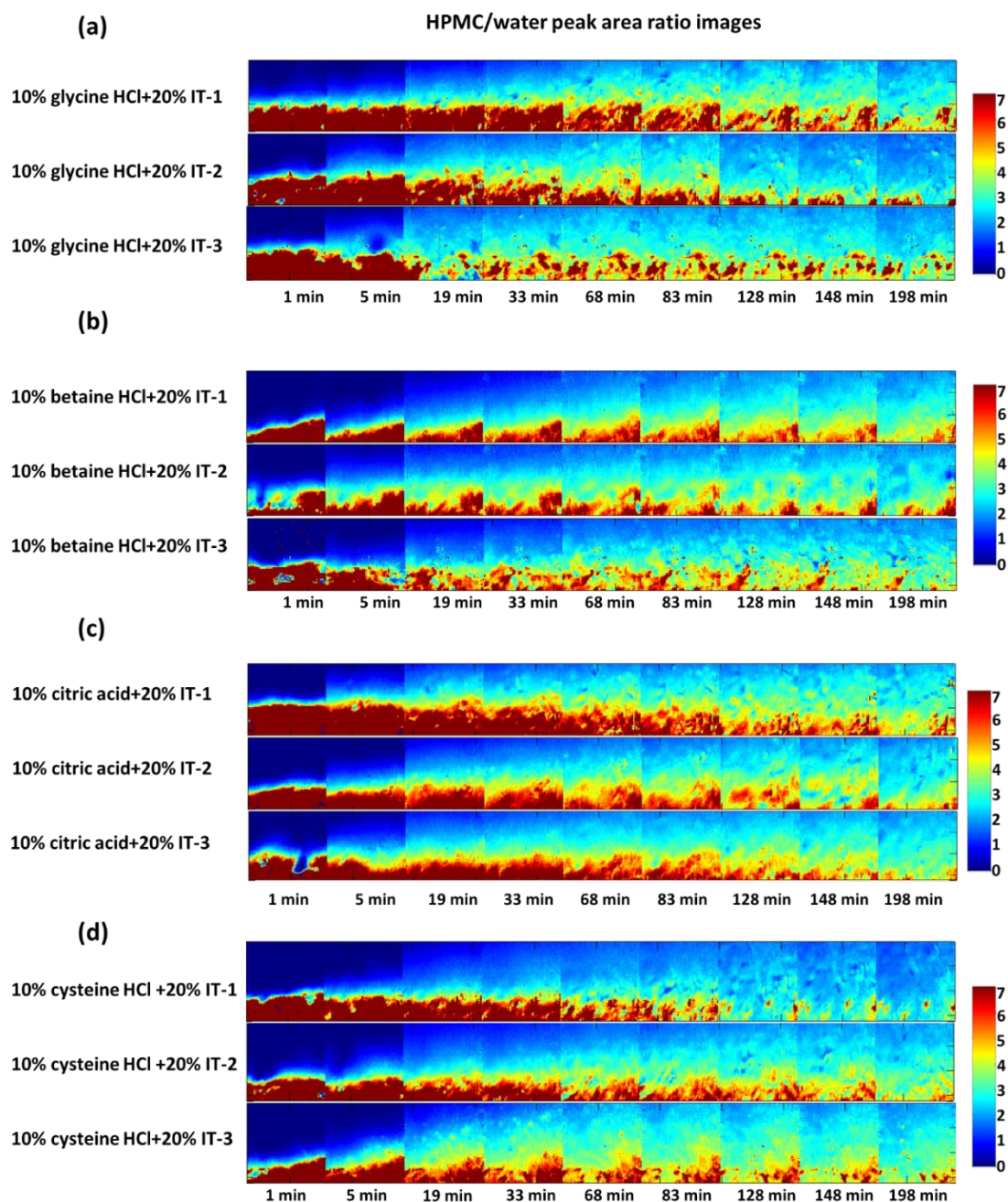


Fig. 13: Selected ATR-FTIR peak area integration ratio images (HPMC:water) showing gel layer evolution for 10% w/w pH modifier+20% w/w IT tablets (n=3) at pH 7 for: (a) glycine HCl; (b) betaine HCl; (c) citric acid and (d) cysteine HCl

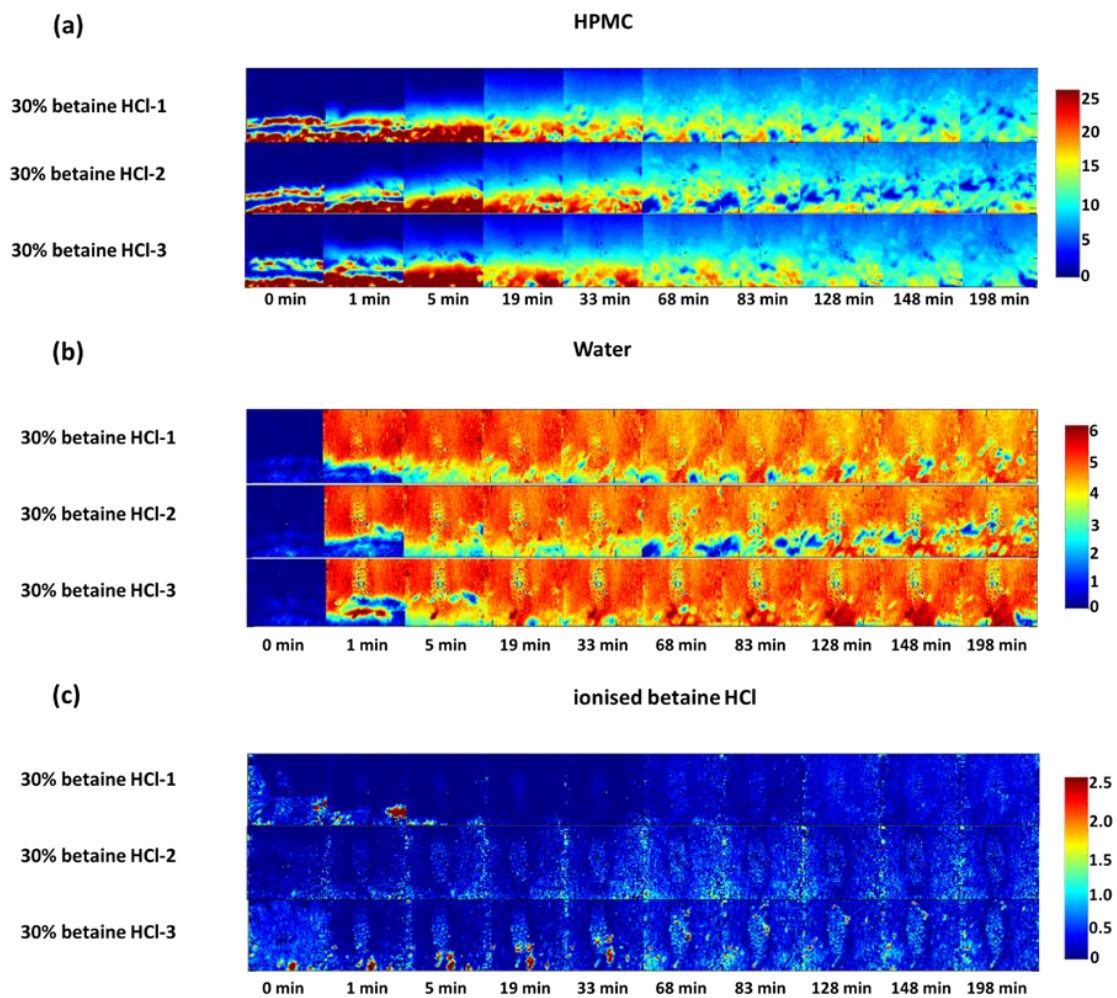


Fig. 14: Selected ATR-FTIR peak area integration images for 30% w/w betaine HCl pH modifier tablets (n=3) over the hydration period, showing distribution of: (a) HPMC; (b) distribution of water; (c) distribution of ionised betaine HCl

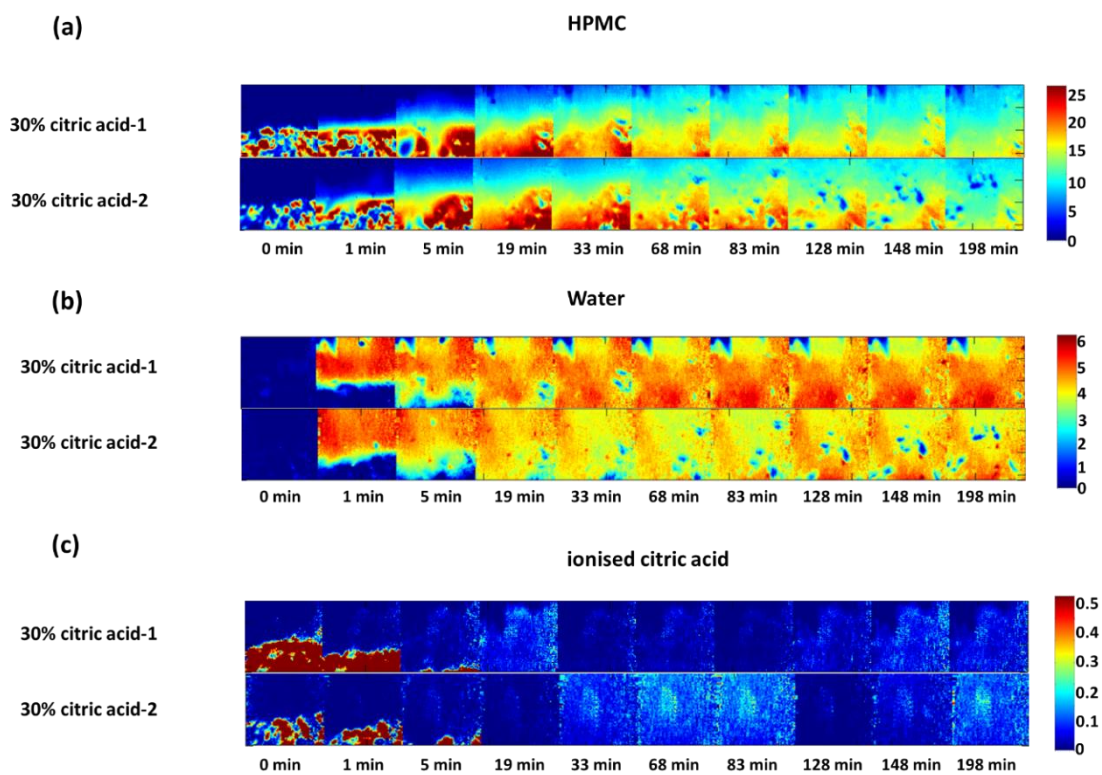


Fig. 15: Selected ATR-FTIR peak area integration images for 30% w/w citric acid pH modifier tablets (n=2) over the hydration period, showing distribution of: (a) HPMC; (b) distribution of water; (c) distribution of ionised citric acid

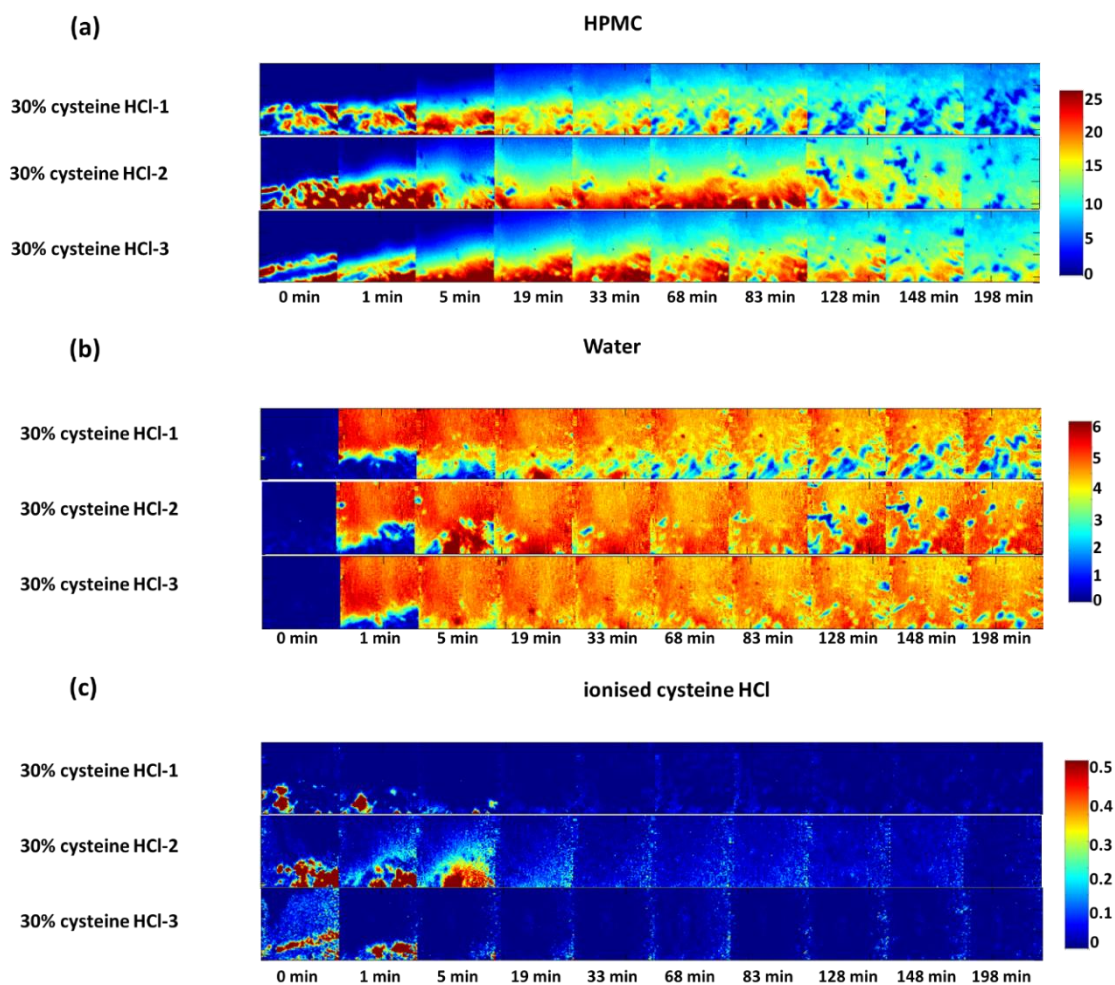


Fig. 16: Selected ATR-FTIR peak area integration images for 30% w/w cysteine HCl pH modifier tablets (n=3) over the hydration period, showing distribution of: (a) HPMC; (b) distribution of water; (c) distribution of ionised cysteine HCl

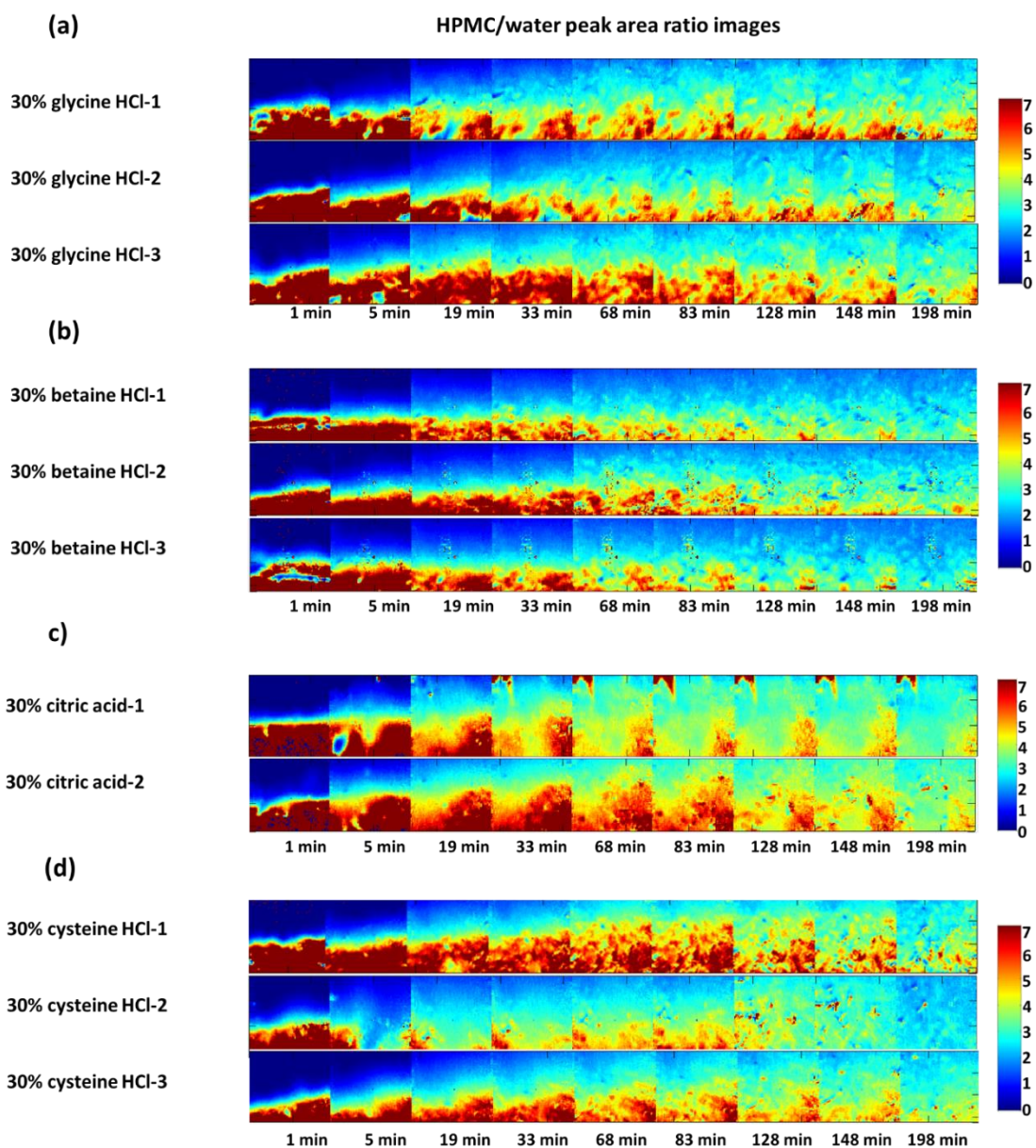


Fig. 17: Selected ATR-FTIR peak area integration ratio images (HPMC:water) showing gel layer evolution for 30% w/w pH modifier for tablets containing (a) glycine HCl (b) betaine HCl; (c) citric acid; and (d) cysteine HCl

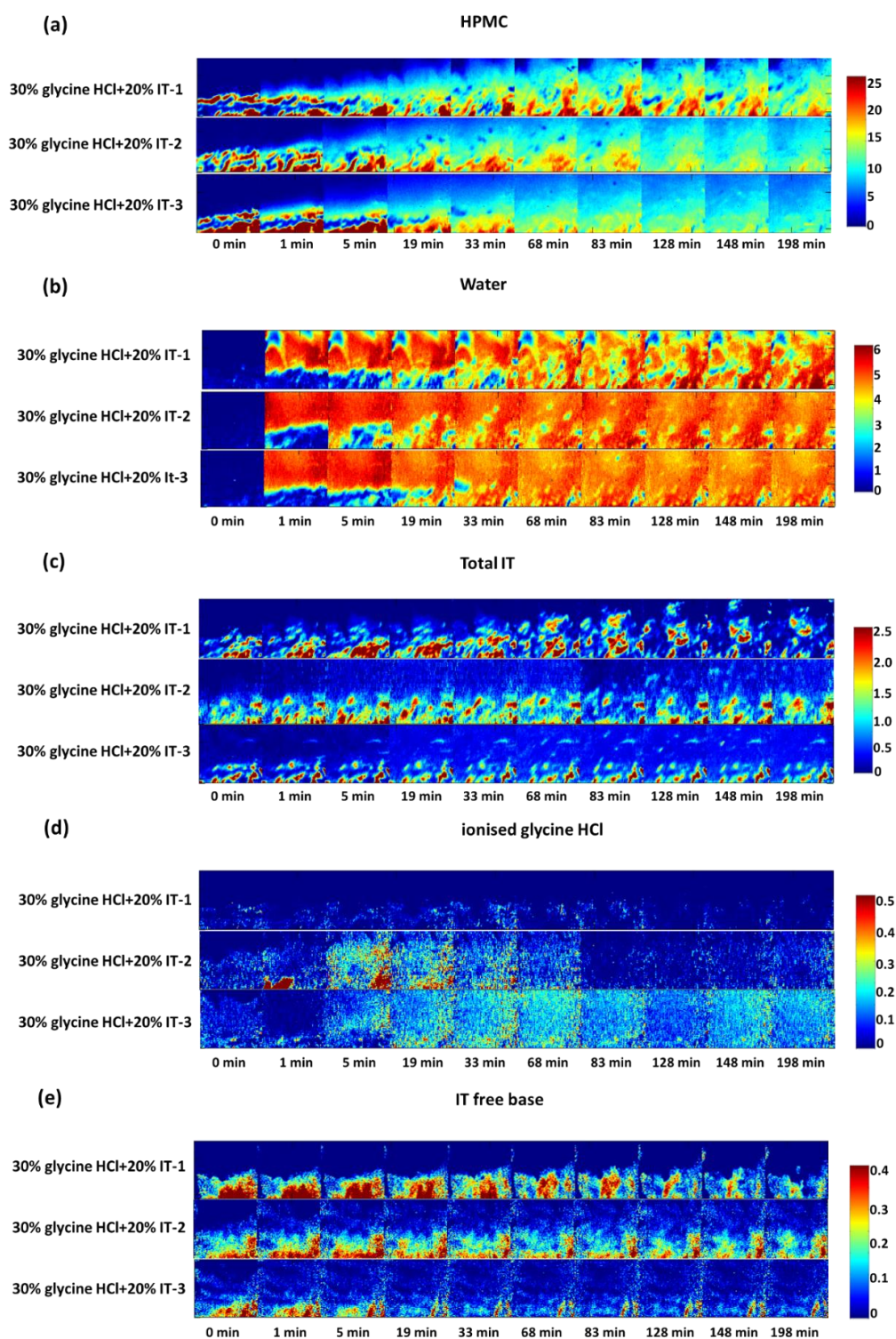


Fig. 18: Selected ATR-FTIR peak area integration images for 20% w/w IT and 30% w/w glycine HCl pH modifier tablets (n=3) over the hydration period, showing distribution of: (a) HPMC; (b) distribution of water; (c) distribution of total IT; (d) distribution of ionised glycine HCl

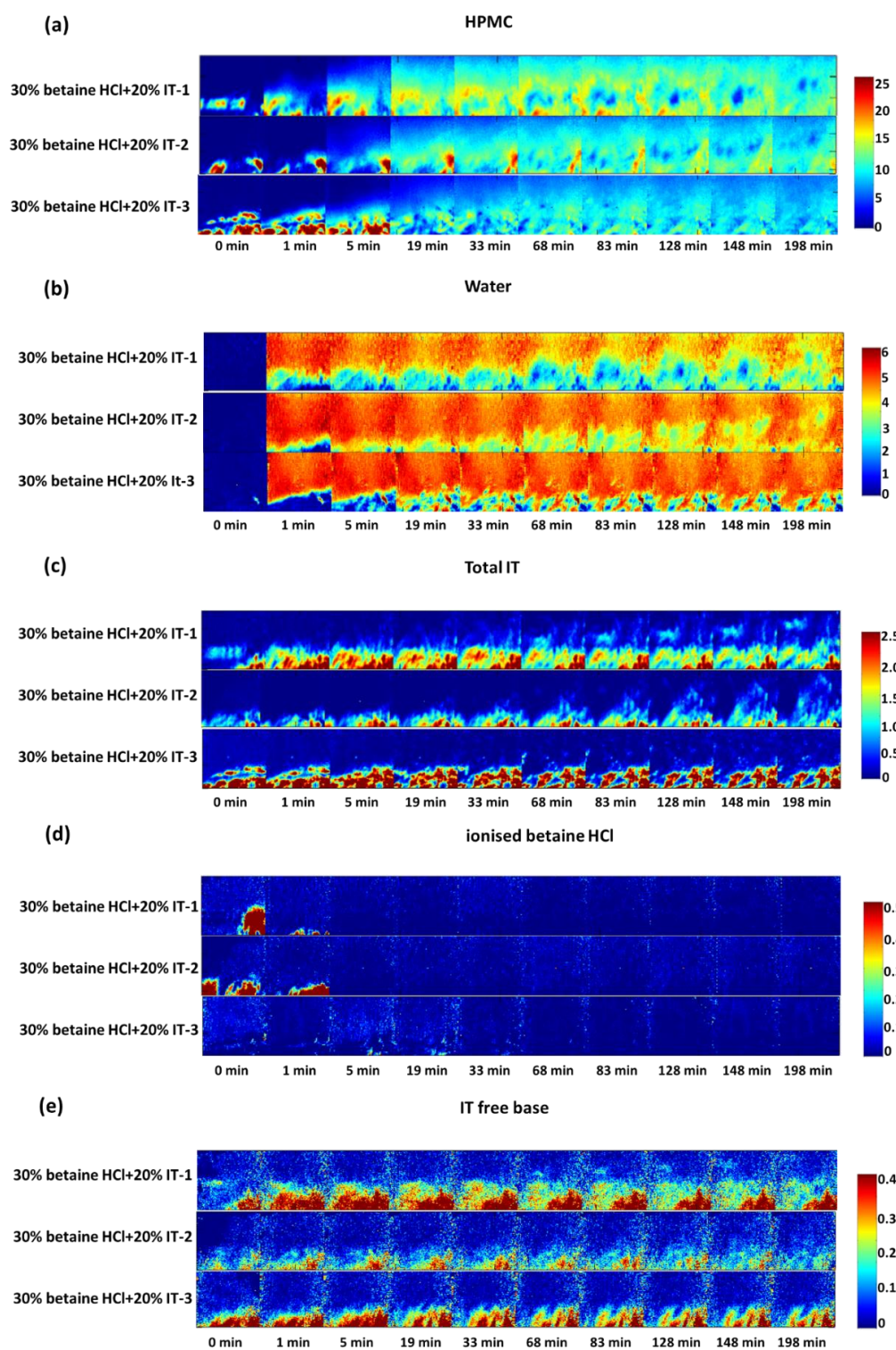


Fig. 19: Selected ATR-FTIR peak area integration images for 20% w/w IT and 30% w/w betaine HCl pH modifier tablets (n=3) over the hydration period, showing distribution of: (a) HPMC; (b) distribution of water; (c) distribution of total IT; (d) distribution of ionised betaine HCl

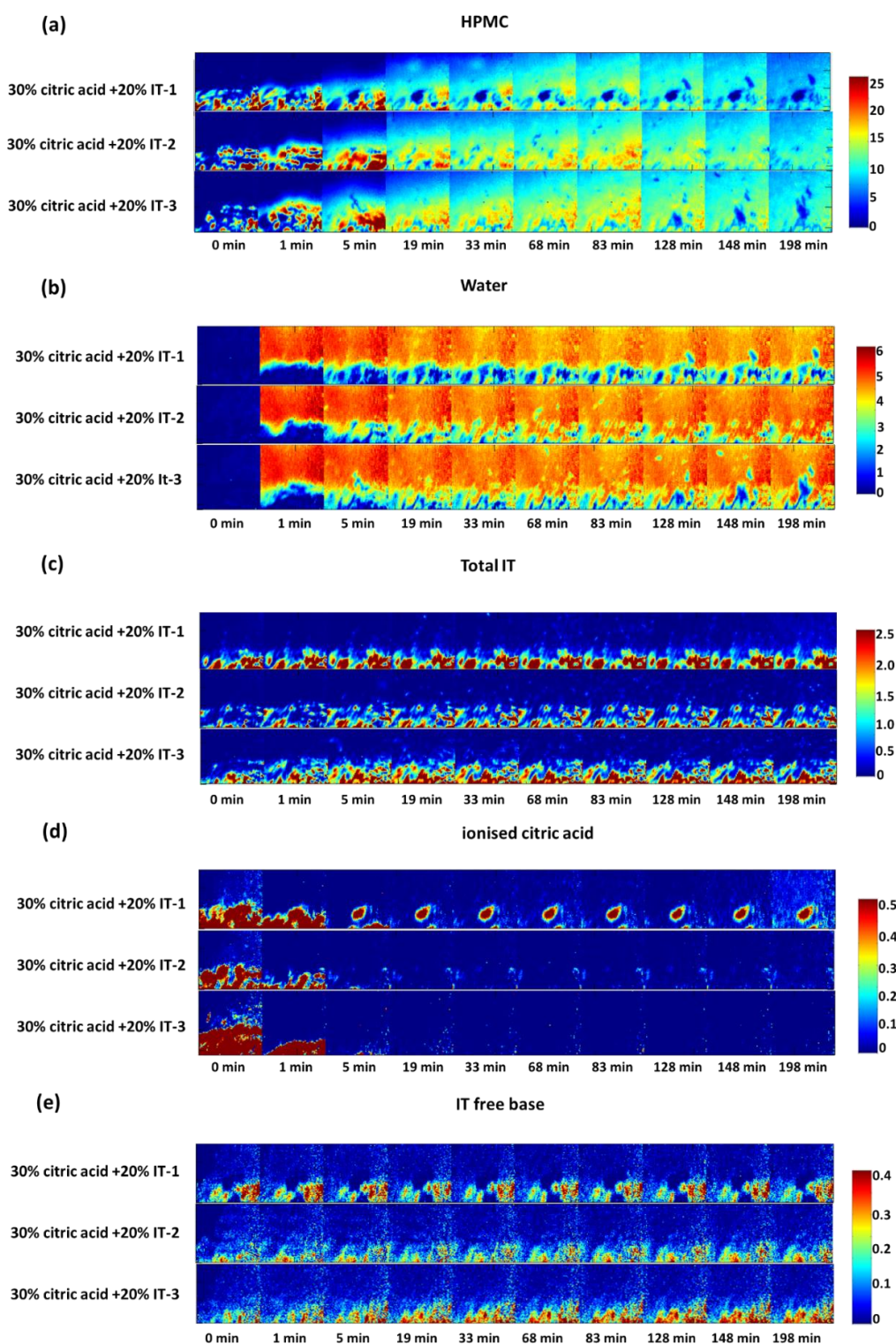


Fig. 20: Selected ATR-FTIR peak area integration images for 20% w/w IT and 30% w/w citric acid pH modifier tablets (n=3) over the hydration period, showing distribution of: (a) HPMC; (b) distribution of water; (c) distribution of total IT; (d) distribution of ionised citric acid

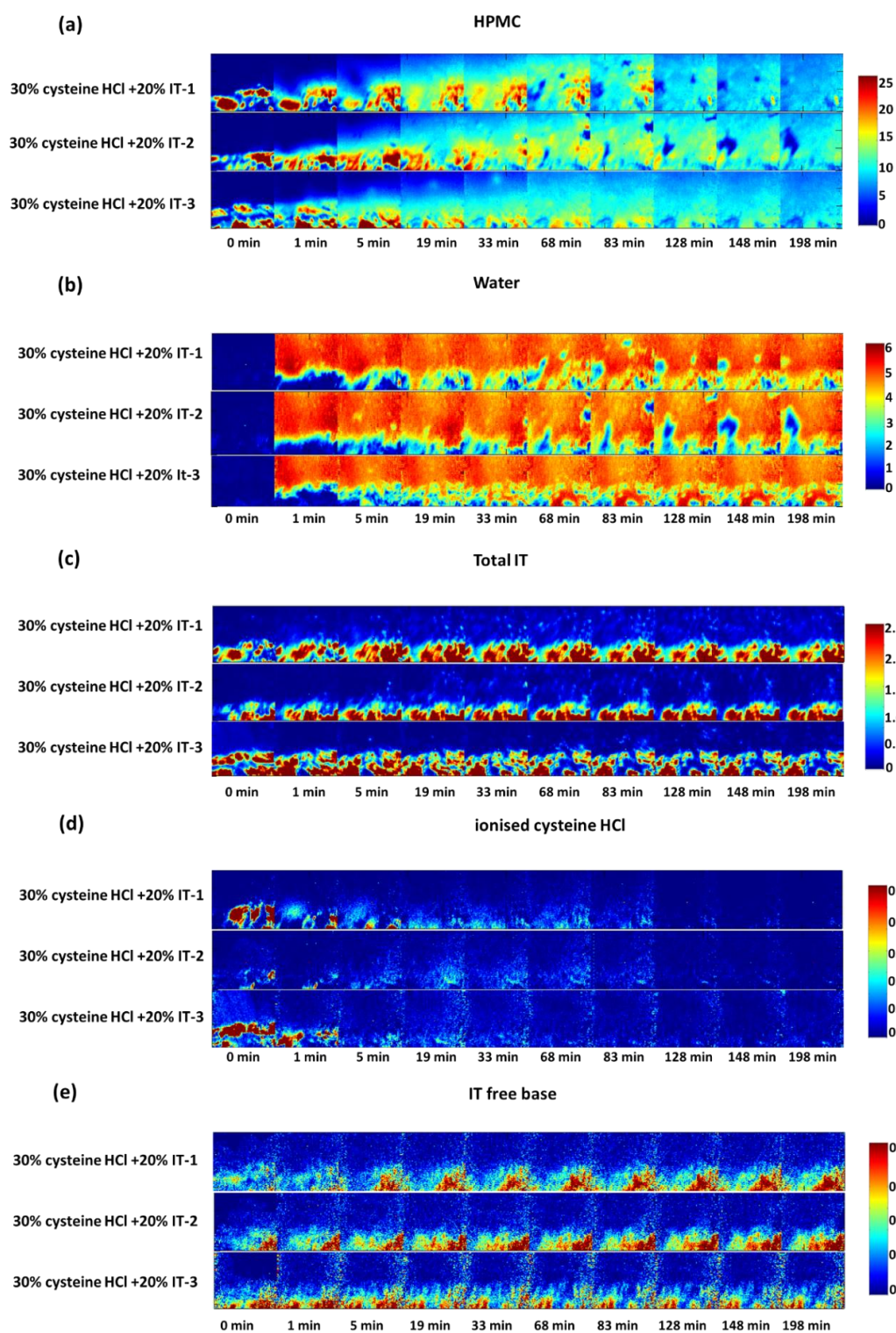


Fig. 21: Selected ATR-FTIR peak area integration images for 20% w/w IT and 30% w/w cysteine HCl pH modifier tablets (n=3) over the hydration period, showing distribution of: (a) HPMC; (b) distribution of water; (c) distribution of total IT; (d) distribution of ionised cysteine HCl

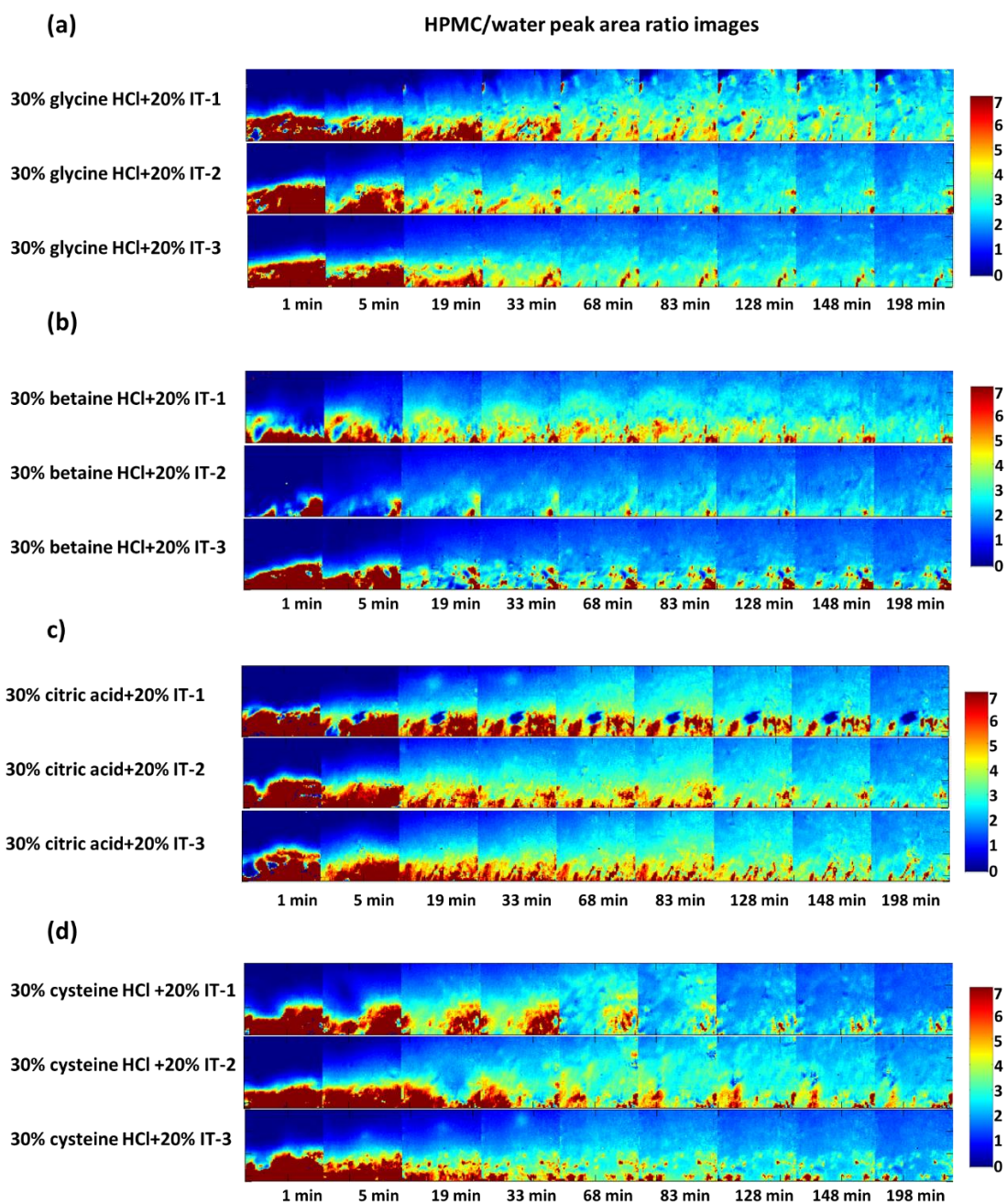


Fig. 22: ATR-FTIR peak area integration ratio images (HPMC:water) showing gel layer evolution for 30% w/w pH modifier+20% w/w IT tablets (n=3) at pH 7 for: (a) glycine HCl; (b) betaine HCl; (c) citric acid and (d) cysteine HCl

Appendix 4

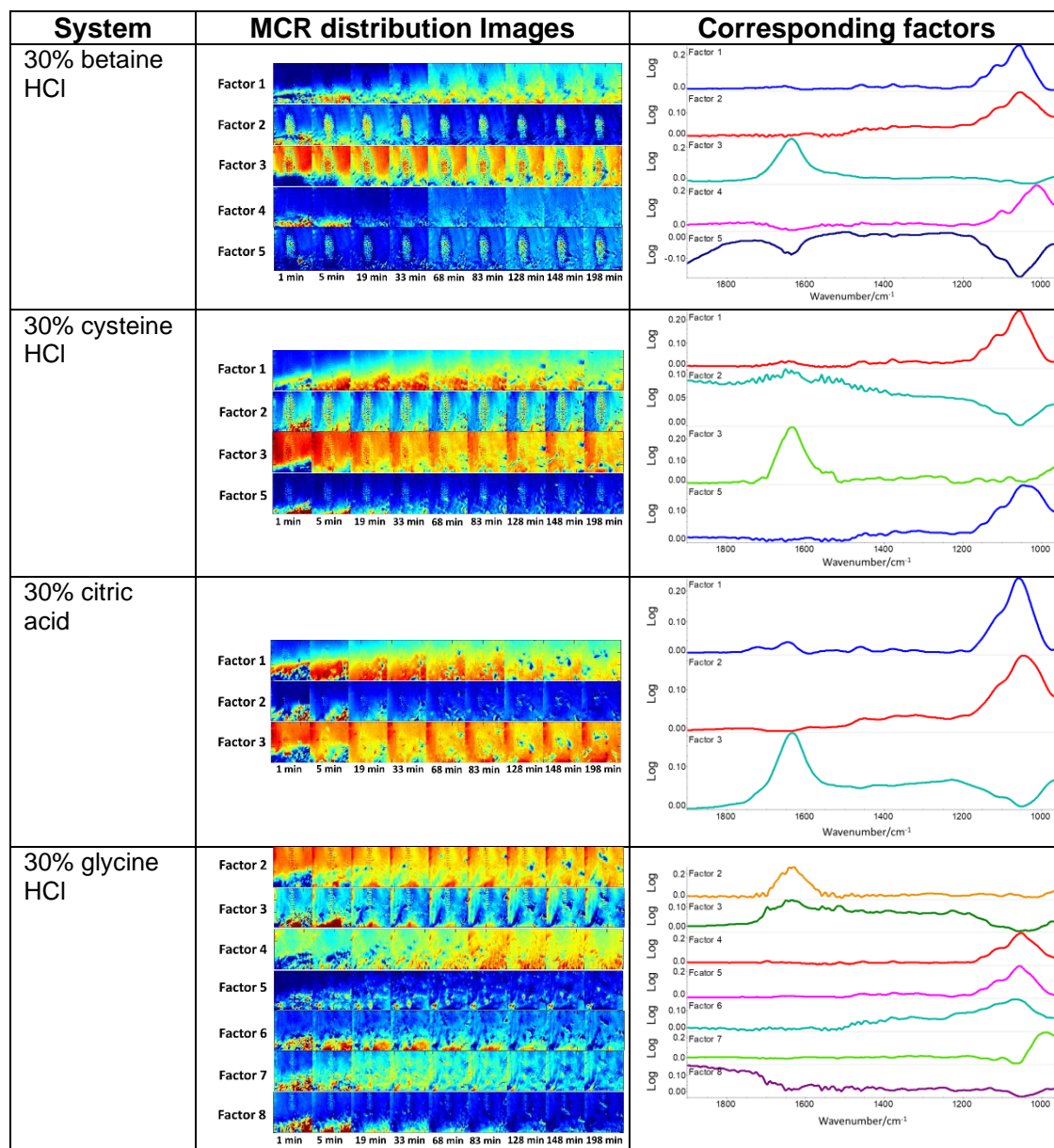


Fig. 23: Selected MCR-ALS distribution images and corresponding factors for 30% w/w modifier placebo tablets for a) betaine HCl; b) cysteine HCl; c) citric acid and d) glycine HCl

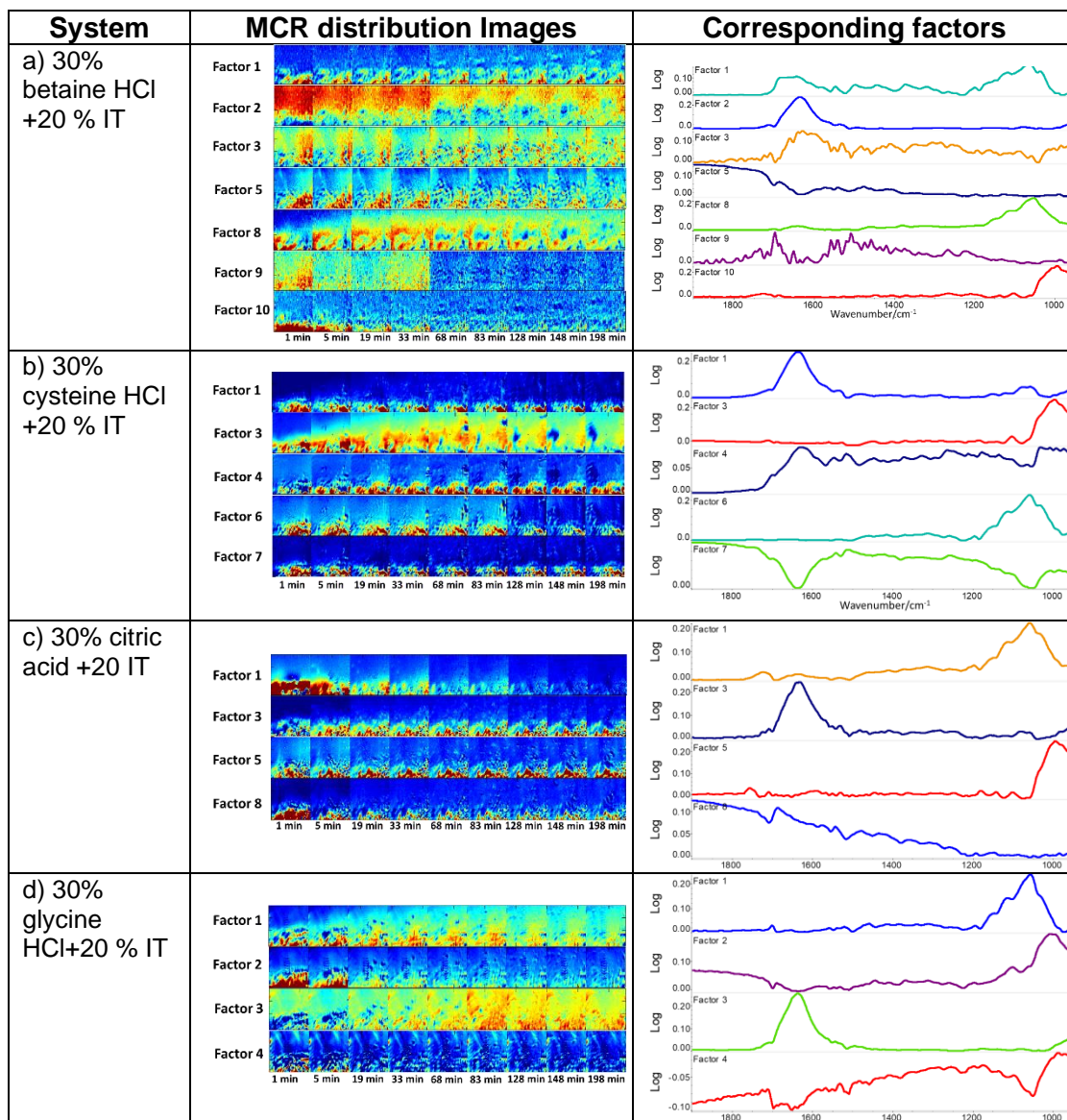
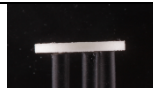
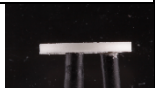
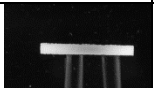
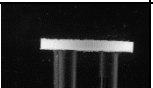
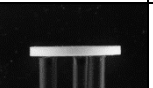
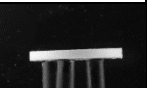
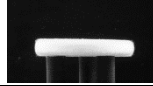
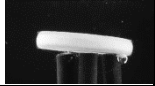
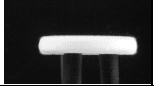
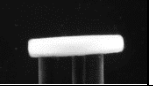
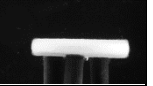
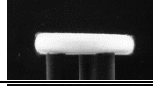
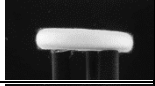
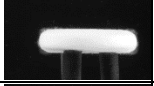
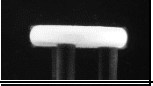
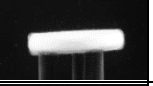
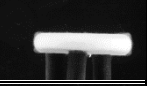
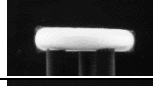
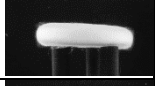
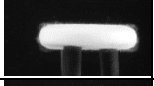
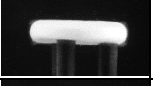
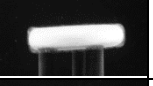
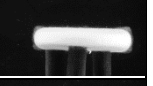
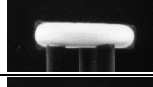
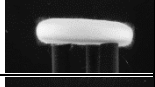
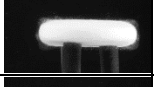
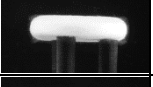
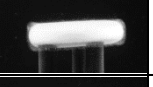
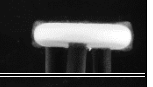
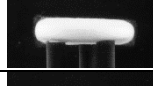
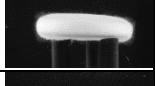
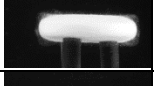
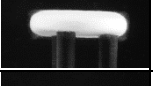
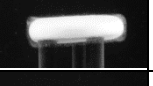
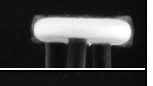
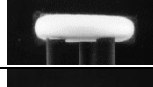
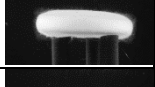
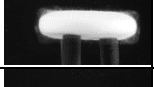
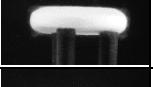
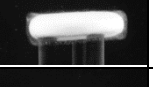
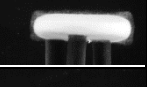
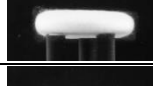
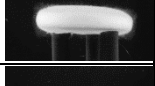
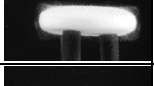
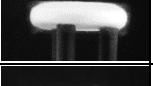
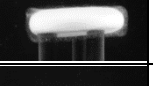
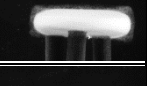
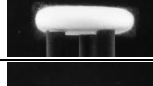
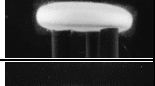
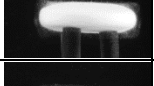
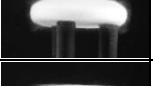
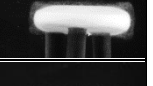
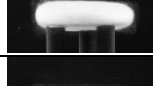
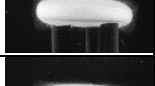
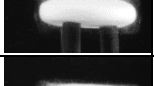
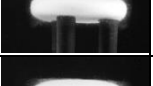
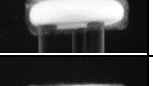
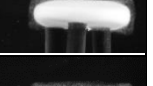
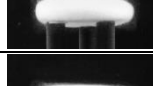
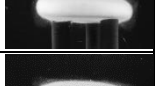
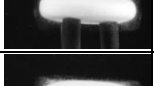
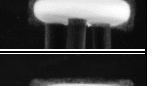
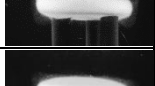
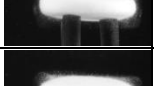
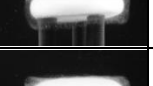
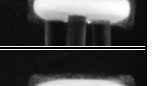
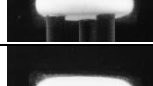
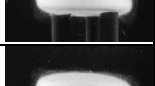
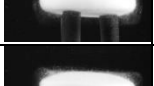
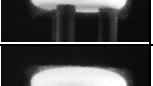
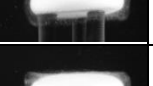
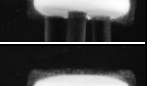
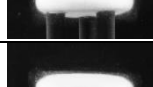
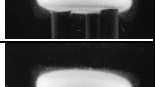
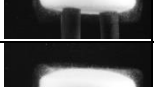
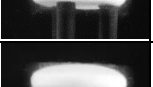
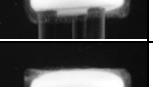
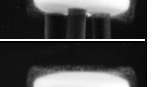
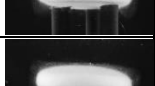
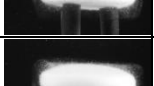
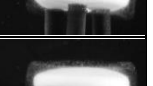
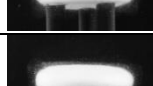
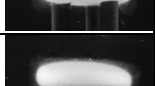
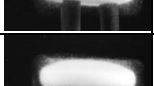
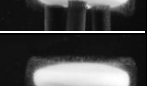
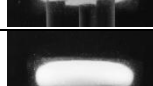
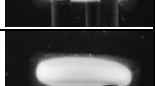
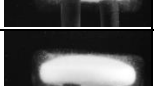
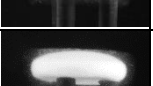
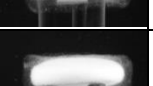
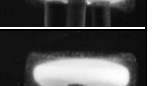
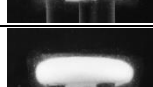
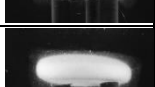
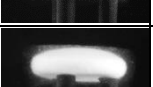
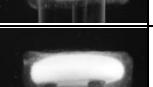
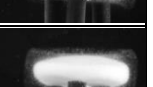
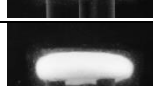
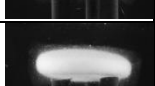
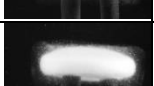
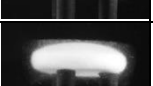
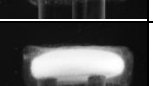
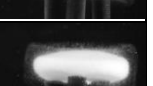


Fig. 24: Selected MCR-ALS distribution images and corresponding factors for 30% w/w modifier with 20% w/w IT tablets for a) betaine HCl; b) cysteine HCl; c) citric acid and d) glycine HCl

Appendix 5

Time/Min	Tablet 1	Tablet 2	Tablet 3	Tablet 4	Tablet 5	Tablet 6
0						
5						
10						
15						
20						
25						
30						
35						
40						
45						
50						
55						
60						
65						
70						
75						
80						
85						
90						
95						

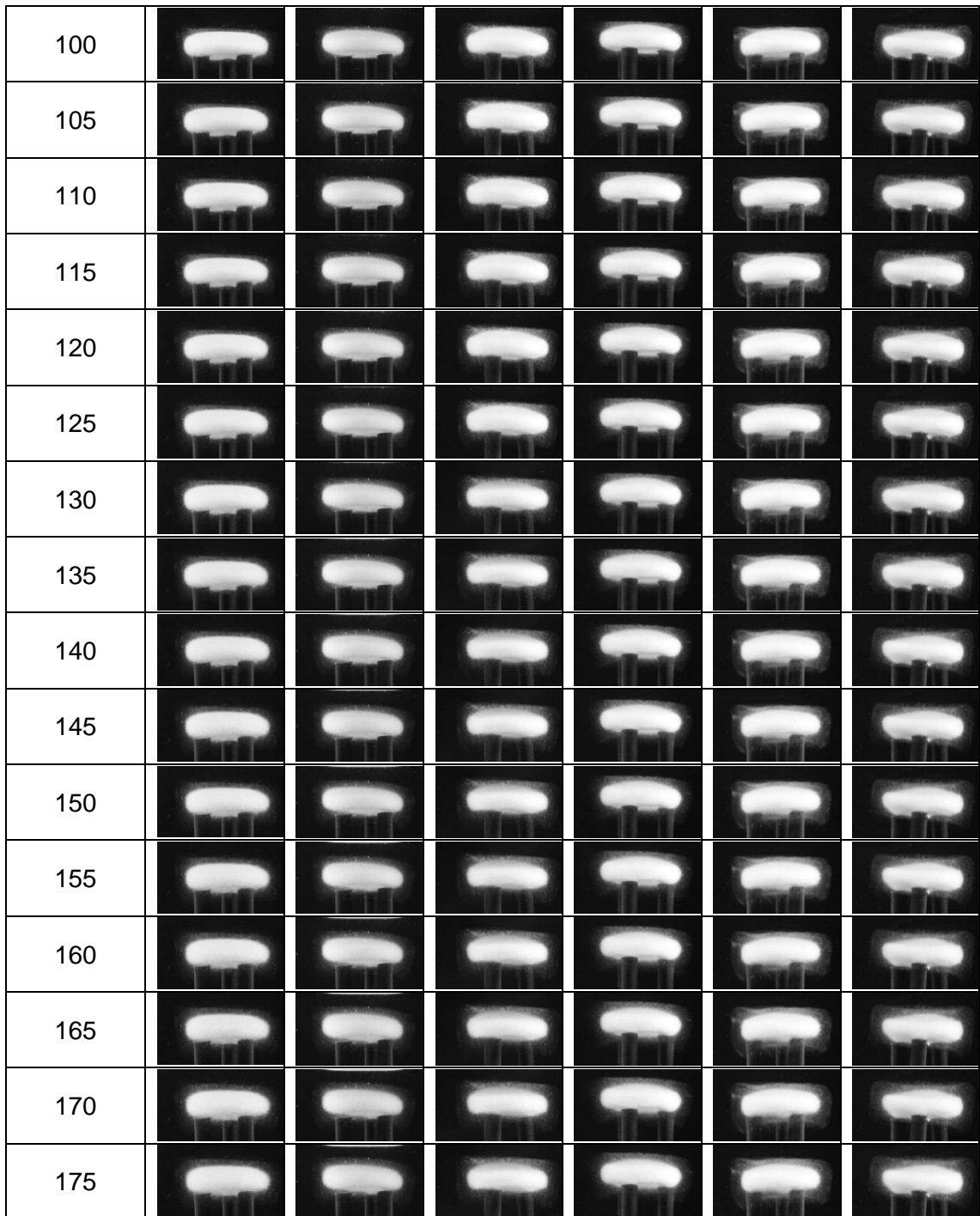


Fig. 25: Axial optical images obtained from swelling experiments (n=6) conducted on placebo tablets at pH 7

Time/Min	Tablet 1	Tablet 2	Tablet 3	Tablet 4	Tablet 5	Tablet 6
0						
5						
10						
15						
20						
25						
30						
35						
40						
45						
50						
55						
60						
65						
70						
75						
80						
85						
90						
95						

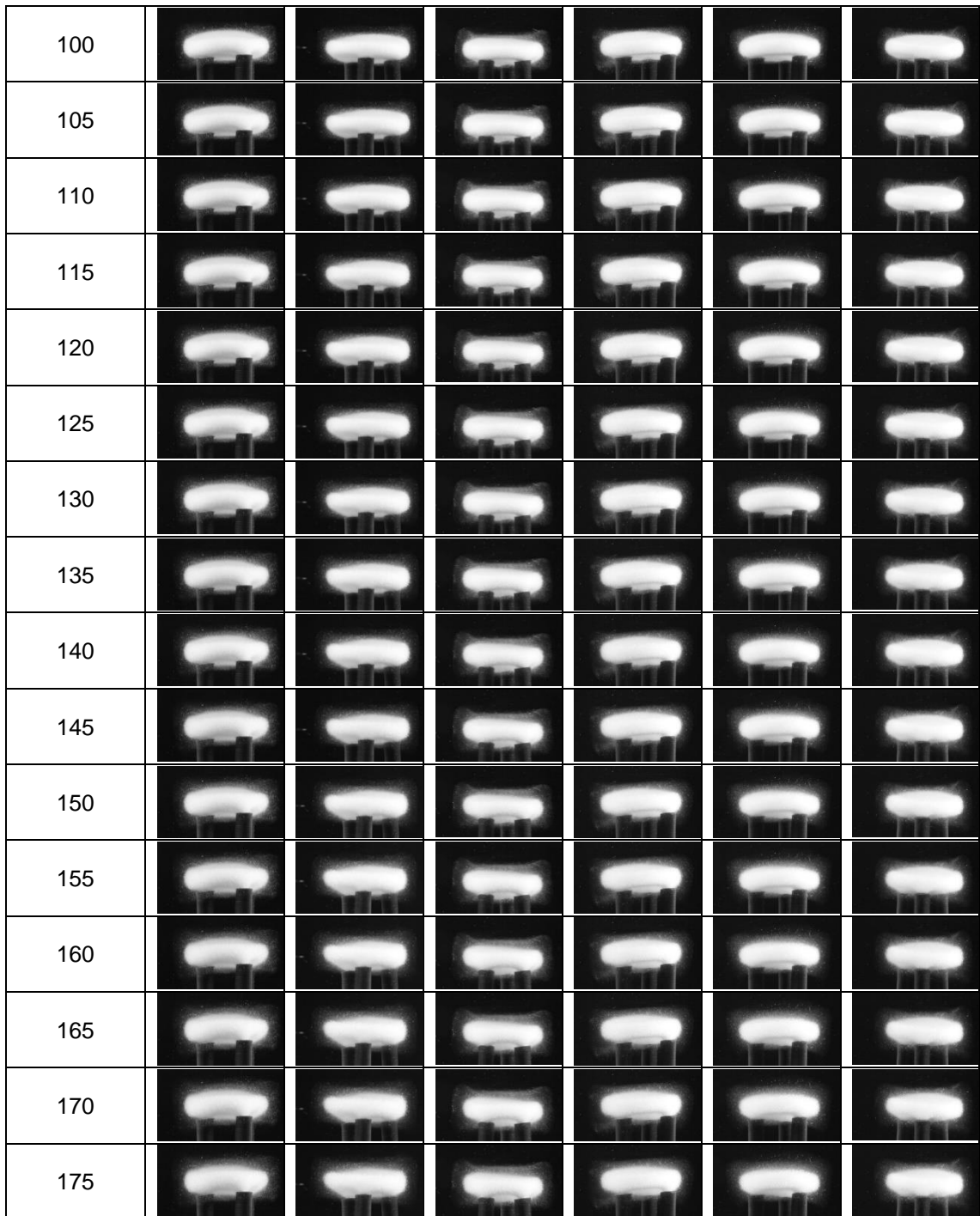


Fig. 26: Axial optical images obtained from swelling experiments (n=6) conducted on placebo tablets at pH 1.5

Time/min	Tablet 1	Tablet 2	Tablet 3	Tablet 4	Tablet 5	Tablet 6
0						
5						
10						
15						
20						
25						
30						
35						
40						
45						
50						
55						
60						
65						

70						
75						
80						
85						
90						
95						
100						
105						
110						
115						
120						
125						
130						
135						

140						
145						
150						
155						
160						
165						
170						
175						

Fig. 27: Radial optical images obtained from swelling experiments (n=6) conducted on placebo tablets at pH 1.5

Time/min	Tablet 1	Tablet 2	Tablet 3	Tablet 4	Tablet 5	Tablet 6
0						
5						
10						
15						
20						
25						
30						
35						
40						
45						
50						
55						
60						
65						

70						
75						
80						
85						
90						
95						
100						
105						
110						
115						
120						
125						
130						
135						

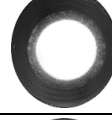
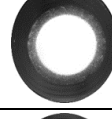
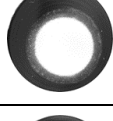
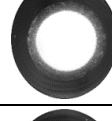
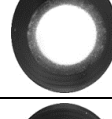
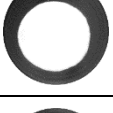
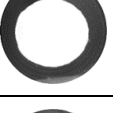
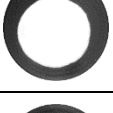
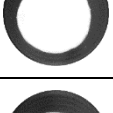
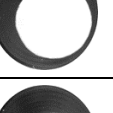
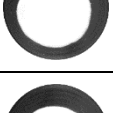
140						
145						
150						
155						
160						
165						
170						
175						

Fig. 28: Radial optical images obtained from swelling experiments (n=6) conducted on 20% w/w IT tablets at pH 7

Time/min	Tablet 1	Tablet 2	Tablet 3	Tablet 4	Tablet 5	Tablet 6
0						
5						
10						
15						
20						
25						
30						
35						
40						
45						
50						
55						
60						
65						

70						
75						
80						
85						
90						
95						
100						
105						
110						
115						
120						
125						
130						
135						

140						
145						
150						
155						
160						
165						
170						
175						

Fig. 29: Radial optical images obtained from swelling experiments (n=6) conducted on 20% w/w IT tablets at pH 1.5

Time/min	Tablet 1	Tablet 2	Tablet 3	Tablet 4	Tablet 5	Tablet 6
0						
5						
10						
15						
20						
25						
30						
35						
40						
45						
50						
55						
60						
65						

70						
75						
80						
85						
90						
95						
100						
105						
110						
115						
120						
125						
130						
135						

140							
145							
150							
155							
160							
165							
170							
175							

Fig. 30: Radial optical images obtained from swelling experiments (n=6) conducted on 20% w/w IT tablets at pH 7

Time/min	Tablet 1	Tablet 2	Tablet 3	Tablet 4	Tablet 5	Tablet 6
0						
5						
10						
15						
20						
25						
30						
35						
40						
45						
50						
55						
60						
65						
70						
75						
80						
85						
90						
95						
100						

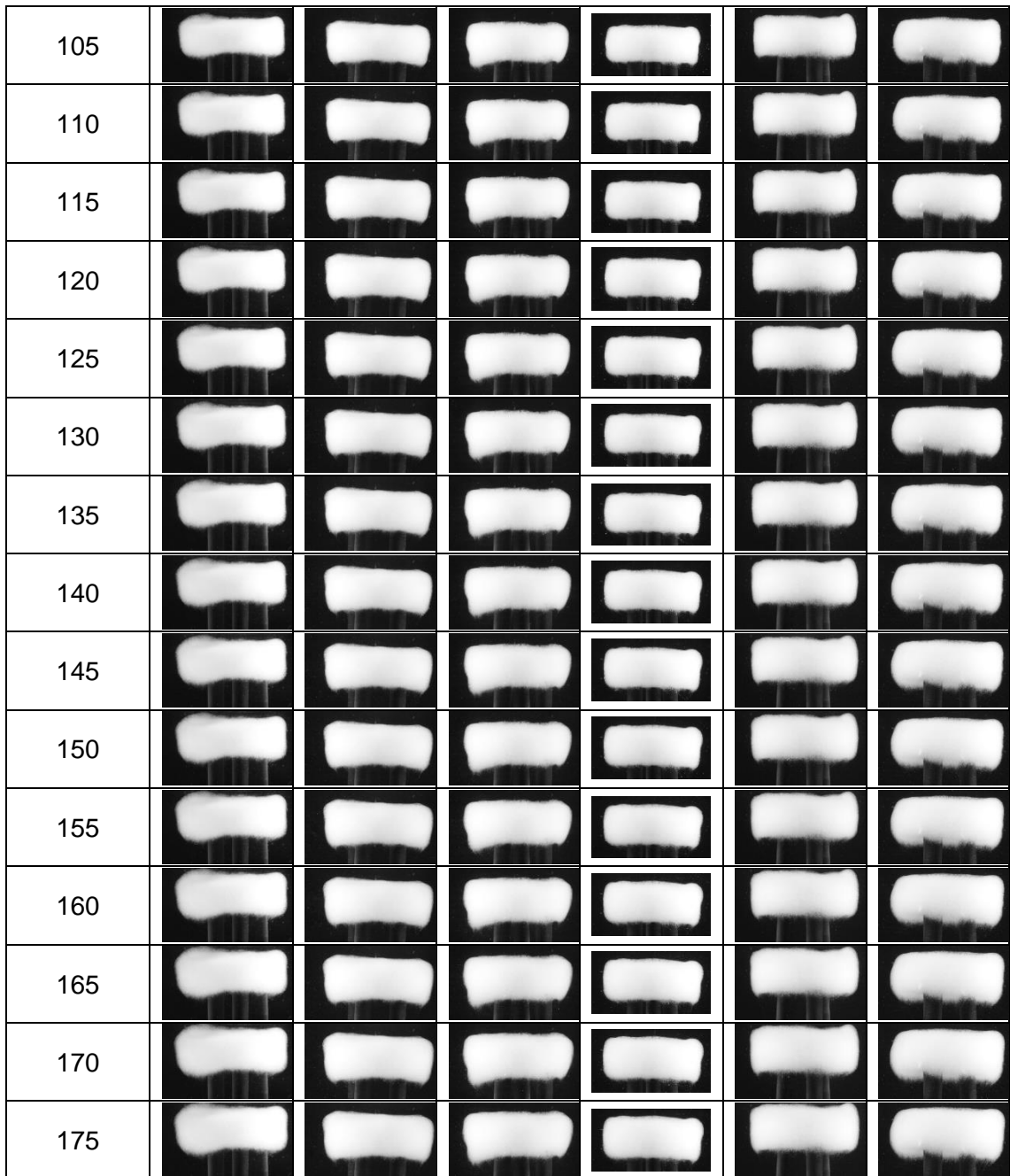
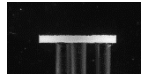
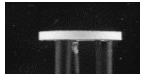
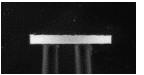
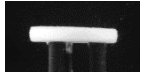
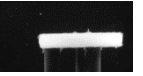
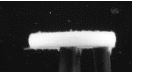
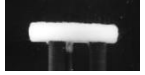
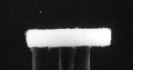
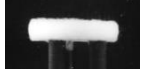
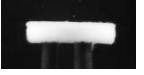
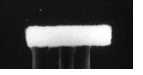
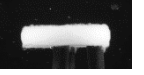
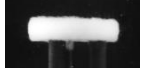
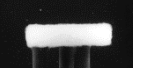
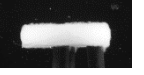
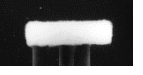
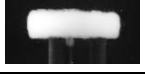
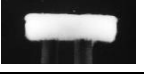
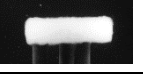
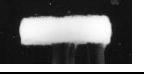
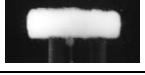
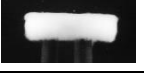
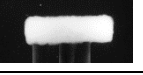
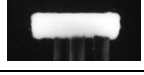
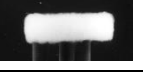
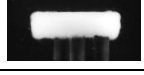
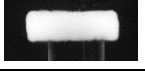
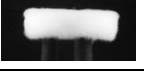
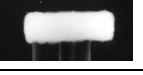
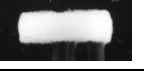
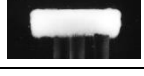
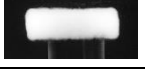
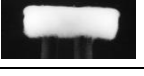
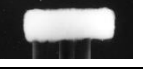
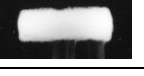
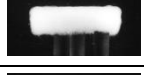
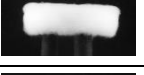
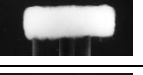
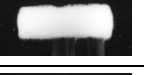
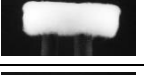
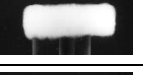
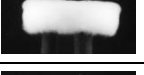
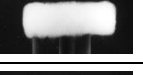
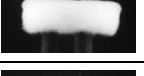
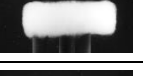
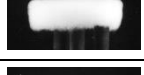
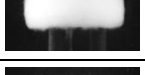
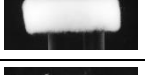
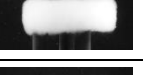
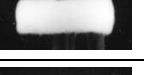
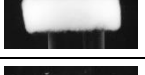
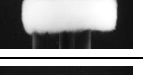
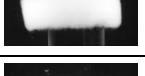
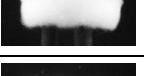
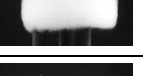
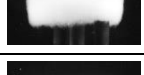
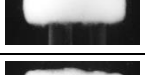
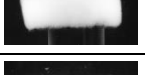
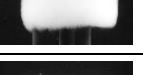


Fig. 31: Axial optical images obtained from swelling experiments (n=6) conducted on 20% w/w IT tablets at pH 7

Time/min	Tablet 1	Tablet 2	Tablet 3	Tablet 4	Tablet 5	Tablet 6
0						
5						
10						
15						
20						
25						
30						
35						
40						
45						
50						
55						
60						
65						
70						
75						
80						
85						
90						
95						
100						

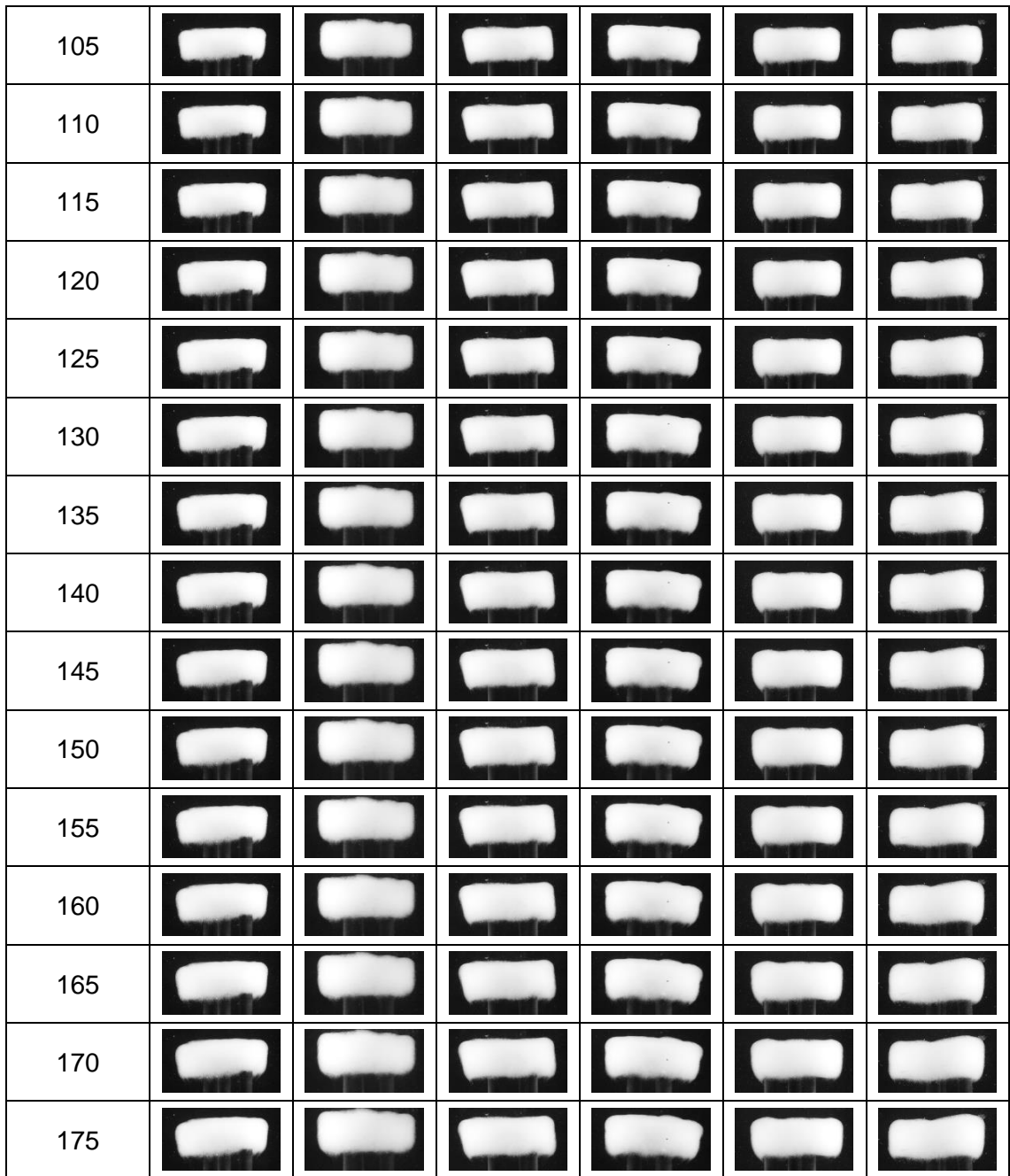
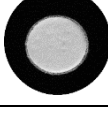
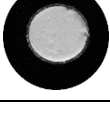
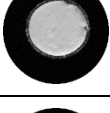
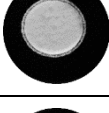
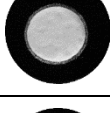
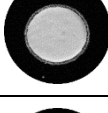
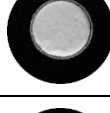
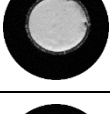
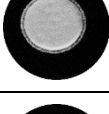
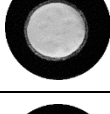
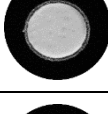
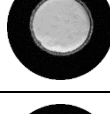
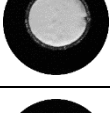
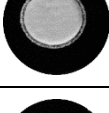
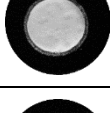
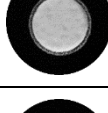
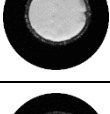
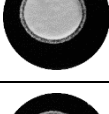
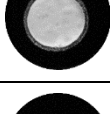
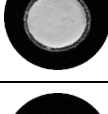
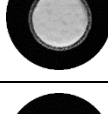
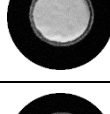
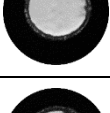
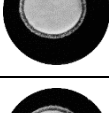
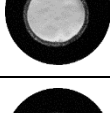
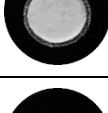
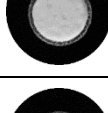
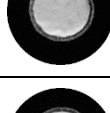
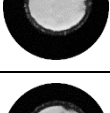
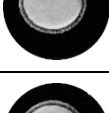
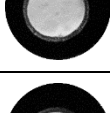
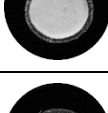
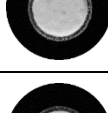
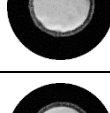
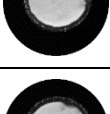
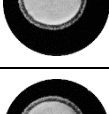
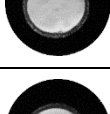
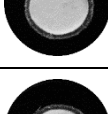
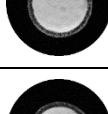
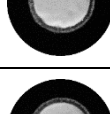
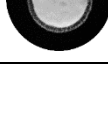
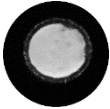
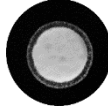
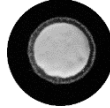
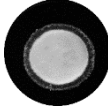
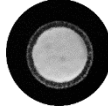
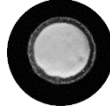
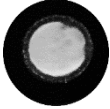
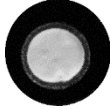
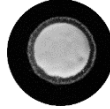
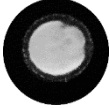
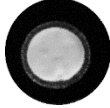
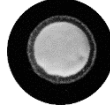
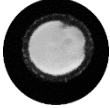
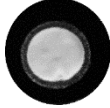
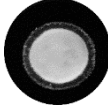
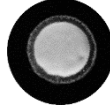
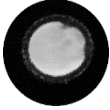
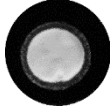
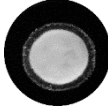
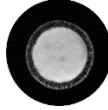
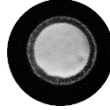
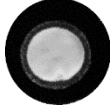
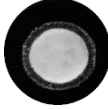
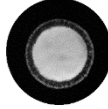
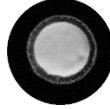
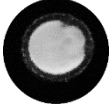
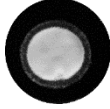
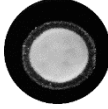
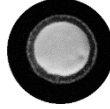
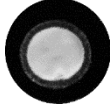
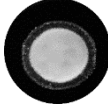
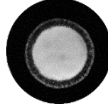
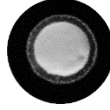
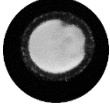
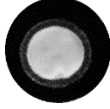
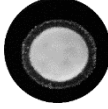
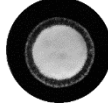
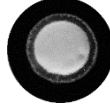
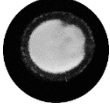
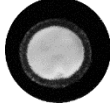
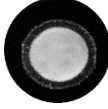
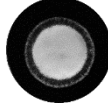
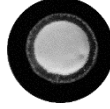
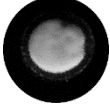
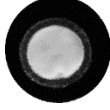
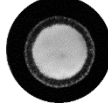
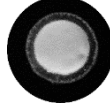


Fig. 32: Axial optical images obtained from swelling experiments (n=6) conducted on 20% w/w IT tablets at pH 1.5

Appendix 6

Time/min	Tablet 1	Tablet 2	Tablet 3	Tablet 4	Tablet 5	Tablet 6
0						
5						
10						
15						
20						
25						
30						
35						
40						
45						
50						
55						
60						

65						
70						
75						
80						
85						
90						
95						
100						
105						
110						
115						
120						
125						
130						

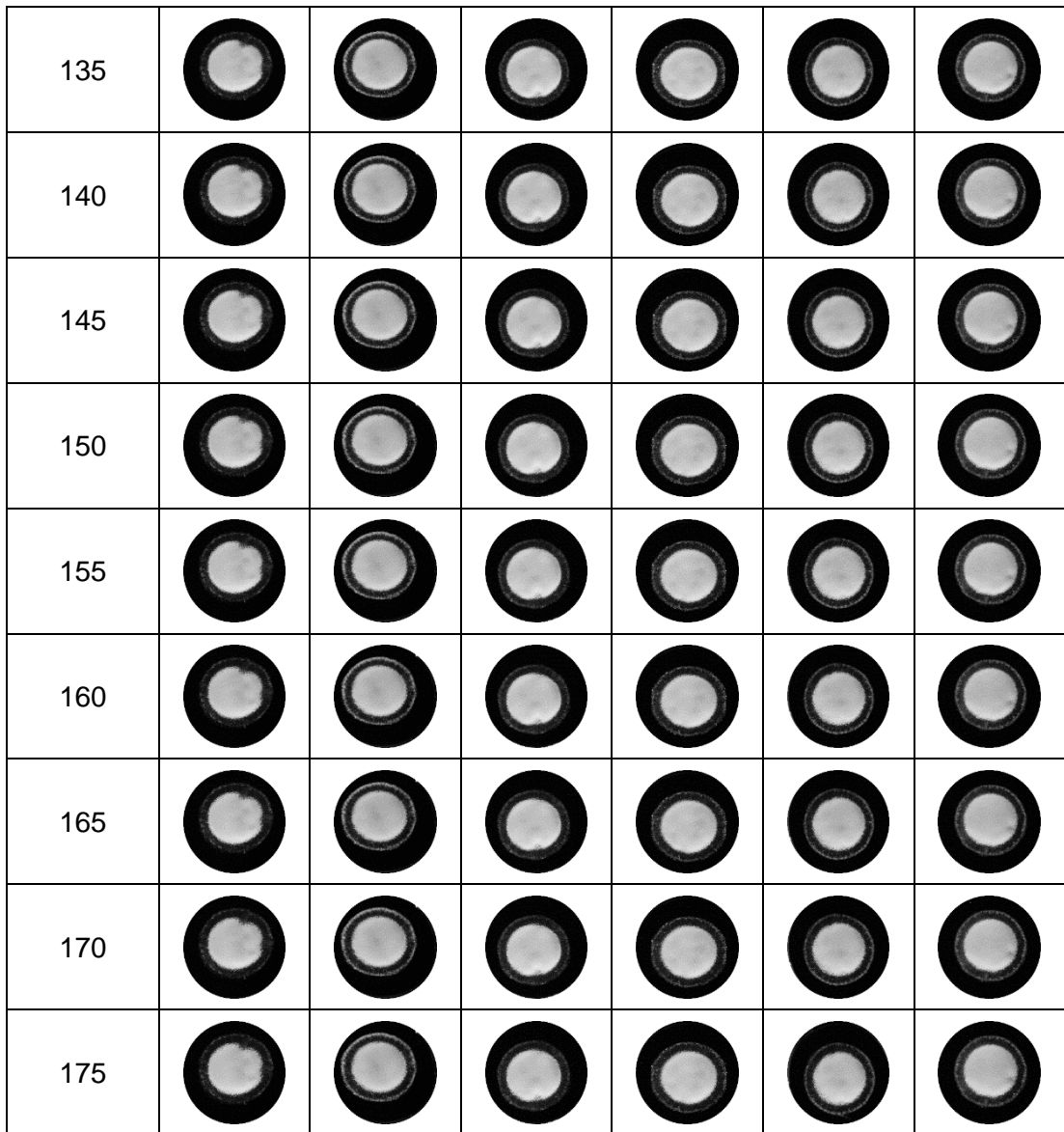
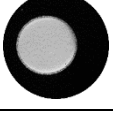
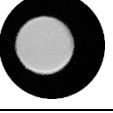
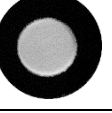
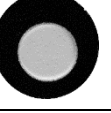
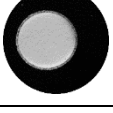
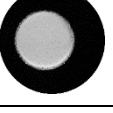
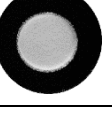
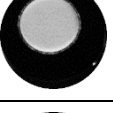
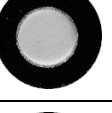
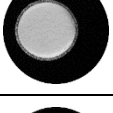
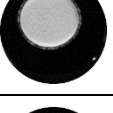
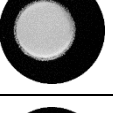
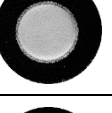
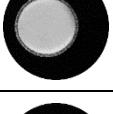
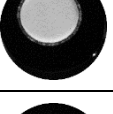
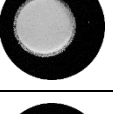
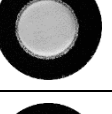
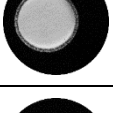
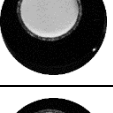
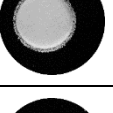
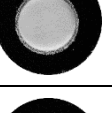
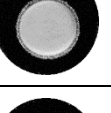
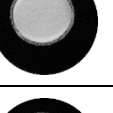
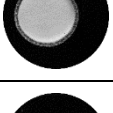
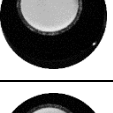
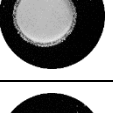
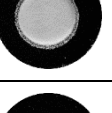
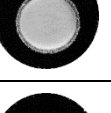
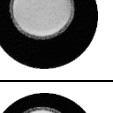
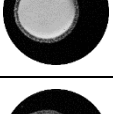
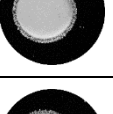
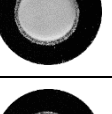
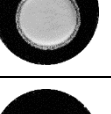
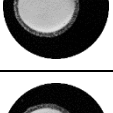
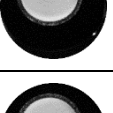
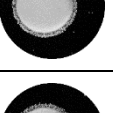
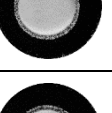
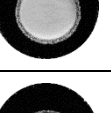
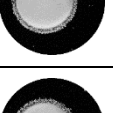
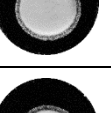
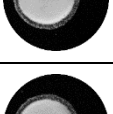
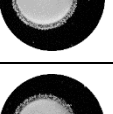
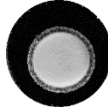
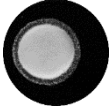
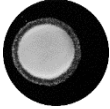
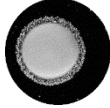
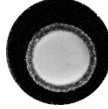
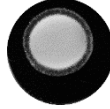
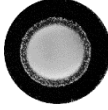
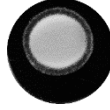
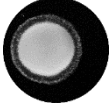
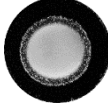
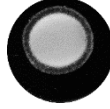
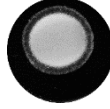
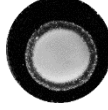
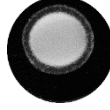


Fig. 33: Radial optical images obtained from swelling experiments (n=6) conducted on tablets containing 10% w/w betaine HCl with 20% w/w IT at pH 7

Time/min	Tablet 1	Tablet 2	Tablet 3	Tablet 4	Tablet 5	Tablet 6
0						
5						
10						
15						
20						
25						
30						
35						
40						
45						
50						
55						
60						
65						

70						
75						
80						
85						
90						
95						
100						
105						
110						
115						
120						
125						
130						
135						

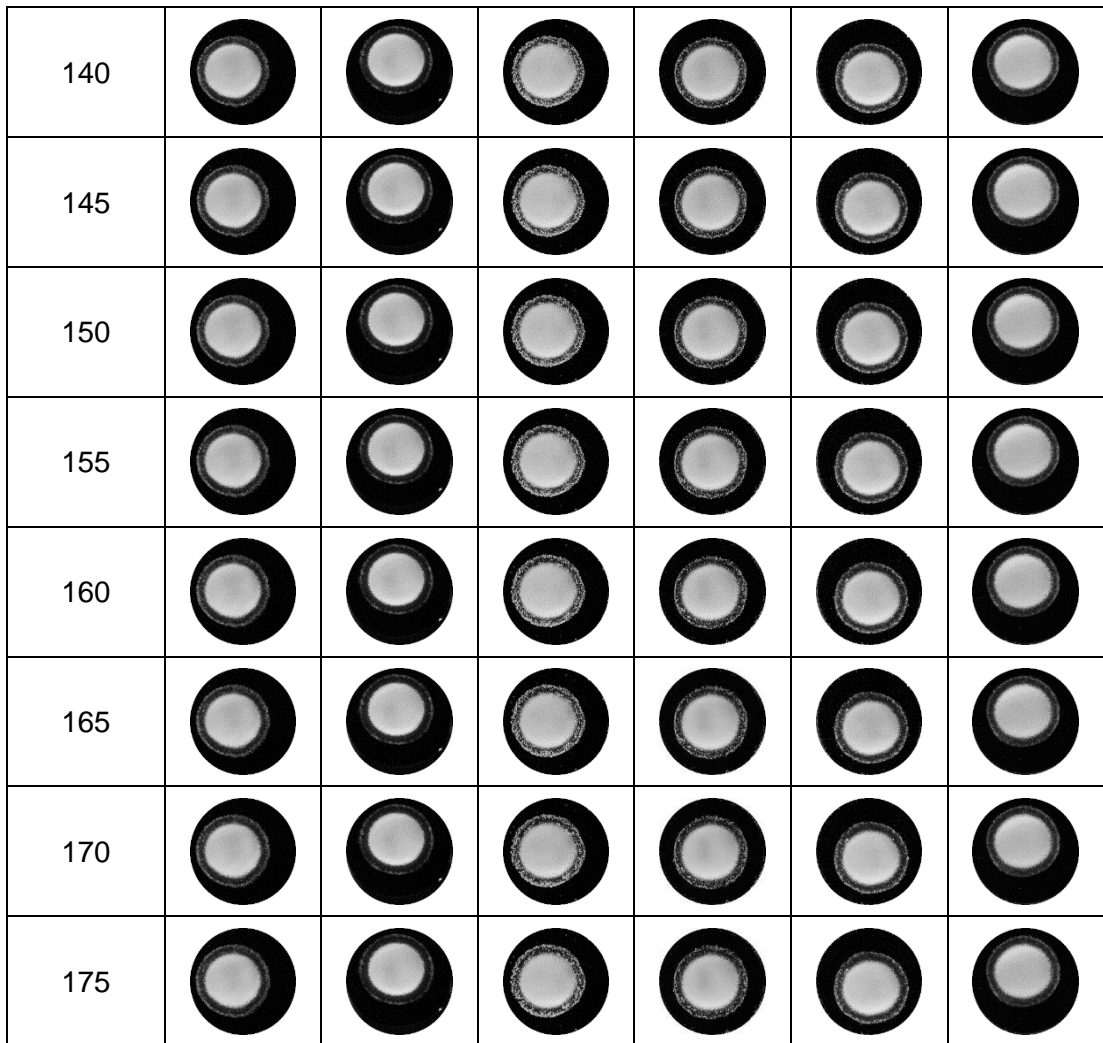
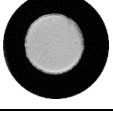
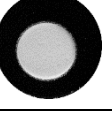
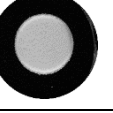
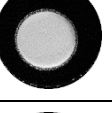
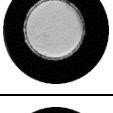
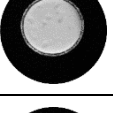
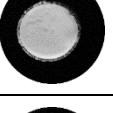
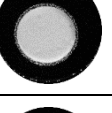
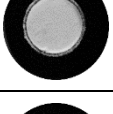
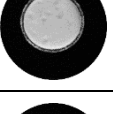
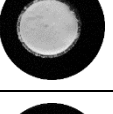
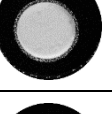
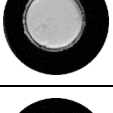
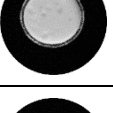
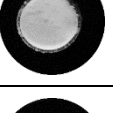
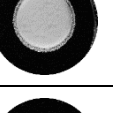
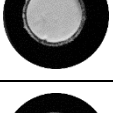
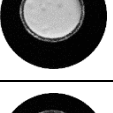
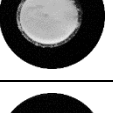
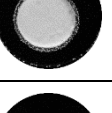
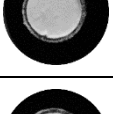
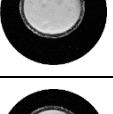
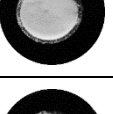
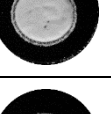
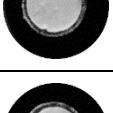
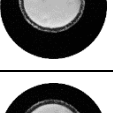
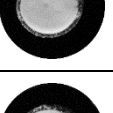
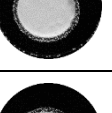
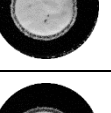
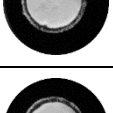
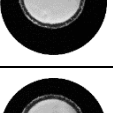
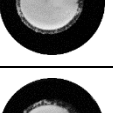
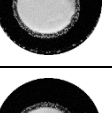
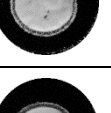
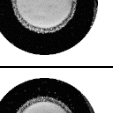
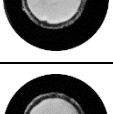
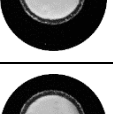
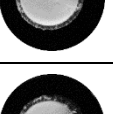
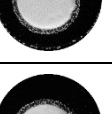
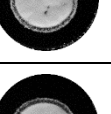
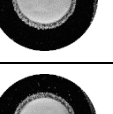
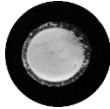
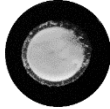
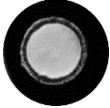
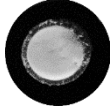
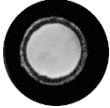
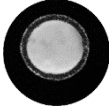
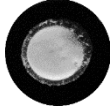
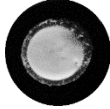
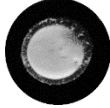
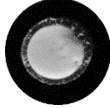
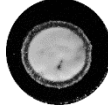
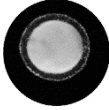
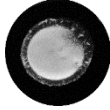
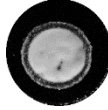
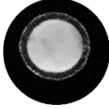
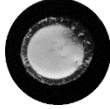
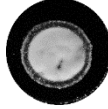
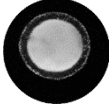
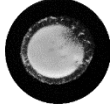
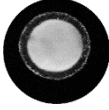
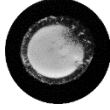
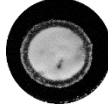
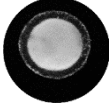
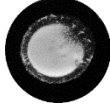
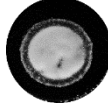
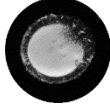
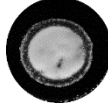
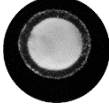
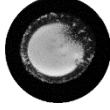
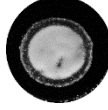


Fig. 34: Radial optical images obtained from swelling experiments (n=6) conducted on tablets containing 10% w/w citric acid at pH 7

Time/min	Tablet 1	Tablet 2	Tablet 3	Tablet 4	Tablet 5	Tablet 6
0						
5						
10						
15						
20						
25						
30						
35						
40						
45						
50						
55						
60						
65						

70						
75						
80						
85						
90						
95						
100						
105						
110						
115						
120						
125						
130						
135						

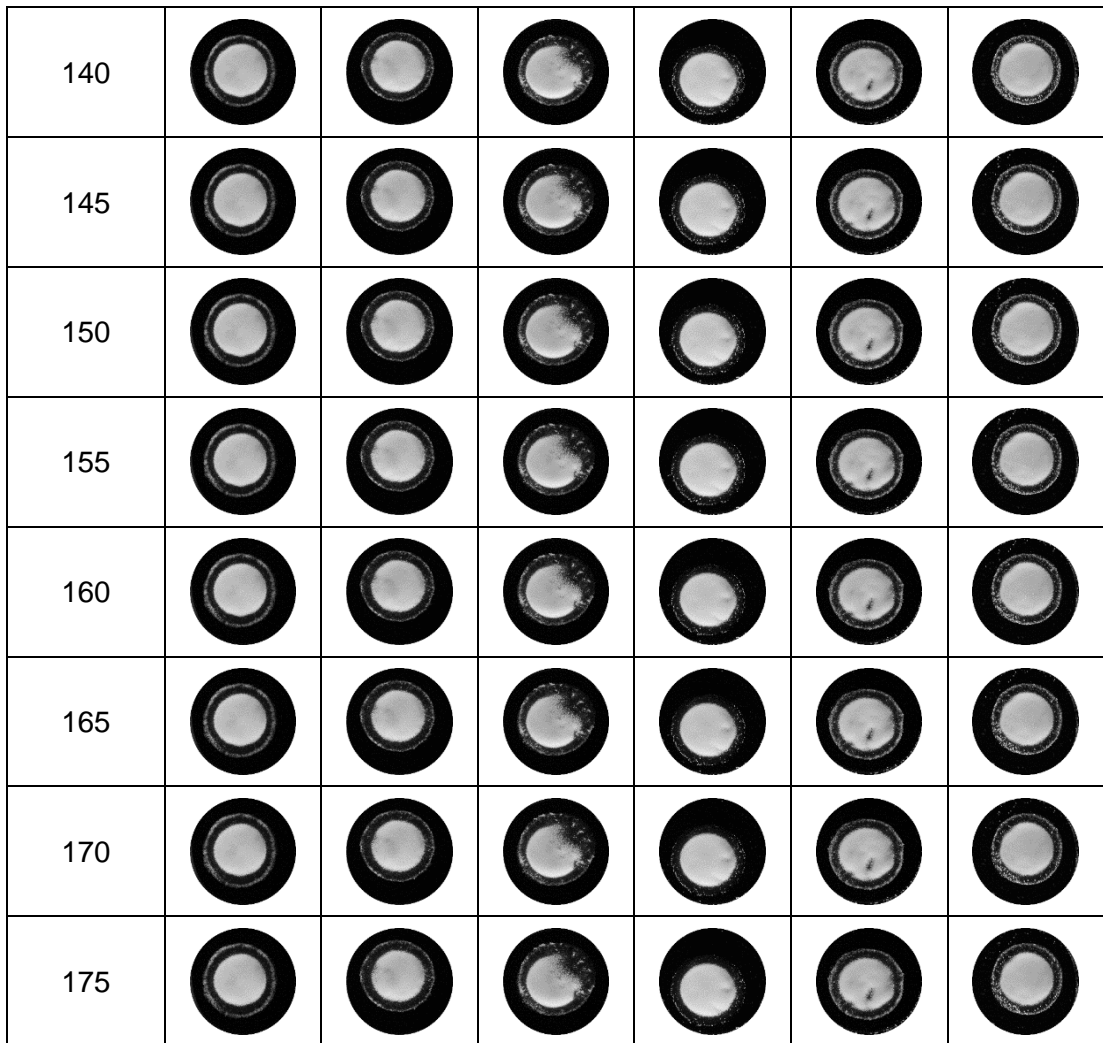
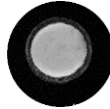
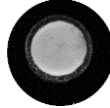
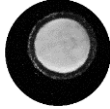
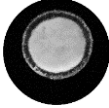
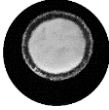
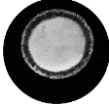
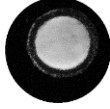
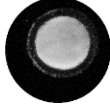
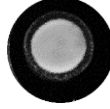


Fig. 35: Radial optical images obtained from swelling experiments (n=6) conducted on tablets containing 10% w/w cysteine HCl at pH 7

Time/min	Tablet 1	Tablet 2	Tablet 3	Tablet 4	Tablet 5	Tablet 6
0						
5						
10						
15						
20						
25						
30						
35						
40						
45						
50						
55						
60						
65						

70						
75						
80						
85						
90						
95						
100						
105						
110						
115						
120						
125						
130						
135						

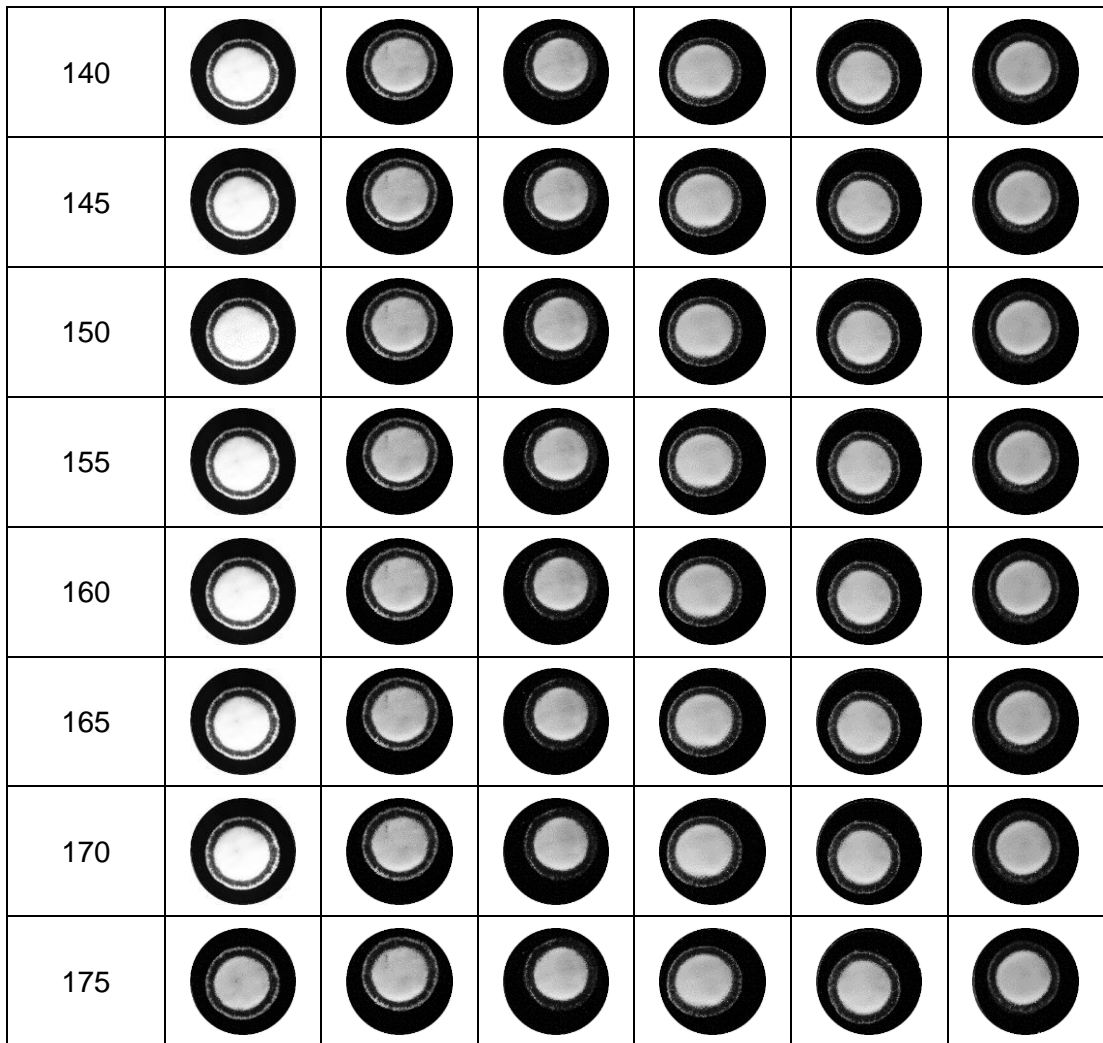
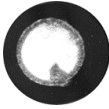
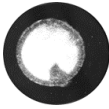
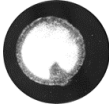
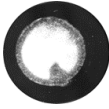
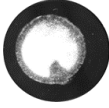
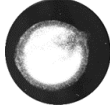
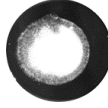
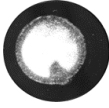
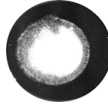
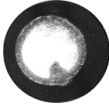
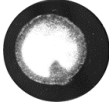
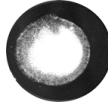
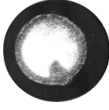
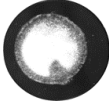
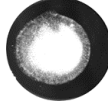
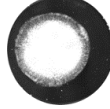
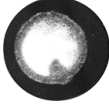
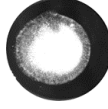
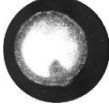
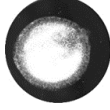
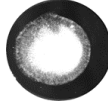


Fig. 36: Radial optical images obtained from swelling experiments (n=6) conducted on tablets containing 10% w/w glycine HCl at pH 7

Time/min	Tablet 1	Tablet 2	Tablet 3	Tablet 4	Tablet 5	Tablet 6
0						
5						
10						
15						
20						
25						
30						
35						
40						
45						
50						
55						
60						
65						

70						
75						
80						
85						
90						
95						
100						
105						
110						
115						
120						
125						
130						
135						

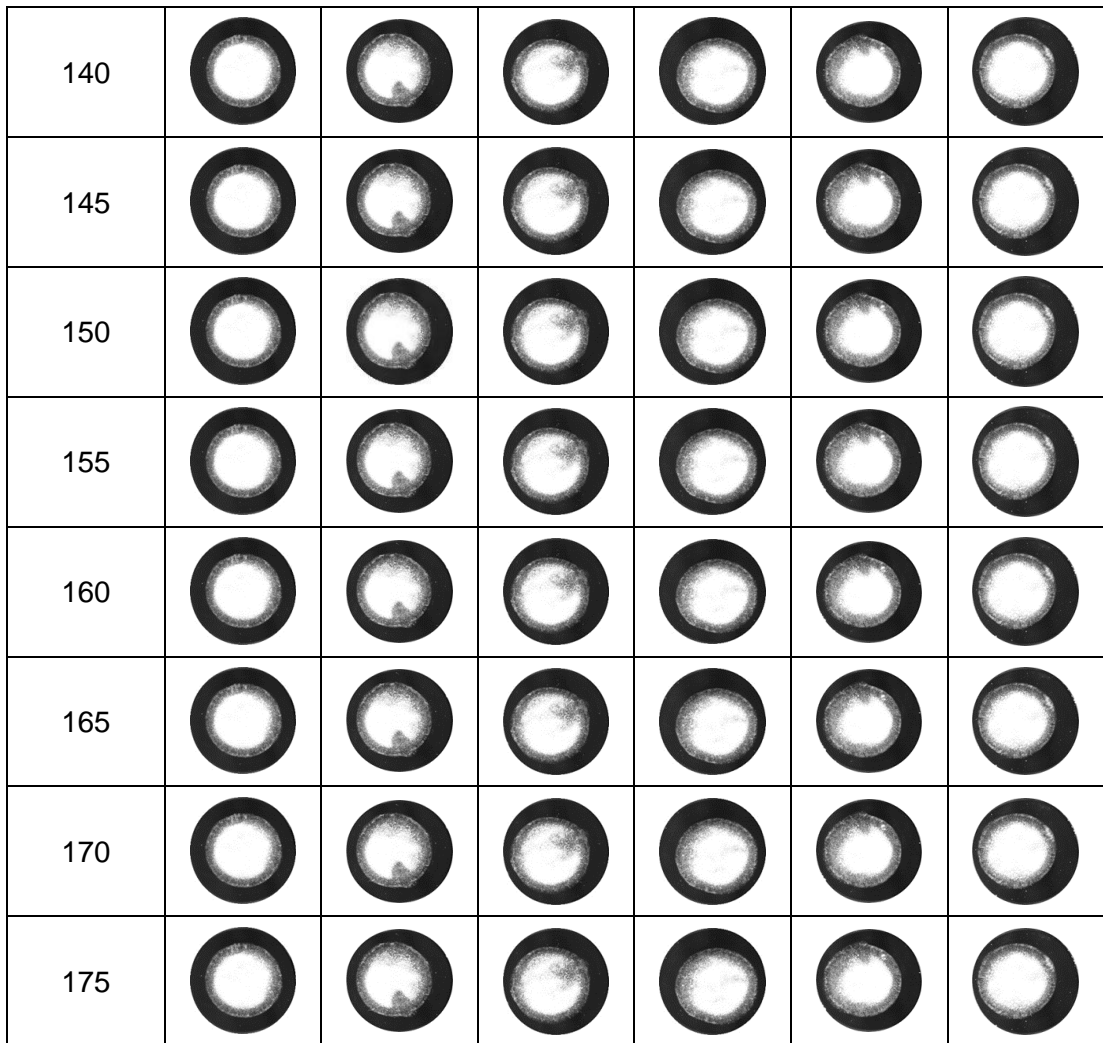
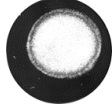


Fig. 37: Radial optical images obtained from swelling experiments (n=6) conducted on tablets containing 30% w/w betaine HCl at pH 7

Time/min	Tablet 1	Tablet 2	Tablet 3	Tablet 4	Tablet 5	Tablet 6
0						
5						
10						
15						
20						
25						
30						
35						
40						
45						
50						
55						
60						
65						

70						
75						
80						
85						
90						
95						
100						
105						
110						
115						
120						
125						
130						
135						

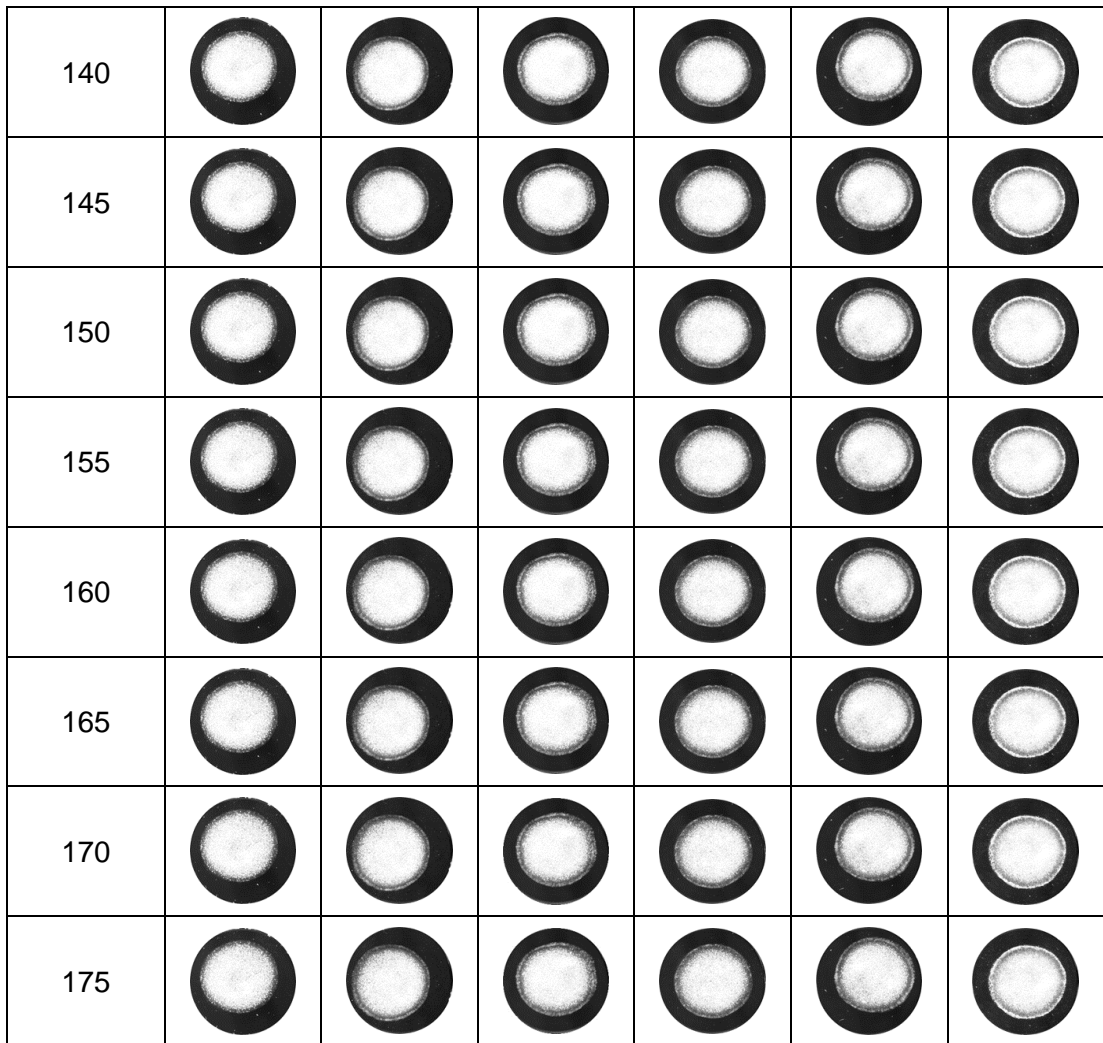
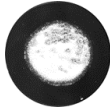
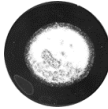
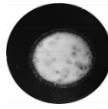
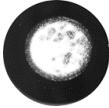
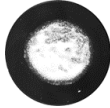
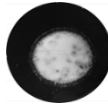
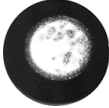
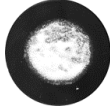
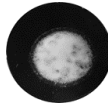
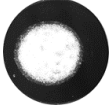
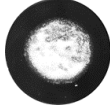
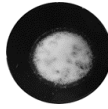
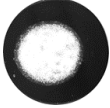
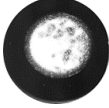
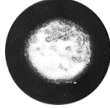
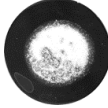
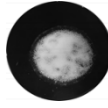
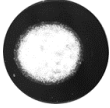
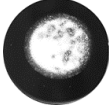
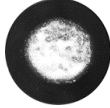
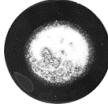
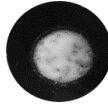
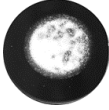
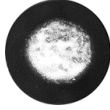
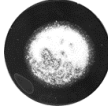
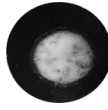
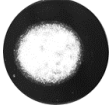
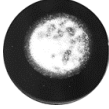
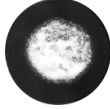
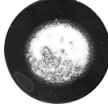
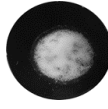
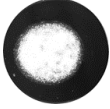
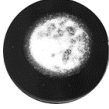
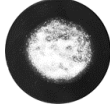
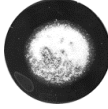
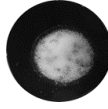
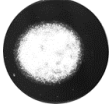
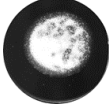
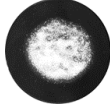
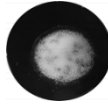
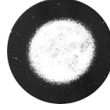
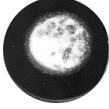
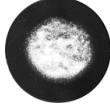
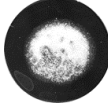
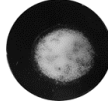
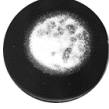
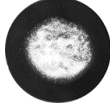
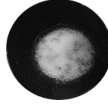
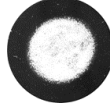
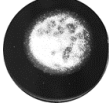
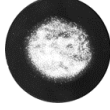
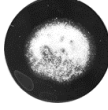
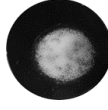
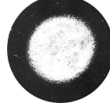


Fig. 38: Radial optical images obtained from swelling experiments (n=6) conducted on tablets containing 30% w/w citric acid at pH 7

Time/min	Tablet 1	Tablet 2	Tablet 3	Tablet 4	Tablet 5	Tablet 6
0						
5						
10						
15						
20						
25						
30						
35						
40						
45						
50						
55						
60						
65						

70						
75						
80						
85						
90						
95						
100						
105						
110						
115						
120						
125						
130						
135						

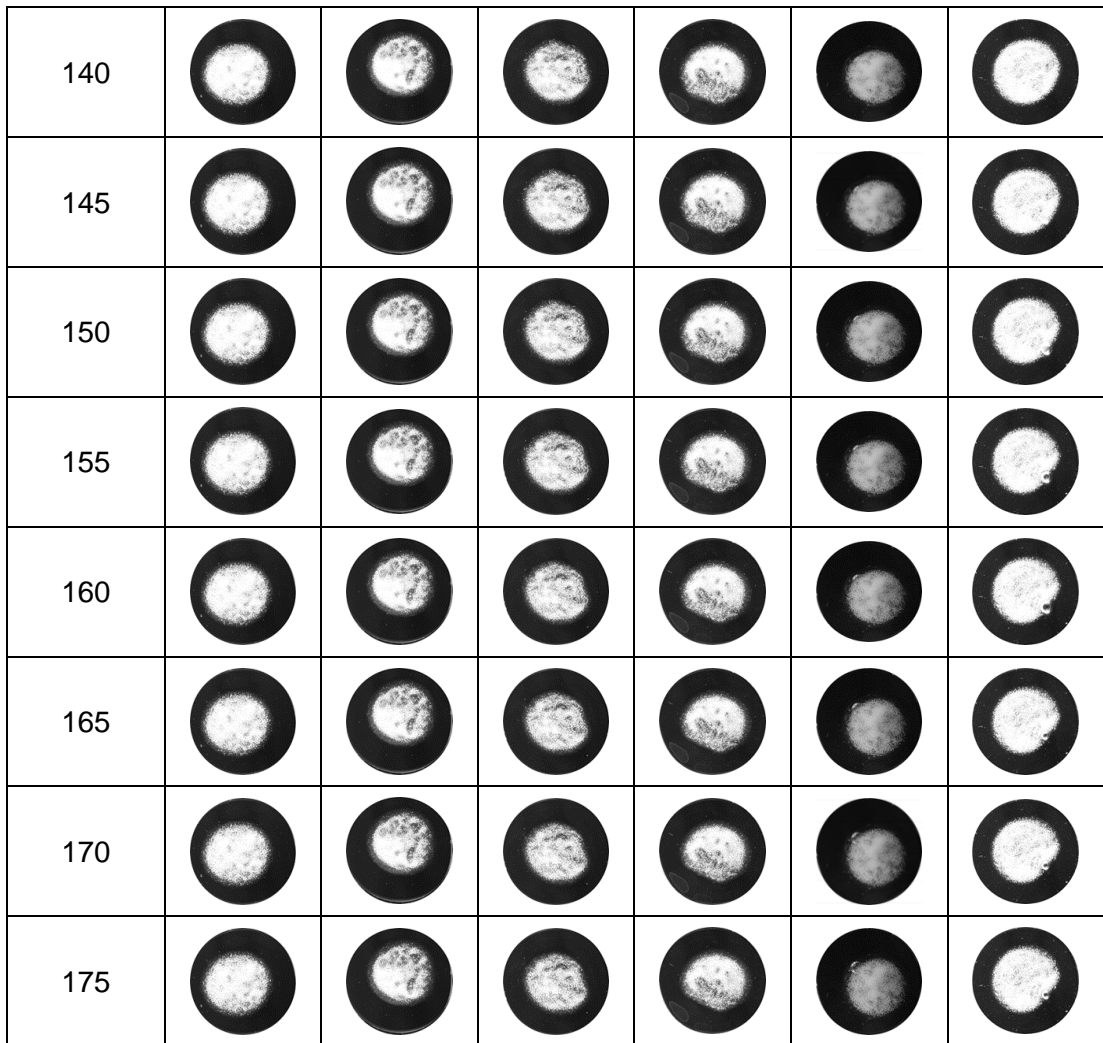


Fig. 39: Radial optical images obtained from swelling experiments (n=6) conducted on tablets containing 30% w/w cysteine HCl at pH 7

Time/min	Tablet 1	Tablet 2	Tablet 3	Tablet 4	Tablet 5	Tablet 6
0						
5						
10						
15						
20						
25						
30						
35						
40						
45						
50						
55						
60						
65						

70						
75						
80						
85						
90						
95						
100						
105						
110						
115						
120						
125						
130						
135						

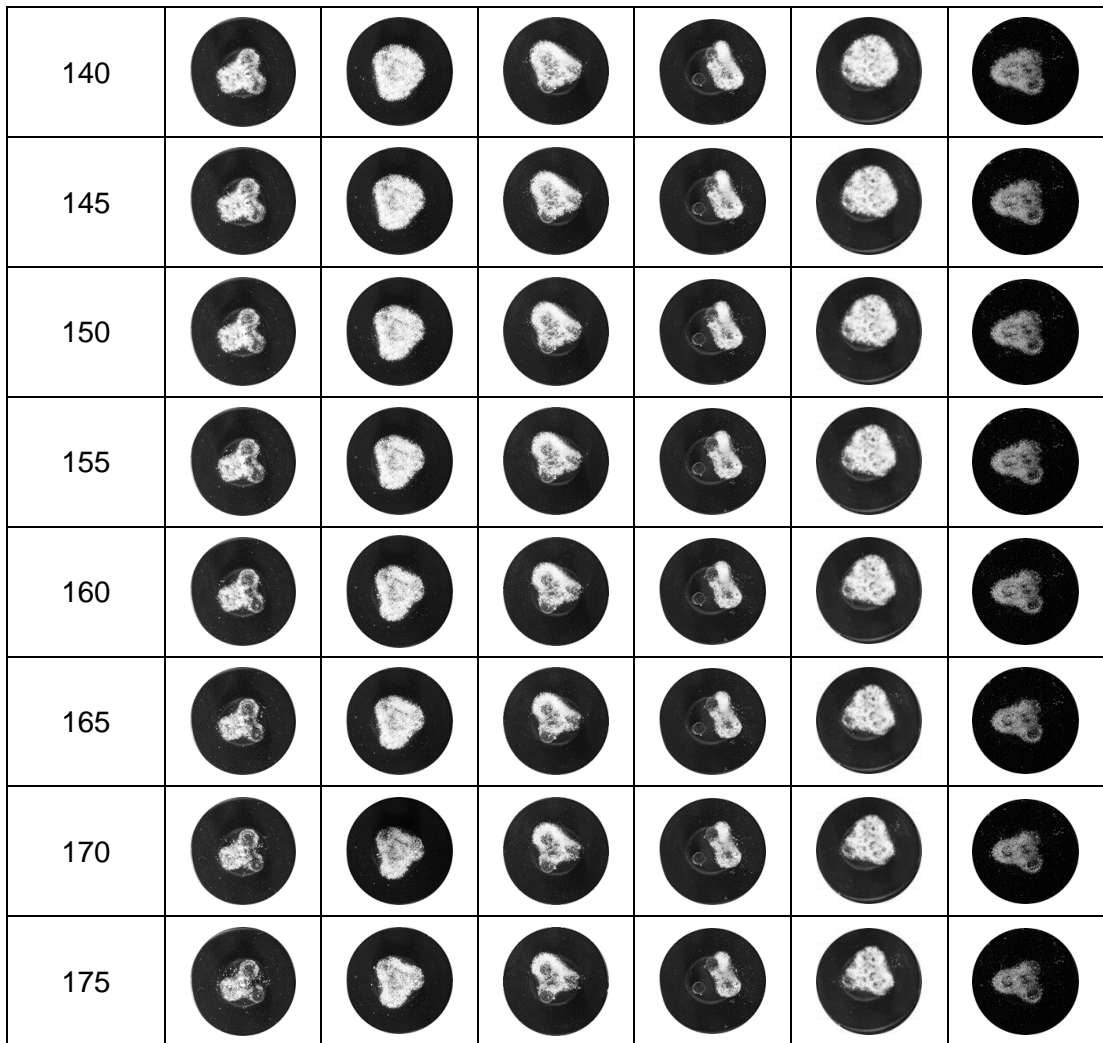
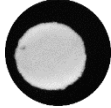
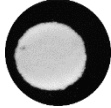
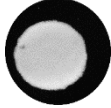
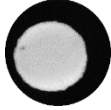
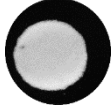
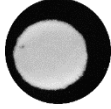
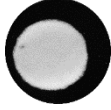
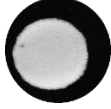


Fig. 40: Radial optical images obtained from swelling experiments (n=6) conducted on tablets containing 30% w/w glycine HCl at pH 7

Time/min	Tablet 1	Tablet 2	Tablet 3	Tablet 4	Tablet 5	Tablet 6
0						
5						
10						
15						
20						
25						
30						
35						
40						
45						
50						
55						
60						
65						

70						
75						
80						
85						
90						
95						
100						
105						
110						
115						
120						
125						
130						
135						

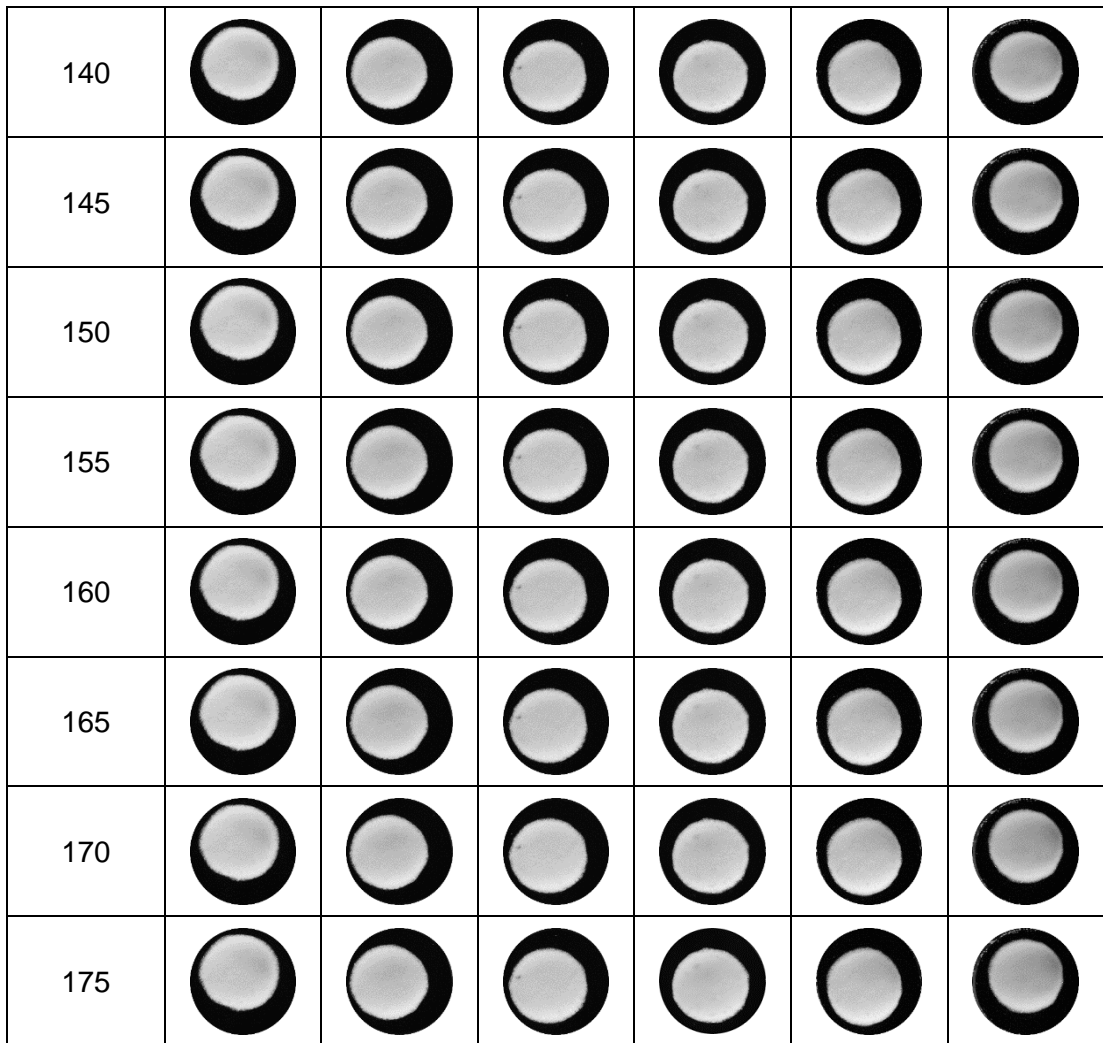
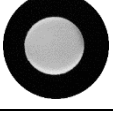
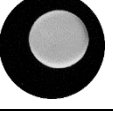
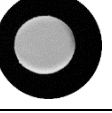
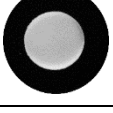
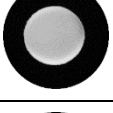
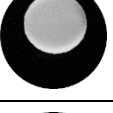
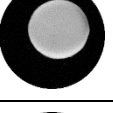
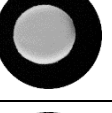
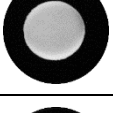
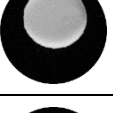
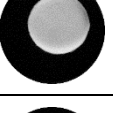
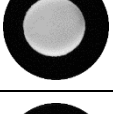
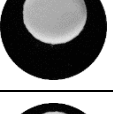
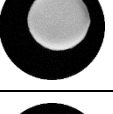
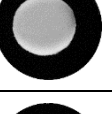
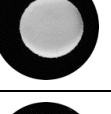
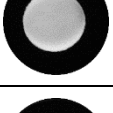
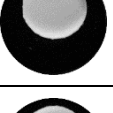
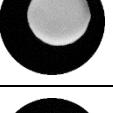
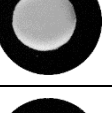
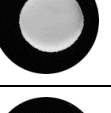
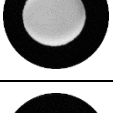
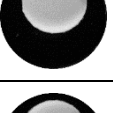
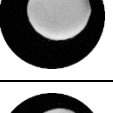
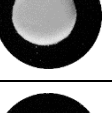
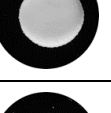
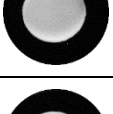
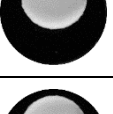
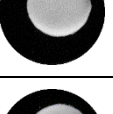
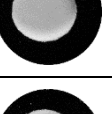
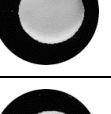
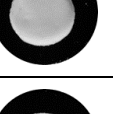
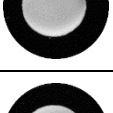
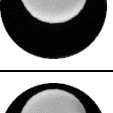
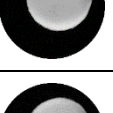
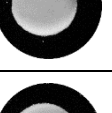
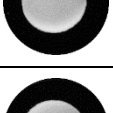
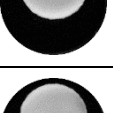
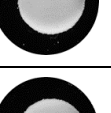
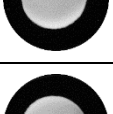
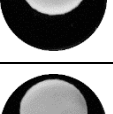
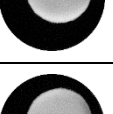
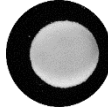
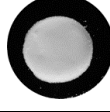
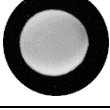
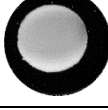
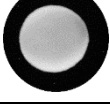
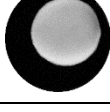
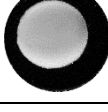
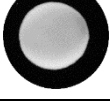
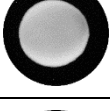
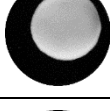
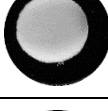
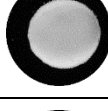
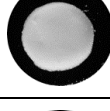
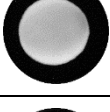
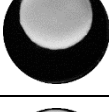
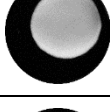
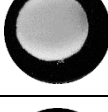
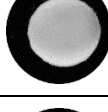
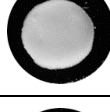
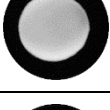
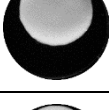
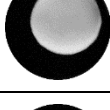
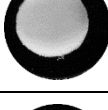
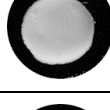
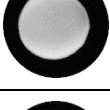
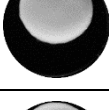
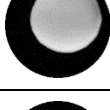
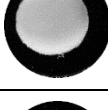
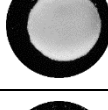
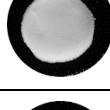
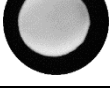
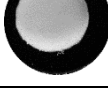


Fig. 41: Radial optical images obtained from swelling experiments (n=6) conducted on tablets containing 10% w/w betaine HCl with 20% w/w IT at pH 7

Time/min	Tablet 1	Tablet 2	Tablet 3	Tablet 4	Tablet 5	Tablet 6
0						
5						
10						
15						
20						
25						
30						
35						
40						
45						
50						
55						
60						
65						

70						
75						
80						
85						
90						
95						
100						
105						
110						
115						
120						
125						
130						
135						

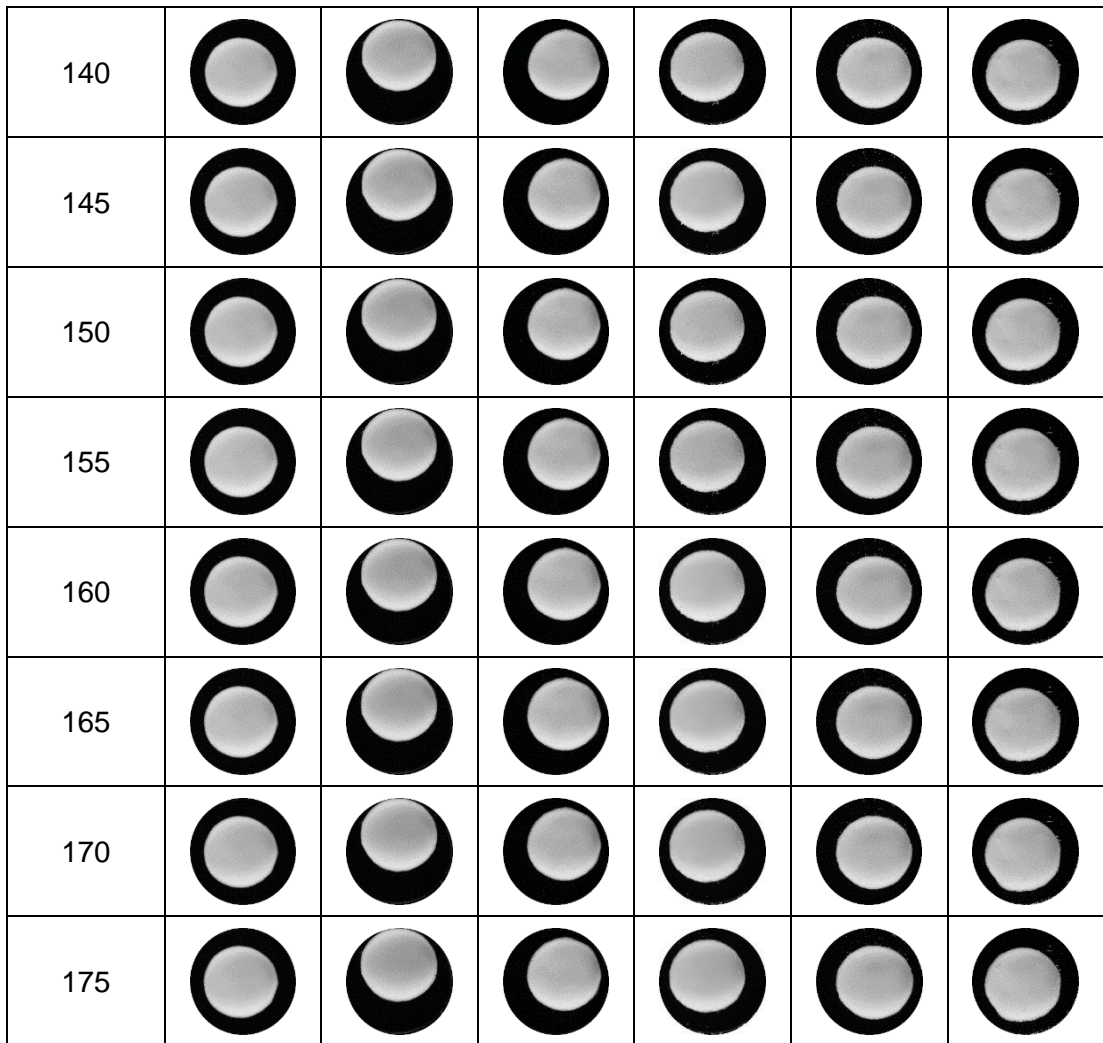
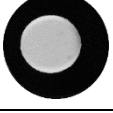
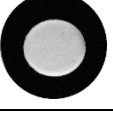
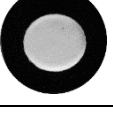
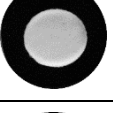
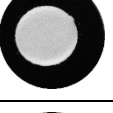
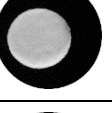
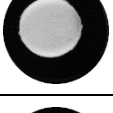
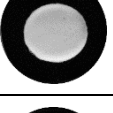
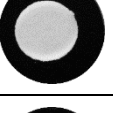
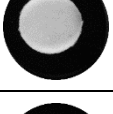
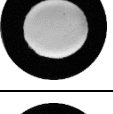
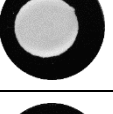
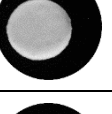
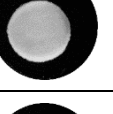
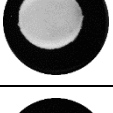
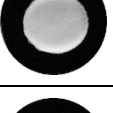
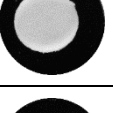
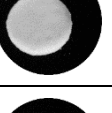
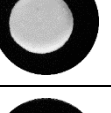
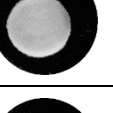
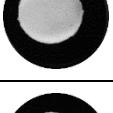
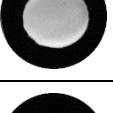
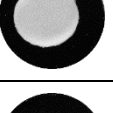
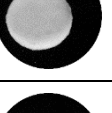
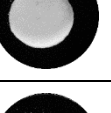
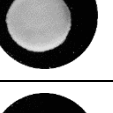
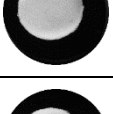
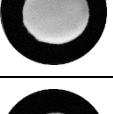
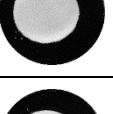
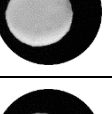
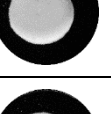
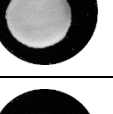
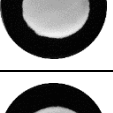
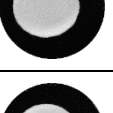
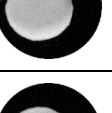
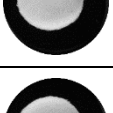
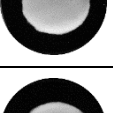
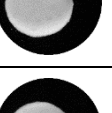
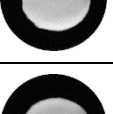
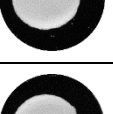
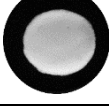
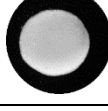
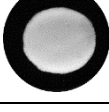
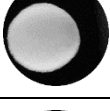
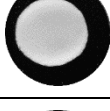
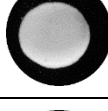
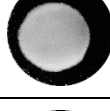
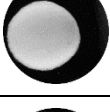
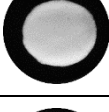
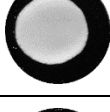
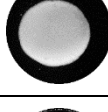
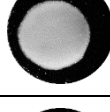
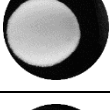
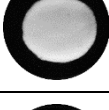
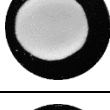
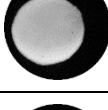
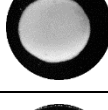
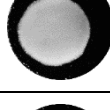
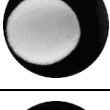
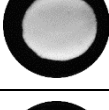
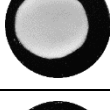
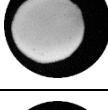
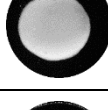
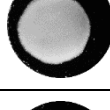
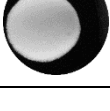
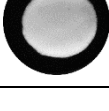


Fig. 42: Radial optical images obtained from swelling experiments (n=6) conducted on tablets containing 10% w/w citric acid with 20% w/w IT at pH 7

Time/min	Tablet 1	Tablet 2	Tablet 3	Tablet 4	Tablet 5	Tablet 6
0						
5						
10						
15						
20						
25						
30						
35						
40						
45						
50						
55						
60						
65						

70						
75						
80						
85						
90						
95						
100						
105						
110						
115						
120						
125						
130						
135						

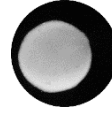
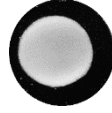
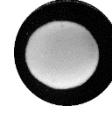
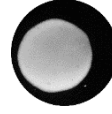
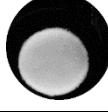
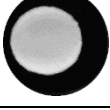
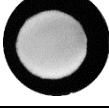
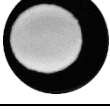
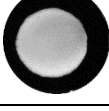
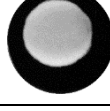
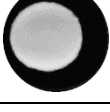
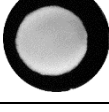
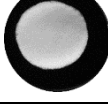
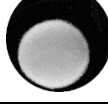
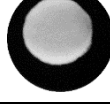
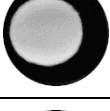
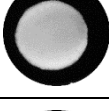
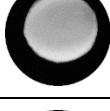
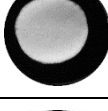
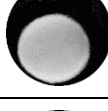
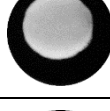
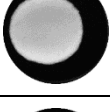
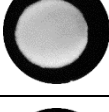
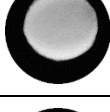
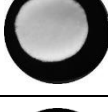
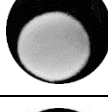
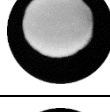
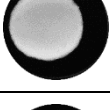
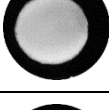
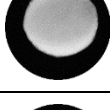
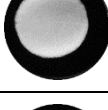
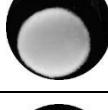
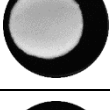
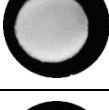
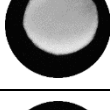
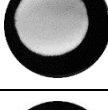
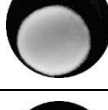
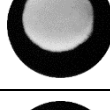
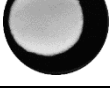
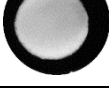
140						
145						
150						
155						
160						
165						
170						
175						

Fig. 43: Radial optical images obtained from swelling experiments (n=6) conducted on tablets containing 10% w/w cysteine HCl with 20% w/w IT at pH 7

Time/min	Tablet 1	Tablet 2	Tablet 3	Tablet 4	Tablet 5	Tablet 6
0						
5						
10						
15						
20						
25						
30						
35						
40						
45						
50						
55						
60						
65						

70						
75						
80						
85						
90						
95						
100						
105						
110						
115						
120						
125						
130						
135						

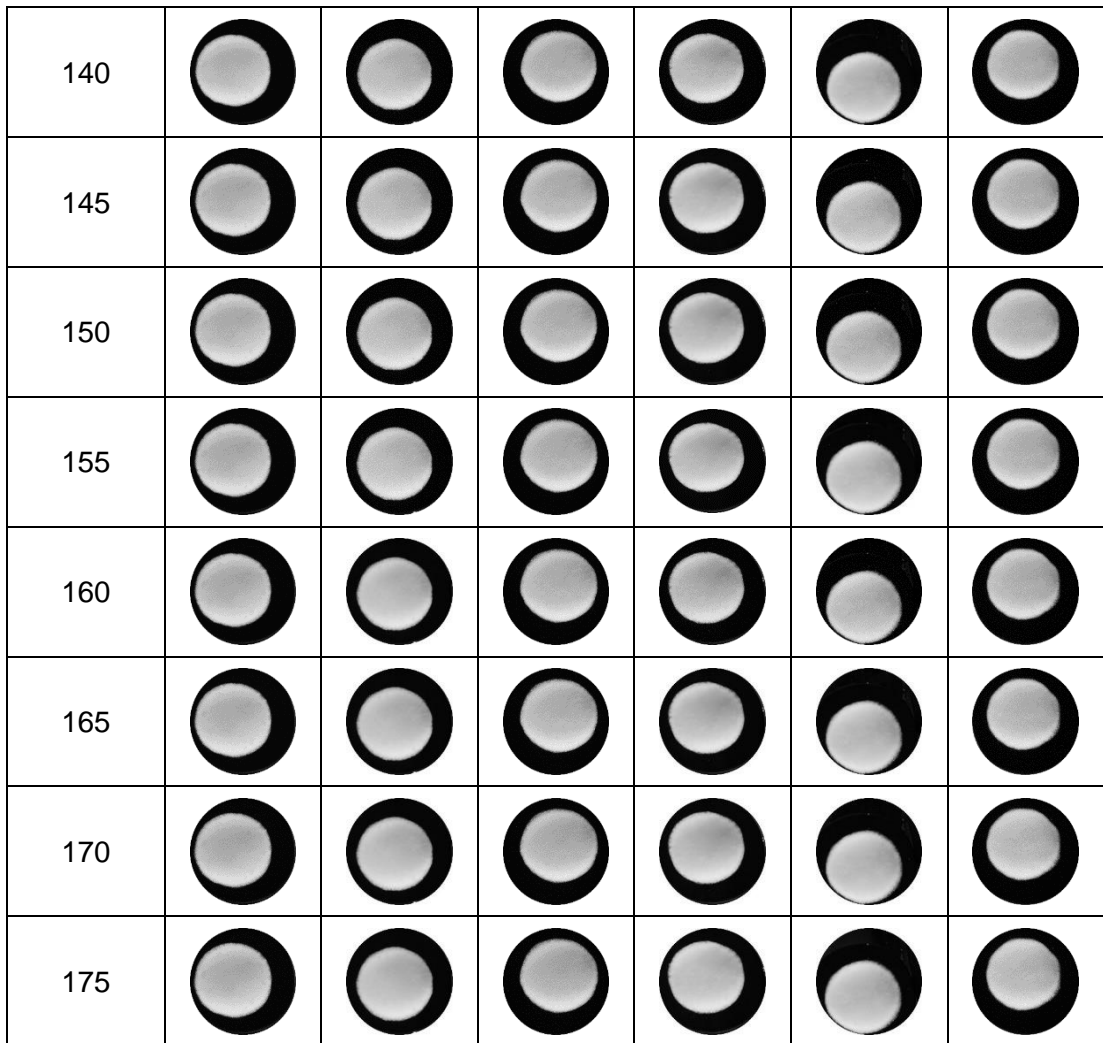
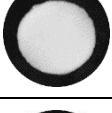
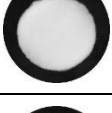
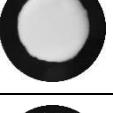
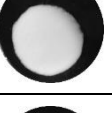
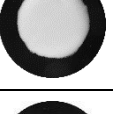
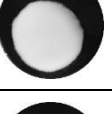
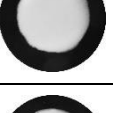
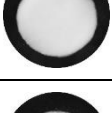
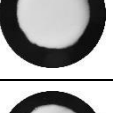
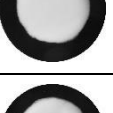
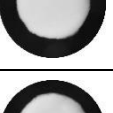
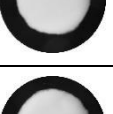


Fig. 44: Radial optical images obtained from swelling experiments (n=6) conducted on tablets containing 10% w/w glycine HCl with 20% w/w IT at pH 7

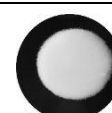
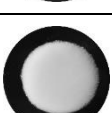
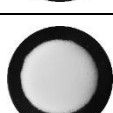
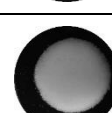
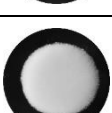
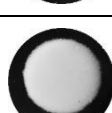
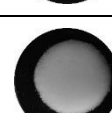
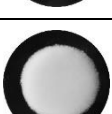
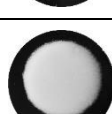
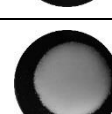
Time/min	Tablet 1	Tablet 2	Tablet 3	Tablet 4	Tablet 5	Tablet 6
0						
5						
10						
15						
20						
25						
30						
35						
40						
45						
50						
55						
60						
65						

70						
75						
80						
85						
90						
95						
100						
105						
110						
115						
120						
125						
130						
135						

140						
145						
150						
155						
160						
165						
170						
175						

Fig. 45: Radial optical images obtained from swelling experiments (n=6) conducted on tablets containing 30% w/w betaine HCl with 20% w/w IT at pH 7

Time/min	Tablet 1	Tablet 2	Tablet 3	Tablet 4	Tablet 5	Tablet 6
0						
5						
10						
15						
20						
25						
30						
35						
40						
45						
50						
55						
60						
65						

70						
75						
80						
85						
90						
95						
100						
105						
110						
115						
120						
125						
130						
135						

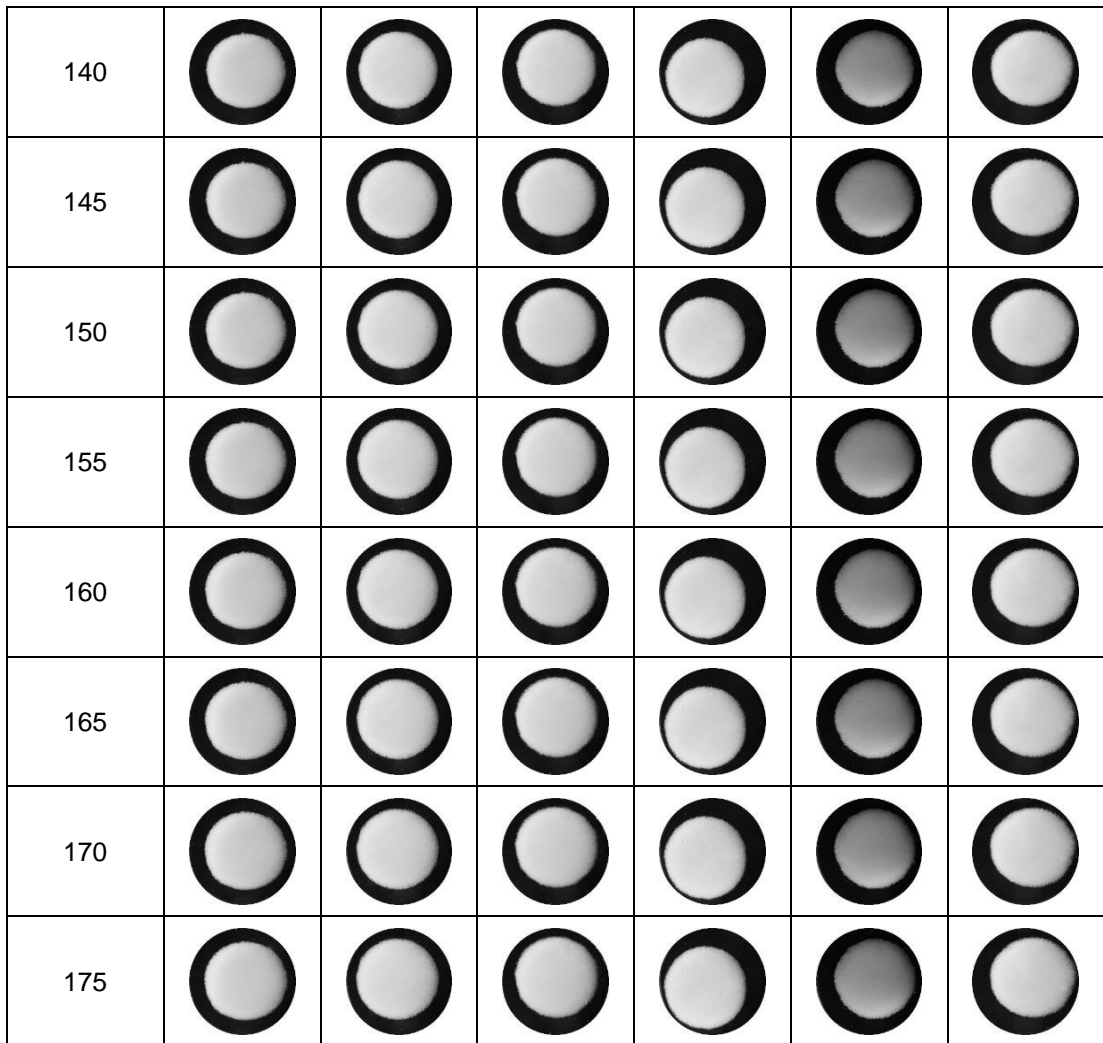
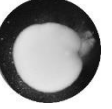


Fig. 46: Radial optical images obtained from swelling experiments (n=6) conducted on tablets containing 30% w/w citric acid with 20% w/w IT at pH 7

Time/min	Tablet 1	Tablet 2	Tablet 3	Tablet 4	Tablet 5	Tablet 6
0						
5						
10						
15						
20						
25						
30						
35						
40						
45						
50						
55						
60						
65						

70						
75						
80						
85						
90						
95						
100						
105						
110						
115						
120						
125						
130						
135						

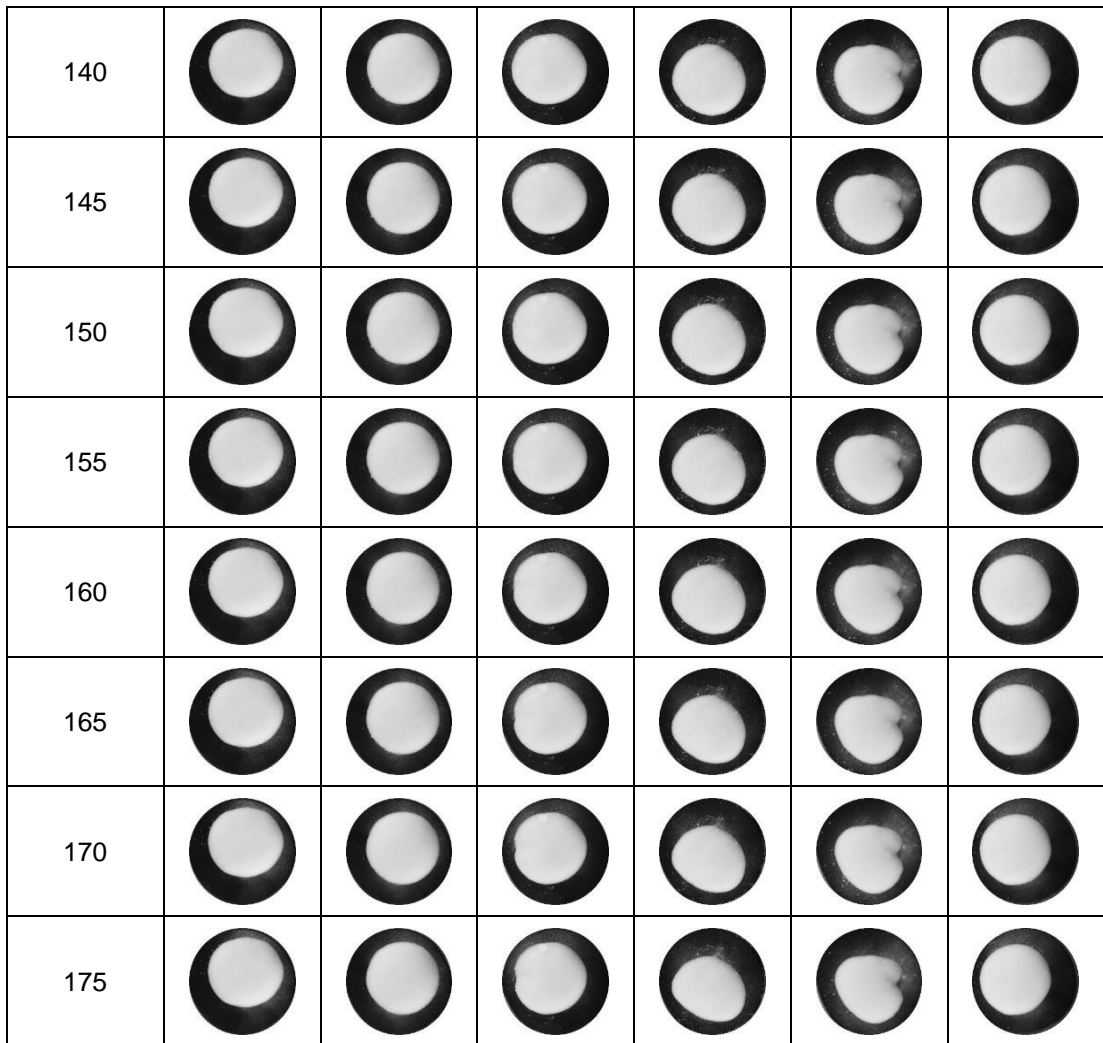
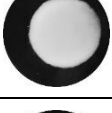
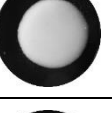
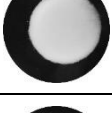
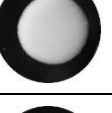
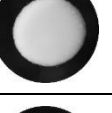
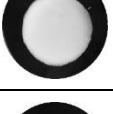
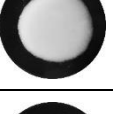
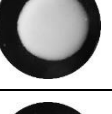
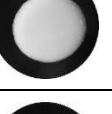
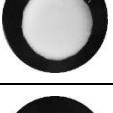
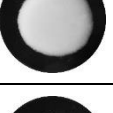
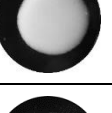
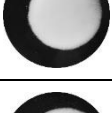
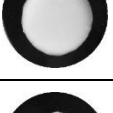
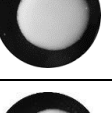
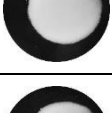
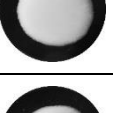
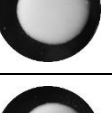
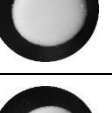
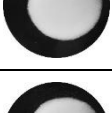
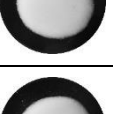


Fig. 47: Radial optical images obtained from swelling experiments (n=6) conducted on tablets containing 30% w/w cysteine HCl with 20% w/w IT at pH 7

Time/min	Tablet 1	Tablet 2	Tablet 3	Tablet 4	Tablet 5	Tablet 6
0						
5						
10						
15						
20						
25						
30						
35						
40						
45						
50						
55						
60						
65						

70						
75						
80						
85						
90						
95						
100						
105						
110						
115						
120						
125						
130						
135						

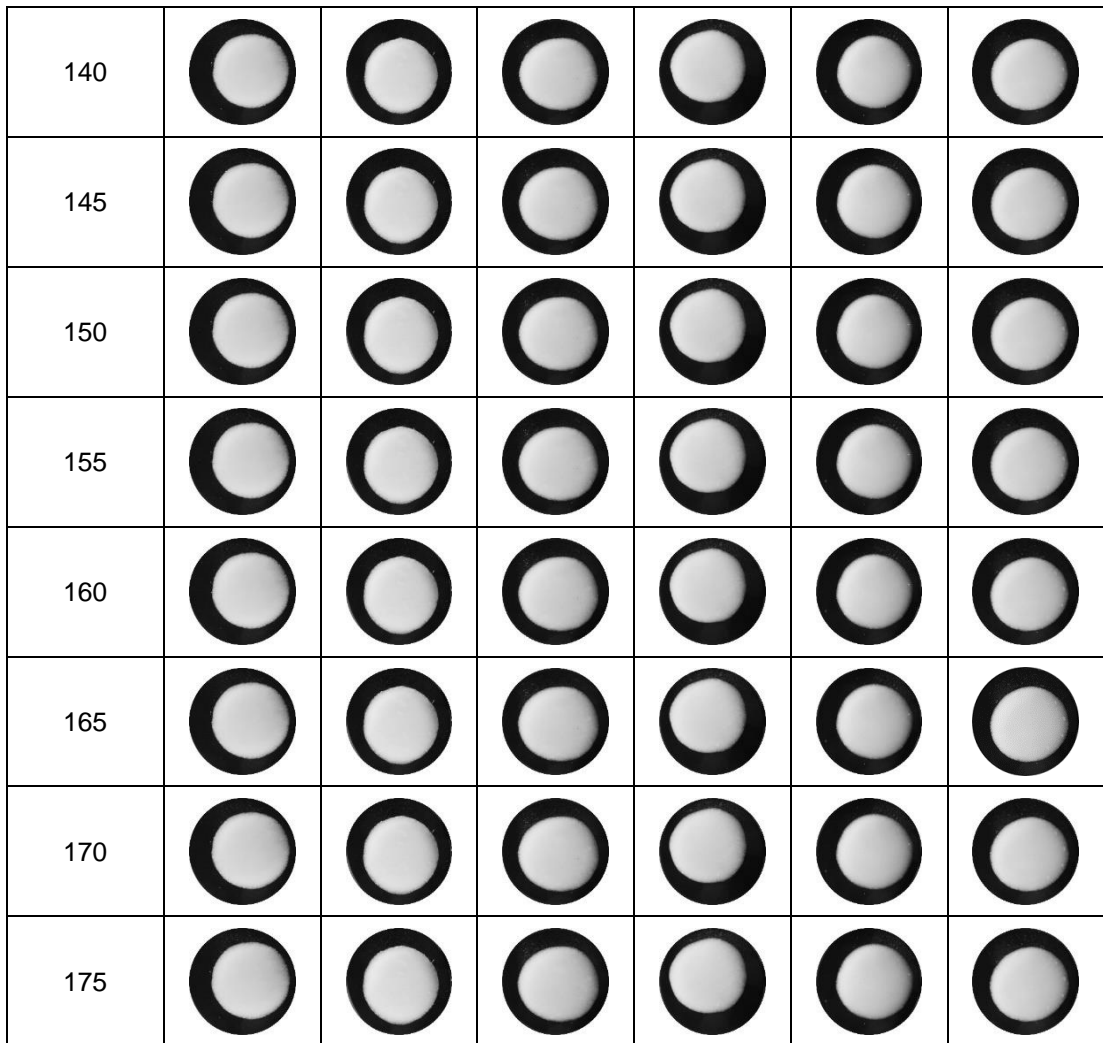


Fig. 48: Radial optical images obtained from swelling experiments (n=6) conducted on tablets containing 30% w/w glycine HCl with 20% w/w IT at pH 7

Appendix 7

A journal article published on the work included in Chapter 5 is presented in this appendix in the original format, as published.

The paper appeared in the Journal of Molecular Pharmaceutics, volume 17, issue 4 (2020), pages 1090-1099.

Investigation of Within-Tablet Dynamics for Extended Release of a Poorly Soluble Basic Drug from Hydrophilic Matrix Tablets Using ATR–FTIR Imaging

Farah Deeba Zahoor, Kerstin T. Mader, Peter Timmins, Jonathan Brown, and Chris Sammon*

Cite This: *Mol. Pharmaceutics* 2020, 17, 1090–1099

Read Online

ACCESS |

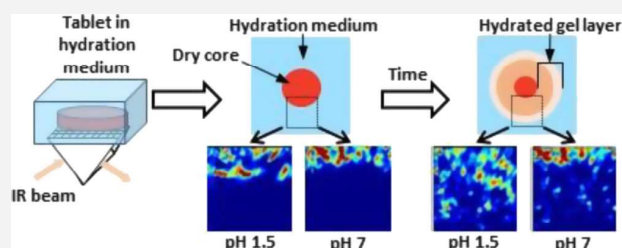
Metrics & More

Article Recommendations

Supporting Information

ABSTRACT: Hydrophilic matrices are an effective option for oral controlled release but can face challenges in terms of bioavailability and efficacy when used in conjunction with poorly soluble, weakly basic drugs. Attenuated total reflectance Fourier transform infrared (ATR–FTIR) imaging provides dynamic information relating to the location and chemical nature of both the sustained release matrix and the active pharmaceutical ingredient (API) during hydration/dissolution. In this study, we have identified a model system combining itraconazole (IT), a poorly soluble, weakly basic API that has pK_a in the physiological range, and hydroxypropyl methylcellulose, which is a commonly used oral tablet matrix. This system was investigated to determine the swelling kinetics at different pH values at a fixed ionic strength and to facilitate the study of the influence of hydrating media pH on the drug particle movement (translocation). Using ATR–FTIR imaging, we were able to show that gel layer formation and swelling were independent of pH but highly dependent on the ionic strength of the hydrating medium in placebo tablets. When the ionic strength was fixed, gel layer formation and radial swelling were both shown to be pH-dependent when IT was incorporated into the matrix. This was verified using optical imaging. The chemical specificity of ATR–FTIR imaging permitted the observation of transformational changes of IT from the free base to the ionized form in the tablet core during hydration. This phenomenon was shown to be greater at pH 1.5 than at pH 7. ATR–FTIR imaging was able to follow drug particle translocation at both pH 1.5 and pH 7; however, the extent of migration away from the tablet core was shown to be greater at lower pH. The location of the translocated particles within the gel layer was different between the two studied pH values, with particles being located close to the swelling front at pH 7 and within the diffusion front at pH 1.5. In both pH environments, the translocated IT particles were shown to be predominantly in the free base form. No evidence of fully solubilized IT was observed in the surrounding medium because of the inherent aqueous solubility of IT being below the instrument detection limits. This work highlighted the value of utilizing a chemically specific spectroscopic tool to increase the understanding of the nature of the factors affecting the release of a pH-dependent, poorly soluble drug from a hydrophilic matrix at different pH values and permitted greater insights into what happens inside the polymer matrix during drug release.

KEYWORDS: real time imaging, poorly soluble drug, itraconazole, gel layer, HPMC, extended release



1. INTRODUCTION

Hydrophilic matrix tablets based on hydroxypropyl methylcellulose (hypromellose, HPMC) are a favorable choice for oral extended drug release dosage forms for a number of reasons, including the knowledge base for technology, regulatory status, low cost of rate control polymer, ease of manufacture, and relative inertness.¹ In contact with water, HPMC rapidly undergoes hydration and swelling with the formation of a gel layer, a dynamic “shell” around the tablet core. The extent of the hydrated polymer increases through ingress of fluid into the tablet over time and contributes to controlling the release of the drug by modulating the rate of water ingress.² Drug dissolution in, and diffusion through, the matrix as well as erosion of the hydrated polymer under shear at the interface between the gel layer and the bulk medium are

processes that contribute to drug release. Understanding the mechanisms controlling the rate of drug release from an HPMC hydrophilic matrix tablet can be pursued by considering the movement of three fronts inside the evolving matrix tablet over time (Figure 1a): the boundary between the yet-to-be hydrated polymer and the hydrated polymer (swelling front), between the hydrated polymer and the bulk

Received: October 15, 2019
Revised: February 14, 2020
Accepted: February 18, 2020
Published: February 18, 2020



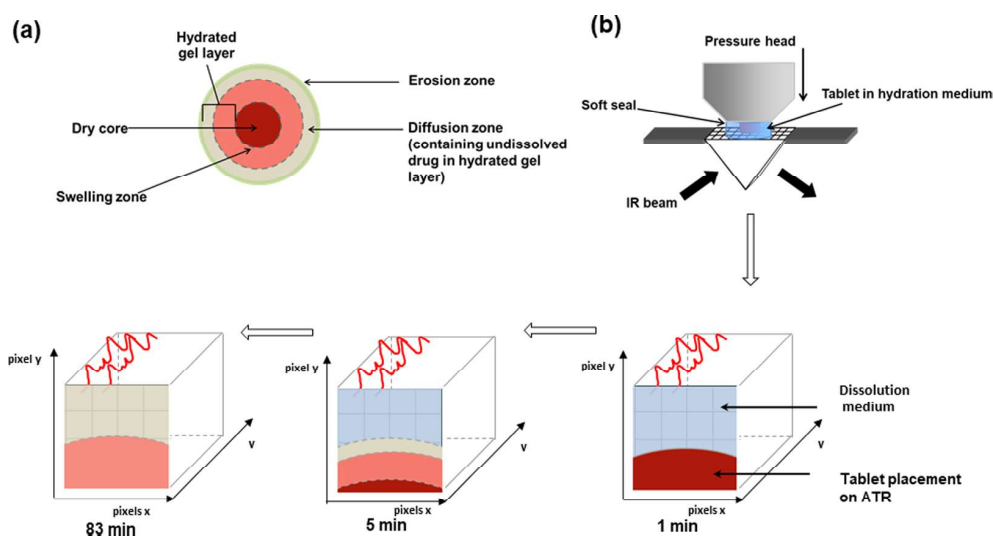


Figure 1. (a) Schematic of different fronts of a hydrating hydrophilic tablet, looking down onto the upper tablet surface as if one could see through it, highlighting the dry core, swelling, diffusion, and erosion fronts, adapted from Timmins et al. and reproduced with permission from Therapeutic Delivery as agreed by Newlands Press Ltd.¹ (b) Schematic of the ATR-FTIR imaging setup over the course of the hydration period using a focal plane array detector.

aqueous medium (erosion front), and within the hydrated gel where the undissolved drug is in equilibrium with the dissolved drug (diffusion front).^{1,3} The presence of solid undissolved drug particles in the hydrated gel layer can impair the swelling of the polymer matrix by restricting the disentanglement of the polymer chains, which may be an important parameter in the case of poorly water-soluble compounds with marked pH-dependent solubility. There is also a correlation between poor drug solubility and erosion of the matrix.⁴ For poorly soluble drugs in hydrophilic matrices, the erosion mechanism of the hydrated polymer is important as it is this erosion that results in the liberation of the undissolved drug.⁴

Previous studies have incorporated nondiffusing insoluble markers to gain insight and quantify swelling within the gel layer of hydrophilic matrix tablets (HPMC). The movement of the fluorescent markers was tracked and observed using a confocal laser scanning microscope.⁵ Interestingly, analysis of the tracks indicated a wave of expansion that started and was the greatest at the exterior, moving toward the core. The findings also suggested that as the deeper layers started to expand, swelling continued in the outer layers.

HPMC is chemically stable over the physiological pH range;⁶ however, the swelling properties of HPMC are strongly influenced by the ionic strength of the medium.^{7,8} The ionic strength can vary considerably in the fluid within the gastrointestinal tract, and depending on fasted and fed states, it can range from 0 to 0.5 mol/L, impacting the drug release from a hydrophilic polymer matrix.⁷ Many different approaches have been used to investigate the formation of the hydrated gel layer and the impact of ionic strength employing a range of techniques.^{9,10} Bajwa et al. used real-time confocal fluorescence imaging to investigate the movement and migration of the early stages of HPMC gel layer formation using the fluorophore Congo red, which selectively binds with the cellulosic unit and hence acts as a marker for the hydrated HPMC.⁸ The authors concluded that the gel layer growth was suppressed with increasing salt concentration of the hydration medium.

Poorly soluble ionizable drugs will exhibit different dissolution behaviors within the physiological pH range. Weakly basic compounds exhibit a marked increase in solubility at low pH while being practically insoluble at neutral pH.^{2,11} A significant number of new drugs in development fall into this category,¹² although the phenomenon may be ameliorated to a degree by incorporating pH modifiers within the matrix to yield improved in vivo performance.¹³ A further method to achieve an improved oral bioavailability is by the creation of a water-soluble salt form of the weakly basic drug.¹⁴

Fourier transform infrared (FTIR) imaging enables multiple spectra to be collected simultaneously, allowing a chemical image of the material to be generated relatively quickly.^{15–17} From this, information about the polymer, drug, and water distribution can be gained simultaneously. The advantage of this approach is the ability to provide characterization of the molecular species present and the morphology of the polymer matrix.¹⁶ FTIR images consist of spectral and spatial information and therefore require additional steps for converting the data into chemically and physically significant information. There are several methodologies for doing this; the simplest involves plotting the peak height or peak area of a band from a known component.

Attenuated total reflectance Fourier transform infrared (ATR-FTIR) imaging has previously been used to study the mechanism of drug release from HPMC matrices.^{18–20} A work by van der Weerd and Kazarian described an approach to study drug release from a tablet by using a combination of chemical imaging via ATR-FTIR imaging and dissolution. Niacinamide incorporated into a HPMC matrix was used as a model system.²¹ Using a partial least-squares regression calibration, quantitative analysis for the concentration of water, polymer, and drug as a function of time was possible.

Hifumi et al. used ATR-FTIR imaging to investigate the influence of different polymer matrices on drug release. They studied ibuprofen-loaded HPMC films as a rapid release model and ibuprofen-loaded polyvinylpyrrolidone films for extended release. By controlling the local pH by incorporating a pH modifier and ionic strength around the HPMC via a

hydrophobicity modifier, the drug release behavior could be controlled.²²

Ewing et al. used ATR–FTIR imaging combined with a polydimethylsiloxane microfluidic device to monitor the behavior and release of ibuprofen in situ under flowing conditions at pH 1 and 7. It was reported that the low pH environment inhibited the release of the drug because of conversion from the molecularly dispersed ibuprofen to the crystalline form.²³

The aim of the current study was to use a poorly water soluble, weakly basic, and lipophilic model drug system to develop an insight into how these types of drugs behave within the tablet matrix. We have selected itraconazole (IT) as the chosen model drug; although it is not a candidate for oral extended delivery from a hydrophilic matrix system, it met the stated criteria for a suitable model compound for this work in that it exhibits pH-dependent poor solubility, close to 1 ng/mL at pH 7 and 4 $\mu\text{g/mL}$ at pH 1,²⁴ with a pK_a of 3.7. This is well inside the physiological pH range and characteristic of the most challenging compounds which might be considered for delivery from hydrophilic matrix systems. It is also very amenable to the spectroscopic imaging approaches we have applied in this work. As a basis for future work, in this exploration of the behavior of IT within the hydrating matrix, the methodology adopted permitted an opportunity to gain an insight into how such drugs behave when the environmental pH changes and in the absence of a pH modifier within the matrix.

This study used ATR–FTIR imaging to monitor the hydration of the polymer and the migration of the drug in the diffusion front over time and examined the influence of ionic strength on the formation of the HPMC gel layer. ATR–FTIR imaging allowed dissolution to be studied in real-time, mapping both the location of the drug and its chemical characteristics (e.g., ionization state) as it dissolved. The behavior of the salt forms of a drug within polymeric systems has been characterized previously. However, the combined assessment of the effects of a poorly soluble and weakly basic drug, of excipients and of water together in a formulation undergoing dynamic changes (including ionisation, dissolution, hydration, swelling and particle dislocation) with a view to informing future product design has not been reported.²³ The application of this approach will permit a greater understanding of the factors controlling the drug release and enable a more effective quality-by-design approach to formulating HPMC matrix tablets.

2. MATERIALS AND METHODS

2.1. Materials. IT (99% Acros Organics) and HPMC (grade METHOCEL K100M CR Premium grade) powders were used as received. For the hydration studies, two different hydrating media were used to investigate the pH effects: 0.1 M HCl solution (pH 1.5) and tris(hydroxymethyl)aminomethane hydrochloride buffer solution (tris buffer, purchased from Sigma-Aldrich, molecular biology grade pH 7.2). In order to explore the influence of ionic strength on the hydration of HPMC, two different ionic strength solutions were investigated. In order to minimize Hofmeister series-like effects, the ionic strength was managed by using monovalent buffering agents.²⁵ HCl (0.1 N) was prepared by diluting concentrated HCl 37% with deionized water having a resistivity of 18.2 M Ω . For the low ionic strength tris buffer, a 0.1 M solution was prepared by carrying a 10-fold dilution of the as-received

solution. In order to obtain high ionic strength solutions, 1 M concentration was used. For the 1 M tris solution, the as-received buffer was used. For the high ionic strength solution at low pH, sodium chloride (general purpose grade, Fischer Scientific) was added to the 0.1 N HCl solution to increase the ionic strength to 1 M.

2.2. Preparation and Characterization of Tablets. HPMC tablets containing 20% w/w IT were prepared by tumble blending (Stuart STR4 rotator drive) for 5 h at approximately 30 rpm. Flat-faced matrix tablets (10 mm) containing 90 mg of total powder were manufactured by direct compression on a Specac Atlas Manual press (Specac, Orpington, UK) using a compaction pressure of 625 MPa and a 5 min compaction time. The average IT content ($n = 6$) was determined using near-infrared (NIR) and shown to be 19.37% w/w with a uniform distribution across the tablet, as determined by Raman microscopy (Supporting Information, Figures S1 and S2). The advantages of using Raman microscopy rather than ATR–FTIR imaging to determine content uniformity of an active pharmaceutical ingredient (API) include enhanced spatial resolution, the possibility of achieving spot sizes less than 2 μm , the ability to map larger areas²⁶ (the mid-IR ATR method is limited to a field of view $\sim 640 \times 640 \mu\text{m}^2$ in our system), and easier discrimination of an aromatic API in an HPMC matrix.

2.3. In Vitro Release Studies. Dissolution studies were carried out by using an Agilent 708 apparatus on the 20% w/w IT formulation ($n = 6$) in 900 mL of 0.1 N HCL and 0.1 M tris buffer using the USP type-II method. A paddle speed of 75 rpm and a temperature of $37 \pm 0.5 \text{ }^\circ\text{C}$ were used in all experiments.²⁷ A 5 mL aliquot was withdrawn at different time intervals and assayed for IT using ultraviolet–visible spectroscopy (Agilent Cary 60) by measuring the absorbance at 257 nm.

2.4. Collection of ATR–FTIR Images. Mid-IR spectroscopic images were collected using a Varian 680-IR spectrometer (Agilent Technologies LDA UK Limited, Stockport, UK) coupled to a variable temperature Golden Gate single reflection ATR-imaging accessory (Specac, Orpington, UK) held at 37 $^\circ\text{C}$. Images were collected at a spectral resolution of 8 cm^{-1} with eight coadditions. It was observed that an S/N advantage can be obtained by using a large number of background scans while maintaining the speed advantage of having fewer sample scans. Therefore, blank ATR crystal images at a resolution of 8 cm^{-1} and 256 coadditions were used as a background reference for image processing.

2.5. Hydration Experiments Using ATR–FTIR Imaging. Hydration studies on the tablets were performed as follows and are shown schematically in Figure 1. Each tablet was placed on the ATR crystal such that approximately one-third of the ATR crystal surface was covered. Pressure was then applied to the tablet using a sapphire anvil, and a good optical contact between the sample and the ATR crystal was confirmed by checking the quality of the image of the dry tablet; this limited the swelling in the axial direction. A polyester ring, of diameter larger than the tablet itself to permit unimpeded radial expansion, was sealed around the tablet, and 5 mL of sonicated pH 7 tris buffer or 0.1 N (pH 1.5) HCl (37 $^\circ\text{C}$) was carefully added from one side of the crystal as the hydrating medium.

Hydration was studied over a 3 h period at a temperature of 37 $^\circ\text{C}$; images were collected every 2 min for the first 10 min, every 10 min over the following 70 min, and every 20 min for

the remainder of the experiment. Chemical images for each component in the system were generated by plotting the peak area of the 1630, 1510, and 1041 cm^{-1} bands to show the distribution of water, IT, and HPMC, respectively, using ISys 5.0 chemical imaging software (Malvern Instruments, Malvern, UK).

It should be noted that this experimental arrangement permits only observation of swelling and water ingress, particle translocation if it occurs, and dissolution/diffusion of the drug in the hydrated matrix. It is not capable of monitoring erosion due to the low shear environment that exists within the cell. However, this is not considered to be a limitation in this context as it still allows assessment of within-tablet dynamics due to hydration and swelling at pH values within the tablet where the drug will be insoluble (high pH medium) or have some solubility (low pH medium).

2.6. Optical Imaging To Determine the Radial and Axial Swelling. Optical images of the axial and radial swelling were collected using two Canon SD MK3 digital cameras equipped with 100 mm macro lenses, arranged to capture axial and radial images of the tablets simultaneously. Images were obtained from the HPMC placebo and the 20% w/w IT-loaded HPMC formulation in dissolution media at pH 1.5 and 7 ($n = 6$). The tablets were placed onto a 3-prong sample holder located in a glass cell, and 40 mL of either 0.1 N HCL or 0.1 M tris buffer was added. Images were collected at 5 min intervals for a period of 180 min. Data analysis was conducted using image analysis software (ImageJ 1.52a) to determine the area change in both the axial and radial dimensions. Dimensional changes of the drug-loaded tablets immersed in media at the two different pH values were statistically compared using two-way analysis of variance (ANOVA) to determine the statistical significance of any differences (Prism V 7.03).

3. RESULTS AND DISCUSSION

3.1. In Vitro Release Studies. Dissolution profiles obtained for the 20% w/w IT-loaded tablets (Figure S3) showed a marked difference in the release rate between the two pH values. At pH 1.5, sustained release of IT was observed over the 24 h experiment, although when the experiment was stopped at this point, only 24% of the contained IT had been released. In contrast, the same IT tablets in the pH 7 medium showed the release to be <1% at 24 h. There was no evidence of burst release during these measurements at either pH for this API/polymer matrix. However, the results showed clear evidence of an increase in both the dissolution rate and the percentage IT release (associated with increased solubility of IT) in the pH 1.5 medium, as anticipated and in full agreement with previous studies.²⁸

3.2. ATR–FTIR Imaging of Reference Materials. Reference spectra for IT, HPMC, 0.1 N HCL, and tris buffer were generated by calculating the mean of the spectra obtained from a single image obtained as described in Section 2.4.

Reference spectra were used to identify species-specific bands from which it was possible to generate chemical images (Figure 2). The bands of interest were shown to be $\delta(\text{OH}) \sim 1620 \text{ cm}^{-1}$ for water (used as a marker for tris buffer and 0.1 N HCL because of water being the main component), $\nu(\text{C–O}) \sim 1041 \text{ cm}^{-1}$ for HPMC, and aromatic $\nu(\text{C=C}) \sim 1510 \text{ cm}^{-1}$ for the total IT distribution.

3.3. ATR–FTIR Imaging of HPMC Placebo Tablets. Mid-IR images of the matrix tablet composed simply of HPMC

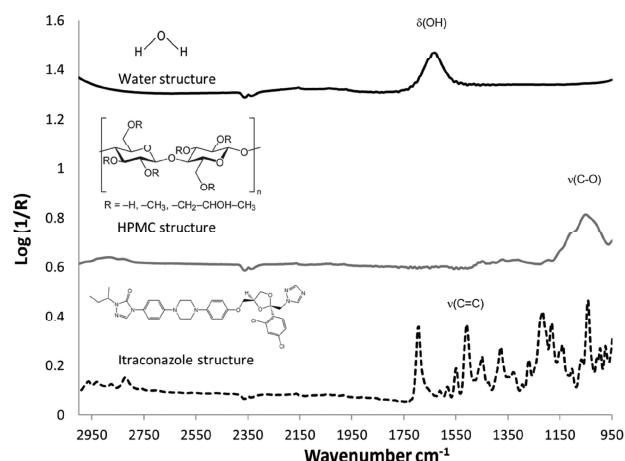


Figure 2. Average ATR–FTIR imaging spectra obtained from reference materials, highlighting $\delta(\text{OH})$, $\nu(\text{C–O})$, and $\nu(\text{C=C})$ in water, HPMC, and IT respectively. Highlighted bands used for peak area integration of images to show distribution of water, IT, and HPMC.

hydrating at pH 1.5 and 7 using low and high ionic strength media over the 3 h hydration period were generated using the bands identified in Section 3.2. The images show the evolution of the ingress of water into the tablet matrix and the growth of the gel layer (Figure 3). High-intensity regions are colored red, whereas low-intensity regions are blue. Increasing intensity is denoted by the numerical values on the accompanying color scale bars.

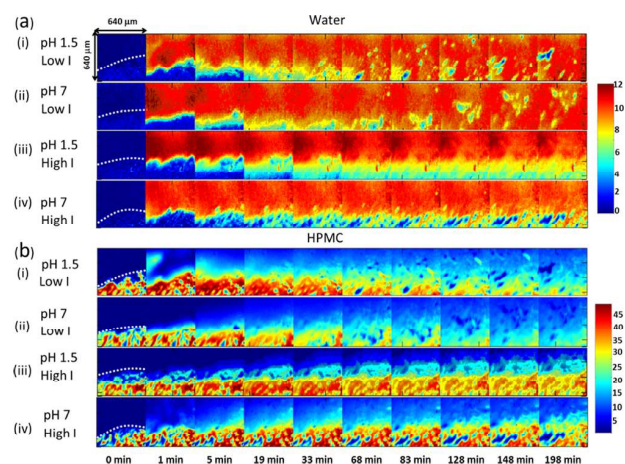


Figure 3. Selected ATR–FTIR images were collected over the time course of hydration experiments for placebo tablets in low and high ionic strength solutions at pH 1.5 and pH 7 showing (a) water and (b) HPMC distributions. Images were generated using methods described in Section 2.5 and 3.2. The dotted lines in the first column of images denotes the boundary between the tablet and air/water.

From the water distribution images (Figure 3a), it is evident that water ingress occurs rapidly, and full penetration throughout the tablet, visible within the field of view, occurs by around 19 min irrespective of the pH or ionic strength environment. HPMC distribution images at t0 show that the (nonhydrated) tablet core is located toward the lower half of the images (Figure 3b). The intensity of this dark red/yellow HPMC distribution in the high ionic strength medium at pH

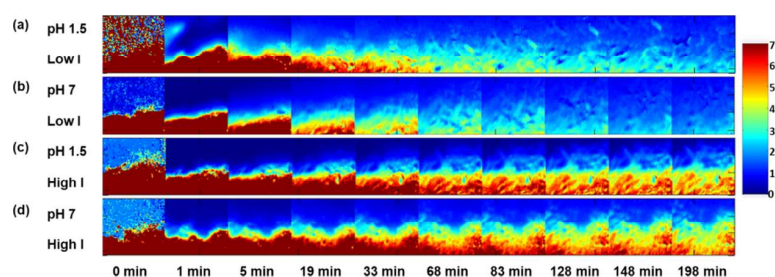


Figure 4. ATR–FTIR images of HPMC/water peak area ratio over the hydration period, showing the HPMC gel layer evolution for (a) pH 1.5 and (b) pH 7 low ionic strength solutions and (c) pH 1.5 and (d) pH 7 high ionic strength solutions.

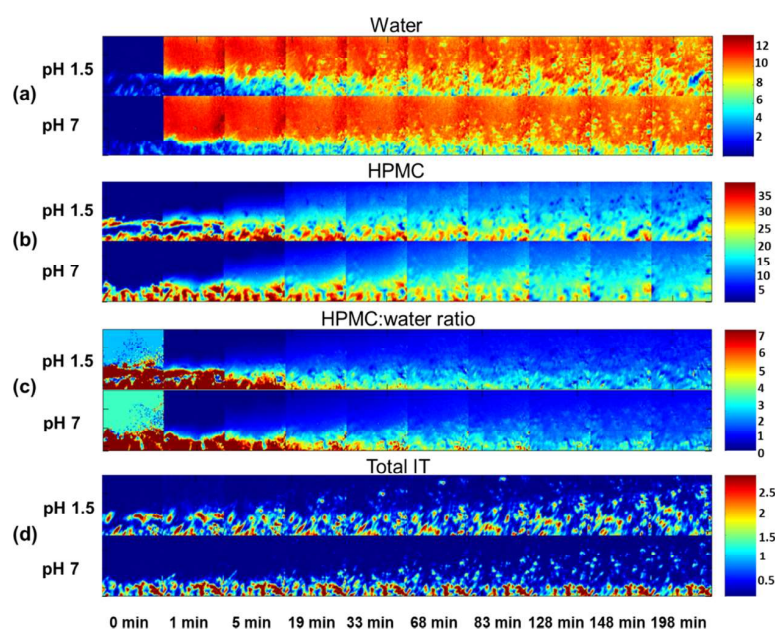


Figure 5. ATR–FTIR peak area integration images over the hydration period, showing the (a) distribution of water, (b) distribution of HPMC, (c) HPMC/water peak area ratio images, showing HPMC gel layer evolution for pH 1.5 and 7, and (d) distribution of total IT.

1.5 and 7 (Figure 3b(iii),(iv)) is far greater throughout the duration of the experiment in comparison to the low ionic strength images (Figure 3b(i),(ii)).

To gain insight into the gel layer behavior, the peak area ratio of $\nu(\text{C}-\text{O})$ in HPMC and $\delta(\text{OH})$ in water was plotted. The gel layer was defined as the cyan zone corresponding to values between 2.2 and 3.8, on the color scale shown in Figure 4 and consisted of a combination of water and polymer at varying concentrations. Figure 4a,b clearly highlights the rapid formation of the gel layer at pH 1.5 and pH 7 in a low ionic strength environment. The dark red color corresponded to regions with a high polymer content. Conversely, regions of hydrated HPMC with increasing water content are denoted by the yellow, green, and cyan zones.

The gel layer behavior is the same between different pH environments for the pure HPMC with the same ionic strength (Figure 4). For the low ionic strength media (Figure 4a,b), at both pH values, initial swelling is observed from the 1 min time point. The dry core diminishes rapidly, and the gel layer recedes toward the edge of the field of view within the time frame of the experiment.

For the high ionic strength images at pH 1.5 and 7, swelling is observed from the outset. The gel layer is much more stable over the duration of the experiment (Figure 4c,d), thus

confirming that the ionic strength of the media had a significant impact on the gel layer behavior. This is consistent with previous studies looking at the impact of ionic strength and HPMC gel formation,^{6,8,10} where the gel layer behavior is shown to be independent of pH but highly dependent on the ionic strength of the medium. At higher ionic strength, less effective penetration of the water into the core and development of hydrated, swollen polymer gel layer are observed.

3.4. FTIR Imaging Hydration Experiments on Pure 20% w/w IT-Loaded Tablets. To determine the influence of pH on IT-containing matrices, the ionic strength of the hydration medium was matched while the pH was modified. The strategy adopted was to use the low ionic strength medium as described in Section 3.3, thereby ensuring that any changes observed to the drug could be attributed to the pH environment alone.

Figure 5 shows the results of the ATR–FTIR imaging hydration experiments performed on 20% w/w IT-loaded tablets hydrated with a low ionic strength medium (0.1 mol/L) at pH 1.5 and 7.

Figure 5a–c shows the water, HPMC distribution, and gel layer evolution over the timeframe of the experiment. These results are similar to those observed with the IT-free HPMC

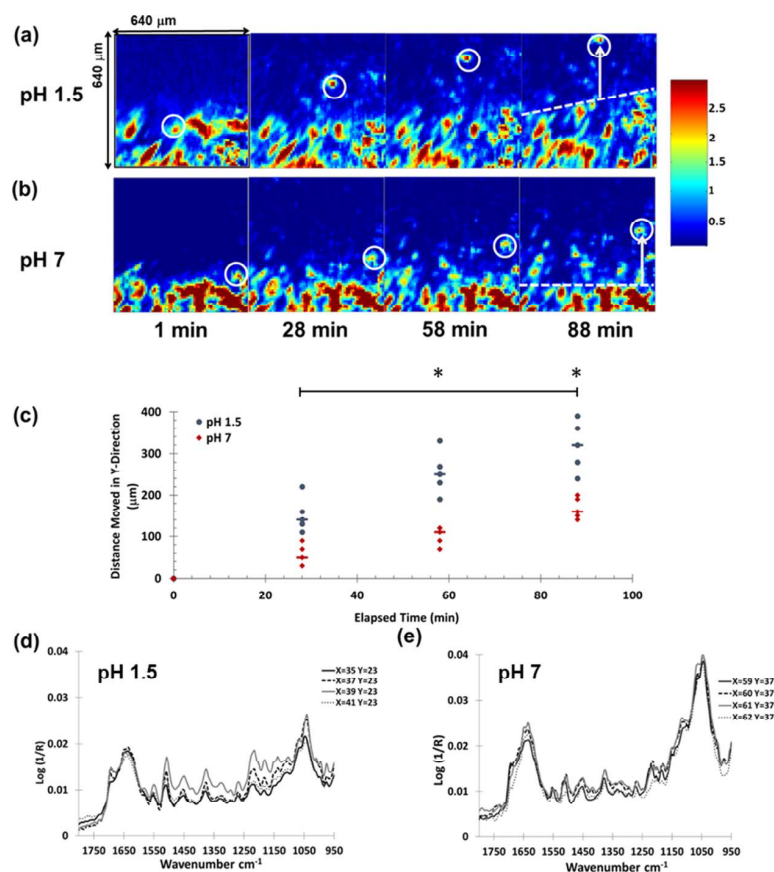


Figure 6. ATR–FTIR images tracking an IT particle at selected time points at (a) pH 1.5 and (b) pH 7 (interface indicated by dashed white line in last pane). (c) Plot showing movement of five discrete particles at each pH over time ($p < 0.05$). FTIR spectra from selected pixels across the IT particle, showing that the particles are IT rich at the 28 min time-point for (d) pH 1.5 and (e) pH 7.

tablets in a low ionic strength medium, as shown in Figures 3 and 4. However, evaluation of the gel layer images shown in Figure 5c over the hydration period appears to show visible differences in the swelling behavior in the two pH environments.

The distribution and dispersion of the total IT over the hydration period (Figure 5d) differ dramatically between the two pH environments. At pH 7, an environment where the drug is very insoluble, the matrix expands and swells, taking some drug particles with it, but the drug predominantly remains in the core and is not readily able to dissolve or disperse into the hydrating matrix, reflecting the *in vitro* dissolution data. However, at pH 1.5, as the HPMC matrix expands and swells, IT shows enhanced mobility and moves with the apparent diffusion front, which has improved definition and has a more inherent structure at this pH. At pH 7, the diffusion front and the swelling front are likely to be almost coincident. As indicated previously, the solubility of IT is very different in the two pH environments. We hypothesize that the additional structure within the diffusion front, evident at pH 1.5, is related to the pH-dependent solubility of IT.^{24,29} This has the potential to impact the mechanism of drug release kinetics.^{30,31}

The FTIR imaging data confirms that the HPMC swelling is similar at each pH for the placebo but is measurably different when IT is incorporated into the tablet. This suggests the possibility of an additional mechanism affecting the drug

release kinetics beyond the pH-enabled drug solubility in the hydrated matrix. To explore this further and to inform the findings observed from the ATR–FTIR imaging, a program of work to determine the swelling kinetics of IT-loaded tablets was conducted using optical imaging (see Section 3.7).

Evidence of undissolved IT particle movement was observed in both the pH environments. This phenomenon of drug particle translocation has previously been studied using optical methods.⁴ Using ATR–FTIR imaging, as the HPMC matrix swells and expands, undissolved drug particles moving outward in the expanding hydrated gel layer can be followed without the need for other markers, such as dyes or glass beads;⁸ advantageously, it is also possible to confirm the chemical form of the drug as the particle is moving.

Expanding the diffusion front area of images at selected time points permits the exploration of the translocation of the IT particles in more detail (Figure 6). In these enlarged images, it is possible to identify and track individual particles; an example of a tracked particle is highlighted at both pH 1.5 (Figure 6a) and pH 7 (Figure 6b) images. At each time point, the change in the position of the interface between the IT rich area and the surrounding medium was calculated. This was then subtracted from the measured distance of particles relative to their original position, giving a measure of the relative movement of the particle and interface at each time point.

Five particles were tracked from the pH 1.5 and 7 datasets, and their movement is plotted in Figure 6c. It should be noted

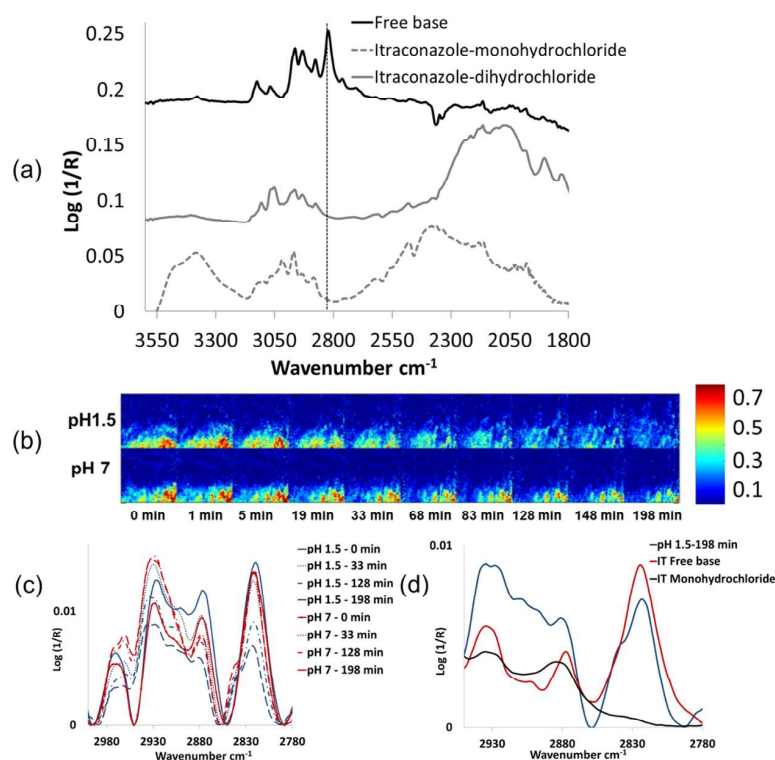


Figure 7. (a) Average ATR–FTIR imaging spectra obtained from IT free base, IT monohydrochloride, and IT dihydrochloride with dotted line indicating $\nu_s(\text{CH})$ at 2821 cm^{-1} . (b) ATR–FTIR peak area integrated images generated using the band at 2821 cm^{-1} . (c) Average ATR–FTIR imaging spectra highlighting $\nu(\text{CH})$ at 0, 33, and 198 min timepoints for 20%w/w IT-loaded tablets at pH 1.5 and 7. (d) Average ATR–FTIR imaging spectra obtained from IT free base, IT monohydrochloride, and 198 min timepoint for 20%w/w IT-loaded tablets at pH 1.5.

that because of the limited field of view of the ATR-imaging experimental setup, distances $>400\ \mu\text{m}$ away from the interface could not be measured. Differences were observed in the distribution and the number of particles between the pH 1.5 and 7 datasets, suggesting that particles at pH 1.5 are moving a greater distance relative to the interface in comparison to those particles present in the pH 7 environment within the same timeframe. A two-way ANOVA determined that there was a statistically significant difference in the distance travelled by the particles in the pH 1.5 and 7 environments after 58 min ($p = <0.05$, $n = 5$). This is most likely attributable to the low solubility of IT at higher pH impacting the water uptake and swelling capacity of the tablet in comparison to that at pH 1.5. For reference, the solubility of IT at pH 7 is reported to be $1\ \text{ng/mL}$, and the solubility at pH 1.5 is $4\ \mu\text{g/mL}$.²⁴

We propose that as IT has much greater solubility at pH 1.5, it therefore will dissolve out of the matrix, effectively leaving a more “porous” structure than that observed at pH 7. This more porous matrix clearly has different expansion properties upon hydration, as evidenced by the different outward IT particle translocation. Differences in the expansion properties were not observed in the placebo. Ultimately, monitoring the actual drug particle movement by ATR–FTIR imaging for a compound that shows pH-dependent solubility reveals more information pertaining to the nuances of the mechanism of drug release when compared to methods lacking chemical specificity, such as optical microscopy, to track glass beads.

3.5. Investigating the Nature of IT Particles within Different pH Environments. IR spectra were extracted across the central line of the highlighted particles in the images obtained after 28 min at pH 1.5 and pH 7 to determine if

changes in the particle mobility were linked to changes in the IT chemistry (Figure 6d,e). The IR spectra from the translocated particles were shown to be IT rich, although evidence of water and HPMC was also observed at both pH values. Interestingly, the particle at pH 7 shows a greater intensity of HPMC across the particle in comparison to that at pH 1.5 as the edge of the diffusion front will be in different places because of the pH effect on IT solubility. Consequently, particles monitored will be located within different evolving fronts (swelling and diffusion)^{1,3,4} depending on the pH. As the tablet hydrates, the polymer chains start to relax, creating the swelling front;³² this and the diffusion fronts move out further as the tablet continues to hydrate, translocating any undissolved particles inside the diffusion front with them.

3.6. Characterization of the Different Forms of IT. FTIR is sensitive to molecular structure, and therefore it is reasonable to assume that spectroscopic differences will be associated with the different forms of IT (ionized/nonionized form). For the images generated here, showing the distribution of IT in Figures 5d and 6a,b, $\nu(\text{C}\equiv\text{C}) \sim 1510\text{ cm}^{-1}$ was used as the spectroscopic marker for IT. However, this band is present in both ionized and unionized forms. Therefore, it only shows the distribution of total IT. In order to ascertain that IR was sensitive to the different forms of IT, ATR–FTIR spectra were collected from IT salts (mono and dihydrochloride) prepared following the procedures outlined previously.^{24,33} Clear differences were observed between the spectra obtained from the free base and IT salts, predominantly in the C–H stretching region. The free base form exhibits a strong band at 2821 cm^{-1} associated with CH symmetric stretching vibrations of the methyl group (Figure 7a), which disappears when the

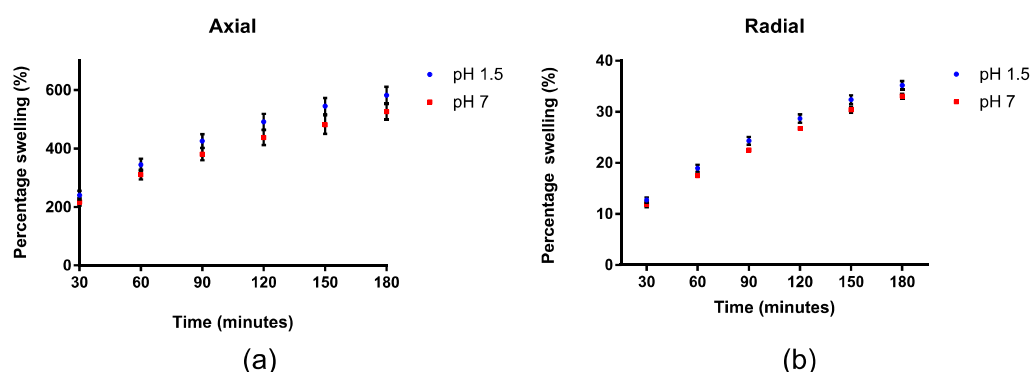


Figure 8. Percentage swelling data obtained from 20% w/w IT-loaded tablets from (a) axial and (b) radial measurements.

drug is ionized. Therefore, the 2821 cm^{-1} band was used to generate peak area distribution images to show changes in IT chemistry over the course of the hydration period (Figure 7b). A greater intensity of undissolved free base is observed in the tablet core (toward the bottom of the image) for the high pH medium over the duration of the experiment. In contrast, for the low pH environment, the intensity of the free base reduces rapidly as it starts to partially ionize, as expected with IT being more soluble at low pH. From this, we can surmise that IT is predominantly in the free base form in the images at the early time points at both pH 1.5 and pH 7. However, IT remains in the free base form for the duration of the experiment behind the swelling front, with a small number of undissolved particles extending toward the diffusion front at pH 7.

Conversely, at pH 1.5, IT is predominantly in the ionized form at later time points, as illustrated by the loss of the free base (Figure 7b), extending through to the outer edge of the diffusion front most probably due to improved solubility. A more detailed evaluation of the changes in the chemistry of IT during the dissolution process can be performed by comparison of the IR data extracted from the lowest six rows of pixels in these images. Binning the spectra within the pixels of the lowest six rows from images at 0, 33, and 198 min at both pH values, it was possible to generate average spectra with sufficient S/N to elucidate differences in the IT chemistry between systems (Figure 7c). It was observed that over the course of the dissolution experiment performed at pH 1.5, there was a subtle reduction in the intensity of the 2821 cm^{-1} band and a shift to higher wavenumber of the 2925 cm^{-1} band over time, which was indicative of a partial transformation of IT from the free base to the monohydrochloride form, shown more clearly in Figure 7d. At pH 7, there is no reduction in the intensity of the 2821 cm^{-1} band indicating that at pH 7, IT remains in the free base form, with an associated lower solubility.

ATR–FTIR imaging studies provide a direct understanding of how the low solubility pH-dependent drug, with a pK_a in the physiological range, changes during the dissolution process. Following matrix swelling and expansion while tracking undissolved drug particles, in the way previous workers have tracked glass beads,⁴ it was possible to directly observe the relationship between particle translocation, drug solubility, ionization state, and distribution across the hydrated matrix at different media pH values. These factors will be important for drug release kinetics at different pH values.

3.7. Physical Swelling Kinetics: Radial and Axial Swelling Results on 20%w/w IT-Loaded Tablets. To

supplement the ATR–FTIR data, a series of swelling experiments were performed on both IT-loaded and placebo tablets at pH 1.5 and pH 7. Examples of the optical images obtained from the placebo and 20% w/w IT-loaded tablets for the 0 and 180 min timepoints at pH 1.5 and 7 for the radial and axial measurements are shown in Figures S4, S5, S7, and S8. The results obtained from the swelling measurements confirmed that the swelling of placebo HPMC tablets was independent of pH; however, there were a distinct difference in the swelling behavior of the 20% w/w IT-loaded tablets in the different pH environments (Figure 8). A greater degree of swelling was observed at pH 1.5 over the period of hydration. Statistical analysis was carried out on the 30, 60, 90, 150, and 180 min time point data using the two-way ANOVA to determine if there is a significant difference in both axial and/or radial swelling between tablets in the pH 1.5 and 7 environments. The results indicate that no statistically significant difference was observed at the 30 min time point; however, a significant difference ($p < 0.05$) was observed for the subsequent time points analyzed. Statistical analysis was also carried out on the placebo data at the same time points; however, no significant difference was found for either the axial or radial dimensions between the pH environments (Figure S6). These findings are in agreement with the FTIR–ATR imaging data presented earlier and support the hypothesis that the reduced swelling capacity of the IT-loaded tablets at pH 7 leads to a reduction in the translocation of IT particles in the diffusion layer and consequently, along with the poor solubility of IT under these conditions, results in the retardation of IT release from these tablets.

4. CONCLUSIONS

This work highlights the value of utilizing ATR–FTIR imaging to elucidate factors affecting the release of a pH-dependent, poorly soluble drug from a hydrophilic matrix. This approach permits an understanding of the within-matrix dynamics of the drug and shows that although evidence of particle translocation was observed in both pH 1.5 and 7 environments, drug mobility was very different between the two.

Using ATR–FTIR imaging to follow matrix swelling and expansion and track undissolved drug particles in the way previous workers have tracked glass beads,⁴ it was possible to observe the changing chemical nature of the drug as a particle moved within the diffusion front. At pH 7, the drug remained in the free base form, which is poorly soluble, and therefore largely stayed within the core and the swelling front. At pH 1.5, however, IT was partially ionized, becoming more soluble, and

was able to migrate into the diffusion front and eventually out into the surrounding medium. The IT-containing tablets exposed to the low pH medium show higher swelling rate and greater overall percentage swelling in comparison to those exposed to the pH 7 environment. No significant differences in the swelling behavior were observed for placebo tablets.

Therefore, we conclude that the differential drug solubility observed across the pH range is not the sole reason for different release rates within different pH environments. Additionally, the presence of a nondissolved drug negatively impacts matrix swelling, resulting in translocated free base drug particles in the swelling front at pH 7 and partially ionized drug particles in the diffusion front at pH 1.5. In combination, differences in the solubility of the drug and the swelling of the matrix affect the rate and percentage drug release at the two different pH values.

■ ASSOCIATED CONTENT

SI Supporting Information

The Supporting Information is available free of charge at <https://pubs.acs.org/doi/10.1021/acs.molpharmaceut.9b01063>.

NIR data for quantification of tablet composition, Raman data to ascertain IT distribution, in vitro dissolution data, and axial and radial swelling data (PDF)

■ AUTHOR INFORMATION

Corresponding Author

Chris Sammon – Sheffield Hallam University, Sheffield S1 1WB, U.K.; Phone: +44 114 2253069; Email: c.sammon@shu.ac.uk

Authors

Farah Deebe Zahoor – Sheffield Hallam University, Sheffield S1 1WB, U.K.; orcid.org/0000-0003-1462-0983

Kerstin T. Mader – Sheffield Hallam University, Sheffield S1 1WB, U.K.

Peter Timmins – University of Huddersfield, Huddersfield HD1 3DH, U.K.; orcid.org/0000-0002-5840-0678

Jonathan Brown – Bristol-Myers Squibb, Moreton, Merseyside CH46 1QW, U.K.

Complete contact information is available at: <https://pubs.acs.org/10.1021/acs.molpharmaceut.9b01063>

Notes

The authors declare no competing financial interest.

■ ACKNOWLEDGMENTS

The authors would like to thank the Sheffield Hallam University for providing funding and Bristol-Myers Squibb for supporting the project and kindly donating the materials. The authors thank the valuable technical assistance offered by Dr Natalka Johnson, Gary Robinson, Paul Allender, and Laura McLaughlin.

■ REFERENCES

(1) Timmins, P.; Desai, D.; Chen, W.; Wray, P.; Brown, J.; Hanley, S. Advances in mechanistic understanding of release rate control mechanisms of extended-release hydrophilic matrix tablets. *Therapeutic delivery* **2016**, *7*, 553–572.

(2) Alderman, D. A. A review of cellulose ethers in hydrophilic matrices for oral controlled-release dosage forms. *Int. J. Pharm. Technol. Prod. Manuf.* **1984**, *5*, 1–9.

(3) Colombo, P.; Bettini, R.; Massimo, G.; Catellani, P. L.; Santi, P.; Peppas, N. A. Drug diffusion front movement is important in drug release control from swellable matrix tablets. *J. Pharm. Sci.* **1995**, *84*, 991–997.

(4) Bettini, R.; Catellani, P. L.; Santi, P.; Massimo, G.; Peppas, N. A.; Colombo, P. Translocation of drug particles in HPMC matrix gel layer: effect of drug solubility and influence on release rate. *J. Controlled Release* **2001**, *70*, 383–391.

(5) Alder, J.; Jayan, A.; Melia, C. A Method for Quantifying Differential Expansion within Hydrating Hydrophilic Matrixes by Tracking Embedded Fluorescent Microspheres. *J. Pharm. Sci.* **1999**, *88*, 371–377.

(6) Ford, J. L. Design and Evaluation of Hydroxypropyl Methylcellulose Matrix Tablets for Oral Controlled Release: A Historical Perspective. In *Hydrophilic Matrix Tablets for Oral Controlled Release*, AAPS Advances in the Pharmaceutical Sciences Series; Timmins, P., Pygall, S. R., Melia, D. R., Eds.; Springer: New York, 2014; Vol 16, pp. 17–51.

(7) Asare-Addo, K.; Levina, M.; Rajabi-Siahboomi, A. R.; Nokhodchi, A. Effect of ionic strength and pH of dissolution media on theophylline release from hypromellose matrix tablets-Apparatus USP III, simulated fasted and fed conditions. *Carbohydr. Polym.* **2011**, *86*, 85–93.

(8) Bajwa, G. S.; Hoebler, K.; Sammon, C.; Timmins, P.; Melia, C. D. Microstructural imaging of early gel layer formation in HPMC matrices. *J. Pharm. Sci.* **2006**, *95*, 2145–2157.

(9) Mikac, U.; Sepe, A.; Kristl, J.; Baumgartner, S. A new approach combining different MRI methods to provide detailed view on swelling dynamics of xanthan tablets influencing drug release at different pH and ionic strength. *J. Controlled Release* **2010**, *145*, 247–256.

(10) Xu, X. M.; Song, Y. M.; Ping, Q. N.; Wang, Y.; Liu, X. Y. Effect of Ionic Strength on the Temperature-Dependent Behavior of Hydroxypropyl Methylcellulose Solution and Matrix Tablet. *J. Appl. Polym. Sci.* **2006**, *102*, 4066–4074.

(11) Timmins, P.; Delargy, A. M.; Howard, J. R. Optimization and Characterization of a pH-Independent Extended-Release Hydrophobic Matrix Tablet. *Pharm. Dev. Technol.* **1997**, *2*, 25–31.

(12) Vasconcelos, T.; Sarmiento, B.; Costa, P. Solid dispersions as strategy to improve oral bioavailability of poor water soluble drugs. *Drug Discovery Today* **2007**, *12*, 1068–1075.

(13) Good, D. J.; Hartley, R.; Mathias, N.; Crison, J.; Tirucherai, G.; Timmins, P.; Hussain, M.; Haddadin, R.; Koo, O.; Nikfar, F.; Fung, N. K. E. Mitigation of Adverse Clinical Events of a Narrow Target Therapeutic Index Compound through Modified Release Formulation Design: An in Vitro, in Vivo, in Silico, and Clinical Pharmacokinetic Analysis. *Mol. Pharm.* **2015**, *12*, 4434–4444.

(14) Serajuddin, A. T. M. Salt formation to improve drug solubility. *Adv. Drug Delivery Rev.* **2007**, *59*, 603–616.

(15) Ewing, A. V.; Clarke, G. S.; Kazarian, S. G. Stability of indomethacin with relevance to the release from amorphous solid dispersions studied with ATR-FTIR spectroscopic imaging. *Eur. J. Pharm. Sci.* **2014**, *60*, 64–71.

(16) Chan, K. L. A.; Kazarian, S. G. Visualisation of the heterogeneous water sorption in a pharmaceutical formulation under controlled humidity via FT-IR imaging. *Vib. Spectrosc.* **2004**, *35*, 45–49.

(17) Ewing, A. V.; Kazarian, S. G. Recent advances in the applications of vibrational spectroscopic imaging and mapping to pharmaceutical formulations. *Spectrochim. Acta, Part A* **2018**, *197*, 10–29.

(18) Punčochová, K.; Ewing, A. V.; Gajdošová, M.; Sarvašová, N.; Kazarian, S. G.; Beránek, J.; Štěpánek, F. Identifying the mechanisms of drug release from amorphous solid dispersions using MRI and ATR-FTIR spectroscopic imaging. *Int. J. Pharm.* **2015**, *483*, 256–267.

(19) Kazarian, S. G.; Chan, K. L. A. Applications of ATR-FTIR spectroscopic imaging to biomedical samples. *Biochim. Biophys. Acta, Biomembr.* **2006**, *1758*, 858–867.

(20) Wray, P. S.; Clarke, G. S.; Kazarian, S. G. Application of FTIR Spectroscopic Imaging to Study the Effects of Modifying the pH Microenvironment on the Dissolution of Ibuprofen from HPMC Matrices. *J. Pharm. Sci.* **2011**, *100*, 4745–4755.

(21) Van der Weerd, J.; Kazarian, S. G. Combined approach of FTIR imaging and conventional dissolution tests applied to drug release. *J. Controlled Release* **2004**, *98*, 295–305.

(22) Hifumi, H.; Ewing, A. V.; Kazarian, S. G. ATR-FTIR spectroscopic imaging to study the drying and dissolution of pharmaceutical polymer-based films. *Int. J. Pharm.* **2016**, *515*, 57–68.

(23) Ewing, A. V.; Clarke, G. S.; Kazarian, S. G. Attenuated total reflection-Fourier transform infrared spectroscopic imaging of pharmaceuticals in microfluidic devices. *Biomicrofluidics* **2016**, *10*, 024125.

(24) Tao, T.; Zhao, Y.; Wu, J.; Zhou, B. Preparation and evaluation of itraconazole dihydrochloride for the solubility and dissolution rate enhancement. *Int. J. Pharm.* **2009**, *367*, 109–114.

(25) Pygall, S. R.; Kujawinski, S.; Timmins, P.; Melia, C. D. The suitability of tris(hydroxymethyl) aminomethane (THAM) as a buffering system for hydroxypropyl methylcellulose (HPMC) hydrophilic matrices containing a weak acid drug. *Int. J. Pharm.* **2010**, *387*, 93–102.

(26) Gordon, K. C.; McGoverin, C. M. Raman mapping of pharmaceuticals. *Int. J. Pharm.* **2011**, *417*, 151–162.

(27) FDA U.S. Food and Drug Administration, “Dissolution Methods-Itraconazole,”. [Online]. Available: https://www.accessdata.fda.gov/scripts/cder/dissolution/dsp_SearchResults.cfm [accessed July 19, 2019].

(28) Qi, J.; Daintree, L. S.; Ding, S.; Ledger, D. M.; Wang, B.; Zhao, W.; Jianping, Q.; Wu, W. Itraconazole solid dispersion prepared by a supercritical fluid technique: preparation, in vitro characterization, and bioavailability in beagle dogs. *Drug Des., Dev. Ther.* **2015**, *9*, 2801–2810.

(29) Peeters, J.; Neeskens, P.; Tollenaere, J. P.; Van Remoortere, P.; Brewster, M. E. Characterization of the interaction of 2-hydroxypropyl- β -cyclodextrin with itraconazole at pH 2, 4, and 7. *J. Pharm. Sci.* **2002**, *91*, 1414–1422.

(30) Ford, J. L.; Mitchell, K.; Rowe, P.; Armstrong, D. J.; Elliott, P. N. C.; Rostron, C.; Hogan, J. E. Mathematical modelling of drug release from hydroxypropylmethylcellulose matrices: effect of temperature. *Int. J. Pharm.* **1991**, *71*, 95–104.

(31) Colombo, P.; Bettini, R.; Santi, P.; De Ascentiis, A.; Peppas, N. A. Analysis of the swelling and release mechanisms from drug delivery systems with emphasis on drug solubility and water transport. *J. Controlled Release* **1996**, *39*, 231–237.

(32) Ghori, M. U.; Conway, B. R. Hydrophilic Matrices for Oral Control Drug Delivery. *Am. J. Pharmacol. Sci.* **2015**, *3*, 103–109.

(33) Bagavatula, H.; Lankalapalli, S.; Tenneti, V.; Beeraka, N.; Bulusu, B. Comparative Studies on Solubility and Dissolution Enhancement of Different Itraconazole Salts and Their Complexes. *Adv. Pharmacol. Pharm.* **2014**, *2*, 85–89.